SOLID-STATE NMR STUDY OF ALKYL CHAIN DYNAMICS IN CRYSTALLINE ORGANIC SOLIDS

a thesis presented by
Jukka Petteri Kujanpää
to the
University of St. Andrews
in application for
THE DEGREE OF DOCTOR OF PHILOSOPHY

St. Andrews November 1999

Declaration

I, Jukka Petteri Kujanpää, hereby certify that this thesis, which is approximately 40,000 words in length, has been written by me, that it is a record of my work carried out by me and that it has not been submitted in any previous application for a higher degree.

signature: date: 4-11-99

I was admitted as a research student in May 1996 and as a candidate for the degree of Ph.D. in October 1997; the higher study for which this is a record was carried out in the University of St. Andrews between 1996 and 1999.

signature: date: 4-11-99

I hereby certify that the candidate has fulfilled the conditions of the Resolution and Regulations appropriate for the degree of Ph.D. in the University of St. Andrews and that the candidate is qualified to submit this thesis in application for that degree.

signature of supervisor: date: 26-11-99

Copyright

Acknowledgements

First of all I would like to thank my supervisor Dr. Frank Riddell for launching this project and kindly taking me to do research in St. Andrews. I am also grateful to Neste Oy's Foundation, especially Dr. Kyösti Riistama there, for the scholarship that made the project possible.

I would like to express my gratitude to all the people in the laboratory during the years. Special thanks go to Diane for correcting my English and for the nights out, Ken and Roger for kindly showing me how golf should be played, Sina for playing golf with me, Jennifer for bringing red roses to the laboratory and Jenny for helping with the syntheses.

Dr. Phil Lightfoot is gratefully acknowledged for solving the crystal structures. Dr. Maryjane Tremayne is thanked for her kind help with the powder diffraction patterns. Dr. Paul Wright is acknowledged for interesting discussions about molecular dynamics and solid-state NMR. I would also like to extend my thanks to Dr. David Tunstall for his help with the spectrometer and allowing me to use equipment belonging to the physics department.

Many thanks go to the technical staff: Melanja for taking care of the spectrometer, Brian for fixing the spectrometer, Bobby for filling the nitrogen dewars, Marjory for delivering the chemicals and Sylvia for making the elemental analyses.

Special thanks are reserved for all my friends for a great three years in St. Andrews. I also wish to thank the people of the Breakaway society for organising numerous trips to the beautiful Scottish Highlands.

My sincerest appreciation goes to my family for their support during these years.

Abstract

Molecular dynamics in short chains of methylene groups were studied in α,ω-diacids and substituted α,ω-alkanediyl diesters using solid-state NMR methods. ^{13}C CP/MAS spectra were measured for all compounds, and interesting dynamic effects were observed in the variable temperature spectra for hexane-1,6-diyl and butane-1,4-diyl bis(*p*-nitrobenzoates). ^{2}H quadrupolar echo spectra were used to characterise the mechanism of the motion. In the theoretical part of this thesis, it was concluded that *trans-gauche* isomerisation is impossible to distinguish from small angle librational motion if ^{2}H quadrupolar echo spectra are measured only with one refocusing delay. Consequently, the ^{2}H quadrupolar echo spectra measured with two different refocusing delays indicated that librational motion describes the dynamics in the these chains better than *trans-gauche* isomerisation. A conical libration model was developed to explain all the ^{2}H quadrupolar echo spectra measured in this thesis.

The ^{2}H quadrupolar echo spectra measured for α,α,ω,ω-tetradeuterated diacids indicated that the chain undergoes a fast and small amplitude librational motion. The amplitude of this librational motion was found to agree with amplitudes obtained previously from neutron diffraction measurements for succinic and suberic acids. For glutaric and pimelic acids, the ^{2}H quadrupolar echo spectra measured above the β to α phase transition suggested that the amplitude of the librational motion increases in the phase transition. For all diacids, ^{2}H spin-lattice relaxation time was found to be nearly temperature independent over a wide temperature range. An odd-even effect was observed near 200 K where the ^{2}H spin-lattice relaxation time increased strongly with decreasing temperature for the odd acids but not for the even acids. All diesters with an all-*trans* chain showed similar temperature independence of the ^{2}H spin-lattice relaxation time, and therefore, this temperature independence was proposed to be a general property of short all-*trans* chains. Diesters with *gauche* bonds in the chain, however, showed linear dependence of $\ln(^{2}H\ T_1)$ on inverse temperature with apparent activation energies between 20 and 80 kJ mol^{-1}. This was proposed to be due to different alignment of bonds in the chain containing *gauche* bonds.

TABLE OF CONTENTS

SYMBOLS

α, β, γ	Euler angles for the transformation form the laboratory frame to the molecular frame
B_0	external magnetic field
B_1	applied radio frequency field
$C_m(t)$	correlation function
χ	quadrupolar coupling constant = e^2qQ/h
e	charge of an electron
E_a	Arrhenius type activation energy
E_R	echo reduction factor, defined as the ratio of intensities of echos measured with 160 μs and 20 μs refocusing delays
ϕ, θ, ψ	Euler angles for the transformation form the molecular frame to the principal axis system of the quadrupolar coupling tensor
$\phi(\theta)$	Gaussian density distribution function
γ	magnetogyric ratio
GB	Gaussian broadening factor
h	Plank´s constant
$H_v(y)$	Hermite polynomials
$J_m(\omega)$	spectral density function
k	rate constant, force constant or Bolzmann constant
M_0	equilibrium magnetisation along the Z-axis
M_Z	magnetisation along the Z-axis
N_α, N_β	populations of α and β energy levels
N_v	normalization constant for the harmonic oscillator
eq	magnitude of the electric field gradient
eQ	nuclear quadrupole moment
R_1	spin-lattice relaxation rate = $1/T_1$
$\Delta\theta$	standard deviation of Gaussian distribution
θ_0	mean of Gaussian distribution
τ	varible time period
τ_c	correlation time
T_1	spin-lattice relaxation time
$T_{1\rho}$	spin-lattice relaxation time in the rotating frame
T_{1S}(ADRF)	relaxation time for adiapatic demagnetisation in the rotating frame
T_2	transverse relaxation time
ν_0, ω_0	Larmor frequency
ν_c, ω_c	correlation frequency
x, y, z	molecular co-ordinates
X, Y, Z	laboratory co-ordinates
1, 2, 3	principal axes of the quadrupolar coupling tensor

1. SOLID STATE NMR METHODS

Our understanding of crystalline solids is largely based on X-ray diffraction structures that often give the impression that atoms and molecules are stationary in the crystal lattice and molecular motion is absent.[1] On the other hand, high resolution nuclear magnetic resonance (NMR) is highly sensitive to molecular motions and chemical exchange.[2] Although molecular motions are generally slower in solids than in liquids, they have an important role in determining macroscopic properties of solid materials. For example, the mechanical properties of solid polymers are closely related to microscopic structure and molecular motions.[3] Also, the conductivity of solid polymer electrolytes[4] and the electrical properties of conducting polymers[5] originate from the motions at molecular level.

NMR of solids is instrumentally more demanding than high resolution NMR in liquids as more and stronger interactions have to be averaged out.[6] In 1975, a combination of cross polarisation and magic angle spinning (^{13}C CP/MAS) was used to obtain a liquid-like high resolution ^{13}C spectrum of a solid polymer for the first time.[7] Since then, the ^{13}C CP/MAS technique has been widely applied to the investigation of solid materials.[8] Furthermore, the ^{13}C CP/MAS technique allows for the measurement of relaxation times for chemically different sites in a molecule, and therefore, facilitates the use of relaxation times in the study of molecular dynamics.[9]

The development of NMR instrumentation has also made it possible to measure deuterium spectra of solids routinely. Although the deuterium is a quadrupolar nucleus, its spectrum is always narrower than *ca.* 200 kHz.[10] Therefore, deuterium NMR is a versatile technique for studying molecular motions in solids.[11] Molecular motions with rate constants from 10^3 to 10^7 s^{-1} induce changes in the spectrum. These changes depend not only on the rate but also on the amplitude and geometry of the motion.[12] The geometry and the rate of the motion can be formulated into a model for computer calculations. Then, the comparison of observed and calculated spectra gives invaluable information about the details of molecular motion in solids.

1.1. SOLID-STATE NMR SPECTRA

1.1.1. ^{13}C CP/MAS experiment[13-15]

In the liquid state, rapid molecular tumbling averages dipolar interactions to zero, and the chemical shielding anisotropy is reduced to its isotropic value. Therefore, the indirect (scalar) coupling is observed, which is characterised by the scalar coupling constant *J*. In solids, however, the dipolar interaction between protons is of the order 50 kHz, and the chemical shielding anisotropy of ^{13}C nuclei can be as high as 25 kHz, if a high external field is used. As a result, peaks in the ^{13}C NMR spectrum are broad, and special techniques are needed to narrow the ^{13}C line width. These line narrowing techniques are high-power decoupling and magic angle spinning. High-power decoupling of protons is used to remove the C-H dipolar interaction whereas spinning the sample at a magic angle greatly reduces the chemical shielding anisotropy.

Another problem in measuring ^{13}C spectra is that the natural abundance of ^{13}C isotope is only 1.1% and its magnetogyric ratio is small compared with protons. As a result, the sensitivity of ^{13}C NMR measurement is low. Sensitivity can be increased by cross-polarisation from protons which enhances the ^{13}C signal by a maximal factor of 4. In general, the cross-polarisation technique is combined with high-power decoupling and magic-angle spinning, and the resulting technique is called the ^{13}C CP/MAS technique.

The cross-polarisation process is closely related to spin diffusion that occurs among abundant nuclei in solids. In organic solids, protons are abundant nuclei and proton spins are strongly coupled to each other by dipolar couplings. If two nuclei are coupled to each other, have the same precessional frequency and anti-parallel spin alignments, they can undergo rapid mutual transitions called flip-flops[16], as shown in figure 1.1. When spin A changes its spin-state, it acts like a resonant radio-frequency field for spin B, and therefore, spin B also changes its spin state. This information proceeds through the whole proton system by these mutual spin flip-flops in a process called spin diffusion. Because of spin diffusion, protons in organic molecules

relax at the same rate, that is, all protons have the same spin-lattice relaxation time T_1. The rate of spin diffusion is of the order of the spin-spin relaxation rate $1/T_2$, or in other words, the total width of proton spectrum.

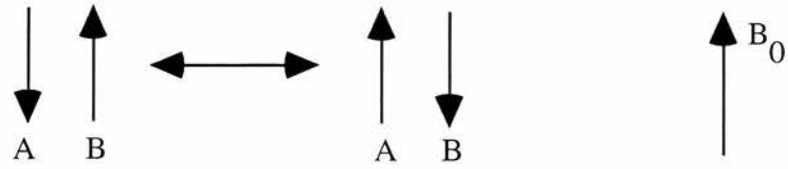

Figure 1.1. Simplified picture of spin flip-flop process for spins A and B. Mutual spin transition occurs when spin B absorbs the photon emitted by spin A.

In organic solids, protons are abundant spins and undergo fast spin flip-flops. Carbon-13 in natural abundance, however, is a dilute spin, and therefore, the mutual spin flip-flop process is weak. In addition, the Larmor frequency of carbon-13 is only a quarter of the corresponding proton frequency. Therefore, the spin flip-flop process between protons and carbons is not energy conserving in the external magnetic field. However, the carbon and proton spins can be aligned, in a process called spin-locking, along applied radio frequency fields B_{1C} and B_{1H}, respectively, so that:

$$\gamma_H B_{1H} = \gamma_C B_{1C} \qquad (1.1.)$$

Under this condition, carbon and proton spins have components precessing at the same frequency, and the spin flip-flop process becomes energy conserving, as shown in figure 1.2.[17,18] This process is called cross-polarisation, and equation 1.1 is called the Hartmann-Hahn condition.

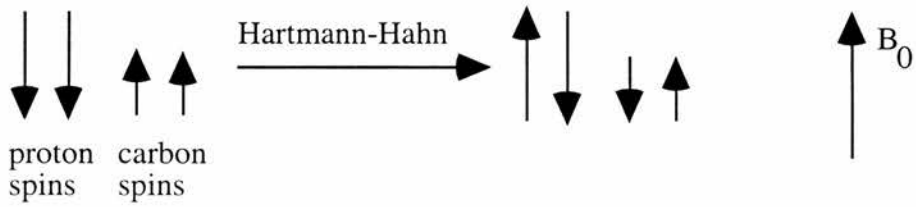

Figure 1.2. During the Hartmann-Hahn condition protons and carbons undergo mutual spin flip-flops. When a proton changes its spin state, it causes a carbon nucleus to change its spin state. As a result, dilute carbon spins adopt the spin alignment of abundant protons, and carbon magnetisation is enhanced by up to a factor of four.

Since the proton spin reservoir is much larger (abundant spins) than the carbon spin reservoir (dilute spins), the carbon spins adopt the alignment of proton spins. It can be shown thermodynamically, that the maximum enhancement of carbon magnetisation is $\gamma_H/\gamma_C = 4$.[19] Since the carbon magnetisation originates from proton magnetisation, the recycling delay in the pulse sequence is determined by the spin-lattice relaxation time of protons rather than carbons. In polymers, for example, the proton spin-lattice relaxation time is much shorter than the corresponding relaxation time for carbons, and therefore, more spectra per unit time can be averaged increasing the signal to noise ratio. If the proton spin-lattice relaxation time is also long, the experiment can be made more effective with a flip-back sequence[20] that returns the proton magnetisation along the external magnetic field with a radio-frequency pulse at the end of the high power decoupling period. The cross-polarisation pulse sequence is shown in figure 1.3.

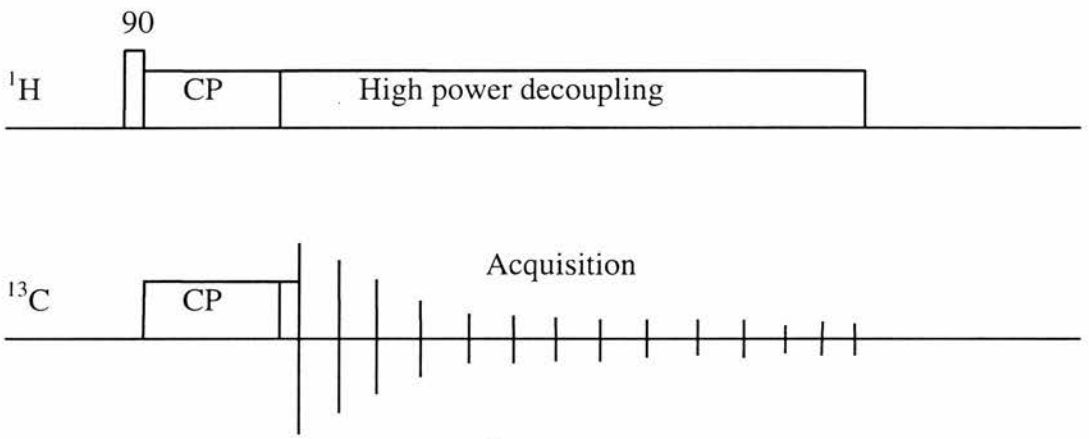

Figure 1.3. Cross-polarisation pulse sequence. 90° pulse is followed by a cross-polarisation period. During the acquisition of ^{13}C signal, protons are decoupled by high-power irradiation.

Molecular motion can cause two different changes in the ^{13}C CP/MAS spectrum. Firstly, a coalescence of peaks occurs if the corresponding sites in the molecule are exchanging at a rate comparable to the difference in their chemical shifts.[21] Secondly, molecular motion can reduce decoupling efficiency, and therefore, broaden the peaks.[22-25] This occurs when the rate of the molecular motion is comparable to the precession frequency of the nuclei in the decoupling field, *i.e.* when

$$\tau_c = \frac{1}{2\pi\upsilon_c} = \frac{1}{\omega_c} = \frac{1}{\gamma B_1} \qquad (1.2.)$$

where υ_c is the correlation frequency.

1.1.2. ^{2}H quadrupolar echo spectrum

The ^{13}C CP/MAS spectrum can give the rate of molecular motion but it fails to give any direct information on the spatial reorientation of C-H bonds. On the other hand, the line shape of the ^{2}H spectrum depends directly on the movement of a C-D bond.[26] The measurement of ^{2}H spectrum, however, has been difficult with conventional NMR techniques and has only recently become possible with the advent of quadrupolar echo pulse sequence. This sequence is needed because the deuteron signal decreases to zero within the dead time of the detector (*ca.* 20 μs), and therefore, the signal cannot be observed by single pulse excitation. The quadrupolar echo pulse sequence generates an echo of the original signal.[27] The echo is well-separated from the last pulse in the sequence, and therefore, the signal can be measured starting from the top of the echo without any loss of information. The quadrupolar echo pulse sequence is shown in figure 2.4.

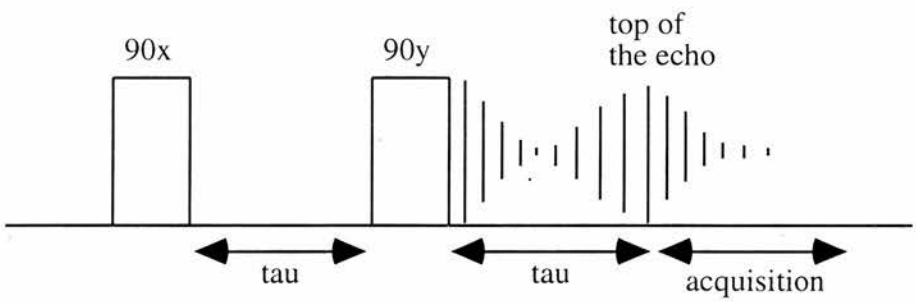

Figure 1.4. The quadrupolar echo sequence. The 90° pulses are separated by a refocusing delay tau, and the acquisition is started from the top of the echo after another tau delay.

Because of instrumental limitations, ^{2}H quadrupolar echo spectra are subject to various line shape artefacts. Most of the artefacts are caused by finite length of the 90° pulse which leads to uneven excitation of the spectrum and to a feedthrough signal or virtual FID.[28,29] However, the program MXET1 that is most often used for the simulation of ^{2}H quadrupolar echo line shape includes a correction procedure for

the 90° pulse length, and consequently, a spectrum for given set of experimental parameters and a given model of C-D bond motion can be calculated.[30]

The calculation of ^{2}H quadrupolar echo line shape that is the basis of the program MXET1[30] is briefly outlined in the following. The orientation dependent frequencies for deuteron (I=1) are:

$$\omega_i = \pm(3/2)^{1/2} T_0^{(2)LAB} \tag{1.3.}$$

where

$$T_0^{(2)LAB} = \sum_{p=-2}^{2} D_{0p}^{(2)*}(\alpha,\beta,\gamma) T_p^{2(PAS)} \tag{1.4.}$$

where the transformation described by Euler angles (α,β,γ) rotates the laboratory axes into the principal axis system (PAS). For deuterons bonded to aliphatic carbons the quadrupolar coupling tensor is symmetric (η=0), and the only nonvanishing element in the PAS system is:

$$T_0^{2(PAS)} = \left(\frac{3}{8}\right)^{1/2} \frac{e^2 qQ}{h} = \left(\frac{3}{8}\right)^{1/2} \chi \tag{1.5.}$$

where χ=e^{2}qQ/h is the quadrupolar coupling constant. Substituting this equation into 1.4 gives:

$$T_0^{(2)LAB} = D_{00}^{(2)*}(\alpha,\beta,\gamma) T_0^{(2)PAS} = \left(\frac{3}{8}\right)^{1/2} \chi D_{00}^{(2)*}(\alpha,\beta,\gamma) \tag{1.6.}$$

The Wigner rotation matrix can be calculated using its definition and tabulated values for the relevant matrix elements:

$$D_{00}^{(2)*}(\alpha,\beta,\gamma) = e^{i\alpha\cdot 0} d_{00}^2(\beta) e^{i\gamma\cdot 0} = d_{00}^2(\beta) = \frac{1}{2}\left(3\cos^2\beta - 1\right) \tag{1.7.}$$

Using equations 1.3, 1.6 and 1.7 gives:

$$\omega = \pm\frac{3}{4}\chi\left(\frac{3\cos^2\beta - 1}{2}\right) \tag{1.8.}$$

Equation 1.8 gives the powder line shape for an infinitely sharp spectrum. This line shape has to be broadened with suitable broadening functions to obtain a more realistic powder pattern. The powder pattern is also known as a Pake doublet (fig. 1.5).

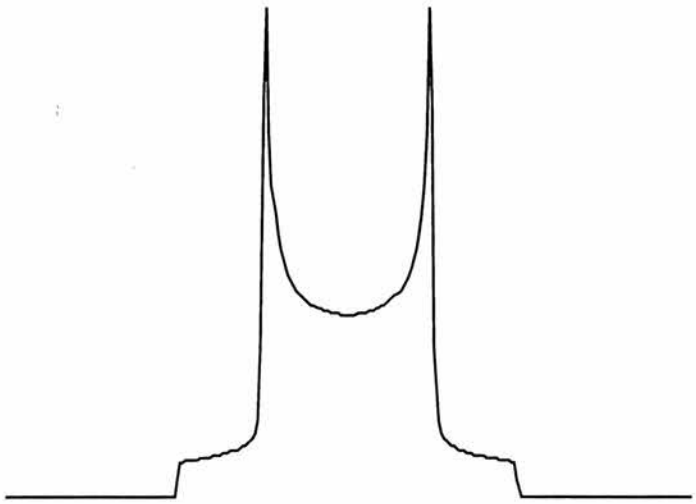

Figure 1.5. ^2H line shape for a powder in the absence of molecular motion or a Pake doublet.

Equation 1.8 describes the dependence of quadrupolar frequency on the angles between the laboratory frame and the principal axis system of the quadrupolar coupling tensor but fails to describe any intramolecular motion. In order to describe intramolecular motion, that is, the dependence of the quadrupolar frequency on the molecular angles, a molecular axis system (x,y,z) has to be defined, as shown in figure 1.6.

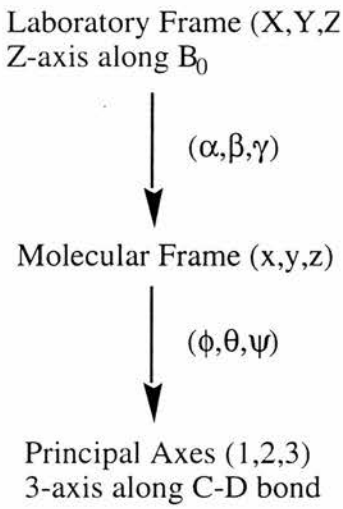

Figure 1.6. The relationship between different co-ordinate systems used in the calculation of deuteron line shape.

This molecular axis system can chosen to describe the molecular motion most conveniently. The z-axis can be, for example, a director axis in a drawn polymer or simply a carbon-carbon bond about which the motion takes place. This intermediate molecular frame can be directly added to equation 1.4:

$$T_0^{(2)LAB} = \sum_{p,q=-2}^{2} D_{0p}^{(2)*}(\alpha,\beta,\gamma) D_{pq}^{(2)*}(\phi,\theta,\psi) T_q^{2(PAS)} \qquad (1.9.)$$

Thus, the angles (ϕ,θ,ψ) have to be determined based on the molecular geometry and an assumed model for the molecular motion generating the different sites. Using the angles (ϕ,θ,ψ) and a sufficient number of random angles (α,β,γ) the site frequencies in a powder can be calculated. If more complicated motions than an uniaxial motion are to be considered, more intermediate frames can be added to equation 1.9.

The equations above give the quadrupolar frequencies for different sites but fail to describe the effect of molecular motion during the refocusing delays. The line shape when molecular motion is present can be calculated by solving equation:

$$\frac{d\sigma}{dt} = [i\Omega + \mathrm{K}]\sigma = \mathbf{A}\sigma \qquad (1.10.)$$

where the elements of σ are the transverse magnetisation vectors, Ω is a diagonal matrix of the site frequencies ω and **K** is a kinetic matrix describing the exchange. Solving this equation leads to an expression for the free induction decay signal starting from the top of the echo:

$$F(t,\tau_1,\tau_2) = \exp[\mathbf{A}t]\exp[\mathbf{A}\tau_2]\exp[\mathbf{A}*\tau_1]\sigma(0) \qquad (1.11.)$$

where $\sigma(0)$ is the vector of fractional site populations. Fourier transform of this free induction decay signal yields the line shape. Terms that account for uneven excitation by finite rf pulses and for contributions from the virtual FID can be added to equation 1.11. The calculation is conveniently done with the program MXET1 that takes the Euler angles for each site together with acquisition and processing parameters as an input and then calculates the powder line shape using the above equations.

1.1.3. Two-dimensional experiment

The angle of C-D bond motion can be directly measured from a two-dimensional deuterium exchange spectrum.[31-35] In the absence of molecular motion, the 2D exchange spectrum consists of a Pake doublet along the diagonal. Molecular motions in the slow exchange regime where the correlation time is longer than a millisecond induce intensity off the diagonal. These off-diagonal ridges are very characteristic to motional modes, and also in favourable cases, allow for the direct measurement of angle of C-D bond motion. Slowly moving deuterons, however, tend to relax very slowly, and therefore in the absence of any additional faster motions, long ^{2}H spin-lattice relaxation time makes the measurement of two-dimensional spectra very time consuming.

1.2. NUCLEAR RELAXATION

In thermal equilibrium, nuclear spins are distributed between the two energy levels (for spin-1/2 nuclei) according to the Bolzmann distribution:[36]

$$\frac{N_\beta}{N_\alpha} = \exp\left(-\frac{\Delta E}{kT}\right) = \exp\left(-\frac{h\nu_0}{kT}\right) \qquad (1.12.)$$

According to eq. 1.12, there is a small excess of spins in the lower level in the equilibrium. In an NMR experiment, however, the population of the higher energy level increases as spins are excited to the higher energy level. For example, the populations of the two energy levels would be equal after applying a saturating pulse sequence to the spin system.

If a spin system with non-equilibrium populations of the energy levels is left undisturbed, it will relax back to the equilibrium state within a time period that depends on how well the energy released in the relaxation process can be transferred to the surroundings of the spin-system. Since both the spin system and its surroundings (the lattice) are involved in this relaxation process, it is called spin-lattice relaxation. The rate of spin-lattice relaxation is characterised by spin-lattice

relaxation time T_1 which is the inverse of the rate constant for the build-up of the magnetisation M_Z:[37]

$$\frac{dM_Z}{dt} = k\left(M_0 - M_Z\right) = \frac{1}{T_1}\left(M_0 - M_Z\right) \qquad (1.13.)$$

where M_0 is the equilibrium magnetisation.

1.2.1. Connection between relaxation and molecular motion

A spin system can relax only if its surroundings (the lattice) can absorb the energy generated in the relaxation process. As the energy difference between the spin levels corresponds to radio frequencies, radio frequencies are emitted in the relaxation process. Therefore, the lattice must be able to absorb radio frequencies. The lattice can interact with electromagnetic radiation via molecular motions that modulate dipolar and electrostatic interactions in the molecules of the lattice. In principle, three types of motion can occur in molecules: translational, vibrational and rotational motions. The vibrational frequencies (IR-frequencies), however, are much higher than the NMR frequencies and, as a result, fail to contribute to NMR relaxation. On the other hand, translational motion is in general absent in solids. Consequently, rotational motions have an important role in spin relaxation in solids.

In order to correlate relaxation with molecular motion, random particle and electromagnetic wave motion are conveniently described with a correlation function $C_m(t)$.[38] In general, $C_m(t)$ is assumed to decay exponentially with time:

$$C_m(t) = A_m \exp\left(-t/\tau_c\right) \qquad (1.14.)$$

In the case of rotational motion, the correlation function represents the fraction of molecules which have not rotated by a characteristic angle during the correlation time τ_c (also called atomic jump time). Very similarly to the NMR spectrum which is a Fourier transform of the free induction decay signal, the spectral density $J_m(\omega)$ which gives the relative amount of power at any given frequency ω is the cosine Fourier transform of the correlation function:[38]

$$J_m(\omega) = 2\int_0^\infty C_m(t)\cos(\omega t)dt = A_m \cdot \frac{\tau_c}{1+\omega^2\tau_c^2} \qquad (1.15.)$$

The relationship between the spectral density function and the spin-lattice relaxation time can be seen if the logarithm of the spectral density is plotted as a function of the logarithm of the frequency for different correlation times (fig. 1.7). The plots shown in figure 1.7 indicate that the spectral density at the Larmor frequency is at maximum when τ_c is equal to $1/\omega_0$. As the spin-lattice relaxation is faster when more frequencies are available near the Larmor frequency, this point corresponds to a spin-lattice relaxation time minimum.

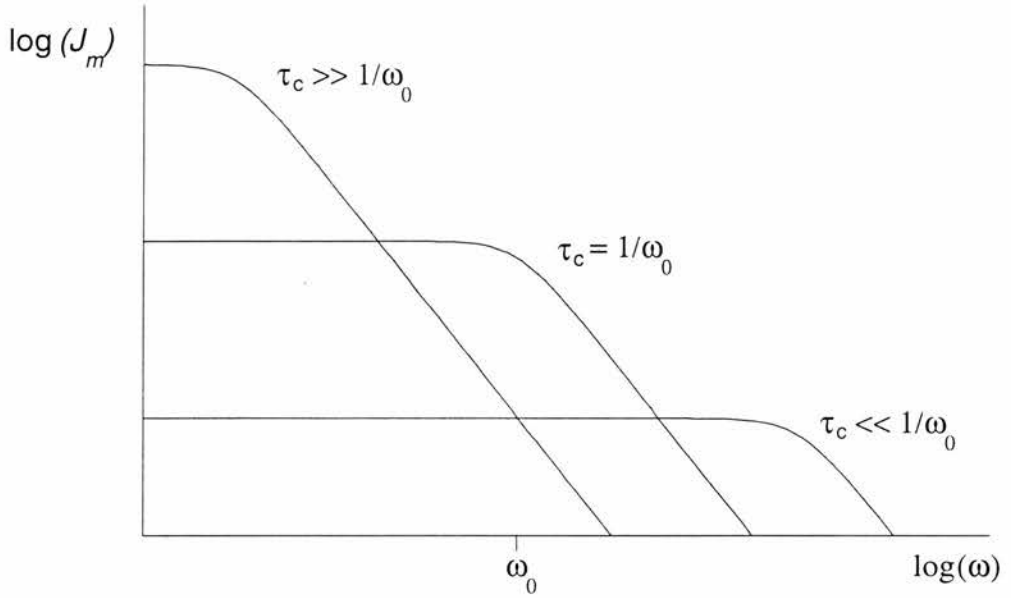

Figure 1.7. Log(J_m) as a function of log(ω). The spectral density reduces sharply, when $\tau_c \sim 1/\omega$. Spectral density at ω_0 is at maximum when $\tau_c = 1/\omega_0$.

1.2.2. Proton spin-lattice relaxation

Proton spins in organic solids are strongly coupled and undergo spin diffusion process as described in section 1.1. As a result, all protons have the same spin-lattice relaxation time, and no information on the motion of different molecular sites can be obtained from the spin-lattice relaxation time even if separate peaks for these sites were obtained with special techniques, such as CRAMPS. This greatly decreases the usefulness of proton spin-lattice relaxation time in characterisation of molecular

motions in organic solids. Therefore, proton spin-lattice relaxation times have mainly been used to study motions in simple compounds, such as benzene, in which all the protons are chemically equivalent, and therefore, no differentiation of molecular sites is needed. The proton relaxation time is given by:[39]

$$\frac{1}{T_1} = \frac{2}{3} < \Delta\omega^2 > \left(\frac{\tau_c}{1+\omega_0^2\tau_c^2} + \frac{4\tau_c}{1+4\omega_0^2\tau_c^2} \right) \qquad (1.16.)$$

where $<\Delta\omega^2>$ is the second moment, which is a measure of the mean square local dipolar field and can be calculated for a given model of motion.

1.2.3. ^{13}C spin-lattice relaxation

The ^{13}C spin-lattice relaxation time is a much more useful parameter than the proton spin-lattice relaxation time since well-resolved carbon spectra can be obtained with the CP/MAS pulse sequence as described in section 1.1. In addition, the spin-diffusion process is essentially absent between ^{13}C spins as they are dilute, and between carbons and protons as this process is not energy conserving. The measurement of ^{13}C spin-lattice relaxation times, however, is complicated by strong dipolar couplings in solids. As the ^{13}C spins are coupled to the proton spins, the relaxation process is characterised by the Solomon equations that describe dipolar relaxation in a two-spin system:[40]

$$\begin{aligned} \frac{dM_Z^H}{dt} &= -R_1^H\left(M_Z^H - M_{eq}^H\right) - \sigma\left(M_Z^C - M_{eq}^C\right) \\ \frac{dM_Z^C}{dt} &= -R_1^C\left(M_Z^C - M_{eq}^C\right) - \sigma\left(M_Z^H - M_{eq}^H\right) \end{aligned} \qquad (1.17.)$$

where $R_1=1/T_1$ and σ is the cross relaxation rate. According to the lower equation, ^{13}C spin-lattice relaxation in this case is biexponential. This can be seen as a transient nuclear Overhauser effect (nOe) in the evolution of the magnetisation.[41] The spin-lattice relaxation becomes exponential, however, if protons are continuously irradiated so that proton magnetisation is zero:

$$\frac{dM_Z^C}{dt} = -R_1^C\left(M_Z^C - M_{stat}^C\right) \qquad (1.18.)$$

where *stat.* refers to stationary state under proton irradiation. Clearly, a long period of relatively high-power decoupling is needed if the ^{13}C spin-lattice relaxation time is long and strong coupling interactions are to be removed. This causes severe heating in the probe and is therefore instrumentally difficult. A favourable situation occurs, however, when the proton spin-lattice relaxation time is much shorter than ^{13}C spin-lattice relaxation time.[42] In this case, eq. 1.18 is obtained without any decoupling as the protons relax quickly back to equilibrium ($M_Z^H \approx M_{eq}^H$).

Signal intensity can be enhanced in the ^{13}C T_1 measurement with the pulse sequence of Torchia.[43] In this sequence, carbon magnetisation is first generated with the cross-polarisation process, and then, an inversion recovery type sequence is used to follow the evolution of magnetisation as a function of time. During the evolution period, protons are decoupled by continuous irradiation to avoid any NOE effects. Finally, the carbon-13 signal is acquired under high-power proton decoupling.

In addition to the problems associated with the measurement of ^{13}C T_1 relaxation time in organic solids, there is a different problem in the interpretation of ^{13}C spin-lattice relaxation time obtained under magic-angle spinning. The magic-angle spinning narrows the powder line shape down to a sharp line at the isotropic chemical shift but it fails to transform the underlying anisotropic[44], non-exponential spin-lattice relaxation into a single exponential.[45] If the anisotropy in spin-lattice relaxation is small, however, this non-exponentiality may be within the experimental error, and therefore unobservable[41].

1.2.4. ^{13}C relaxation in the rotating frame

The ^{13}C spin-lattice relaxation time is sensitive to molecular motions occurring at frequencies near the Larmor frequency of the carbon-13 nucleus. Many motional processes occur, however, at much lower frequencies in the mid kilohertz range. ^{13}C relaxation time in the rotating frame ^{13}C $T_{1\rho}$ is sensitive to these lower frequency motions.[46,47] Instead of letting the spins relax in the external magnetic field B_0, the

spins are forced to relax in an applied spin-lock field B_1.[48] ^{13}C $T_{1\rho}$ relaxation time depends on the correlation time, τ_c, according to:[49]

$$\frac{1}{T_{1\rho}} = \frac{B^2 \tau_c}{1 + \omega_1^2 \tau_c^2} \qquad (1.19.)$$

where B^2 is a measure of the ^{13}C-^{1}H dipolar interaction strength and ω_1 is the frequency of the spin-locking field. ^{13}C $T_{1\rho}$ relaxation can be modulated either by molecular motions or by the proton spin diffusion process. If the spin diffusion contribution is high, as is the case in strongly coupled spin systems, the interpretation of ^{13}C $T_{1\rho}$ relaxation time is difficult.[50] This often limits the use of ^{13}C $T_{1\rho}$ relaxation time in studies of molecular dynamics in highly crystalline polymers.[51] In principle, the contribution of the spin-spin process could be reduced with multipulse proton homonuclear decoupling during the evolution of magnetisation under ^{13}C $T_{1\rho}$ relaxation.[52]

1.2.5. ^{2}H spin-lattice relaxation

The ^{2}H spin-lattice relaxation time is the most unambiguous relaxation time as it depends solely on molecular motion. For powder samples, however, its interpretation is complicated by the anisotropy of spin-lattice relaxation as the relaxation time depends on the orientation of the unique principal axis with respect to the external magnetic field. In other words, different parts of the powder pattern relax with different rates. Fortunately, this anisotropy of spin-lattice relaxation is small in general, and therefore, the powder average spin-lattice relaxation time often describes the crystalline relaxation process well:[44]

$$\frac{1}{T_1} = \frac{3\pi^2 \chi^2}{4}\left[J_1(\omega_0) + 4J_2(2\omega_0)\right] \qquad (1.20.)$$

The powder average spectral densities can be calculated from equation 1.15 using powder average autocorrelation functions. Expressions for autocorrelation functions for various models have been derived[44] and are discussed in chapter 3.

1.2.6. Arrhenius equation

As spin-lattice relaxation times depend on the correlation time τ_c but are measured as a function of temperature, a connection between the correlation time and temperature is needed. The correlation time for a rate-activated process depends on temperature according to the Arrhenius equation:

$$\tau_c = \tau_\infty \exp\left(\frac{E_a}{RT}\right) \tag{1.21.}$$

where τ_∞ is the correlation time at infinite temperature, E_a is the activation energy and R is the gas constant. Then, using equations 1.20 and 1.15, for example, gives for the dependence of the ^{2}H spin-lattice relaxation time on correlation time:

$$\frac{1}{T_1} = C \cdot \left(\frac{\tau_c}{1+\omega_0^2\tau_c^2} + \frac{4\tau_c}{1+4\omega_0^2\tau_c^2}\right) \tag{1.22.}$$

where all constants have been combined into constant C. Two regions occur depending on the magnitude of the correlation time. On the low temperature side of the T_1 minimum the motion is slower than at minimum, i.e. $\omega_0\tau_c >> 1$, and therefore, the natural logarithm of the spin-lattice relaxation time depends on inverse temperature:

$$\ln T_1 = \frac{E_a}{RT} + \ln\left(\frac{\omega_0^2\tau_\infty}{2C}\right) \tag{1.23.}$$

where the Arrhenius equation has been used. On the high temperature side of the minimum the motion is faster than at minimum, i.e. $\omega_0\tau_c << 1$, and therefore:

$$\ln T_1 = -\frac{E_a}{RT} - \ln\left(5C\tau_\infty\right) \tag{1.24.}$$

Thus, the Arrhenius activation energy can be obtained from the slope of a plot of the natural logarithm of the spin-lattice relaxation time as a function of the inverse temperature if the motion is rate-activated and if the spin-lattice relaxation time depends only on the rate of the motion. Quite often, however, the spin-lattice relaxation time depends also on the amplitude of the motion, and therefore, the above equations fail to give the Arrhenius activation energy. In this case, the parameter E_a given by equations 1.23 and 1.24 is called the apparent activation energy.

2. OBSERVED MOLECULAR MOTIONS IN ALKYL CHAINS

Conformational changes in short sequences of bonds are often characterised using Helfand's classification.[53] This classification is based on the effect that the isomerisation has on the ends of the sequence. Helfand used a notation: P*gtt*Q <-> P'*ttg*Q', where P and Q represent the polymer tails and *g* and *t* refer to *gauche* and *trans* conformations, to denote an isomerisation from a *gauche*, *trans*, *trans* conformation to a *trans*, *trans*, *gauche* conformation. A co-ordinate frame where P is equal to P' was chosen, and consequently, three groups were defined depending on the effect of conformational transformation on Q relative to P.

Type I motion occurs so that the chain ends remain at their original positions. In other words, Q is equal to Q'. Type I motion requires two parallel bonds in the sequence. An example of type I motion is crankshaft motion. The crankshaft motion involves seven bonds. Five central bonds keep their conformation and rotate along the parallel first and seventh bonds. Using Helfand's notation, this mode of motion can be represented as P$t(tg^+tg^+t)t$Q <-> P$g^+(tg^+tg^+t)g^-$Q. Another important motion of type I is so called three bond motion. The three bond motion actually involves five bonds. The three central bonds rotate along the first and fifth bond to form the other half of the cyclohexane ring. This motion is denoted as Pttg^+ttQ <-> P$g^+tg^-tg^+$Q.

Type II motion involves a translation of Q relative to P whereas type III motion changes the orientation of Q relative to P. An example of type II motion is *gauche* migration, which can be represented as Pg^+ttQ <-> Pttg^+Q'. Another example of type II motion is a pair *gauche* production, which is denoted as P$tttt$Q <-> Pg^+tg^-Q'. The simplest example of type III motion is a single bond rotation PtQ <-> Pg^+Q'.

Type I motions are the most likely mode of local motion in polymers, since they do not involve any modifications at ends of the sequence. Helfand calculated that the rate of type II transitions are comparable to the rate of type I in the amorphous state. He also suggested that the phase transition from the glassy state to the amorphous state could be regarded as the limit where type II transitions become possible.[53]

2.1. *N*-palmitoylgalactosylceramide

Trans-gauche isomerisation in polymethylene chains was observed for the first time in a glycolipid bilayer using ^{2}H quadrupolar echo measurements.[54] ^{2}H quadrupolar echo spectra for the ordered lamellar crystalline phase of *N*-palmitoylgalactoceramide selectively labelled at the 6 position of the *N*-acyl chain showed changes typical for a two-site tetrahedral jump. At -40 °C, an axially symmetric Pake doublet was observed indicating that the acyl chain was nearly static. As the temperature was increased, the centre of the spectrum filled in, and then, a flat top spectrum was observed at 0 °C. At 20 °C, the central area was rounded, and finally, a completely axially asymmetric spectrum was observed at 40 °C.

All spectra were simulated using a two-site exchange model with a jump angle of 109.5°. The spectra were very sensitive to the populations of the two sites and to the rate constant for the exchange. Interestingly, the flat top spectrum was simulated with a rate constant of 2.5×10^{5} s^{-1} and populations of 0.8 and 0.2 for the two sites. Although only two sites of the diamond lattice were needed to explain the results for the 6 position, the authors suggested that at least a third or perhaps even a fourth site is involved in the isomerisation of the other chain positions.

2.2. Chain motion in polyethylene

Because of the strong dipolar coupling between protons in crystalline polyethylene, the ^{13}C $T_{1\rho}$ relaxation time is determined by spin-spin effects rather than by molecular motion at low temperatures.[50] Although the motional contribution increases with temperature, and at high temperatures and for large ^{13}C spin-locking fields the ^{13}C $T_{1\rho}$ relaxation time is indeed determined by molecular motion, the interpretation of ^{13}C $T_{1\rho}$ data is generally difficult for highly crystalline systems. Motional details can, however, be obtained from deuteron NMR measurements.

Spiess *et al.* have studied chain motions in perdeuterated low density polyethylene (LPE) isothermally crystallised from the melt.[55,56] The ^2H quadrupolar echo spectrum for this perdeuterated LPE was a superposition of a static Pake doublet for the deuterons in the rigid crystalline regions and a broad spectrum that narrowed upon heating for mobile amorphous regions. The spectra for these two regions could be separated with a saturation recovery pulse sequence since the deuterons in the two regions had considerably different spin-lattice relaxation times. The spectrum for the crystalline regions was slightly narrowed and broadened by the α-process that involves 180° jumps of the chains about their long axes and additional small angle fluctuations. More spectral changes were, however, observed in the spectrum for the amorphous regions. Near the γ-transition at 143 K, the spectrum was similar to that observed for the crystalline regions indicating that large scale molecular motions were absent. Upon heating, the central regions first filled in above 200 K, and then above 313 K, only a single peak was observed.

All spectra were simulated by assuming localised motions of short flexible units. The partially narrowed room temperature spectrum was simulated with a superposition of line shapes for exchange between 2 and 3 tetrahedral sites arising from motions of flexible units of 3 and 5 bonds long, respectively. Below 200 K, the spectra were a superposition of a rigid lattice spectrum and a spectrum for 3-bond motions. Above 300 K, motions over 7 bonds became possible as the free volume increased and the number of localised constraints due to the interaction with neighbouring chains decreased. The existence of these constraints was proven by Monte Carlo calculations[57] and also by spin alignment measurements[58].

2.3. Molecular motions in poly(ethylene terephthalate)

Sefcik *et al.* have studied molecular motions in various poly(ethylene terephthalates) at room temperature using ^{13}C $T_{1\rho}$ measurements.[59] The samples studied were quenched, annealed at 61 °C, annealed at 140 °C, annealed at 200 °C and a biaxially drawn film. The resolution of ^{13}C CP/MAS spectra measured at 15.09 MHz was good enough to resolve ethylene (63 ppm), aromatic (133 ppm) and carbonyl carbon

(165 ppm) peaks. For the quenched PET, these peaks were fairly broad with widths of 90, 100 and 60 Hz, respectively. To determine whether this broadening was due to motional effects (homogeneous broadening) or to distributions of chemical shifts, homogeneous line widths were measured from the decay of cross-polarisation magic-angle spinning echo amplitudes. This homogeneous line width was larger for the ethylene carbons (35 Hz), which experience larger dipolar interactions, than for the aromatic (13 Hz) and carbonyl carbons (8 Hz). Interactions with γ-substituents were expected to be small, and therefore, different ethylene conformations were not believed to broaden the ethylene carbon line. The ethylene carbon line width was, however, comparable to $1/T_{1\rho}$, since the echo amplitudes decayed at the same rate as $T_{1\rho}$. Thus, it was concluded that much of the broadening was caused by molecular motion which decreases dipolar-decoupling efficiency. Also the broadening of the aromatic and carbonyl carbon lines was consistent with substantial homogeneous broadening from molecular motion.

$T_{1\rho}$ relaxation times were compared with T_{IS}(ADRF) relaxation times (adiabatic demagnetisation in the rotating frame). For the amorphous samples, T_{IS}(ADRF) was more than an order of magnitude larger than $T_{1\rho}$. This indicated that $T_{1\rho}$ for the ethylene carbons of amorphous PET was determined by molecular motion.[43] Instead for the crystalline PET, $T_{1\rho}$ was equal to T_{IS}(ADRF). Thus, relaxation in crystalline regions was spin-spin dominated and no information about molecular motion was available. The broadening of peaks in the ^{13}C CP/MAS spectra indicated that molecular motions with frequencies comparable to the decoupling field (*ca.* 40 kHz) were present. Further evidence was obtained from the dependence of $T_{1\rho}$ on the spin-locking frequency ω_1. $T_{1\rho}$ for the ethylene carbon of quenched PET and PET annealed below the glass transition temperature depended on the square of ω_1, thus indicating that molecular motions were slower than ω_1. $T_{1\rho}$ for the aromatic carbon was only slightly dependent on ω_1, which suggested that phenyl reorientation may occur at higher frequencies than ω_1.

The authors compared this information about molecular motion with the mechanical properties of PET. The increase in ethylene carbon $T_{1\rho}$ when quenched films were

annealed at 61 °C was accompanied with a decrease in the impact strength. This was consistent with the fact that a short main-chain $T_{1\rho}$ often corresponds to high impact strength.[60,61] It was also suggested that ductile behaviour in quenched PET was due to co-operative high-frequency components of ethylene group motion.

2.4. Molecular motions in poly(butylene terephthalate)

Jelinski *et al.* have reported solid state NMR evidence for three-bond motion as an isolated motional mode in poly(butylene terephthalate).[62] The alkyl portion of poly(butylene terephthalate) is the shortest sequence which can undergo three-bond motions, but is unable to undergo longer range motional modes. Thus, poly(butylene terephthalate) was considered as an ideal compound to study three-bond motions. Jelinski *et al.* have shown by ^{13}C NMR relaxation data and carbon-13 chemical shift anisotropy measurements that the terephthalate groups can be considered as static compared with the motions of the alkyl portions.[63-65] The relaxation times for the alkyl residues suggested a correlation time of *ca.* 10^{-5}-10^{-6} s^{-1} for the alkyl chain motion. These chain motions were characterised further by ^{2}H quadrupolar echo spectra measured for 2,2,3,3-d_4-labelled poly(butylene terephthalate) in a temperature range from -88 °C to +85 °C.

A deuteron powder pattern of a rigid lattice was observed at -88 °C and a quadrupolar coupling constant of 165 kHz was measured from this spectrum.[62] At higher temperatures the spectra showed motional averaging. The centre of the pattern filled in but the total width of the pattern remained at a value of *ca.* 120 kHz. A flat top spectrum was observed at +5 °C. Between +5 and 85 °C, the central area of the spectrum was rounded, and finally in the fast exchange limit at 85 °C, the spectrum was an asymmetric (η=1) pattern. At even higher temperatures, other spectral features took place, and a spike grew in the centre of the spectrum.

The spectra were simulated with a model that involves a C-D bond hopping between two equally populated sites separated by a dihedral angle of 103°. These hops were interpreted as arising from *trans-gauche* conformational isomerisations. The

calculated spectra were very sensitive to the jump angle, and jump angles of 100° or 110° failed to produce the observed spectra. Rate constants for the isomerisation process were estimated from the deuteron spectra. The rate constant was smaller than 1×10^4 s^{-1} at -88 °C and increased to 5.7×10^5 s^{-1} at 85 °C. The flat top spectrum was produced with a rate constant of 7.1×10^4 s^{-1}. A plot of the natural logarithm of the rate constants as a function of the inverse temperature yielded an apparent activation energy of 24 kJ mol^{-1} for the isomerisation.

A flat top quadrupolar echo spectrum was measured for 1,1,4,4-d_4-labelled poly(butylene terephthalate) at 85 °C, where the spectrum for the 2,2,3,3-d_4-labelled derivative was a totally axially asymmetric spectrum, indicating that the chain end deuterons undergo motions different from those of the central deuterons.[62] Consequently, the authors concluded that the chain end deuterons are not involved in large-scale and rapid motions at temperatures where the central deuterons are in the fast exchange limit.

The NMR data was interpreted as being in agreement with a model that involves some PtttQ <-> Pg±tg∓Q and Pttg±Q<-> Pg±ttQ motions as the predominant modes. The sites for the two-site model used for the simulations were interpreted as being g^+tg^- and g^-tg^+.

2.5. Bulk hard-segment polyurethanes

A deuteron NMR study has also been carried out on bulk hard-segment polyurethanes.[66] The two polyurethanes were semicrystalline bis(4-isocyanophenyl)methane (MDI-BDO), and completely amorphous 2,4-toluenediyl diisocyanate (TDI-BDO), both chain extended with butanediol-2,2,3,3-d_4 (fig. 2.1). For MDI-BDO, spin-lattice relaxation time data indicated that two different components were present, a short-T_1 component with T_1 of order 20 ms and a long T_1 component with T_1 of order 0.5 s. The short T_1 component was due to deuterons in the amorphous regions of the polymer.

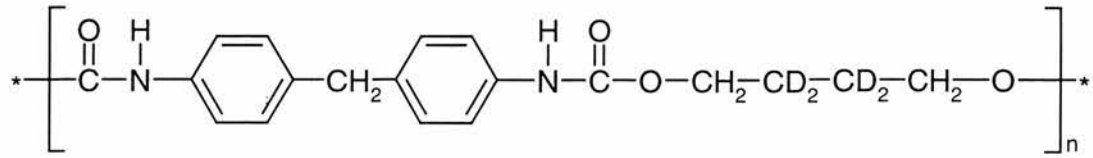

MDI-BDO

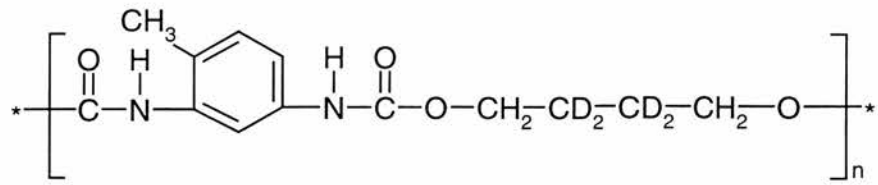

TDI-BDO

Figure 2.1. The structures of the hard-segment polyurethanes MDI-BDO and TDI-BDO.

Spectra obtained with an amorphous quadrupolar echo sequence, which involves a saturating sequence before the standard quadrupolar echo sequence, indicated that *ca.* 70 % of the deuterons were in the amorphous regions. Spectra for these deuterons were domelike above room temperature suggesting that the motionally averaged electric field gradient tensor was axially asymmetric and that the corresponding motion had two-fold symmetry. Thus, the room temperature spectrum, whose overall width was *ca.* 120 kHz, was simulated using a two-site jump model with a jump angle of 114° and a single correlation time in the fast-motion limit. In addition, small torsional oscillations (±10°) of the methylene group about a C-C bond were added to reduce the width from a rigid lattice value of 125 kHz to the observed value of 120 kHz. Remaining differences between the observed and calculated spectra were attributed to distributions in the frequencies of motion. It was suggested that the frequency distribution was due to differences in local packing density.

At higher temperatures, further narrowing of the line shape was observed. The width of the spectrum was *ca.* 105 kHz at 83 °C. This narrowing was taken into account by including a fast, small-amplitude diffusion of the butanediol chain to the model used to simulate the room temperature spectra. A reasonable fit between the observed and calculated spectra was obtained by assuming that the butanediol chain was diffusing within a cone of semiangle of 12 ° at 62 °C and 16° at 83 °C. A T_1 minimum was

observed at *ca.* 45 °C suggesting that the average correlation time for the motion was *ca.* 2 ns at this temperature. While the motion was in the fast-motion limit above room temperature, a flat top spectrum was observed at -45 °C, suggesting that the correlation time for the two-site hopping motion was in the intermediate rate regime at this temperature. For the deuterons in the crystalline region, a rigid lattice Pake doublet with a quadrupole splitting of 125 kHz was observed at -45 °C. As the temperature was increased the centre of the pattern filled in and a flat-top spectrum was observed at 73 °C. This was explained as being due to *trans-gauche* conformational transitions in the intermediate rate region.

Very similar spectral changes were observed for TDI-BDO. The main difference was that the total spectral intensity decreased sharply above 40 °C. The glass transition temperature for this polymer is 40 °C, and therefore, the loss in intensity was due to large-angle motions above the glass transition temperature. This decrease in intensity was not observed for MDI-BDO since the glass transition temperature for this polymer is at *ca.* 110 °C, near the highest temperature 120 °C that was studied.

2.6. Chain motion in nylon 66

Segmental dynamics in selectively deuterated nylon 66 polymers have been studied both in the crystalline[67] and in the amorphous phases[68] using deuteron NMR techniques. In contrast to the commonly used model of jumps in the diamond lattice, the chain motion in nylon 66 was interpreted by a harmonic oscillator model with a single correlation time and a distribution of librational angles. Gaussian distribution with a standard deviation of $\Delta\theta$ was used to describe the libration because the ensemble average probability distribution for the 11 lowest eigenstates of ethane with $\nu_0 = 300\ cm^{-1}$ could well be approximated as Gaussian. This approximation was assumed to be valid if the barrier to internal methylene group rotation in nylon 66 was larger or comparable to that in ethane. However, this single distribution of librational angles failed to produce the rather featureless observed spectra. This featureless shape of the observed spectra indicated that the C-D bond motion was spatially inhomogeneous, that is, C-D bonds in different regions of the polymer were

undergoing different motions. This was in agreement with the small average length of crystallite stems, which was *ca.* five repeat units. Consequently, an additional distribution P($\Delta\theta$) for the standard deviation of the Gaussian distribution was added to account for this spatially inhomogeneous distribution.

^{2}H quadrupolar echo spectra were nearly identical for all methylene groups in each moiety and at every temperature studied. Pake doublets were observed at room temperature. As the temperature was increased, the central area filled in and above 160 °C the spectra were close to an axially asymmetric spectra. Although the line shape changes were very similar to those observed for poly(butyleneterephthalate) and for the polyurethanes, the *trans-gauche* isomerisation model was considered to be inconsistent with the shortening of the chain axis and also with the line shapes. Instead, the librational model described above was used to explain the data. The motion was assumed to be in the fast-motion limit and all spectral changes were due to changes in the amplitude of the motion. The inhomogeneous distribution P($\Delta\theta$) was chosen to be half Gaussian below the Brill transition (130-170 °C) and an additional Gaussian distribution was added above the Brill transition. The inhomogeneous distribution spread from *ca.* 5° to *ca.* 20° at room temperature whereas at 228.1 K it spread from *ca.* 50 to 90°.

The spectral changes for the amorphous regions below the glass transition temperature were fairly similar to those observed for the crystalline regions. Rigid lattice Pake doublets were observed at -183 K. Upon heating, the central area of the spectra filled in, and then at 50° C, the central area was rounded. The glass transition temperature for nylon 66 is dependent on the frequency of the measurement but is *ca.* 100 °C at the frequency relevant to the line shape analysis. The line shapes were simulated using a bimodal model consisting of a fast librational motion similar to used for the crystalline region and an inhomogeneous distribution of *trans-gauche* jumps. The distribution of the *trans-gauche* jumps was also assumed to be Gaussian and was centred at the tetrahedral jump angle.

Above the glass transition temperature, a very sharp peak appeared in the spectra of all methylene sites and also in the spectra for the N-D sites. This was interpreted as

being due to the α-relaxation or to the glass transition. The spectra for the methylene sites were simulated as a composite of three components undergoing fast, intermediate and slow exchange. The broad component was assumed to be very similar to that observed below the glass transition temperature whereas the fast- and intermediate components were fitted by Lorentzian line shapes with line widths of 1-2 and 10 kHz, respectively, representing isotropic motion.

2.7. Molecular motions in liquid-crystalline poly(ester amides)

Molecular motions have been studied in liquid crystalline poly(ester amides) below their glass transition temperature using ^{13}C $T_{1\rho}$ measurements.[69] These polymers exhibit thermotropic liquid crystallinity, and the number and magnitude of phase transitions depend on the length of the ester and amide moieties. The amide moieties are in all-*trans* conformation whereas the ester moieties are a mixture of *trans* and *gauche* bonds. The ^{13}C $T_{1\rho}$ relaxation time for these polymers was assumed to be dominated by motional processes and to be inversely proportional to molecular motion. The ^{13}C $T_{1\rho}$ relaxation time was measured for the resonances for the methylene groups adjacent to the ester group and adjacent to the amide group for polymers prepared with different lengths of the ester and amide moieties, respectively. Longer ^{13}C $T_{1\rho}$ relaxation times were observed for the ester site which suggested that the ester site was less mobile than the amide site. Therefore, it was proposed that the chain in an all-*trans* conformation may provide more freedom of movement than the chain containing *gauche* bonds.

Whereas mobility in the amide site was almost independent of the chain length, the ester site showed an odd-even effect in which the motion was more restricted in chains with even number of methylene groups.[69] An odd-even effect is also observed in the thermal behaviour of these polymers. Polymers with 2 or 4 carbons exhibit only very few endothermic transitions whereas polymers with 3 or 5 carbons in the ester chain exhibit many endotherms. As a result, the authors concluded that when the mobility of the α-carbon in the ester moiety is restricted, the polymer melts in a

single step at a relatively high temperature but when the α-carbon is more mobile, the libration occurs in several small increments covering a broad temperature range.

2.8. Two-dimensional NMR studies

Zemke *et al.* have studied the *trans-gauche* conformational exchange in atactic polypropylene near the glass transition.[70] At 250 K, above the glass transition temperature of 239 K, two peaks were observed for the methylene carbons. The peak at 48.6 ppm was for the methylene carbons with two *trans* carbons in the γ-positions whereas the peak at 44.9 ppm was for the methylene carbons in a *trans-gauche* environment. At 262 K, these two peaks were coalesced into one peak at 46.6 ppm. A 2D ^{13}C CP/MAS spectrum measured at 250 K showed cross peaks for the two methylene carbons indicating that a *trans-gauche* conformational transition occurred in the amorphous phase. In the glassy phase, however, both the *trans-gauche* exchange and the diffusive rotational process were slower than 1 s, the time scale of these NMR experiments.

Hirschinger *et al.* have applied two-dimensional deuteron exchange NMR to study the chain motion in the crystalline α-phase of poly(vinylidene fluoride).[71] Mechanical and dielectric studies have indicated that the α-relaxation at high temperature is caused by molecular motion in the crystalline regions. The 2D deuteron exchange spectrum at 370 K showed elliptical exchange ridges indicating large-scale molecular motion. A comparison of a calculated and the experimental spectra yielded reorientation angle distribution function (RAD) that consisted of two peaks centred at 0 ° and 67 °. The latter indicated a two-site C-D bond motion by an angle of 67 ° or 113° in the crystal lattice. The correlation time of 20 ± 5 ms for this motion at 370 K was calculated from the RAD function, well in agreement with dielectric relaxation studies. By comparing this NMR result with published X-ray and dielectric relaxation studies the authors arrived at an unique conclusion that the observed motion was P*tgtg*$^-$Q<-> P*g*$^-$*tg*Q.

Schaefer *et al.* have used both one- and two-dimensional deuteron NMR techniques to study segmental dynamics in poly[(dimethylimino)decamethylene-tetrafluoroborate], $[-(CH_2)_{10}-N^+(CH_3)_2-]_n \cdot nBF_4$.[72,73] The methyl groups and the α-, β- and γ-positions of the methylene chain were selectively deuterated for deuteron NMR studies. At 220 K, a rigid lattice Pake doublet was observed for all the chain deuterated samples indicating that molecular motions with correlation times shorter than 1 ms were absent. Significant spectral changes were observed on heating the sample. Essentially the same changes were observed for all the chain deuterated samples but at different temperatures. These changes indicated that mobility increased with distance from the cationic centres. As the temperature was increased, the central area of the Pake pattern filled in and the spectra became domelike, similarly to those observed for poly(butyleneterephthalate) and polyurethanes.

Above the glass transition temperature (313 K) at 360 K the spectra were triangular with a very sharp peak on the top. The 2D-exchange spectra failed to show any elliptical ridges typical for discrete *trans-gauche* isomerisation but rather showed features of large angle reorientation. High intensity along the diagonal indicated that a substantial number of C-D bonds were static on the time scale of the experiment. On the other hand, spectra measured with a longer mixing time (200 ms) showed broadening of the spectrum along the diagonal indicating small angle reorientations. Nevertheless, these results were explained with *trans-gauche* exchange but assuming that the tetrahedral jumps were not accurate but rather ill-defined. This explanation was consistent with the quadrupolar echo spectra that showed high intensity in the central area. This high intensity in the central area was explained to be generated by tetrahedral jumps but was smeared out by an inhomogeneous distribution of libration angles. Above the glass transition, the 2D spectra showed exchange over the entire spectral region indicating that a slow motion onsets at the glass transition process.

3. MODELS OF MOTION

In this chapter, various models of motion are discussed and simulated ^{2}H quadrupolar echo spectra for these models are shown. When using ^{2}H quadrupolar echo spectra for differentiating between models of motion, it is important that spectra are measured with different refocusing delays and these spectra are compared with simulated spectra. The measurement of quadrupolar echo spectra in the intermediate exchange rate regime, however, is very time consuming for long refocusing delays as the echo intensity decreases exponentially with the refocusing delay:[74]

$$I(2\tau) = I(0)\exp\left(-2\tau/T_2^*\right) \tag{3.1.}$$

where $I(0)$ is the initial intensity and T_2^* is the effective transverse relaxation time. In addition to motional effects in the intermediate exchange regime, the echo intensity is also decreased by dipolar couplings between deuterons and protons as the quadrupolar echo pulse sequence fails to refocus these couplings.[56,74] Dipolar couplings also broaden the line shape, and their effect can be taken into account by multiplying the free induction decay signal by a few kilohertz wide Gaussian broadening function.[75-77] Such a broadening has a fairly small effect on the line shape, but the decrease in the echo intensity during the refocusing delay is considerable. For example, a 2 kHz Gaussian broadening (*GB*) gives for the echo reduction factor E_r, defined as the ratio of intensities of echoes measured with 160 μs and 20 μs refocusing delays:

$$E_R = \frac{\exp\left(-\left(GB\cdot 2\tau_2\right)^2\right)}{\exp\left(-\left(GB\cdot 2\tau_1\right)^2\right)} = \frac{\exp\left(-\left(2000\cdot 320\cdot 10^{-6}\right)^2\right)}{\exp\left(-\left(2000\cdot 40\cdot 10^{-6}\right)^2\right)} = 0.67 \tag{3.2}$$

Similarly, 3 kHz of Gaussian broadening gives 0.40 for the echo reduction factor. Thus, the dipolar couplings decrease the echo intensity to about half of its original value. Four times as many transients are therefore needed for the spectrum measured with a 160 μs delay to obtain the same signal to noise ratio as in the spectrum measured with a 20 μs delay. Because of this severe decrease in echo intensity, and

very limited instrumental time in use, spectra were measured only with two different refocusing delays. A short delay of 20 μs was used to avoid probe recovery problems and to maximise the signal intensity, whereas a long delay of 160 μs was used to maximise the effect of anisotropic T_2 relaxation. The same delays were used in the simulations.

3.1. Two-site exchange.

The simplest model of motion is two-site exchange. This model involves a C-D bond exchanging between two different orientations separated by an angle of 2β (half angle β). 2β is chosen to represent the angle because this leads to a convenient expression for the ^{2}H spin-lattice relaxation time.[67] Euler angles (φ,θ,ψ) for this model are readily obtained if molecular co-ordinates are chosen so that the z-axis bisects the D-C-D angle and y-axis is perpendicular to both C-D bonds, as shown in figure 3.1. Then, θ is equal to β for both sites and φ is zero for site 1 and 180° for site 2.

Figures 3.2-3.6 show spectra simulated with different half angles β. Half angles of 1.0, 2.5, 10.0, 20.0 and 54.7 degrees were chosen to represent the changes in line shape as the angle is increased. For each angle, the rate constant k was varied from slow exchange values of *ca.* 10^3 s^{-1} to fast exchange values of 10^9 s^{-1}. In the intermediate regime, rate constants best representing the line shape changes were used. All spectra were broadened with 1 kHz Lorentzian and 2 kHz Gaussian broadening functions.

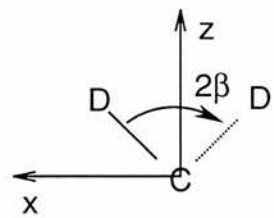

Figure 3.1. C-D bond exchanging between two different orientations separated by an angle of 2β. The y-axis of the molecular co-ordinate system is pointing out of the paper plane.

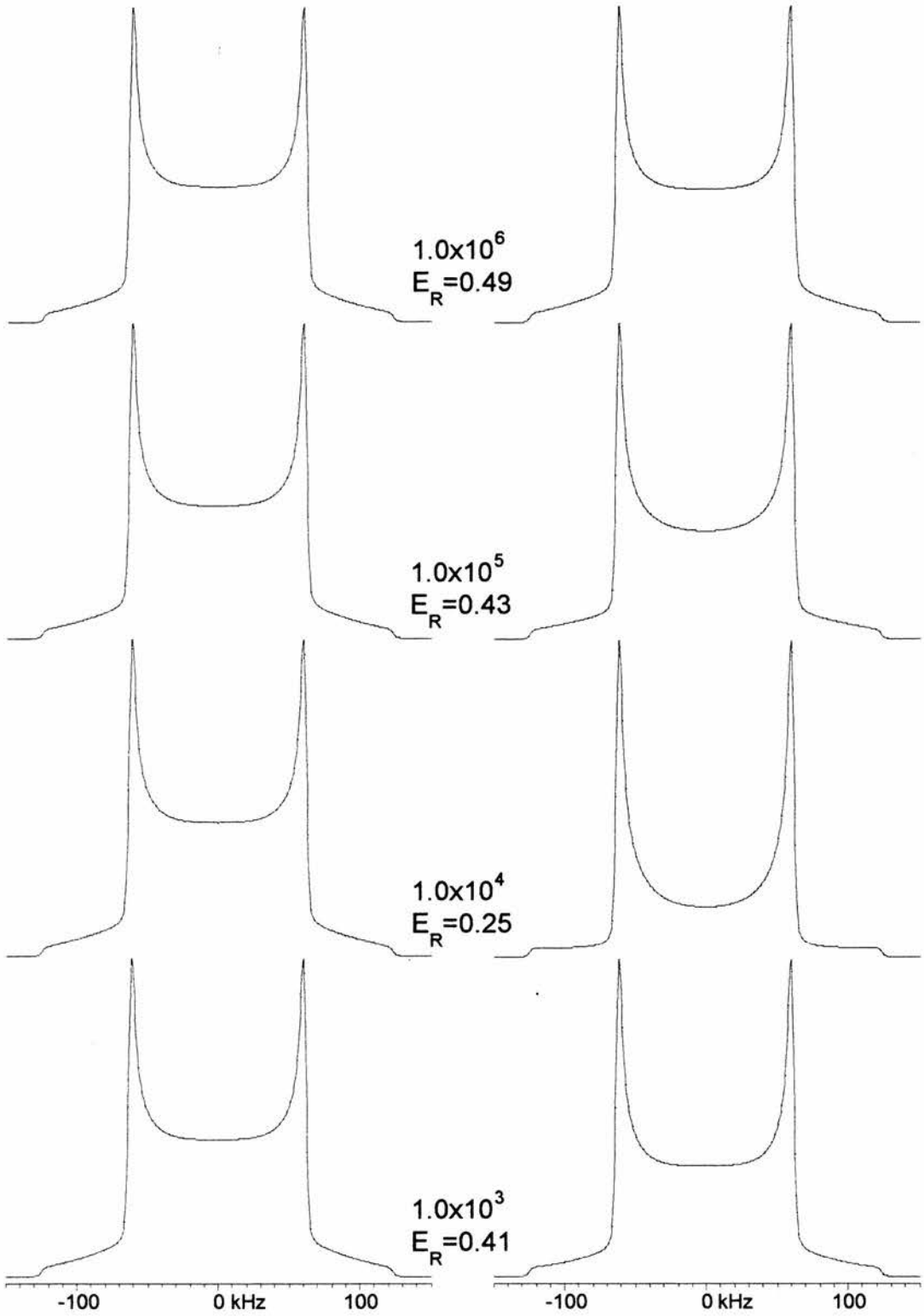

Figure 3.2. Simulated spectra for two-site exchange with a half angle of 1.0 degree. Refocusing delays are 20 μs (left) and 160 μs (right). 90° pulse length is 3.8 μs. Rate constants (s^{-1}) and echo reduction factors are shown in the figure.

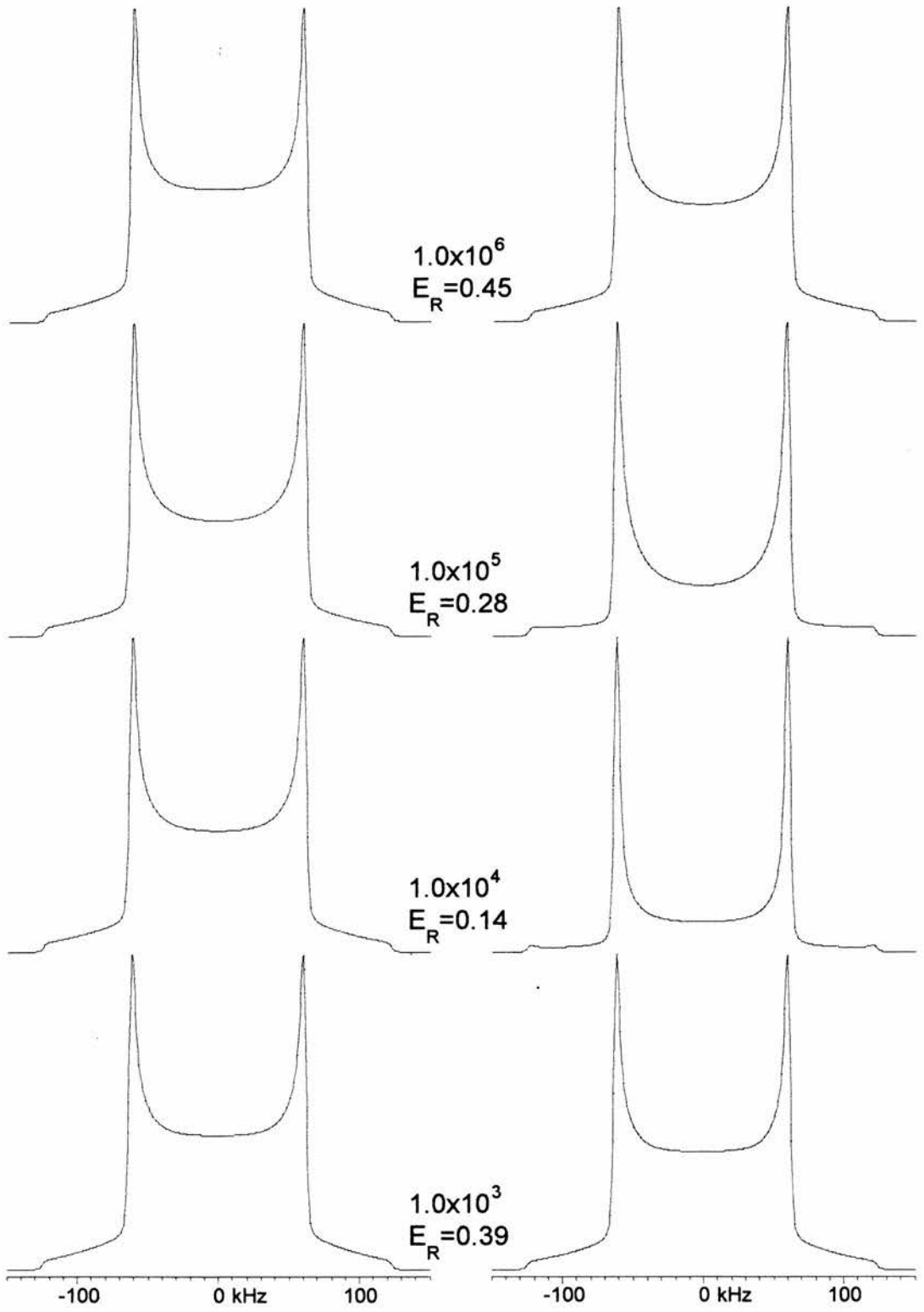

Figure 3.3. Simulated spectra for two-site exchange with a half-angle of 2.5 degrees. Refocusing delays are 20 μs (left) and 160 μs (right). 90° pulse length is 3.8 μs. Rate constants (s^{-1}) and echo reduction factors are shown in the figure.

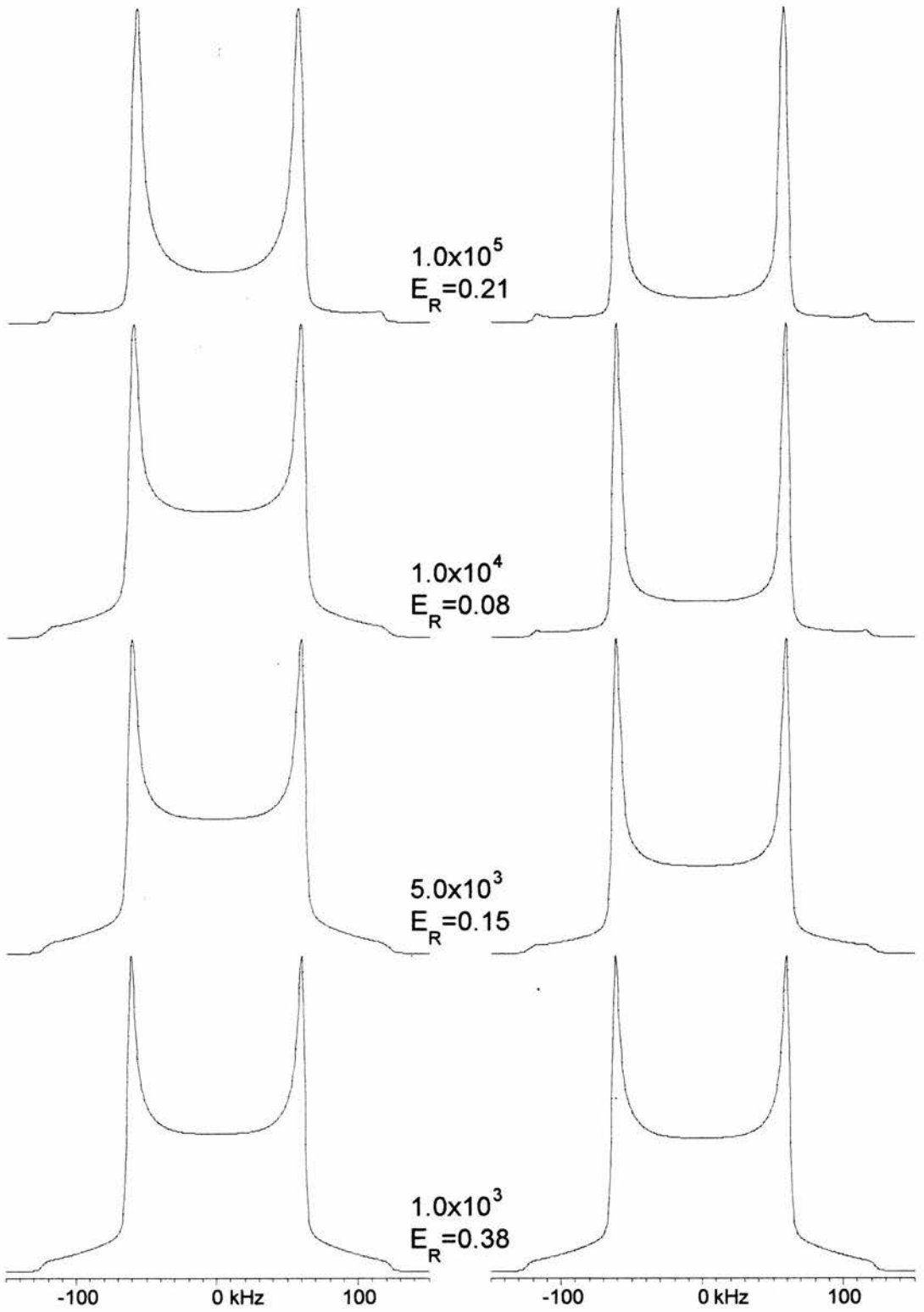

Figure 3.4. Simulated spectra for two-site exchange with a half angle of 10.0 degrees. Refocusing delays are 20 μs (left) and 160 μs (right). 90° pulse length is 3.8 μs. Rate constants (s^{-1}) and echo reduction factors are shown in the figure.

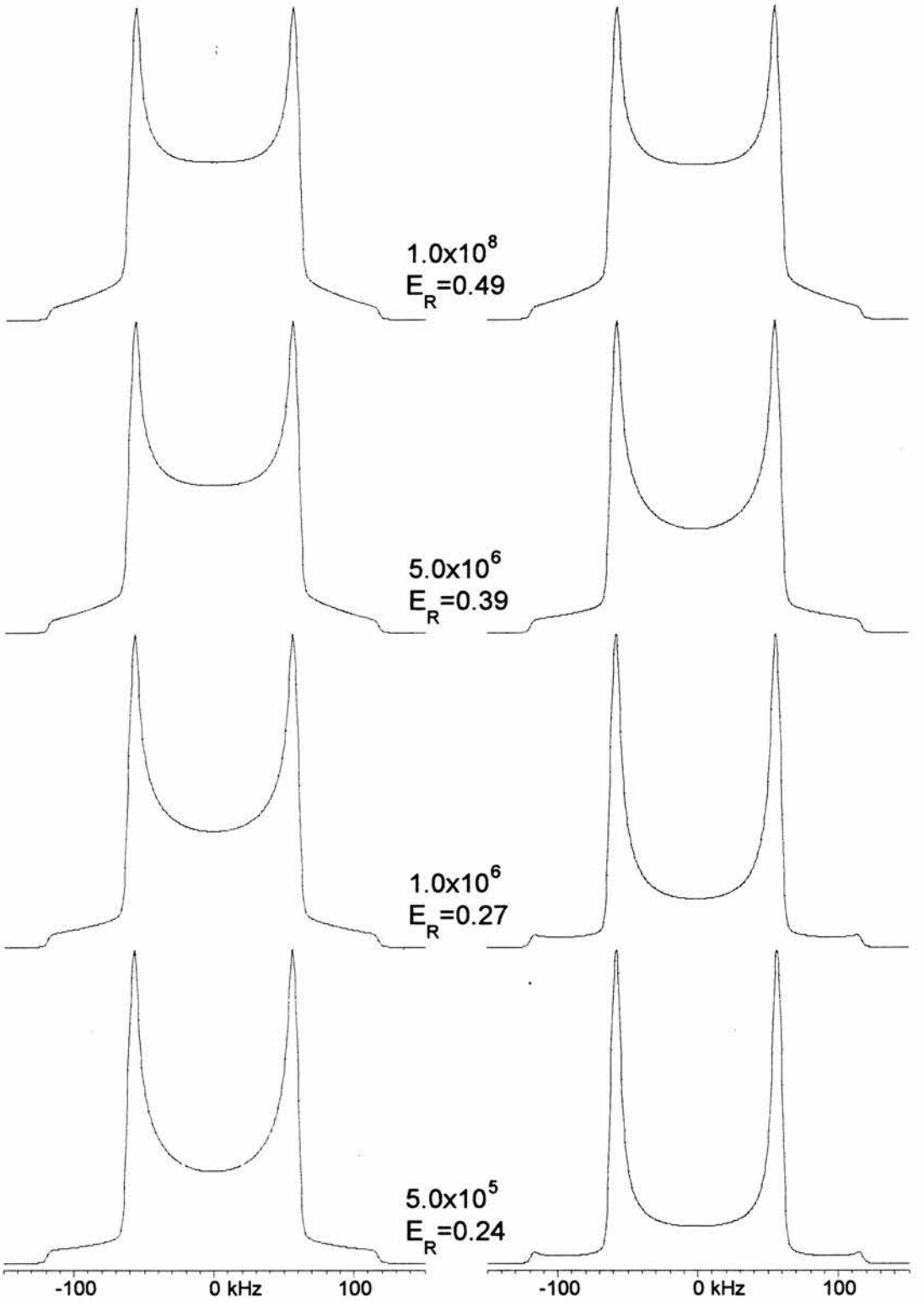

Figure 3.4. (continued) Simulated spectra for two-site exchange with a half angle of 10.0 degrees. Refocusing delays are 20 μs (left) and 160 μs (right). 90° pulse length is 3.8 μs. Rate constants (s^{-1}) and echo reduction factors are shown in the figure.

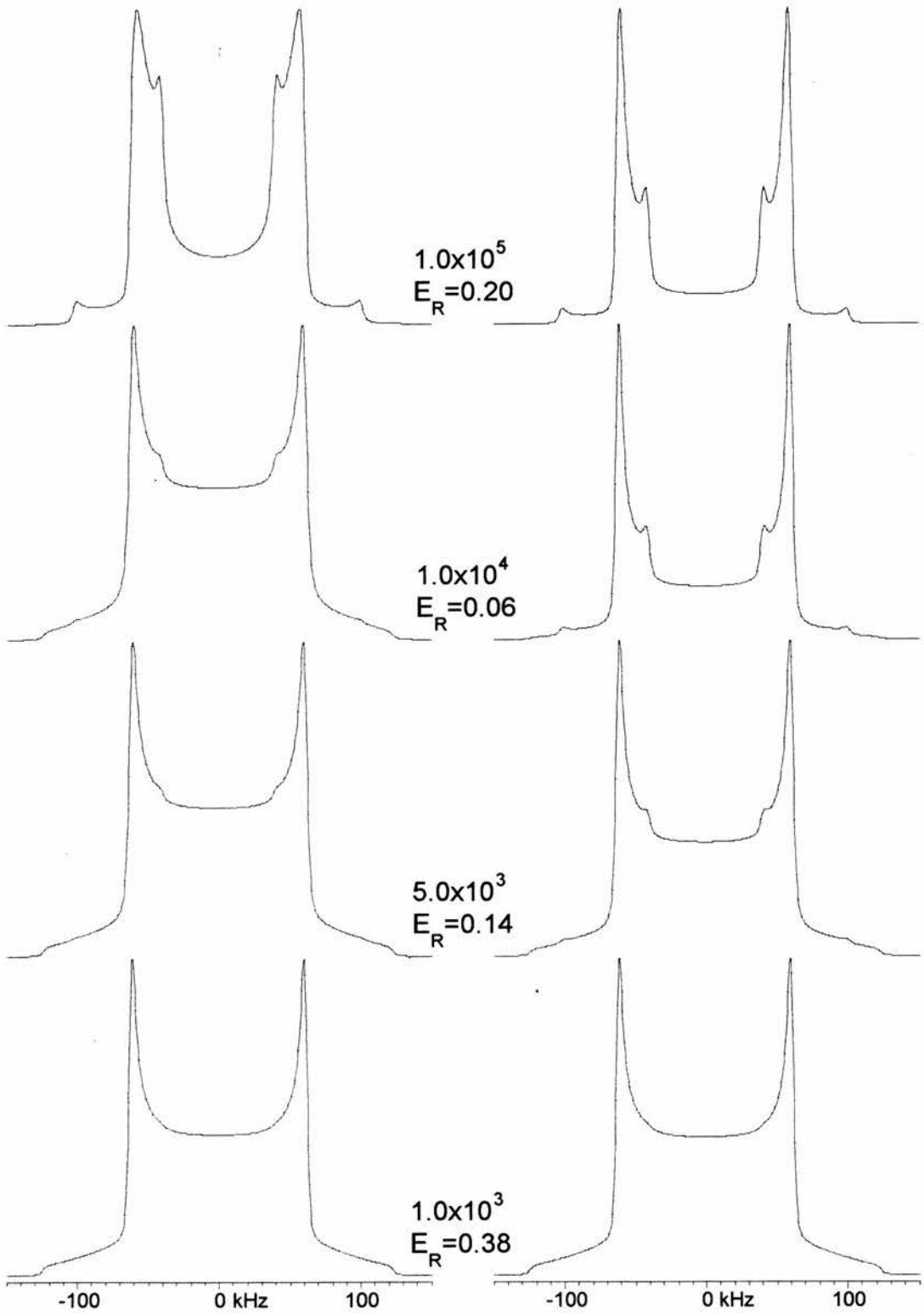

Figure 3.5. Simulated spectra for two-site exchange with a half angle of 20.0 degrees. Refocusing delays are 20 μs (left) and 160 μs (right). 90° pulse length is 3.8 μs. Rate constants (s^{-1}) and echo reduction factors are shown in the figure.

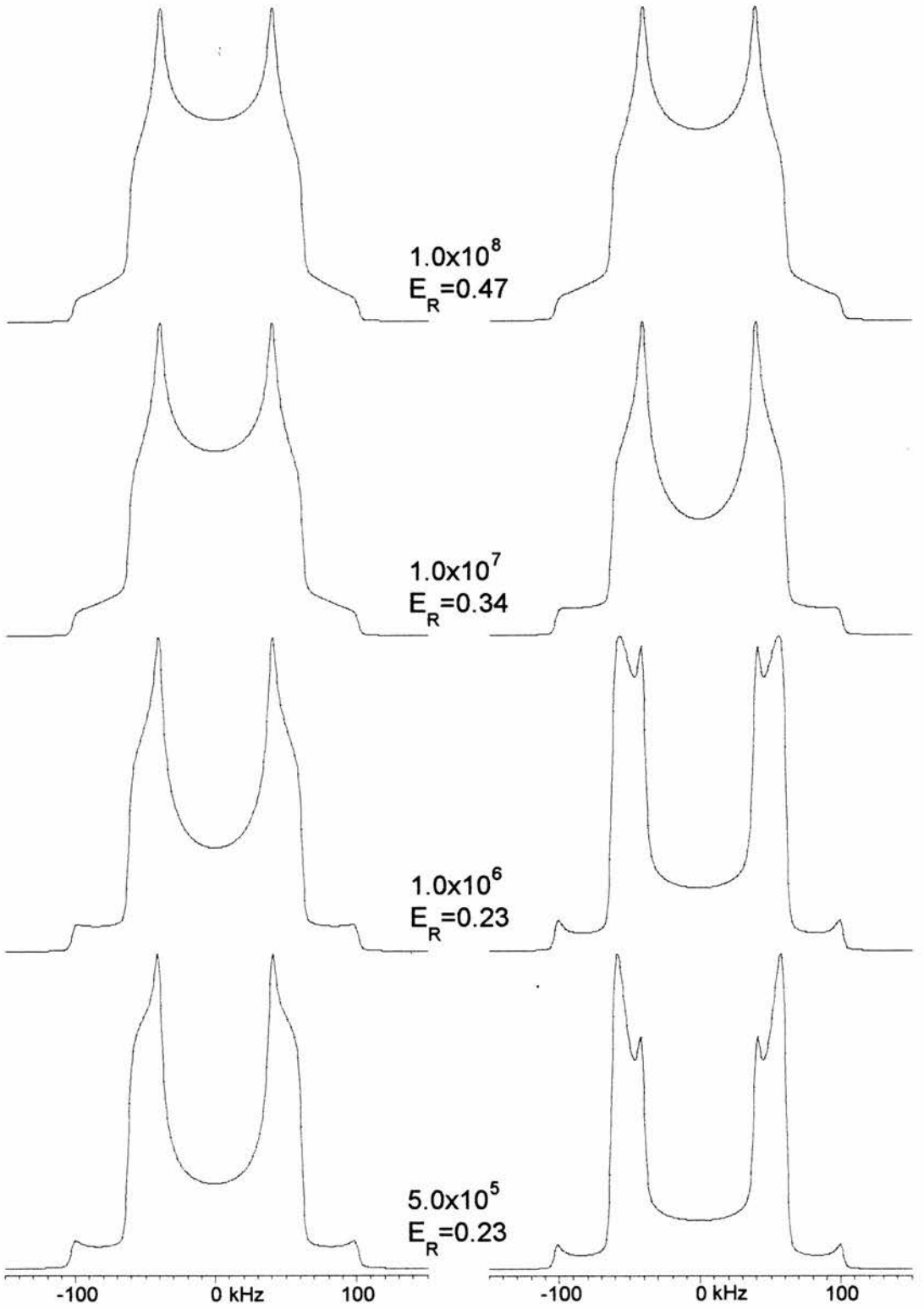

Figure 3.5. (continued) Simulated spectra for two-site exchange with a half angle of 20.0 degrees. Refocusing delays are 20 μs (left) and 160 μs (right). 90° pulse length is 3.8 μs. Rate constants (s^{-1}) and echo reduction factors are shown in the figure.

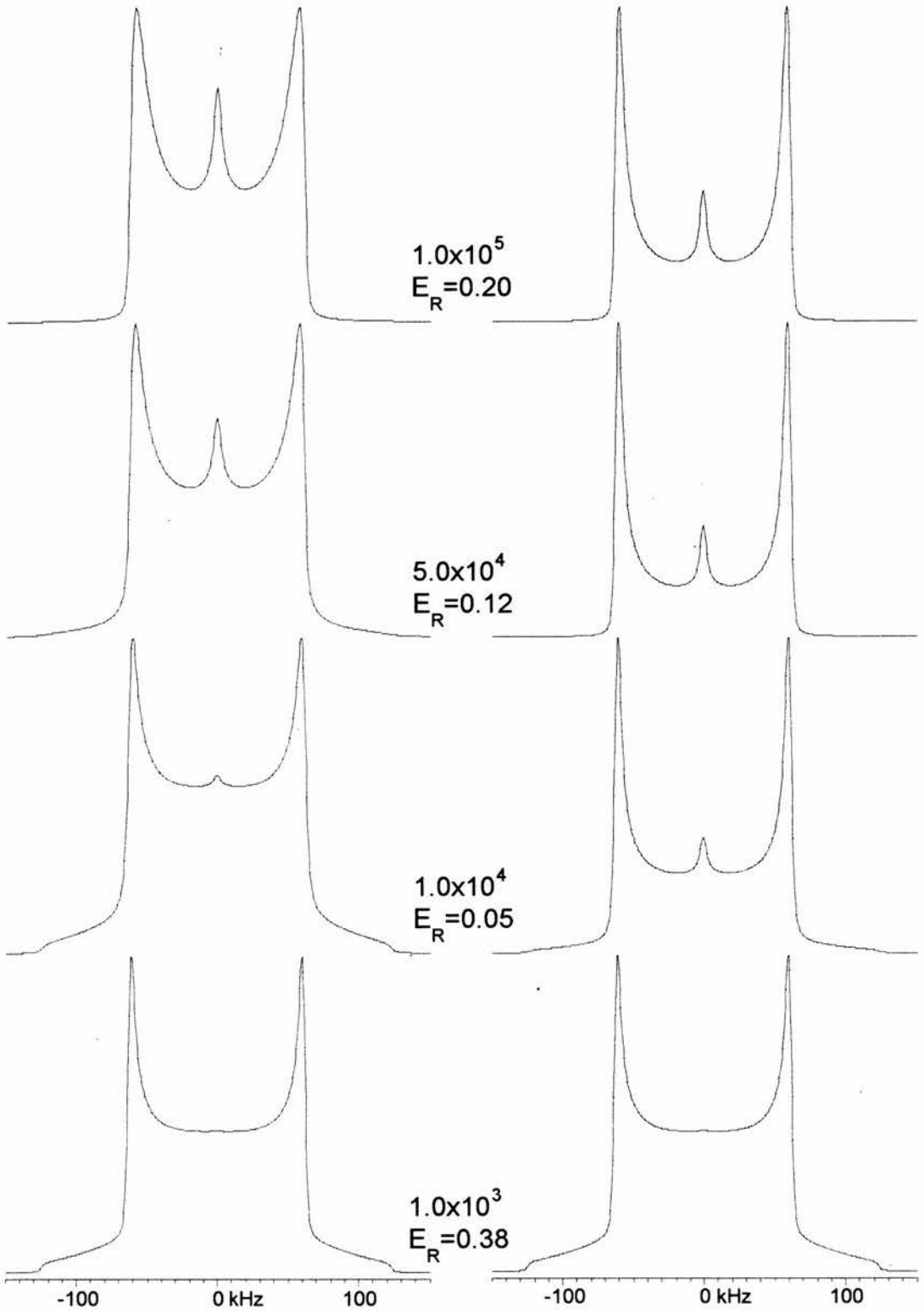

Figure 3.6. Simulated spectra for two-site exchange with a half angle of 54.7 degrees, or "magic angle". Refocusing delays are 20 μs (left) and 160 μs (right). 90° pulse length is 3.8 μs. Rate constants (s^{-1}) and echo reduction factors are shown in the figure.

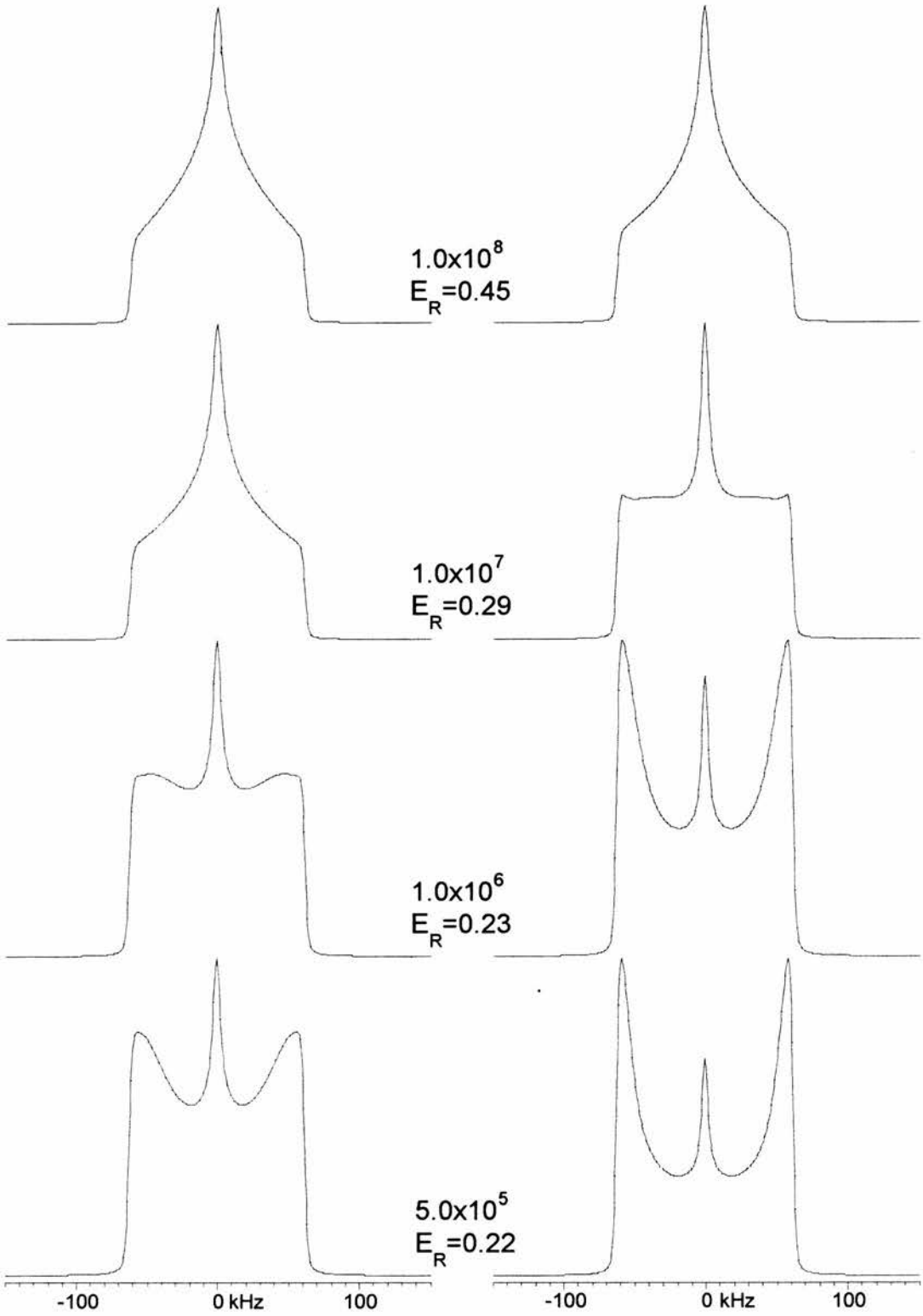

Figure 3.6. (continued) Simulated spectra for two-site exchange with a half angle of 54.7 degrees, or "magic angle". Refocusing delays are 20 μs (left) and 160 μs (right). 90° pulse length is 3.8 μs. Rate constants (s^{-1}) and echo reduction factors are shown in the figure.

For rate constants smaller than *ca.* 10^3 s^{-1}, a rigid lattice Pake doublet is observed for both refocusing delays. However, as the rate constant increases from 10^3 s^{-1}, the intensity of the central area of the Pake doublet decreases. This decrease is more pronounced on the spectra simulated with a 160 μs refocusing delay because of a longer evolution time under anisotropic T_2 relaxation. Even for a very small half angle of 1.0 degree (fig. 3.2), the intensity in the central area has considerably decreased when the exchange rate is 10^4 s^{-1}. The longer evolution time under anisotropic T_2 relaxation also means that less signal is refocused after 320 μs. Consequently, the intensity of the 160 μs spectrum is smaller than the intensity of the 20 μs spectrum.

Figure 3.7 shows the dependence of echo reduction factor, defined as the ratio of the intensity of the spectrum measured with a 160 μs refocusing delay to the intensity of the spectrum measured with a 20 μs refocusing delay, on the rate constant for different half angles β. Echo reduction factors in the absence of dipolar couplings can be obtained from the echo intensities calculated with the MXET1 program. These ideal echo reduction factors are often reported in the literature but are rather misleading if dipolar couplings are present. As explained at the beginning of this chapter, the dipolar couplings reduce the echo reduction factor to about half of its original value, and therefore, the values obtained from the MXET1 program are divided by two to obtain more realistic values. Echo reduction factors obtained this way are shown in figure 3.7. Clearly, the echo reduction factor is at minimum when the rate constant is *ca.* 10^4 s^{-1}. As the rate constant becomes larger than this, the echo reduction factor and the intensity in the central area of the spectrum increase until the fast exchange limit is reached at *ca.* 10^9 s^{-1}.

Another important change in the spectrum is that fast motion induces asymmetry ($\eta \neq 0$) for large half-angles. This is especially clear in the spectra shown in figure 3.5 for a half angle of 20 degrees. The two-site motion is planar, and therefore, the motionally induced asymmetry is characteristic for highly planar motions.[78] For example, phenyl ring flipping is often well described by two-site exchange with the angle 2β equal to 120 degrees.[79] Also, ND_2 group flipping has been simulated with the two-site model using 2β of 59.5°.[80]

The spectra for which 2β equals the tetrahedral angle, however, are significantly different. Because the motion averages the C-D bond orientation at magic angle, a spike grows in the centre of the spectrum (zero frequency) as the rate constant is increased. In the fast motion limit, a completely axially asymmetric (η=1) spectrum is observed.

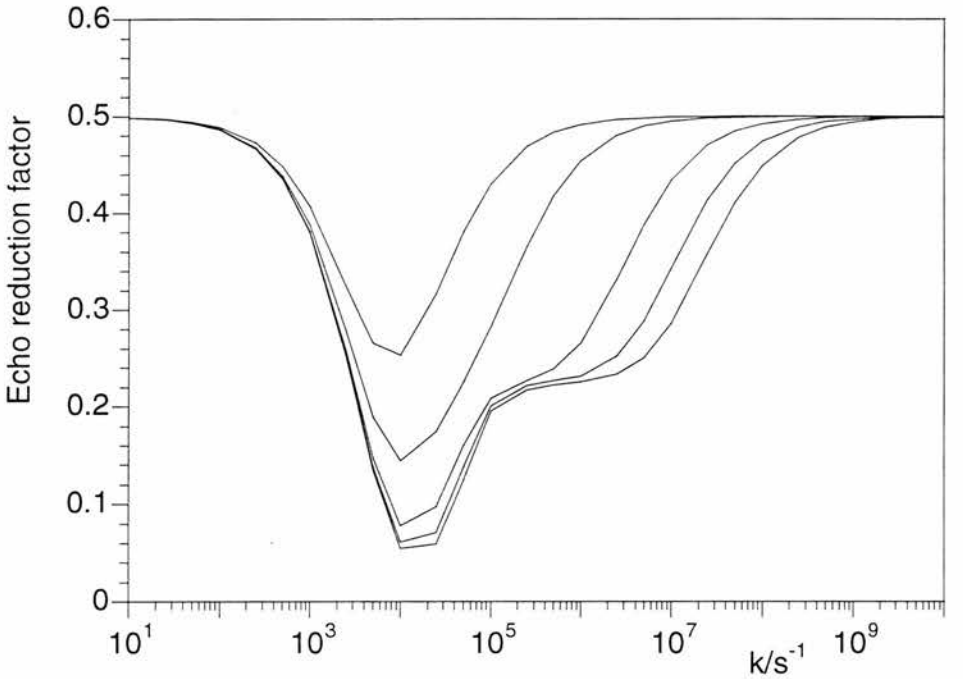

Figure 3.7. Dependence of echo reduction factor on the rate constant k and on the half-angle β. Half-angles for top to bottom are: 1.0°, 2.5°, 10.0°, 20.0° and 54.7°.

If the two-site model with 2β equal to the tetrahedral angle is used to describe *trans-gauche* exchange, different populations for the two sites should be considered as it is highly unlikely that a *trans* and a *gauche* conformation would occur with the same probability. Figure 3.8 shows simulated spectra for exchange between two sites of populations 0.1 (p_1, site 1) and 0.9 (p_2, site 2) and an angle 2β of 109.5 degrees. The rate constants shown in the figure are the rate constants from site 2 to site 1, denoted as k_{12}.[30,81] The spectra were calculated using an exchange matrix

$$\mathbf{K} = \begin{pmatrix} -k_{21} & k_{12} \\ k_{21} & -k_{12} \end{pmatrix} = \begin{pmatrix} -9 & 1 \\ 9 & -1 \end{pmatrix} \tag{3.3}$$

where the rate constant from site 1 to site 2, k_{21}, is nine times k_{12} to fulfil the principle of microscopic reversibility $k_{12} \cdot p_2 = k_{21} \cdot p_1$.

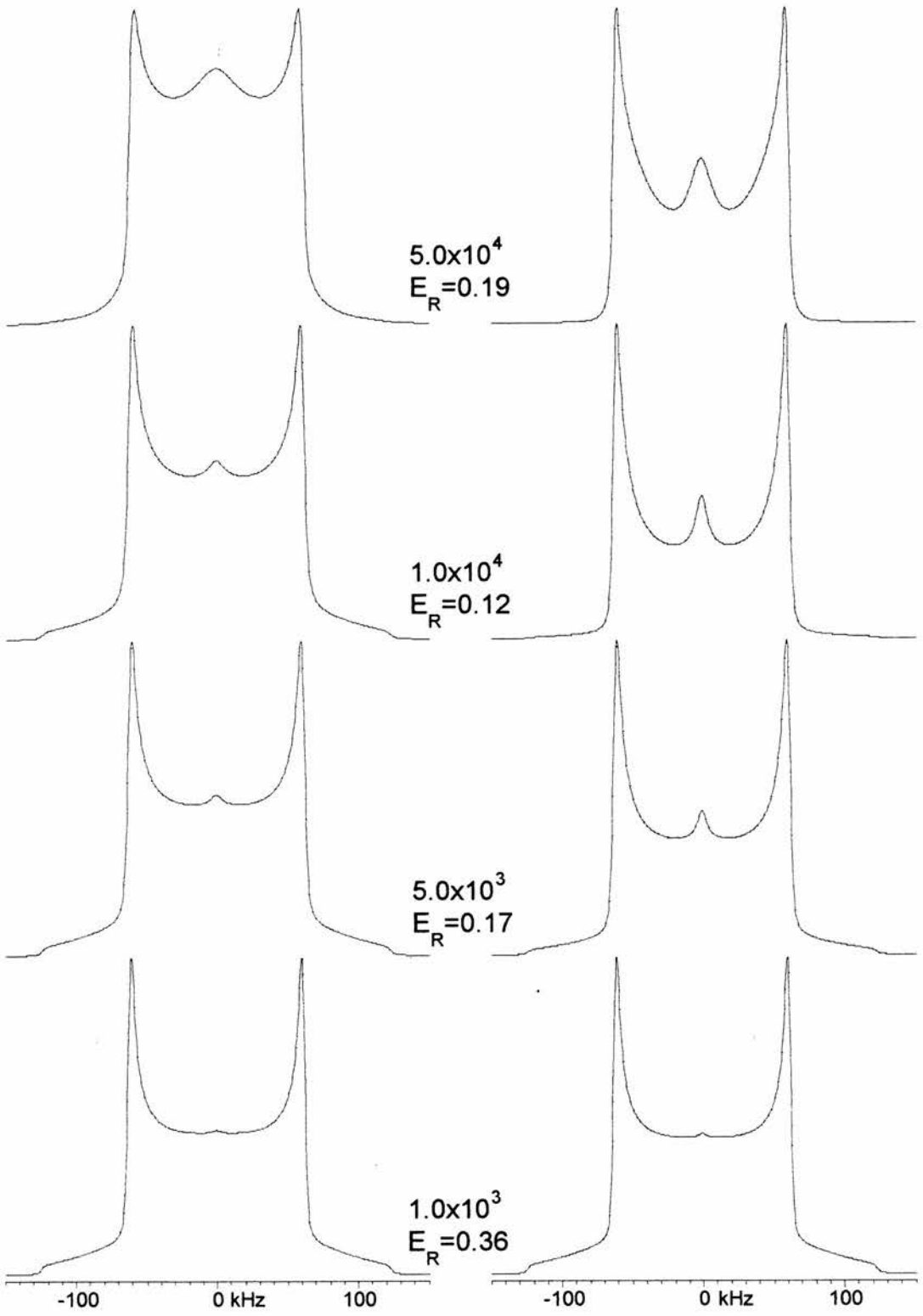

Figure 3.8. Simulated spectra for two-site exchange with a half angle of 54.7° and with populations of 0.1 and 0.9 for the two sites. Refocusing delays are 20 μs (left) and 160 μs (right). 90° pulse length is 3.8 μs. Rate constants (s^{-1}) and echo reduction factors are shown in the figure.

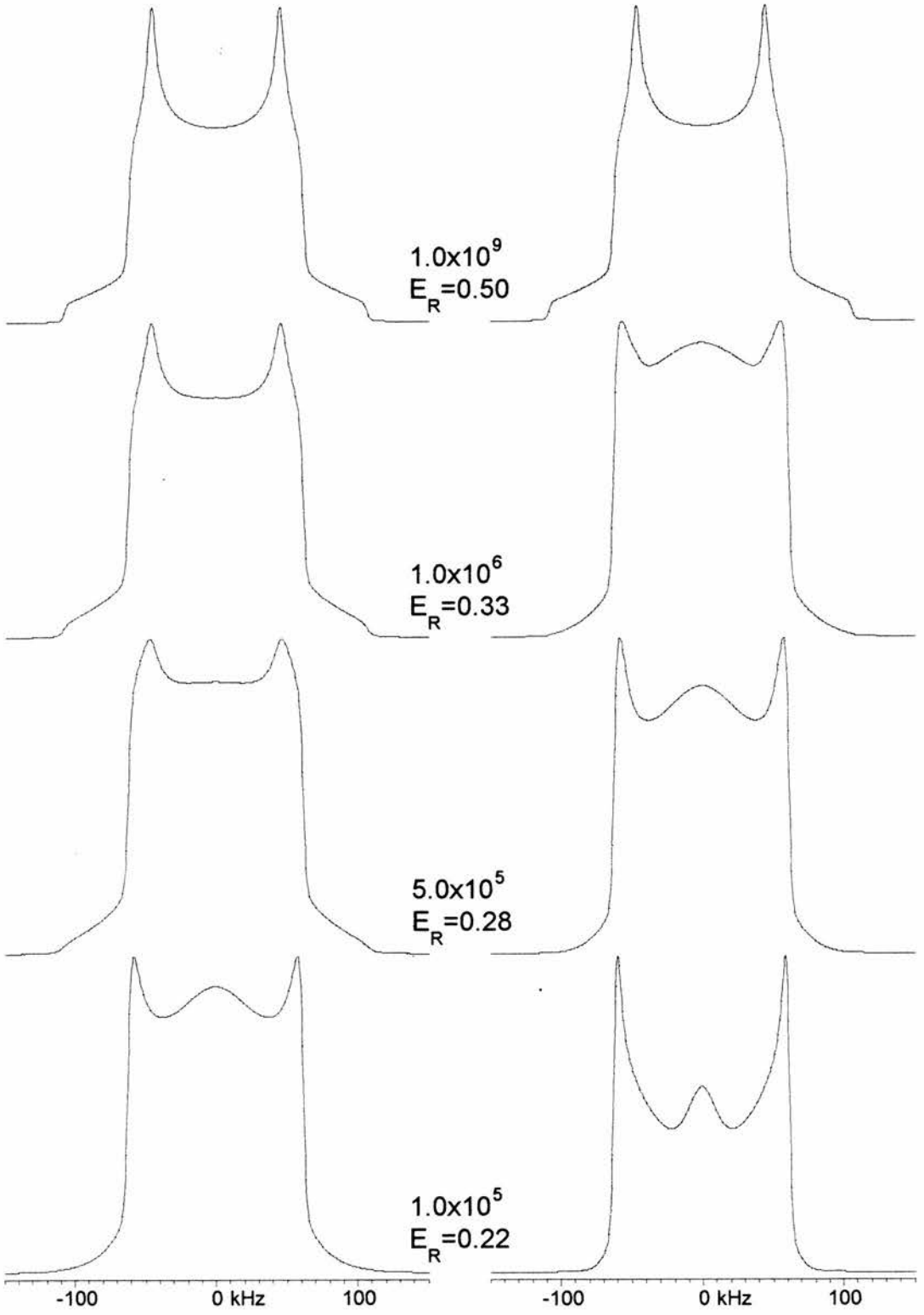

Figure 3.8. (continued) Simulated spectra for two-site exchange with a half angle of 54.7° and with populations of 0.1 and 0.9 for the two sites. Refocusing delays are 20 μs (left) and 160 μs (right). 90° pulse length is 3.8 μs. Rate constants (s^{-1}) and echo reduction factors are shown in the figure.

The ^2H spin-lattice relaxation time is readily calculated for this simple two-site exchange model. The powder average autocorrelation function for a two-site jump of angle 2β with populations P_1 and P_2 is:[67]

$$C_m(t) = \frac{3}{5} P_1 P_2 \sin^2(2\beta) \exp(-t/\tau_c) \tag{3.4.}$$

where $(\tau_c)^{-1} = k_{12} + k_{21}$. Substituting this into eqs. 1.15 and 1.20 gives for the ^2H spin-lattice relaxation rate:

$$R_1 = \frac{1}{T_1} = \frac{9}{10} P_1 P_2 (\pi\chi)^2 \sin^2(2\beta) \left(\frac{\tau_c}{1+\omega_0^2\tau_c^2} + \frac{4\tau_c}{1+4\omega_0^2\tau_c^2} \right) \tag{3.5.}$$

According to eq. 3.5, the spin-lattice relaxation time depends both on the half-angle β and on the correlation time τ_c. Figure 3.9. shows a contour plot of the spin-lattice relaxation time as a function of the half-angle and the correlation time for equal populations and a quadrupolar constant of 165 kHz. The half-angle β in this plot is varied from 0.1° to half of a tetrahedral angle whereas the correlation time is varied from a slow exchange value of 10^{-3} s to a fast exchange value of 10^{-15} s.

The contour plot indicates two important facts. Firstly, spin-lattice relaxation times shorter than 100 s, which are readily measurable, occur between correlation times 10^{-4} and 10^{-14} s. In other words, a C-D bond that is moving slower than 10^4 s^{-1} or faster than 10^{14} s^{-1} is difficult to observe with the basic quadrupolar echo sequence. Secondly, very short spin-lattice relaxation times of the order 10 ms can only be observed if the correlation time is of order of a nanosecond and the half-angle β is larger than 20°. The ^2H spin-lattice relaxation time at the minimum is obtained from:

$$\frac{1}{T_{1,\min}} = \frac{9}{10} P_1 P_2 (\pi\chi)^2 \sin^2(2\beta) \cdot \frac{1.42}{\omega_0} = 178 \cdot \sin^2(2\beta) \tag{3.6.}$$

for equal populations, a quadrupolar constant of 165 kHz and deuteron Larmor frequency of 77 MHz. According to eq. 3.6, the shortest possible ^2H spin-lattice relaxation time for this model is 5.6 ms when the half-angle β equals 45°.

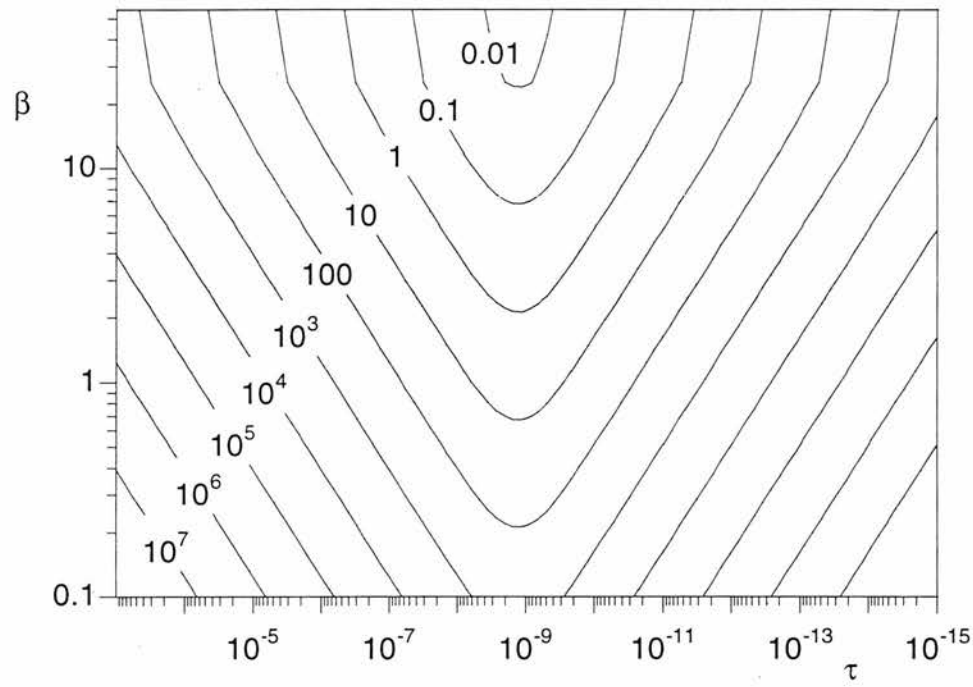

Figure 3.9. Contour plot of ^{2}H spin-lattice relaxation time (T_1) as a function of the half-angle β and the correlation time τ_c for the two-site model. T_1 in seconds is shown in contours. T_1 minimum is at $\tau_c=1.3\cdot10^{-9}$ s.

Jelinski *et al.* used the two-site model with an angle of 103° to describe *trans-gauche* exchange in poly(butylene terephthalate).[62] Hirschinger *et al.*[67] later suspected that the simulated spectra of Jelinski *et al.* had been multiplied by large broadening factors, and therefore, might not reflect the actual motion. Because the repeat unit of poly(butylene terephthalate) is equal to that of the three butanediol derivatives discussed in chapter 5, and therefore, the simulation of Jelinski *et al.* is of great importance, attempts were made to repeat the simulation with the MXET1 program. Figure 3.10 shows spectra simulated with the two-site model using an angle 2β of 103° and experimental values of Jelinski *et al.*, that is, 90° pulse length of 4.3 μs and refocusing delay τ of 30 μs. In addition, the spectra shown on the left were apodised with reasonable broadening factors of 1 kHz Lorentzian and 2 kHz Gaussian broadening whereas the spectra on the right were apodised with large Lorenzian broadening factors from 8 to 30 kHz to reproduce the observed spectra of Jelinski *et al.* Clearly, the details of the original spectra are obscured by these large broadening functions, and therefore, no conclusions about the mechanism of the motion can be made.

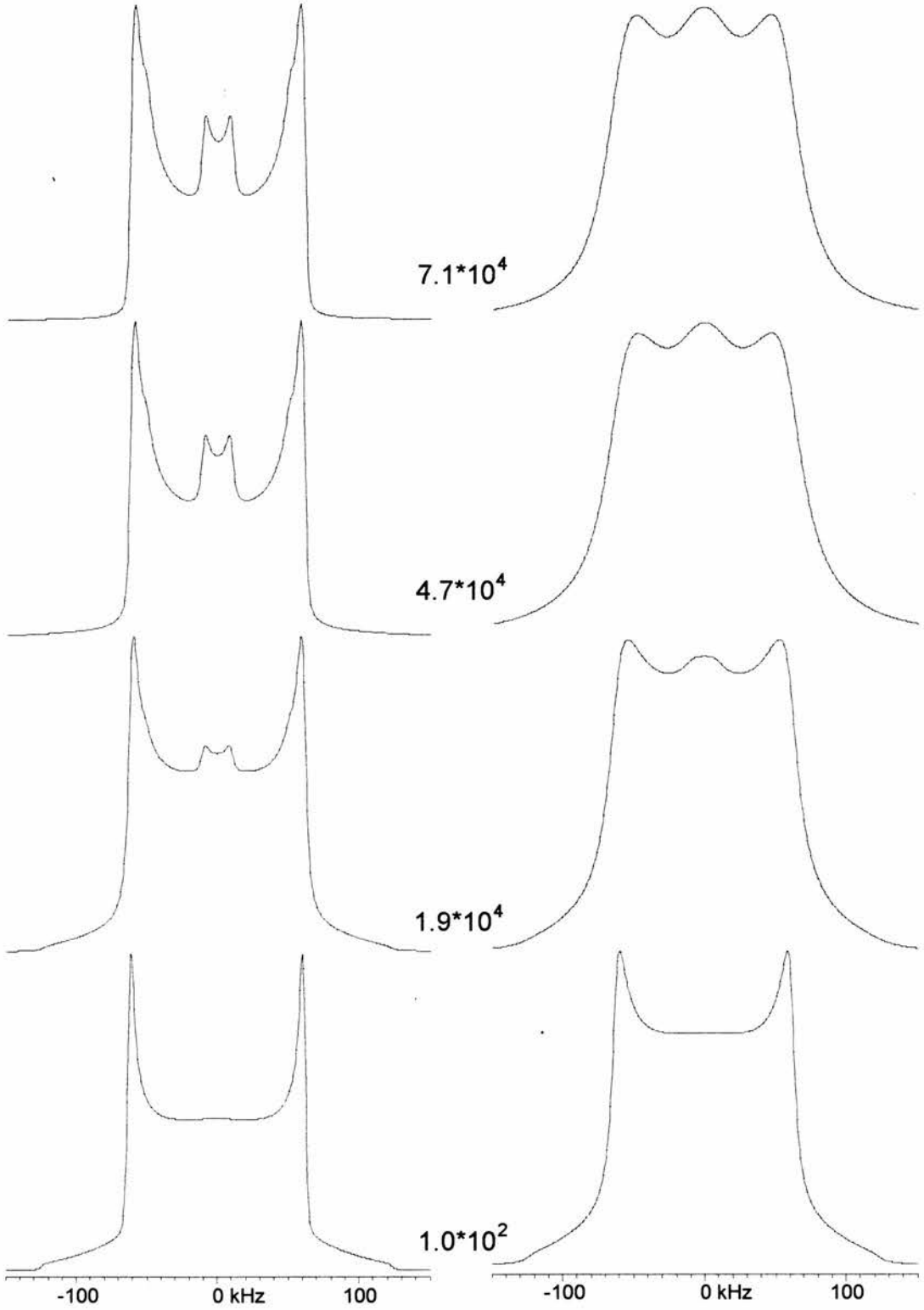

Figure 3.10. Reproduction of spectra of Jelinski *et al.*[62] Rate constants (s^{-1}) are shown in spectra. Before Fourier transformation, the fid was multiplied by 1 kHz of Lorentzian and 2 kHz of Gaussian broadening (left) or by 8, 15, 30 and 30 kHz of Lorenzian broadening (right). The spectra on the right resemble closely those of Jelinski *et al.*[62]

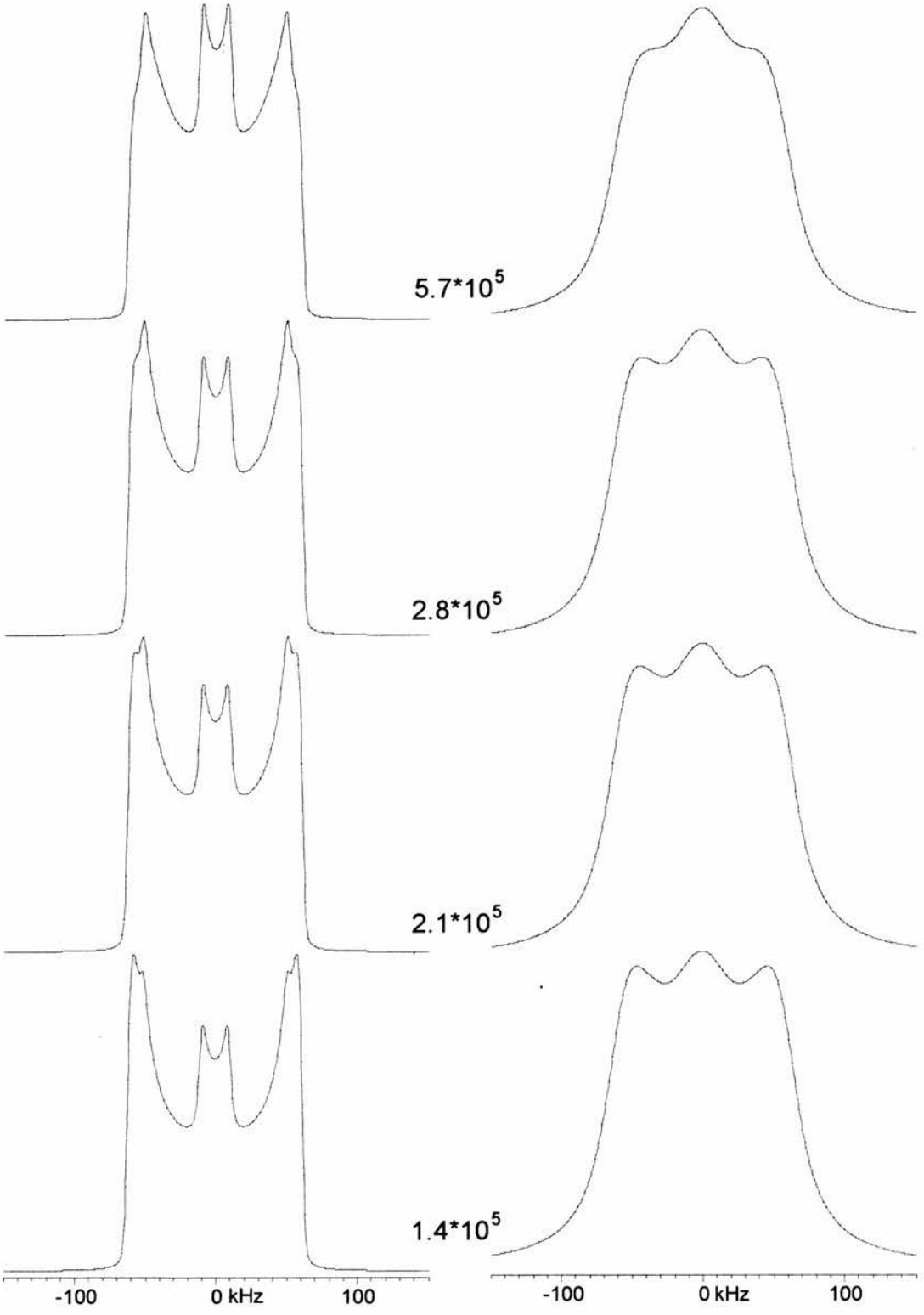

Figure 3.10. (continued) Reproduction of spectra of Jelinski *et al.*[62] Rate constants (s^{-1}) are shown in spectra. Before Fourier transformation, the fid was multiplied by 1 kHz of Lorentzian and 2 kHz of Gaussian broadening (left) or 30 kHz of Lorenzian broadening (right). The spectra on the right resemble closely those of Jelinski *et al.*[62]

3.2. Three-site conical motion

The two-site model describes highly planar motion and produces a totally axially asymmetric (η=1) ^{2}H quadrupolar echo spectrum in the fast exchange limit. On the other hand, conical motion is cylindrically symmetric, and therefore, produces an axially symmetric spectrum in the fast motion limit. The spectrum is readily calculated for a given number of sites on a cone of half-angle β.

Methyl group rotation is a simple three site conical motion involving a C-D bond exchanging between three sites on a cone of half-angle 70.5°. Because the C-D bond is exchanging between three-sites of a tetrahedron, this model also describes *trans-gauche* exchange with equal populations for *trans* and *gauche* conformations.

The Euler angles (table 3.1) for this model are readily obtained in a molecular co-ordinate system where the z-axis is the cone axis. Calculated spectra with different rate constants are shown in figure 3.11. A Pake doublet is observed when the rate constant is smaller than 10^3 s^{-1}. Considerable distortion of the Pake doublet is observed for rate constants larger than 10^3 s^{-1}. Between 10^4 and 10^5 s^{-1}, a triplet appears in the central area of the Pake doublet, and then, the original Pake doublet disappears. When the rate constant exceeds 10^6 s^{-1}, the triplet transforms into a motionally narrowed Pake doublet.

The width, defined as the separation of the 90° orientation spikes, of the motionally narrowed Pake doublet for fast diffusion on a cone of half-angle of 70.5° is given by[82]

$$\Delta = \frac{3}{8}\chi\left|3\cos^2 70.5° - 1\right| = 0.250\chi \qquad (3.7.)$$

The three site model approximates continuous diffusion fairly well. The width of the calculated spectrum is 37 kHz which agrees well with 41 kHz obtained from equation 3.7 using a quadrupolar constant of 165 kHz.

Table 3.1. The Euler angles for methyl group rotation.

Site	ϕ	θ	ψ
1	0	70.5	0
2	120	70.5	0
3	240	70.5	0

Although this model is very simple, the equation for the ^{2}H spin-lattice relaxation time is rather cumbersome.[44] Taking the powder average, however, greatly simplifies the equation. The powder average spin-lattice relaxation time for methyl group rotation can be calculated from equation:[82]

$$\frac{1}{T_1} = \frac{\chi^2}{15}\left[\frac{\tau}{1+\omega^2\tau^2} + \frac{4\tau}{1+4\omega^2\tau^2}\right] \qquad (3.8.)$$

Because motions that average the C-D bond orientation at the magic angle produce very special line shapes, it is interesting to simulate three-site motion on a cone with a half-angle equal to magic angle. Since the conical three-site motion averages the C-D bond orientation about an axis oriented at the magic angle, it is similar to magic angle spinning, and an isotropic peak should be observed in the fast motion limit.

Calculated spectra for different rate constants are shown in figure 3.12. As expected, a spike appears in the centre (zero frequency) of the Pake doublet as the rate constant is increased. Only this isotropic peak is observed in the fast-motion limit. The averaging is more effective for the longer 160 μs refocusing delay. For this delay, the isotropic peak is observed when the rate exceeds 10^4 s^{-1} whereas for the 20 μs delay the isotropic peak is observed for rates faster than 10^5 s^{-1}.

This motion could describe three dimensional librational motion of a C-D bond in a methylene group. However, a six-site cone is the preferred model for this three-dimensional librational motion. Two sites are generated by the libration of the C-D bond about the chain axis, and additional four sites are created by rotations about the C-C bonds in both directions. This model is discussed further in section 3.4.

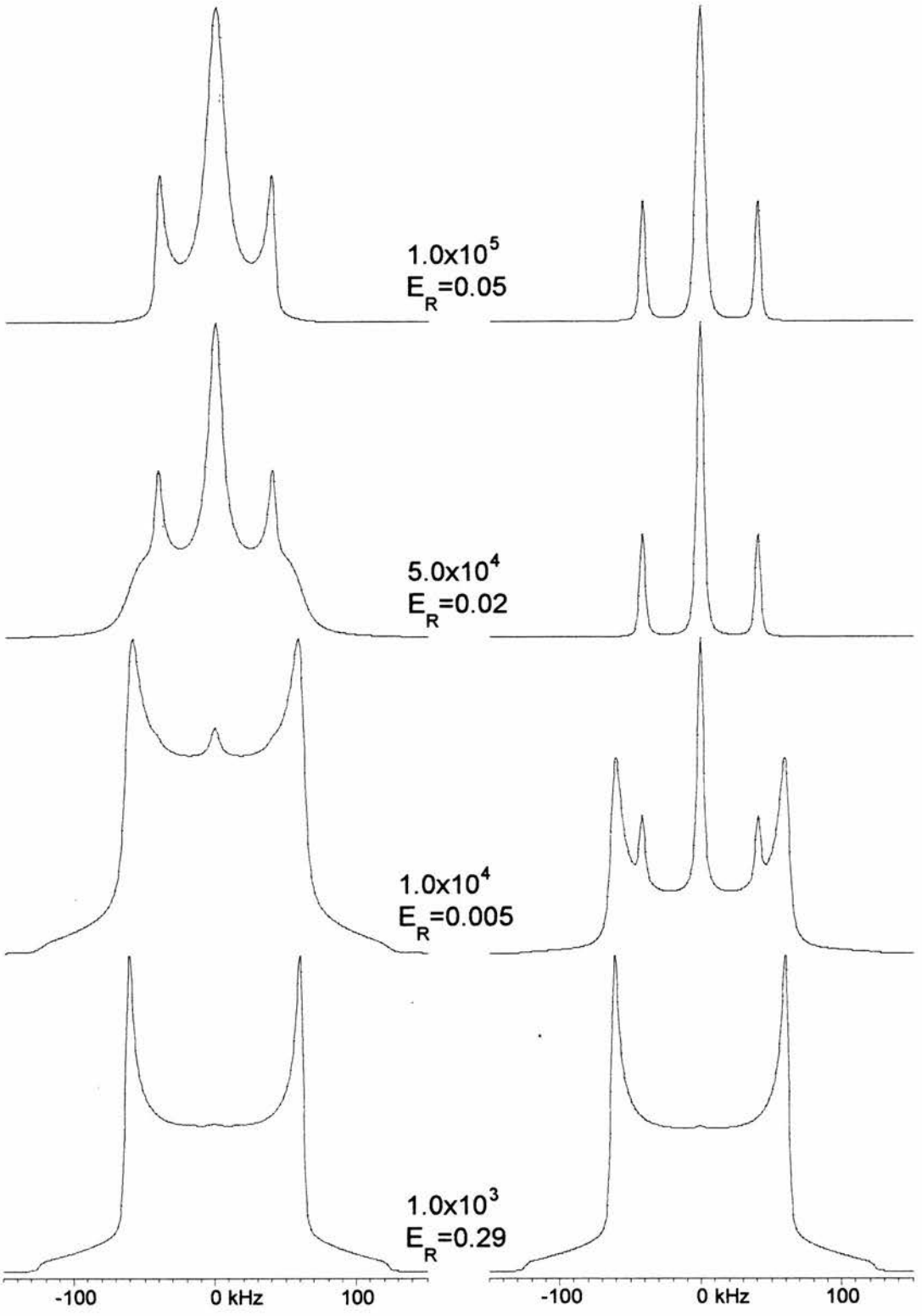

Figure 3.11. Simulations for methyl group rotation. Refocusing delays are 20 μs (left) and 160 μs (right). 90° pulse length is 3.8 μs. Rate constants (s^{-1}) and echo reduction factors are shown in the figure.

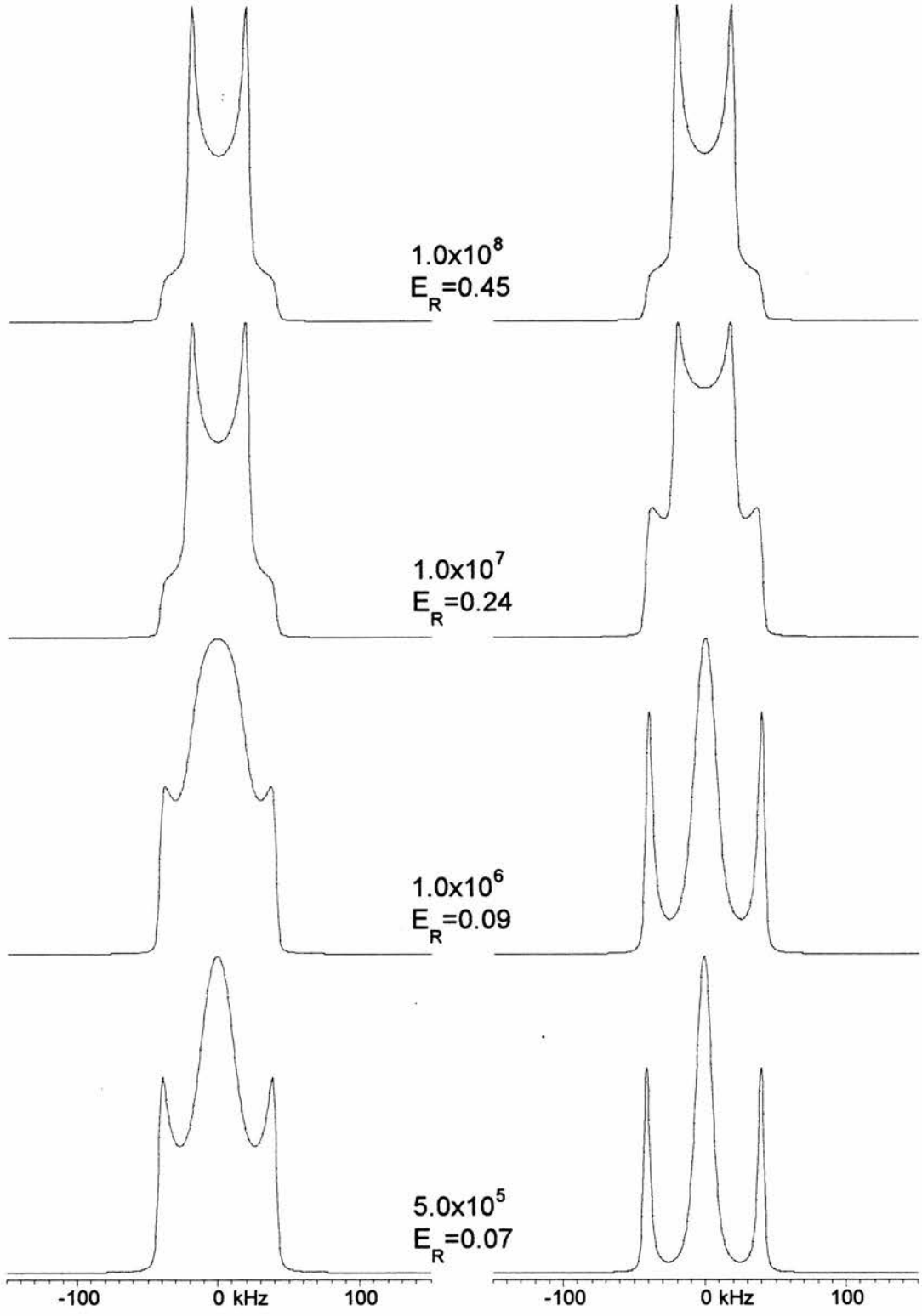

Figure 3.11. (continued) Simulations for methyl group rotation. Refocusing delays are 20 μs (left) and 160 μs (right). 90° pulse length is 3.8 μs. Rate constants (s^{-1}) and echo reduction factors are shown in the figure.

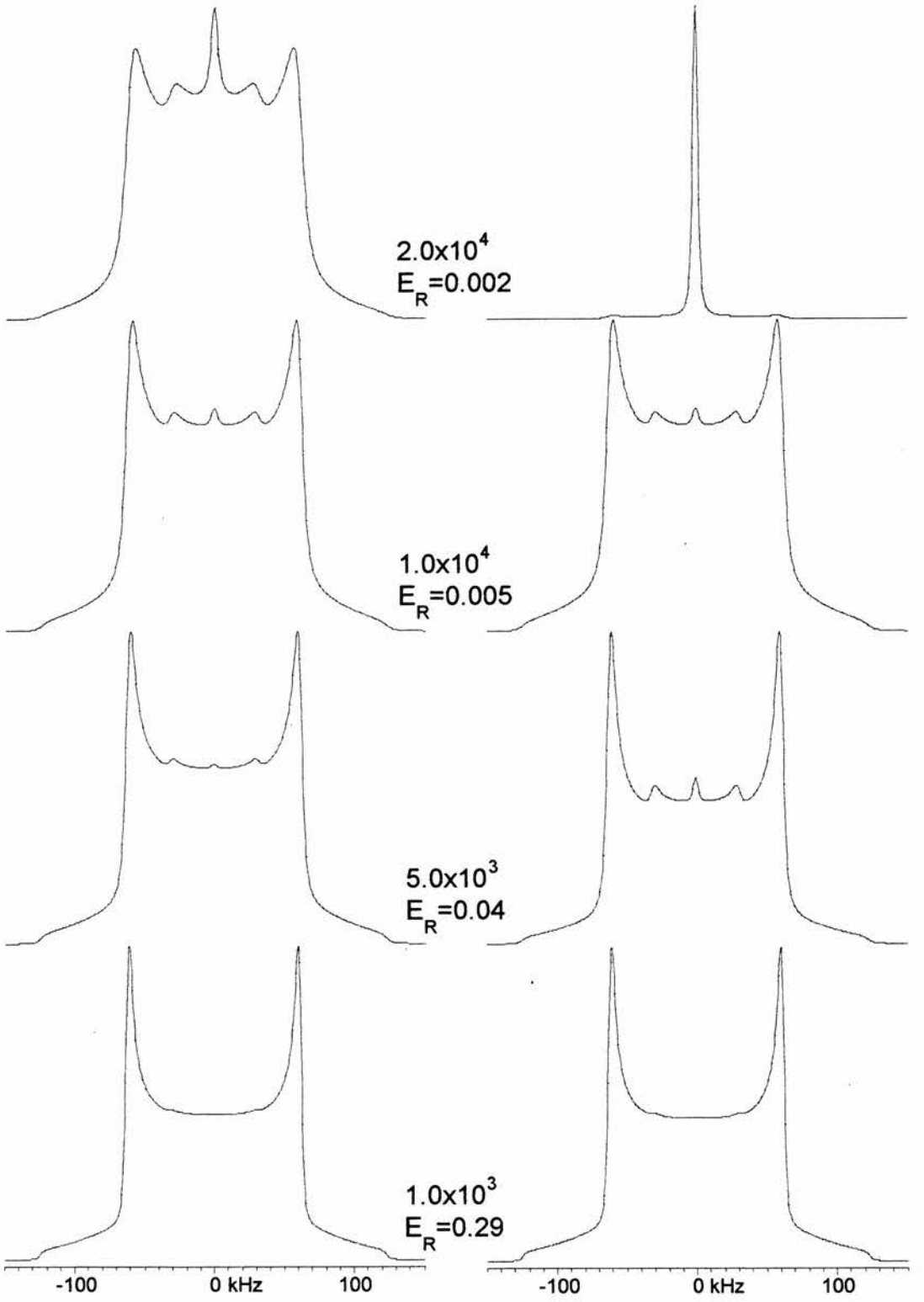

Figure 3.12. Simulations for three sites on a cone of half-angle 54.7°. Refocusing delays are 20 μs (left) and 160 μs (right). 90° pulse length is 3.8 μs. Rate constants (s^{-1}) and echo reduction factors are shown in the figure.

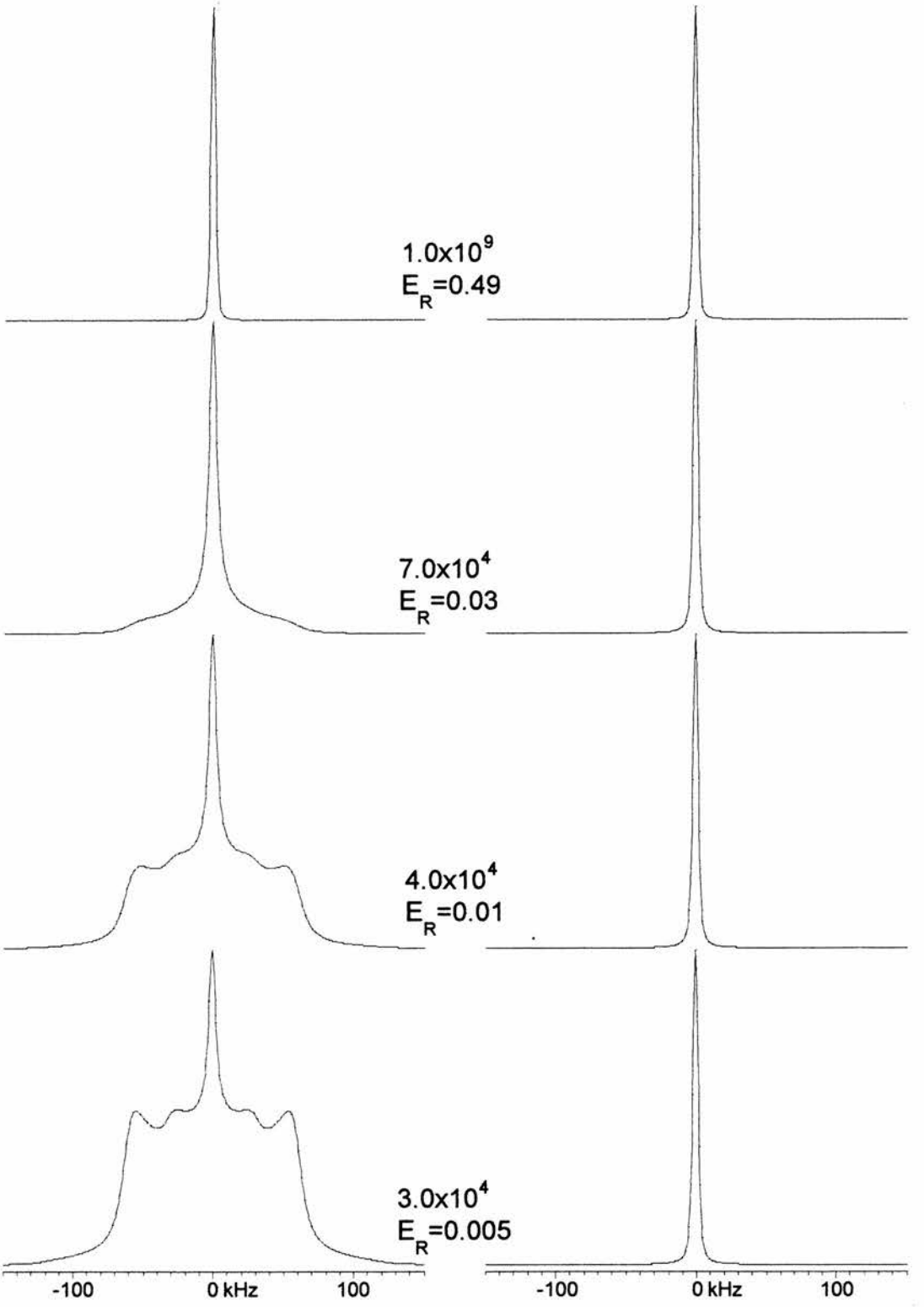

Figure 3.12. (continued) Simulations for three sites on a cone of half-angle 54.7°. Refocusing delays are 20 μs (left) and 160 μs (right). 90° pulse length is 3.8 μs. Rate constants (s^{-1}) and echo reduction factors are shown in the figure.

3.3. Motion in the diamond lattice

Exchange in a diamond lattice, or exchange between all four tetrahedral sites has been widely used to describe molecular motion of polymer chains in solution.[83] In solids, however, the full four site exchange involves large displacements of the polymer tail, and therefore, is more likely in the amorphous phase than in the crystalline phase. Other examples of molecular motion in the diamond lattice are solid D_2O[84] and solid cyclopentane[85].

Euler angles for the four sites in the diamond lattice can be readily obtained if molecular axes are chosen so that the y-axis bisects the D-C-D angle of the methylene group and the z-axis is along the chain axis, that is, perpendicular to y-axis and the two C-D bonds. Euler angles in this co-ordinate system are listed in table 3.2.

Calculated spectra for exchange between the four sites in the diamond lattice with different rate constants are shown in figure 3.13. As expected for averaging over the magic angle, only an isotropic peak remains in the fast motion limit. This limit occurs at a rate constant of *ca.* 10^5 s^{-1}. Interestingly, these line shapes are very similar to those produced by the three site conical motion with the half-angle equal to magic angle. The motional modes are, however, very different. The three site conical motion could represent three-dimensional librational motion that does not require large displacements for the carbon chain whereas the exchange in the diamond lattice requires very large displacements for the chain carbons.

Table 3.2. Euler angles for exchange in the diamond lattice.

Site	ϕ	θ	ψ
1	144.75 (=90+54.75)	90.00	0
2	35.25 (=90-54.75)	90.00	0
3	90.00	215.25 (=270-54.75)	0
4	90.00	324.75 (=270+54.75)	0

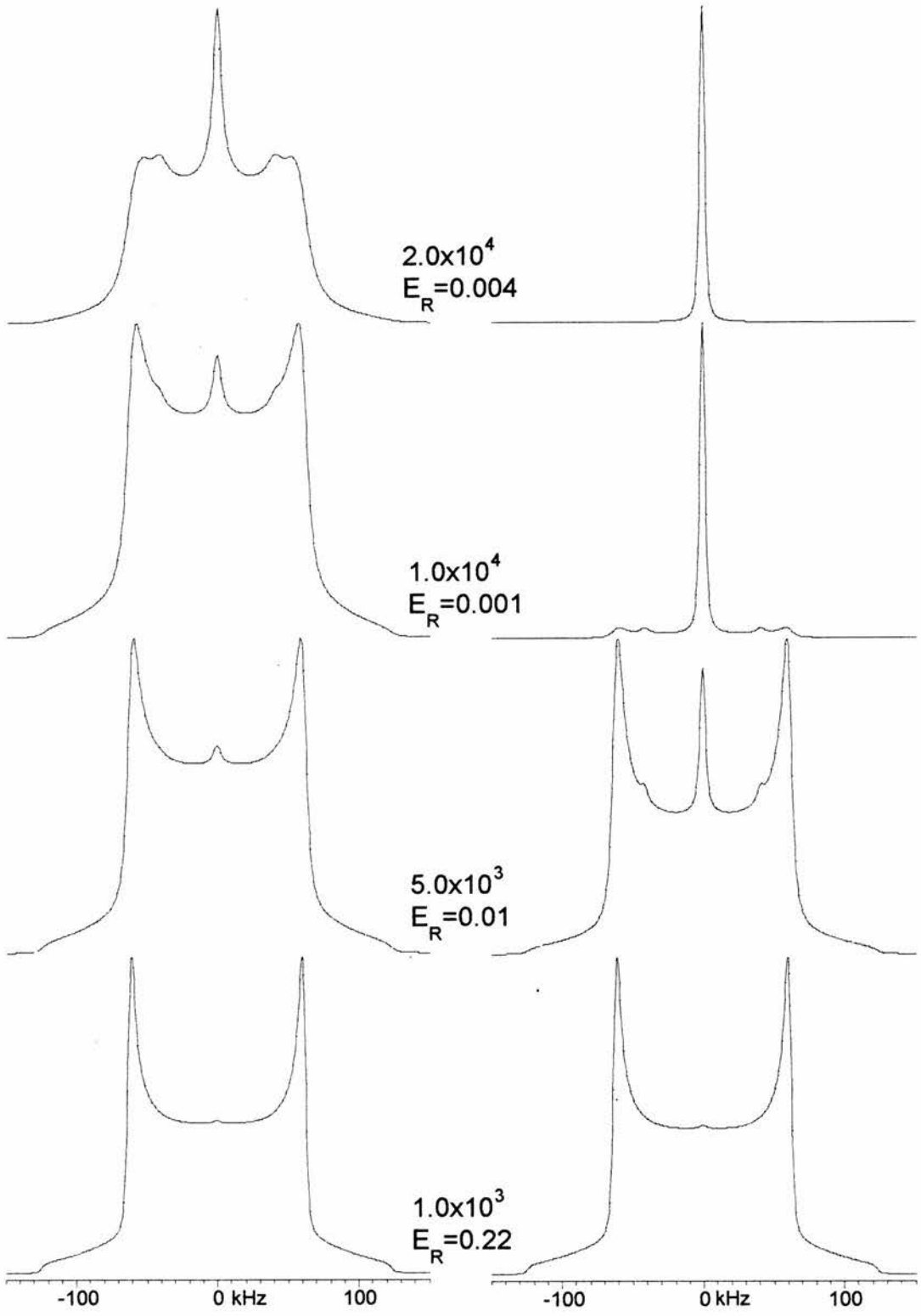

Figure 3.13. Calculated spectra for four site exchange in the diamond lattice. Refocusing delays are 20 μs (left) and 160 μs (right). 90° pulse length is 3.8 μs. Rate constants (s^{-1}) and echo reduction factors are shown in the figure.

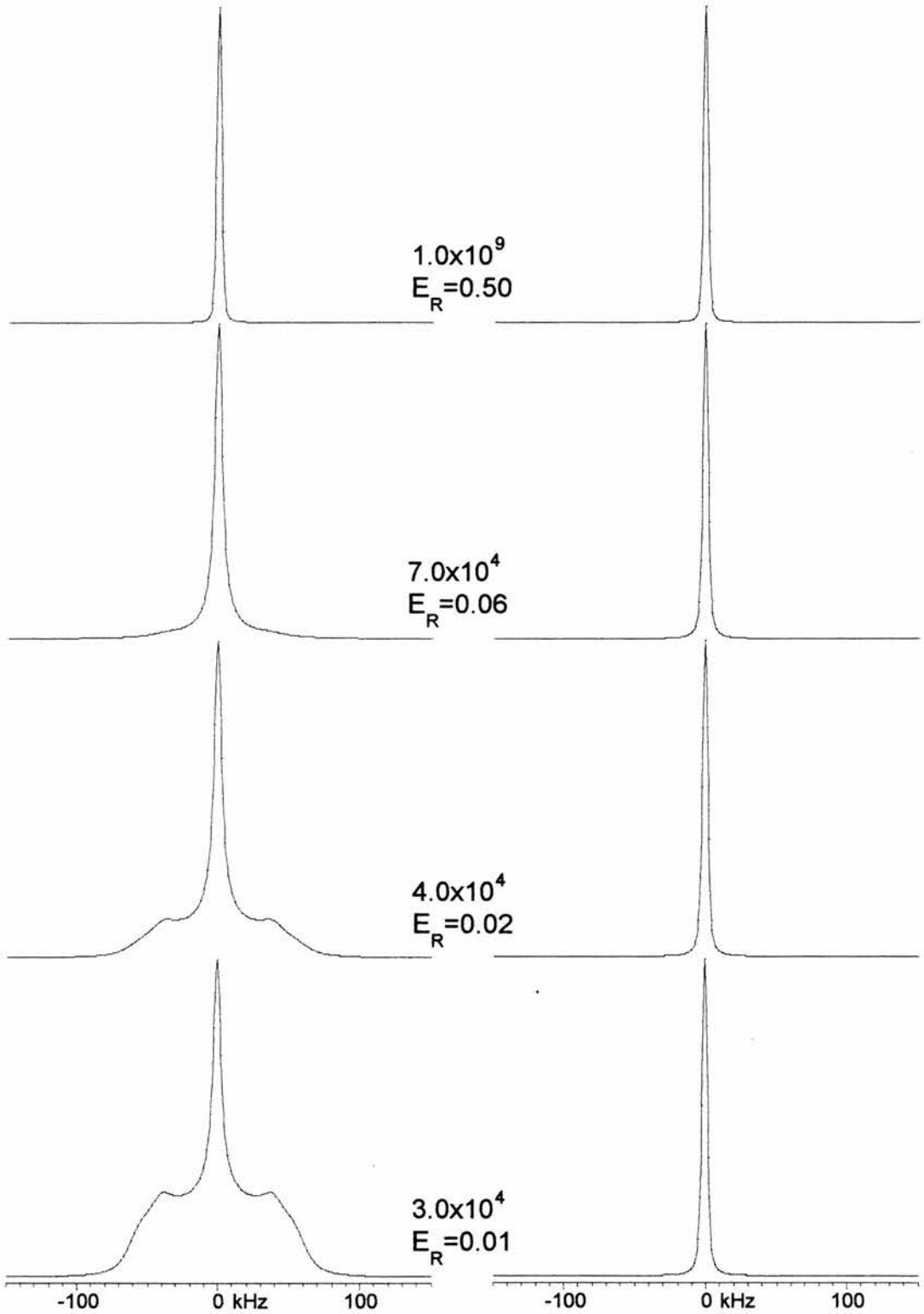

Figure 3.13. (continued) Calculated spectra for four site exchange in the diamond lattice. Refocusing delays are 20 μs (left) and 160 μs (right). 90° pulse length is 3.8 μs. Rate constants (s^{-1}) and echo reduction factors are shown in the figure.

Three-site exchange in the diamond lattice describes *trans-gauche* exchange about one carbon-carbon bond. Table 3.3 assigns Euler angles to different conformations. It should be mentioned again that if the *trans*-site can only exchange with one *gauche* site, this model is equal to the two-site exchange model with 2β equal to 109.5°. On the other hand, if all three sites can exchange with each other and all sites have equal populations, this model is equal to methyl group rotation.

As it is unlikely that the *trans* and *gauche* conformations would occur with equal probabilities, non-equal populations for the *trans* and *gauche* conformations are used in this model. It is also assumed that the *trans*-site can exchange with either of the two *gauche* sites but the *gauche* sites can not exchange with each other. This can be obtained with an exchange matrix

$$\mathbf{K} = \begin{pmatrix} -k_{21} & k_{12} & 0 \\ k_{21} & -(k_{12}+k_{32}) & k_{23} \\ 0 & k_{32} & -k_{23} \end{pmatrix} \qquad (3.9.)$$

where k is the rate constant. Calculated spectra for populations of 0.25, 0.5 and 0.25 for *gauche* (site1), *trans* (site 2) and *gauche* (site 3) conformations, respectively, and for different rate constants are shown in figure 3.14.

The rate constants shown in the figure are for the exchange from *trans* to *gauche*, that is, rate constants k_{12} and k_{32} of equation 3.9. The other two rate constants are twice larger to fulfil the principle of microscopic reversibility. The changes in the line shape are very similar to those for the methyl group rotation (corresponding equal populations of 0.33 for each site). The main difference is that an axially asymmetric spectrum rather than a motionally narrowed Pake doublet is observed in the fast exchange limit.

Table 3.3. Euler angles for three-site *trans-gauche* exchange.

Site	ϕ	θ	ψ
1 (gauche)	90.00	215.25	0
2 (trans)	144.75	90	0
3 (gauche)	35.35	90	0

Different line shape changes are observed, however, if the populations of the *gauche* sites are reduced to 0.05 leaving 0.9 for the *trans* site. Spectra simulated with these populations are shown in figure 3.15. For small rate constants, a spike grows in the centre of the spectrum. For a rate constant of *ca.* 10^5 s^{-1}, the central area of the 20 μs spectrum has nearly filled in and the 20 μs spectrum for a rate constant of 10^6 s^{-1} is domelike.

The 20 μs spectrum for a rate constant of 10^6 s^{-1} is very similar to that observed for 2,2,5,5-d_4-hexane-1,6-diyl bis(*p*-nitrobenzoate) at 250 K in the diester series (chapter 5). Although the simulated and measured spectra for the 20 μs refocusing delay match reasonably well, and therefore, could be taken as evidence for *trans-gauche* exchange, the spectra fail to match for the 160 μs delay. In the simulated spectra, the central dome is more pronounced in the spectrum measured with the 160 μs delay whereas in the observed spectrum the dome is more pronounced in the spectrum measured with the 20 μs delay. Furthermore, the simulated spectrum for a rate constant of 10^7 s^{-1} and 20 μs refocusing closely resembles the 160 μs spectrum observed for the 2,2,5,5-d_4-hexane-1,6-diyl bis(*p*-nitrobenzoate) at 250 K whereas the simulated spectrum for the 160 μs delay resembles the observed 20 μs spectrum. This clearly demonstrates that no conclusions about the mechanism of molecular motion can be made if ^2H quadrupolar echo spectra are measured with only one refocusing delay.

Obviously, there is a large number of different combinations of populations for the *trans-gauche* exchange model, but the observed spectra shown in chapters 4 and 5 could not be simulated using the *trans-gauche* model. In addition, none of the crystal structures for the diacids nor the diesters showed evidence of large scale displacements required by the *trans-gauche* model. Therefore, a librational model similar to that of Hirschinger *et al.*[67] was considered to be more adequate. After introducing a basic six-site librational model in the next section, this model is discussed in section 3.5.

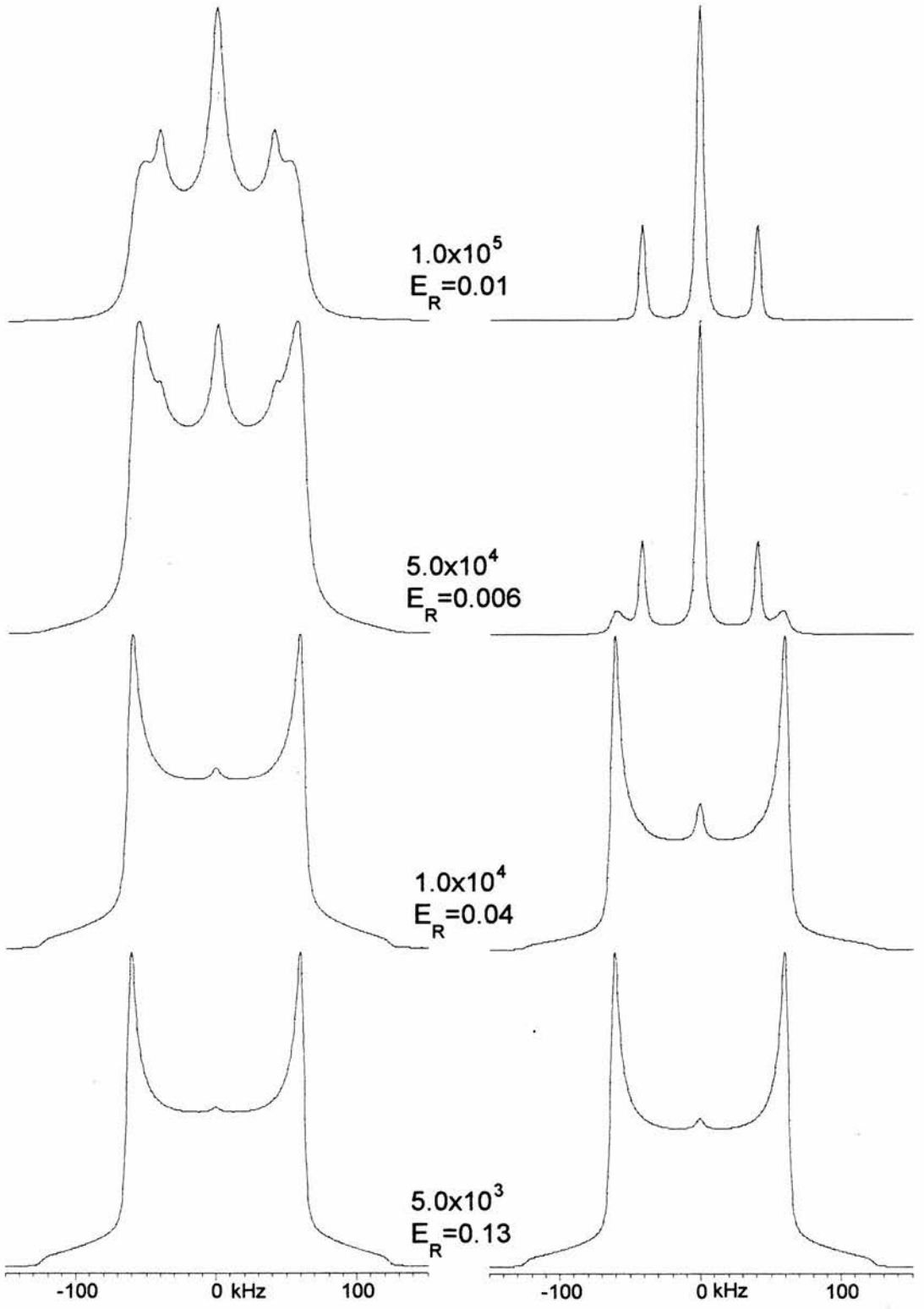

Figure 3.14. Simulations for three-site *trans-gauche* exchange model with 25 % of *gauche* and 50 % of *trans*. Refocusing delays are 20 μs (left) and 160 μs (right). 90° pulse length is 3.8 μs. Rate constants (s^{-1}) and echo reduction factors are shown in the figure.

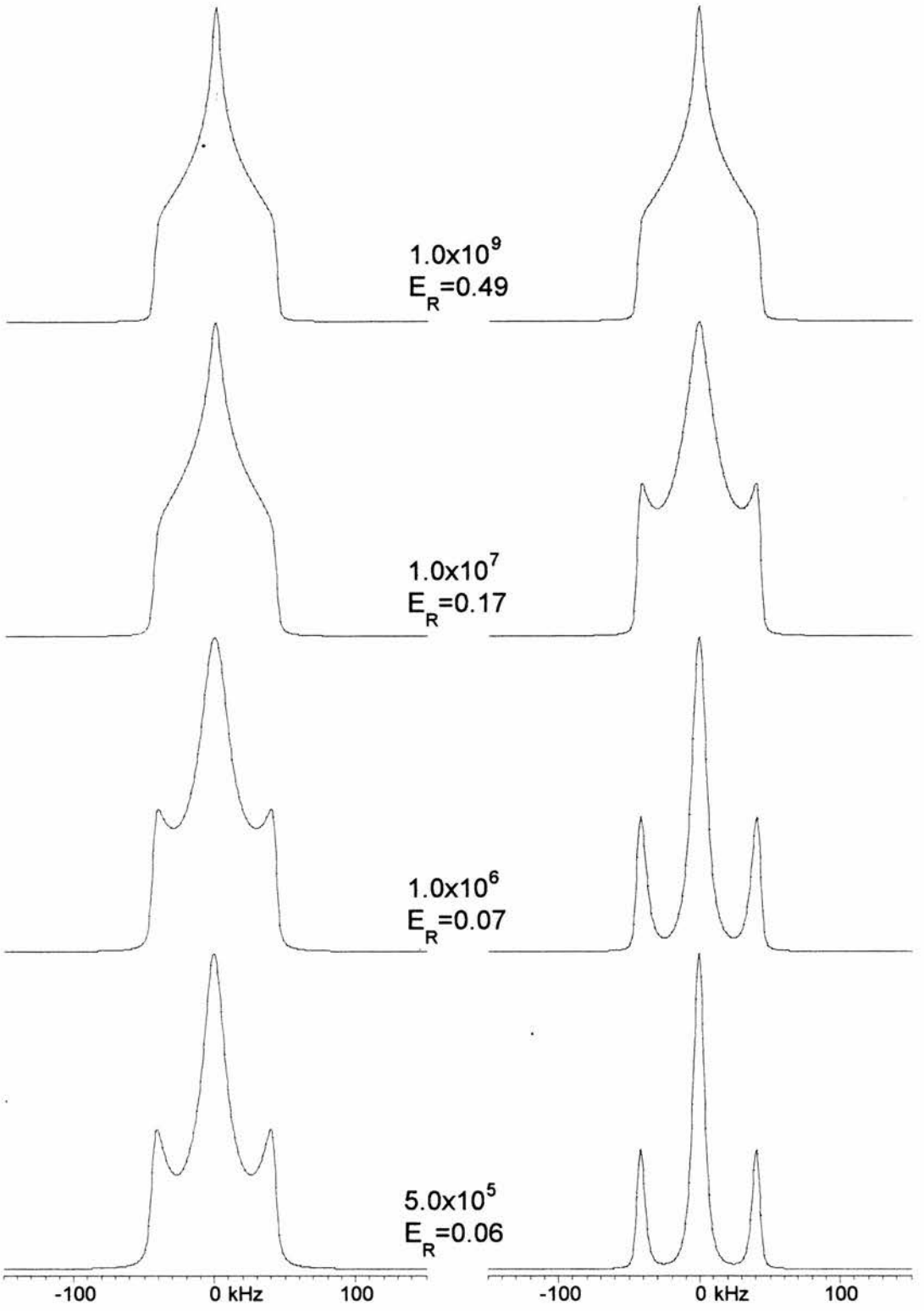

Figure 3.14. (continued) Simulations for three-site *trans-gauche* exchange model with 25 % of *gauche* and 50 % of *trans*. Refocusing delays are 20 μs (left) and 160 μs (right). 90° pulse length is 3.8 μs. Rate constants (s^{-1}) and echo reduction factors are shown in the figure.

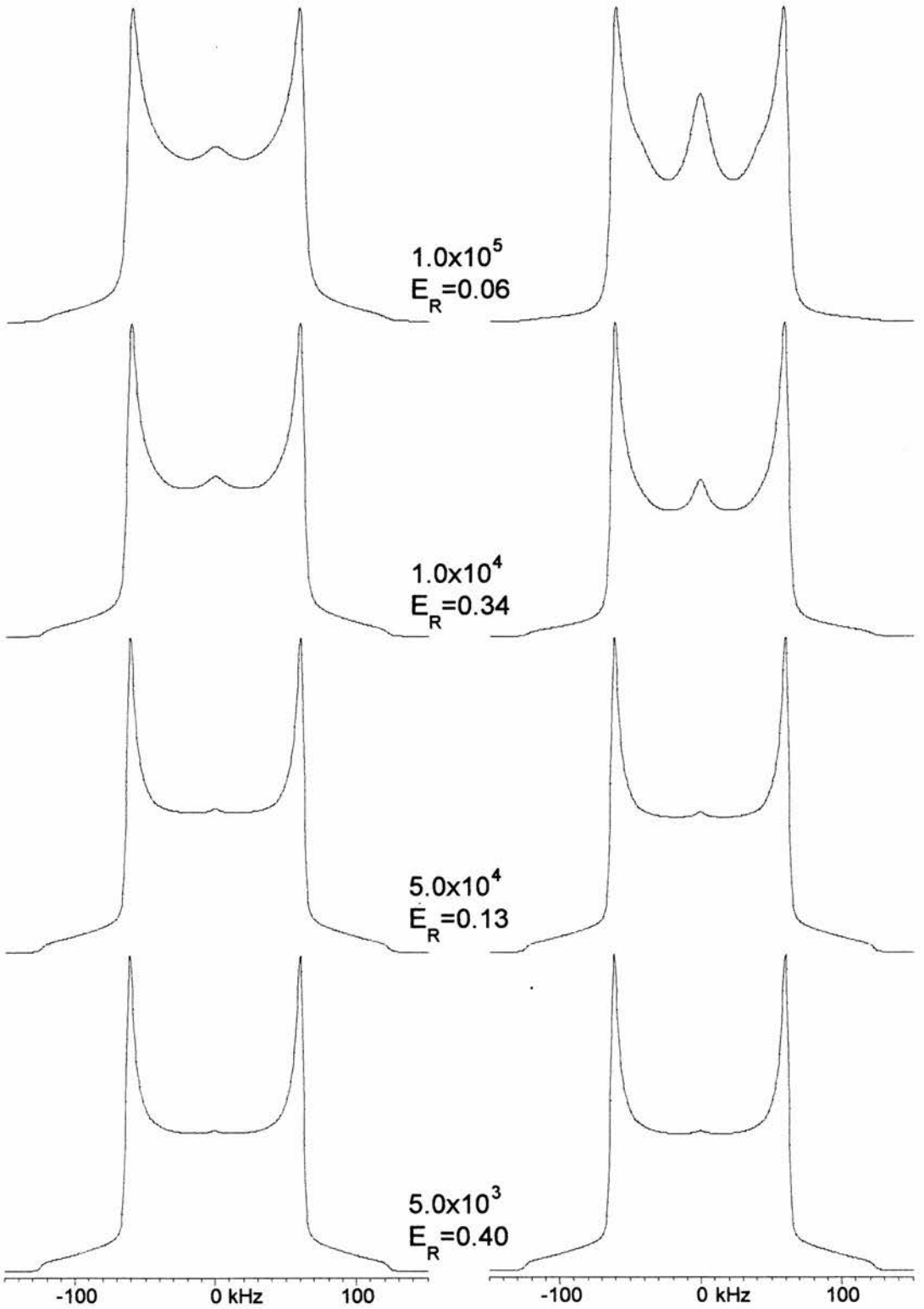

Figure 3.15. Simulated spectra for *trans-gauche* exchange with 5 % of *gauche* and 90 % of *trans*. Refocusing delays are 20 μs (left) and 160 μs (right). 90° pulse length is 3.8 μs. Rate constants (s^{-1}) and echo reduction factors are shown in the figure.

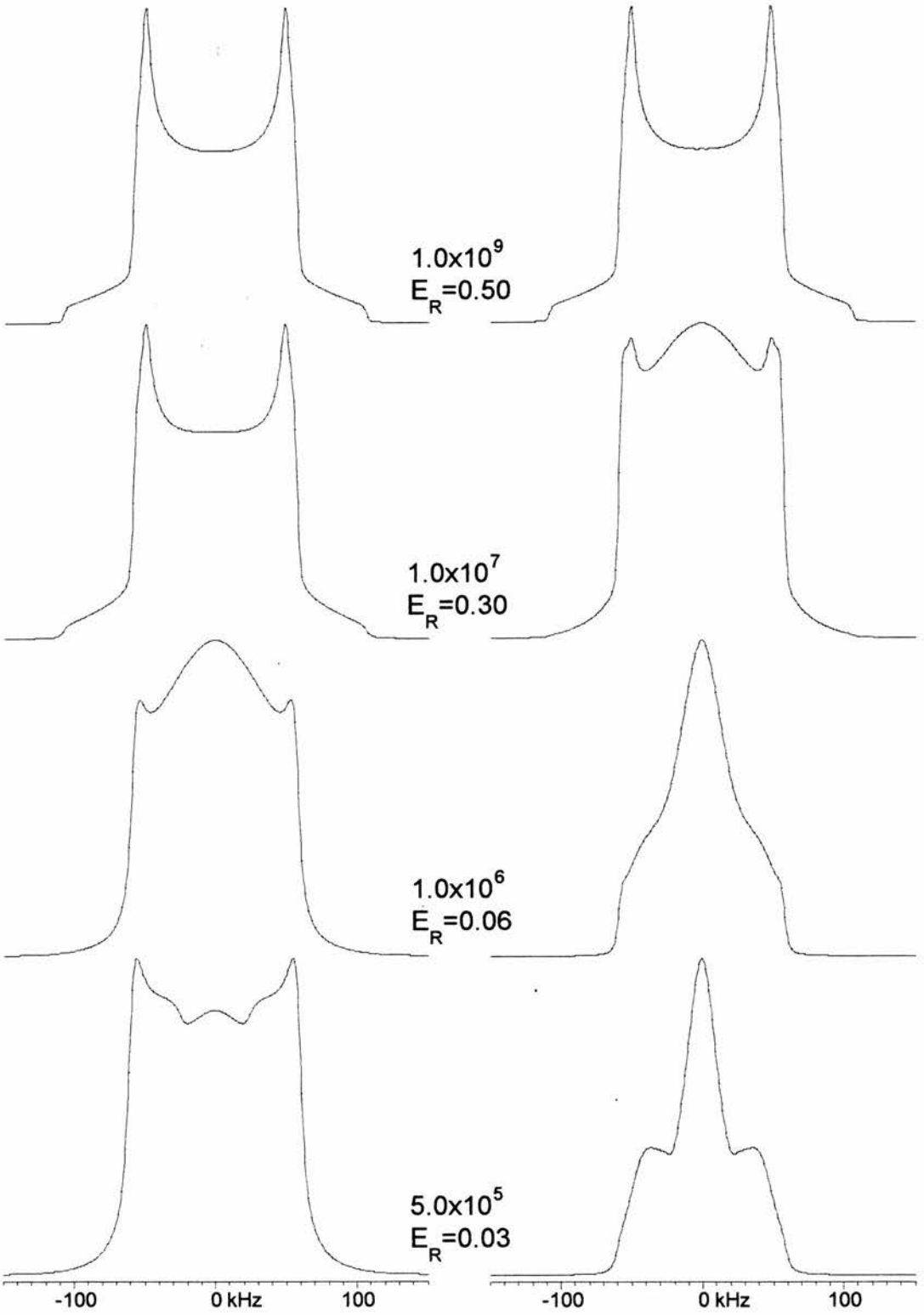

Figure 3.15. (continued) Simulated spectra for *trans-gauche* exchange with 5 % of *gauche* and 90 % of *trans*. Refocusing delays are 20 μs (left) and 160 μs (right). 90° pulse length is 3.8 μs. Rate constants (s^{-1}) and echo reduction factors are shown in the figure.

3.4. Six-site conical motion

As was mentioned in section 3.2, a six-site cone is preferred over the three site cone to describe three dimensional libration of a C-D bond in a methylene group. Two of the six sites originate from libration of the chain about its chain axis (fig. 3.16, left) or from simultaneous rotation of the two C-C bonds is opposite directions, and the other four sites are generated by rotations of the two C-C bonds in both directions (fig. 3.16, right). These rotations are assumed to be restricted within half of the tetrahedral angle in each direction because larger rotations would result in *trans-gauche* exchange that was discussed in previous sections. Rotation of one C-C bond by half of a tetrahedral angle would require *ca.* 1 Å displacement for the other carbon atom bonded to the methylene group. However, since this three dimensional libration occurs simultaneously in all the chain carbons, only half of that displacement, *ca.* 0.5 Å, is required for the chain carbons.

Although the sites on the cone produced with rotations of fig. 3.16 are not equally spaced, this random librational motion is modelled as a motion on a six-site cone with a half-angle β and with all the sites 60° apart from each other to facilitate calculations. This model serves mainly as a basis for the distributional model of section 3.5, and therefore, the line shape simulations would be difficult without a supercomputer if this basic motion was made more complex. The Euler angles for this model are shown in table 3.4. As this model describes random three dimensional libration of the C-D bond, an exchange model where all sites exchange with all the other sites was chosen.

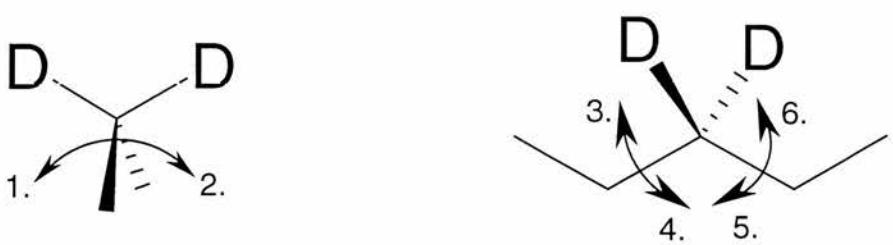

Figure 3.16. The origin of the six-site conical motion. Two sites are generated by libration of the chain about its axis (left), or equally, by a simultaneous rotation of the two bonds in different directions. The other four sites are obtained by rotations of the two C-C bonds in both directions (right).

Table 3.4. Euler angles for the six-site conical motion.

Site	ϕ	θ	ψ
1	0	β	0
2	60	β	0
3	120	β	0
4	180	β	0
5	240	β	0
6	300	β	0

Figures 3.17-3.20 show quadrupolar echo spectra simulated for all sites exchange with different half angles β and for different rate constants *k*. When the half-angle is 1.0 degree, small decrease in the intensity of central region of the spectrum is observed for rate constants from 10^3 to 10^4 s^{-1}. These spectra are practically indistinguishable from the spectra for the two-site model. For larger half-angles, however, the decrease in the central area of the spectrum is more severe than for the two-site model.

In the spectrum simulated for a half angle of 5.0 degrees, rate constant of 10^4 s^{-1} and a refocusing delay of 160 μs, the intensity of the central area is nearly zero and only two peaks remain for the 90° orientations. For a half-angle of 20.0 degrees, even the 90° orientation spikes are reduced to nearly zero in the 160 μs spectrum, but spikes are observed at the first turning point of the spectrum. The echo reduction factors shown in the figure indicate, however, that the intensity of the spectra for the 160 μs delay is nearly zero for rate constants of the order 10^4 s^{-1}, and therefore, these spectra are difficult to observe.

When the half-angle equals the magic angle (fig. 3.20), the spectra are again very different. A spike grows in the centre of the spectrum as the rate constant is increased. For rate constants larger than *ca.* 10^5 s^{-1}, only this isotropic peak remains. The changes in the line shape are very similar to those for the exchange in the diamond lattice, and therefore, these two models are difficult to distinguish from each other. In the next section, this six-site cone model is used as a basis for a model involving a distribution of librational angles.

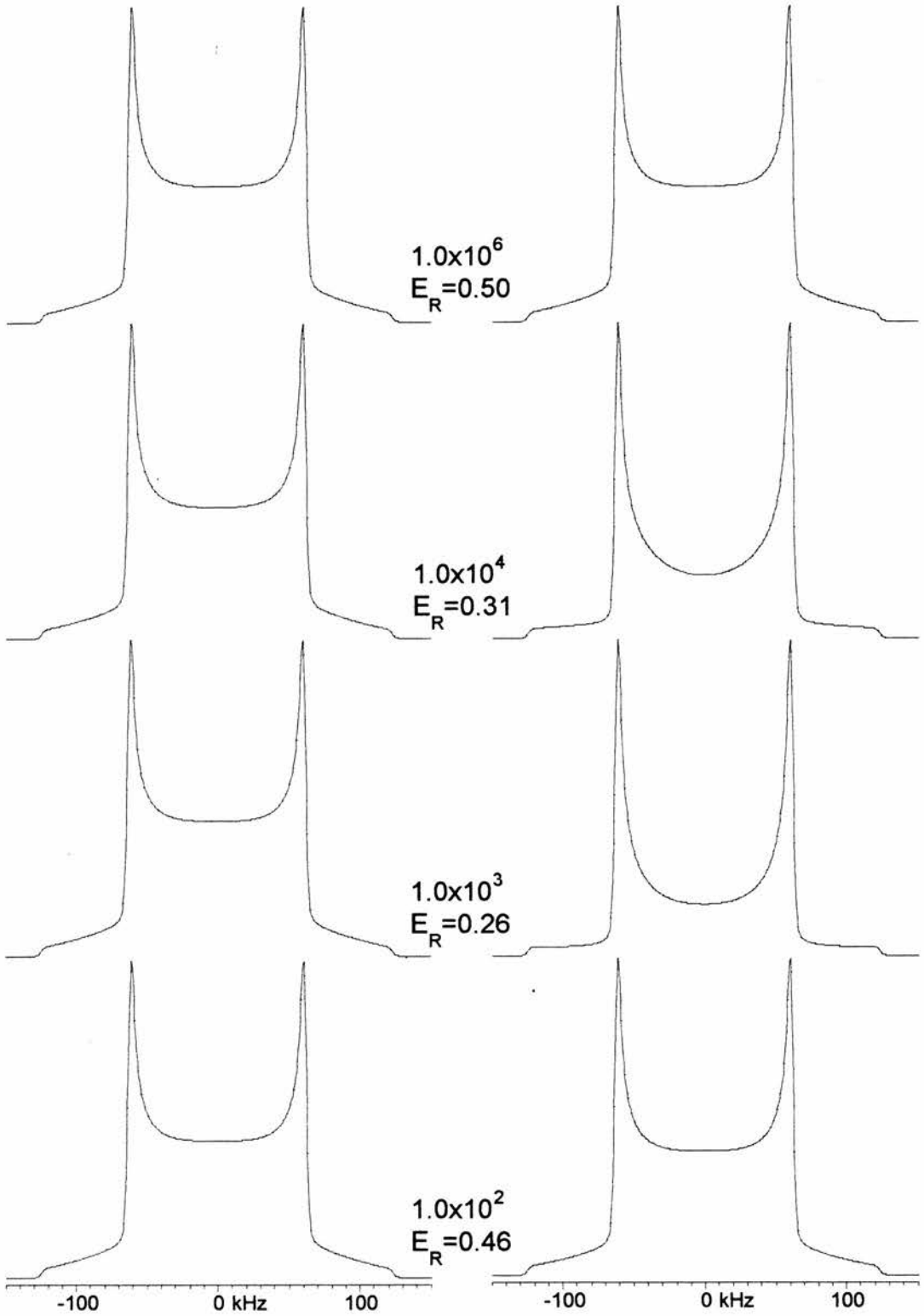

Figure 3.17. Simulated spectra for conical six-site motion with a half-angle of 1.0 degree. Refocusing delays are 20 μs (left) and 160 μs (right). 90° pulse length is 3.8 μs. Rate constants (s^{-1}) and echo reduction factors are shown in the figure.

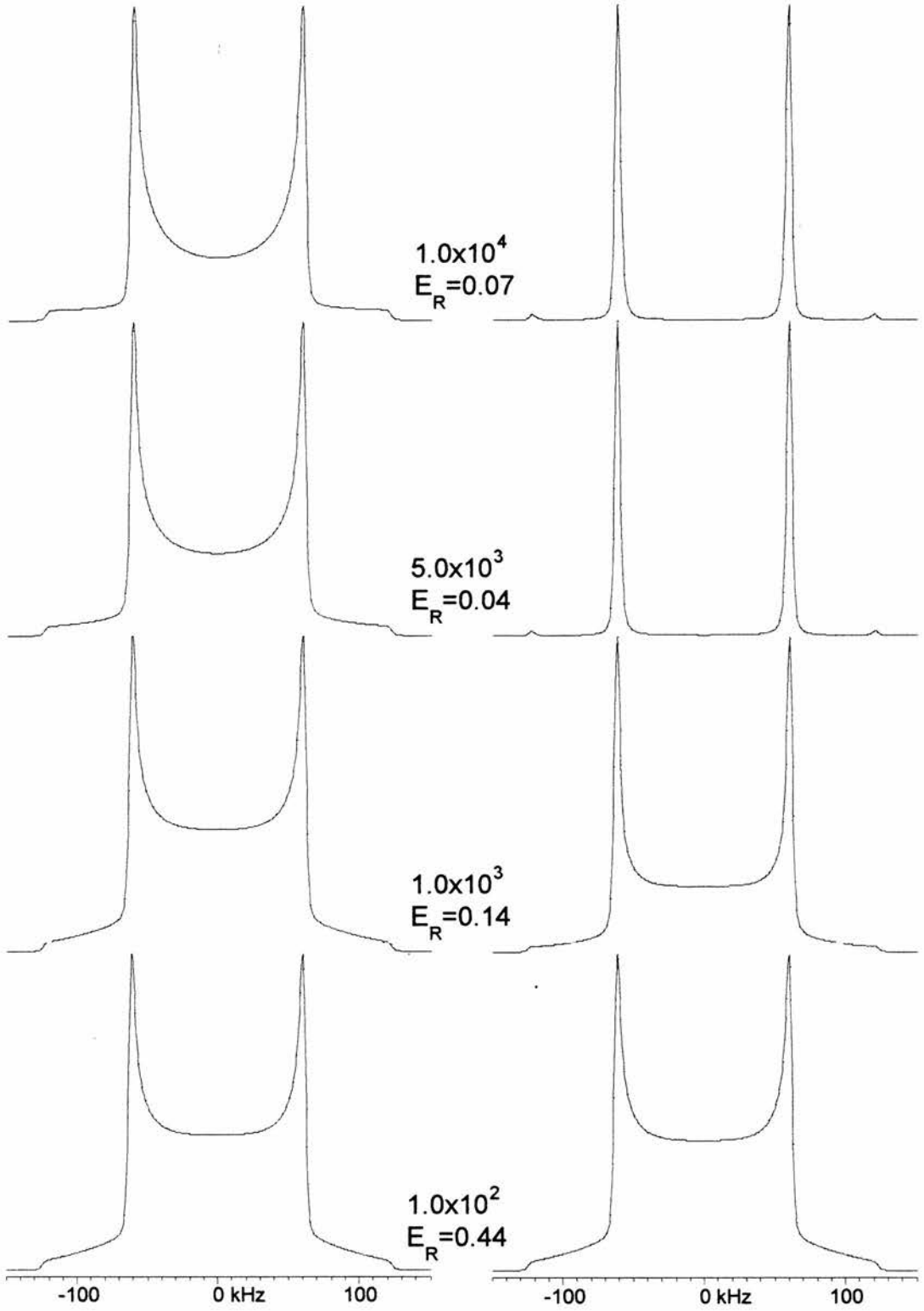

Figure 3.18. Simulations for cone motion of 5.0 degrees half-angle and all-sites exchange. Refocusing delays are 20 μs (left) and 160 μs (right). 90° pulse length is 3.8 μs. Rate constants (s^{-1}) and echo reduction factors are shown in the figure.

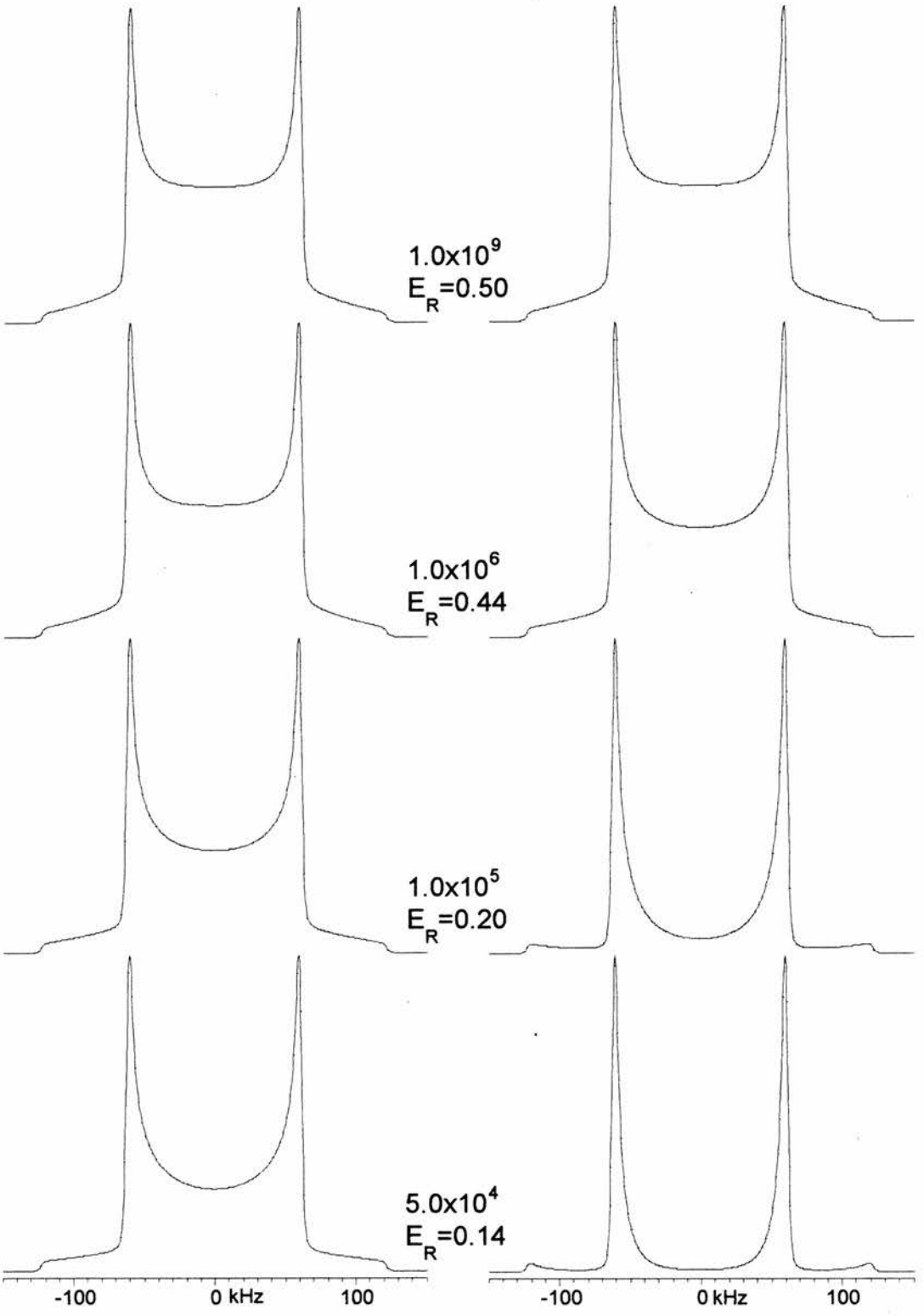

Figure 3.18. (continued). Simulations for cone motion of 5.0 degrees half-angle and all-sites exchange. Refocusing delays are 20 μs (left) and 160 μs (right). 90° pulse length is 3.8 μs. Rate constants (s^{-1}) and echo reduction factors are shown in the figure.

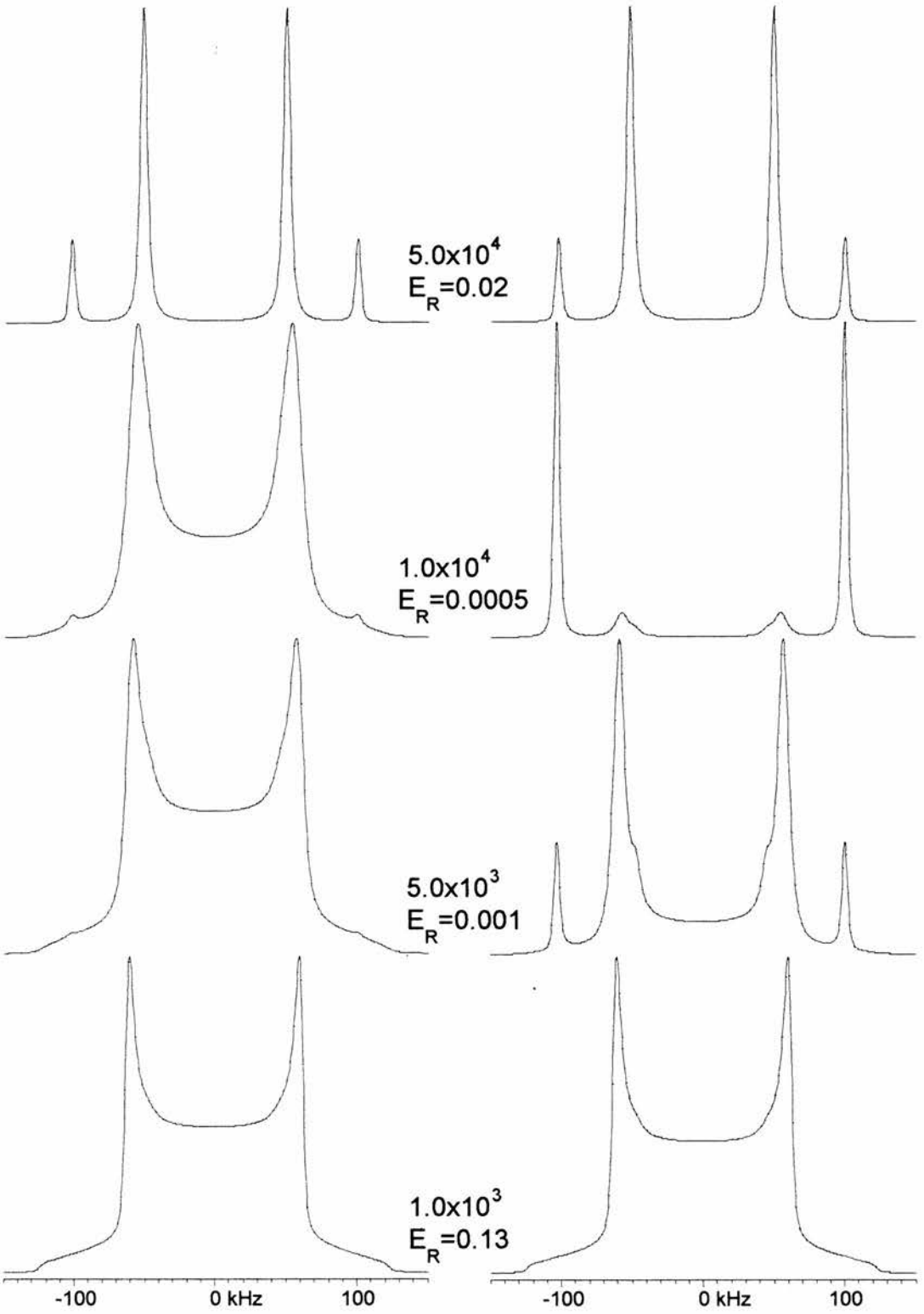

Figure 3.19. Simulations for cone motion of 20 degrees half-angle and all-sites exchange. Refocusing delays are 20 μs (left) and 160 μs (right). 90° pulse length is 3.8 μs. Rate constants (s^{-1}) and echo reduction factors are shown in the figure.

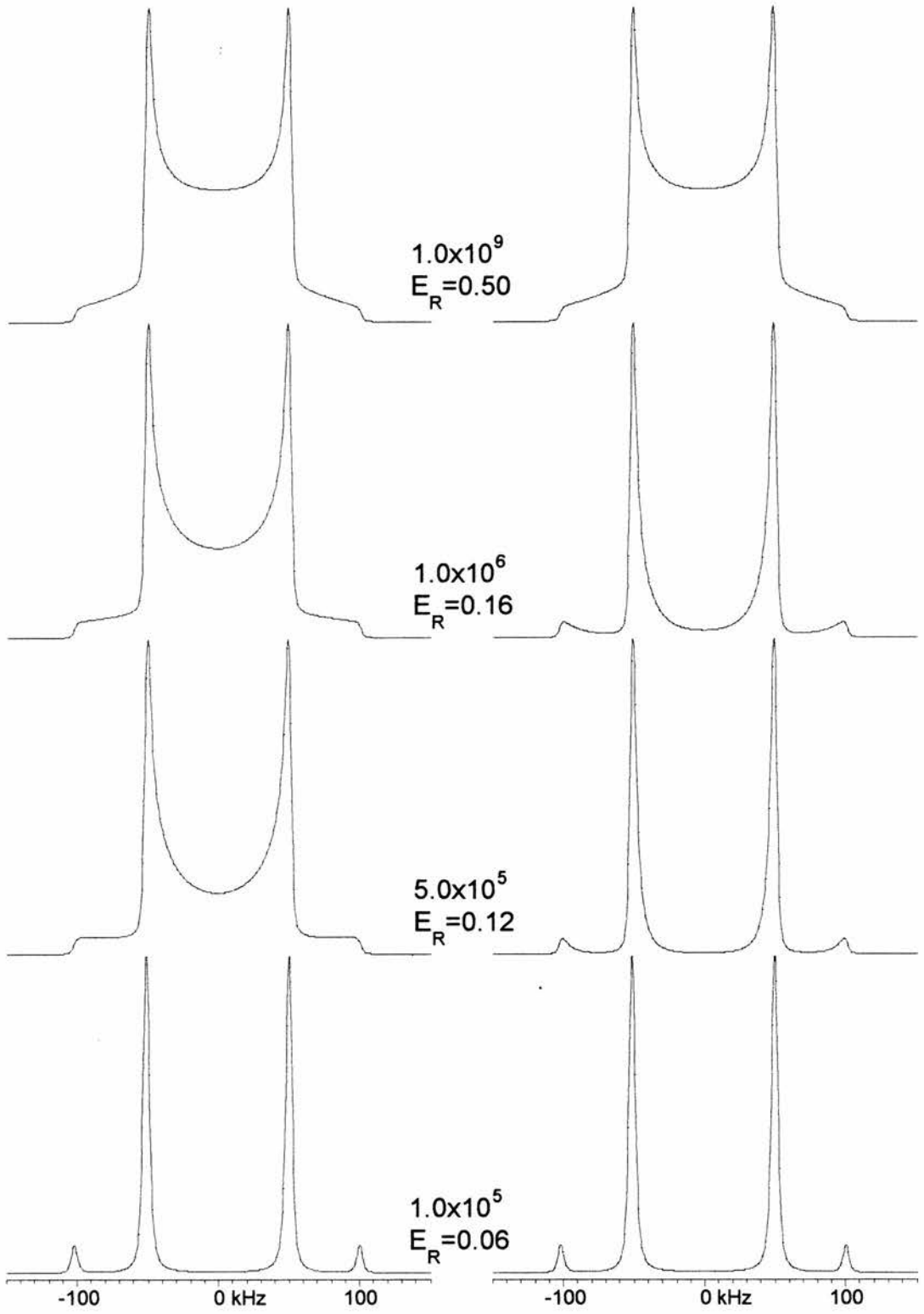

Figure 3.19. (continued) Simulations for cone motion of 20 degrees half-angle and all-sites exchange. Refocusing delays are 20 μs (left) and 160 μs (right). 90° pulse length is 3.8 μs. Rate constants (s^{-1}) and echo reduction factors are shown in the figure.

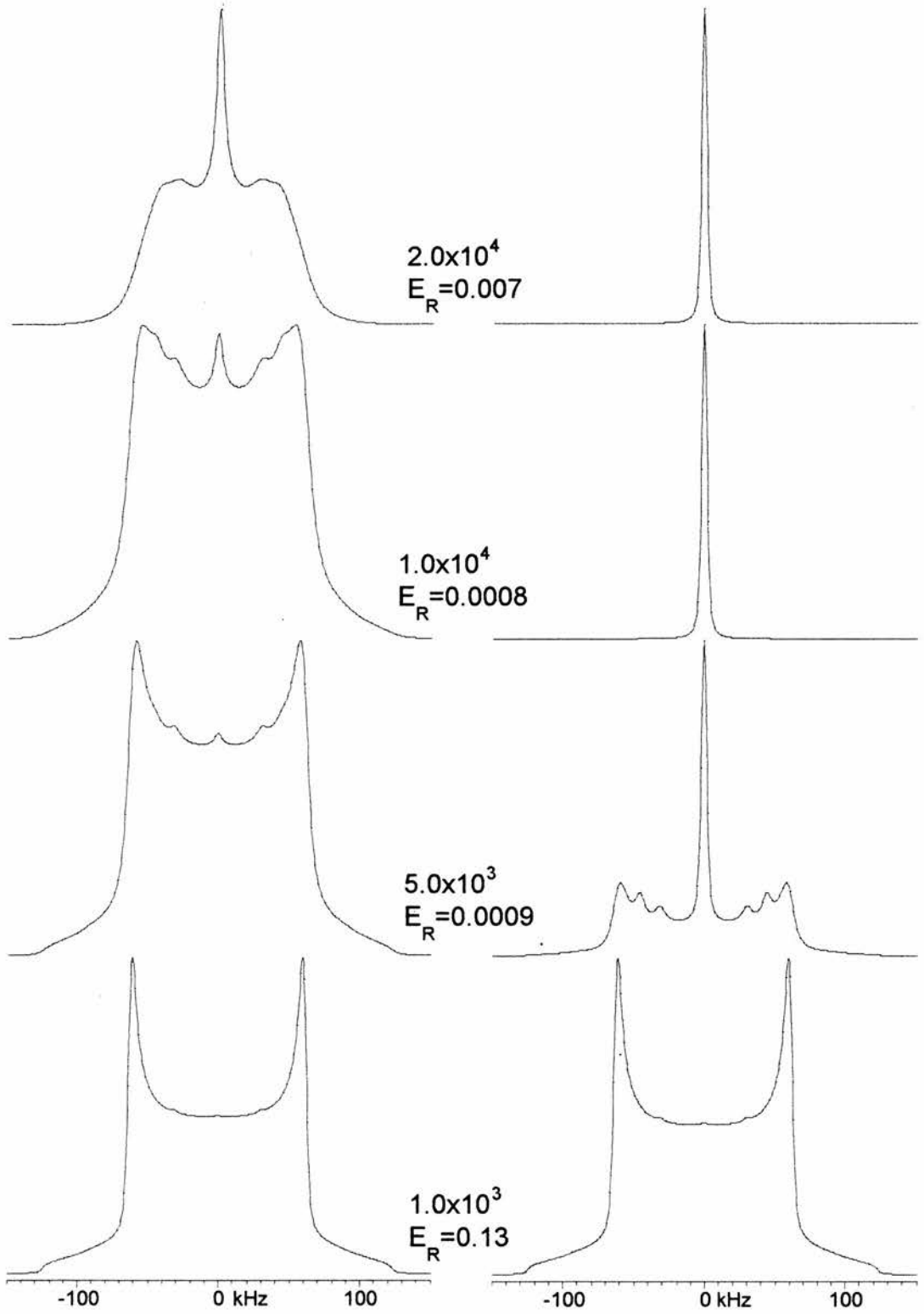

Figure 3.20. Simulations for cone motion of 54.7 degrees half-angle and all-sites exchange. Refocusing delays are 20 μs (left) and 160 μs (right). 90° pulse length is 3.8 μs. Rate constants (s^{-1}) and echo reduction factors are shown in the figure.

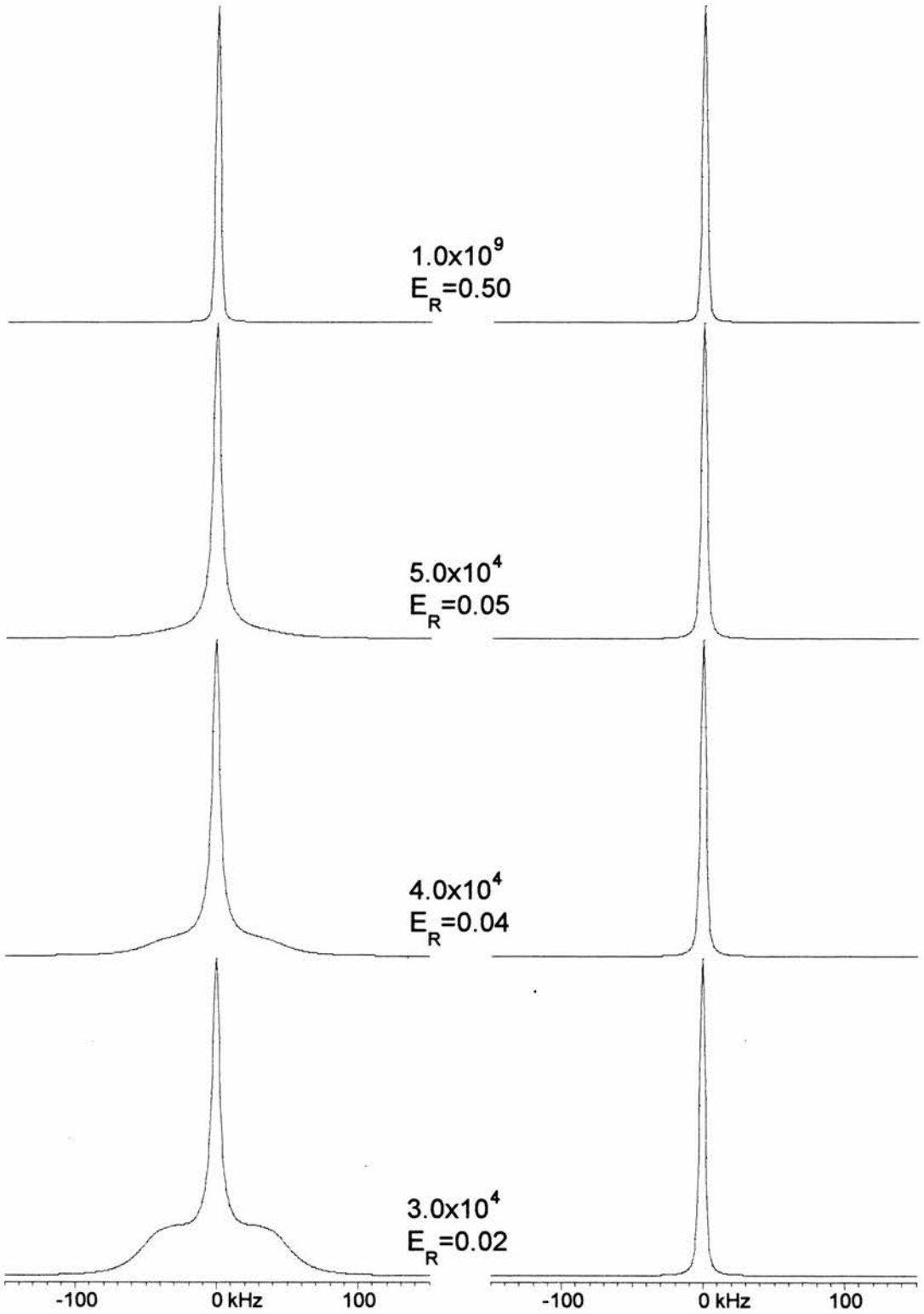

Figure 3.20. (continued) Simulations for cone motion of 54.7 degrees half-angle and all-sites exchange. Refocusing delays are 20 μs (left) and 160 μs (right). 90° pulse length is 3.8 μs. Rate constants (s^{-1}) and echo reduction factors are shown in the figure.

For the all sites exchange model the autocorrelation function can be derived by substituting[44]

$$\begin{aligned} \Gamma_{aa'}(t) &= 1 && a = a' = 0 \\ &= \exp(-Nkt) && a = a' (\mathrm{mod}\ N) \\ &= 0 && otherwise \end{aligned} \qquad (3.10.)$$

where $Nk=1/\tau_c$ and $N=6$, into the equation for the powder average autocorrelation function[67] and using the Wigner rotation matrix elements

$$d^2_{00} = \frac{1}{2}\left(3\cos^2\beta - 1\right); \quad d^2_{01} = -d^2_{0-1} = \sqrt{\frac{3}{8}}\sin^2(2\beta); \quad d^2_{02} = d^2_{0-2} = \sqrt{\frac{3}{8}}\sin^2\beta$$

gives for the powder average autocorrelation function

$$\begin{aligned} C_m(t) &= \frac{1}{5}\sum_{a=-2}^{2}\left[d^2_{0a}(\beta)\right]^2\Gamma_{aa}(t) \\ &= \frac{1}{5}\left[\left(d^2_{0-2}(\beta)\right)^2 + \left(d^2_{0-1}(\beta)\right)^2 + \left(d^2_{01}(\beta)\right)^2 + \left(d^2_{02}(\beta)\right)^2\right]\exp\left(-t/\tau_c\right) + \frac{1}{5}\left(d^2_{00}(\beta)\right)^2 \\ &= \frac{3}{20}\left(\sin^4\beta + \sin^2(2\beta)\right)\exp\left(-t/t_c\right) + \frac{1}{20}\left(9\cos^4\beta - 6\cos^2\beta + 1\right) \end{aligned} \qquad (3.11.)$$

Using equations 1.15 and 1.20 gives for the relaxation rate

$$R_1 = \frac{1}{T_1} = \frac{9}{40}(\pi\chi)^2\left(\sin^4\beta + \sin^2(2\beta)\right)\left(\frac{\tau_c}{1+\omega_0^2\tau_c^2} + \frac{4\tau_c}{1+4\omega_0^2\tau_c^2}\right) \qquad (3.12)$$

Comparing eq. 3.12 with eq. 3.5 for the two-site model indicates that the spin-lattice relaxation rates for these two models differ only by the term $\sin^4\beta$ if equal populations are used in the two-site model. This term is very small for half-angles smaller than *ca.* 30 degrees, and therefore, the spin-lattice relaxation times for these two models are practically the same for small half-angles. This is also evident from the contour plot of the spin-lattice relaxation time as a function of the cone half-angle β and the correlation time shown in figure 3.21. Again, the experimentally measurable region of spin-lattice relaxation time shorter than 100 s is between 10^{-4} and 10^{-14} s. Very short T_1 of order 10 ms is observed if the half-angle β is of order 30 degrees. The ^{2}H spin-lattice relaxation time at the minimum is given by:

$$\frac{1}{T_{1,\min}} = 182\cdot\left[\sin^4\beta + \sin^2(2\beta)\right] \qquad (3.13.)$$

Thus, a minimum value of 4.1 ms for the spin-lattice relaxation time is obtained when β is equal to 55 degrees.

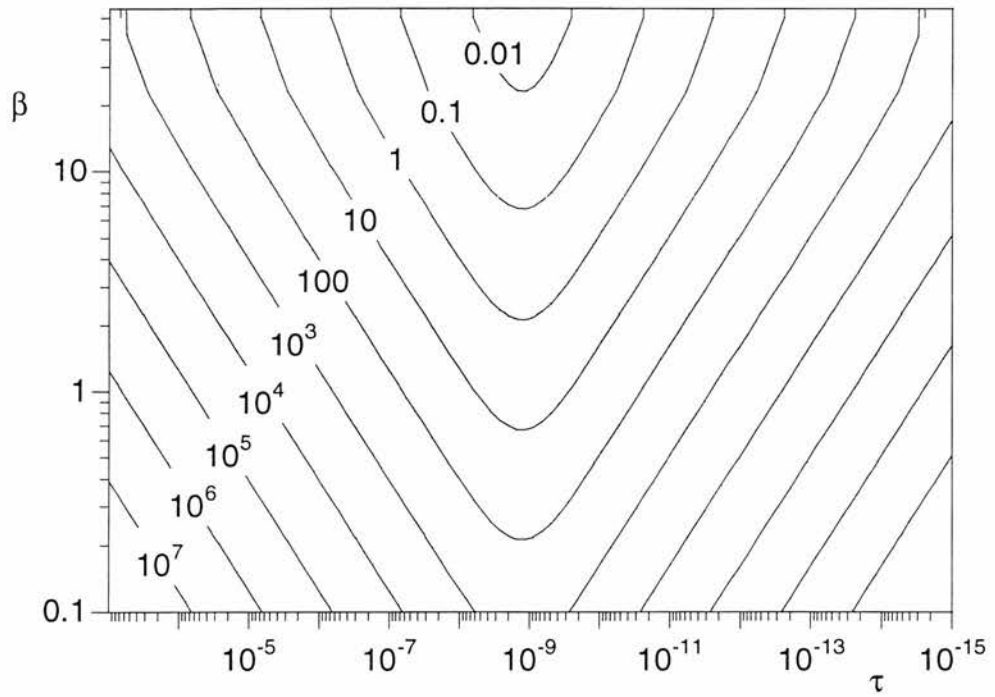

Figure 3.21. Contour plot of T_1 as a function of half-angle β and τ_c for the six-site cone model. T_1 in seconds are shown in contours. T_1 minimum is at $\tau_c=1.3\times10^{-9}$ s.

In principle, any of the conical models could be combined with another model, for example the two-site model or the *trans-gauche* model, to describe an additional libration of the C-D bond or the libration axis.[30,86] This can be easily done with the MXET1 program by adding a co-ordinate system and the Euler angles describing the motion of these co-ordinates with respect to an existing co-ordinate system, for example the principal axis system of the quadrupolar coupling tensor. This addition of co-ordinate systems, however, increases the number of exchange sites rapidly, and consequently, the calculation becomes too time consuming to be done on normal workstation level computers, and therefore, a supercomputer is needed to do these calculations. The basic models presented in this chapter, however, failed to produce the line shape changes for most of the compounds discussed in chapters 4 and 5. Therefore, the distributional model of Hirchinger *et al.*[67] was used as a basis in these simulations. As the distribution function covers a wide range of angles, it will take any additional librations into account, and therefore, there is no need to add these librations in the six-site cone model used as a basis for the distribution model.

3.5. Conical libration model.

Hirschinger *et al.*[67] in their simulation of the line shapes for selectively deuterated nylon 66 polymer took a whole different approach to the calculation of deuteron spectra. Instead of using the simple models described in the previous sections, they assumed that the C-D bond was librating over a wide range of angles. They also assumed that this librational motion was well described by a harmonic oscillator in its 11 lowest energy levels, and therefore, the probability distribution for the librational angles was well approximated by Gaussian density function.

The harmonic oscillator model of Hirschinger *et al.*[67], however, fails to explain the results shown in chapters 4 and 5 since it requires very large displacements for the atoms in the chain to produce domelike spectra, and also, fails to produce a sharp peak in the centre of the spectrum. Miura *et al.*[68] used a different model for amorphous nylon 66 for which a sharp peak in the centre was observed. This model consisted of three different component spectra that were summed in different ratios to produce the observed spectra. The components represented different segments of the polymer undergoing slow, intermediate and slow exchange. The component spectra therefore originated from the amorphous nature of the polymer rather than a specific model of motion. The sharp peak was assumed to reflect fast and nearly isotropic motion.

For the diacids and diesters discussed in chapters 4 and 5, however, domelike features and a sharp peak in the centre of the spectrum were observed although these compounds are purely crystalline and contain no segments that could undergo isotropic motion. Therefore, these spectral features have to originate from a different mode of motion of the C-D bonds than isotropic motion. It is proposed that the underlying motion is three dimensional librational motion of the C-D bonds, and this motion is described with the six-site conical model. As described in section 3.4., this model results naturally from rotations of the C-C bonds and also produces a sharp peak in the centre. Furthermore, this model requires only rather small displacements of the chain carbons, and therefore, is preferred over models that involve motion in the diamond lattice requiring large displacements. The C-D bond librates, however,

over a range of angles rather than on a well-defined cone, and therefore, the half-angle of the cone has to be distributed using a suitable distribution function.

The motion is not assumed to be strictly harmonic but the shape of the distribution function is derived form the harmonic oscillator model. Although harmonically oscillating C-H bonds that vibrate at IR-frequencies in the million megahertz range are in their ground state, many energy levels are excited for the C-C bonds in the alkyl chain oscillating at frequencies near the Larmor frequency of deuteron (77 MHz at 11.7 tesla). Thus, the distribution is not Gaussian but rather the probability at the turning points of the oscillation increases with temperature as increasingly higher energy levels are excited. Figure 3.22 shows the probability density functions for energy levels 0, 5 and 15 of a harmonic oscillator together with population weighted sum of the probability density functions at different temperatures. At low temperatures, only a few levels are excited and the population weighted sum is satisfactorily Gaussian. As the temperature increases, the probability at the turning points increases at the expense of the central region. At high temperatures, the classical picture where the oscillator spends most of its time at the turning points is reached. These turning points for very high levels of excitation are assumed to be at or near 55°, taken as half of the tetrahedral angle, as the potential energy would increase rapidly at this angle because of the restrictions imposed by the chain and its end groups.

The motion involves, however, rather large displacements and high excitation levels, and therefore, may not be strictly harmonic. Furthermore, the results shown in chapter 5 indicate that the rate of the motion changes with temperature, also indicating that the motion is not strictly harmonic. Thus, a distribution function that reasonably approximates the behaviour of a harmonic oscillator is chosen, and the changing rate is accounted for in the simulation of the spectra for the six-site cone model. A distribution function

$$y = \sum_{i=1}^{n} p_i \exp\left(\frac{-\left(\theta - \theta_{0,i}\right)^2}{2\Delta\theta_i^2}\right) \qquad (3.14.)$$

where p_i is the proportion, $\theta_{0,i}$ is the centre and $\Delta\theta_i$ is the standard deviation of the i:th Gaussian distribution, was chosen for simplicity. Up to three terms were needed in the simulations of the observed spectra, and therefore, this model is very similar to that of Miura *et al.*[68] although the reasoning is very different. Lorentzian terms could be used in eq. 3.14 to account for the sharp peak in the centre but Gaussian terms were used for simplicity.

Equation 3.14 is plotted with different parameters in figure 3.23. The graph on the bottom of figure 3.23 represents low temperatures where only the first term of eq. 3.14 with a centre at 0° is used to produce a Gaussian distribution similar to the ground state of the harmonic oscillator. As the harmonic oscillator spends increasingly more time at its turning points at higher temperatures, a second term with its centre moving towards half of a tetrahedral angle with temperature is included to account for the population distribution at the turning points.

The graph in the middle of figure 3.23 represents medium temperatures where the second Gaussian distribution is centred between 0 and 55 degrees. At high temperatures, represented by the graph on the top of figure 3.24, the second Gaussian term is centred at the half of a tetrahedral angle describing oscillation occurring at maximum displacement. The distribution function cuts off at the magic angle excluding any displacement beyond half of a tetrahedral angle.

In practice, a set of free induction decays are calculated for each rate constant using the six-site cone model for half-angles from 0 to 55 degrees with 0.5° increment. This is done with the MXET1 program that corrects for the finite pulse length and calculates the line shape for a given set of parameters. This set of free induction decays is then multiplied by the distribution function of equation 3.14. with suitable parameters to obtain a distribution that best produces the observed spectra. Then, the resultant free induction decay is multiplied with Lorentzian and Gaussian broadening factors to account for the spectral processing and for the dipolar couplings, respectively. Finally, the free induction decay is Fourier transformed to produce the spectrum in the frequency domain. This model is named as 'conical libration model' and is used in all simulations in chapters 4 and 5.

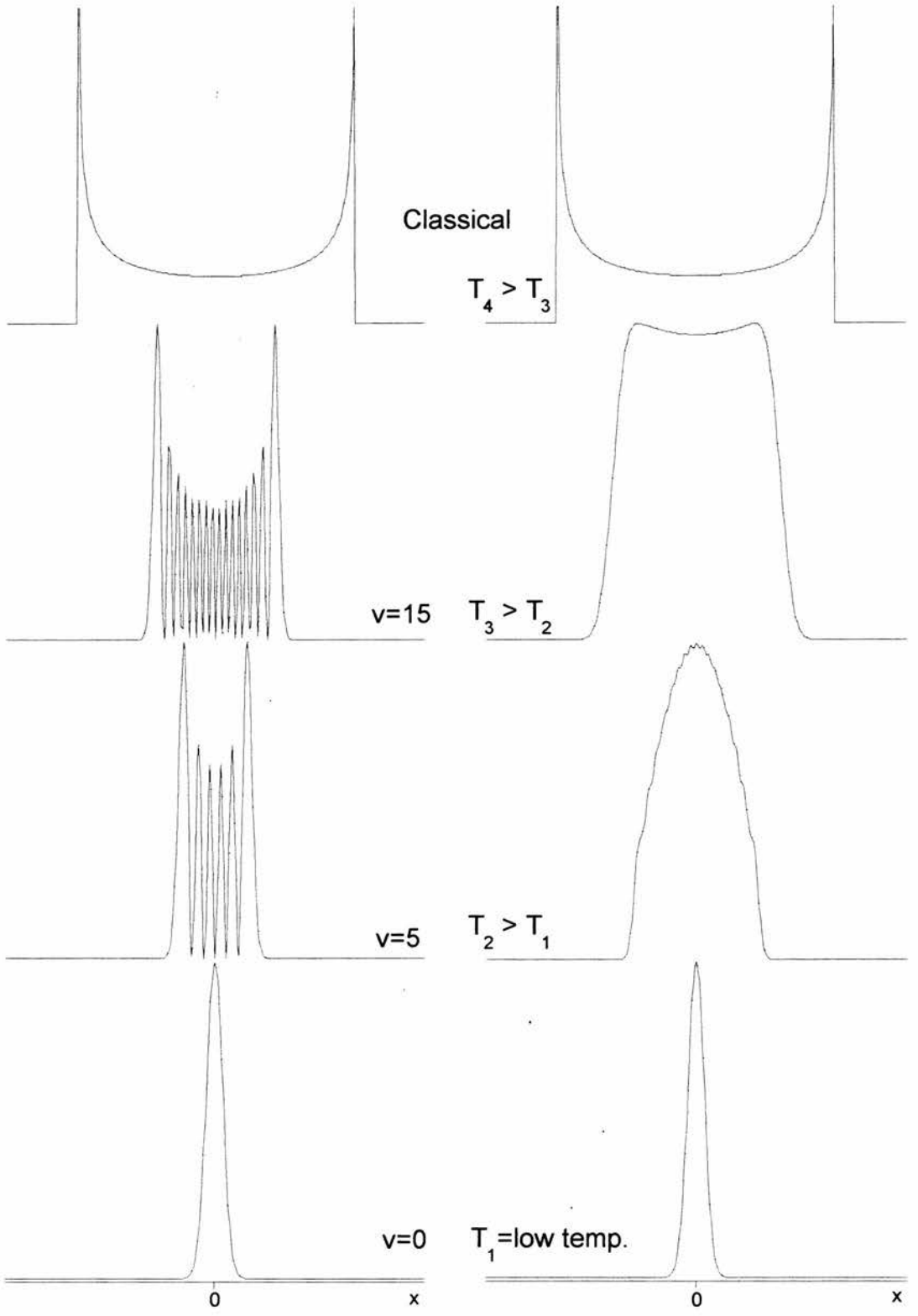

Figure 3.22. Probability density $\psi_v^2 = N_v^2 H_v^2(y)\exp(-y^2)$ for some quantum states v of a harmonic oscillator (left) together with population weighted sum $\Sigma p_v \psi_v^2$ as a function of temperature (right).[88] Populations for the different quantum states v are given by $p_v = (1-\exp(-h\nu/kT))\exp(-vh\nu/kT)$. The displacement variable x is given by $x = \alpha y$ where $\alpha = (\hbar^2/(mk))^{1/4}$. The classical behaviour is reached at high temperatures (top). All scales are arbitrary.

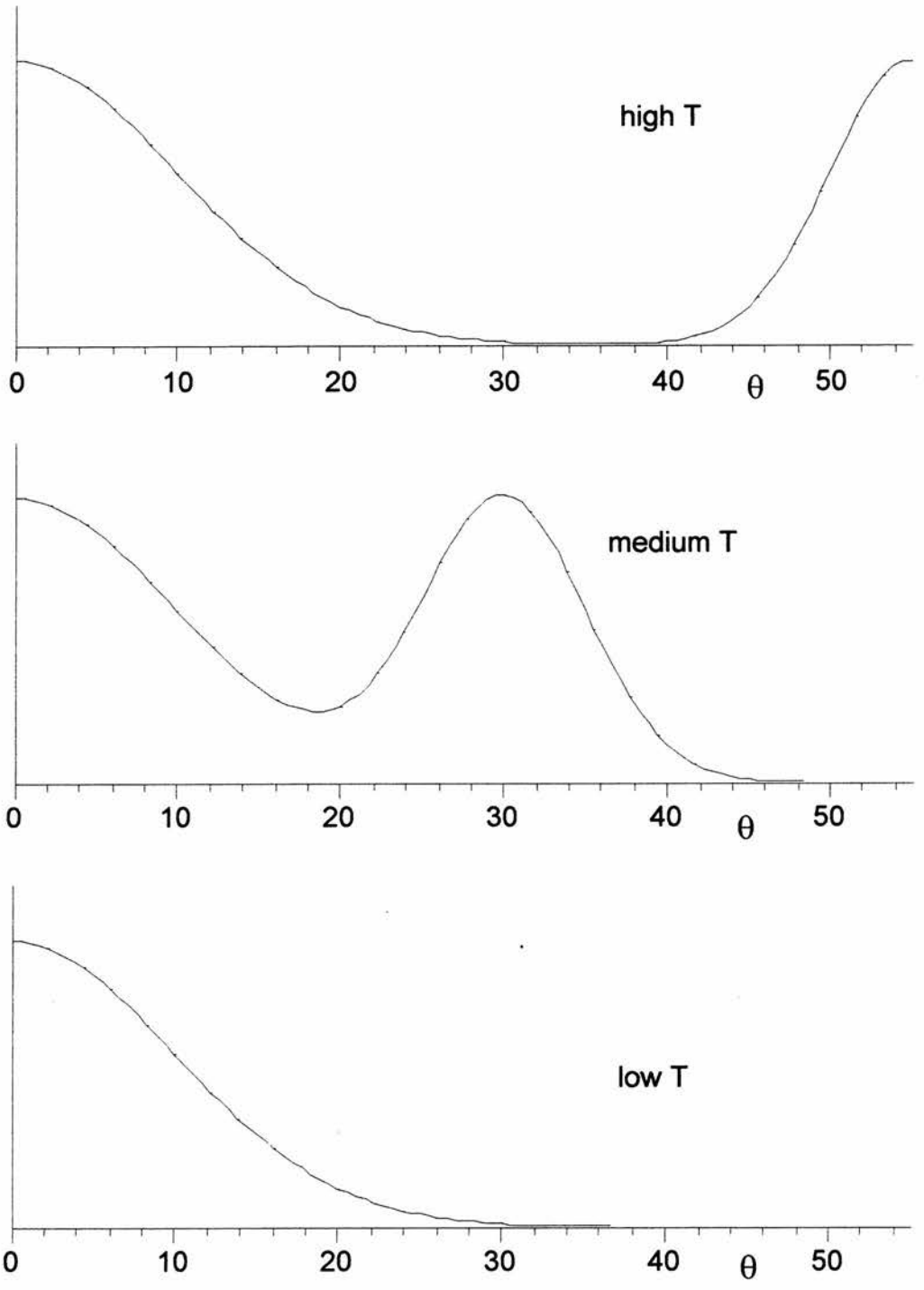

Figure 3.23. Plots of equation 3.14. showing how the centre of the distribution moves from zero at low temperatures to half of a tetrahedral angle at high temperatures. The scale is arbitrary for y.

Figures 3.24 and 3.25 show the effect of changing rate constant on spectra simulated with two different distribution functions. In both simulations, two terms of eq. 3.14 are included and the first is the same with the centre at 0° and standard deviation of 10°. Also, the proportions of the two terms are equal with $p_1=p_2=1$.

The spectra shown in figure 3.24 were simulated with the second term of eq. 3.14 centred at 45° and having a standard deviation of 10°. As expected, a Pake doublet is observed for very slow motion with a rate constant smaller than 10^2 s^{-1}. Increasing the rate constant to 10^5 s^{-1} results in a decrease in the intensity of the central region of the spectrum, the effect being more pronounced in the spectra calculated with a 160 μs refocusing delay. When the rate constant is larger than 10^5 s^{-1}, however, the intensity of the central region increases creating a dome in the centre. This dome occurs first in the spectra with a 20 μs refocusing delay ($k=5\text{x}10^5$ s^{-1}) and then also in the spectra with 160 μs refocusing delay ($k=5\text{x}10^6$ s^{-1}). At even larger rate constants, the dome sharpens a little but is still present in the fast motion limit.

It is interesting to compare these spectra with the spectra simulated for *trans-gauche* exchange model with 5% of *gauche* and 90% of *trans* conformations, for which a dome was also observed in the central region for rate constants of order 10^6 s^{-1}. However, the changes for the *trans-gauche* model occur in the opposite order, that is, the changes occur first in the spectra for 160 μs refocusing delay as the rate constant is increased. This again shows, that spectra have to be measured and simulated for different refocusing delays and at different temperatures if conclusions about the motional model are to be made.

The spectra shown in figure 3.25 are simulated with the second term of eq. 3.14 centred at 55° (taken as the magic angle) and having a standard deviation of 1°. As expected, this second term creates a spike in the centre of the spectrum for large rate constants whereas a Pake doublet is observed in the slow motion limit.

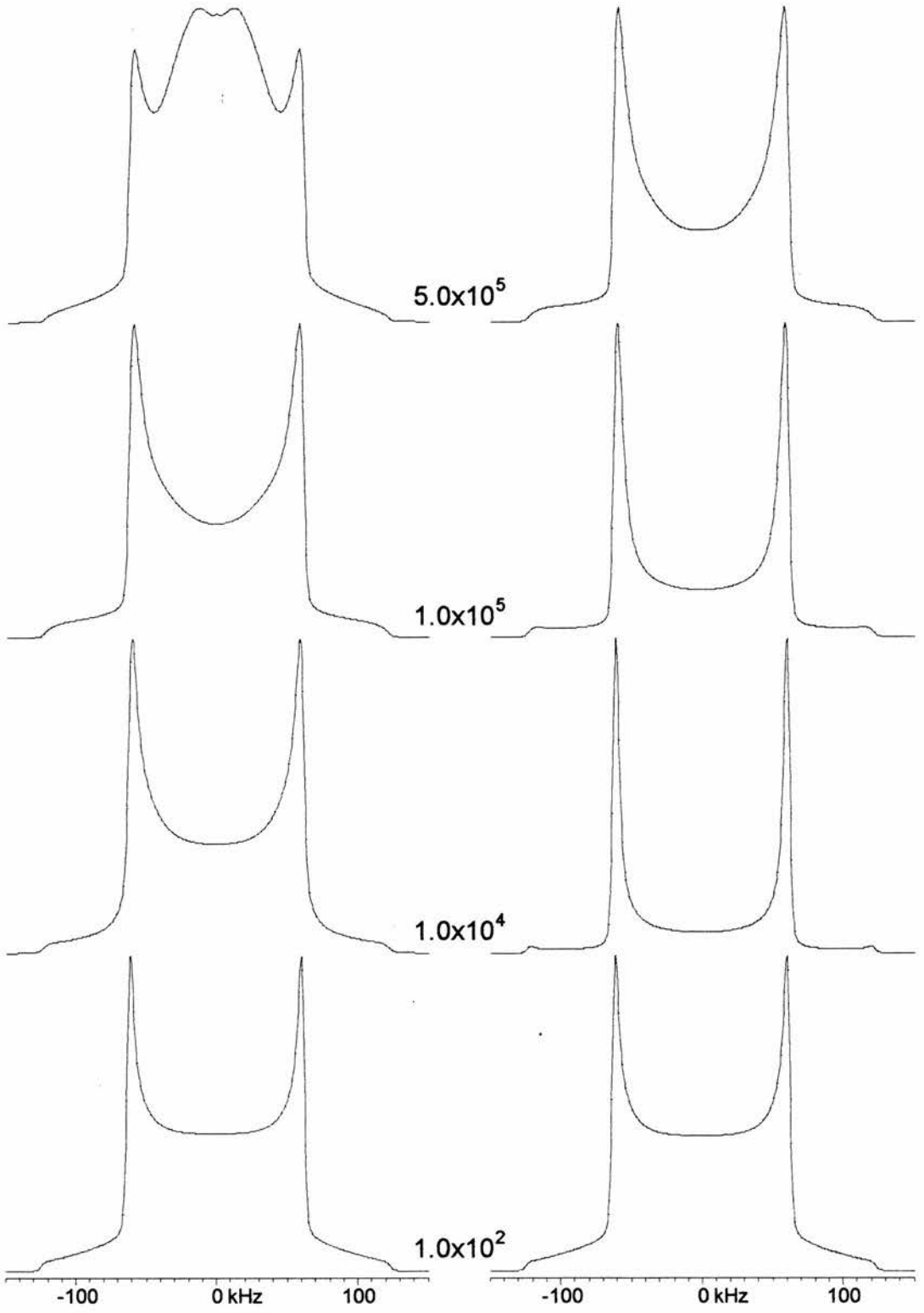

Figure 3.24. Simulated spectra for the distribution function of eq. 3.14. Parameters are: p_1=1, s_1=10, c_1=0, p_2=1, s_2=10 and c_2=45°. Refocusing delays are 20 μs (left) and 160 μs (right). 90° pulse length is 3.8 μs. Rate constants (s^{-1}) are shown in the figure.

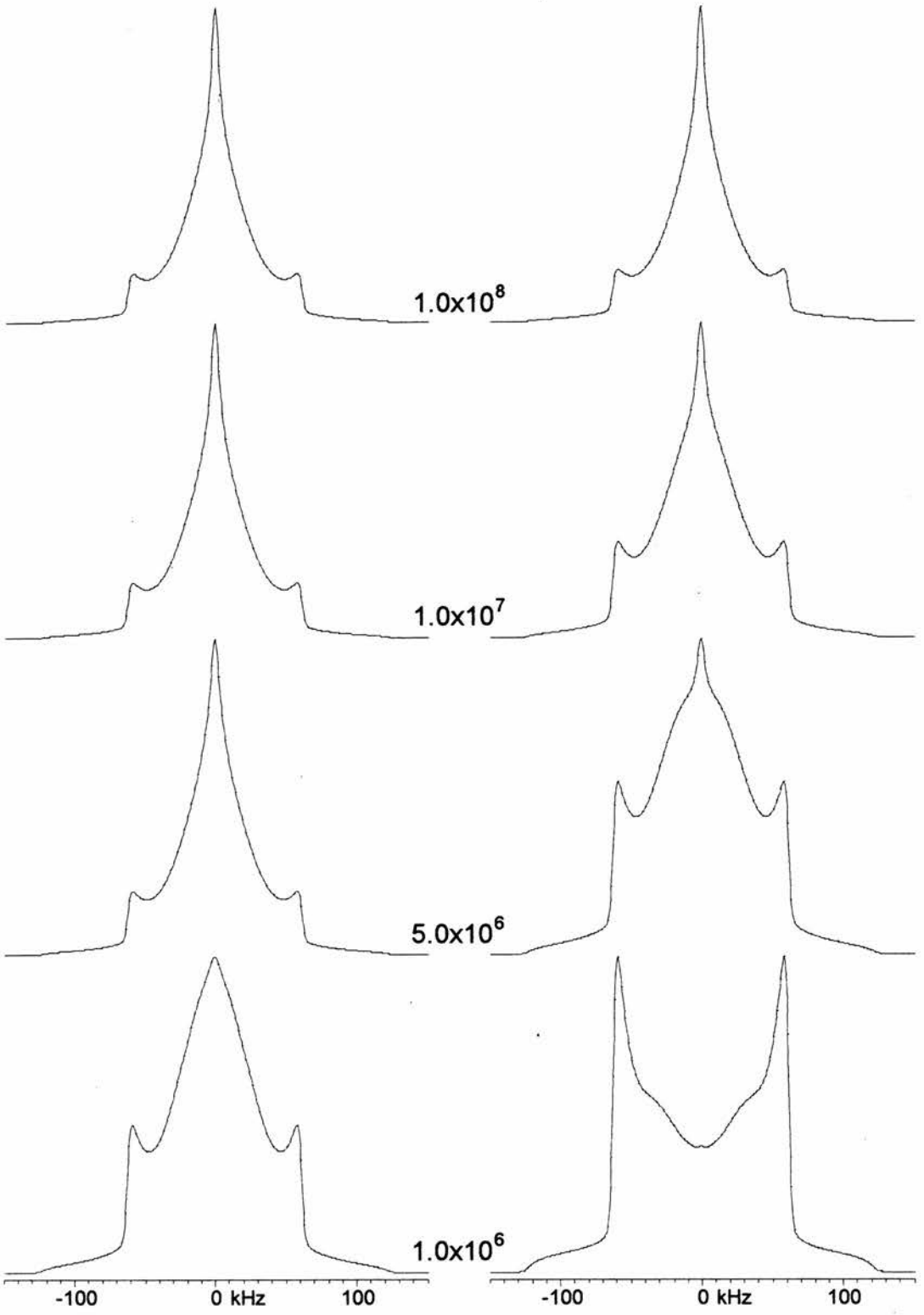

Figure 3.24. (continued) Simulated spectra for the distribution function of eq. 3.14. Parameters are: p_1=1, s_1=10, c_1=0, p_2=1, s_2=10 and c_2=45°. Refocusing delays are 20 μs (left) and 160 μs (right). 90° pulse length is 3.8 μs. Rate constants (s^{-1}) are shown in the figure.

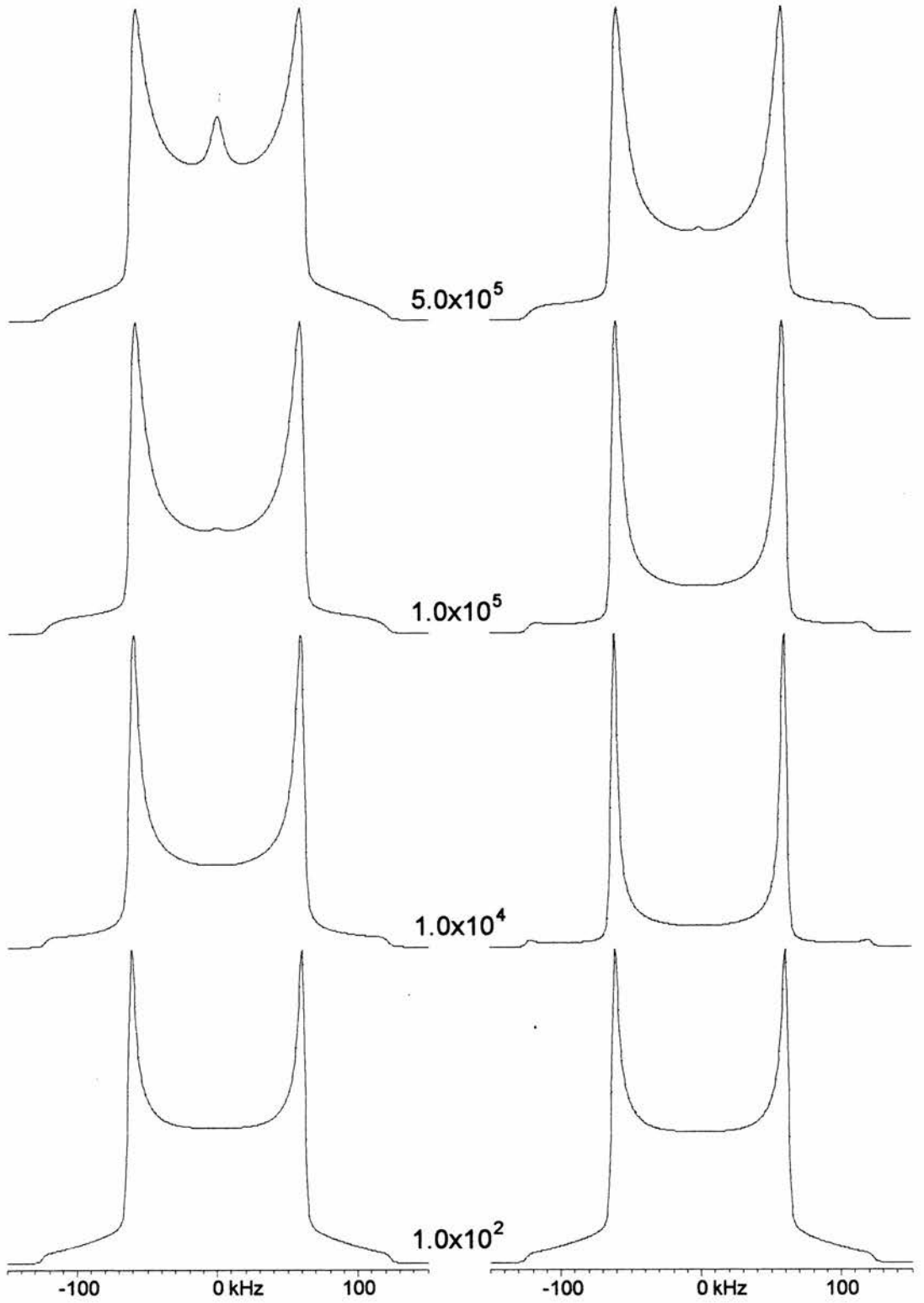

Figure 3.25. Simulated spectra for the distribution function of eq. 3.14. Parameters are: p_1=1, s_1=10, c_1=0, p_2=1, s_2=1 and c_2=55°. Refocusing delays are 20 μs (left) and 160 μs (right). 90° pulse length is 3.8 μs. Rate constants (s^{-1}) are shown in the figure.

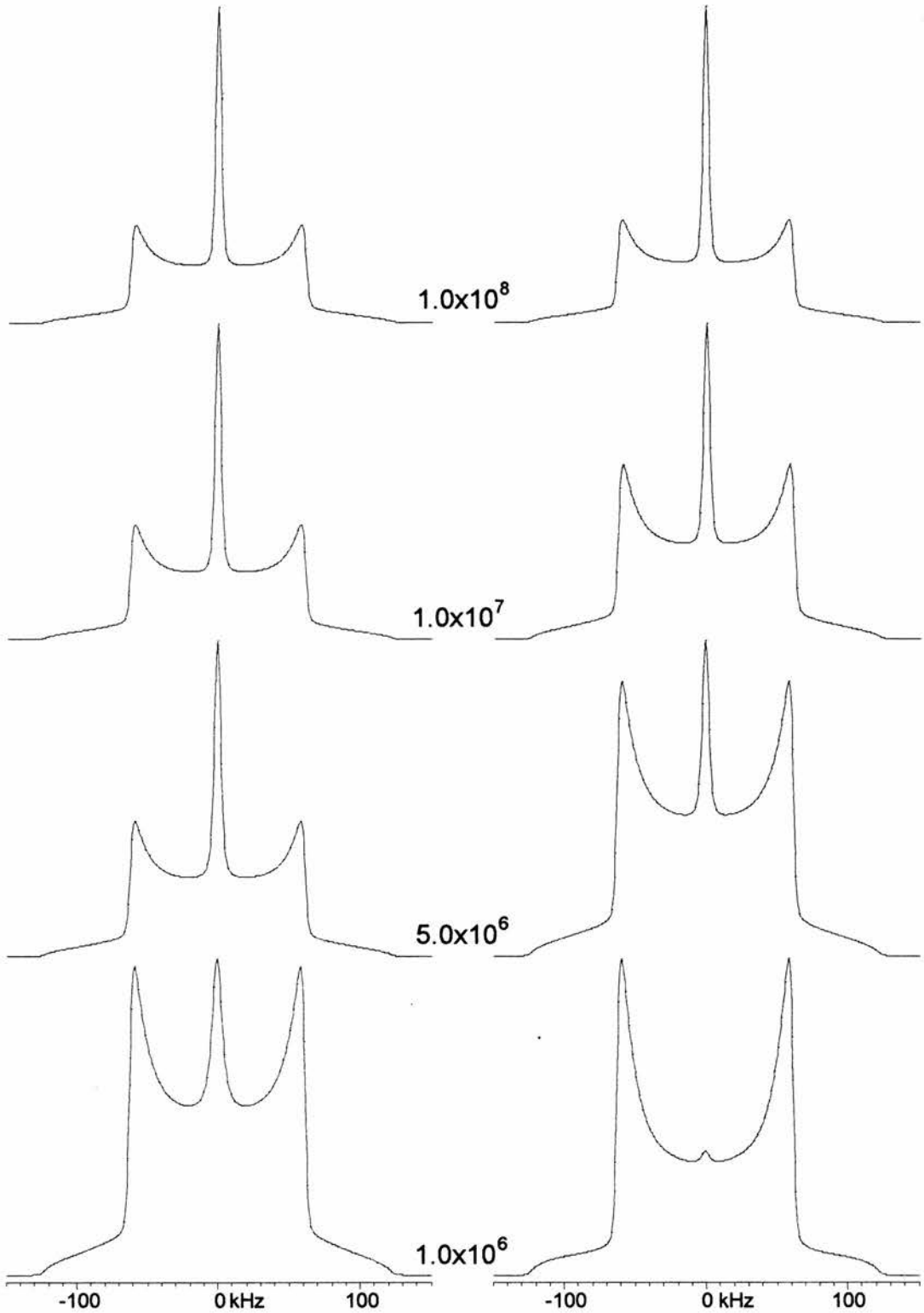

Figure 3.25. (continued) Simulated spectra for the distribution function of eq. 3.14. Parameters are: p_1=1, s_1=10, c_1=0, p_2=1, s_2=1 and c_2=55°. Refocusing delays are 20 μs (left) and 160 μs (right). 90° pulse length is 3.8 μs. Rate constants (s^{-1}) are shown in the figure.

4. THE DIACID SERIES

A series of simple diacids from succinic to suberic acid was studied for two different reasons. First, the structures of succinic and suberic acids have been determined by neutron diffraction which gives nuclear anisotropic displacement parameters for hydrogens. Secondly, two members of this series with odd number of carbons, glutaric and pimelic acids, undergo phase transitions well below their melting points, and therefore, the effect of these phase transitions on chain mobility can be studied.

4.1. Succinic acid

Two different phases are known for succinic acid, $HOOC(CH_2)_2COOH$.[98] The phase that is stable above 137 °C is called the α-phase. Its crystal structure has been solved from x-ray[89-90] diffraction data but since this phase is stable only above the high temperature limit of the NMR probes the structure is irrelevant to this study. The structure of the β-phase, which is stable below 137 °C, has been solved from both x-ray[90-91] and neutron diffraction[92] data. The neutron diffraction study of Leviel *et al.*[92] is considered to be the most accurate and is only discussed here. The structure (appendix, p. A-21) was solved from data collected at 77 and 300 K thus giving invaluable information on the increase of the amplitude of molecular libration. The authors called this librational motion "an oscillatory motion of the molecule around its minimal inertial axis" and showed that the angle of libration increases with temperature.

Nuclear anisotropic displacement parameters (ADP) obtained from the refinement of neutron diffraction data reflect both static and dynamic disorder in the crystal. Static disorder is mainly due to crystal defects and impurities whereas dynamic disorder is caused by thermal motion in the crystal. ADP's also refer to an atom that is an average over all the unit cells in the crystal.[93] Therefore, in order to compare neutron diffraction data with NMR data, the contribution of the dynamic disorder has to be

extracted from the nuclear anisotropic displacement parameters and the motional information thus obtained has to be transformed into angular terms.

The simplest and commonly used approach is to analyse molecular motion with a simple rigid-body model of Schomaker and Trueblood.[94] In this model, it is assumed that the whole molecule librates about an axis with an angle of libration λ. The rigid-body analysis gives two tensors, namely the translation tensor **T** and the libration tensor **L**. The libration tensor is interesting as its diagonal elements are squares of the libration angles about principal axes of motion. In other words, the angle of libration in each principal axis direction is obtained as the square root of the corresponding diagonal element of the libration tensor **L**.

The largest element of the libration matrix for succinic acid was L_{11} at both temperatures, and the authors therefore concluded that the librational motion occurred mainly about the I_x inertia axis that is approximately in the chain direction. At 77 K, the value of L_{11} corresponded to an angle of libration of 5.4°. On heating to 300 K this angle increased to 9.2°. It is interesting to compare the angles obtained from the neutron diffraction data with solid-state NMR data. The NMR data should be consistent with the angular increase of librational motion. In addition, NMR data should give an approximate rate for the librational motion. This information is not obtained from neutron diffraction data.

Figure 4.1 shows ^{13}C CP/MAS spectra measured at different temperatures. In the whole temperature range from 198 K to 358 K, there are only two peaks in the spectrum. The peaks are at 28.4 ppm ($\underline{C}H_2$) and 180.3 ppm ($\underline{C}$=O). The spectra show no evidence of dynamic dipolar broadening nor effects of short ^{13}C $T_{1\rho}$ relaxation time. Therefore, no attempt was made to measure ^{13}C $T_{1\rho}$ relaxation time at any temperature.

The methylene groups of succinic acid were deuterated, and the ^2H spin-lattice relaxation time of this 2,2,3,3-d_4-succinic acid was measured in a temperature range from 109 K to 400 K. Measured ^2H spin-lattice relaxation times are listed in table 4.1 and shown as a function of temperature in figure 4.2.

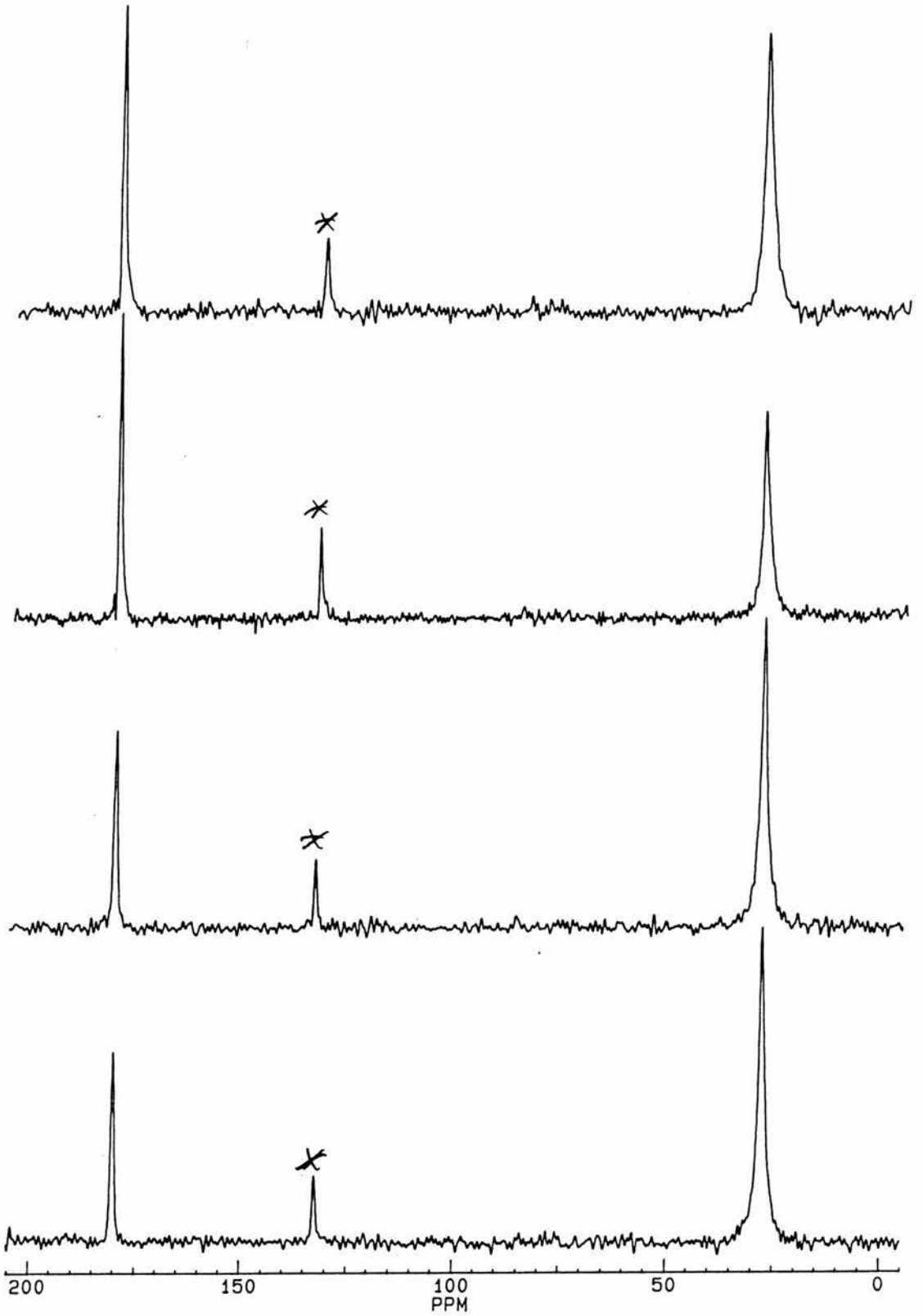

Figure 4.1. ^{13}C CP/MAS spectra for succinic acid at different temperatures. Temperatures are from top to bottom: 358, 298, 246 and 198 K. Spinning sidebands (at 6 kHz) are asterisked.

Table 4.1. Measured ^{2}H spin-lattice relaxation time for 2,2,3,3-d_4-succinic acid.

T(vtu)/K	T/K	^{2}H T_1/s
108	109	177
130	131	163
150	150	150
170	170	133
190	189	137
210	208	146
230	228	132
250	247	152
270	267	120
292	288	143
310	306	139
330	325	157
350	345	122
370	364	89.6
390	383	72.1
410	403	35.7

Perhaps surprisingly, the ^{2}H spin-lattice relaxation time changes little over this wide temperature range being *ca.* 150 s between 109 K and 325 K. Above 325 K, it decreases slowly with temperature to 36 s at 403 K. Assuming that the libration is unaffected by deuteration, the angle of libration increases from 5.4° at 77 K to 9.2° at 300 K according to the neutron diffraction study of Leviel *et al.*[92] Therefore, a qualitative explanation for the ^{2}H T_1 plateau is that the rate of librational motion is in the fast motion limit where the spin-lattice relaxation time increases as the correlation time shortens with temperature. The increase in the angle of libration, however, decreases the spin-lattice relaxation time, and therefore, compensates for the increase caused by the shortening correlation time. As a result, a fairly temperature independent spin-lattice relaxation time is observed.

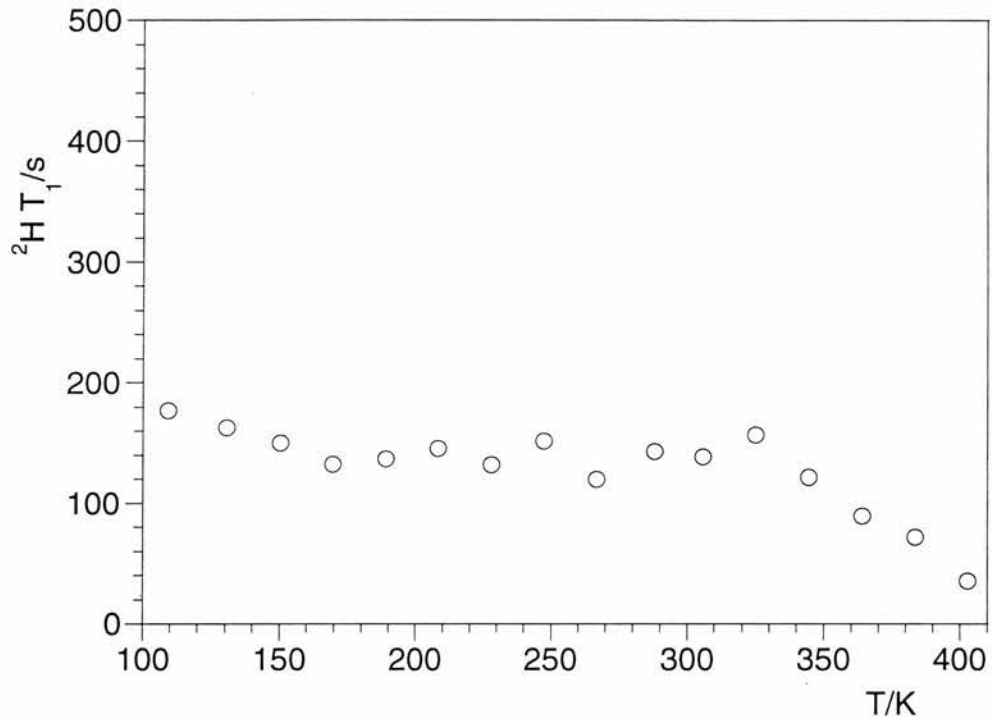

Figure 4.2. Measured ^2H spin-lattice relaxation time as a function of temperature for 2,2,3,3-d_4-succinic acid.

In the fast motion limit, any narrowing of the deuteron powder pattern is caused by an increase in the angle of motion, and therefore, the angle can be obtained by comparing observed spectra with calculated spectra. Then, the rate of motion can be obtained from the corresponding ^2H spin-lattice relaxation time. Unfortunately, the ^2H spin-lattice relaxation time was long in the whole temperature range, and therefore, made the measurement of quadrupolar echo spectra very time-consuming. Another difficulty was that the Bruker MSL spectrometer could only generate delays up to 100 seconds directly. As the spin-lattice relaxation time was of the order 150 s at low temperatures, a recycle delay of 800 s was needed to prevent saturation. Long delays were generated by replacing the single recycle delay with a loop of recycle delays as explained in chapter 6. This worked well in general, except that the spectra measured at very low temperatures with only one or two phase cycles were slightly out of phase.

^2H quadrupolar echo spectra were measured at four different temperatures from 111 K to 403 K (fig. 4.3). The spectrum at 111 K was measured with a recycle delay of 1000 s and only one phase cycle of 4 transients, and therefore, is slightly out of

phase. The width of this spectrum, however, is 122 kHz indicating a very small angle of libration. Line shape calculations using the two-site model indicate that the angle of libration is smaller than 5°. The line shape analysis fails to give an accurate angle but agrees well with the small angle of 5.4° obtained from neutron diffraction data for a non-deuterated sample. A crude estimate for the correlation time at 110 K can be obtained from the measured ^{2}H spin-lattice relaxation time of 177 s. Using equation 3.5 with an angle 2β of 5° and equal populations gives 3×10^{-12} s for the correlation time.

A 116 kHz wide powder pattern was observed at room temperature (289 K) indicating a larger angle of libration. Again, the line shape analysis fails to give an accurate angle, but simulations using the two-site model indicate that the angle of libration is *ca.* 15°. Considering the approximate nature of both techniques and that the sample used in the neutron diffraction was not deuterated, this angle is in reasonable agreement with the value of 9.2° obtained from the neutron diffraction data. Interestingly, the conical libration model gives 5° for the cone half-angle corresponding to 10° cone angle. This agrees better with the angle obtained from neutron diffraction suggesting that motion may deviate from planar at high temperatures. The rate of exchange can be estimated from the measured ^{2}H spin-lattice relaxation time of 143 s. Equation 3.5 gives *ca.* 3×10^{-13} s^{-1} for the correlation time using the angle 15°. Again, this value is highly approximate but is consistent with the qualitative explanation that the correlation time decreases with temperature. Interestingly, the decrease in correlation time from 3×10^{-12} s at 111 K to 3×10^{-13} s at 289 K corresponds to activation energy of 3 kJ mol^{-1}.

The quadrupolar echo spectrum measured at 345 K is a superposition of two powder patterns. The outer doublet is 120 kHz wide whereas the inner doublet is only 110 kHz wide corresponding to *ca.* 5° and 20° angles of libration, respectively. Interestingly, this splitting of the quadrupolar echo spectrum occurs above 330 K where the ^{2}H spin-lattice relaxation time begins to decrease with temperature. Therefore, a change in motional mode may occur at 330 K. Apart from the explanation given in section 3.5 (chapter 3) there are two other possible explanations for the observation of the superimposed powder patterns. Firstly, there could be two

different molecules with different motional modes in the unit cell. According to the neutron diffraction study of Leviel *et al.*[92], however, all the molecules are equal. Alternatively, one of the two CD_2 groups might be librating at larger angles than the other thus producing a narrower doublet. This would be similar to the powder patterns observed for phospholipids in cell membranes where the motion increases with distance from the end group along the chain thus producing narrower doublets towards the end of the chain.[95] For succinic acid, however, this would require unequal hydrogen bonding for the two carboxylic groups. No evidence of any disorder of the O-H hydrogen was found in the neutron diffraction study of Leviel *et al.*[92] Disorder could occur, however, at 345 K as the highest temperature studied by neutron diffraction was only 300 K.

At 403 K, further narrowing of both doublets is observed. The outer doublet is 117 kHz wide whereas the inner doublet is only 99 kHz wide. In addition, an isotropic peak is observed at zero frequency. Figure 4.3 shows simulated spectra using the conical libration model with parameters given in table 4.2. The result is very similar to that obtained with the two-site model. Two-site or almost any other model could have been used in the simulation of the low temperature spectra but the conical libration model was used in all simulations as it conveniently produces the peak in the centre of the spectrum. The appearance of this central peak suggests that the motion deviates from planar at high temperatures where the libration occurs at angles comparable to magic angle and in three dimensions.

Table 4.2. Parameters used in simulations of ^2H quadrupolar echo spectra.

spectrum	p	θ_0	$\Delta\theta$	$W_{calc.}$	$W_{obs.}$
403 K outer	100	10	1	116	117
inner	40	20	1	100	99
peak	3	55	1	-	-
345 K outer	100	5	1	119	120
inner	45	15	1	109	110
289 K outer	100	5	1	119	-
inner	45	10	1	116	116
111 K	100	0	1	122	122

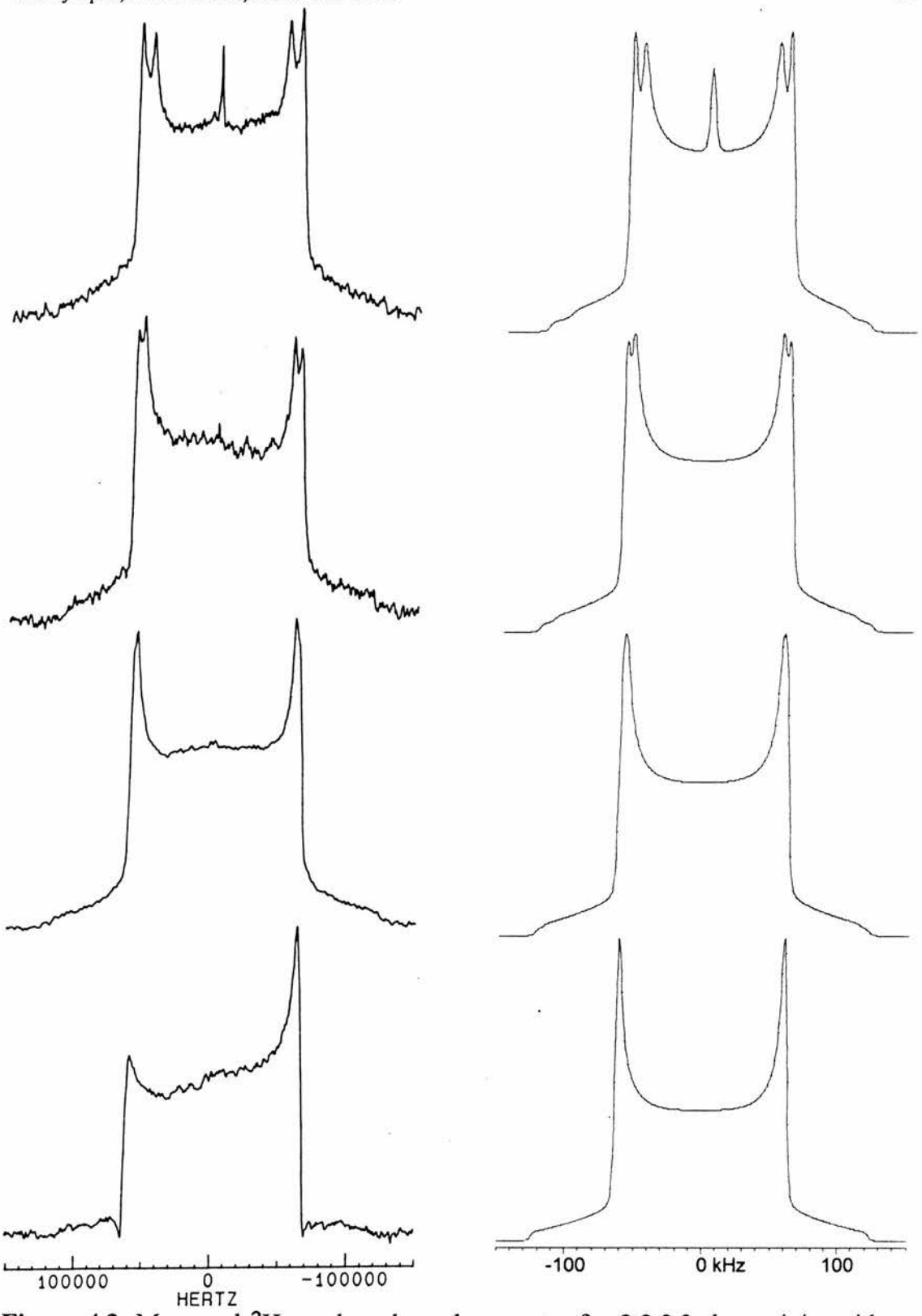

Figure 4.3. Measured ^2H quadrupolar echo spectra for 2,2,3,3-d_4-succinic acid at different temperatures (left) together with simulated spectra using the conical libration model (right). Refocusing delay is 20 μs. Temperatures are from top to bottom: 403, 345, 289 and 111 K. Parameters for the simulations are given in table 4.2. Rate constant is 1×10^8 s^{-1}.

4.2. Glutaric acid

There are three known phases for glutaric acid, $HOOC(CH_2)_3COOH$.[96-98] However, only the crystal structure of the β-phase that is stable at room temperature is known. The structure was first solved by Macgillavry *et al.*[97] and then by Morrison *et al.*[96] The structure (appendix, p. A-22) is very similar to that of pimelic acid, the other member of the odd series. For the interpretation of ^{13}C CP/MAS spectra it is important to note that there is a C_2 symmetry axis perpendicular to the molecular axis through the central carbon. Therefore, three peaks are expected in the ^{13}C CP/MAS spectrum.

As expected, there are three peaks in the ^{13}C CP/MAS spectrum for the β-phase at 53 °C (fig. 4.4). Peaks are at 18.7 (-$\underline{C}H_2CH_2COOH$), 33.7 (-$CH_2\underline{C}H_2COOH$) and 181.5 ppm (-$CH_2CH_2\underline{C}OOH$). The spectrum remains the same on cooling to -75 °C. At 61 °C, however, two peaks are observed for the carbonyl carbons and for the α-carbons. This indicates that the β to α phase transition occurs below 61 °C in the MAS conditions and that glutaric acid lacks a C_2 symmetry axis in the α-phase. The temperatures measured in the MAS conditions, however, are inaccurate because of a temperature gradient in the sample. Peaks in the high temperature spectrum are at 18.5 (-$\underline{C}H_2CH_2COOH$), 33.0 and 33.8 (-$CH_2\underline{C}H_2COOH$), 179.8 and 181.8 ppm (-$CH_2CH_2\underline{C}OOH$). The spectrum remains the same on heating up to 85 °C.

The phase transition was confirmed by differential scanning calorimetry. An endotherm was observed at 67 °C (onset, peak at 70 °C). This temperature (340 K) is lower than 348.5 K reported by Cingolani *et al.*[99a] but agrees well with 338.0 K reported by Petropavlov *et al.*[99b] A sample of 2,2,4,4-d_4-glutaric acid prepared for ^2H NMR studies was also scanned. For this sample, the phase transition occurred at a higher temperature of 82 °C (onset, peak at 85 °C). The low temperature phase was confirmed to be the β-phase by powder diffraction (fig. 4.5). A simulated pattern generated from the structure of Morrison *et al.*[96] agrees well with the observed pattern. A powder pattern was also measured above the β to α phase transition. The sample could not be spun in the furnace, and therefore, the pattern was not good enough for structure determination. This pattern is, however, clearly different from the low temperature pattern.

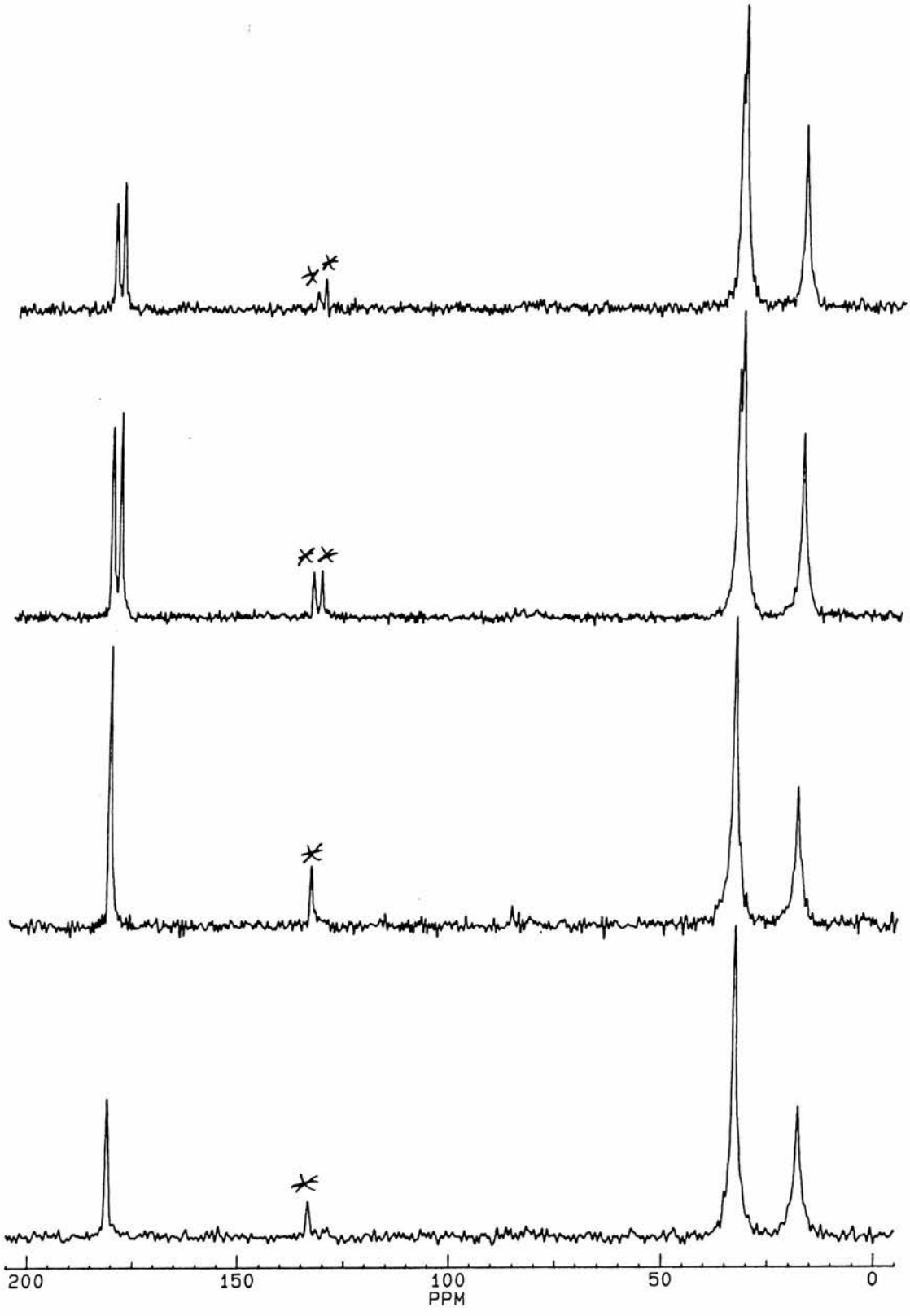

Figure 4.4. ^{13}C CP/MAS spectra of glutaric acid at different temperatures. Temperatures are from top to bottom: 358, 334, 326 and 198 K. Spinning sidebands (at 6 kHz) are asterisked.

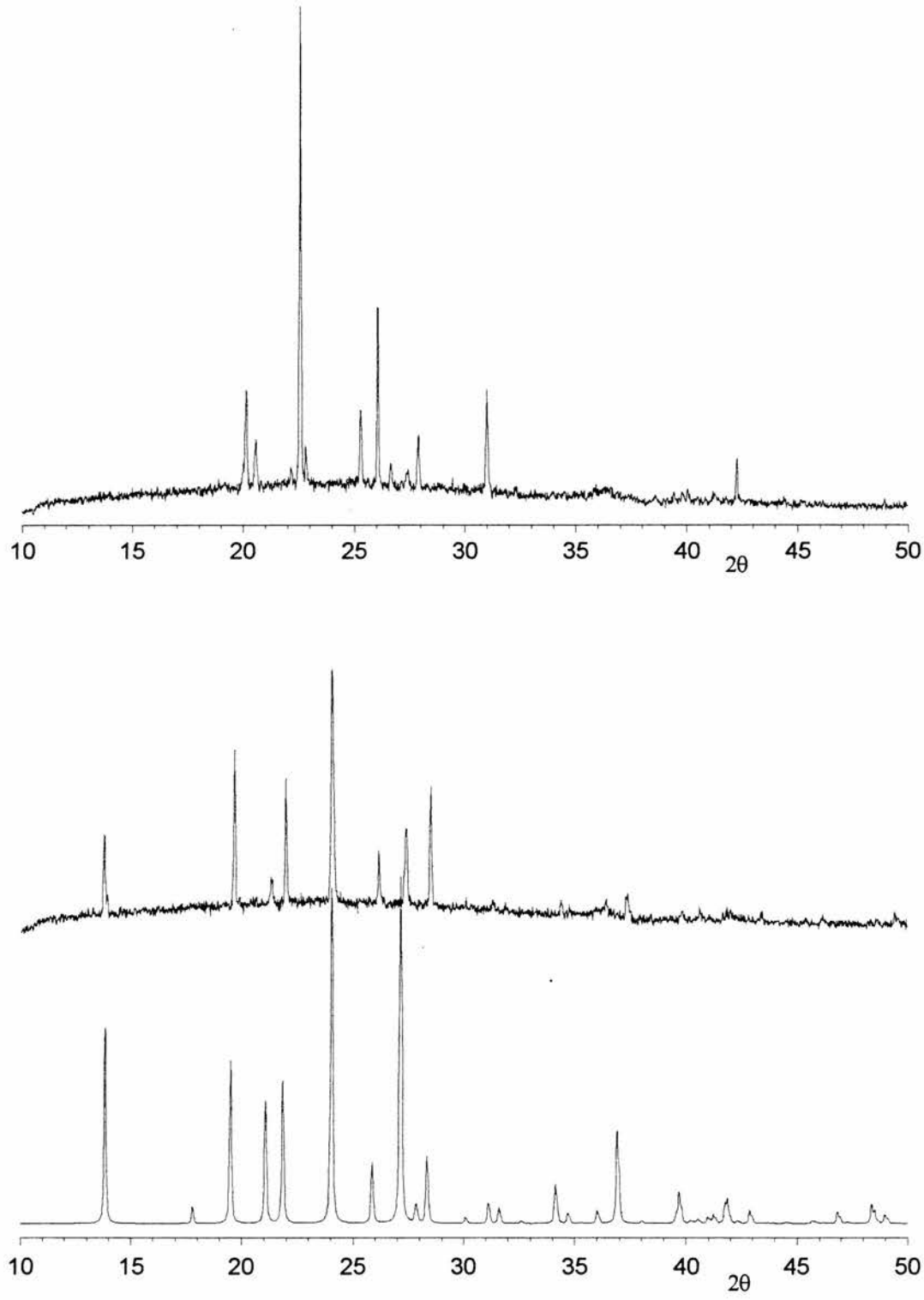

Figure 4.5. Powder diffraction pattern for glutaric acid at 18 °C together with a simulated pattern for the β-phase (bottom). The powder pattern measured at 85 °C (top) is clearly different from the low temperature pattern.

MacGillavry *et al.*[97] have proposed that one reason for the alternating physical properties of even and odd diacids is the twisting of odd diacids that increases their free energy in the solid state. Therefore, it is interesting to compare the mobility in the odd and even acids by ^{2}H NMR. First, ^{2}H spin-lattice relaxation time was measured for 2,2,4,4-d_4-glutaric acid at different temperatures. The measured values are listed in table 4.3 and shown as a function of temperature in figure 4.6. Clearly, the dependence of the ^{2}H spin-lattice relaxation time on temperature for 2,2,4,4-d_4-glutaric acid is very different from that observed for 2,2,3,3-d_4-succinic acid, an even acid. At 350 K, near the β to α phase transition at 355 K, a clear change from increasing to decreasing ^{2}H spin-lattice relaxation with temperature is observed indicating increasing angle of motion above the phase transition. Interestingly, a T_1 minimum is observed at *ca.* 150 K.

Table 4.3. Measured ^{2}H spin-lattice relaxation times for 2,2,4,4-d_4-glutaric acid.

T(vtu)/K	T/K	^{2}H T_1/s
109	110	37.1
120	121	16.6
130	131	8.50
150	150	5.59
170	170	5.79
190	189	6.71
210	208	9.51
230	228	11.5
250	247	12.7
270	267	15.8
290	286	19.1
310	306	22.5
330	325	23.5
350	345	26.7
360	354	25.9
370	364	23.6

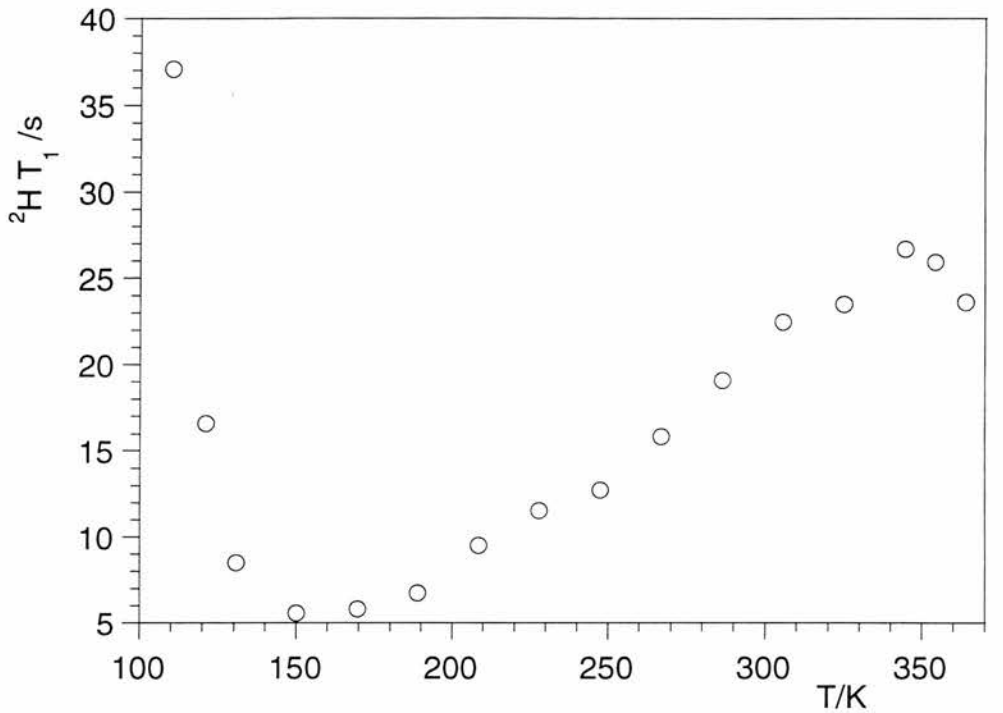

Figure 4.6. ^{2}H spin-lattice relaxation time (T_1) as a function of temperature for 2,2,4,4-d_4-glutaric acid. The β to α phase transition occurs at 355 K.

The dependence of ^{2}H spin-lattice relaxation on temperature around the T_1 minimum resembles very closely a curve that is obtained when an Arrhenius type dependence for the correlation time on temperature is used. Figure 4.7 shows the natural logarithm of the spin-lattice relaxation time as a function of inverse temperature together with least squares fits to the linear portions of the curve. The slopes of the least squares lines give 7 and 5 kJ mol^{-1} for the apparent activation energy on the low and high temperature sides of the minimum, respectively.

The Arrhenius type activation energy is only related to the change in the rate of motion with temperature whereas the apparent activation energy also reflects the change in the amplitude of the motion. Therefore, the apparent activation energy is unequal to the Arrhenius activation energy. The contribution of the rate change has to be extracted from the spin-lattice relaxation time data to obtain Arrhenius activation energy, and therefore, the angular change has to be estimated from quadrupolar echo spectra.

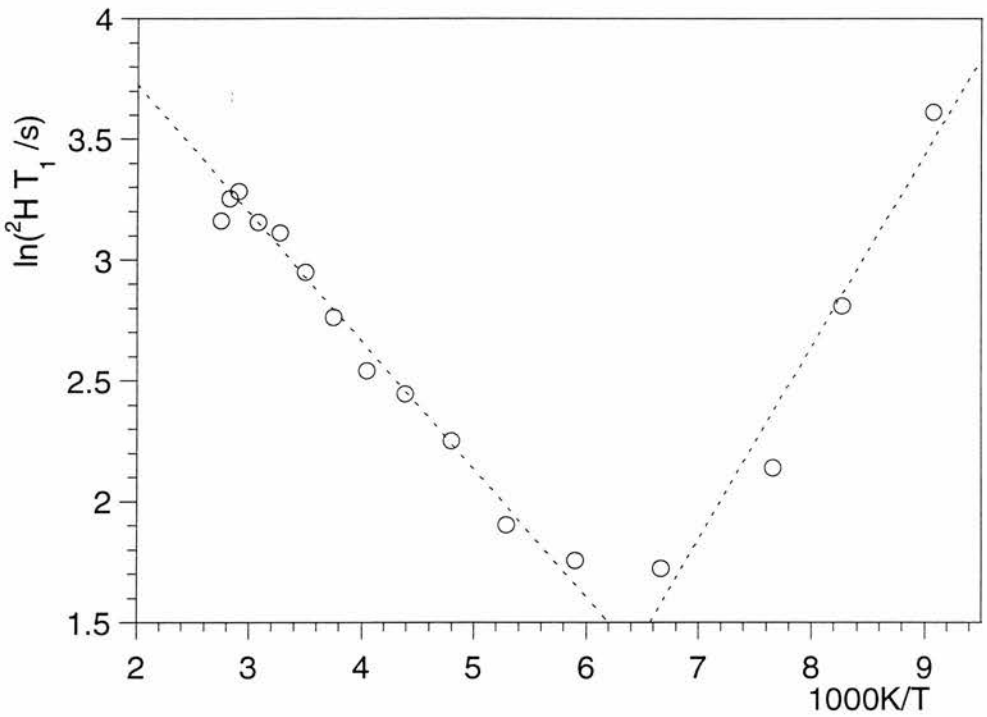

Figure 4.7. A plot of $\ln(^2H\ T_1)$ as a function of 1000K/T together with linear least squares fits for 2,2,4,4-d_4-glutaric acid. Apparent activation energy from the slope is 7 kJ mol^{-1} and 5 kJ mol^{-1} on the low and high temperature sides of the minimum, respectively.

The quadrupolar echo spectra shown in figure 4.8 are independent of the length of the refocusing delay indicating that the rate of the motion is in the fast motion limit, and therefore, consistent with the observation of the T_1 minimum. As expected, they also indicate that not only the rate but also the amplitude of the motion changes with temperature. The width of the spectrum is 119 kHz at 150 K whereas it is only 112 kHz at 286 K. In the fast motion limit this kind of narrowing can only be caused by an increase in the angle of motion but not by a further increase in rate.

It is interesting to analyse the spin-lattice relaxation time data similarly to that of succinic acid. At the T_1 minimum (150 K) the correlation time is 1×10^{-9} s, and the two-site model indicates that the librational angle is smaller that 5°. On the other hand, the spectrum is only 112 kHz wide at 286 K and is further narrowed down to 107 kHz at 345 K indicating *ca.* 20° angle of motion. This angle and the measured spin-lattice relaxation time of 26.7 s give 1×10^{-12} s for the correlation time using eq.

3.5. The decrease in correlation time from 1×10^{-9} s at 150 K to 1×10^{-12} s at 345 K corresponds to an activation energy of 15 kJ mol^{-1}.

The spectra measured at 364 K, above the β to α phase transition, however, are very different from those observed for the β-phase. As for the high temperature spectra of 2,2,3,3-d_4-succinic acid, there is an isotropic peak at zero frequency. Although the melting point is very near to 369 K, the sample was a fine powder and did not show any evidence of melting when removed form the probe after cooling. The remaining powder pattern consists of two Pake doublets. The widths of the outer and inner doublets are 104 and 74 kHz, respectively, indicating librational angles of the order 25 and 40 degrees, respectively.

Figure 4.9 shows simulated spectra using the conical libration model with parameters given in table 4.4. The result for the low temperature spectra is very similar to that discussed above for the two-site model, and therefore, these two models are impossible to distinguish from each other. The spectrum for the α-phase, however, is readily reproduced with the conical libration model but cannot be obtained with the two-site model. This suggests that the motion deviates increasingly from planar at higher temperatures and the phase transition facilitates this change in the mode of motion. Above the melting point, of course, the motion would be isotropic and only the isotropic peak would be observed.

Table 4.4. Parameters used in simulations of ^{2}H quadrupolar echo spectra.

spectrum	p	θ_0	$\Delta\theta$	$W_{calc.}$	$W_{obs.}$
364 Kouter	100	15	1	108	104
inner	45	30	1	74	74
peak	50	55	1	-	-
345 K	100	15	1	108	107
286 K	100	13	1	112	112
150 K	100	5	1	119	119

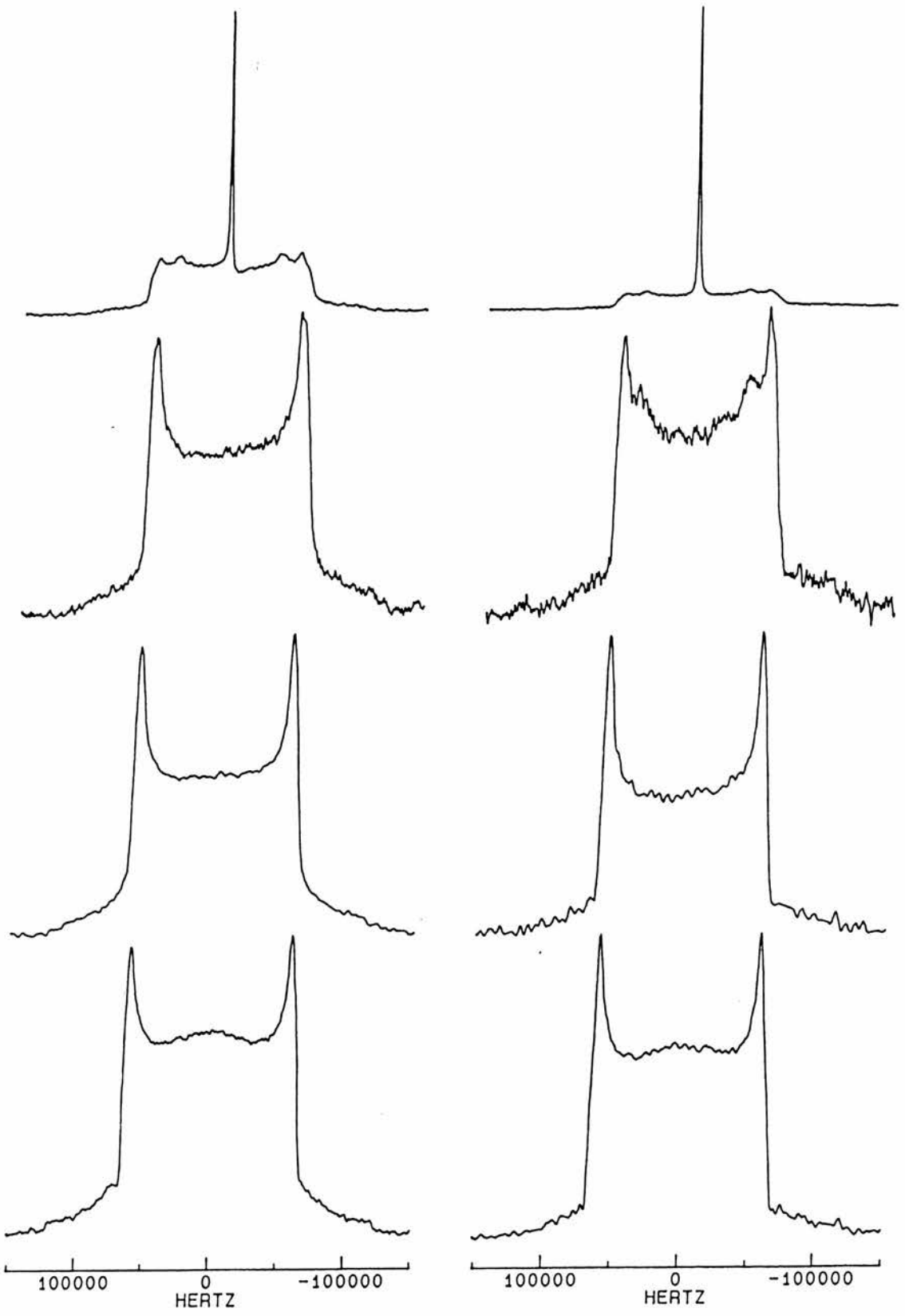

Figure 4.8. Measured ^2H quadrupolar echo spectra for 2,2,4,4-d_4-glutaric acid at different temperatures. Refocusing delay is 20 μs (left) and 160 μs (right). Temperatures are from top to bottom: 364, 345, 286 and 150 K.

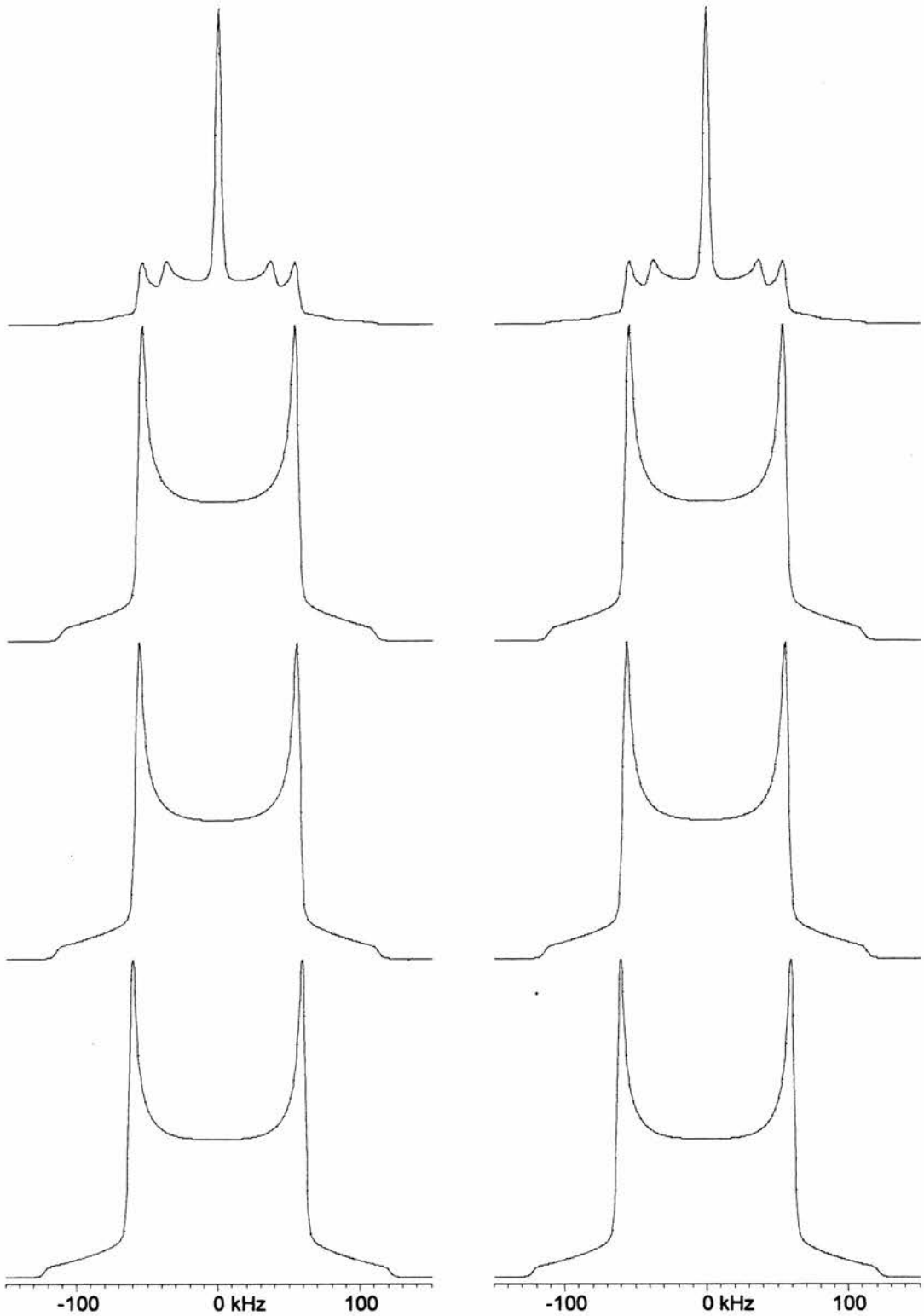

Figure 4.9. Simulated ^2H quadrupolar echo spectra for 2,2,4,4-d_4-glutaric acid for a refocusing delay of 20 μs (left) and 160 μs (right) using the conical libration model. Parameters for the simulations are given in table 4.4. Rate constant is 1×10^8 s^{-1}.

4.3. Adipic acid

Adipic acid, $HOOC(CH_2)_4COOH$, is another member of the even series. Its crystal structure has been studied by various groups.[100-102] The most reliable (R=8.0) of these structures is the one by Housty and Hospital.[102] The molecule is nearly planar and has a centre of symmetry between the two central carbons (appendix, p. A-24). Therefore three peaks are expected in the ^{13}C CP/MAS spectrum.

Figure 4.10 shows ^{13}C CP/MAS spectra measured at different temperatures. As expected, only three peaks are observed. The peaks are at 23.8 ($\underline{C}H_2CH_2COOH$), 34.7 ($CH_2\underline{C}H_2COOH$) and 182.1 ppm ($\underline{C}OOH$). The ^{13}C CP/MAS spectra show no evidence of dynamic dipolar broadening, and therefore, no attempt was made to measure ^{13}C $T_{1\rho}$ relaxation time at any temperature.

The α-carbons of adipic acid were deuterated and ^2H spin-lattice relaxation time for this 2,2,5,5-d_4-adipic acid was measured between 110 K and 393 K. As for succinic acid, the first member of the even series, the ^2H spin-lattice relaxation time is fairly constant over the whole temperature range.115 s was measured at 110 K and 41 s at 393 K for the ^2H spin-lattice relaxation time. The measured values are listed in table 4.5 and shown as a function of temperature in figure 4.11. As for succinic acid, the temperature independent spin-lattice relaxation time is a result of the balance between the increase caused by the shortening correlation time in the fast motion limit and the decrease caused by the increasing amplitude of the motion.

Unfortunately, long ^2H spin-lattice relaxation times made a detailed quadrupolar echo study prohibitively time-consuming, and therefore, only three spectra with a 20 μs refocusing delay were measured at different temperatures. At the lowest temperature 110 K, a 121 kHz wide powder pattern was observed indicating smaller than 5° angle of libration. This spectrum could not be phased for the reasons explained in section 4.1 for succinic acid. The measured spin-lattice relaxation time of 115 s corresponds to a correlation time of 4×10^{-12} s. A 118 kHz wide powder pattern was observed at room temperature (289 K) indicating that the angle of motion increases with temperature.

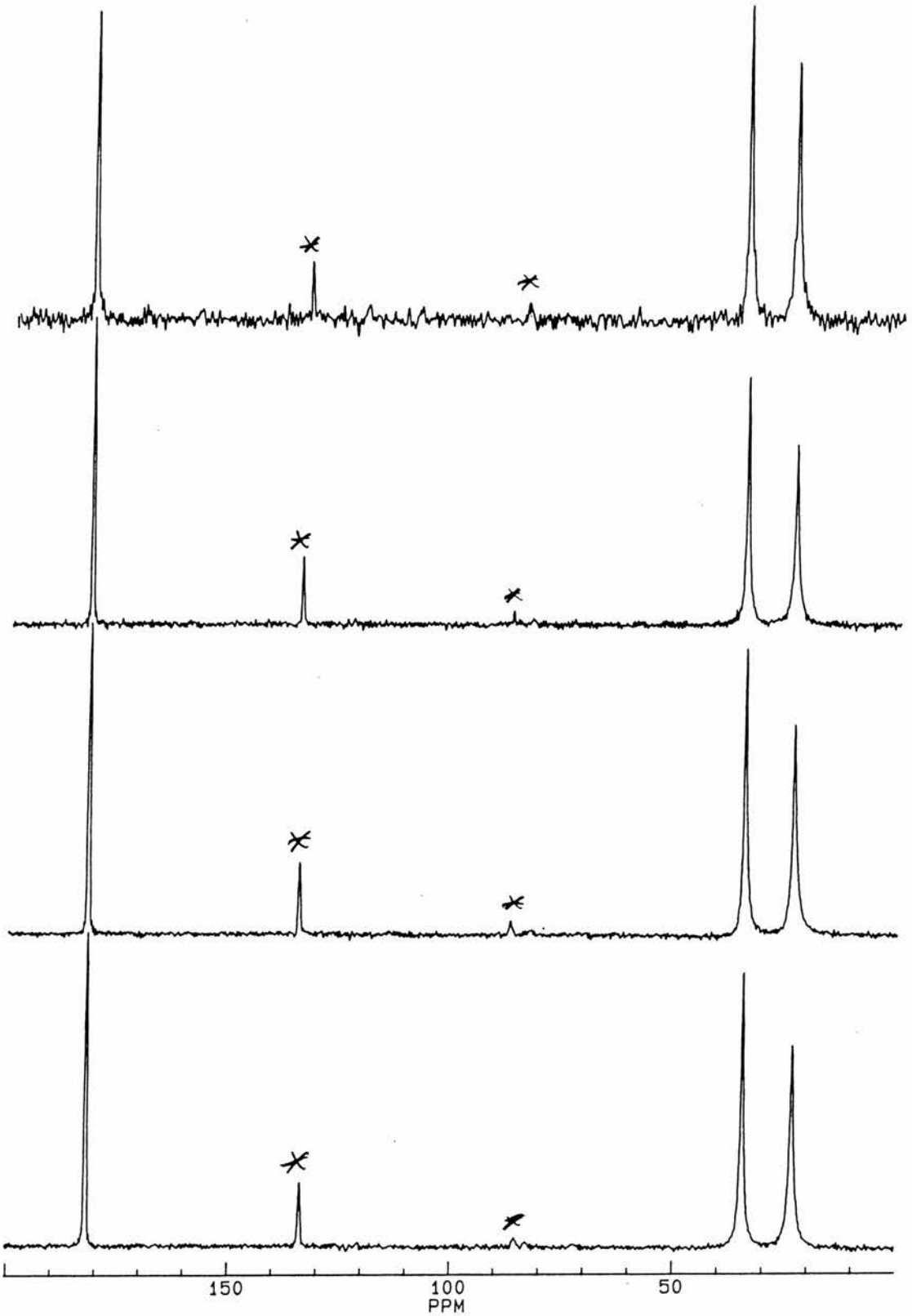

Figure 4.10. ^{13}C CP/MAS spectra for adipic acid at different temperatures. Temperatures are from top to bottom: 358, 296, 238 and 190 K. Spinning sidebands (at 6 kHz) are asterisked.

Table 4.5. Measured ^{2}H T_1 relaxation times for 2,2,5,5-d_4-adipic acid.

T(vtu)/K	T/K	^{2}H T_1/s
109	110	115
130	131	84
140	140	67
160	160	45
180	179	60
200	199	64
220	218	55
240	238	57
260	257	78
280	276	69
300	296	71
320	315	67
340	335	78
360	354	64
380	374	73
400	393	41

At 393 K, a 109 kHz wide powder pattern was observed indicating librational angle of *ca.* 20°. Again, there is a small isotropic peak at zero frequency, but no evidence of melting could be seen in the sample. The measured spin-lattice relaxation time of 41 s corresponds to a correlation time of 7×10^{-13} s.

Interestingly, the observed decrease in correlation time from 4×10^{-12} s at 110 K to 7×10^{-13} s at 393 K corresponds to an activation energy of 2 kJ mol^{-1}, well in agreement with the value of 3 kJ mol^{-1} estimated for 2,2,3,3-d_4-succinic acid (section 4.1).

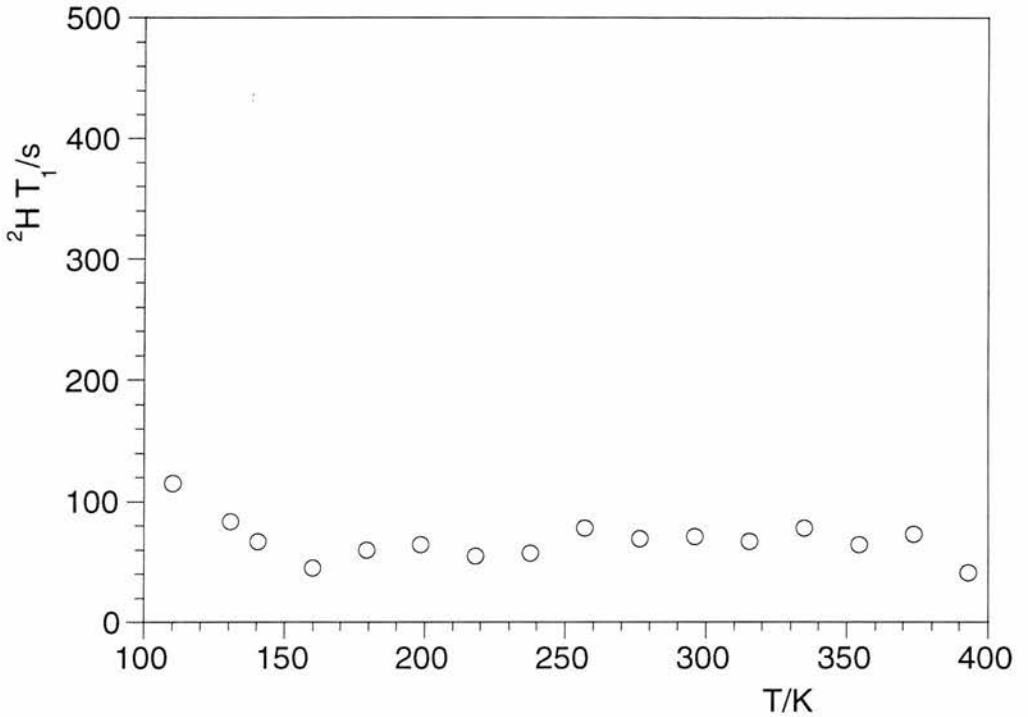

Figure 4.11. ^{2}H spin-lattice relaxation time (T_1) as a function of temperature for 2,2,5,5-d_4-adipic acid.

Figure 4.12 shows simulated spectra using the three dimensional librational model. The parameters used in the simulations are listed in table 4.6. Again, the result for the low temperature spectra is very similar to that discussed above for the two-site model. The isotropic peak is, however, conveniently produced with the conical libration model suggesting that the motion deviates from planar at high temperatures.

Table 4.6. Parameters used in simulations of ^{2}H quadrupolar echo spectra.

spectrum	p	θ_0	$\Delta\theta$	$W_{calc.}$	$W_{obs.}$
393 Kouter	100	15	1	108	109
peak	3	55	1	-	-
289 K	100	5	1	119	118
110 K	100	0	1	122	121

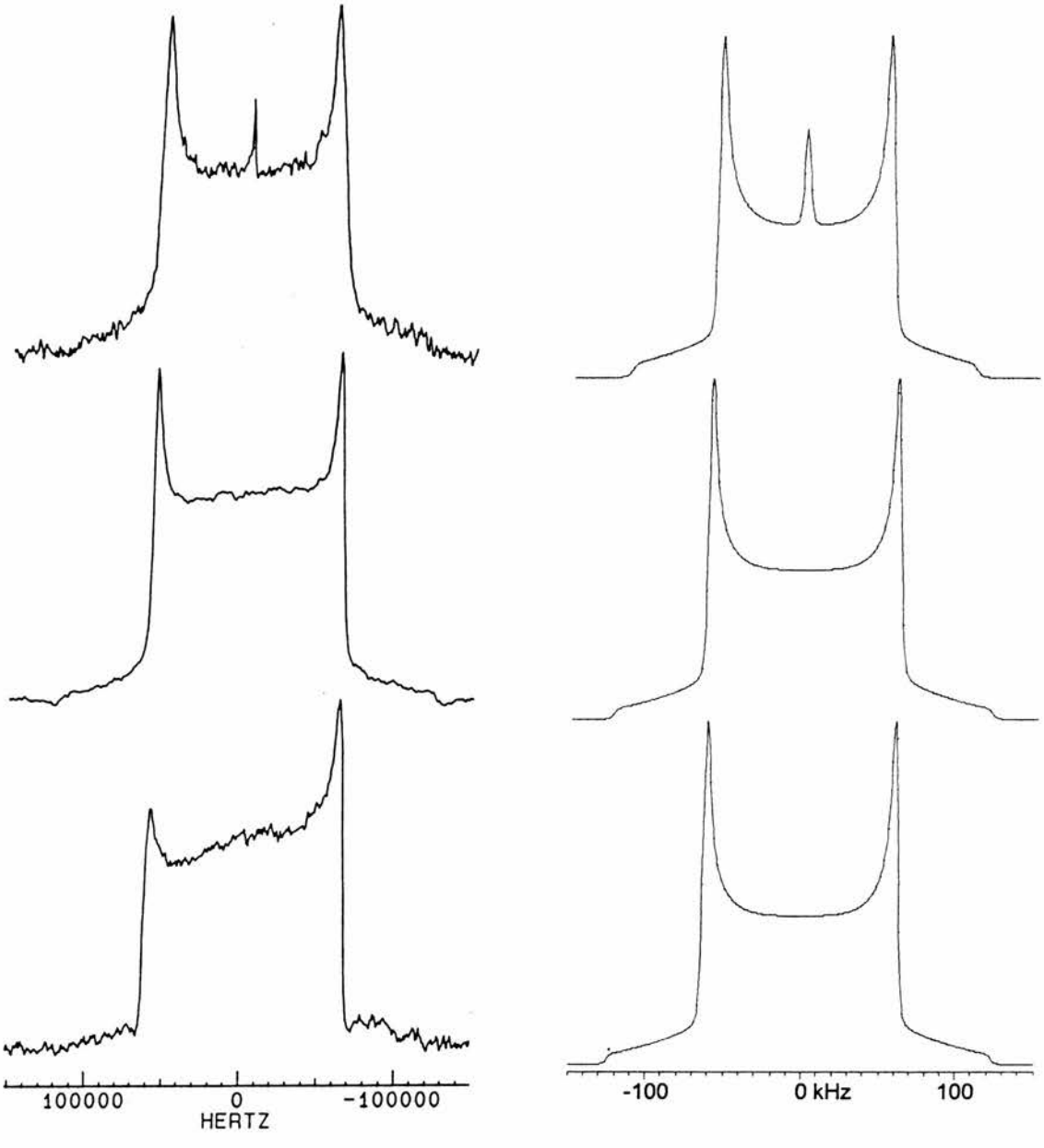

Figure 4.12. Measured ^2H quadrupolar echo spectra for 2,2,5,5-d_4-adipic acid at different temperatures (left) together with simulated spectra using the three dimensional librational model with parameters given in table 4.6. (right). Refocusing delay is 20 μs. Temperatures are from top to bottom: 393, 289 and 110 K. Rate constant is 1×10^8 s^{-1} in the simulations.

4.4. Pimelic acid

Pimelic acid, $HOOC(CH_2)_5COOH$, is another member of the odd series and has a phase change well below its melting point. According to Dupre la Tour the phase change occurs at *ca.* 75 °C.[98] The crystal structures for both phases are known. The phase that is stable at room temperature is called β-phase whereas the α-phase is stable above 75 °C. There is a third phase change near the melting point, but the structure of this γ-phase is unknown.

Macgillavry *et al.* have solved the x-ray structure of the β-phase.[103] The crystals were obtained by recrystallising from water. As for the glutaric acid, there is a C_2 symmetry axis perpendicular to the molecular axis through the central carbon (appendix, p. A-25). This is because the carboxylic groups are equally twisted (*ca.* +30° and -30°) with respect to the molecular plane. Therefore, a total of four peaks are expected in the ^{13}C CP/MAS spectrum for the β-phase.

Kay and Katz have grown crystals in the α-phase from melt.[104] The structure was solved from x-ray diffraction data collected at room temperature. The reliability factor *R* for this refinement was poor, only 20 %, but the authors claim that "for a number of reasons to be mentioned later it appears that the structure is correct, albeit not highly accurate".

Housty and Hospital have solved the structure of α-phase again to determine the positions of hydrogen atoms.[105] Their crystals were obtained by recrystallising from formic acid. They also obtained a rather poor reliability factor of 9.5 %. The structure indicates, however, that there is no axis of symmetry through the central carbon in the α-phase (appendix, p. A-26).

The reason for this lack of symmetry is that the carboxylic groups are differently twisted (+49° and -12°) with respect to the molecular plane. Thus, all the carbon atoms are not magnetically equivalent in the α-phase, and therefore, a total of seven peaks are expected in the ^{13}C CP/MAS spectrum. ^{13}C CP/MAS spectra for pimelic acid recrystallised from formic acid are shown in figure 4.13.

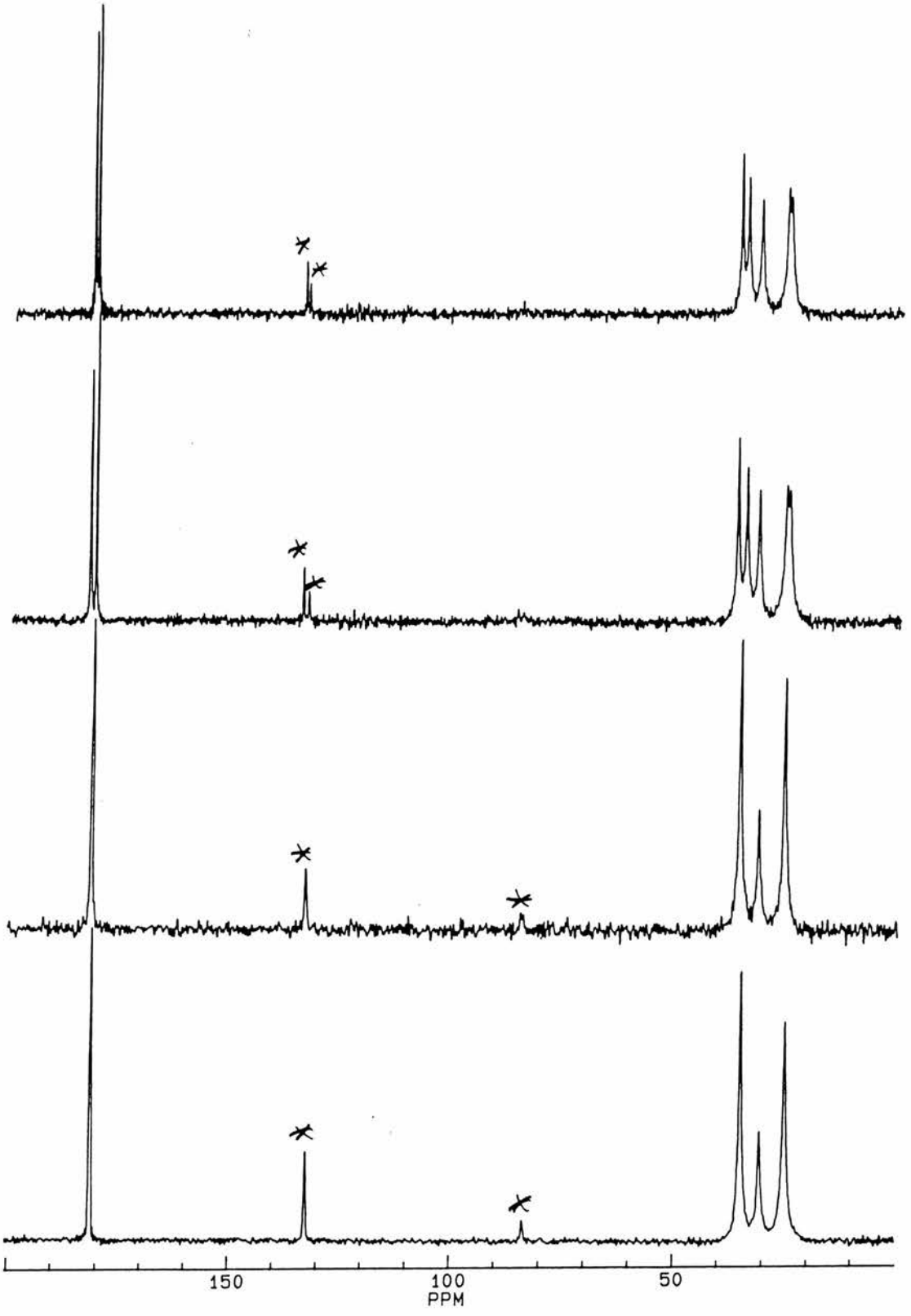

Figure 4.13. ^{13}C CP/MAS spectra for pimelic acid at different temperatures. Temperatures are from top to bottom: 358, 338, 326 and 190 K. Spinning sidebands (at 6 kHz) are asterisked.

Although Housty and Hospital could keep their α-phase crystals for weeks at room temperature, this sample is clearly of β-phase as there are four peaks in the ^{13}C CP/MAS spectrum at 53 °C. Peaks are at 25.3 ppm ($HOOCCH_2\underline{C}H_2CH_2$-), 31.2 ppm ($HOOCCH_2CH_2\underline{C}H_2$-), 35.3 ppm ($HOO\underline{C}CH_2CH_2CH_2$-) and 181.3 ppm ($HO\underline{O}CCH_2CH_2CH_2$-). The spectrum remains the same on cooling to -83 °C indicating the lack of phase transitions between -83 and 53 °C. As expected for the α-phase, all peaks but the peak for the central carbon are split at 65 °C. Peaks are now at 25.4 and 26.0 ppm ($HOOCCH_2\underline{C}H_2CH_2$-), 32.0 ppm ($HOOCCH_2CH_2\underline{C}H_2$-), 34.9 and 36.4 ppm ($HOO\underline{C}CH_2CH_2CH_2$-), 181.5 and 182.3 ($HO\underline{O}CCH_2CH_2CH_2$-). The spectrum remains the same on heating up to 85 °C. After cooling down to 53 °C, the spectrum for the α-phase was still observed but a further cooling down to 45 °C induced a change back to the spectrum for the β-phase. This suggests that the phase transition is reversible but rather slow, and also, that the α-phase is not stable at room temperature.

The phase transition temperatures of pimelic acid and 2,2,6,6-d_4-pimelic acid prepared for ^2H NMR studies were confirmed by differential scanning calorimetry (DCS). The two phase transitions were clearly visible for both samples. The onset of the β to α phase change was at 67 °C for pimelic acid and at 66 °C for 2,2,6,6-d_4-pimelic acid. Again, the phase transition occurs at a lower temperature (below 65 °C) in MAS conditions, probably because of a temperature gradient in the sample. Interestingly, the deuteration affects more the α to γ phase transition, the onset being at 96 °C for pimelic acid and 88 °C for 2,2,6,6-d_4-pimelic acid. The temperature gap between the α to γ phase transition and the melting point is still very small for the deuterated sample, and therefore, no attempt was made to collect a powder diffraction pattern for the γ-phase. The crystal structures of the β and α phases were confirmed by powder diffraction. The powder diffraction patterns for the β and α phases together with simulated patterns generated from the structures of Macgillavry *et al.*[103] for the β-phase and of Housty and Hospital[105] for the α-phase are shown in figure 4.14. Because a non-spinning sample was used, the peak intensities are unreliable in the measured patterns, but otherwise the agreement between the simulated and measured patterns is good.

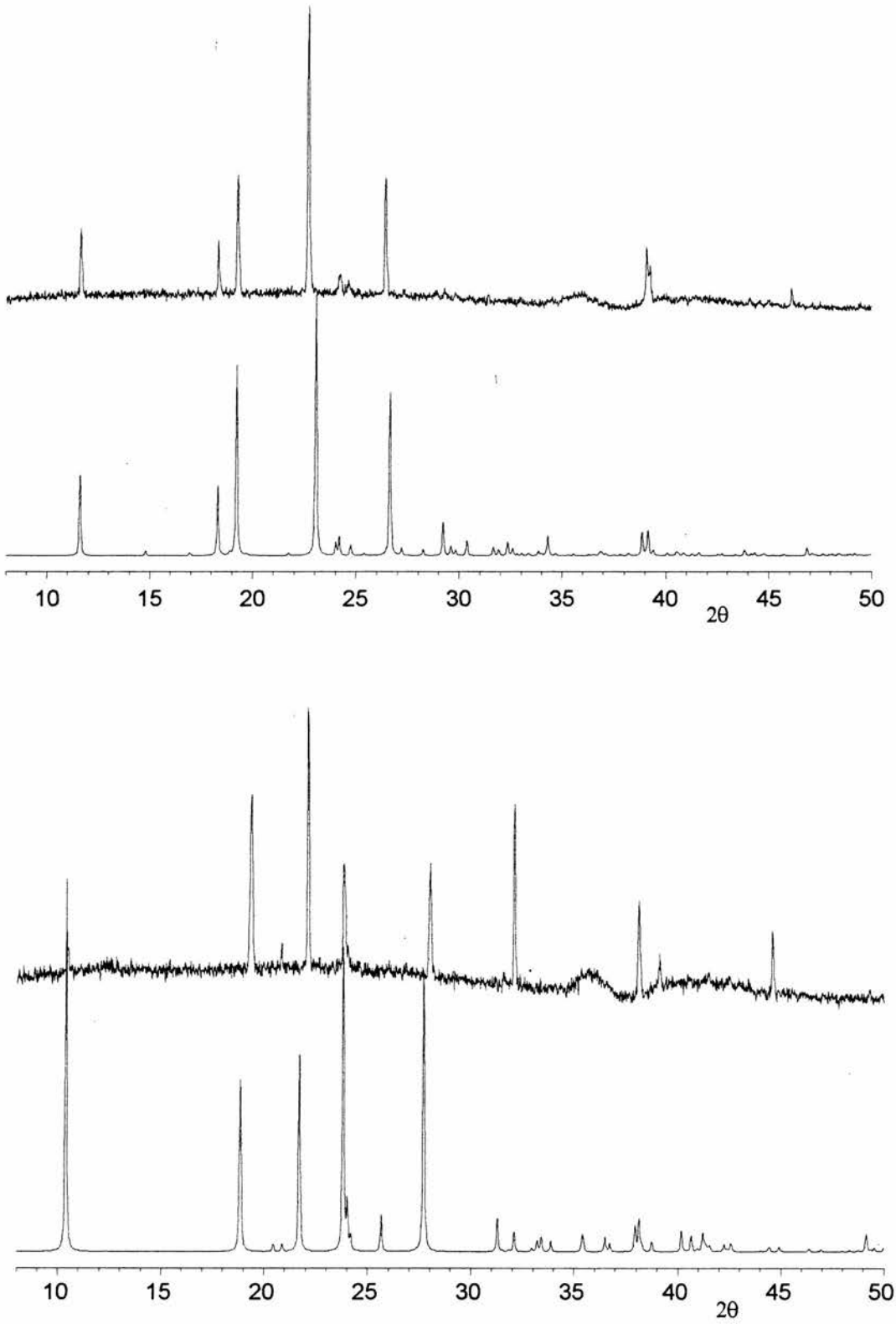

Figure 4.14. Powder diffraction patterns for pimelic acid at 16 °C together with a simulated pattern for the β-phase (bottom) and at 85 °C together with a simulated pattern for the α-phase (top).

The ^{2}H spin-lattice relaxation time was measured for 2,2,6,6-d_4-pimelic acid in a temperature range from 110 K to 375 K. The measured values are listed in table 4.7 and shown as a function of temperature in figure 4.15.

Table 4.7. Measured ^{2}H T_1 relaxation times for 2,2,6,6-d_4-pimelic acid.

T(vtu)/K	T/K	^{2}H T_1/s
109	110	135
112	113	60
116	117	20
123	124	14
133	134	10
153	153	7.0
173	172	9.0
193	192	11
213	211	13
233	231	17
253	250	20
273	270	24
292	288	28
303	299	25
313	309	28
323	318	27
333	328	27
343	338	26
353	347	25
360	354	26
368	362	23
372	366	20
376	370	13
380	374	9.9
381	375	8.0

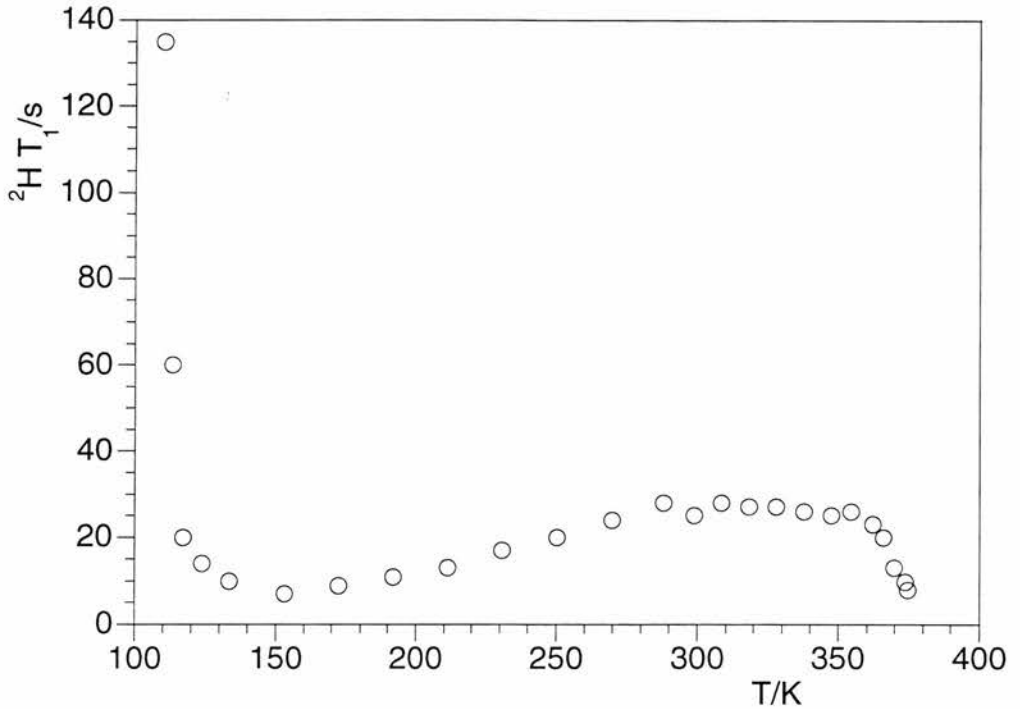

Figure 4.15. Measured ^{2}H spin-lattice relaxation (T_1) time as a function of temperature for 2,2,6,6-d_4-pimelic acid.

The ^{2}H spin-lattice relaxation time decreases rapidly with temperature until a minimum occurs at *ca.* 150 K. Above 150 K, the ^{2}H spin-lattice relaxation time increases with temperature until a plateau occurs from 280 K to 350 K. The increase in the ^{2}H spin-lattice relaxation time has to be due to shortening correlation time for the librational motion in the fast motion limit. As for the 2,2,4,4-d_4-glutaric acid, the increase in spin-lattice relaxation time is partly compensated by a decrease due to increasing amplitude of the motion. Between 280 K and 350 K, the increase in the amplitude fully compensates for the shortening correlation time, and consequently, a plateau of constant spin-lattice relaxation time is observed.

Above 350 K, the spin-lattice relaxation time decreases strongly with temperature. As the onsets of the β to α and α to γ phase transitions are at 340 and 361 K, respectively, this decrease in the spin-lattice relaxation time indicates that the amplitude of the motion increases strongly with temperature in the α-phase (below 361 K) and γ-phase (above 361 K) before the sample melts at 376 K. Above the melting point, of course, the motion would be isotropic.

Figure 4.16 shows the natural logarithm of the spin-lattice relaxation time as a function of inverse temperature together with least squares fits to the linear portions of the curve. The slopes of the least squares lines give 29, 4 and 4 kJ mol^{-1} for the apparent activation energies in the order of increasing temperature. These apparent activation energies relate to changes both in the rate and the amplitude of the motion, and therefore, are unequal to Arrhenius activation energy that relates only to the change in the rate for the motion. The slope above the β to α phase transition gives formally -91 kJ mol^{-1} for the apparent activation energy referring almost purely to the rapid change in the amplitude of the motion.

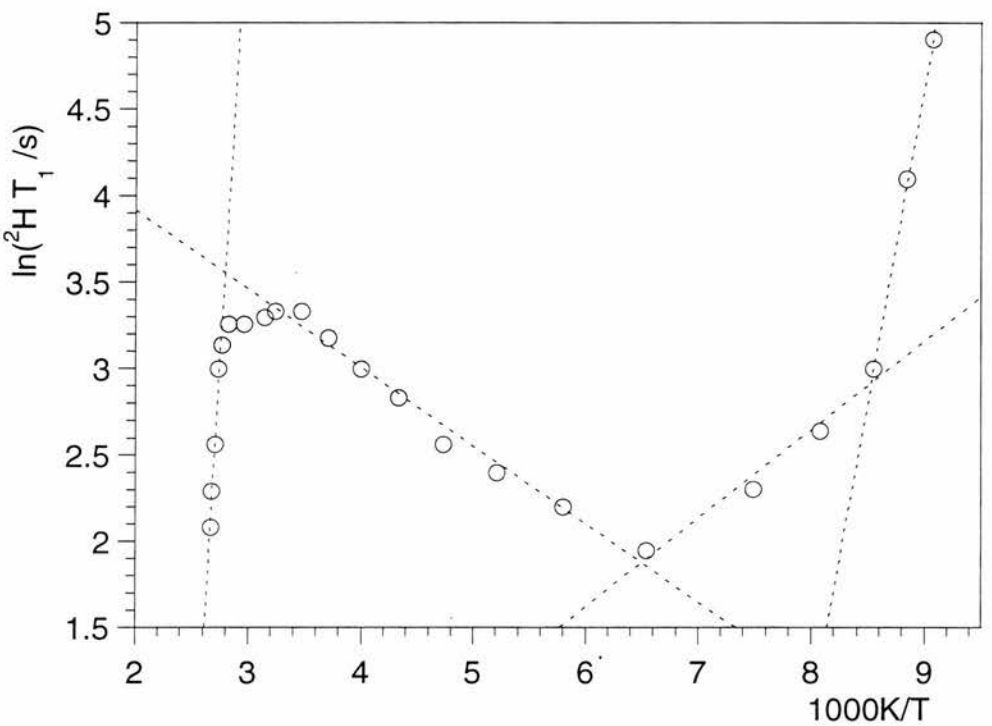

Figure 4.16. A plot of ln(^{2}H T_1) as a function of inverse temperature together with least-squares lines for the four linear regions. Apparent activation energies are from right to left: 29, 4, 4 and formally -91 kJ mol^{-1}.

The increase in the amplitude of the motion should result in narrowing of the quadrupolar echo spectra. Therefore, ^{2}H quadrupolar echo spectra were measured between 120 and 370 K. The measured spectra are shown in figure 4.17. At the lowest temperature 124 K, the quadrupolar echo spectrum is 121 kHz wide indicating a librational motion with the angle smaller than 5°. Little narrowing is

observed on heating to 211 K. The spectrum is still 120 kHz wide indicating that the librational angle is still smaller than 5°. At 288 K, however, more narrowing of the quadrupolar echo spectrum is observed. The spectrum is 116 kHz wide indicating a librational angle of *ca.* 15°. At the highest temperature for the β-phase, 347 K, the quadrupolar echo spectrum is 109 kHz wide indicating an angle of *ca.* 20° for the libration. The spin-lattice relaxation time of 25 s corresponds to a correlation time of 1×10^{-12} s. Again, it is interesting to estimate the activation energy for the decrease in correlation time. A decrease from 1×10^{-9} s at 150 K to 1×10^{-12} s at 347 K corresponds to an activation energy of *ca.* 15 kJ mol^{-1}, the same value as that obtained for 2,2,4,4-d_4-glutaric acid.

Figure 4.19 shows ^2H quadrupolar echo spectra for the α and γ phases. Above the β to α phase transition at 354 K, the spectrum is still 109 kHz wide but with an additional sharp peak at zero frequency suggesting that the phase transition induces an additional mode of motional averaging occurring at the magic angle. As was discussed above, the C_2 symmetry axis is lost on the phase change from β- to α-phase. Therefore, the two CD_2 groups might not only be differently twisted with respect to the molecular plane but also moving differently. At 370 K, above the α to γ phase transition, the sharp peak at zero frequency is more intense, and the remaining powder pattern is 95 kHz wide indicating *ca.* 30° angle of libration.

As before, the low temperature spectra could be simulated with almost any model. The peak in the centre of the high temperature spectra, however, is conveniently produced with the conical libration model, and therefore, this model was used in all simulations. The parameters used in the simulations are listed in table 4.8 and the simulated spectra are shown in figure 4.18 for the β-phase and in figure 4.20 for the α- and γ-phases. The appearance of the peak to the centre of spectrum at high temperatures suggest that the motion increasingly deviates from planar at higher temperatures.

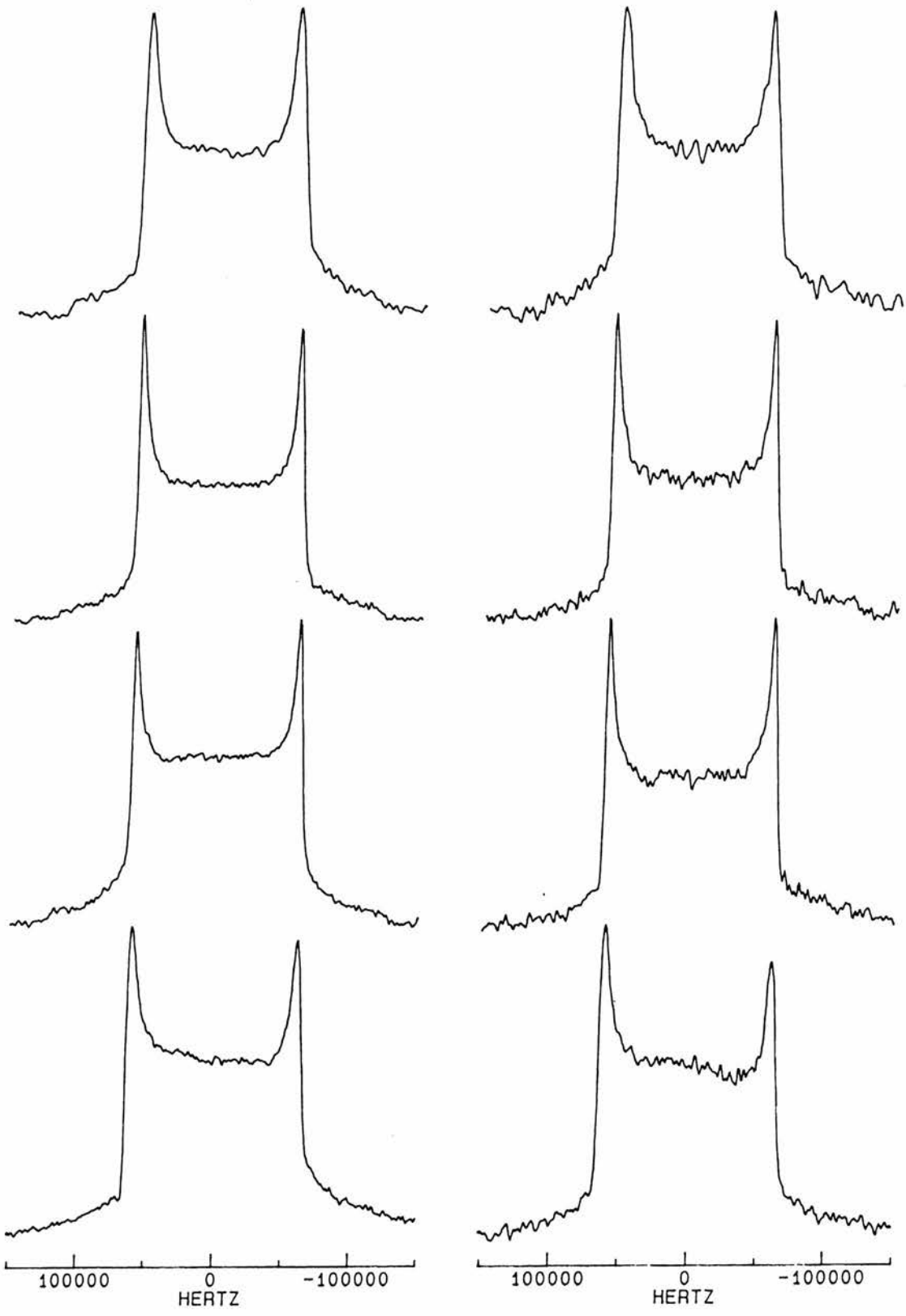

Figure 4.17. ^{2}H quadrupolar echo spectra of 2,2,6,6-d_4-pimelic acid at different temperatures. Temperatures are from top to bottom: 347, 288, 211 and 124 K.

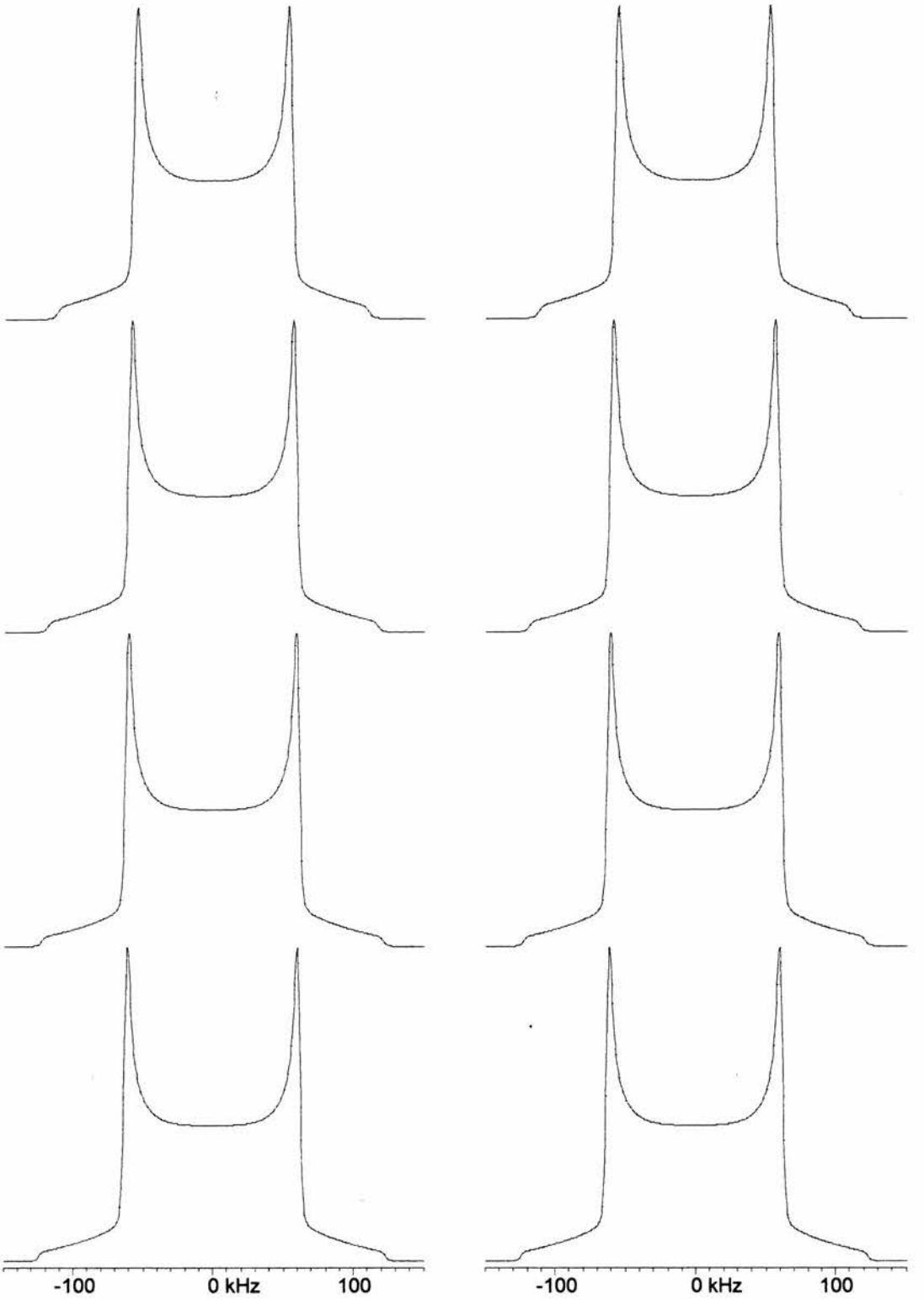

Figure 4.18. Simulated ^2H quadrupolar echo spectra for 2,2,6,6-d_4-pimelic acid with a 20 μs (left) and 160 μs (right) refocusing delays using the three dimensional librational model. Parameters for simulations are given in table 4.8. Rate constant is 1×10^8 s^{-1}.

Table 4.8. Parameters used in the simulations of ^{2}H quadrupolar echo spectra in figures 4.18 and 4.20.

spectrum	p	θ_0	$\Delta\theta$	$W_{calc.}$	$W_{obs.}$
370 K outer	80	15	1	-	-
inner	100	22	1	95	95
peak	50	55	1	-	-
354 K outer	100	15	1	108	109
peak	10	55	1	-	-
347 K	100	15	1	108	109
288 K	100	10	1	116	116
211 K	100	5	1	119	120
124 K	100	0	1	122	121

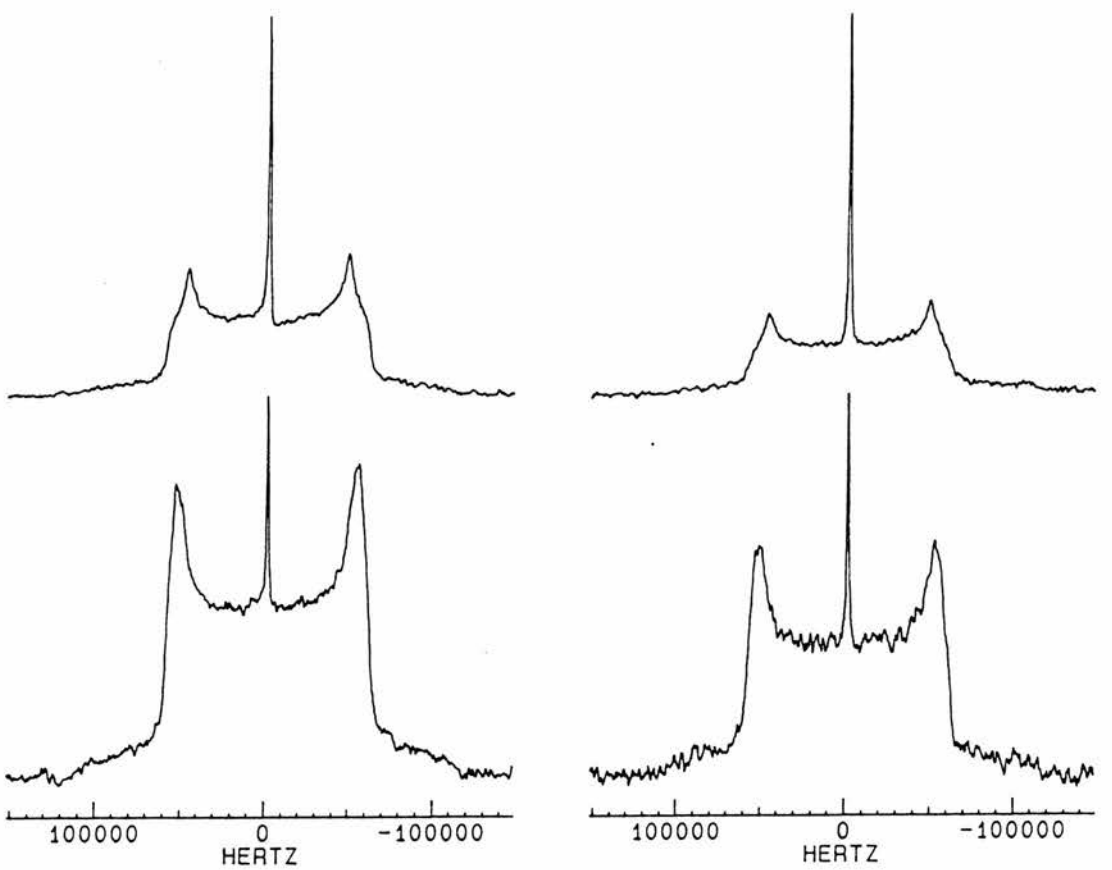

Figure 4.19. Measured ^{2}H quadrupolar echo spectra for 2,2,6,6-d_4-pimelic acid above the β to α phase change (354 K, bottom) and above the α to γ phase change (370 K, top). Refocusing delay is 20 μs (left) and 160 μs (right).

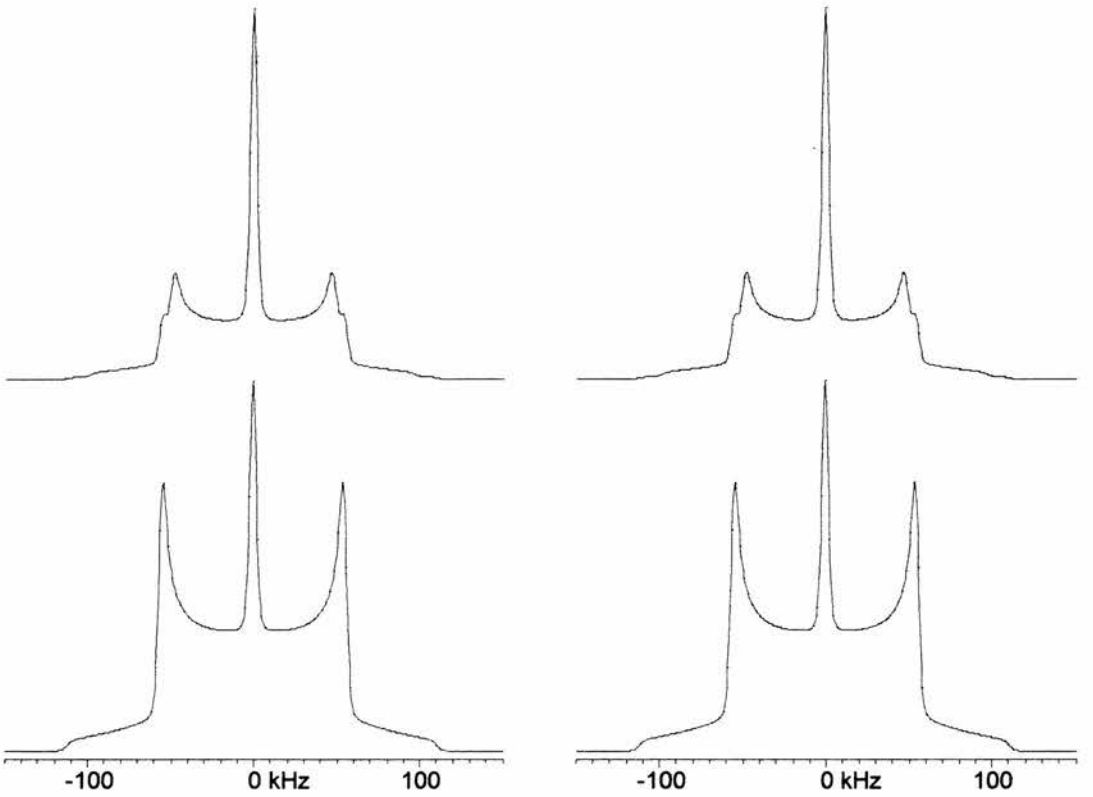

Figure 4.20. Simulated ^2H quadrupolar echo spectra for 2,2,6,6-d_4-pimelic acid above the β to α phase change (bottom) and above the α to γ phase change (top) using the conical libration model. Refocusing delay is 20 μs (left) and 160 μs (right). Parameters for simulations are given in table 4.8. Rate constant is 1×10^8 s^{-1}.

4.5. Suberic acid

Housty *et al.*[106] have solved the crystal structure of suberic acid, $HOOC(CH_2)_6COOH$, from single crystal x-ray data. On the other hand, Gao *et al.*[107] have solved the structure from neutron diffraction data collected at 18.4, 75 and 123 K to obtain nuclear anisotropic displacement parameters for the thermal motion of the protons and to study the librational motion of the molecule (appendix, p. A-27). Although the crystals used in this study were twinned, the authors believe that their analysis is nevertheless correct. The librational motion was first analysed with the rigid-body model of Shoemaker and Trueblood[94] and then further with the segmented body model of He and Craven[108]. However, the rigid-body analysis is assumed to be accurate enough for comparison of the librational angle with the angle obtained from the relaxation time and line shape analysis.

The matrix elements of the librational **L** tensor indicated that the librational motion was characterised by the L_{33} element alone, and therefore, the authors concluded that the motion occurred about the molecular long axis. The square root of the L_{33} element gave 3.0, 4.0 and 5.5° for the angle of libration at 18.4, 75 and 123 K, respectively. Again, it is interesting to compare these values with solid-state NMR data.

^{13}C CP/MAS spectra measured at different temperatures are shown in figure 4.21. Peaks are at 25.5 ($-\underline{C}H_2CH_2CH_2COOH$), 31.1 ($-CH_2\underline{C}H_2CH_2COOH$), 34.9 ($-CH_2CH_2\underline{C}H_2COOH$) and 181.9 ppm ($-\underline{C}OOH$). The spectra show no significant changes in the intensities of the peaks for CH_2 carbons, and therefore, no attempt was made to measure ^{13}C $T_{1\rho}$ relaxation time at any temperature.

The α-carbons of suberic acid were deuterated and the ^2H spin-lattice relaxation time for this 2,2,7,7-d_4-suberic acid was measured in a temperature range from 110 K to 400 K. The measured values are listed in table 4.9 and shown as a function of temperature in figure 4.22. As for the other two members of the even series, succinic and adipic acids, ^2H spin-lattice relaxation time changes little over the whole temperature range. 16 s was measured for the spin-lattice relaxation time at 110 K whereas 38 s was measured at 393 K.

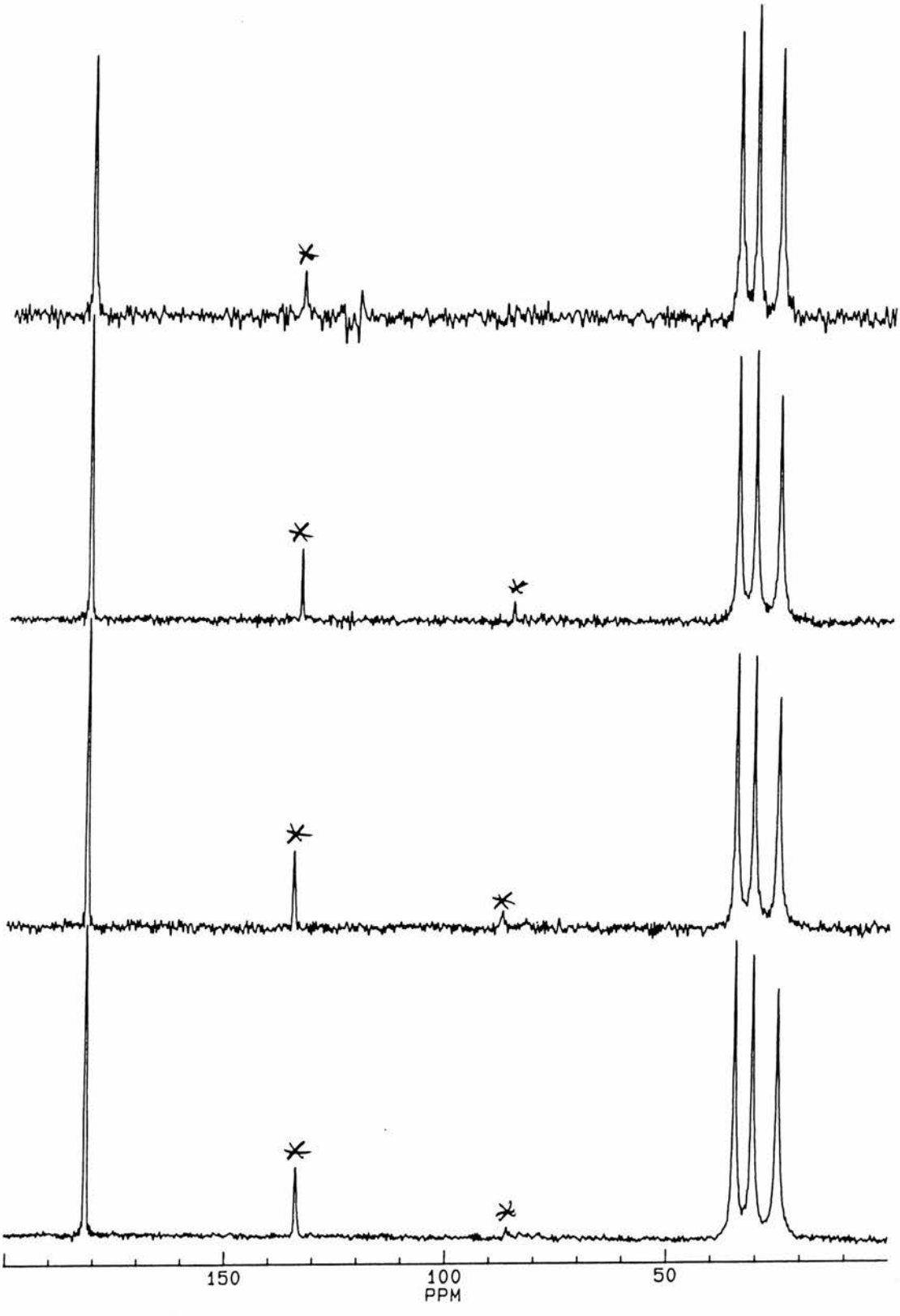

Figure 4.21. ^{13}C CP/MAS spectra for suberic acid at different temperatures. Temperatures are from top to bottom: 358, 296, 238 and 190 K. Spinning sidebands (at 6kHz) are asterisked.

Table 4.9. Measured ^{2}H T_1 relaxation times for 2,2,7,7-d_4-suberic acid.

T(vtu)/K	T/K	^{2}H T_1/s
109	110	16
123	124	12
138	138	14
153	153	12
173	172	20
193	192	28
213	211	38
233	231	38
253	250	55
273	270	71
303	299	68
323	318	64
343	338	62
363	357	55
383	377	43
400	393	38

At low temperatures, ^{2}H spin-lattice relaxation time increases with temperature. Therefore, the rate of the motion has to be in the fast motion limit where a decrease in the correlation time increases the spin-lattice relaxation time. As for the other diacids studied, this increase is partly compensated by a decrease due to increasing amplitude of the motion, and therefore, the spin-lattice relaxation time only slowly increases with temperature. At 270 K, the contribution of the increasing amplitude overtakes the contribution of the shortening correlation time, and as a result, the spin-lattice relaxation time begins to decrease with temperature.

Unfortunately, the ^{2}H spin-lattice relaxation time was too long for effective ^{2}H quadrupolar echo measurements, and consequently, spectra were measured only at three different temperatures. At the lowest temperature 124 K, spectra were measured with 20 μs and 160 μs refocusing delays (fig. 4.23). The spectrum is

independent of the refocusing delay and 124 kHz wide indicating fast and very small angle motion. As before, the angle of libration is estimated to smaller than 5°. This is consistent with the angle of 5.5° obtained from the neutron diffraction data for a non-deuterated sample at 123 K. Using an angle of 5°, the measured spin-lattice relaxation time of 12 s gives 4×10^{-11} s for the correlation time.

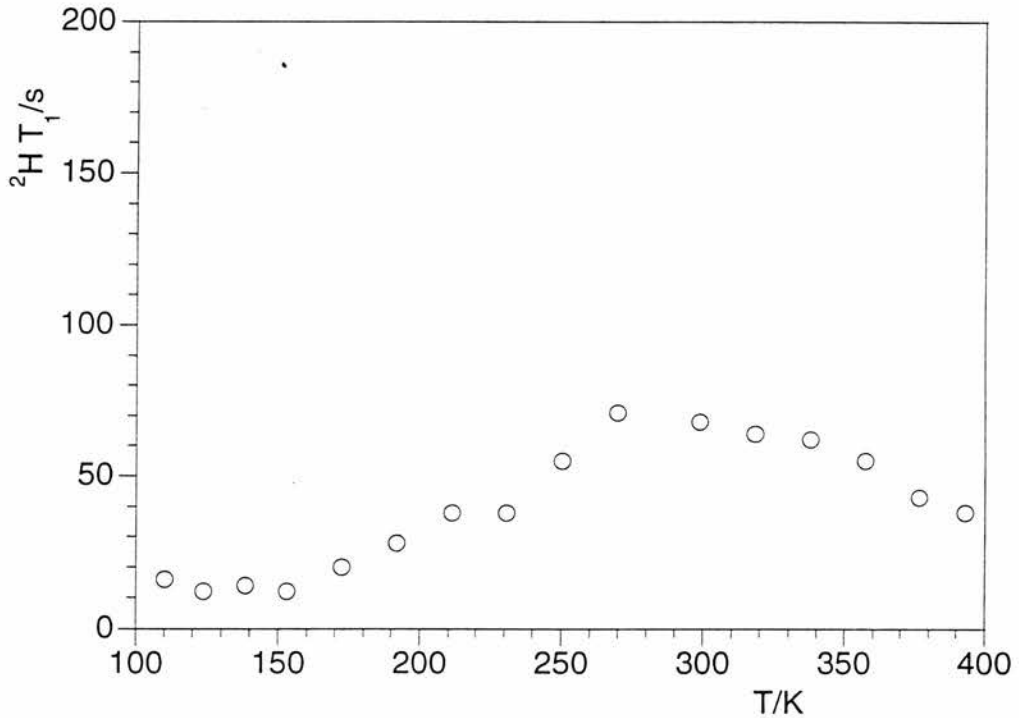

Figure 4.22. ^{2}H T_1 relaxation time as a function of temperature for 2,2,7,7-d_4-suberic acid.

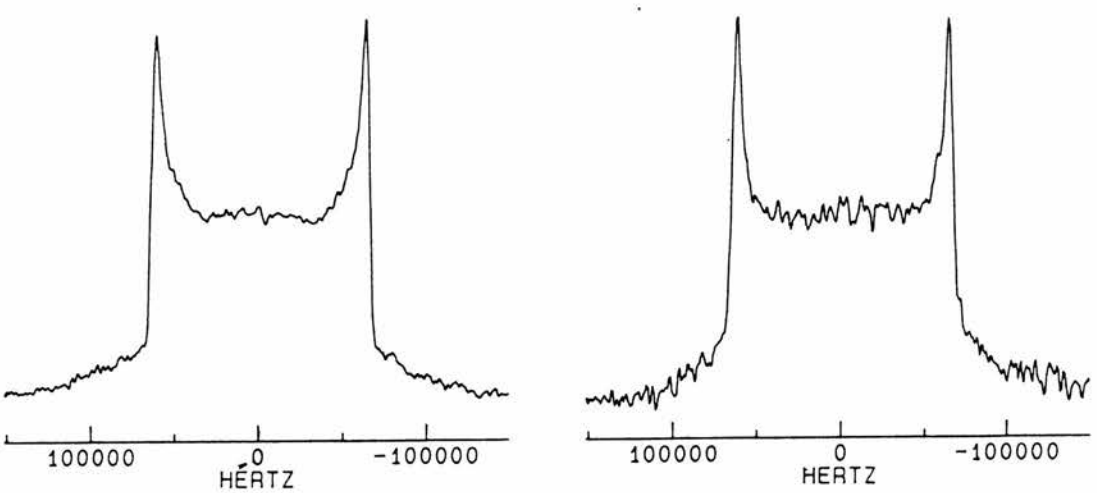

Figure 4.23. Measured ^{2}H quadrupolar echo spectra for 2,2,7,7-d_4-suberic acid at 124 K. Refocusing delay is 20 μs (left) and 160 μs (right).

The angular increase in evident from the ^{2}H quadrupolar echo spectra measured at different temperatures with a 20 μs refocusing delay (fig. 4.24). A 117 kHz wide powder pattern was observed at 289 K, corresponding to an angle of *ca.* 15° for the librational motion. At 393 K, further narrowing of the powder pattern was observed. The width of the powder pattern is 103 kHz indicating a librational angle of order 25°. Moreover, a small peak at zero frequency indicates that the motion also averages C-D bond orientation at a magic angle. Using the angle 25° and eq. 3.5, the ^{2}H spin-lattice relaxation time of 38 s corresponds to a correlation time of 5×10^{-13} s. Interestingly, this decrease in correlation time form 4×10^{-11} s at 123 K to 5×10^{-13} s at 393 K corresponds to activation energy of 7 kJ mol^{-1}.

Also shown in figure 4.24 are spectra simulated with the conical libration model. The parameters used in the simulation are listed in table 4.10. The result is very similar to those of succinic and adipic acids. Again, any model could have been used in the simulation of the low temperature spectra. As the conical libration model conveniently produces the peak in the centre of the spectrum it was used in all simulations. The appearance of the peak in the centre of the powder pattern at high temperatures suggests that the motion deviates increasingly from planar with temperature.

Table 4.10. Parameters used in simulations of ^{2}H quadrupolar echo spectra shown in figure 4.24.

spectrum	*p*	θ_0	$\Delta\theta$	$W_{calc.}$	$W_{obs.}$
393 K outer	100	18	1	103	103
peak	5	55	1	-	-
289 K	100	5	1	119	117
124 K	100	0	1	122	124

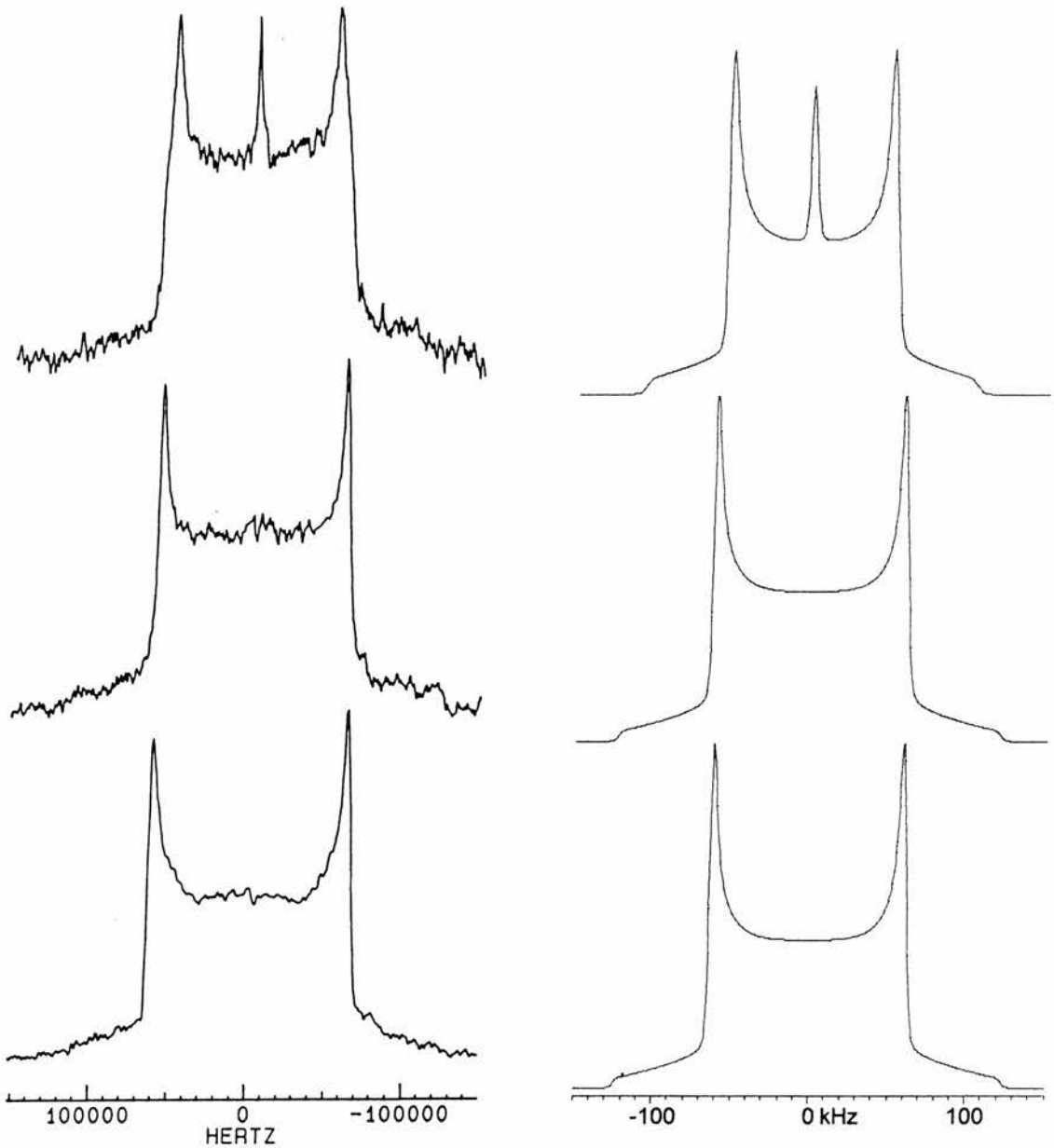

Figure 4.24. Measured ^2H quadrupolar echo spectra for 2,2,7,7-d_4-suberic acid with a 20 μs refocusing delay together with simulated spectra using the three dimensional librational model. Temperatures are from top to bottom: 393, 289 and 124 K. Parameters for the simulations are given in table 4.10.

4.6. Conclusions from the diacid series

This series shows that a temperature independent spin-lattice relaxation time is observed when the increase in the angle of motion compensates for the decrease in correlation time in the fast motion limit. For all the diacids studied, a nearly temperature independent part in the spin-lattice relaxation time curve was observed, and therefore, activation energies for the motion could not be obtained directly. Because of the inherent inaccuracy of the ^{2}H NMR technique for small changes in rate and angle of motion in the fast motion limit and the uncertainty in the actual mode of motion, only very crude estimates for the motional parameters were obtained.

An interesting odd-even effect was observed in the activation energy for the librational motion of these diacids. The activation energy was of the order 5 kJ mol^{-1} for the even diacids while it was of the order 15 kJ mol^{-1} for the odd diacids. This is in agreement with the theory of MacGillavry *et al.*[97] who have proposed that one reason for the alternating physical properties of even and odd diacids is the twisting of odd diacids that increases their free energy in the solid state. According to this NMR study, the twisting of the odd acids also increase the activation energy for the librational motion, and therefore, the libration of the odd diacids is slower than the libration of the even diacids.

Finally, it is interesting to formulate a rule of thumb for the position of the ^{2}H spin-lattice relaxation time minimum for these diacids and similar compounds. Substituting the observed position of the minimum 150 K for the odd diacíds and the activation energy 15 kJ mol^{-1} into the Arrhenius equation indicates that τ_∞ is 1×10^{-14} s. As a result, the position of the ^{2}H spin-lattice relaxation time minimum in kelvins is ten times the activation energy in kJ mol^{-1}. According to this simple rule, the T_1 minimum for the even diacids would be at 50 K, and therefore, is well below the low temperature limit of the probe. *ca.* 110 K. Consequently, only the high temperature side of the minimum was observed for the even diacids.

5. THE DIESTER SERIES

The diacid series gave invaluable information on the dependence of the ^2H spin-lattice relaxation time on temperature when the amplitude of librational motion increases in all-*trans* chains. On the other hand, this diester series was chosen to compare molecular motions in all-*trans* chains with motions in chains containing *gauche* bonds and to study the effect of chain length on the chain motion. The following compounds were chosen to represent these changes in the chain:

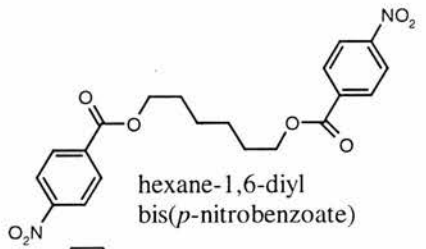

hexane-1,6-diyl
bis(*p*-nitrobenzoate)

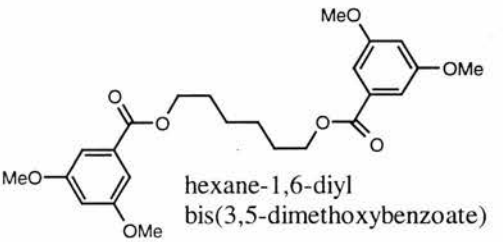

hexane-1,6-diyl
bis(3,5-dimethoxybenzoate)

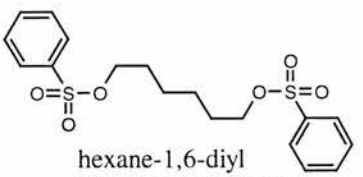

hexane-1,6-diyl
dibenzenesulphonate

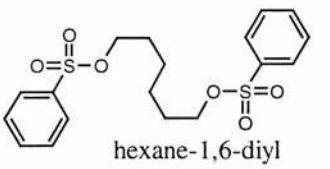

hexane-1,6-diyl
ditosylate

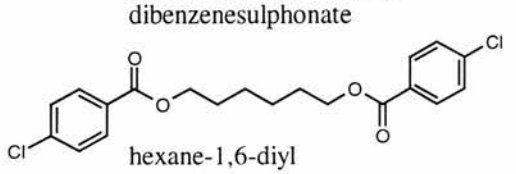

hexane-1,6-diyl
bis(*p*-chlorobenzoate)

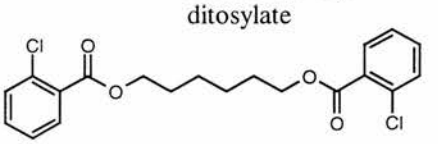

hexane-1,6-diyl
bis(*o*-chlorobenzoate)

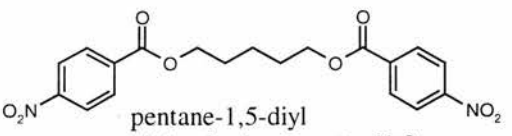

pentane-1,5-diyl
bis(*p*-nitrobenzoate)

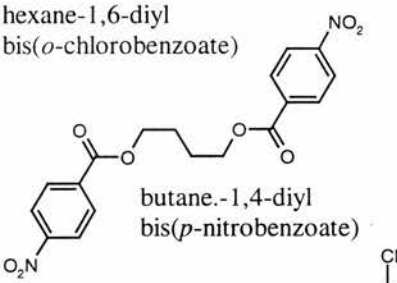

butane.-1,4-diyl
bis(*p*-nitrobenzoate)

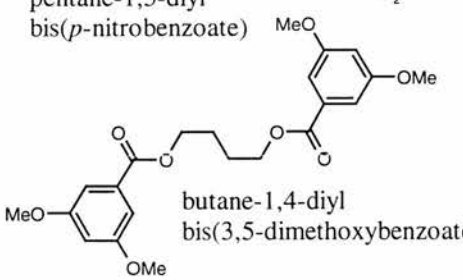

butane-1,4-diyl
bis(3,5-dimethoxybenzoate)

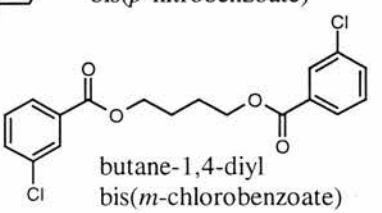

butane-1,4-diyl
bis(*m*-chlorobenzoate)

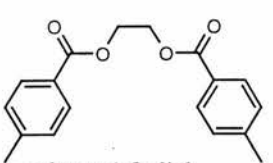

ethane-1,2-diyl
bis(*p*-methylbenzoate)

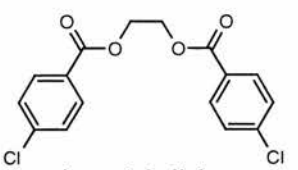

ethane-1,2-diyl
bis(*p*-chlorobenzoate)

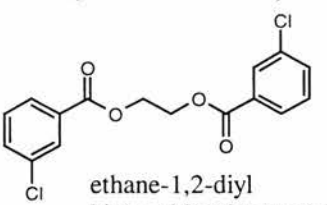

ethane-1,2-diyl
bis(*m*-chlorobenzoate)

5.1. Hexane-1,6-diyl bis(*p*-nitrobenzoate)

The crystal structure of hexane-1,6-diyl bis(*p*-nitrobenzoate) was solved from single crystal x-ray diffraction data. Structural details and views of the unit cell are given in the appendix (p. A-1 and A-28). The molecule is symmetric with a centre of symmetry between the carbons at positions 3 and 4 in the chain. The bond between the carbons at positions 1 and 2 and the symmetrically related bond between the carbons at positions 5 and 6 are in a *gauche* conformation. All other chain carbon-carbon bonds are in a *trans* conformation. Anisotropic displacement parameters for the chain carbons are typical for a small organic compound and fail to indicate any large-scale motion in the chain. Therefore, *trans-gauche* isomerisation is an unlikely mode of motion for this chain.

Figure 5.1 shows ^{13}C CP/MAS spectra measured at different temperatures. A short contact time of 200 μs was used to reduce the intensities of the peaks for the aromatic carbons. Peaks in the room temperature spectrum are at 27.4 ppm ($OCH_2CH_2\underline{C}H_2$), 30.9 ($OCH_2\underline{C}H_2$), 66.4 ($O\underline{C}H_2$), 123.4 ($\underline{C}_{Ar}$(2,6)), 129.7 and 131.8 ($\underline{C}_{Ar}$(3,5)), 134.8 ($\underline{C}_{Ar}$-C=O), 148.7 and 151.0 ($\underline{C}_{Ar}$-NO_2) and 164.7 ppm ($\underline{C}$=O).

The high temperature spectra are very similar to the room temperature spectrum. Instead of two peaks at 148.7 and 151.0 ppm, however, only one peak is observed for the aromatic ring carbons bonded to nitro group in the spectrum measured at 367 K. This could reflect some reorientation process of nitro groups but was not studied further. Otherwise this spectrum is similar to that measured at room temperature.

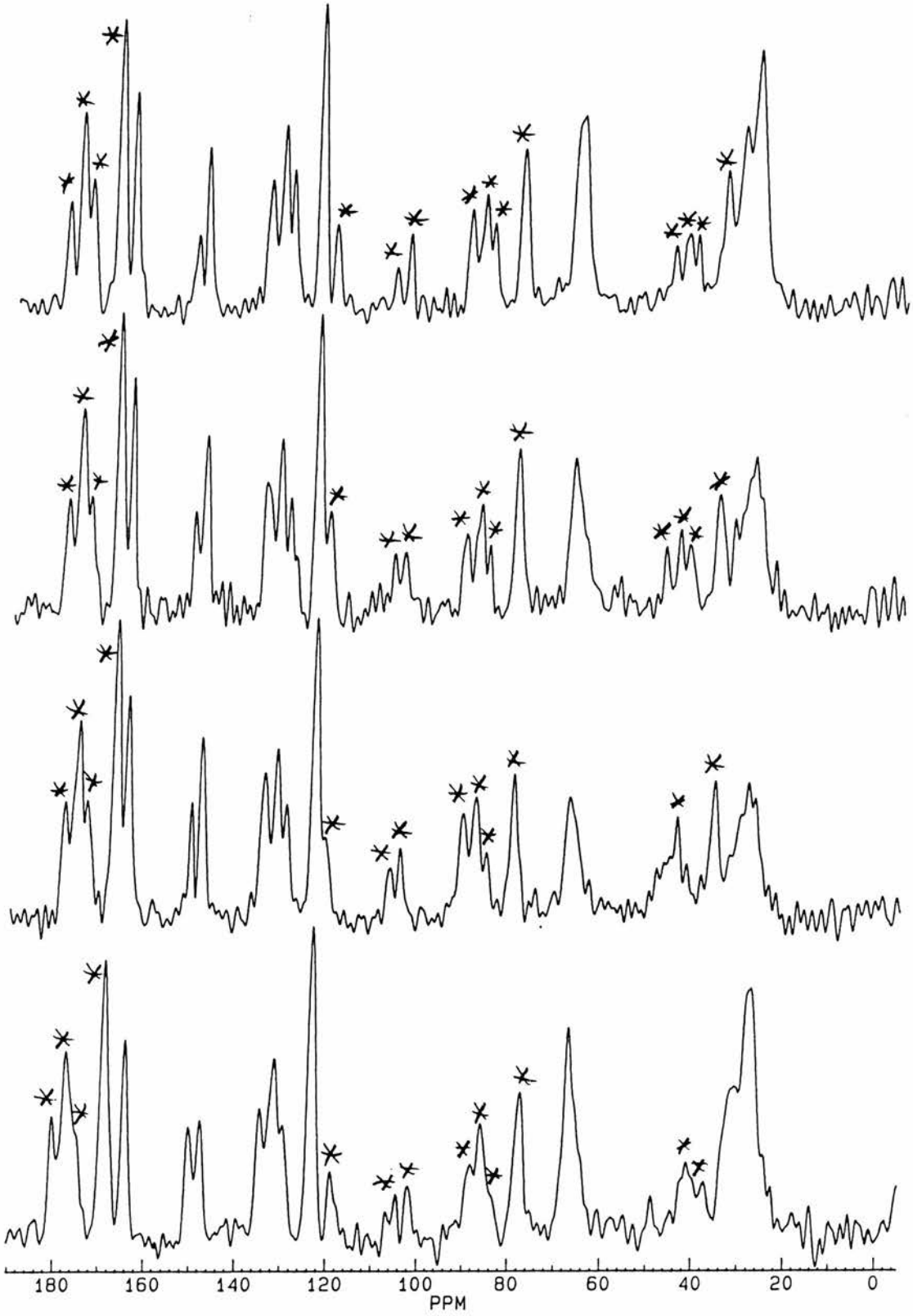

Figure 5.1. ^{13}C CP/MAS spectra for hexane-1,6-diyl bis(*p*-nitrobenzoate) at different temperatures. Temperatures are from top to bottom: 246, 234, 222 and 206 K. Spinning sidebands (at 5.5 kHz) are asterisked.

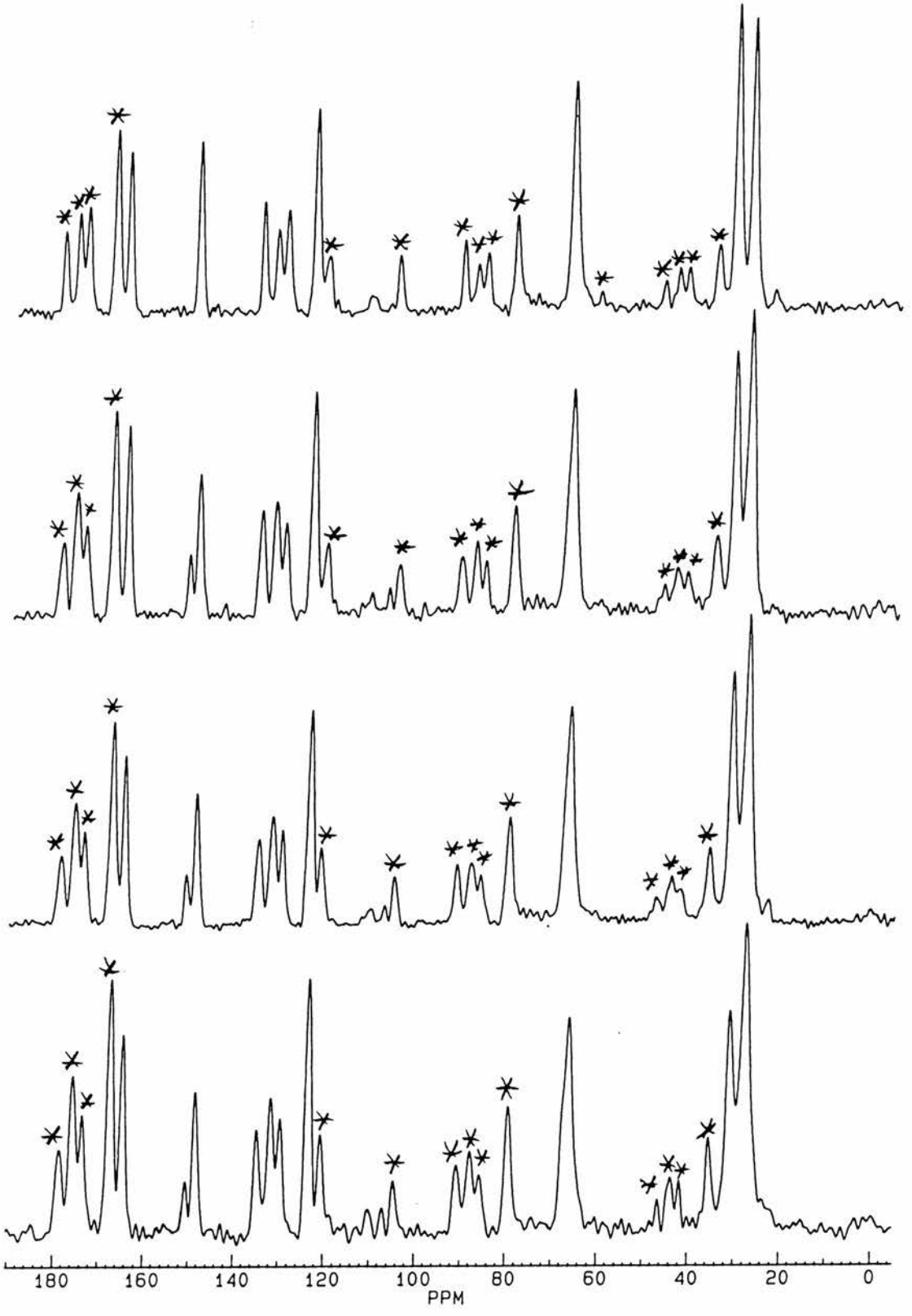

Figure 5.1. (continued) ^{13}C CP/MAS spectra for hexane-1,6-diyl bis(*p*-nitrobenzoate) at different temperatures. Temperatures are from top to bottom: 367, 318, 298 and 270 K. Spinning sidebands (at 5.5 kHz) are asterisked.

Interesting changes occur in the ^{13}C CP/MAS spectra on cooling down from room temperature. At 270 K, the peaks for chain carbons are broader and less intense than at room temperature. At 234 K, further broadening of these peaks occur and their intensity is nearly equal to the intensity of the spinning sideband at 37 ppm, that is, *ca.* 20% of their intensity at room temperature. Maximum broadening and loss of intensity is observed at 222 K. At the lowest temperature achieved 206 K, the peaks sharper and more intense than at 222 K.

The observed broadening of the peaks for the chain carbons is due to dynamic dipolar broadening that is caused by molecular motion and decreases decoupling efficiency when the frequency of molecular motion is comparable to the precession frequency of the protons in the decoupling field. The decoupling frequency in these measurements was 63 kHz, and therefore, the broadening of the peaks indicates that the chain undergoes molecular motion with frequencies of the order 60 kHz at 220 K.

As the spin-locking frequency was equal to the decoupling frequency, maximum dipolar broadening occurs simultaneously with a ^{13}C $T_{1\rho}$ minimum, and therefore, the loss of signal intensity is partially caused by a short ^{13}C $T_{1\rho}$ relaxation time. Consequently, the observation of dynamic dipolar broadening suggests that a ^{13}C $T_{1\rho}$ minimum should occur near 220 K.

^{13}C $T_{1\rho}$ relaxation time was measured for the chain carbons at different temperatures using the same spin-locking frequency of 63 kHz. The measured values are listed in table 5.1 and shown as a function of temperature in figure 5.2. The lines in figure 5.2 are best-fitting lines to equation

$$y = \frac{1 + c \cdot \exp(2b / x)}{a \cdot \exp(b / x)} \tag{5.1.}$$

where the Arrhenius equation 1.21 has been substituted into eq. 1.19 and all constants have been combined into parameters *a, b* and *c*.

Table 5.1. ^{13}C $T_{1\rho}$ relaxation time for the chain carbons of hexane-1,6-diyl bis(*p*-nitrobenzoate). Peaks are at 27.4, 30.9 and 66.4 ppm.

T/VTU	*T*/K	27.4 ppm	30.9 ppm	66.4 ppm
280	285	18.2	20.0	25.6
275	281	15.9	12.2	-
270	277	12.7	10.4	20.8
265	273	9.1	14.3	10.4
260	269	5.9	5.9	11.5
255	266	5.8	6.4	6.7
250	261	4.7	4.9	5.9
245	257	4.1	4.7	4.9
240	253	4.8	4.8	4.2
230	245	2.4	1.4	2.5

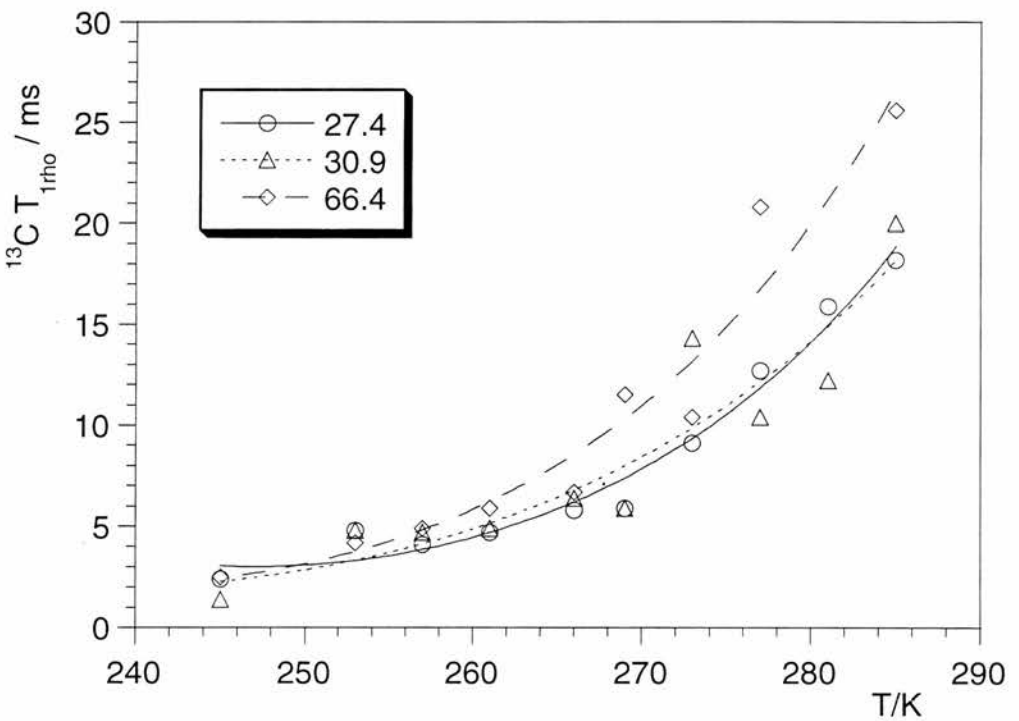

Figure 5.2. Dependence of ^{13}C $T_{1\rho}$ on temperature for the chain carbons of hexane-1,6-diyl bis(*p*-nitrobenzoate) together with least-squares fits to eq. 5.1.

The best-fitting lines suggest that the ^{13}C $T_{1\rho}$ minimum is below 240 K for all chain carbons. This consistent with the observation of maximum dipolar broadening at 220 K. Unfortunately, the proton spin-lattice relaxation time for this compound increases

with decreasing temperature. A recycle delay of 10 s was used at room temperature but delays longer than 30 s were needed to prevent saturation below 240 K. This made the measurement of ^{13}C $T_{1\rho}$ relaxation time prohibitively time-consuming below 240 K. For the same reason, the signal-to-noise ratio was rather poor in the spectra used in the calculation of the ^{13}C $T_{1\rho}$ relaxation times. This is seen as scattering of the data points from the fitted lines. Comparing equation 5.1 with equation 1.19 indicates that the parameter b equals the apparent activation energy E_a. Apparent activation energies were calculated, however, from the slopes of plots of $\ln(^{13}C\ T_{1\rho})$ as a function of inverse temperature.

Figure 5.3 shows plots of $\ln(^{13}C\ T_{1\rho})$ as a function of reciprocal temperature (1000K/T) for all chain carbons together with least-squares lines. Again, the scattering of the data points from the fitted straight lines is due to the low signal-to-noise ratio in the spectra. The slopes of the fitted lines indicate that apparent activation energies are nearly equal for all the chain carbons. The apparent activation energy is 30 kJ/mol for carbons at positions 1 and 6 (at 66.4 ppm) and 34 kJ/mol for all the other chain carbons (at 30.9 and 27.4 ppm).

Unfortunately, the ^{13}C $T_{1\rho}$ relaxation time fails to give any direct information about the details of the molecular motion. Furthermore, the proton spin diffusion rate can be very high in crystalline compounds, thus making the ^{13}C $T_{1\rho}$ relaxation time more dependent on the spin-spin process than on the spin-lattice relaxation.[50] The total width of the proton spectrum was *ca.* 100 kHz between 200 and 360 K indicating a proton spin diffusion rate of the same order. This spin diffusion rate is high compared with the spin-locking frequency 63 kHz used to measure ^{13}C $T_{1\rho}$ relaxation times suggesting that the contribution of the spin-spin process to the relaxation is high. In principle, the contribution of spin diffusion could be measured by comparing ^{13}C T_{IS}(ADRF) relaxation times with ^{13}C $T_{1\rho}$ relaxation times but the measurement of ^{13}C T_{IS}(ADRF) is instrumentally very demanding and was not attempted. The contribution of spin diffusion, however, is fairly constant because the width of the proton spectrum is independent of temperature between 200 and 360 K, and therefore, does not affect the calculation of apparent activation energy from the

slope of $\ln(^{13}C\ T_{1\rho})$ vs. $1/T$ but rather affects the intercept and thus makes the calculation t_∞ and B^2 from the intercept difficult.

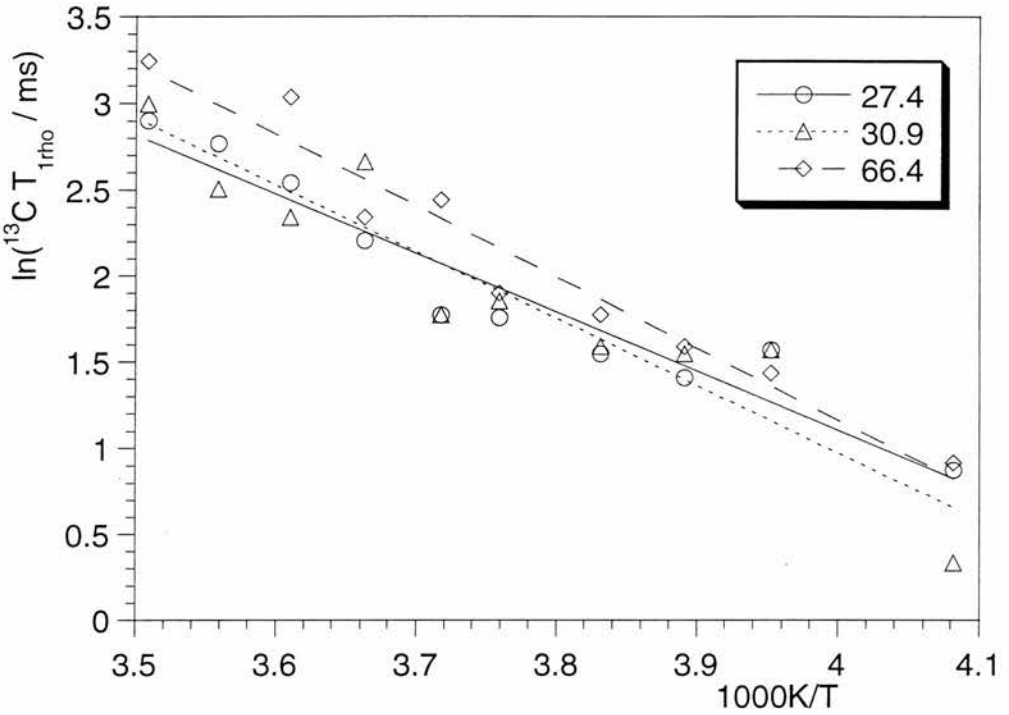

Figure 5.3. Dependence of $\ln(^{13}C\ T_{1\rho})$ on inverse temperature for the chain carbons of hexane-1,6-diyl bis(*p*-nitrobenzoate). Apparent activation energies are 34, 34 and 30 kJ mol^{-1} for the peaks at 27.4, 30.9 and 66.4 ppm, respectively.

The ^{13}C CP/MAS spectrum was inverted at 358 K with the pulse sequence of Torchia.[43] Magnetisation was left to evolve under ^{13}C spin-lattice relaxation for different time periods (fig. 5.4). During this delay, a train of saturating 90° pulses was applied on the proton channel to avoid any cross-polarisation effects. The spectrum at the bottom of fig. 5.4 was measured after a short evolution delay of 5 ms, and consequently, all the peaks are inverted. The next spectrum was measured after a longer delay of 0.5 s. The peaks for the chain carbons have considerably decreased in intensity. Moreover, the peaks for the central carbons are smaller than the peaks for the chain end carbons indicating that the central carbons relax faster than the chain end carbons. The second topmost spectrum was measured after a 0.85 s delay. The peaks for the central carbons are comparable to the noise level but the peak for the chain end carbons is still of considerable intensity. Finally, all chain carbons have fully relaxed in 2.5 seconds after inversion (fig. 5.4, top).

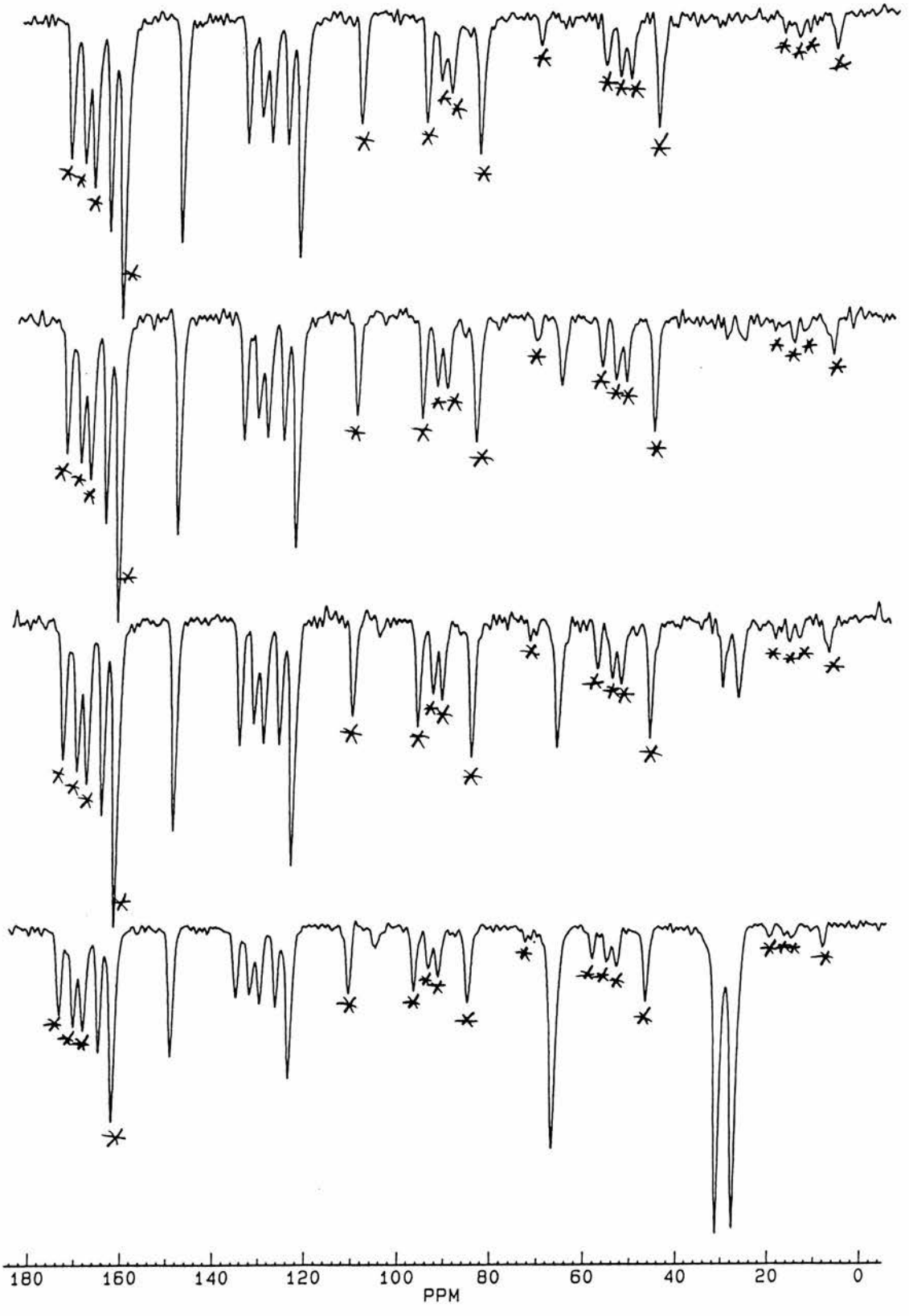

Figure 5.4. Recovery of an inverted ^{13}C CP/MAS spectrum under ^{13}C spin-lattice relaxation. Evolution delays are from top to bottom: 2.5 s, 0.85 s, 0.5 s and 5 ms. Spinning sidebands (at 4.8 kHz) are asterisked.

^{13}C spin-lattice relaxation was adequately described with a single exponential for all chain carbons, and therefore, ^{13}C spin-lattice relaxation times were calculated from exponential fits to the evolution of peak intensity as a function of time. ^{13}C spin-lattice relaxation times were 490 ± 35 ms for carbons at 1 and 6 positions, 245 ± 14 ms for carbons at 2 and 5 positions and 270 ± 16 ms for carbons at 3 and 4 positions in the chain. These values indicate that the central carbons relax about twice as fast as the chain end carbons. Interestingly, aromatic and carbonyl carbons fail to relax at all during the time in which the chain carbons relax fully, and therefore, the *p*-nitrophenyl groups in this compound can be considered as static compared with the alkyl chain.

Two different chain deuterated samples were prepared for deuterium NMR studies. The alkyl chain was deuterated at the 1 and 6 positions yielding 1,1,6,6-d_4-hexane-1,6-diyl bis(*p*-nitrobenzoate) and in the 2 and 5 positions yielding 2,2,5,5-d_4-hexane-1,6-diyl bis(*p*-nitrobenzoate). The ^{2}H spin-lattice relaxation time was measured for both samples at different temperatures. These values are listed in table 5.2 and shown as a function of temperature in figure 5.5.

For both samples, ^{2}H spin-lattice relaxation time decreases strongly with temperature until a minimum occurs at *ca.* 350 K. According to the rule of thumb formulated in section 4.6 (chapter 4) this temperature for the minimum corresponds to an activation energy of 35 kJ mol^{-1}. Figure 5.6 shows the natural logarithm of the ^{2}H spin-lattice relaxation time as a function of inverse temperature for both samples. The plots are satisfactorily linear from *ca.* 290 K to 200 K. Also shown in figure 5.6 are linear least-squares fits to the data in this region. The slopes of these lines give 35 and 36 kJ mol^{-1} for the apparent activation energy of the 1,1,6,6-d_4 and 2,2,5,5-d_4 derivatives, respectively, satisfactorily in agreement with the value 34 kJ mol^{-1} obtained from the ^{13}C $T_{1\rho}$ data for the same positions. It is interesting to estimate the position of the ^{13}C $T_{1\rho}$ minimum from the ^{2}H T_1 relaxation time data. The correlation time is 1.2×10^{-9} s at the ^{2}H T_1 minimum where $\omega_0\tau_c=0.6$ while it is only 2.5×10^{-6} s at the ^{13}C $T_{1\rho}$ minimum where $\omega_1\tau_c=1$. Using these values and an activation energy of 35 kJ mol^{-1} the Arrhenius equation gives 210 K for the position of the ^{13}C $T_{1\rho}$ minimum, satisfactorily in agreement with the observed 220 K.

Table 5.2. Measured ^{2}H spin-lattice relaxation times for 1,1,6,6-d_4-hexane-1,6-diyl and 2,2,5,5-d_4-hexane-1,6-diyl bis(*p*-nitrobenzoates).

T(vtu)/K	T/K	^{2}H T_1/s 1,1,6,6-d_4	^{2}H T_1/s 2,2,5,5-d_4
190	189	812	-
192	190	209	-
193	192	381	-
195	194	68.0	-
198	197	48.0	-
203	202	27.0	12.9
208	206	16.0	-
213	211	7.70	9.3
223	221	3.50	4.1
233	231	1.41	2.3
243	241	0.752	0.772
253	250	0.384	0.351
263	260	0.240	0.236
273	270	0.149	0.111
283	279	0.0940	0.0650
290	286	0.0700	-
293	289	-	0.0457
303	299	0.0480	0.0333
313	309	0.0340	0.0284
323	318	0.0280	0.0250
333	328	0.0220	0.0222
343	338	0.0203	0.0217
348	343	0.0186	-
353	347	0.0182	0.0213
358	352	0.0178	-
363	357	0.0186	0.0217
373	367	0.0188	0.0236
383	377	0.0204	0.0247
388	381	0.0232	-

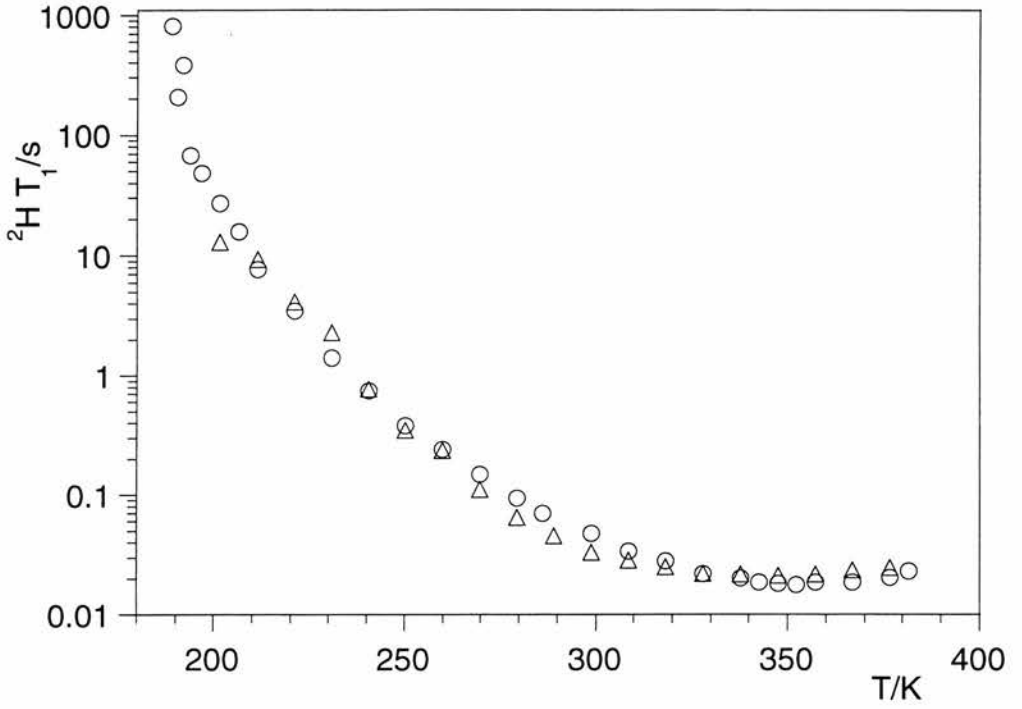

Figure 5.5. ^{2}H spin-lattice relaxation time as a function of temperature for 1,1,6,6-d_4- (o) and 2,2,5,5-d_4-hexanediyl bis(*p*-nitrobenzoates) (Δ).

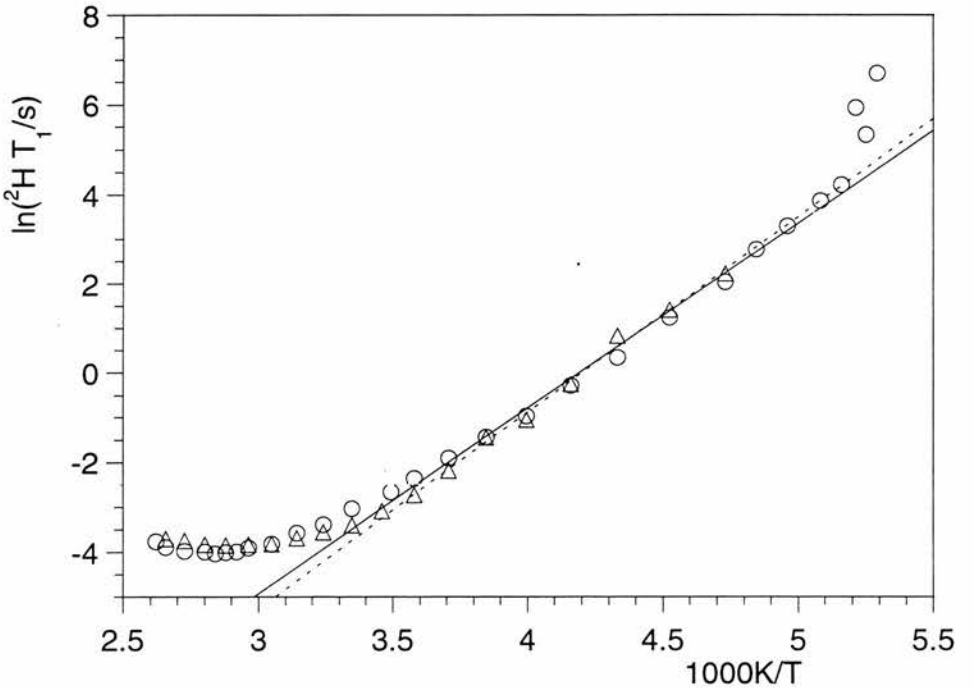

Figure 5.6. Dependence of ln(^{2}H T_1) on 1000K/T for 1,1,6,6-d_4- (o) and 2,2,5,5-d_4-hexane-1,6-diyl bis(*p*-nitrobenzoates) (Δ) together with linear least-squares fits. Apparent activation energies from the slopes are 35 and 36 kJ/mol, respectively.

^{2}H quadrupolar echo spectra were measured at different temperatures using 20 μs and 160 μs refocusing delays. Measured spectra for the 1,1,6,6-d_4-labelled derivative are shown in figure 5.8. Above 290 K, the line shape is independent of the length of the refocusing delay indicating that the frequency of molecular motion is in the fast motion limit. Below 290 K, however, the intensity in the central area of the spectra decreases suggesting that the frequency of molecular motion is in the intermediate rate regime, *i.e.* smaller than 10^7 Hz. This is consistent with the observation of the dipolar broadening in the ^{13}C CP/MAS spectrum and short ^{13}C $T_{1\rho}$ relaxation times below 270 K. At 357 K, an apparent third inflection point is observed in the line shape suggesting the molecular motion induces asymmetry to the spectrum. A spectrum measured at 367 K (fig. 5.7), however, indicates that the spectrum is actually a superposition of two slightly different spectra.

The ^{2}H quadrupolar echo spectra were best simulated using the conical libration model with parameters given in table 5.3 (fig. 5.9). The spectra could also have been simulated with the two-site model but as the conical libration model conveniently produced the spectra for the 2,2,5,5-d_4-labelled derivative, the same model was used also for the 1,1,6,6-d_4-labelled derivative. The spectra measured at 357 K and above were simulated using two distributions. Interestingly, only a small change in the standard deviation of the distribution broadens the spectrum so that the splitting clearly visible in the spectrum measured at 367 K is invisible in the spectra measured at 357 and 377 K.

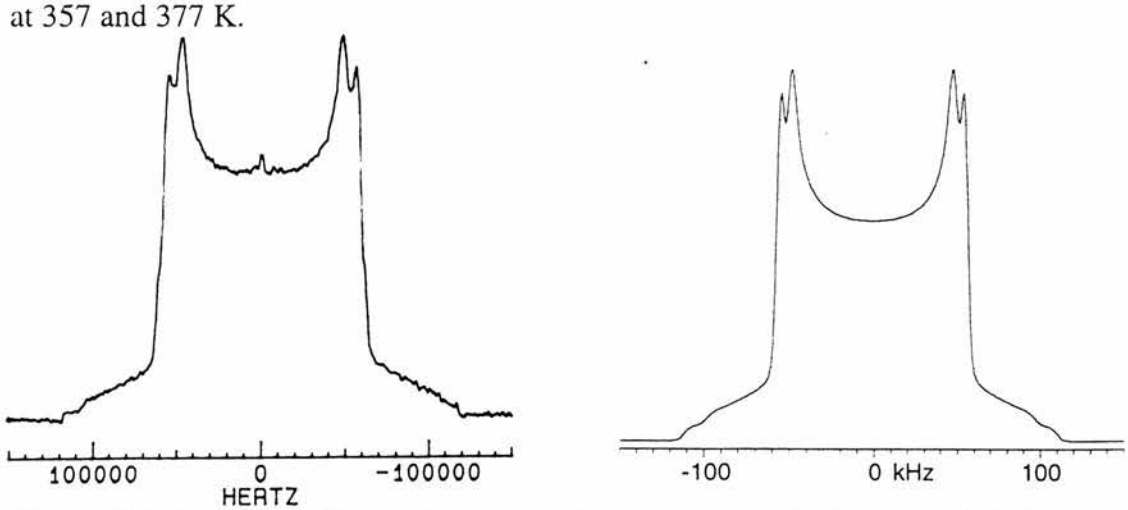

Figure 5.7. Measured ^{2}H quadrupolar echo spectrum (left) for 1,1,6,6-d_4-hexane-1,6-diyl bis(*p*-nitrobenzoate) at 367 K together with a simulated spectrum (right) using the conical libration model with parameters given in table 5.3.

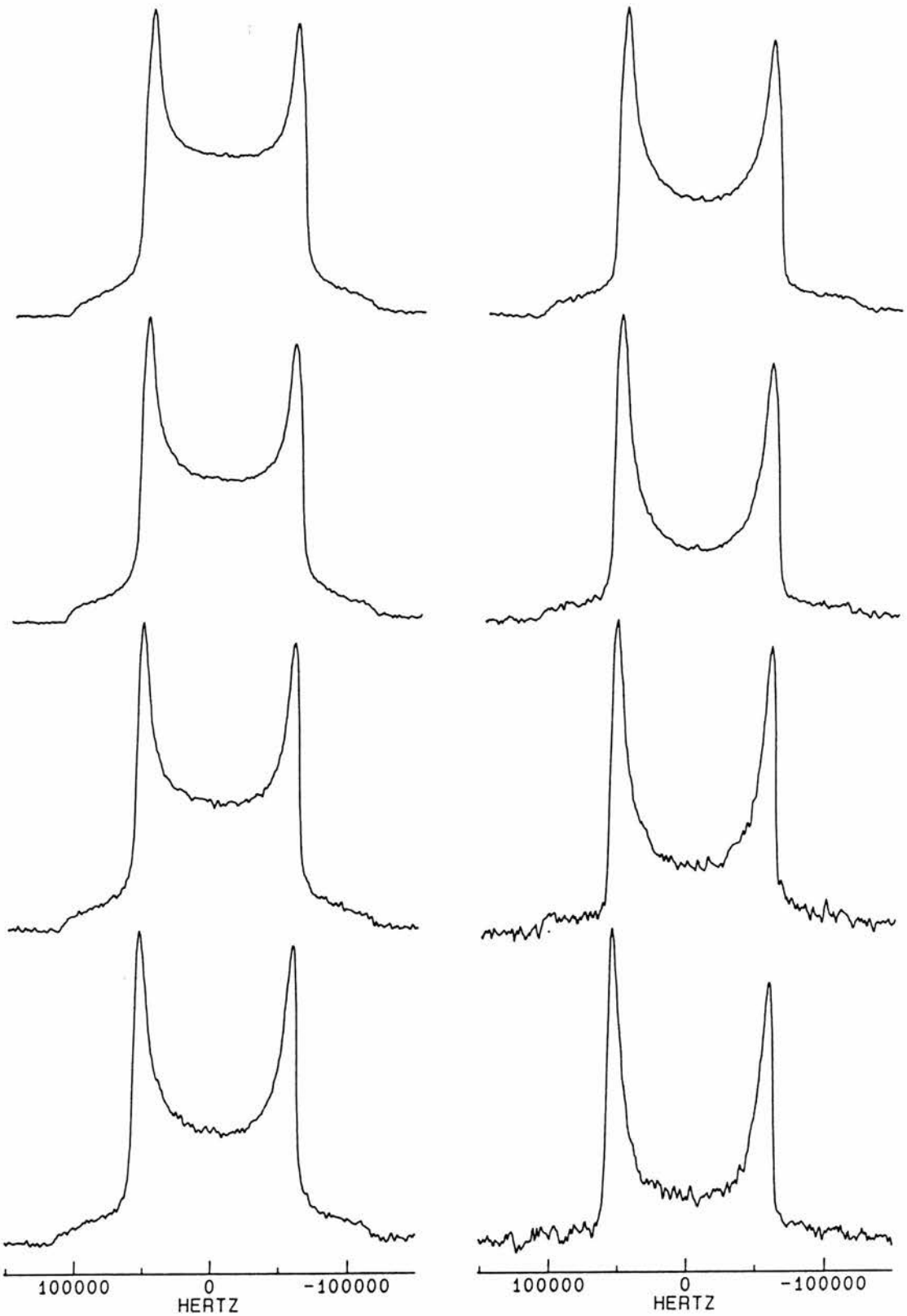

Figure 5.8. Measured ^2H quadrupolar echo spectra for 1,1,6,6-d_4-hexane-1,6-diyl bis(*p*-nitrobenzoate) at different temperatures. Refocusing delay is 20 μs (left) and 160 μs (right). Temperatures are from top to bottom: 270, 250, 240 and 231 K.

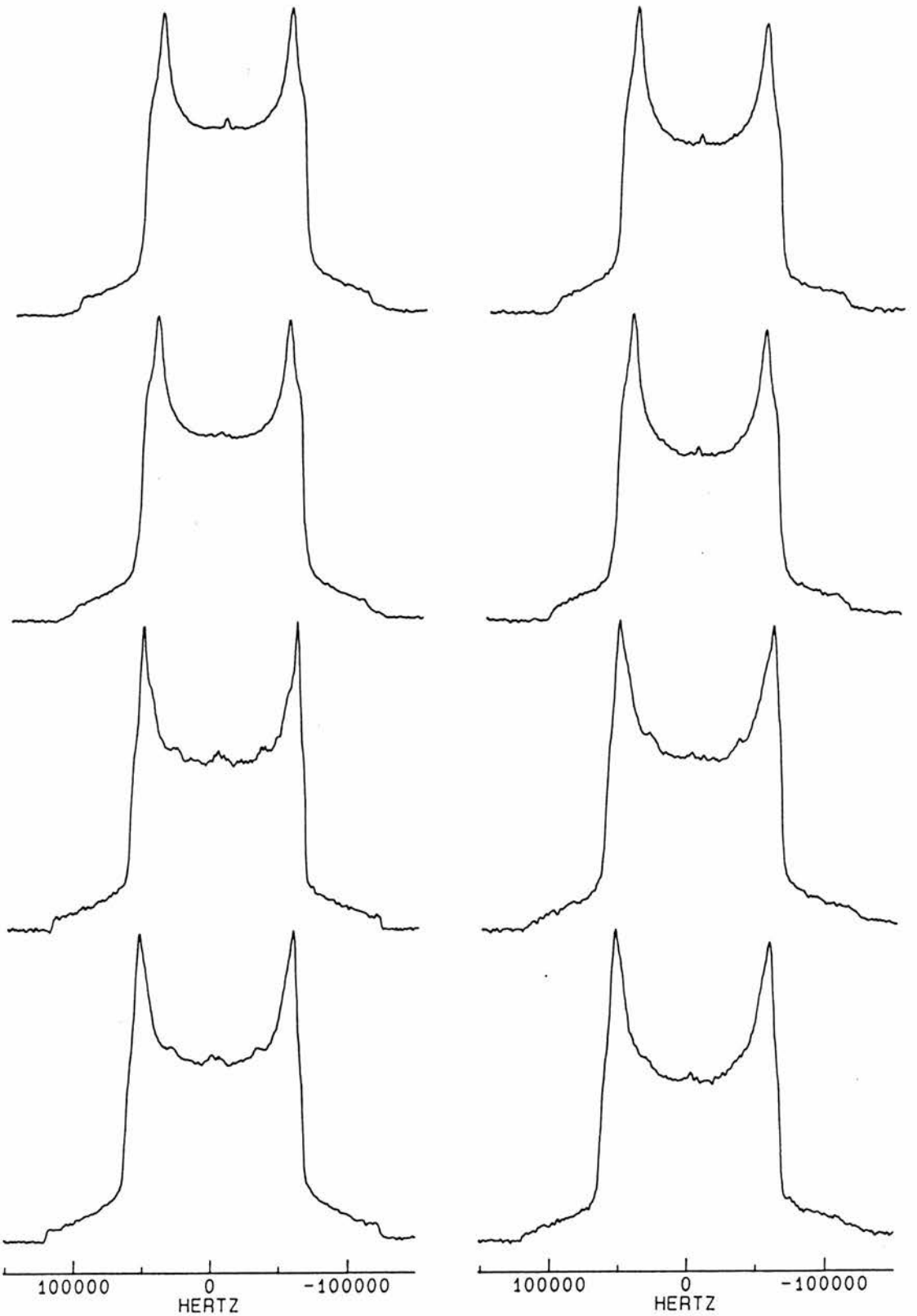

Figure 5.8. (continued) Measured ^2H quadrupolar echo spectra for 1,1,6,6-d_4-hexane-1,6-diyl bis(*p*-nitrobenzoate) at different temperatures. Refocusing delay is 20 μs (left) and 160 μs (right). Temperatures are from top to bottom: 377, 357, 328 and 289 K.

Table 5.3. Parameters for simulations of ^{2}H quadrupolar echo spectra.

spectrum	k / s^{-1}	p	θ_0	$\Delta\theta$	$W_{calc.}$ kHz	$W_{obs.}$ kHz
1,1,6,6-d_4						
377 K outer	1×10^8	80	15	3	-	-
inner		100	22	1	96	94
367 K outer	1×10^8	100	15	1	108	111
inner		50	22	1	96	95
357 K outer	1×10^8	80	15	3	-	-
inner		100	22	1	96	96
328 K	1×10^8	100	15	3	107	112
289 K	1×10^7	100	15	3	107	112
270 K	5×10^6	100	15	3	107	106
250 K	2×10^6	100	15	3	107	108
240 K	1×10^6	100	10	3	114	115
231 K	5×10^5	100	10	3	114	115
2,2,5,5-d_4						
377 K outer	1×10^8	2	15	5	-	-
inner		1	45	10	-	-
peak		100	55	1	-	-
328 K outer	1×10^8	2	15	5	-	-
inner		1	45	10	-	-
peak		100	55	1	-	-
288 K outer	1×10^8	10	15	5	-	-
inner		5	45	10	-	-
peak		100	55	1	-	-
279 K outer	1×10^7	30	15	5	-	-
inner		15	45	10	-	-
peak		100	55	1	-	-
270 K outer	5×10^6	100	15	5	108	104
inner		100	45	5	-	-
250 K outer	5×10^6	100	15	5	108	108
inner		30	45	5	-	-
231 K	2×10^6	100	10	10	108	113
211 K	1×10^6	100	10	10	108	114

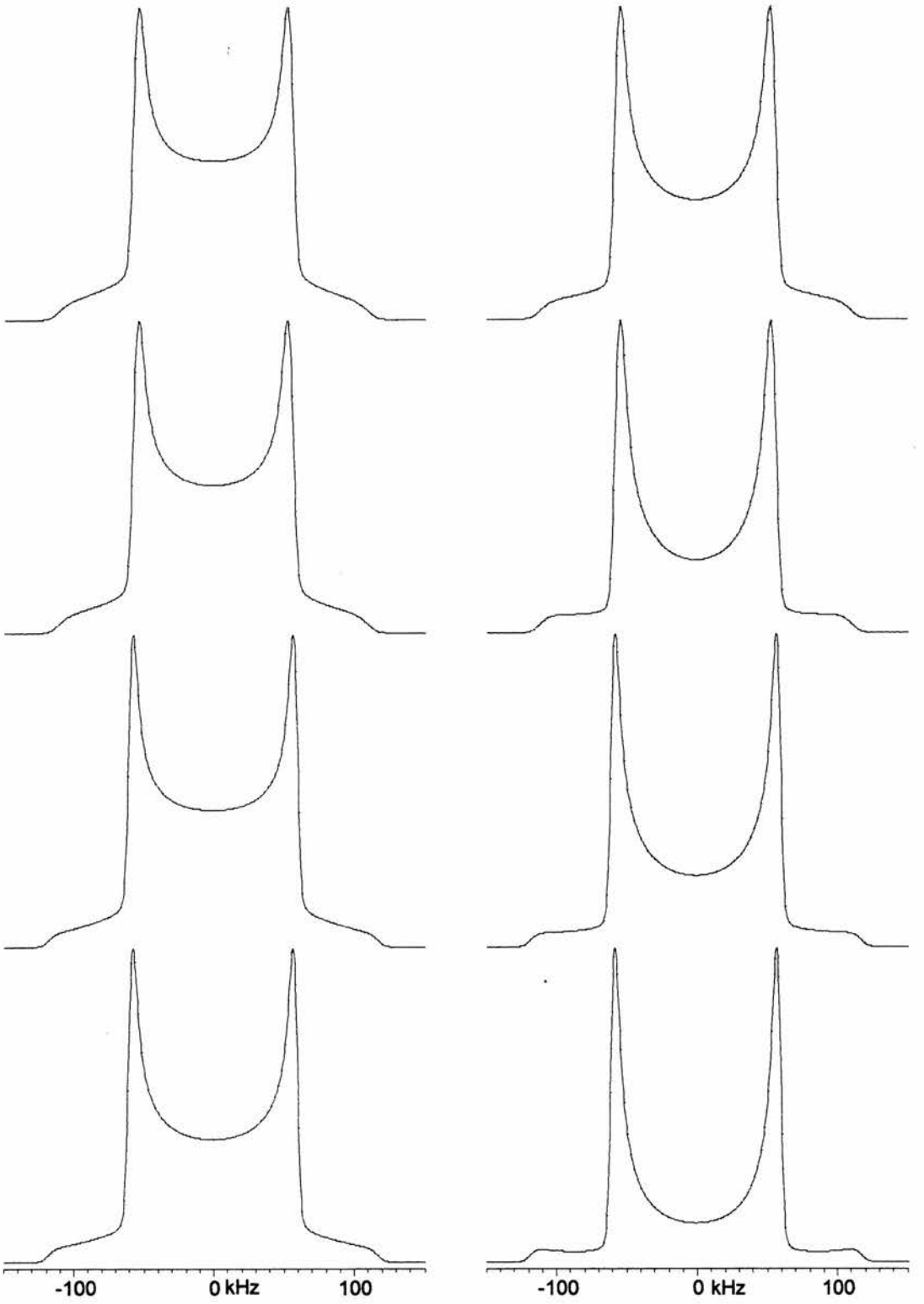

Figure 5.9. Calculated ^2H quadrupolar echo spectra of 1,1,6,6-d_4-hexane-1,6-diyl bis(*p*-nitrobenzoate) using the conical libration model. Parameters for the simulations are given in table 5.3.

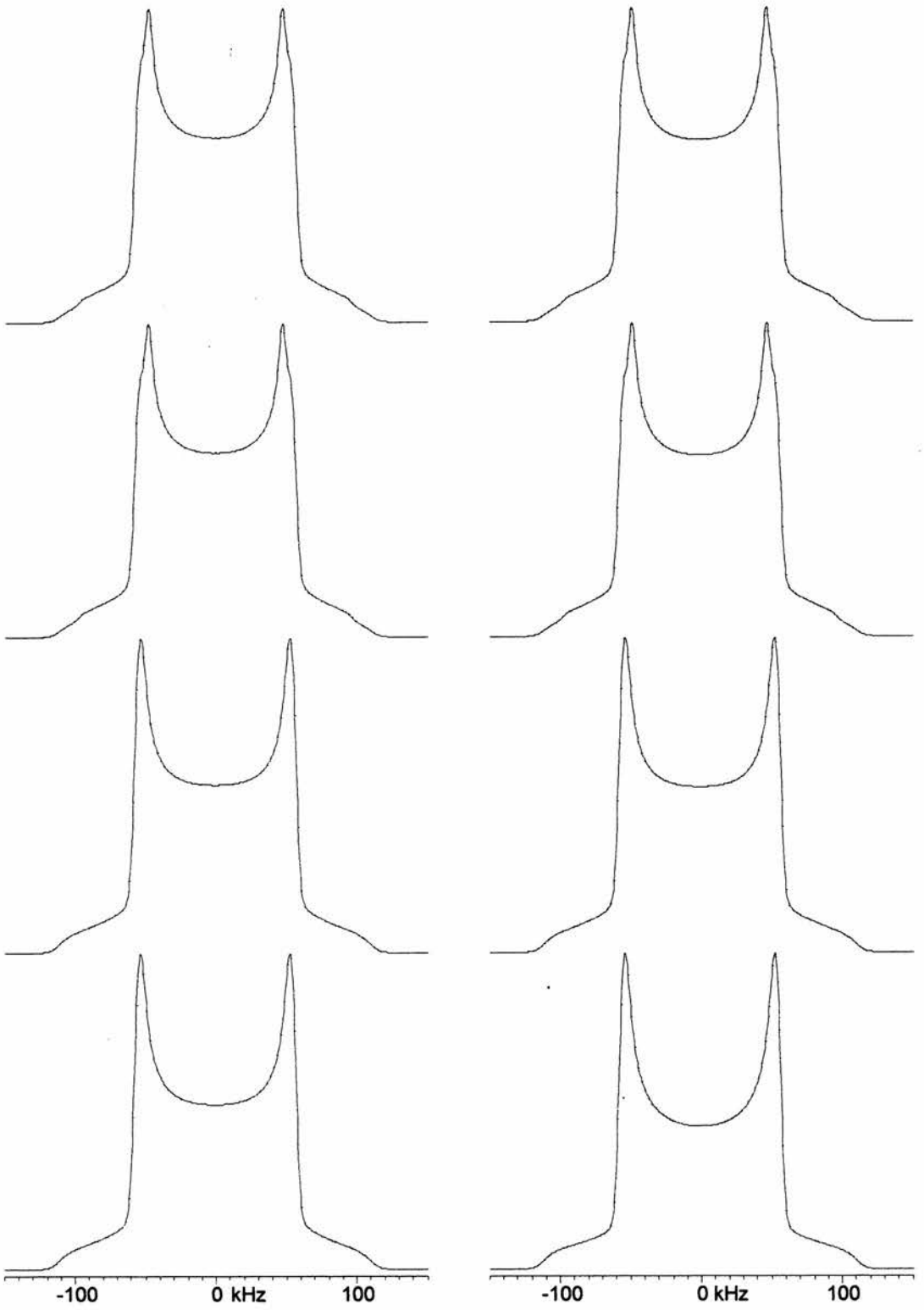

Figure 5.9. (continued) Calculated ^2H quadrupolar echo spectra for 1,1,6,6-d_4-hexane-1,6-diyl bis(*p*-nitrobenzoate) using the conical libration model. Parameters for the simulations are given in table 5.3.

Figure 5.10 shows ^{2}H quadrupolar spectra for the 2,2,5,5-d_4-labelled derivative. 114 and 113 kHz wide powder patterns were observed at 211 and 231 K, respectively. At these temperatures, the intensity in the central area of the spectrum decreases with the refocusing delay indicating that the rate of librational motion is in the intermediate rate regime, in keeping with the ^{13}C CP/MAS spectra and ^{13}C $T_{1\rho}$ relaxation times. At 250 K, the central region of the spectrum measured with 20 μs delay is domelike while only a small hump is observed in the spectrum measured with 160 μs delay. The dome of the 20 μs spectrum sharpens at 270 K and also the 160 μs spectrum becomes domelike at this temperature.

The observation of different spectra for the two different refocusing delays indicates that the rate of librational motion is in the intermediate regime. At 279 K, however, the spectra are nearly equal indicating that the rate of the motion is almost in the fast motion limit, i.e. the rate of the motion is *ca.* 10^7 s^{-1}. The dome in the central area has sharpened into a peak at zero frequency. At higher temperatures the proportion of the peak increases and the proportion of the remaining powder pattern decreases indicating that the motion increasingly mimics isotropic motion at higher temperatures.

^{2}H quadrupolar echo spectra were best simulated using the conical libration model with parameters given in table 5.3. The simulated spectra are shown in figure 5.11. As for the 1,1,6,6-d_4-labelled derivative, the simulation is difficult since the rate and the amplitude of the motion change simultaneously. Also the conical libration model is only a very crude model for the actual libration of the C-D bonds in the chain. Refinement of the model, however, would be very difficult and the calculations would probably require a supercomputer. Nevertheless, the simple conical libration model satisfactorily produces the observed spectra.

The simulation produces the changes in the central area of the spectrum in the right order, that is, the dome first appears in the 20 μs spectrum and then in the 160 μs spectrum as temperature increases. As was discussed in section 3.3 (chapter 3), the *trans-gauche* model produces these changes in the opposite order, and therefore, fails to explain these results.

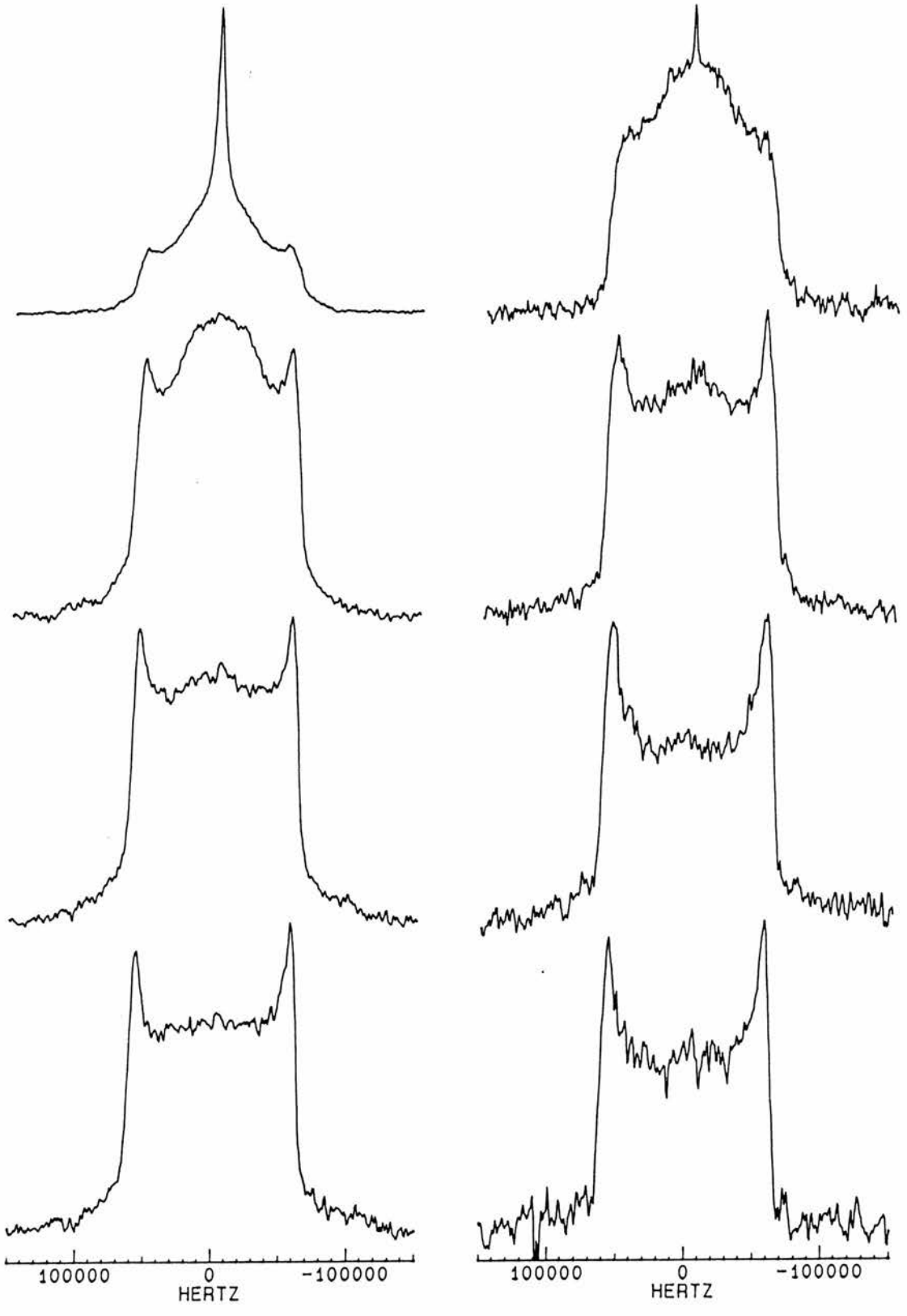

Figure 5.10. Measured ^{2}H quadrupolar echo spectra of 2,2,5,5-d_4-hexane-1,6-diyl bis(*p*-nitrobenzoate) at different temperatures. Refocusing delay is 20 μs (left) and 160 μs (right). Temperatures are from top to bottom: 270, 250, 231 and 211 K.

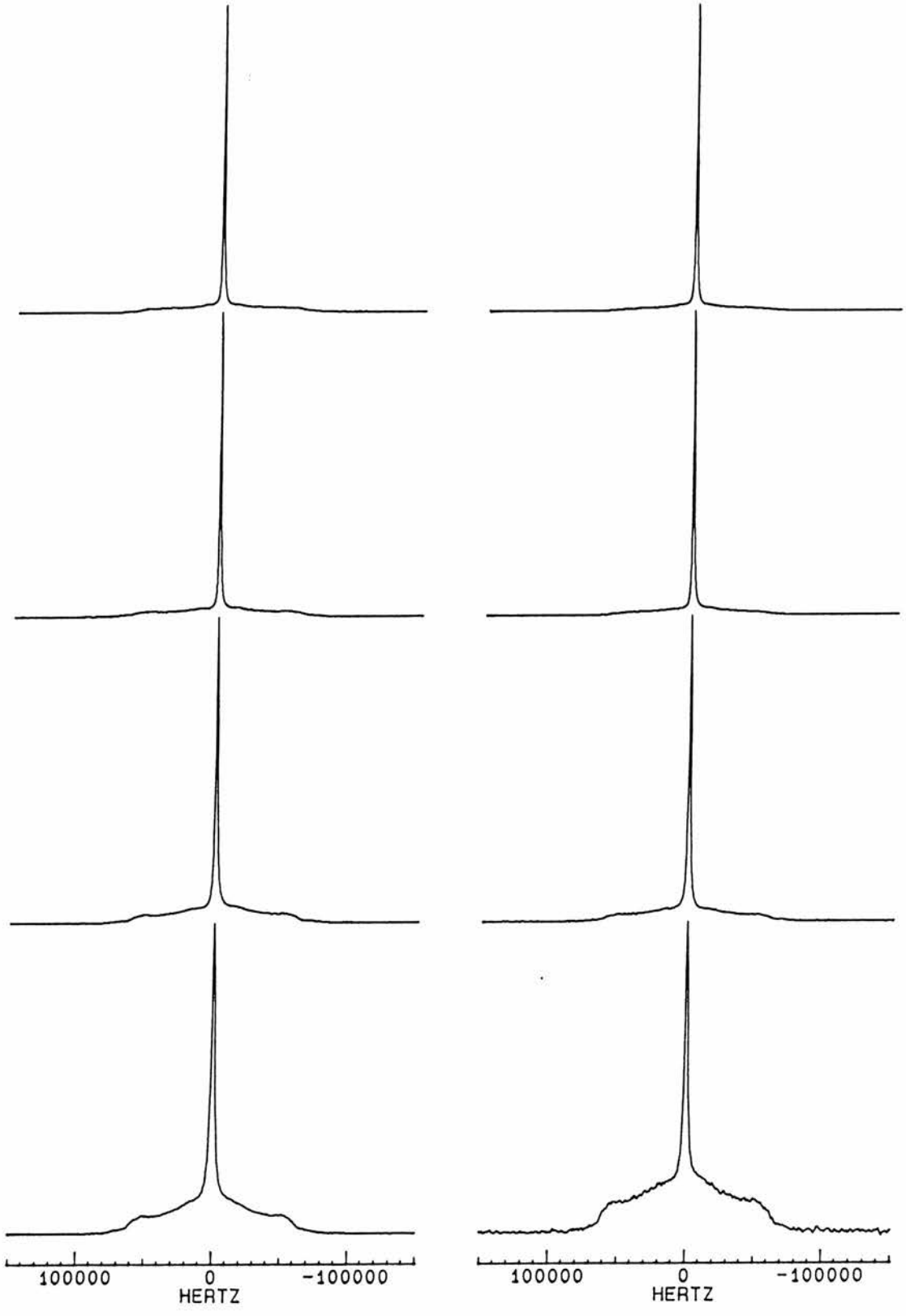

Figure 5.10. (continued) Measured ^2H quadrupolar echo spectra of 2,2,5,5-d_4-hexane-1,6-diyl bis(*p*-nitrobenzoate) at different temperatures. Refocusing delay is 20 μs (left) and 160 μs (right). Temperatures are from top to bottom: 377, 328, 288 and 279 K.

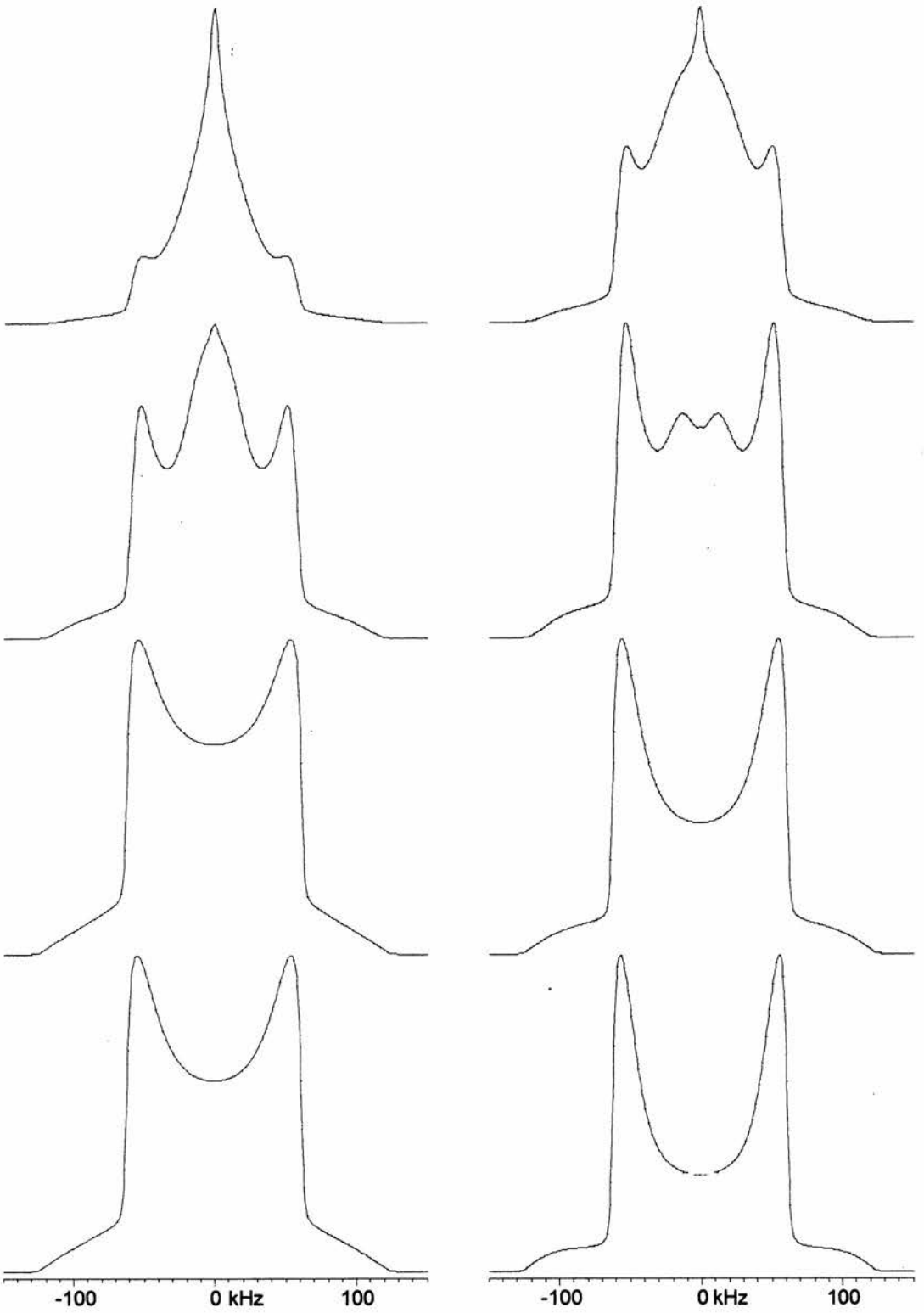

Figure 5.11. Calculated ^2H quadrupolar echo spectra for 2,2,5,5-d_4-hexane-1,6-diyl bis(*p*-nitrobenzoate) using the conical libration model. Parameters for the simulations are given in table 5.3.

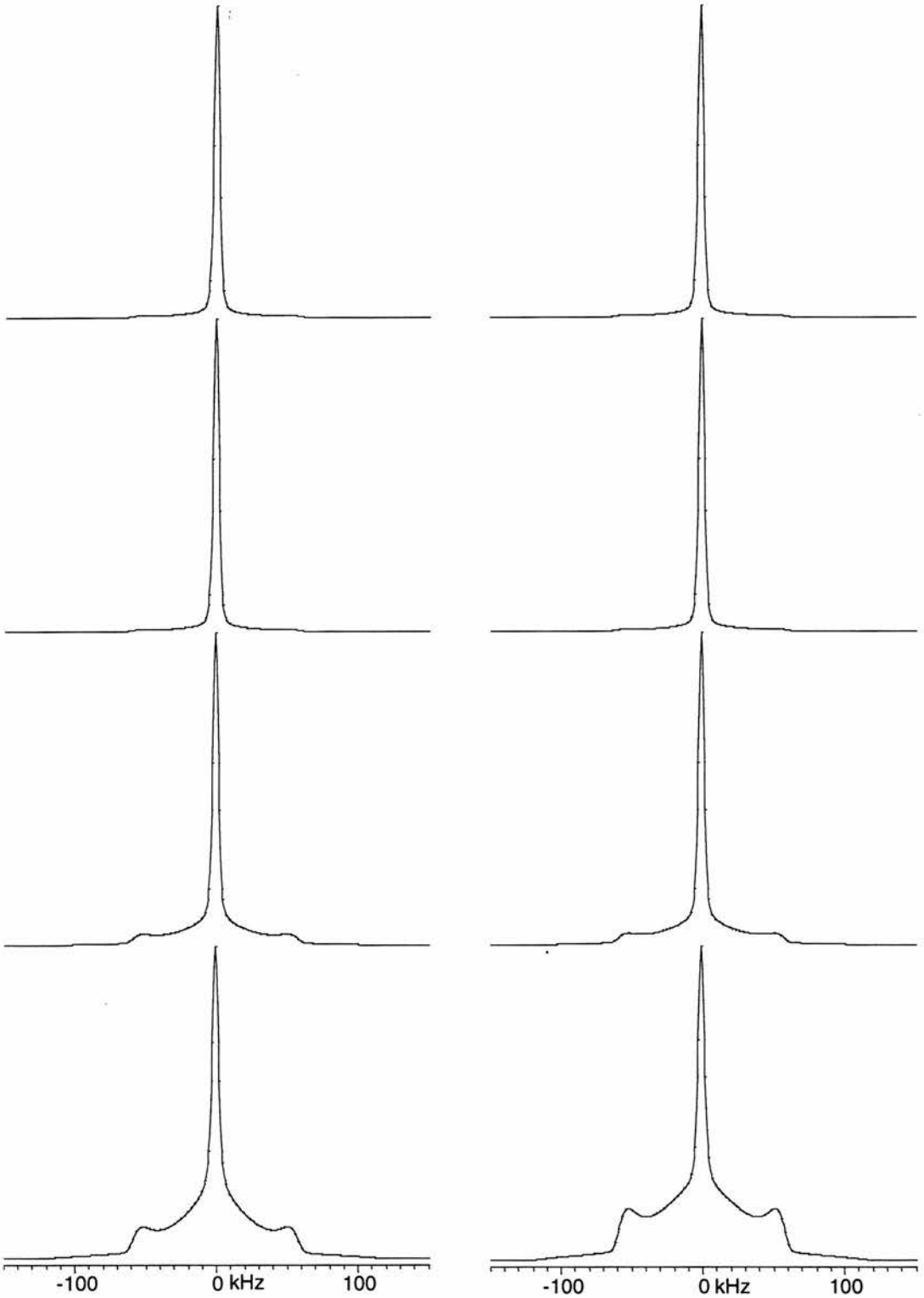

Figure 5.11. (continued) Calculated ^2H quadrupolar echo spectra for 2,2,5,5-d_4-hexane-1,6-diyl bis(*p*-nitrobenzoate) using the conical libration model. Parameters for the simulations are given in table 5.3.

^{13}C CP/MAS spectra, ^{13}C $T_{1\rho}$ relaxation times, ^{2}H quadrupolar echo spectra and ^{2}H spin-lattice relaxation times are all consistent with decreasing rate of the librational motion on cooling. Further evidence for this decrease is obtained from the temperature dependence of echo reduction factor (fig. 5.12), defined as the ratio of the intensity of the echoes for 160 μs and 20 μs refocusing delays. The echo reduction factor for the 1,1,6,6-d_4-labelled derivative increases from 0.3 at 220 K to a plateau of *ca.* 0.5 above 300 K indicating that rate of librational motion increases from the intermediate rate region of the quadrupolar echo experiment (slower than *ca.* 10^7 Hz) to the fast motion limit. For the 2,2,5,5-d_4-labelled derivative the dependence of echo reduction factor on temperature is similar although not quite as smooth as for the 1,1,6,6-d_4-labelled derivative. The echo reduction factor increases from 0.35 at 210 K to 0.75 at 375 K. The large value of 0.75 for the echo reduction factor suggests that the dipolar coupling weakens at high temperatures, in keeping with the observation of the isotropic peak in the quadrupolar echo spectra.

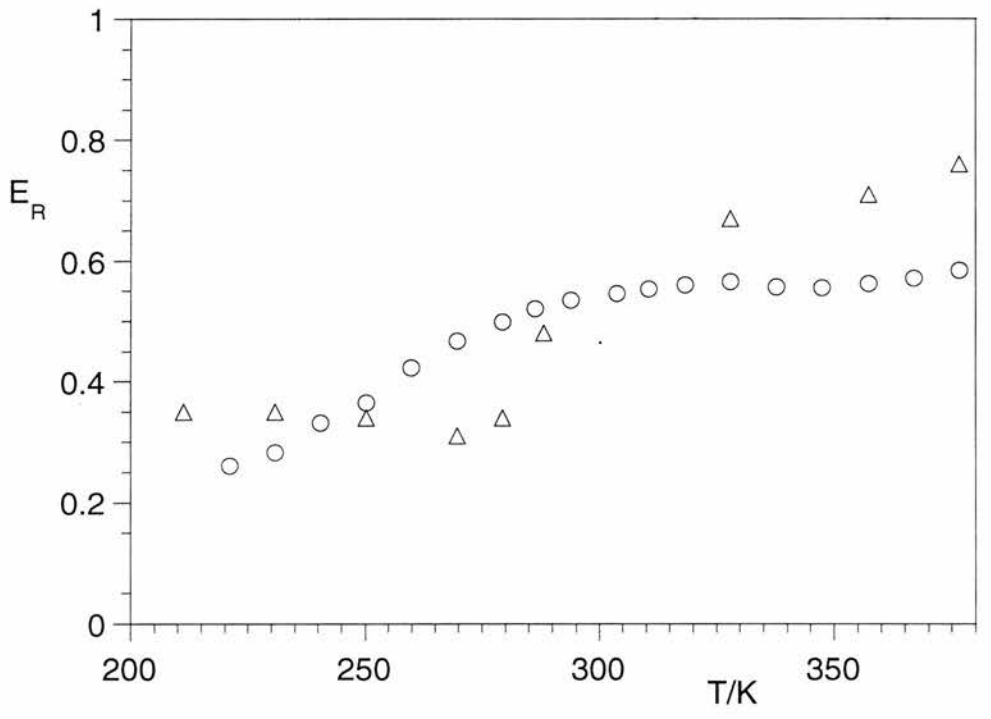

Figure 5.12. Echo reduction factor as a function of temperature for 1,1,6,6-d_4-hexane-1,6-diyl (o) and 2,2,5,5-d_4-hexane-1,6-diyl (Δ) bis(*p*-nitrobenzoates).

5.2. Hexane-1,6-diyl bis(3,5-dimethoxybenzoate)

Because the measurement of the ^{13}C $T_{1\rho}$ relaxation time was tedious for hexane-1,6-diyl bis(*p*-nitrobenzoate) and other similar derivatives, and the measurement of the ^{13}C $T_{1\rho}$ relaxation time being the original purpose of this thesis, efforts were made to find a compound that has much shorter proton spin-lattice relaxation time. In polymers such as polythene, proton spin-lattice relaxation occurs mainly in the chain terminating methyl or methoxy groups that rotate fast, and therefore, generate spectral density at the proton Larmor frequency. Then, the other protons in the polymer also relax fast as they are connected to these rapidly moving protons by the spin diffusion process. Thus, proton spin-lattice relaxation can be enhanced by adding methyl or methoxy groups. Therefore, the *p*-nitrobenzoyl groups were replaced with 3,5-dimethoxybenzoyl groups, which were chosen to minimise overlapping with the peaks for alkyl chain carbons.

The crystal structure of hexane-1,6-diyl bis(3,5-dimethoxybenzoate) was solved from single crystal x-ray data. Structural details and views of the unit cell are given in the appendix (p. A-5 and A-31). The structure shows that the chain conformation is very similar to that of hexane-1,6-diyl bis(*p*-nitrobenzoate). The bond between the chain carbons at positions 1 and 2 and the symmetrically related bond between the carbons at positions 5 and 6 are in the *gauche* conformation whereas all the other bonds in the chain are in the *trans* conformation.

^{13}C CP/MAS spectra were measured at different temperatures (fig. 5.13). Because of fast proton spin-lattice relaxation, good quality spectra were obtained in the whole temperature range of the probe. The peaks for the hexyl chain are at 27.9 ($OCH_2CH_2\underline{C}H_2$), 29.9 ($OCH_2\underline{C}H_2$) and 66.8 ppm ($O\underline{C}H_2$) well-resolved from other signals. The other signals are at: 55.2 and 57.1 ($O\underline{C}H_3$), 102.0 and 104.8 ($\underline{C}_{Ar}$ 2 and 6), 112.8 ($\underline{C}_{Ar}$ 4), 131.9 ($\underline{C}_{Ar}$ 1), 160.3 and 160.9 ($\underline{C}_{Ar}$ 3 and 5) and 167.2 ppm ($\underline{C}$=O). Unfortunately, the ^{13}C CP/MAS spectra fail to show any evidence of dynamic dipolar broadening or shortening of ^{13}C $T_{1\rho}$ relaxation time. This is rather odd as the alkyl chain is very similar to that of hexane-1,6-diyl bis(*p*-nitrobenzoate) which showed these effects suggesting that the chain dynamics are very sensitive to the molecular environment around the chain.

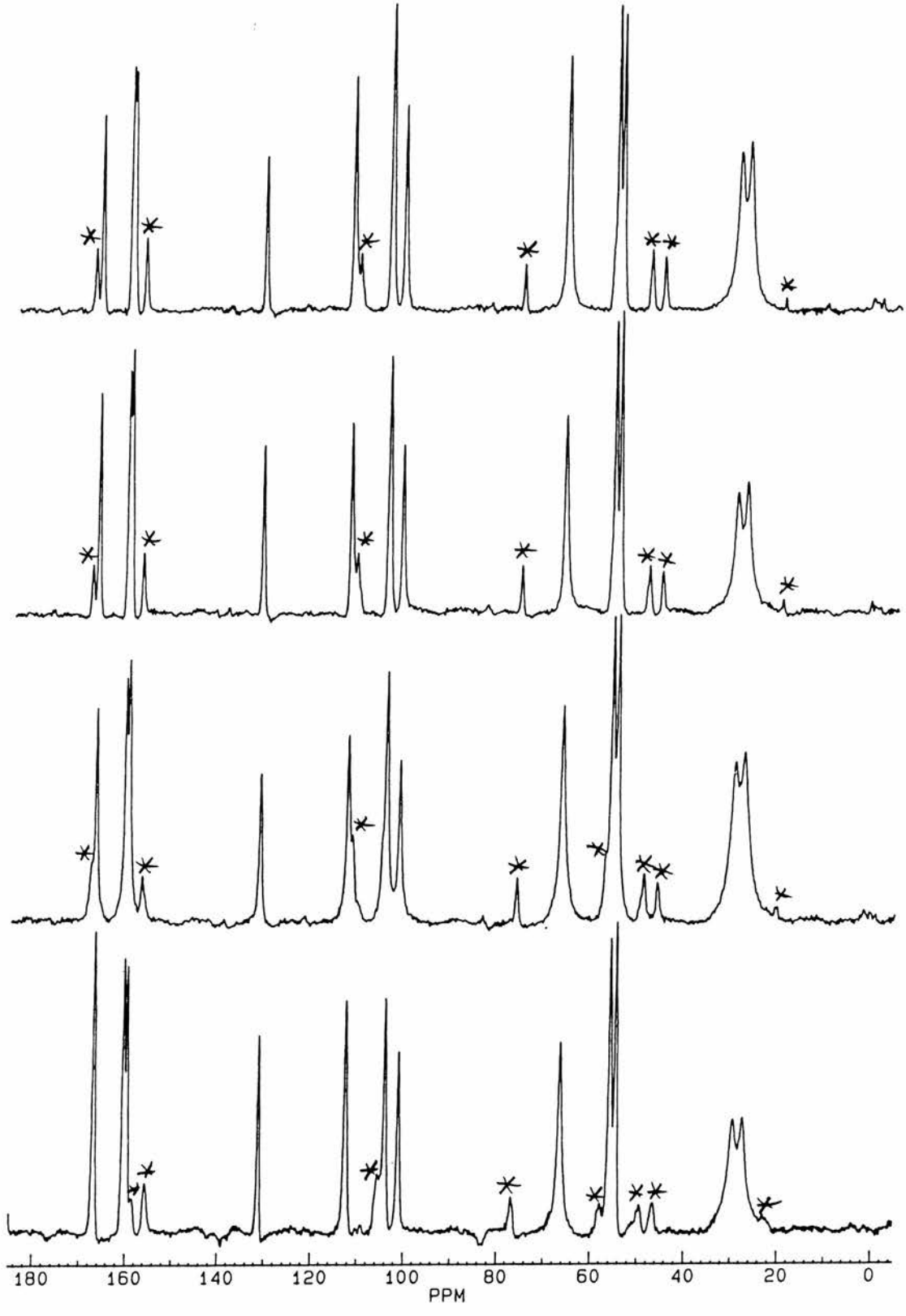

Figure 5.13. ^{13}C CP/MAS spectra for hexane-1,6-diyl bis(3,5-dimethoxybenzoate) at different temperatures. Temperatures are from top to bottom: 270, 246, 222 and 190 K. Spinning sidebands (at 7 kHz) are asterisked.

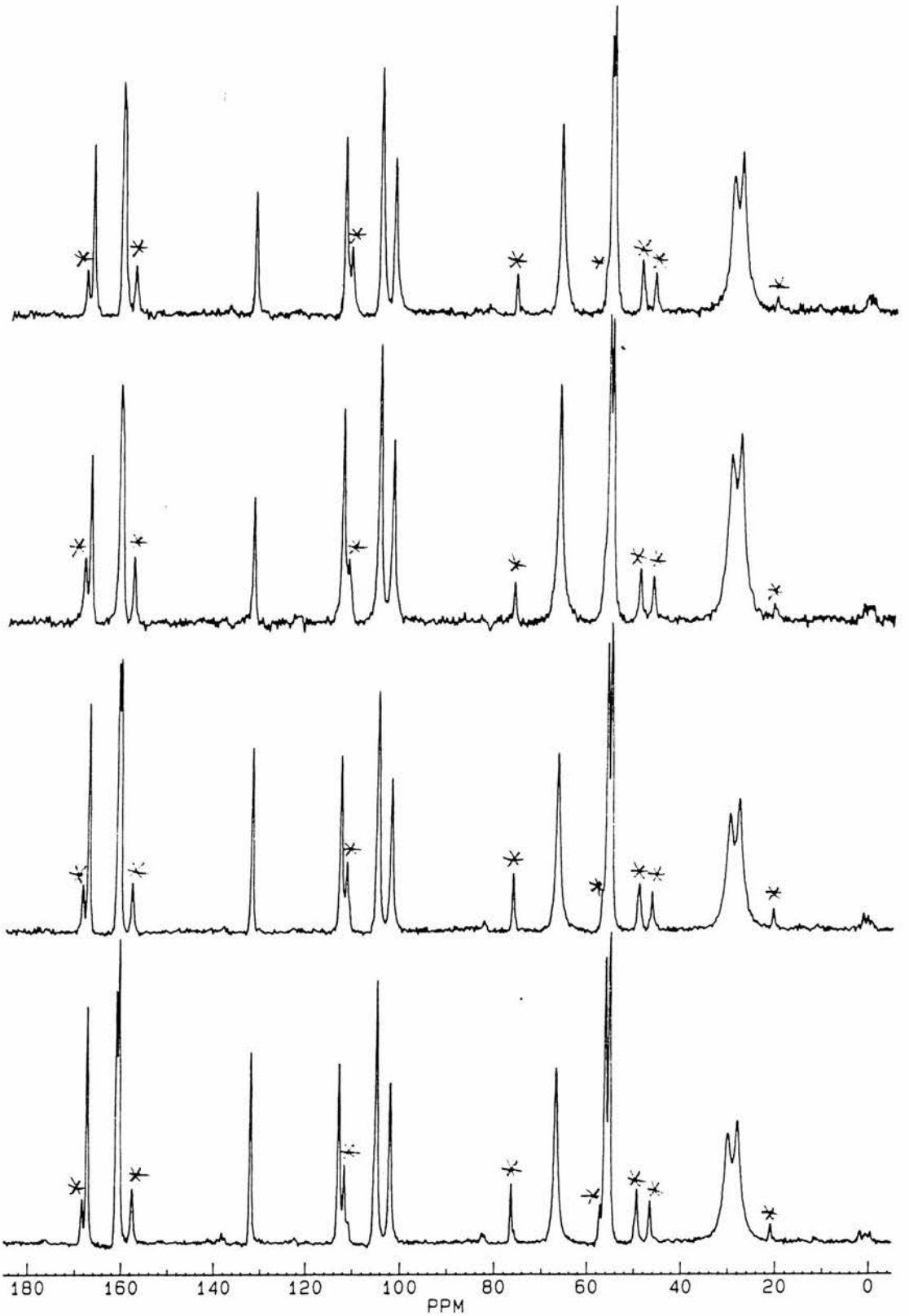

Figure 5.13. (continued) ^{13}C CP/MAS spectra for hexane-1,6-diyl bis(3,5-dimethoxybenzoate) at different temperatures. Temperatures are from top to bottom: 358, 338, 318 and 297 K. Spinning sidebands (at 7 kHz) are asterisked.

The methylene groups in the chain ends were deuterated and the ^{2}H spin-lattice relaxation time for this 1,1,6,6-d_4-hexane-1,6-diyl bis(3,5-dimethoxybenzoate) was measured at different temperatures between 190 and 360 K. The measured ^{2}H spin-lattice relaxation times are listed in table 5.4 and shown as a function of temperature in figure 5.14.

The ^{2}H spin-lattice relaxation time decreases from 61 s at 192 K to 0.2 s at 357 K. This decrease is similar but the values are larger than for 1,1,6,6-d_4-hexane-1,6-diyl bis(*p*-nitrobenzoate) suggesting that the amplitude of the librational motion is smaller for 3,5-dimethoxybenzoyl derivative and might be too small to cause dipolar broadening effects in the ^{13}C CP/MAS spectrum and considerably shorten the ^{13}C $T_{1\rho}$ relaxation time. Figure 5.15 shows a plot of ln(^{2}H T_1) as a function of 1000K/T together with a best-fitting least squares line. The slope of the least-squares line gives 27 kJ mol^{-1} for the apparent activation energy.

Table 5.4. Measured ^{2}H spin-lattice relaxation times for 1,1,6,6-d_4-hexane-1,6-diyl bis(3,5-dimethoxybenzoate).

T(vtu)/K	T/K	^{2}H T_1/s
193	192	61.0
203	202	41.0
213	211	30.0
223	221	11.2
233	231	4.01
253	250	1.45
273	270	0.767
292	288	0.524
303	299	0.421
313	309	0.360
323	318	0.355
333	328	0.289
343	338	0.305
353	347	0.275
363	357	0.209

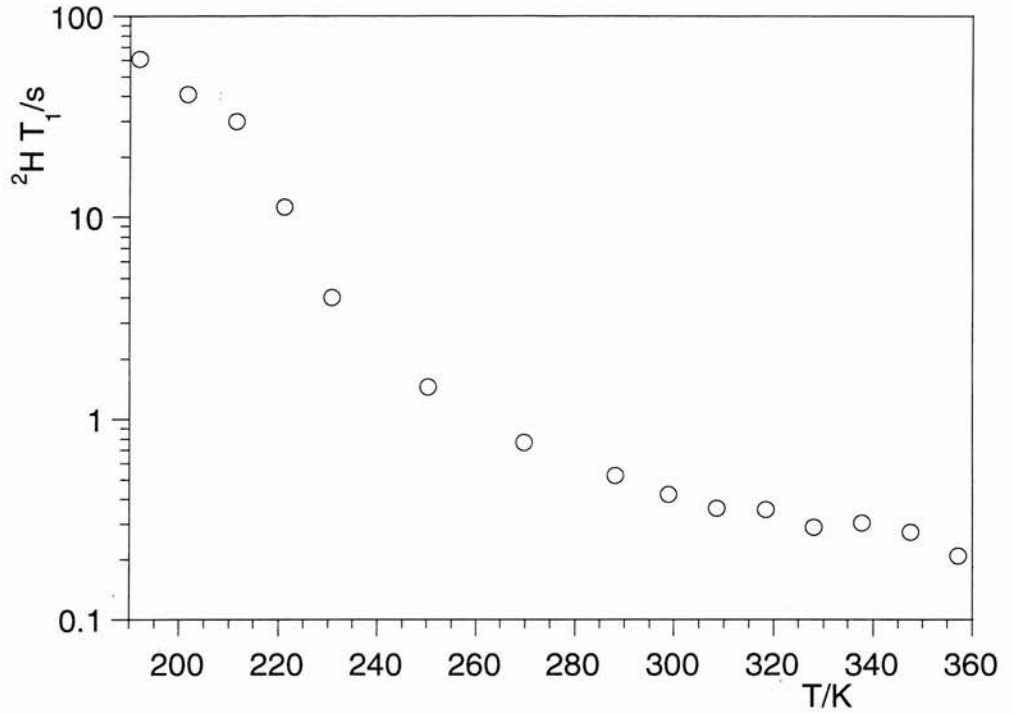

Figure 5.14. Measured ^{2}H T_1 relaxation time as a function of temperature for 1,1,6,6-d_4-hexane-1,6-diyl bis(3,5-dimethoxybenzoate).

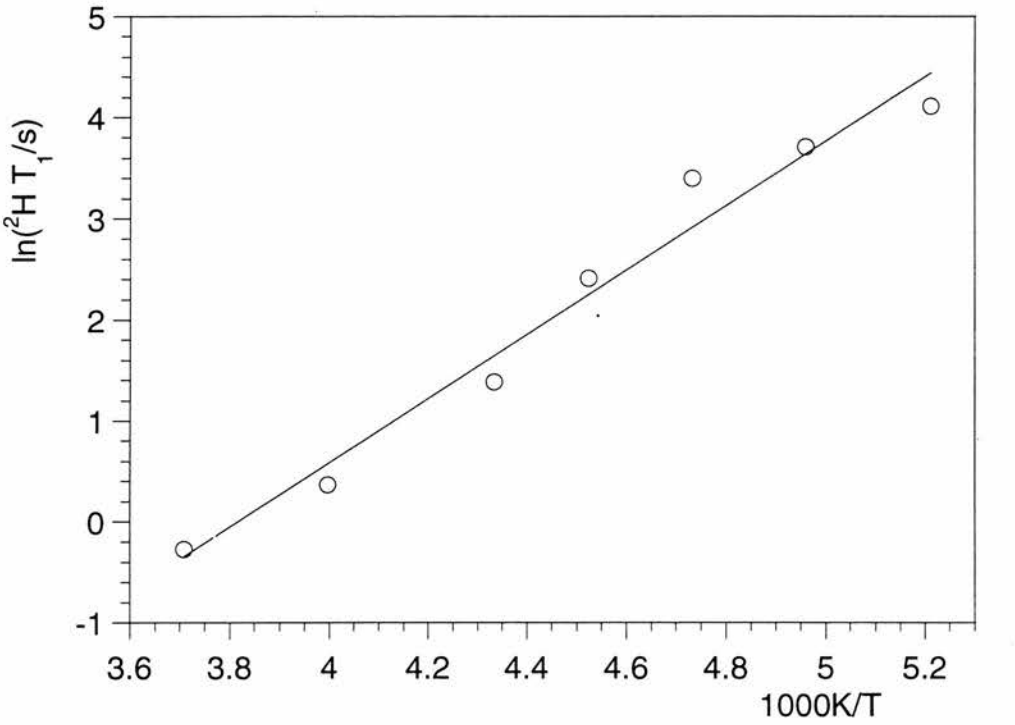

Figure 5.15. Plot of ln(^{2}H T_1) as a function of 1000K/T for 1,1,6,6-d_4-hexane-1,6-diyl bis(3,5-dimethoxybenzoate). Apparent activation energy from the slope is 27 kJ mol^{-1}.

^{2}H quadrupolar echo spectra were measured at three different temperatures with 20 and 160 μs refocusing delays. The measured spectra are shown in figure 5.16. The 116 kHz wide spectrum is independent of temperature and the length of the refocusing delay indicating small amplitude motion in the fast motion limit, in keeping with the failure to observe dynamic dipolar broadening. Figure 5.17 shows simulated spectra using the conical libration model. The rate constant was set to 1×10^8 s^{-1} and the distribution was centred at 10° with a standard deviation of 1°.

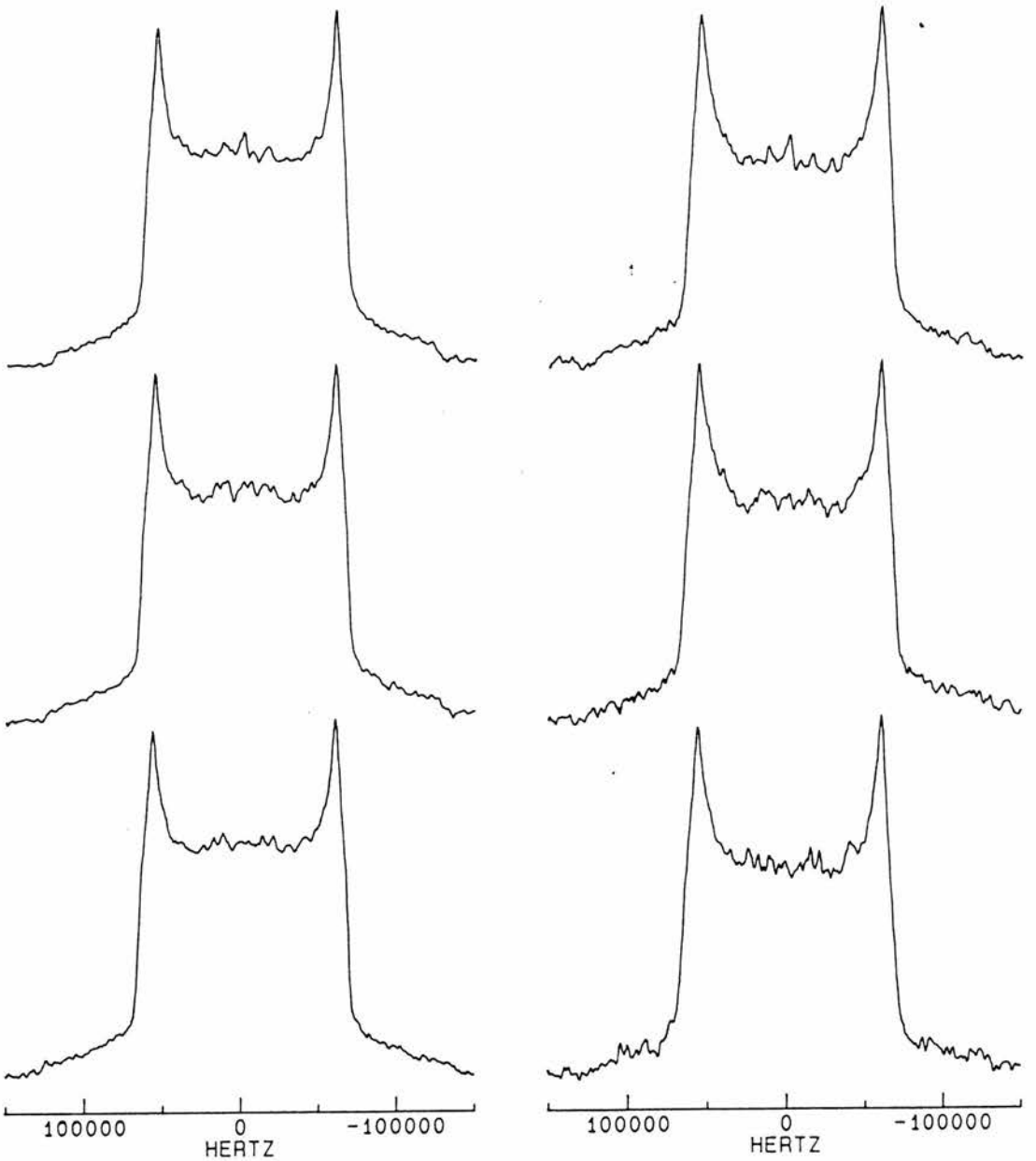

Figure 5.16. Measured ^{2}H quadrupolar echo spectra for 1,1,6,6-d_4-hexane-1,6-diyl bis(3,5-dimethoxybenzoate) at different temperatures. Refocusing delay is 20 μs (left) and 160 μs (right). Temperatures are from top to bottom: 338, 288 and 250 K.

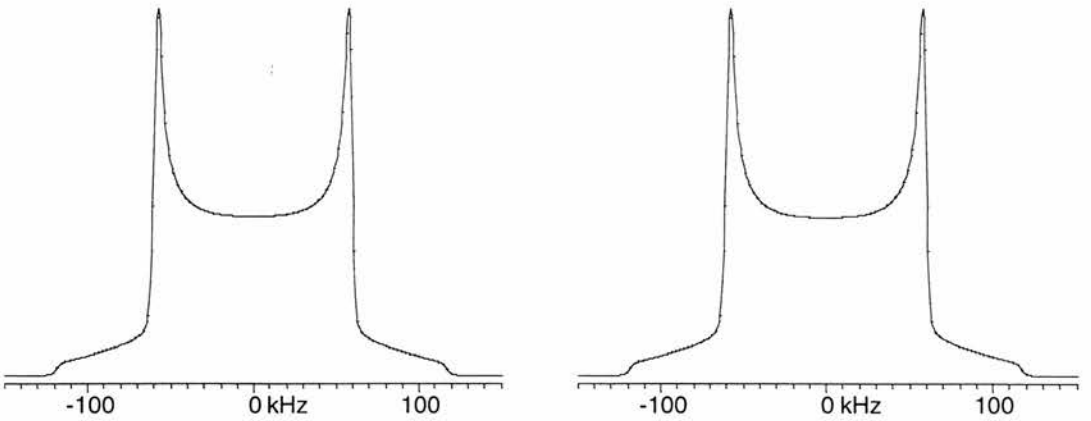

Figure 5.17. Simulated ^{2}H quadrupolar echo spectra for 1,1,6,6-d_4-hexane-1,6-diyl bis(3,5-dimethoxybenzoate).

5.3. Hexane-1,6-diyl dibenzenesulfonate

The crystal structure of hexane-1,6-diyl dibenzenesulfonate was solved from single crystal x-ray diffraction data. Structural details and views of the unit cell are given in the appendix (p. A-9 and A-32). The alkyl chain is very similar to that of the *p*-nitro and 3,5-dimethoxy derivatives. The bond between the chain carbons at positions 1 and 2 and the symmetrically related bond between carbons 5 and 6 are in *gauche* conformation while all the other chain bonds are in *trans* conformation.

The ^{13}C CP/MAS spectrum was measured only at room temperature because of slow proton spin-lattice relaxation and a low melting point at 59 °C. Increasing the contact time from the standard 1 ms failed to improve the signal-to-noise ratio (fig. 5.18). Peaks in the ^{13}C CP/MAS spectrum are at 27.2 ($OCH_2CH_2\underline{C}H_2$), 28.4 ($OCH_2\underline{C}H_2$), 73.1 ($O\underline{C}H_2$), 128.2 ($\underline{C}_{Ar}$), 129.8 ($\underline{C}_{Ar}$), 134.3 ($\underline{C}_{Ar,4}$) and 137.1 ppm ($\underline{C}_{Ar}$-S). The spectrum shows no effects of short ^{13}C $T_{1\rho}$ relaxation time, and therefore, no attempt was made to measure it.

Two samples were prepared for deuteron NMR studies. The methylene groups in the chain ends were deuterated yielding 1,1,6,6-d_4-hexane-1,6-diyl dibenzenesulfonate and the neighbouring methylene groups were deuterated producing 2,2,5,5-d_4-

hexane-1,6-diyl dibenzenesulfonate. The ^{2}H spin-lattice relaxation time was measured between 218 and 325 K for both samples. The measured values are listed in table 5.5 and shown as a function of time in figure 5.19. Figure 5.20 shows plots of ln(^{2}H T_1) as a function of 1000K/T.

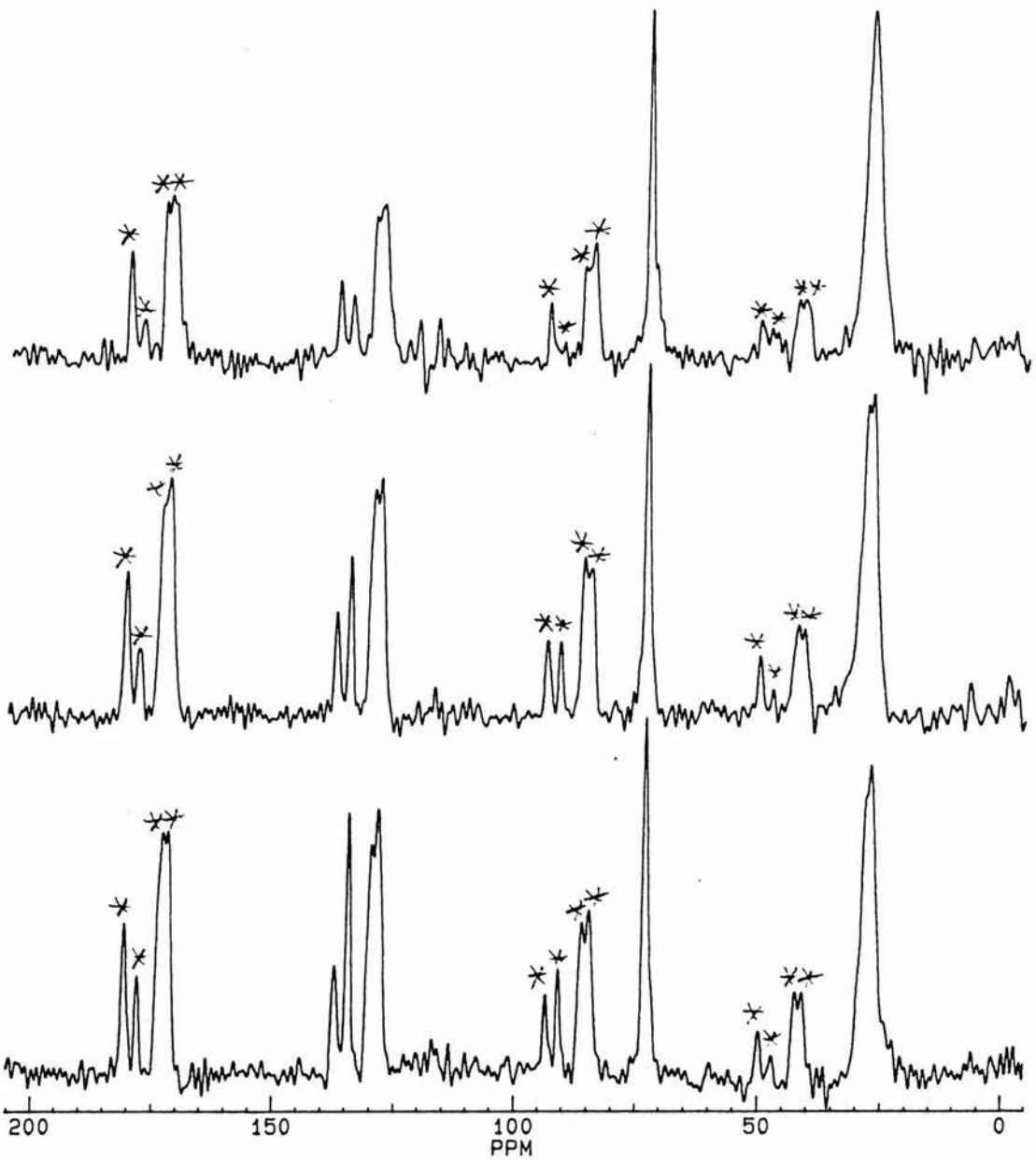

Figure 5.18. ^{13}C CP/MAS spectra for hexane-1,6-diyl dibenzenesulfonate at room temperature. Contact times are from top to bottom: 1, 4 and 12 ms. Spinning sidebands (at 5.5 kHz) are asterisked.

Table 5.5. Measured ^{2}H T_1 relaxation time for 1,1,6,6-d_4- and 2,2,5,5-d_4-hexane-1,6-diyl dibenzenesulfonates.

T(vtu)/K	T/K	^{2}H T_1/s 1,1,6,6-d_4	^{2}H T_1/s 2,2,5,5-d_4
220	218	118	75.7
230	228	49.0	37.1
240	238	22.2	18.3
250	247	11.3	8.48
260	257	6.68	4.17
270	267	3.73	2.19
280	276	2.31	1.25
293	289	1.22	0.645
300	296	0.875	0.429
310	306	0.633	0.317
320	315	0.436	0.229
330	325	0.318	0.172

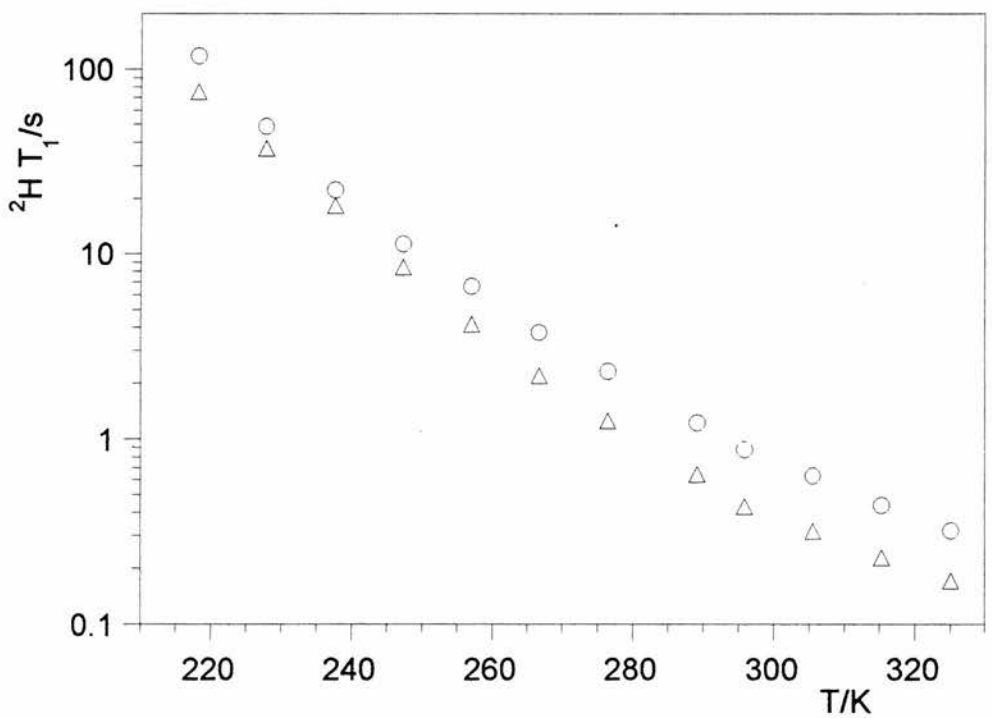

Figure 5.19. Measured ^{2}H spin-lattice relaxation time as a function of temperature for 1,1,6,6-d_4- (o) and 2,2,5,5,-d_4-hexane-1,6-diyl dibenzenesulfonates (Δ).

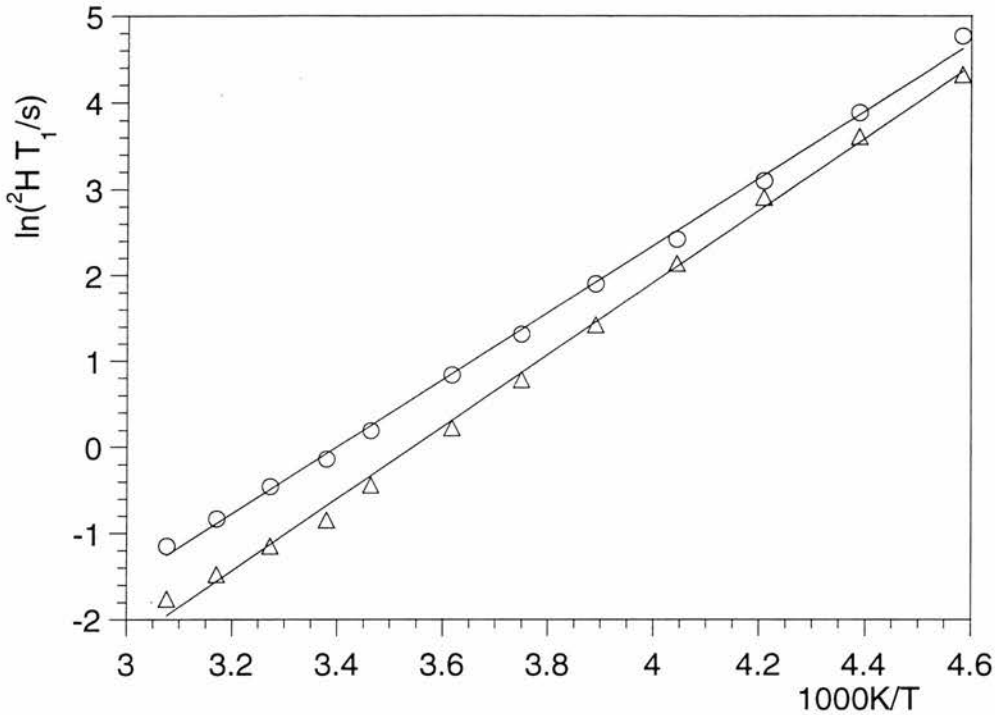

Figure 5.20. Plot of ln(^{2}H T_1) as a function of 1000K/T for 1,1,6,6-d_4- (o) and 2,2,5,5-d_4-hexane-1,6-diyl dibenzenesulfonate (Δ). Apparent activation energies from the slopes are 32.4 and 34.9 kJ mol^{-1}, respectively.

The ^{2}H spin-lattice relaxation time depends very similarly on temperature for both samples. Perhaps surprisingly, the measured relaxation times are only slightly smaller for the 2,2,5,5-d_4-labelled derivative. For both samples, the ^{2}H spin-lattice relaxation time is of order 100 s at 220 K and decreases strongly with temperature to *ca.* 100 ms at 325 K. Plots of ln(^{2}H T_1/s) as a function of 1000K/T (fig. 5.20) are satisfactorily linear for both samples. The slopes of the least-squares lines give 32.4 ± 0.8 and 34.9 ± 1.2 kJ mol^{-1} for the apparent activation energies of 1,1,6,6-d_4- and 2,2,5,5-d_4-hexane-1,6-diyl dibenzenesulfonates, respectively.

For the1,1,6,6-d_4-labelled derivative, ^{2}H quadrupolar echo spectra were measured with 20 and 160 μs refocusing delays at room temperature (fig. 5.21). The observed 112 kHz wide spectrum is independent of the length of the refocusing delay indicating small amplitude motion in the fast motion limit. The spectrum was simulated using the conical libration model with a rate constant of 1×10^8 s^{-1} and the distribution centred at 13° with a standard deviation of 1°.

For the 2,2,5,5-d_4-labelled derivative, ^{2}H quadrupolar echo spectra were measured at four different temperatures between 257 and 325 K (fig. 5.22). The spectra are different from those of the 1,1,6,6-d_4 derivative as there is a sharp peak at zero frequency, indicating that the librational motion averages the C-D bond orientation at magic angle. As for the 1,1,6,6-d_4 derivative, the spectrum is independent of the length of the refocusing delay, and therefore, the rate of motion is in the fast motion limit. The spectra were simulated with the conical libration model (fig. 5.23). Two distributions were needed to reproduce the measured spectra. The first distribution has standard deviation of 1° and centre at 0° at 257 and 267 K. The centre is at 5° at 288 K and 10° at 328 K. The second distribution accounts for the sharp peak and is centred at 55° with a standard deviation of 1°. These distributions were added in ratios 100:6, 100:8, 100:50 and 50:100 at 257, 267, 288 and 328 K, respectively, indicating that the amplitude of the libration increases with temperature.

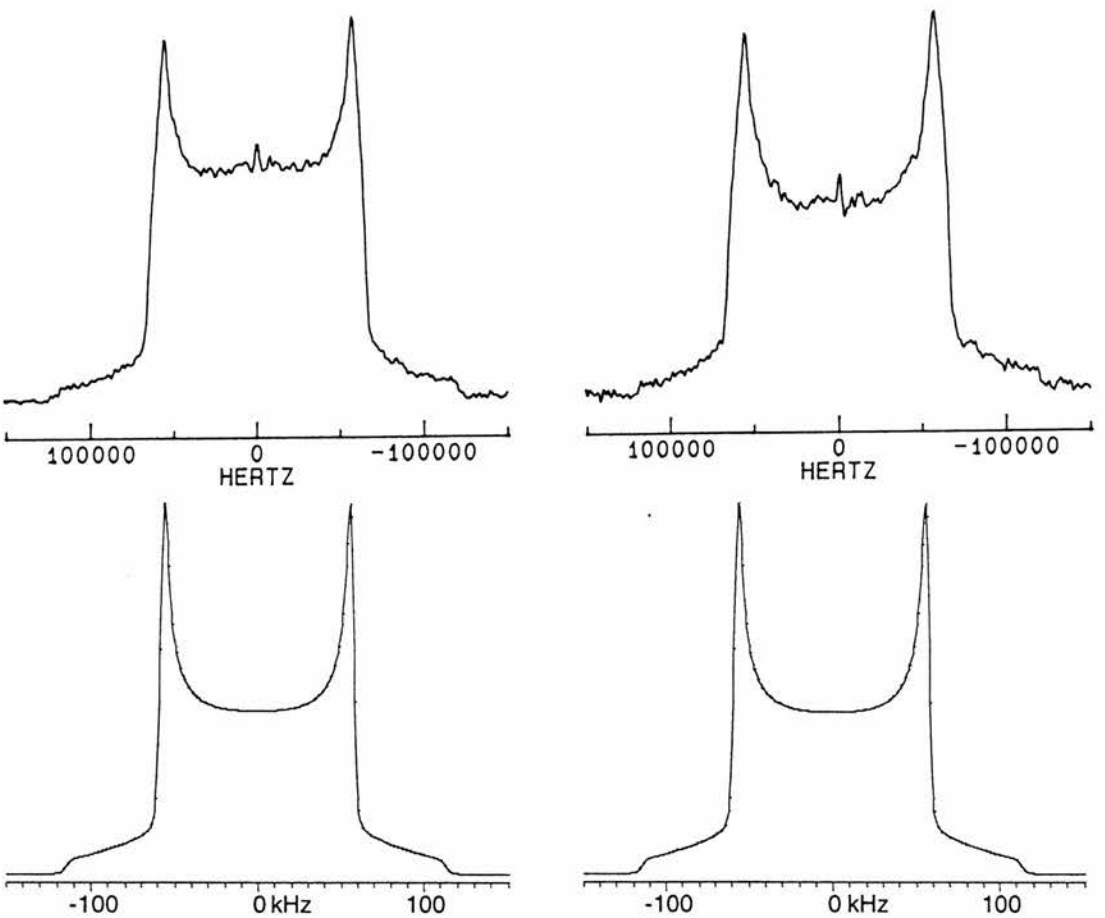

Figure 5.21. Measured ^{2}H quadrupolar echo spectra (top) for 1,1,6,6-d_4-hexane-1,6-diyl dibenzenesulfonate at 289 K together with simulated spectra (bottom). Refocusing delay is 20 μs (left) and 160 μs (right).

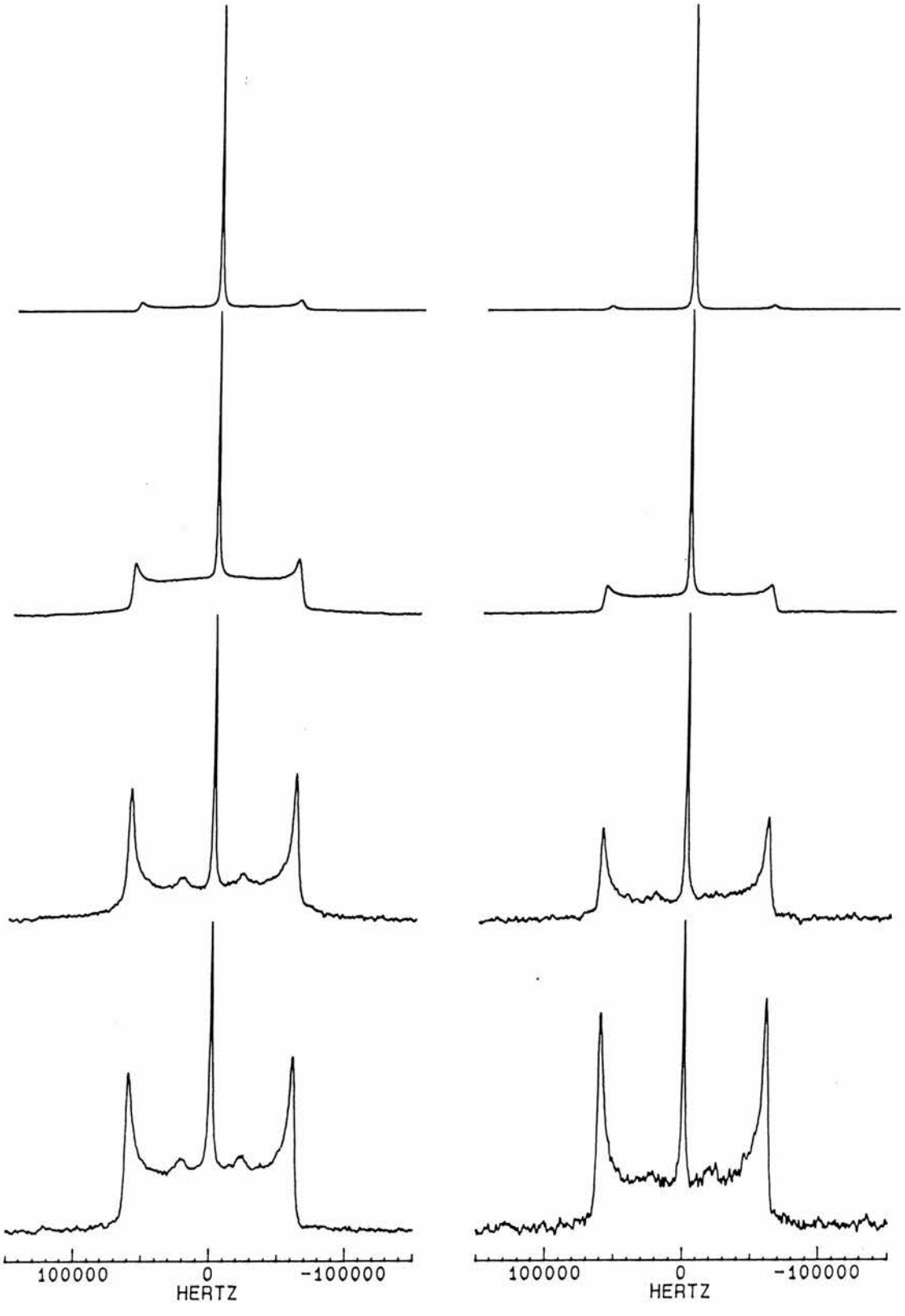

Figure 5.22. Measured ^2H quadrupolar echo spectra for 2,2,5,5-d_4-hexane-1,6-diyl dibenzenesulfonate at different temperatures. Refocusing delay is 20 μs (left) and 160 μs (right). Temperatures are from top to bottom: 325, 288, 267 and 257 K.

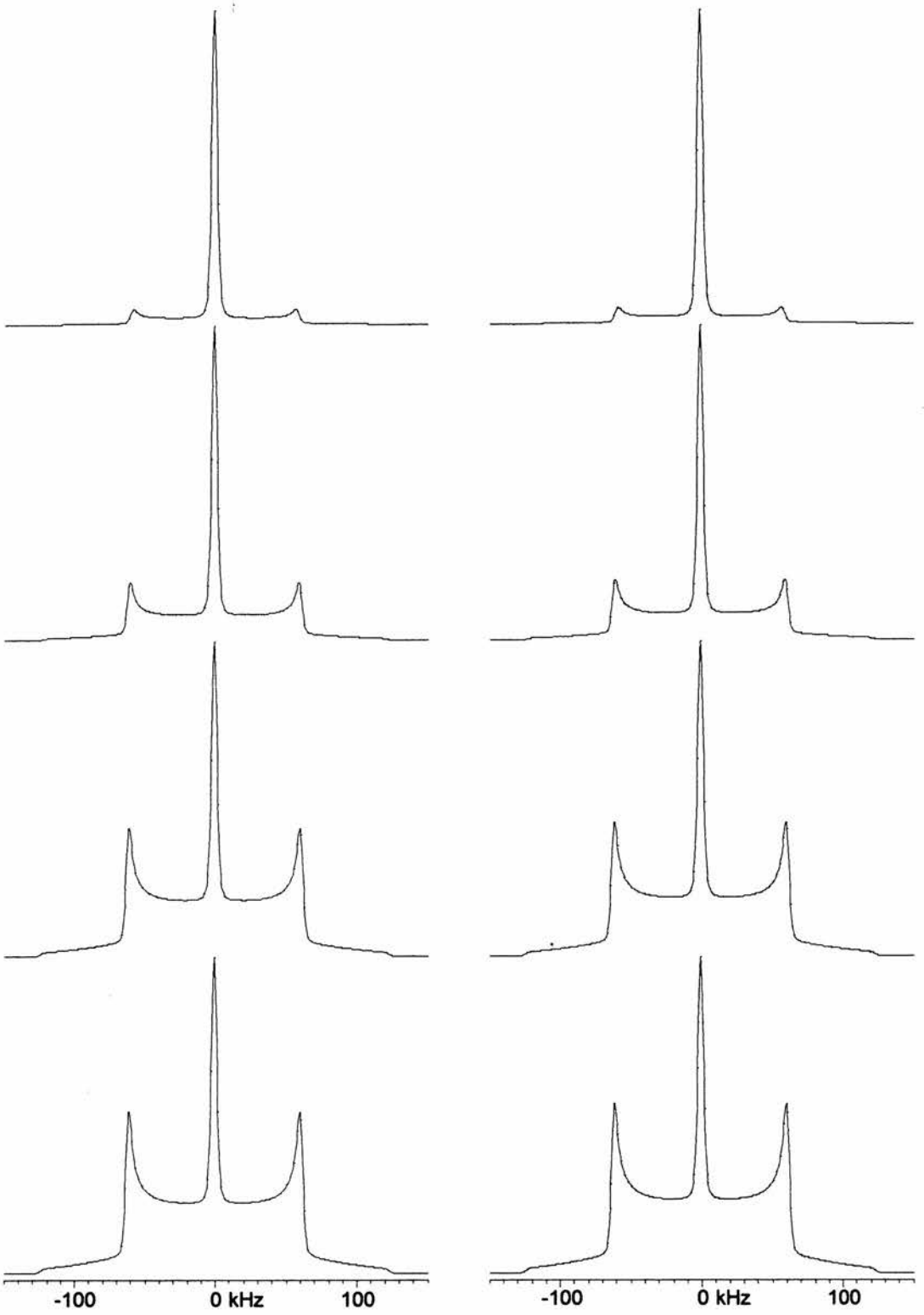

Figure 5.23. Simulated ^2H quadrupolar echo spectra for 2,2,5,5-d_4-hexane-1,6-diyl dibenzenesulfonate.

5.4. Hexane-1,6-diyl ditosylate

The crystal structure of hexane-1,6-diyl ditosylate was solved from single crystal x-ray diffraction data. Structural details and views of the unit cell are given in the appendix (p. A-13 and A-35). The structure shows that all carbon-carbon bonds in the alkyl chain but the central bond are in *gauche* conformation, and therefore, it is interesting to study the effect of these *gauche* bonds on the molecular dynamics in the alkyl chain.

Unfortunately, proton spin-lattice relaxation was slow for this compound, and therefore, ^{13}C CP/MAS spectrum was only measured at room temperature. Also, increasing the contact time from the standard 1 ms failed to improve the signal-to-noise ratio (fig. 5.24). Peaks in the ^{13}C CP/MAS spectrum are at 20.9 ($OCH_2CH_2\underline{C}H_2$), 22.1 (Ar-$\underline{C}H_3$), 27.4 ($OCH_2\underline{C}H_2$), 69.0 ($O\underline{C}H_2$), 127.7 ($\underline{C}_{Ar}$), 130.0 ($\underline{C}_{Ar}$), 132.3 ($\underline{C}_{Ar,4}$) and 144.5 ppm ($\underline{C}_{Ar}$-S). The spectrum shows no effects of short ^{13}C $T_{1\rho}$ relaxation time, and therefore, no attempt was made to measure it.

As for hexane-1,6-diyl dibenzenesulfonate, two samples were prepared for deuteron NMR studies, namely 1,1,6,6-d_4-hexane-1,6-diyl and 2,2,5,5-d_4-hexane-1,6-diyl ditosylates. For both samples, the ^2H spin-lattice relaxation time was measured between 238 and 335 K. The measured values are listed in table 5.6 and shown as a function of temperature in figure 5.25.

Perhaps surprisingly, the ^2H spin-lattice relaxation time is nearly independent of the position of the deuteron label in the chain. For both samples the ^2H spin-lattice relaxation time decreases from order of 100 s at 238 K to *ca.* 0.5 s at 340 K. Interestingly, this decrease is very similar to that observed for the benzenesulfonate derivatives in the previous section although the alkyl chain in the benzenesulfonate derivatives has only two *gauche* bonds. Therefore, the number of *gauche* bonds in the chain is unimportant.

Again, the plot of $\ln(^2H\ T_1)$ as a function of 1000K/T is satisfyingly linear for both samples. These plots are shown in figure 5.26 together with best-fitting least-squares lines. The slopes of the least-squares lines give 36.9 ± 1.0 and 32.3 ± 1.7 kJ mol^{-1} for

the apparent activation energy of 1,1,6,6-d_4- and 2,2,5,5-d_4-hexane-1,6-diyl ditosylate, respectively. These values agree well with the values 32.4 ± 0.8 and 34.9 ± 1.2 kJ mol^{-1} obtained for 1,1,6,6-d_4-hexane-1,6-diyl and 2,2,5,5-d_4-hexane-1,6-diyl dibenzenesulfonate, respectively.

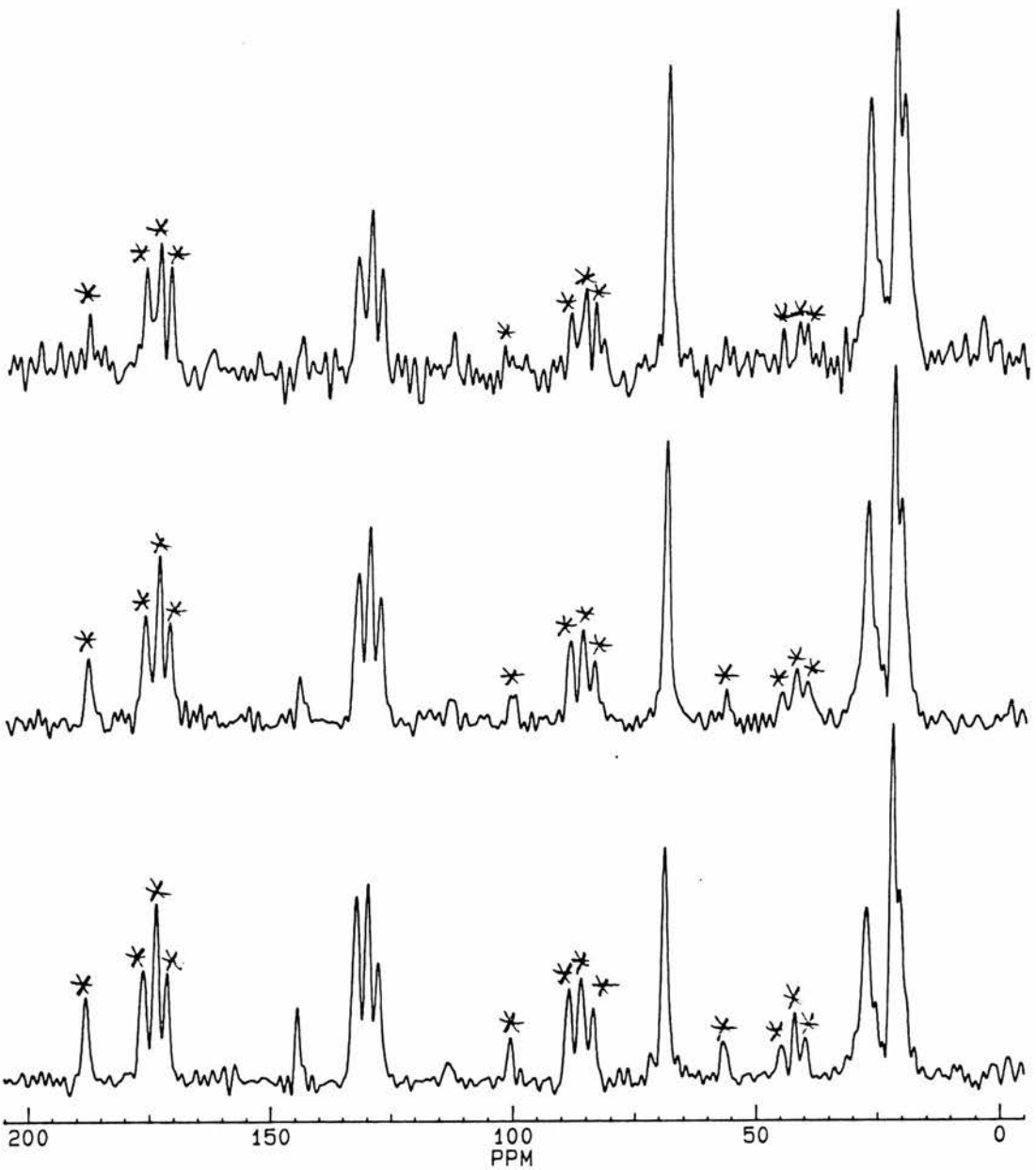

Figure 5.24. ^{13}C CP/MAS spectra for hexane-1,6-diyl ditosylate at room temperature. Contact times are from top to bottom: 1, 4 and 12 ms. Spinning sidebands (at 5.5 kHz) are asterisked.

Table 5.6. Measured ^{2}H spin-lattice (T_1) relaxation times for 1,1,6,6-d_4- and 2,2,5,5-d_4-hexane-1,6-diyl ditosylate.

T(vtu)/K	T/K	^{2}H T_1/s 1,1,6,6-d_4	^{2}H T_1/s 2,2,5,5-d_4
240	238	108	54.3
250	247	62.6	36.2
260	257	27.8	23.9
270	267	16.2	12.4
280	276	9.66	7.93
290	286	5.49	-
293	289	-	4.29
300	296	3.18	3.08
310	306	1.99	1.79
320	315	1.26	1.23
330	325	0.793	0.773
340	335	0.472	0.551

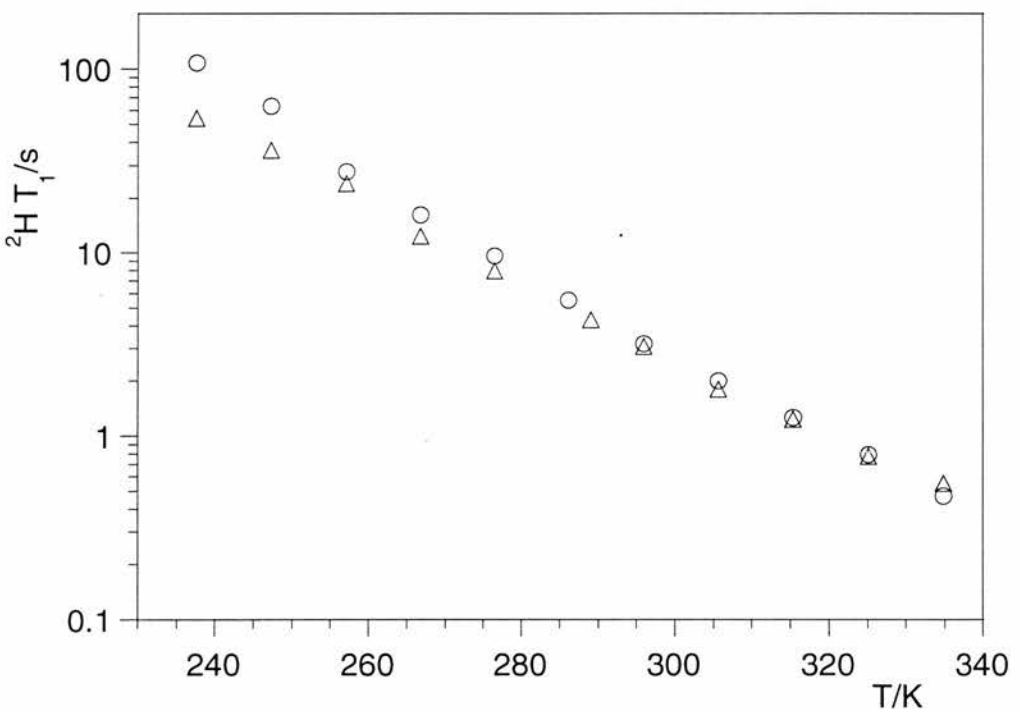

Figure 5.25. Measured ^{2}H spin-lattice relaxation time (T_1) as a function of temperature for 1,1,6,6-d_4- (o) and 2,2,5,5-d_4-hexane-1,6-diyl ditosylate (Δ).

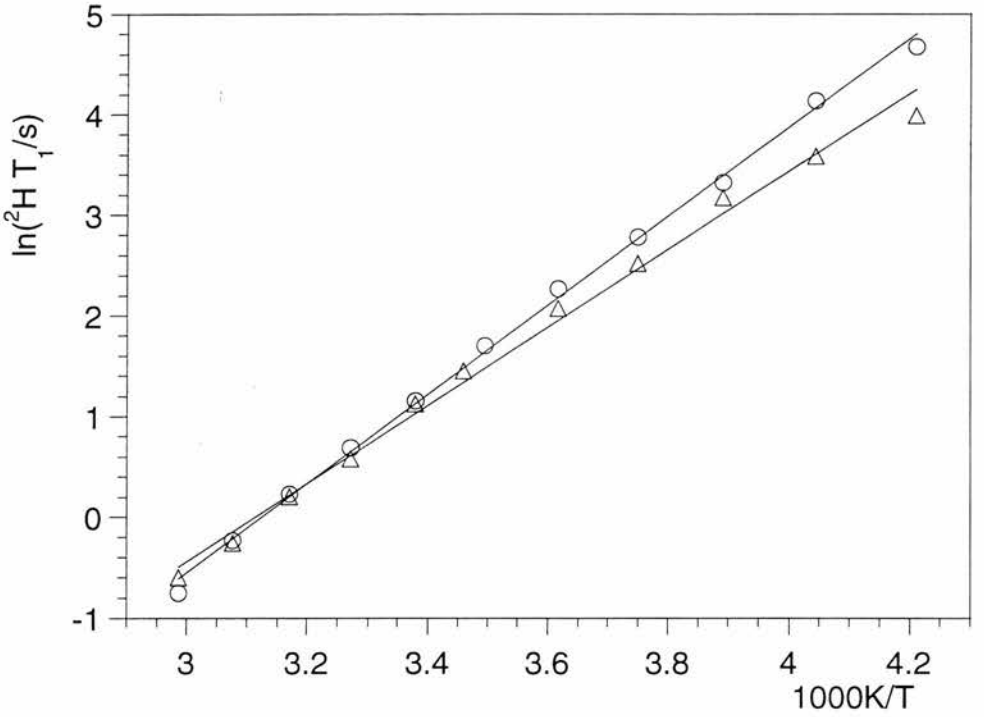

Figure 5.26. Plot of $\ln(^2H\ T_1)$ as a function of 1000K/T for 1,1,6,6-d_4- (o) and 2,2,5,5-d_4-hexane-1,6-diyl ditosylate (Δ). Apparent activation energies from the slopes are 36.9 and 32.3 mol^{-1}, respectively.

For the 1,1,6,6-d_4 derivative, ^2H quadrupolar echo spectra were measured with 20 μs and 160 μs refocusing delays at 315 and 335 K (fig. 5.27). The observed 113 kHz wide spectrum is independent of temperature and the length of the refocusing delay indicating small amplitude motion in the fast motion limit. The spectrum was simulated using the conical libration model with a rate constant of 1×10^8 s^{-1} and with the distribution centred at 10° and having a standard deviation of 5° (fig. 5.28).

For the 2,2,5,5-d_4 derivative, ^2H quadrupolar echo spectra were measured with 20 μs and 160 μs refocusing delays at 267, 288 and 335 K (fig. 5.29). The spectrum is independent of the length of the refocusing delay and there is sharp peak at zero frequency. The spectra are very similar to those of 2,2,5,5-d_4-hexane-1,6-diyl dibenzenesulphonate and were simulated with two distributions having a standard deviation of 1° and centred at 0 and 55° (fig. 5.30). These distributions were added in ratios 100:15, 100:30 and 100:100 at 267, 288 and 335 K, respectively, indicating that the average amplitude of the motion increases with temperature.

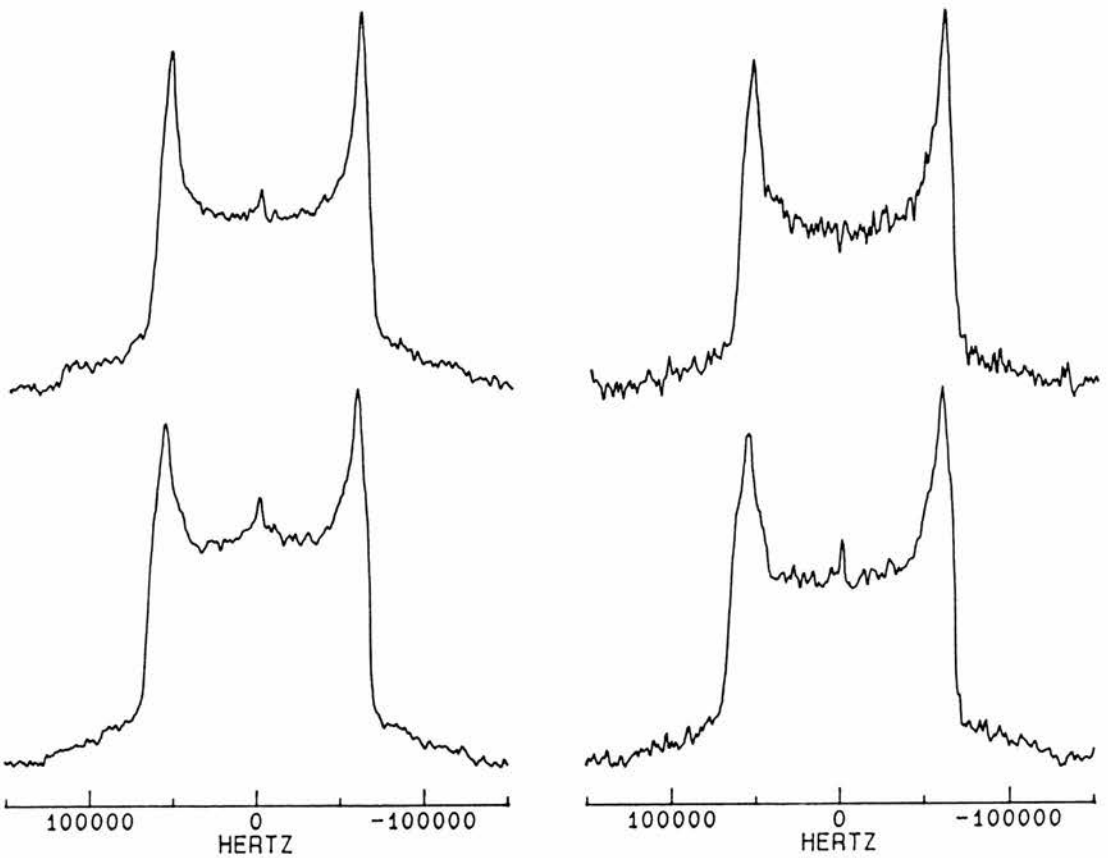

Figure 5.27. Measured ^{2}H quadrupolar echo spectra for 1,1,6,6-d_4-hexane-1,6-diyl ditosylate at 335 K (top) and 315 K (bottom). Refocusing delay is 20 μs (left) and 160 μs (right).

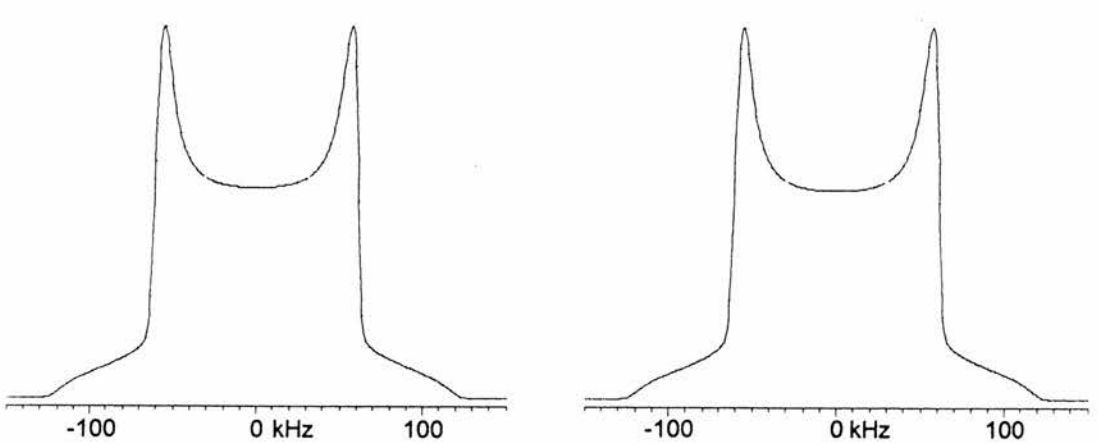

Figure 5.28. Simulated ^{2}H quadrupolar echo spectra for 1,1,6,6-d_4-hexane-1,6-diyl ditosylate.

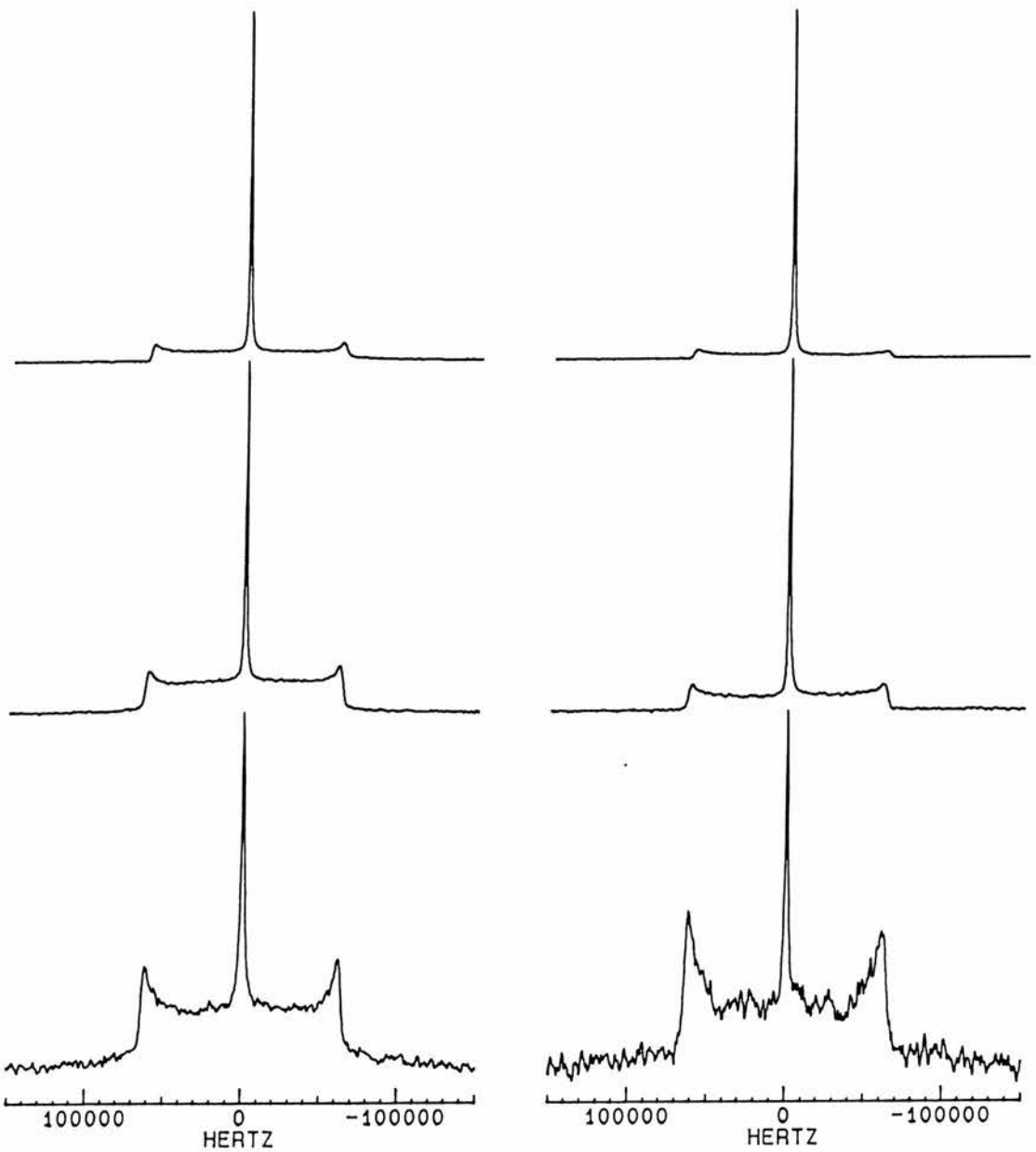

Figure 5.29. Measured ^2H quadrupolar echo spectra for 2,2,5,5-d_4-hexane-1,6-diyl ditosylate at different temperatures. Refocusing delay is 20 μs (left) and 160 μs (right). Temperatures are from top to bottom: 335, 288 and 267 K.

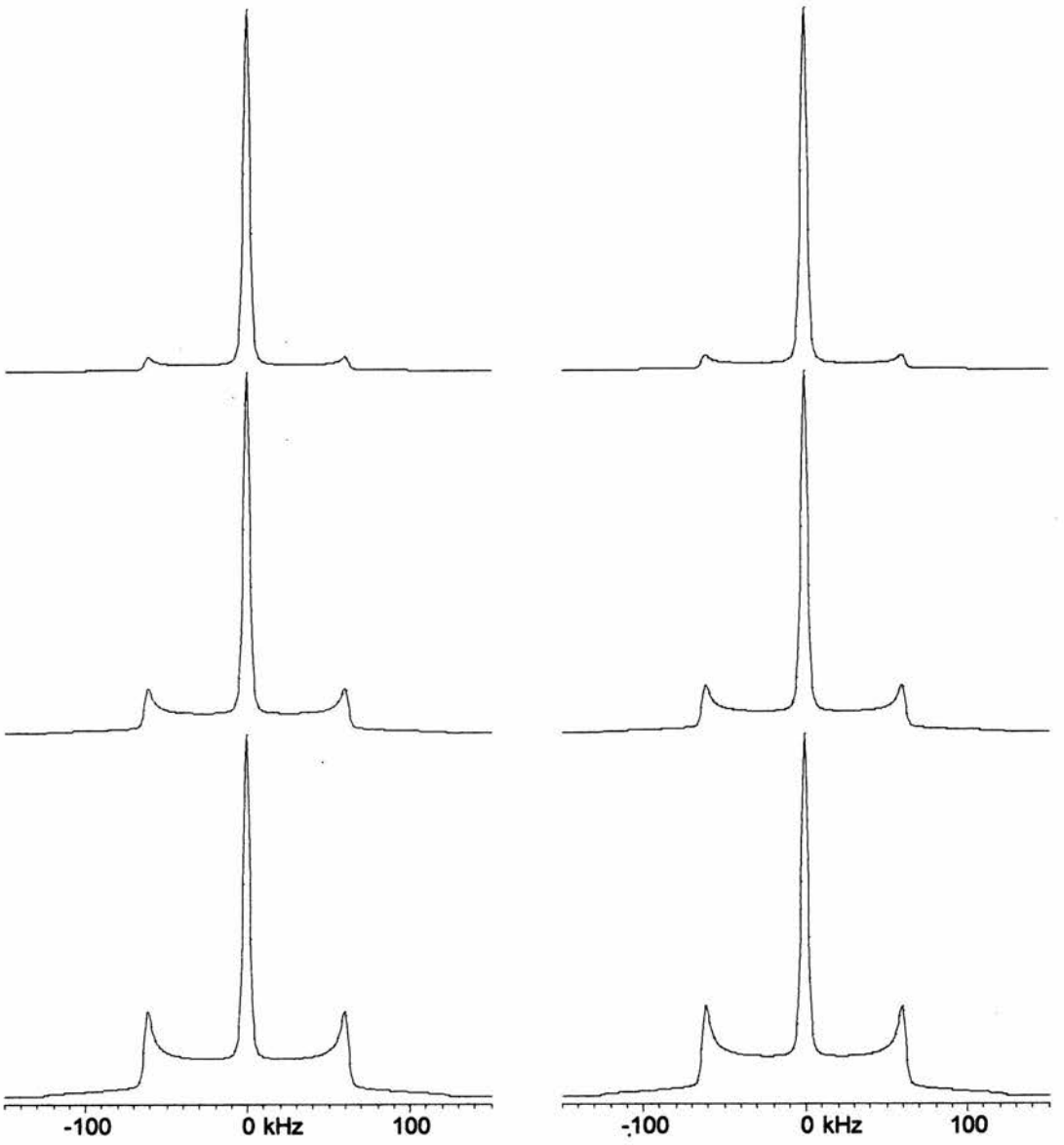

Figure 5.30. Simulated ^2H quadrupolar echo spectra for 2,2,5,5-d_4-hexane-1,6-diyl ditosylate.

5.5. Hexane-1,6-diyl bis(*p*-chlorobenzoate)

All the hexane-1,6-diyl derivatives discussed so far have had *gauche* bonds in the alkyl chain. However, it is interesting to compare molecular dynamics in chains that have *gauche* bonds with chains that are in all-*trans* conformation. The crystal structure of hexane-1,6-diyl bis(*p*-chlorobenzoate) has been solved from single crystal x-ray diffraction data and indicates that the chain is in an all-*trans* conformation.[109,110] Views of the structure are given in the appendix (p. A-36).

Figure 5.31 shows ^{13}C CP/MAS spectra for hexane-1,6-diyl bis(*p*-chlorobenzoate) measured at different temperatures. Peaks are at 28.3 (-$OCH_2\underline{C}H_2\underline{C}H_2$-), 66.2 (-$O\underline{C}H_2CH_2CH_2$-), 129.0 ($\underline{C}_{Ar}$-H) 133.3 ($\underline{C}_{Ar}$-C=O), 138.9 and 141.5 ($\underline{C}_{Ar}$-Cl) and 164.8 ($\underline{C}$=O). These spectra show no evidence of dipolar broadening nor effects of short ^{13}C $T_{1\rho}$ relaxation time, and therefore, no attempt was made to measure the ^{13}C $T_{1\rho}$ relaxation time.

Two chain deuterated samples were prepared for deuterium NMR studies, namely 1,1,6,6-d_4- and 2,2,5,5-d_4-hexane-1,6-diyl bis(*p*-chlorobenzoates). ^2H spin-lattice relaxation times were measured for both samples between 153 and 338 K. The measured values are listed in table 5.7 and shown as function of temperature in figures 5.32 and 5.33.

For the 1,1,6,6-d_4-labelled derivative, the ^2H spin-lattice relaxation time decreases strongly with temperature from 465 s at 182 K to 24.1 s at 250 K. At higher temperatures the ^2H spin-lattice relaxation time is nearly independent of temperature. For the 2,2,5,5-d_4-labelled derivative, the dependence of the ^2H spin-lattice relaxation time with temperature above 210 K is similar to that of the 1,1,6,6-d_4 derivative but the ^2H spin-lattice relaxation times are much shorter indicating larger angle librations towards the centre of the chain. The ^2H spin-lattice relaxation time decreases from 42.1 s at 211 K to 2.19 at 288 K. At higher temperatures, the ^2H spin-lattice relaxation time is nearly independent of temperature. Below 211 K, the ^2H spin-lattice relaxation is bi-exponential with relaxation time for one component of order 40 s and much longer for the other component.

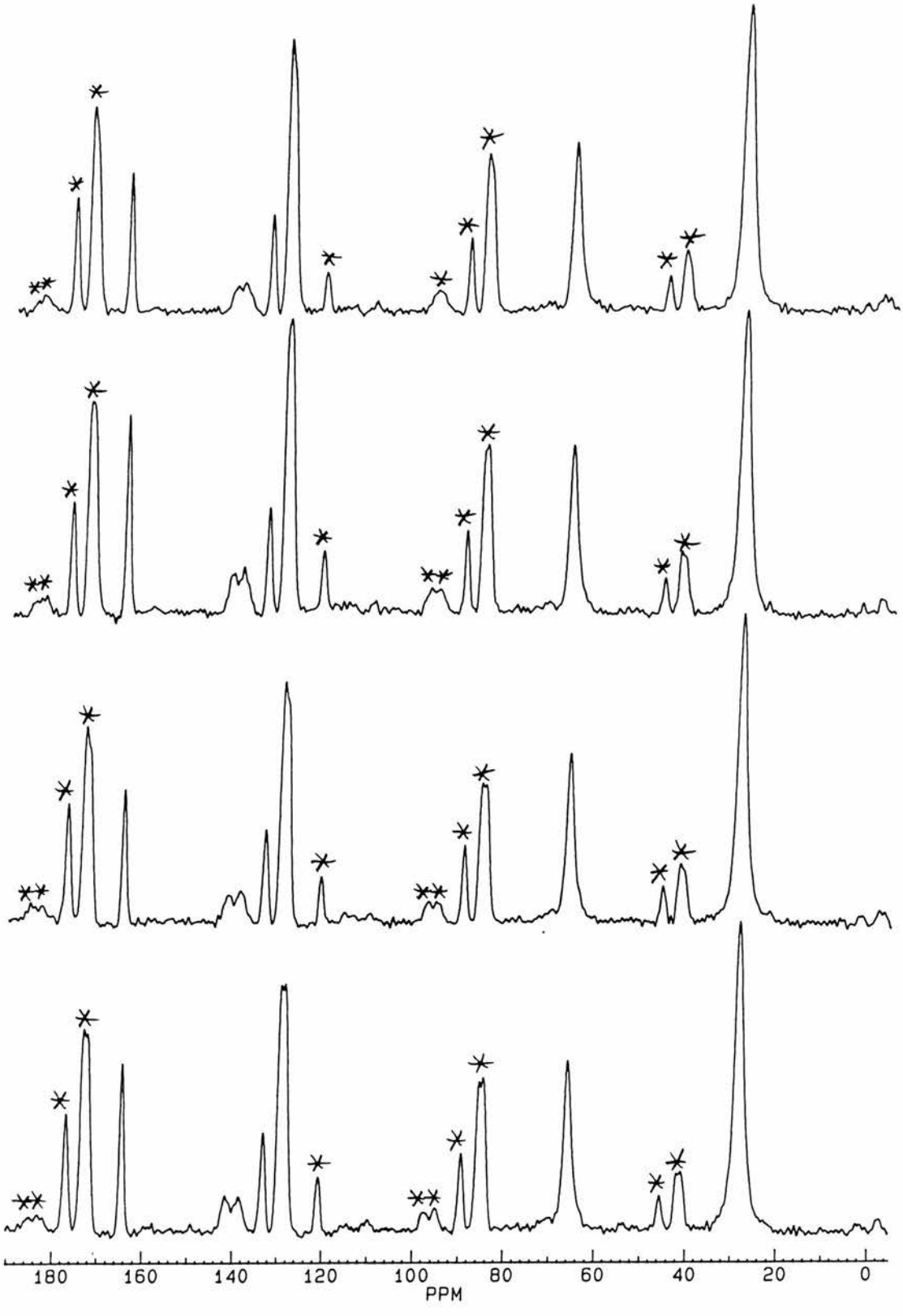

Figure 5.31. ^{13}C CP/MAS spectra for hexane-1,6-diyl bis(*p*-chlorobenzoate) at different temperatures. Temperatures are from top to bottom: 326, 296, 270 and 246 K. Spinning sidebands (at 5.5 kHz) are asterisked.

Table 5.7. Measured ^{2}H T_1 relaxation time for 1,1,6,6-d_4- and 2,2,5,5-d_4-hexane-1,6-diyl bis(*p*-chlorobenzoates).

T(vtu)/K	T/K	^{2}H T_1/s 1,1,6,6-d_4-	^{2}H T_1/s 2,2,5,5-d_4-
183	182	465	-
184	183	377	-
185	184	221	-
186	185	163	-
188	187	113	-
193	192	72.6	-
203	202	52.0	-
213	211	43.0	42.1
233	231	35.6	24.1
253	250	24.1	7.41
273	270	27.3	4.47
292	288	22.9	2.19
313	309	22.8	1.88
333	328	22.6	1.55
343	338	21.5	1.63

The observation of a temperature independent ^{2}H spin-lattice relaxation time for these *p*-chlorobenzoyl derivatives is similar to that observed for the diacids in chapter 4. For the diacids, it was shown that the temperature independence occurs when the increase in the amplitude of motion compensates for the increase in ^{2}H spin-lattice relaxation time caused by a shortening of the correlation time in the fast motion limit. As all the diacids were in all-*trans* conformation, this could be a general property of all-*trans* alkyl chains.

^{2}H quadrupolar echo spectra were measured for the 1,1,6,6-d_4-labelled derivative with 20 μs refocusing delay at 231, 288 and 338 K (fig. 5.33, left). The spectrum is nearly independent of temperature and only narrows down from 117 kHz at 231 K to 115 kHz at 338 K. The spectrum was simulated with the conical libration model with a rate constant of 1×10^8 s^{-1} and the distribution centred at 10° with a standard deviation of 1° (fig. 5.33, right).

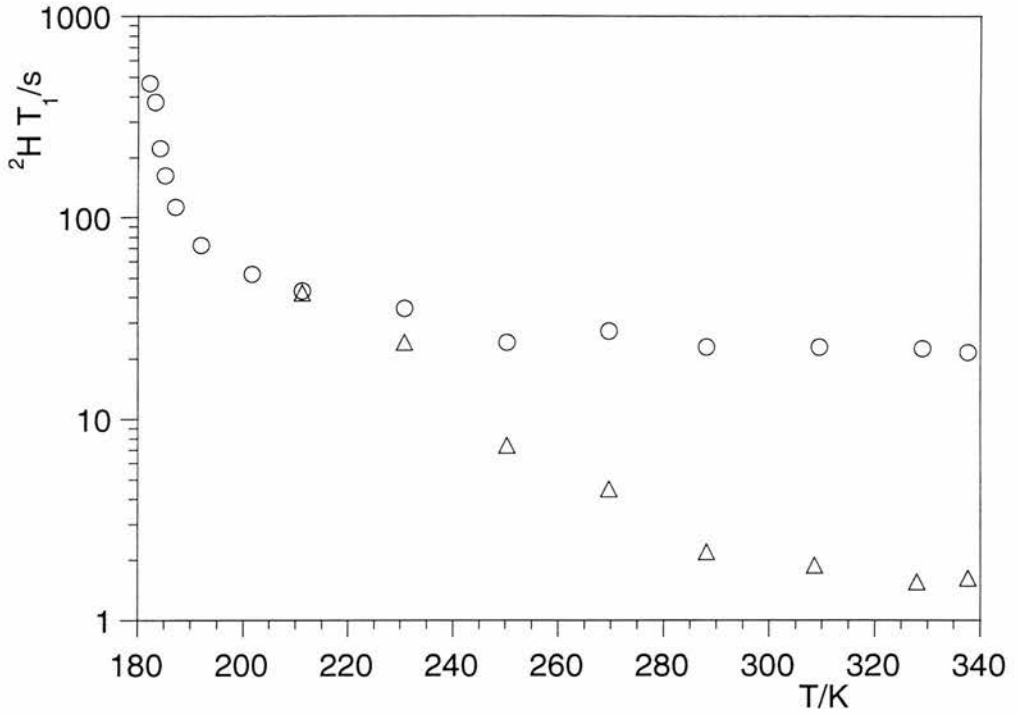

Figure 5.32. Measured ^{2}H spin-lattice relaxation time as a function of temperature for 1,1,6,6-d_4- (o) and 2,2,5,5-d_4-hexane-1,6-diyl bis(*p*-chlorobenzoate) (Δ).

For the 2,2,5,5-d_4-labelled derivative, ^{2}H quadrupolar echo spectra were measured with a 20 μs refocusing delay at 231 K and with 20 and 160 μs refocusing delays at 288 and 338 K. The spectrum measured at 231 K is 122 kHz wide indicating only very small amplitude motion (fig. 5.34, left). The spectrum was simulated using the conical libration model with a rate constant of 1×10^8 s^{-1} and the distribution centred at 0° with a standard deviation of 1° (fig. 5.34, right).

The spectra measured at 288 K and 338 K have a sharp peak at zero frequency (fig. 5.35). The proportion of the peak increases with temperature indicating that the average amplitude of the motion increases with temperature. Further evidence of the increase in the amplitude of motion is observed in the narrowing of the remaining powder pattern from 119 kHz at 288 K to 115 kHz at 338 K. The spectrum is independent of the length of the refocusing delay indicating that the rate of the motion is in the fast motion limit.

The spectra were simulated with the conical libration model using a rate constant of 1×10^8 s^{-1} and two different distributions. The first distribution was centred at 5° and had a standard deviation of 1°. The other distribution accounts for the sharp peak, and therefore, is centred at 55° and has a standard deviation of 1°. These two distributions were added in ratios 100:7 at 288 K and 100:15 at 338 K to reproduce the measured spectra (fig. 5.36). The increase in the proportion of the second distribution indicates that the average amplitude of the motion increases with temperature.

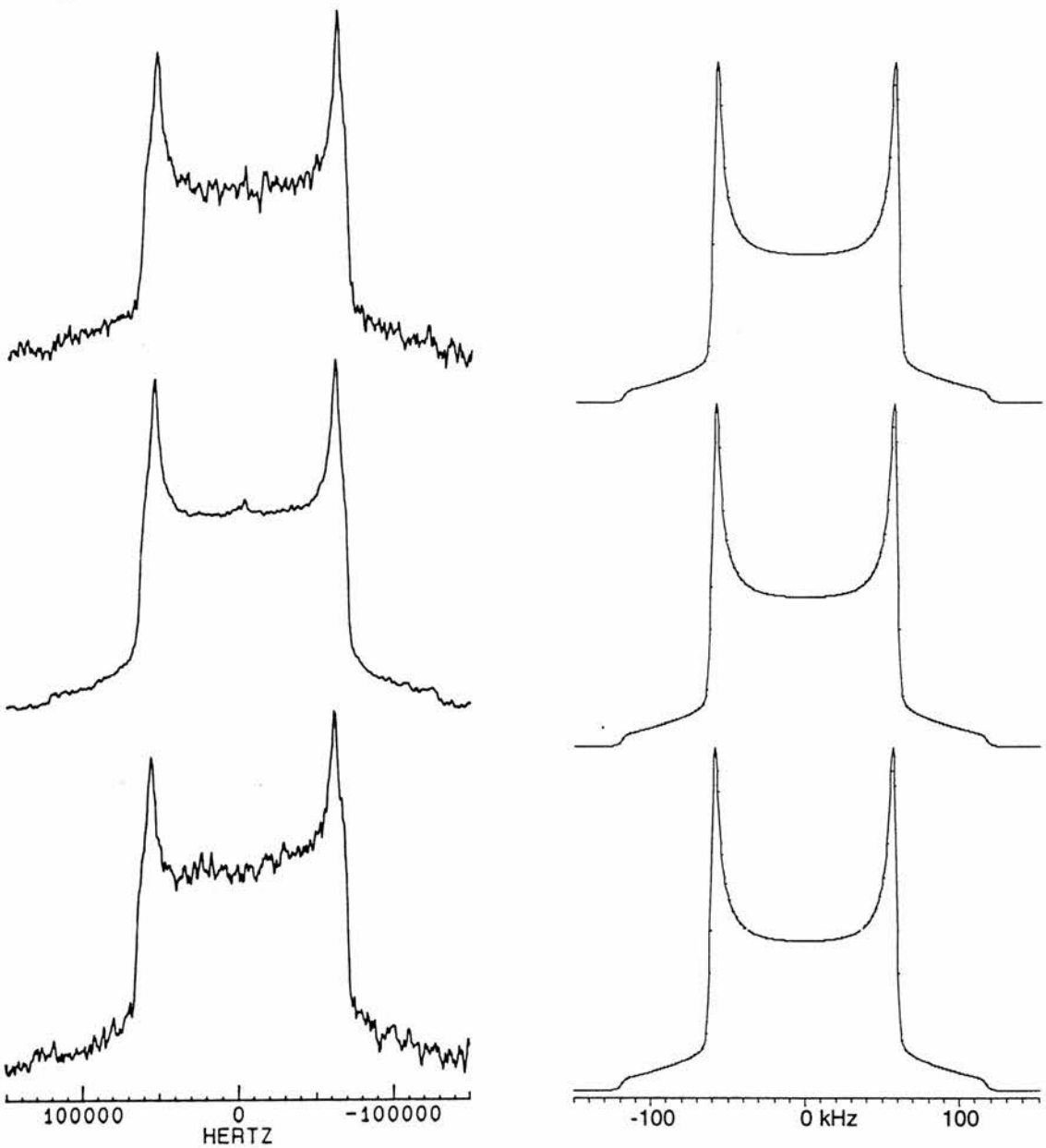

Figure 5.33. Measured ^2H quadrupolar echo spectra (left) for 1,1,6,6-d_4-hexyl 1,6-bis(*p*-chlorobenzoate) at different temperatures together with simulated spectra (right). Temperatures are from top to bottom: 338, 288 and 231 K.

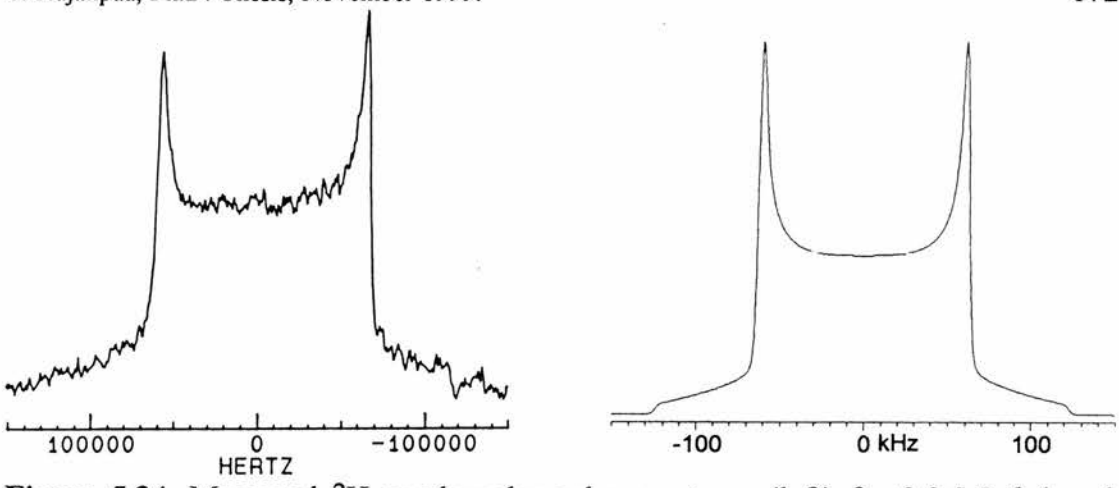

Figure 5.34. Measured ^{2}H quadrupolar echo spectrum (left) for 2,2,5,5-d_4-hexyl 1,6-bis(*p*-chlorobenzoate) at 231 K together with a simulated spectrum (right).

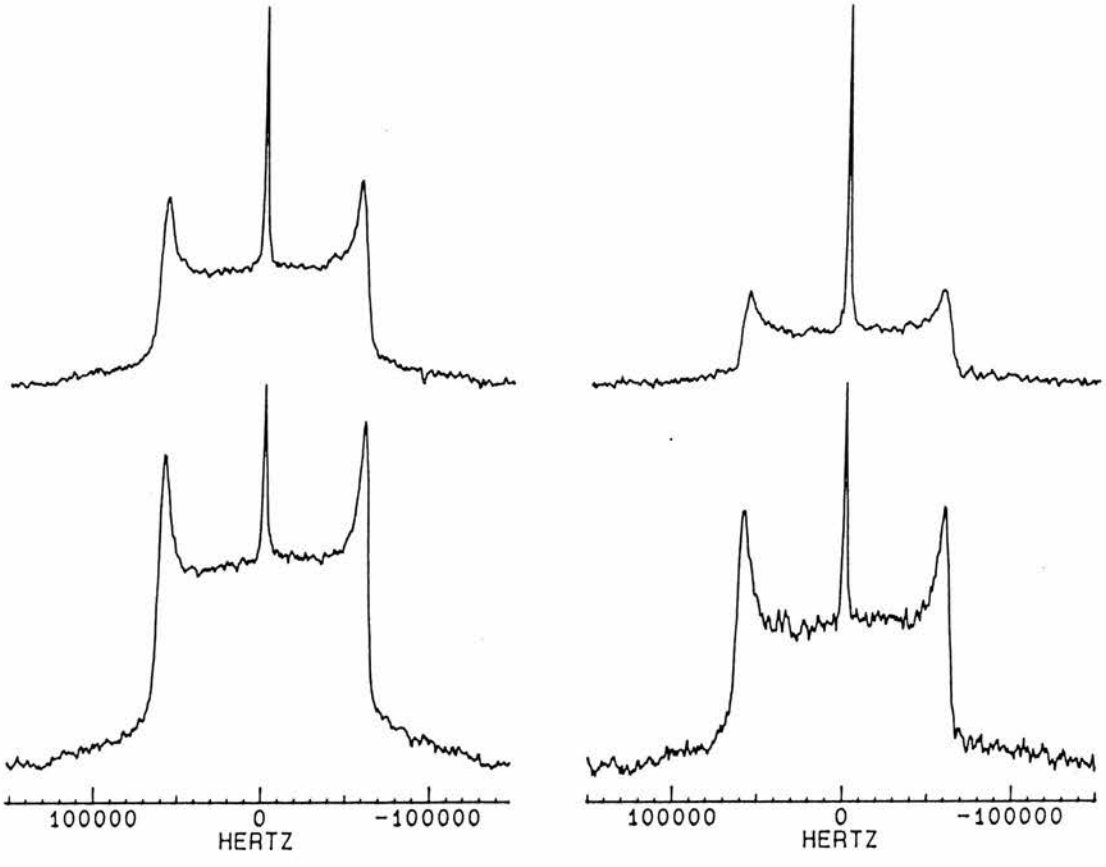

Figure 5.35. Measured ^{2}H quadrupolar echo spectra for 2,2,5,5-d_4-hexyl 1,6-bis(*p*-chlorobenzoate) at 338 K (top) and 288 K (bottom). Spectra were measured with 20 μs (left) and 160 μs (right) refocusing delays.

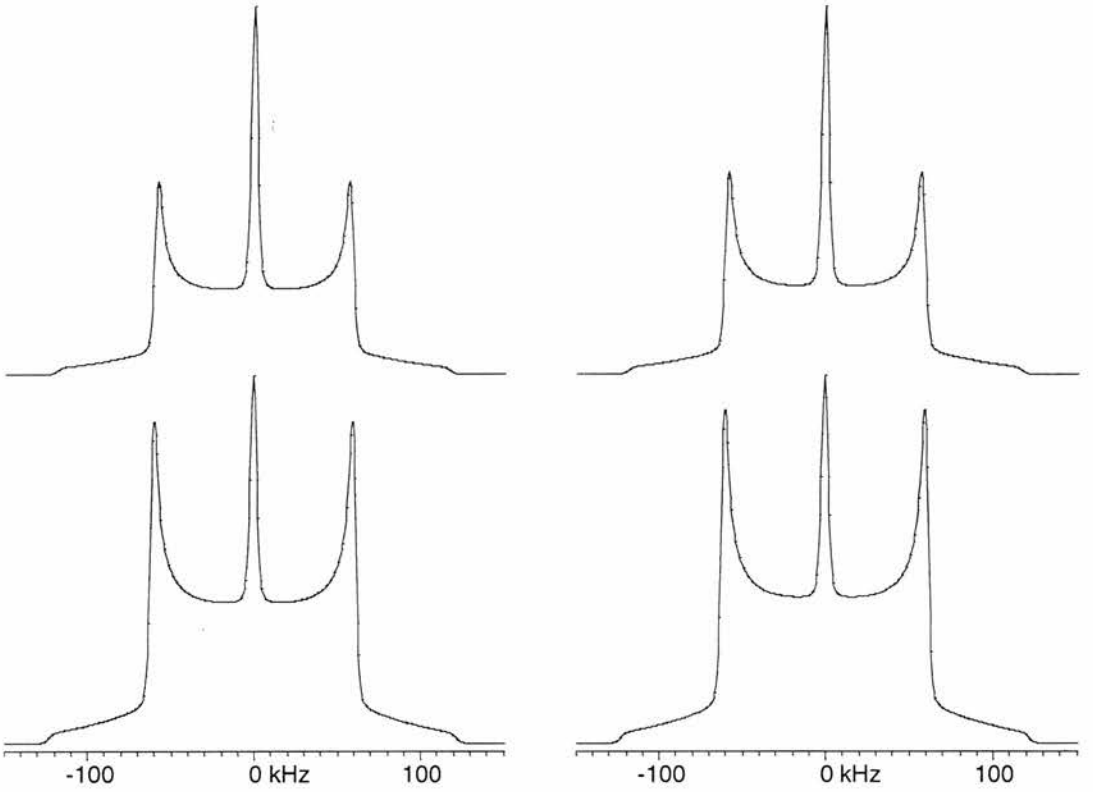

Figure 5.36. Simulated ^{2}H quadrupolar echo spectra for 2,2,5,5-d_4-hexyl 1,6-bis(*p*-chlorobenzoate).

5.6. Hexane-1,6-diyl bis(*o*-chlorobenzoate)

All the compounds studied so far that have an all-*trans* alkyl chain, namely the diacids and hexane-1,6-diyl bis(*p*-chlorobenzoate), show temperature independence of ^{2}H spin-lattice relaxation time. To investigate whether this phenomenon is a more general property of all-*trans* chains, hexane-1,6-diyl bis(*o*-chlorobenzoate) was studied. Its crystal structure (appendix, p. A-38) indicates that the chain is in an all-*trans* conformation.[109]

Figure 5.37 shows ^{13}C CP/MAS spectrum measured at room temperature. Peaks are at 26.6 (-OCH$_2$CH$_2$<u>C</u>H$_2$-), 29.0 and 31.3 (-OCH$_2$<u>C</u>H$_2$CH$_2$-), 66.7 (-O<u>C</u>H$_2$CH$_2$CH$_2$-), 127.2, 131.9 (<u>C</u>$_{Ar}$-H), 134.3, 136.3 and 164.4 ppm (<u>C</u>=O). Two peaks are observed for the chain carbons at positions 2 and 5 because of crystal packing effects as the molecule is asymmetric. Slow proton spin-lattice relaxation made the measurement of variable temperature spectra prohibitively time-consuming.

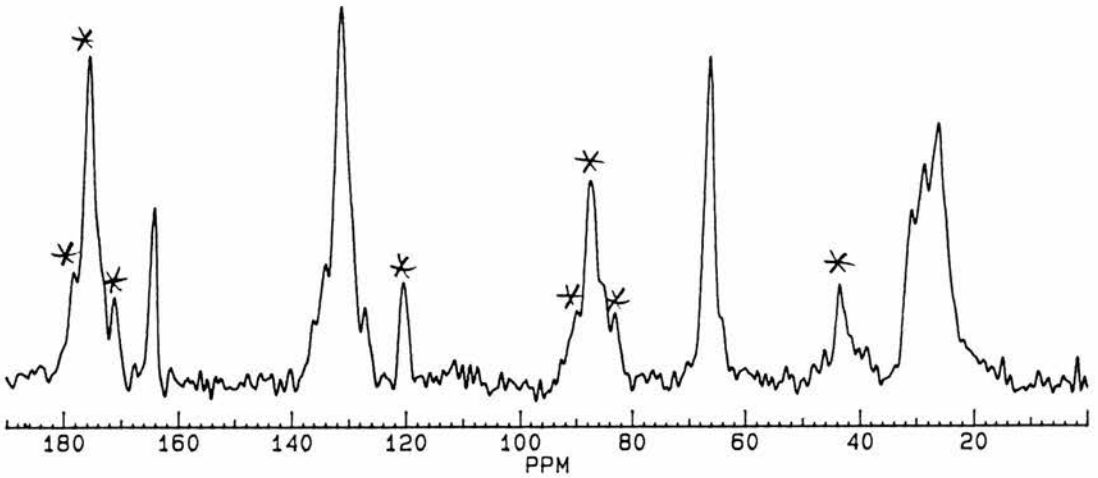

Figure 5.37. ^{13}C CP/MAS spectrum for hexane-1,6-diyl bis(*o*-chlorobenzoate) at room temperature. Spinning sidebands are asterisked.

The chain end methylene groups were deuterated, and ^{2}H spin-lattice relaxation time for this 1,1,6,6-d_4-hexane-1,6-diyl bis(*o*-chlorobenzoate) was measured between 199 and 296 K. The measured values are listed in table 5.8 and shown as a function of temperature in figure 5.38.

As expected for an all-*trans* chain, the ^{2}H spin-lattice relaxation time is nearly independent of temperature decreasing only from *ca.* 75 s at 199 K to *ca.* 40 s at 296 K. This is consistent with the other all-*trans* compounds all of which show temperature independence of ^{2}H spin-lattice relaxation time.

Table 5.8. Measured ^{2}H spin-lattice relaxation times for 1,1,6,6-d_4-hexane-1,6-diyl bis(*o*-chlorobenzoate).

T(vtu)/K	T/K	^{2}H T_1/s
200	199	74.5
220	218	77.8
240	238	73.9
260	257	50.8
280	276	45.9
300	296	39.2

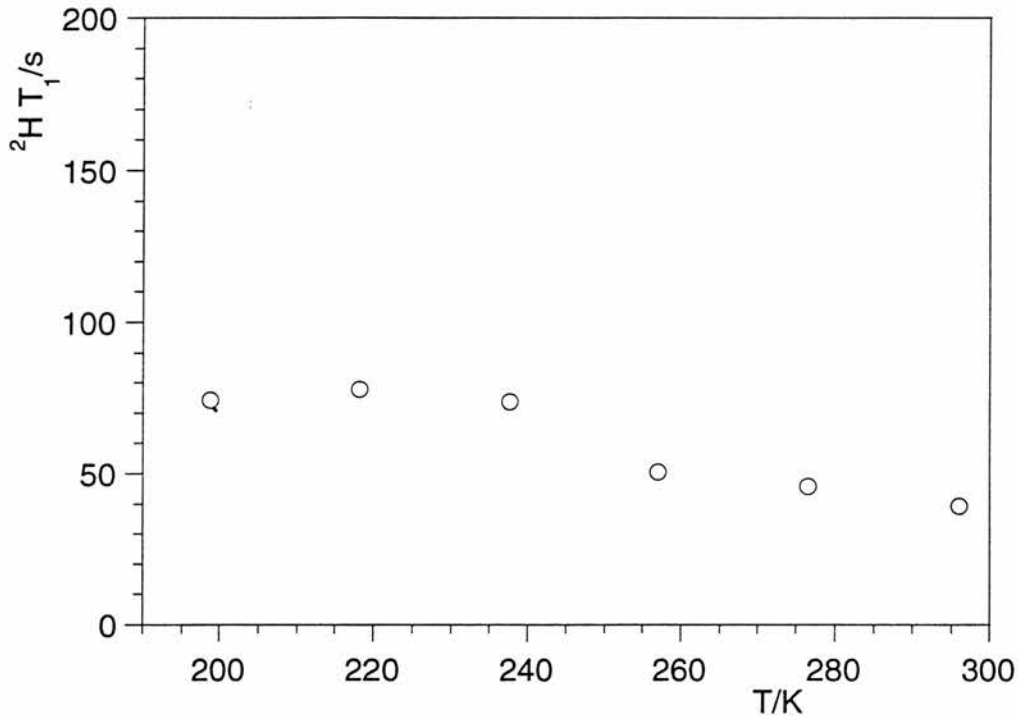

Figure 5.38. Measured ^2H spin-lattice relaxation time as a function of temperature for 1,1,6,6-d_4-hexane-1,6-diyl bis(*o*-chlorobenzoate).

Because of slow ^2H spin-lattice relaxation, only one quadrupolar echo spectrum was measured at room temperature with a 300 s recycle delay (fig. 5.39, left). A 112 kHz wide spectrum was observed indicating only small amplitude motion. The spectrum was simulated using the conical libration model with a rate constant of 1×10^8 s^{-1} and the distribution centred at 13 ° and having a standard deviation of 1°.

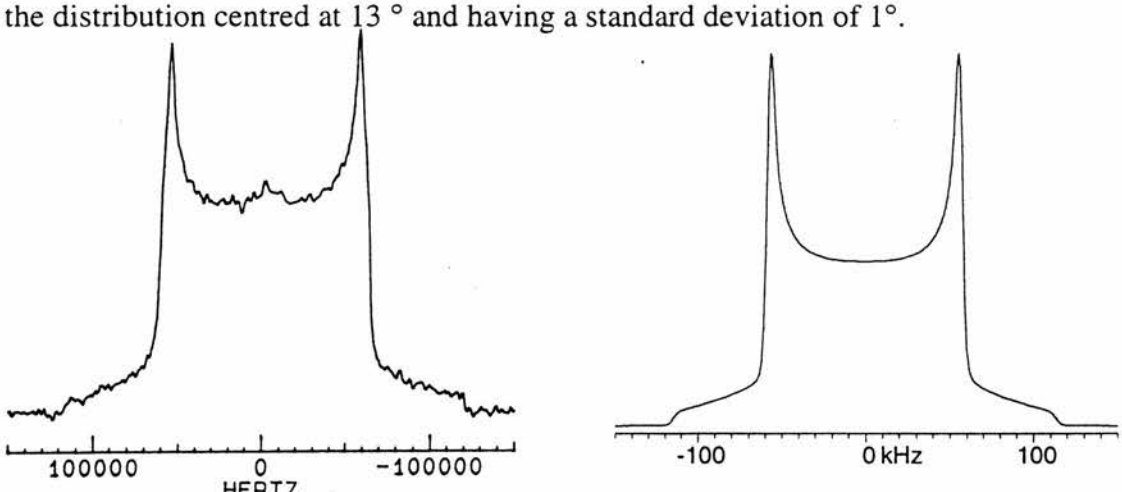

Figure 5.39. Measured ^2H quadrupolar echo spectrum (left) for 1,1,6,6-d_4-hexane-1,6-diyl bis(*o*-chlorobenzoate) at room temperature together with a simulated spectrum (right).

5.7. Pentane-1,5-diyl bis(*p*-nitrobenzoate)

As for the diacid series, the effect of chain length on the chain dynamics was studied also in this diester series. Pentane-1,5-diyl bis(*p*-nitrobenzoate) has five carbons in the alkyl chain that is in an all-*trans* conformation.[111]

Figure 5.40 shows ^{13}C CP/MAS spectrum measured at room temperature. Peaks are at 20.5 ppm ($OCH_2CH_2\underline{C}H_2$), 29.0 ($OCH_2\underline{C}H_2$), 67.4 ($O\underline{C}H_2$), 123.9 ($\underline{C}_{Ar}$(2,6)), 130.0 and 132.0 ($\underline{C}_{Ar}$(3,5)), 135.8 ($\underline{C}_{Ar}$-C=O), 151.0 ($\underline{C}_{Ar}$-NO2) and 164.0 ppm ($\underline{C}$=O). Unfortunately, proton spin-lattice relaxation was slow at room temperature, and consequently, a recycle delay of 90 s was needed to prevent saturation. Because of the slow proton relaxation, the spectrum was measured only at room temperature.

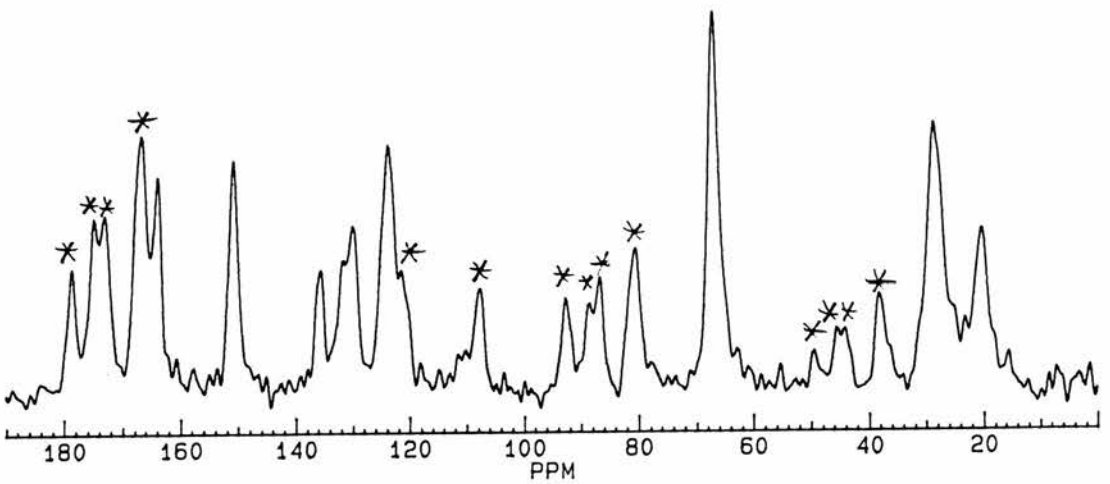

Figure 5.40. ^{13}C CP/MAS spectrum for pentane-1,5-diyl bis(*p*-nitrobenzoate). Spinning sidebands are astered.

The methylene groups in the chain ends were deuterated and ^2H spin-lattice relaxation time for this 1,1,5,5-d_4-pentane-1,5-diyl bis(*p*-nitrobenzoate) was measured between 228 and 364 K. The measured ^2H spin-lattice relaxation times are listed in table 5.9 and shown as a function of temperature in figure 5.41. The dependence of ^2H spin-lattice relaxation time on temperature is very similar to that of 1,1,6,6-d_4-hexane-1,6-diyl bis(*p*-chlorobenzoate). The ^2H spin-lattice relaxation time decreases from *ca.* 800 s at 228 K to *ca.* 90 s at 267 K, and then only slowly decreases with temperature to *ca.* 50 s at 364 K. Again, a nearly temperature independent ^2H spin-lattice relaxation time is observed for an all-*trans* compound.

Table 5.9. Measured ^{2}H spin-lattice relaxation time for 1,1,5,5-d_4-pentane-1,5-diyl bis(*p*-nitrobenzoate).

T(vtu)/K	T/K	^{2}H T_1/s
230	228	826
240	238	252
250	247	176
270	267	92.9
280	276	125
285	281	130
294	290	98.0
300	296	86.0
310	306	80.6
320	315	83.4
330	325	78.0
340	335	73.0
350	345	54.4
360	354	57.9
370	364	47.9

Because of the slow ^{2}H spin-lattice relaxation, the ^{2}H quadrupolar echo spectrum for 1,1,5,5-d_4-pentyl 1,5-(*p*-nitrobenzoate) was only measured at room temperature with a 20 μs refocusing delay. The measured spectrum is shown in figure 5.42. The spectrum is 114 kHz wide and has a small peak at zero frequency.

The spectrum was simulated using the three conical libration model with a rate constant of 1×10^8 s^{-1} and two different distributions (fig. 5.42, right). The first distribution is centred at 10° and has a standard deviation of 1° whereas the other distribution is centred at 55° and has a standard deviation of 1°. These two distributions were added in a ratio of 100:1 indicating that only a small fraction of the C-D bonds is averaged at the magic angle.

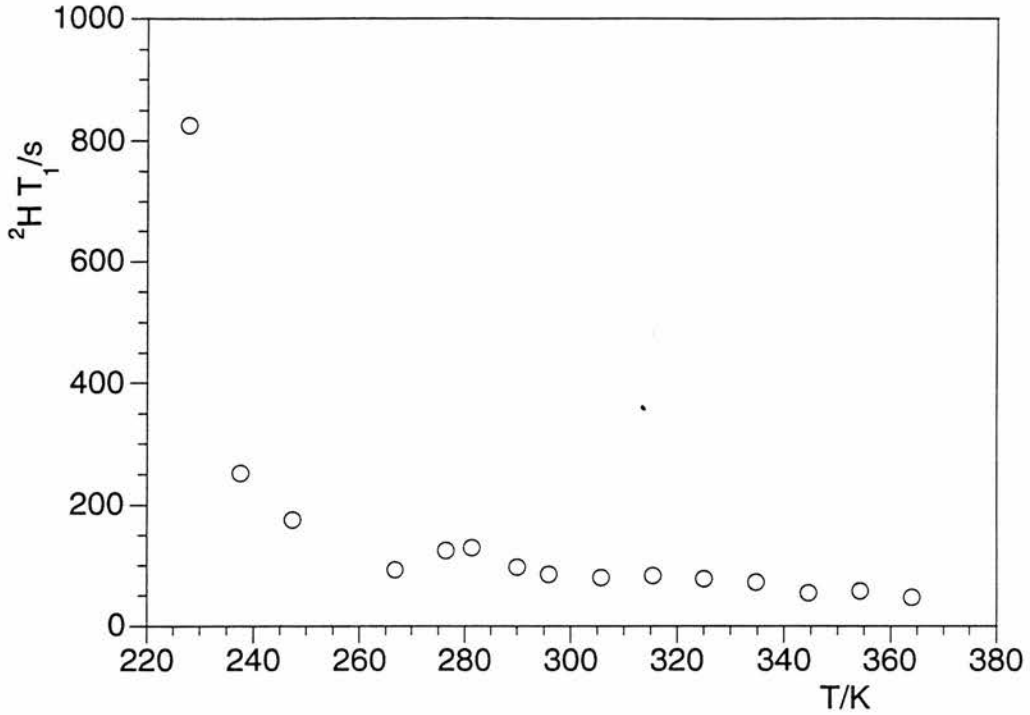

Figure 5.41. Measured ^{2}H spin-lattice relaxation time as a function of temperature for 1,1,5,5-d_4-pentane-1,5-diyl (*p*-nitrobenzoate).

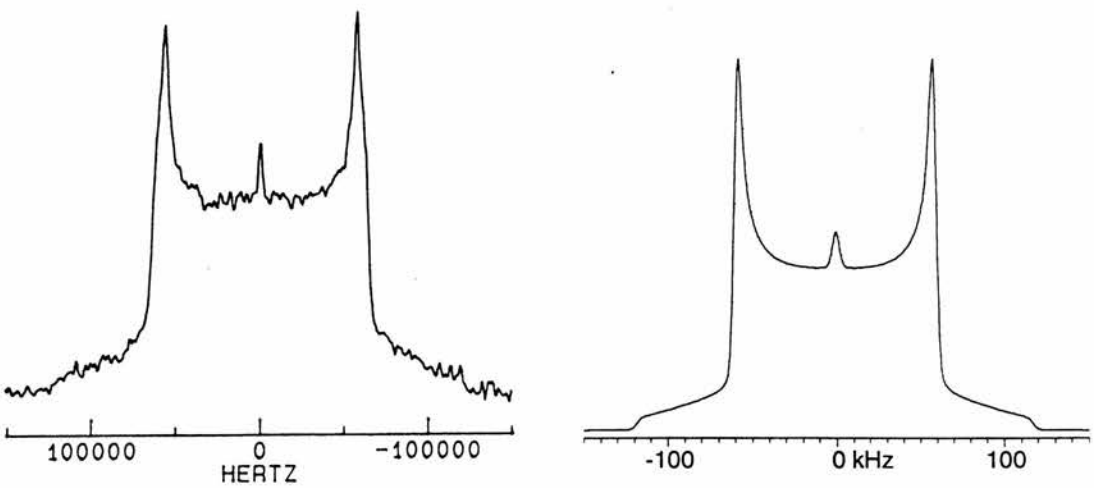

Figure 5.42. ^{2}H quadrupolar echo spectrum for 1,1,5,5-d_4-pentane-1,5-diyl bis(*p*-nitrobenzoate) at room temperature (left) together with a simulated spectrum (right).

5.8. Butane-1,4-diyl bis(*p*-nitrobenzoate)

Butane-1,4-diyl bis(*p*-nitrobenzoate) is one of the three compounds with a four-carbon alkyl chain studied in this thesis. Its crystal structure has been solved from single crystal x-ray data.[112] The structure (appendix, p. A-39) indicates that the bond between the chain carbons at positions 1 and 2 and the symmetrically related bond between the carbons 3 and 4 are in *gauche* conformation whereas the central carbon-carbon bond is in *trans* conformation.

Figure 5.43 shows ^{13}C CP/MAS spectra measured at different temperatures. Peaks in the room temperature spectrum are at 25.4 ($OCH_2\underline{C}H_2$), 65.4 ($O\underline{C}H_2CH_2$), 122.8 ($\underline{C}_{Ar}(2,6)$), 132.4 ($\underline{C}_{Ar}(3,5)$), 135.7 ($\underline{C}_{Ar}$-C=O), 149.4 ($\underline{C}_{Ar}$-NO_2) and 164.3 ppm ($\underline{C}$=O). In the spectrum measured at 270 K, the peaks for the alkyl chain carbons have decreased in intensity indicating dipolar broadening and shortening of ^{13}C $T_{1\rho}$ relaxation time. The frequency of the spin-locking field was 63 kHz, and therefore, the rate of the molecular motion is of the same order at 270 K. The decrease in intensity is more severe for the central carbons than for the chain end carbons indicating that the central carbons are more mobile than the chain end carbons. Unfortunately, the measurement of ^{13}C CP/MAS spectra was very time-consuming below room temperature where recycle delays of 90 s were needed to prevent saturation. Therefore, no attempt was made to measure ^{13}C $T_{1\rho}$ relaxation time at any temperature.

Two chain deuterated samples were prepared for deuterium NMR studies, namely 1,1,4,4-d_4-butane-1,4-diyl bis(*p*-nitrobenzoate) and 2,2,3,3-d_4-hexane-1,4-diyl bis(*p*-nitrobenzoate). The ^2H spin-lattice relaxation time was measured for both samples between 228 and 403 K. The measured values are listed in table 5.10 and shown as function of temperature in figure 5.44.

For both samples, ^2H spin-lattice relaxation time decreases from *ca.* 100 s to less than 0.1 s at 403 K. Perhaps surprisingly, the ^2H spin-lattice relaxation time for the 2,2,3,3-d_4-labelled derivative is only slightly smaller than for the 1,1,4,4-d_4-labelled derivative in the whole temperature range.

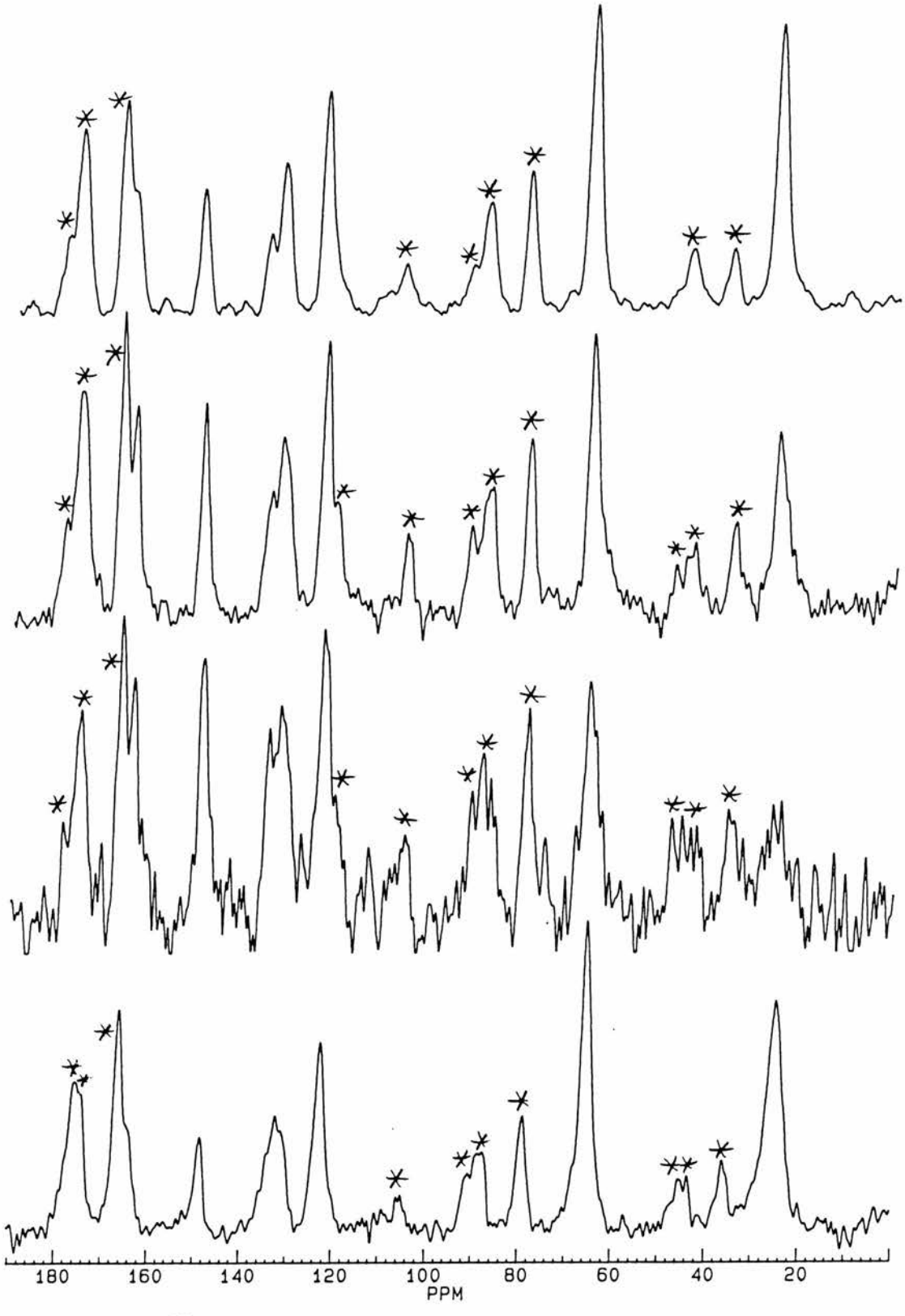

Figure 5.43. ^{13}C CP/MAS spectra for butane-1,4-diyl bis(*p*-nitrobenzoate) at different temperatures. Temperatures are from top to bottom: 374, 296, 270 and 222 K. Spinning sidebands (at 5.5 kHz) are asterisked.

Table 5.10. Measured ^{2}H spin-lattice relaxation times for 1,1,4,4-d_4- and 2,2,3,3-d_4-butane-1,4-diyl bis(*p*-nitrobenzoate).

T(vtu)/K	*T*/K	^{2}H T_1/s 1,1,4,4-d_4-	^{2}H T_1/s 2,2,3,3-d_4-
230	228	-	243
240	238	134	88.3
250	247	43.0	26.5
260	257	17.9	12.8
270	267	7.65	5.18
290	286	-	1.60
292	288	2.15	-
310	306	1.05	0.566
330	325	0.462	0.250
350	345	0.274	0.114
370	364	0.158	0.0535
390	383	0.102	0.0324
400	393	0.0810	0.0241
410	403	0.0670	0.0174

Figure 5.45 shows plots of ln(^{2}H T_1) as a function of inverse temperature for both samples. The dependence is not linear over the whole temperature range but rather a change in the slope is observed at *ca.* 280 K. This change in the slope could indicate that a phase transition occurs near 280 K but no phase transitions were observed in the DSC scan. It is striking, however, that this change in the slope occurs around the same temperature where the intensities of peaks for the alkyl chain carbons decrease in the ^{13}C CP/MAS spectrum. These changes therefore reflect a change in the motional behaviour of the alkyl chain, probably associated to the angle of libration.

The change in the motional behaviour of the alkyl chain is also seen in the apparent activation energies. The slopes of the least-squares lines give 28.8 ± 0.9 and 36.8 ± 1.4 kJ mol^{-1} above 280 K, and 51.6 ± 4.9 and 50.3 ± 4.1 kJ mol^{-1} below 280 K for the apparent activation energy of the 1,1,4,4-d_4 and 2,2,3,3-d_4 derivatives, respectively, indicating that the activation energy is smaller above 280 K.

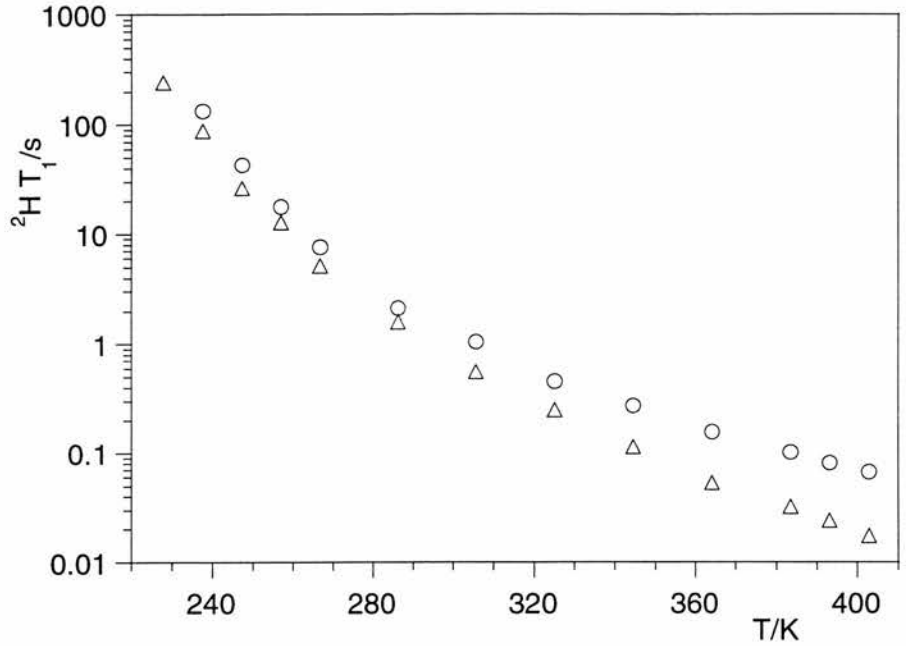

Figure 5.44. Measured ^{2}H spin-lattice relaxation time as a function of temperature for 1,1,4,4-d_4- (o) and 2,2,3,3-d_4-butane-1,4-diyl bis(*p*-nitrobenzoate) (Δ).

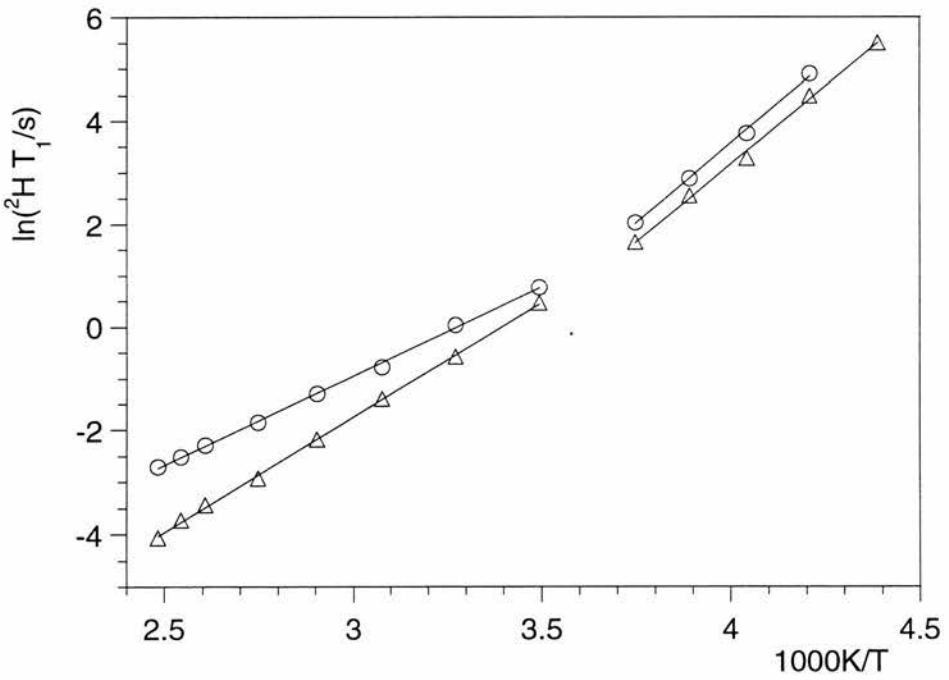

Figure 5.45. Plot of ln(^{2}H T_1/s) as a function of 1000K/T for 1,1,4,4-d_4- (o) and 2,2,3,3-d_4-butanediyl bis(*p*-nitrobenzoate) (Δ) together with linear least-squares fits. Apparent activation energies are 28.8 and 36.8 kJ mol^{-1}, respectively, at high temperatures and 51.6 and 50.3 kJ mol^{-1}, respectively, at low temperatures.

^{2}H quadrupolar echo spectra were measured with 20 μs and 160 μs refocusing delays between 288 and 403 K for both samples (fig. 5.46 and 5.48). For the 1,1,4,4-d_4-labelled derivative, a small decrease in intensity is observed in the central region of the spectrum measured with 160 μs refocusing delay at 288 K indicating that the rate of the motion is in the intermediate rate regime, *i.e.* less that 10^7 Hz, in keeping with the observed dynamic dipolar broadening in the ^{13}C CP/MAS spectrum at 270 K. The spectrum is 114 kHz wide at 288 K, and it narrows only a little to 111 kHz at 403 K. At high temperatures, a small peak is observed at zero frequency indicating that part of the motion averages the C-D bond at the magic angle.

The spectra for the 1,1,4,4-d_4 derivative were simulated using the conical libration model with all distributions having a standard deviation of 1° (fig. 5.47). At 288 K, the rate constant was set to 1×10^6 s^{-1} and the distribution was centred at 11°. The same distribution was used at 325 K but the rate constant was increased to 5×10^6 s^{-1}. At 364 K, the rate constant was increased to 1×10^7 s^{-1} and the distribution was centred at 12°. In addition, another distribution centred at 55° was added in 1:100 ratio to account for the small peak in the centre. Finally at 403 K, the rate constant was increased to 1×10^8 s^{-1} and the first distribution was centred at 14° and the second distribution was added in 2:100 ratio.

Very different changes are observed for the 2,2,3,3-d_4-labelled derivative (fig. 5.48). At 288 K, the central area of the spectrum is nearly full, and almost a flat-top spectrum is observed. The intensity of the central area decreases at higher temperatures and asymmetry appears in the spectrum. The spectrum is 114 kHz wide at 288 K and narrows down to 68 kHz at 403 K. In the whole temperature range, the spectrum is independent of the length of the refocusing delay indicating that the rate of the motion is in the fast motion limit. Therefore, spectra were simulated with a rate constant of 1×10^8 s^{-1} (fig. 5.49) using the conical libration model. At 288 K, one distribution centred at 0° and with a standard deviation of 17° was used. At 325 K, one distribution centred at 15° with a standard deviation of 10° was added to another distribution centred at 24° with a standard deviation of 3° in 1:1 ratio. At the two highest temperatures, the two-site model was used. The half-angle β was set to 20° at 364 K and to 23° at 403 K.

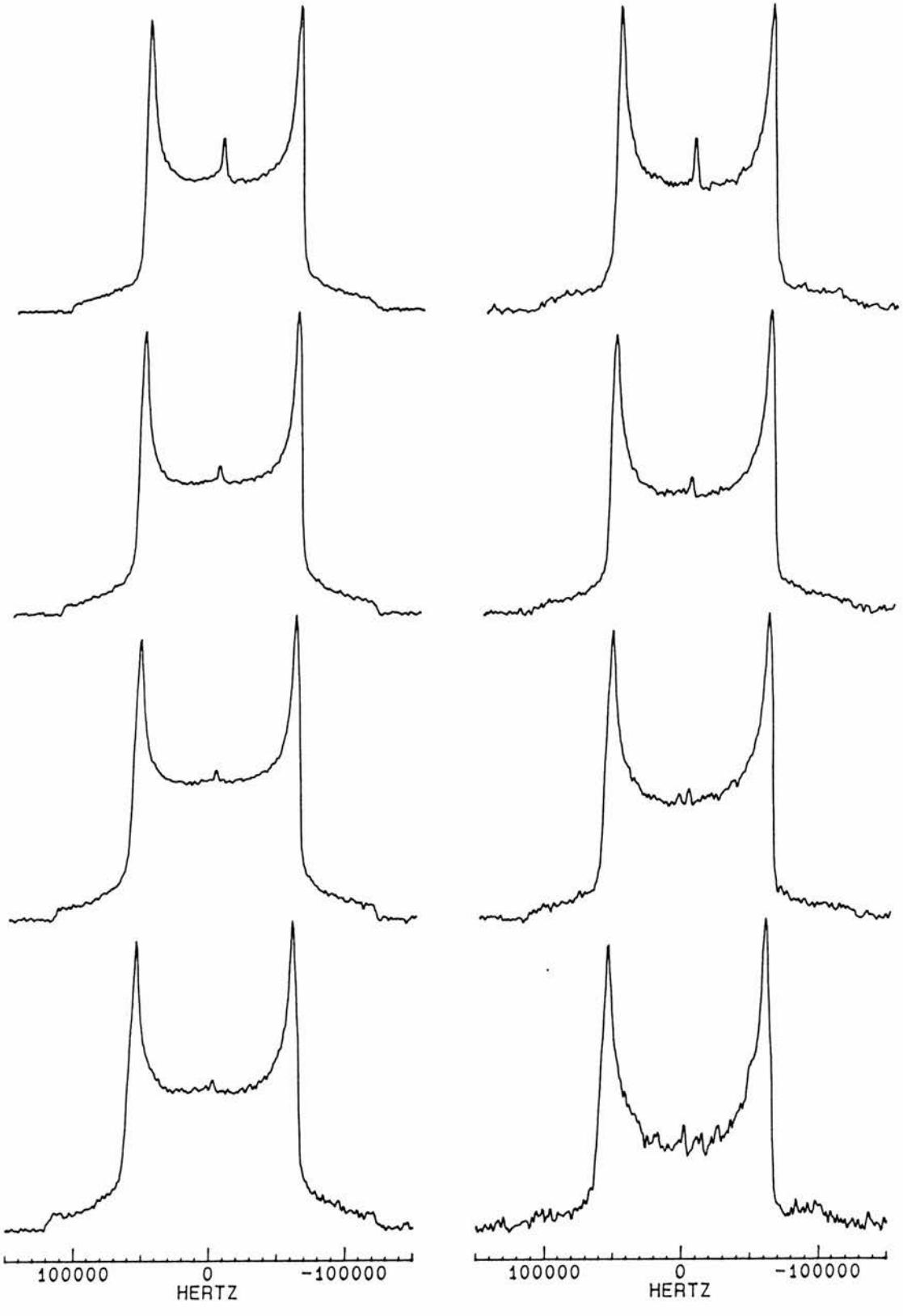

Figure 5.46. Measured ^{2}H quadrupolar echo spectra for 1,1,4,4-d_4-butane-1,4-diyl bis(*p*-nitrobenzoate) at different temperatures. Refocusing delay is 20 μs (left) and 160 μs (right). Temperatures are from top to bottom: 403, 364, 325 and 288 K.

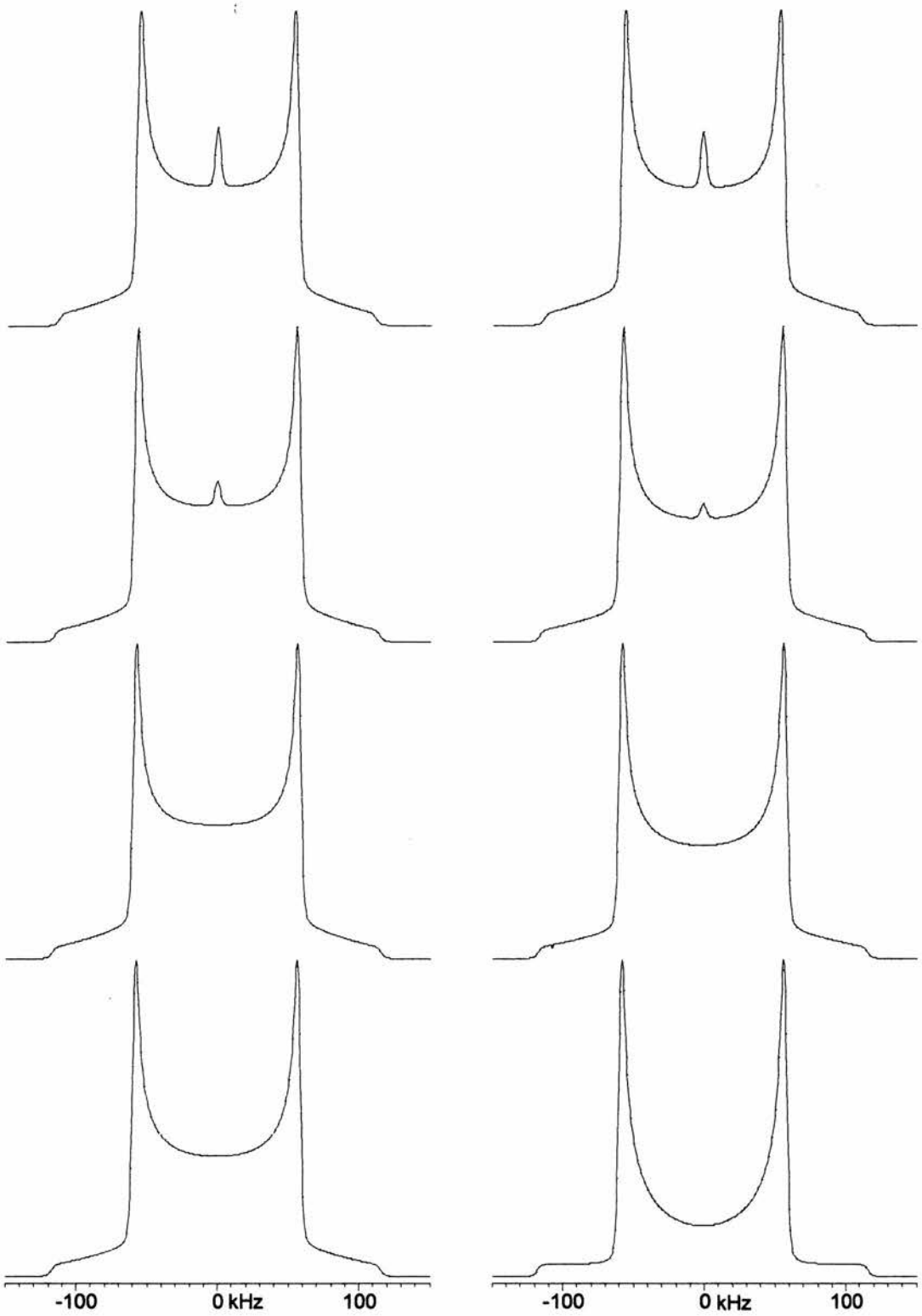

Figure 5.47. Simulated ^2H quadrupolar echo spectra for 1,1,4,4-d_4-butane-1,4-diyl bis(*p*-nitrobenzoate) at different temperatures.

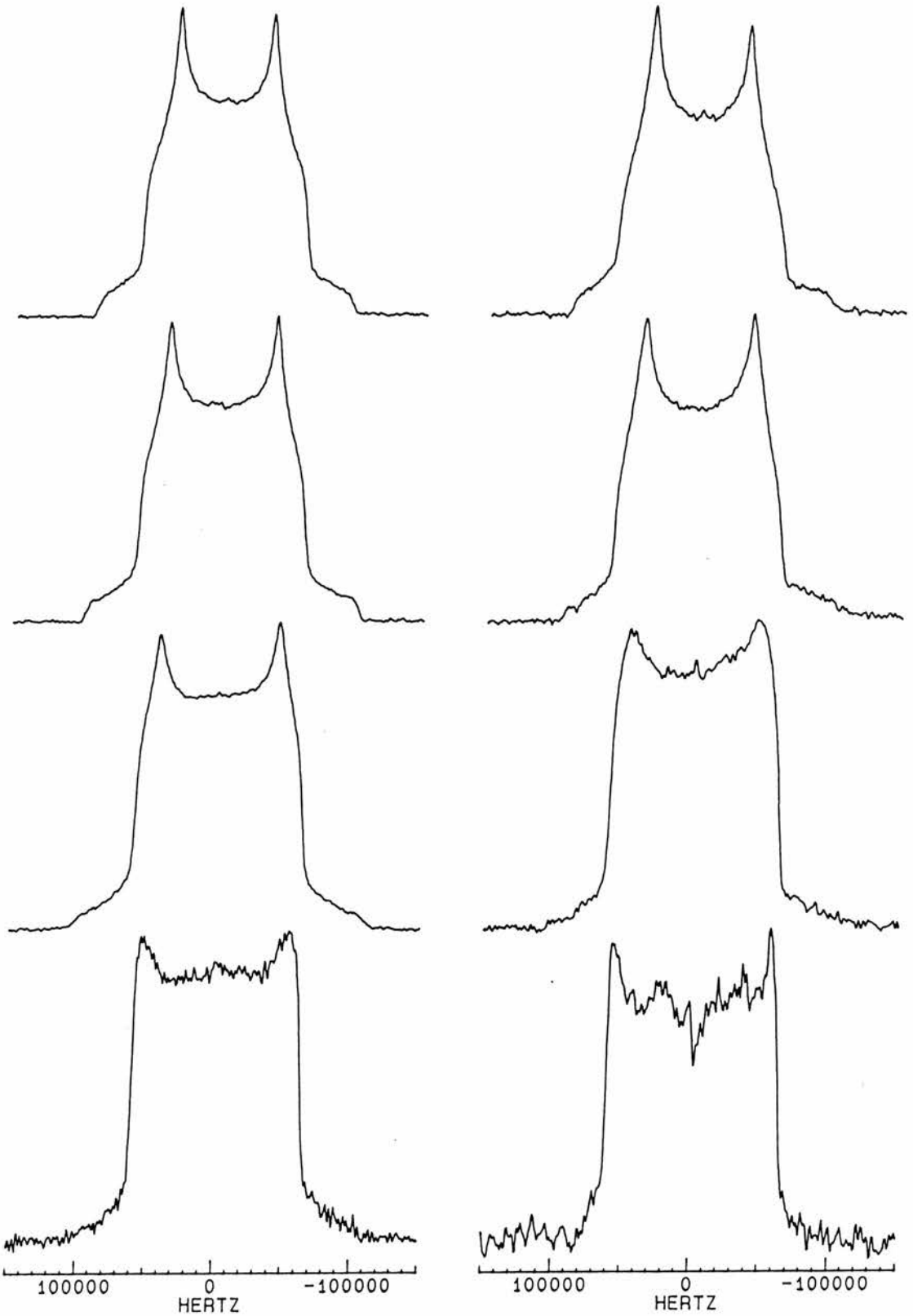

Figure 5.48. Measured ^2H quadrupolar echo spectra of 2,2,3,3-d_4-butane-1,4-diyl bis(*p*-nitrobenzoate) at different temperatures. Refocusing delay is 20 μs (left) and 160 μs (right). Temperatures are from top to bottom: 403, 364, 325 and 288 K.

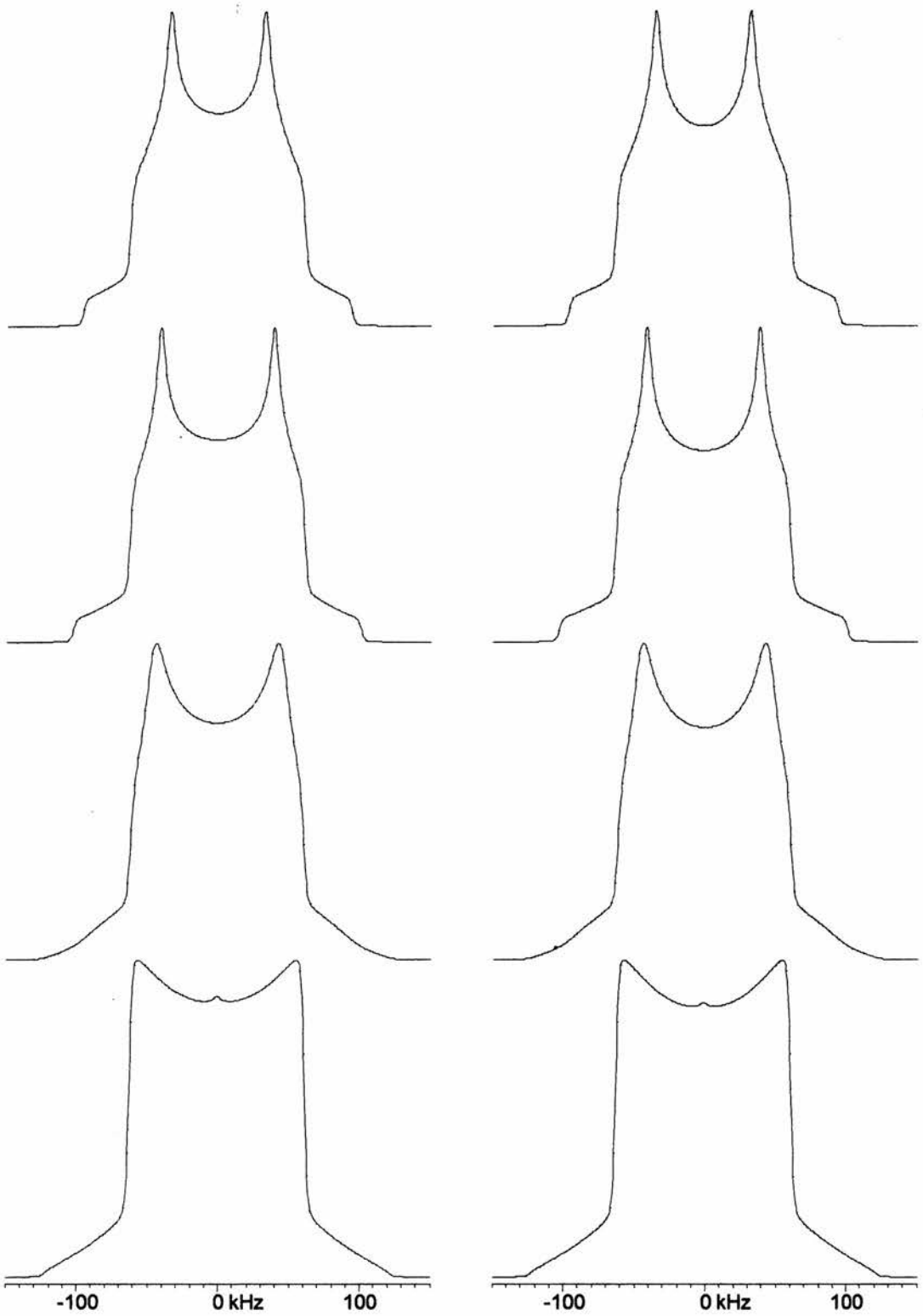

Figure 5.49. Simulated ^2H quadrupolar echo spectra of 2,2,3,3-d_4-butane-1,4-diyl bis(*p*-nitrobenzoate).

5.9. Butane-1,4-diyl bis(3,5-dimethoxybenzoate)

As for the hexane-1,6-diyl bis(3,5-dimethoxybenzoate), butane-1,4-diyl bis(3,5-dimethoxybenzoate) was chosen because the fast rotating methoxy groups enhance proton spin-lattice relaxation, and therefore, facilitate the measurement of ^{13}C CP/MAS spectra. The crystal structure of butane-1,4-diyl bis(3,5-dimethoxybenzoate) was solved from single crystal x-ray data. Structural details and views of the unit cell are given in the appendix (p. A-17 and A-41). The structure indicates that the bond between the chain carbons at positions 1 and 2 and the symmetrically related bond between the carbons at position 3 and 4 are in a *gauche* conformation while the central C-C bond is in a *trans* conformation, similar to that observed for butane-1,4-diyl bis(*p*-nitrobenzoate).

Figure 5.50 shows ^{13}C CP/MAS spectra measured at different temperatures. Good quality spectra were obtained in *ca.* 20 minutes with a 5 s recycle delay and 256 transients. Peaks are at 25.8 (-O-CH_2-$\underline{C}H_2$-), 55.7 (-O-$\underline{C}H_3$), 66.2 (-O-$\underline{C}H_2$-CH_2-), 103.6 and 105.8 ($\underline{C}_{Ar}$(2,6)), 111.5 ($\underline{C}_{Ar}$(4)), 130.5 ($\underline{C}_{Ar}$-C=O) 160.0 ($\underline{C}_{Ar}$-OCH_3) and 164.8 ppm (-$\underline{C}$=O). The ^{13}C $T_{1\rho}$ relaxation time would be readily measured for this sample but, unfortunately, the spectra show no evidence of dipolar broadening nor the associated ^{13}C $T_{1\rho}$ minimum. Therefore, no attempt was made to measure the ^{13}C $T_{1\rho}$ relaxation time at any temperature.

Instead, the ^{13}C CP/MAS spectrum was inverted at 350 K and was left to evolve under ^{13}C spin-lattice relaxation while saturating protons with a train of saturating 90° pulses to avoid any cross-relaxation effects. The spectra measured with different evolution times are shown in figure 5.51. The spectrum at the bottom of fig. 5.51 was measured with a 100 ms evolution time, and consequently, all the peaks are inverted. A 5.0 s evolution delay was used for the next spectrum. The intensity of the peaks for the chain carbons and for the methoxy group carbon has clearly decreased because of ^{13}C spin-lattice relaxation. Interestingly, the central chain carbons (25.8 ppm) relax faster than the carbons bonded to the ester oxygen (66.2 ppm). After an evolution time of 15.0 s, the peak for the central carbons has almost disappeared but the peak for the chain end carbons is still clearly visible. Finally, both peaks have disappeared after 75.0 s evolution delay indicating that all chain carbons relax fully in 75 s.

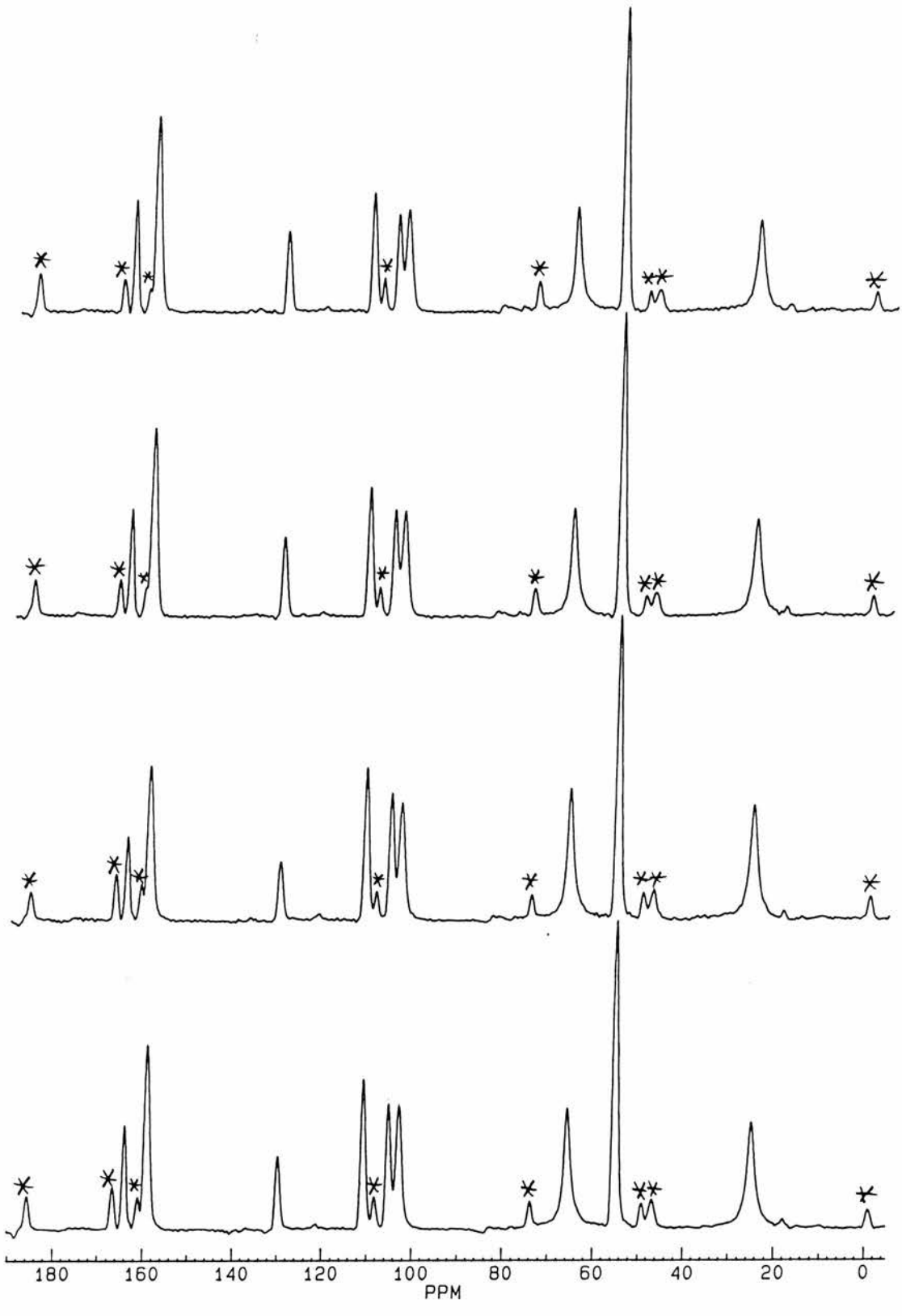

Figure 5.50. ^{13}C CP/MAS spectra for butane-1,4-diyl bis(3,5-dimethoxybenzoate) at different temperatures. Temperatures are from top to bottom: 270, 246, 222 and 190 K. Spinning sidebands (at 7 kHz) are asterisked.

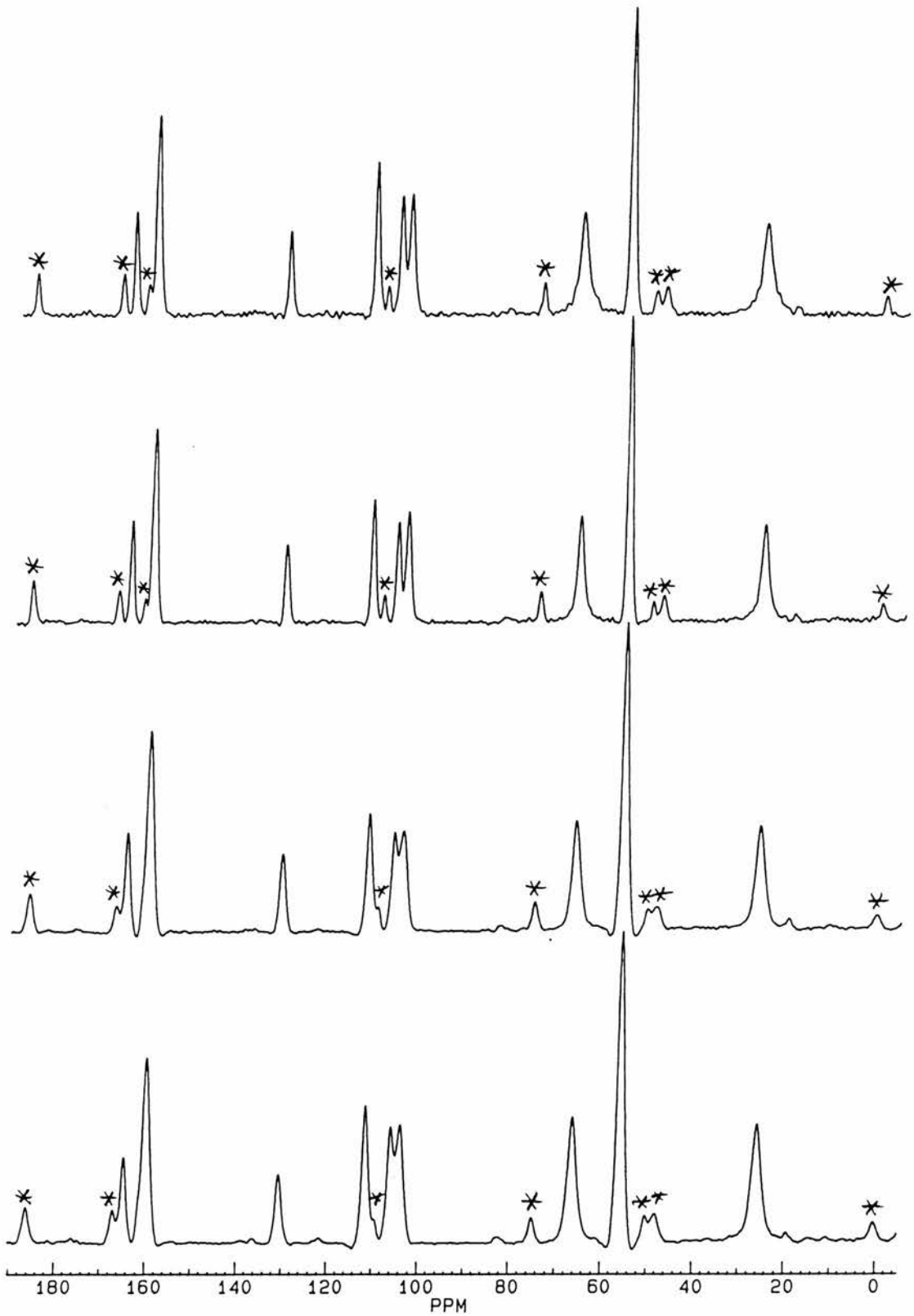

Figure 5.50. (continued) ^{13}C CP/MAS spectra for butane-1,4-diyl bis(3,5-dimethoxybenzoate) at different temperatures. Temperatures are from top to bottom: 366, 342, 318 and 296 K. Spinning sidebands (at 7 kHz) are asterisked.

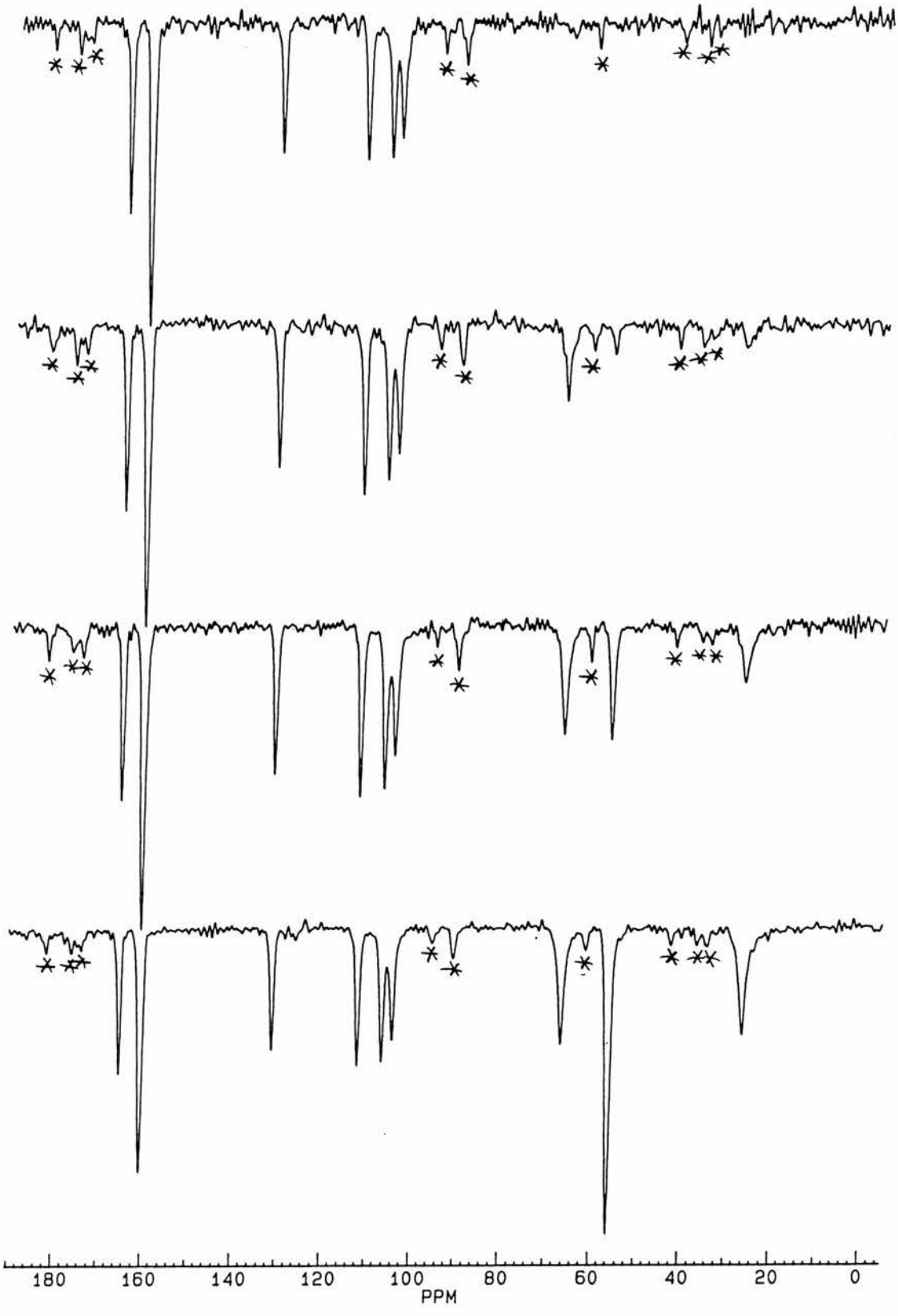

Figure 5.51. Recovery of an inverted ^{13}C CP/MAS spectrum for butane-1,4-diyl bis(3,5-dimethoxybenzoate) at 350 K. Evolution delays are from top to bottom: 75.0 s, 15.0 s, 5.0 s and 100 ms. Spinning sidebands (at 8.7 kHz) are asterisked.

The experiment was repeated at different temperatures using more evolution delays, and ^{13}C spin-lattice relaxation times were calculated from exponential fits to the evolution of peak intensity as a function of time. The measured ^{13}C spin-lattice relaxation times are listed in table 5.11. At 350 K, the ^{13}C spin-lattice relaxation time is 6.48 s for the central chain carbons and 17.1 s for the chain end carbons indicating that the central chain carbons relax about three times faster than the chain end carbons. This faster relaxation of the central carbons suggests that the central carbons undergo larger amplitude motion than the chain end carbons or that the rate of the central carbon motion is nearer to the ^{13}C Larmor frequency.

The phenyl ring and the carbonyl carbons, however, show no evidence of ^{13}C spin-lattice relaxation in any of the measured spectra. The quaternary ring carbons and the carbonyl relax slowly because of the lack of directly attached protons. Assuming that the molecule would librate about the long axis, the ring carbon between the two methoxy groups would relax slowly because the motion would be of very small angle at this site. The other two non-quaternary ring carbons, however, should relax at a comparable rate to the chain carbons since these ring carbons are off the long axis and would experience large angle motion if the molecule would librate about the long axis. Clearly, these ring carbons fail to relax at all during 75 s, the longest delay used, indicating that the 3,5-dimethoxybenzoyl group is static compared with the alkyl chain.

Unfortunately, the ^{13}C spin-lattice relaxation time data for the chain carbons are too bad to obtain reliable activation energies. The data for the methoxy group, however, indicate a T_1 minimum at 190 K (fig. 5.52), and the activation energy for the methoxy group rotation can be obtained from the data on the high temperature side of the minimum. In the fast motion limit, the ^{13}C T_1 relaxation time for a rotating methyl group is given by[44]

$$\frac{1}{T_1} = \frac{\omega_D^2 \tau}{9}\left(7 + 3\cos^2\theta\right) \qquad (5.2.)$$

where $\omega_D = \hbar \gamma_C \gamma_H / r^3$ and θ is the angle between the C_3-symmetry axis of the methyl group and the direction of the external magnetic field B_0. In the following it is assumed that the ^{13}C spin-lattice relaxation time obtained from a peak in the ^{13}C CP/MAS spectrum is satisfactorily approximated by the powder average value.

Table 5.11. Measured ^{13}C spin-lattice relaxation time for butane-1,4-diyl bis(3,5-dimethoxybenzoate).

T(vtu)/K	T/K	^{13}C T_1/s C-$\underline{C}H_2$ 25.6 ppm	^{13}C T_1/s O$\underline{C}H_3$ 55.7 ppm	^{13}C T_1/s O-$\underline{C}H_2$ 66.3 ppm
160	190	-	0.150	-
180	206	-	0.162	-
200	222	-	0.220	-
220	238	-	0.346	-
240	254	-	0.489	-
260	270	-	0.800	-
280	286	-	1.15	-
300	302	long[1]	1.58	long[1]
320	318	long[1]	2.15	long[1]
340	334	15.3	2.79	25.9
350	342	13.5	3.14	24.8
360	350	6.48	3.42	17.1
370	358	3.71	4.11	16.0
380	366	2.71	4.75	7.91

1) No significant change in peak intensity with a delay of 10 s.

The powder average value is obtained from

$$\frac{1}{T_1} = \frac{\omega_D^2 \tau}{36\pi} \int_0^{2\pi} \int_0^{\pi} \left(7 + 3\cos^2\theta\right) \sin\theta d\theta d\phi = \frac{8}{9} \omega_D^2 \tau \qquad (5.3.)$$

Substituting the Arrhenius equation and taking natural logarithm on both sides gives

$$\ln T_1 = -\frac{E_a}{RT} - \ln\left(\frac{8\omega_D^2 \tau_\infty}{9}\right) \qquad (5.4.)$$

Thus, the slope of eq. 5.4 gives the activation energy for the methyl group rotation. Figure 5.53. shows a plot of $\ln(^{13}C\ T_1)$ as a function of 1000K/T together with a best-fitting least-squares line. The slope of the best-fitting line gives 14.5 ± 0.4 kJ mol^{-1} for the activation energy.

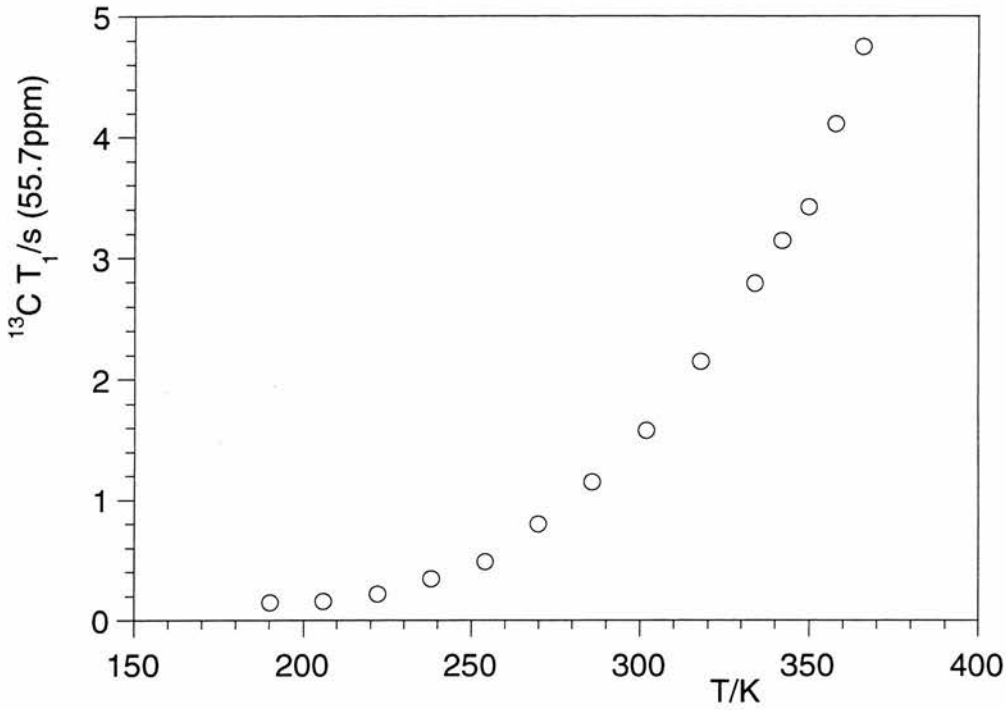

Figure 5.52. Measured ^{13}C spin-lattice relaxation time as a function of temperature for methoxy groups of butane-1,4-diyl bis(3,5-dimethoxybenzoate).

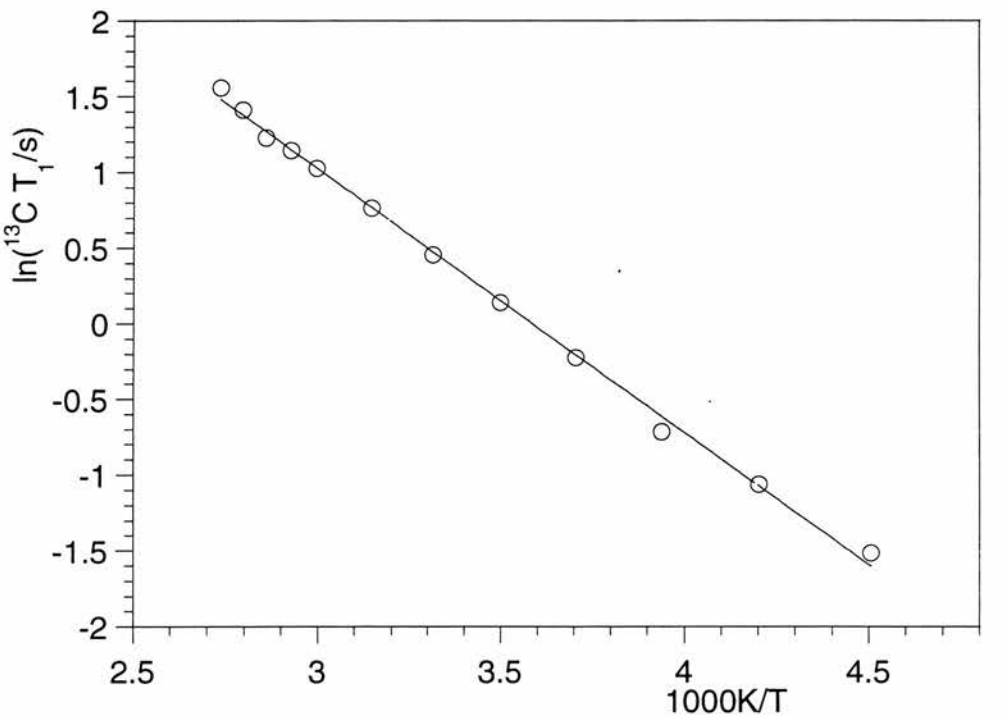

Figure 5.53. Plot of ln(^{13}C T_1) as function of 1000K/T for the methoxy carbons (55.7 ppm) of butane-1,4-diyl bis(3,5-dimethoxybenzoate).

Proton spin-lattice relaxation is a complex process in which all protons relax at the same rate because of the spin-diffusion process between the nuclei. The four fast rotating methoxy groups in butyl 1,4-bis(3,5-dimethoxybenzoate), however, act as a sink of relaxation, and consequently, the proton spin-lattice relaxation is mediated by the methoxy group rotation. Therefore, the same activation energy of 14.5 kJ mol^{-1} that was obtained from the ^{13}C spin-lattice relaxation time data should also be obtained from proton spin-lattice relaxation time data (table 5.12 and fig. 5.54).

Table 5.12. Measured ^{1}H spin-lattice relaxation times for butane-1,4-diyl bis(3,5-dimethoxybenzoate).

T(vtu)/K	T/K	^{1}H T_1/s
140	174	2.13
150	182	1.62
160	190	1.31
170	198	1.21
180	206	1.11
190	214	1.07
200	222	1.04
210	230	1.04
220	238	0.90
240	254	1.31
260	270	1.85
280	286	2.76
296	299	3.58
310	310	4.68
320	318	5.26
330	326	5.99
340	334	6.89
350	342	8.05
360	350	8.92
370	358	9.91
380	366	10.57

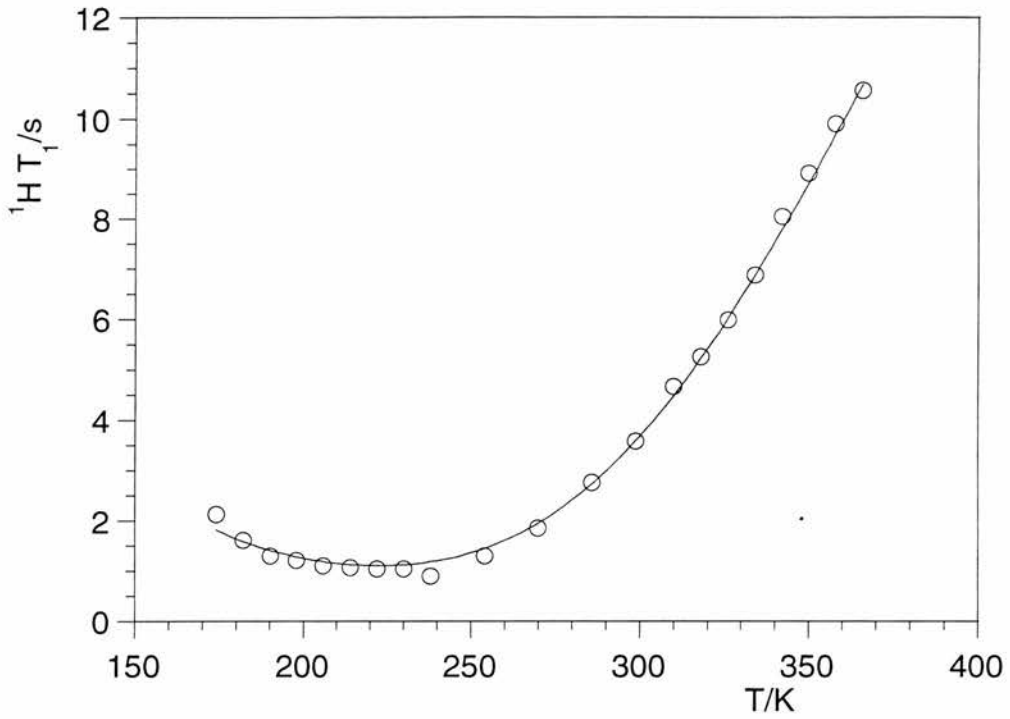

Figure 5.54. Measured ^{1}H spin-lattice relaxation time as a function of temperature for butane-1,4-diyl bis(3,5-dimethoxybenzoate).

A T_1 minimum is observed at *ca.* 220 K indicating that the rate of the rotation is near the Larmor frequency of the protons. The observation of a proton T_1 minimum is consistent with the observation of the ^{13}C T_1 minimum at lower temperature (190 K) as the Larmor frequency of proton is four times larger than the Larmor frequency of carbon-13. Using equation 1.16 for the proton spin-lattice relaxation rate and the Arrhenius equation (eq. 1.21) gives in the fast-motion limit

$$\ln T_1 = -\frac{E_a}{RT} - \ln\left(\frac{10 < \Delta\omega^2 > \tau_\infty}{3}\right) \qquad (5.5.)$$

Thus, the activation energy is obtained from the slope of eq. 5.5. Figure 5.55 shows a plot of ln(^{1}H T_1) as a function of 1000K/T together with a best-fitting least-squares line. The slope of the least-squares line gives 14.9 ± 0.4 kJ mol^{-1} for the activation energy, satisfyingly in agreement with the value of 14.5 ± 0.4 kJ mol^{-1} obtained from the ^{13}C spin-lattice relaxation time data. The fact that the same value is obtained for the activation energy from both ^{13}C and proton spin-lattice relaxation time data confirms that the proton spin-lattice relaxation is mediated by the fast rotation of the

methoxy groups and that the original idea of trying to enhance proton spin-lattice relaxation by adding methoxy groups is valid.

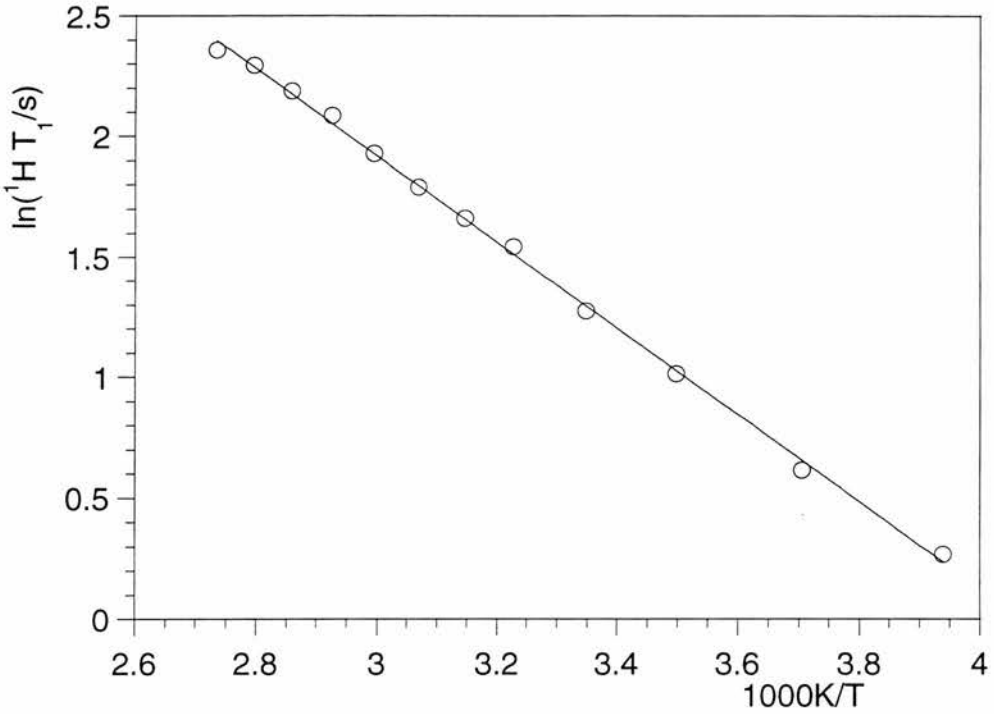

Figure 5.55. Plot of ln(^{1}H T_1) as a function of 1000/T for butane-1,4-diyl bis(3,5-dimethoxybenzoate).

As before, the method of studying molecular motion in the alkyl chain is deuteron NMR. Therefore, two different chain deuterated samples were prepared, namely 1,1,4,4-d_4-butane-1,4-diyl bis(3,5-dimethoxybenzoate) and 2,2,3,3-d_4-butane-1,4-diyl bis(3,5-dimethoxybenzoate). ^{2}H spin-lattice relaxation time was measured for both samples between 238 and 373 K. The measured values are listed in table 5.13 and shown as a function of temperature in figure 5.56.

For both samples, the ^{2}H spin-lattice relaxation time depends strongly on temperature and decreases from *ca.* 100 s at 238 K to less than 1 s at 373 K. In the whole temperature range, the ^{2}H spin-lattice relaxation time is smaller for the 2,2,3,3-d_4-labelled derivative than for the 1,1,4,4-d_4-labelled derivative indicating that the central carbons are more mobile than the chain end carbons.

Figure 5.57 shows plots of ln(^{2}H T_1/s) as a function of 1000K/T together with the best-fitting least-squares lines. The slopes of these lines give 31.7 ± 1.0 kJ mol^{-1} and 37.9 ± 1.3 kJ mol^{-1} for the apparent activation energy of 1,1,4,4-d_4- and 2,2,3,3-d_4-butane-1,4-diyl bis(3,5-dimethoxybenzoates), respectively. The values agree well with the values 28.8 and 36.8 kJ mol^{-1} obtained for the 1,1,4,4-d_4- and 2,2,3,3-d_4-butane-1,4-diyl bis(*p*-nitrobenzoates) above 280 K.

Table 5.13. Measured ^{2}H spin-lattice relaxation time for 1,1,4,4-d_4-butane-1,4-diyl and 2,2,3,3-d_4-butane-1,4-diyl bis(3,5-dimethoxybenzoate).

T(vtu)/K	*T*/K	^{2}H T_1/s 1,1,4,4-d_4-	^{2}H T_1/s 2,2,3,3-d_4-
240	238	-	91.0
250	247	86.9	51.0
255	252	57.0	-
260	257	39.5	32.0
270	267	28.2	17.9
280	276	18.7	10.3
292	288	10.4	-
293	289	-	4.90
300	296	7.63	2.70
310	306	5.10	1.79
320	315	3.37	1.05
330	325	2.23	0.660
340	335	1.59	0.448
350	345	1.00	0.287
360	354	0.763	0.206
370	364	0.572	0.154
380	374	0.410	0.110

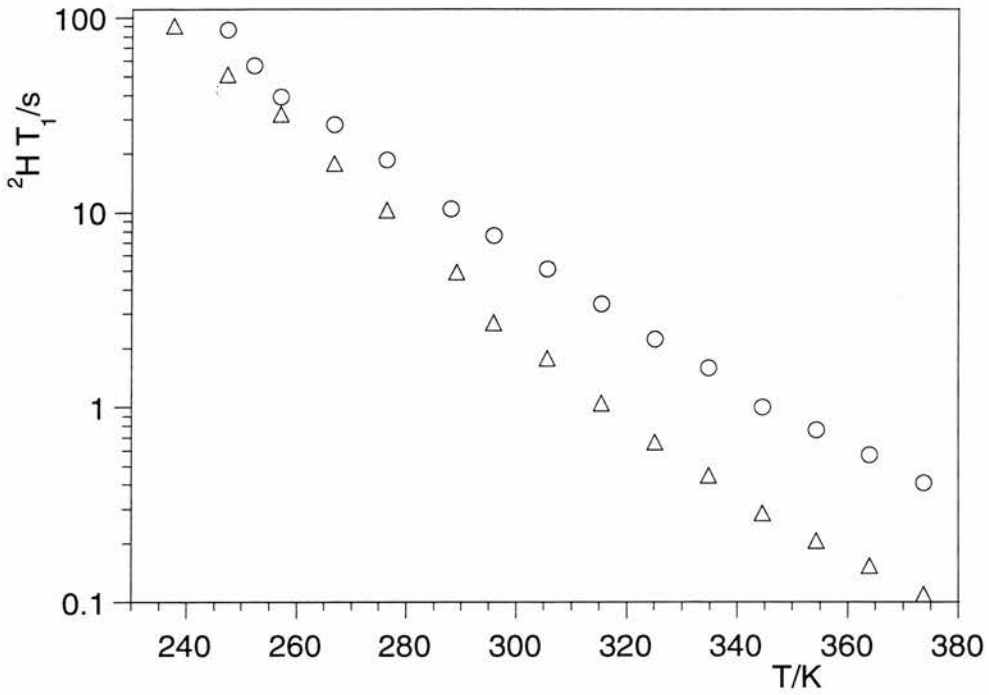

Figure 5.56. Measured ^{2}H spin-lattice relaxation time as a function of temperature for 1,1,4,4-d_4- (o) and for 2,2,3,3-d_4-butane-1,4-diyl bis(3,5-dimethoxybenzoate) (Δ).

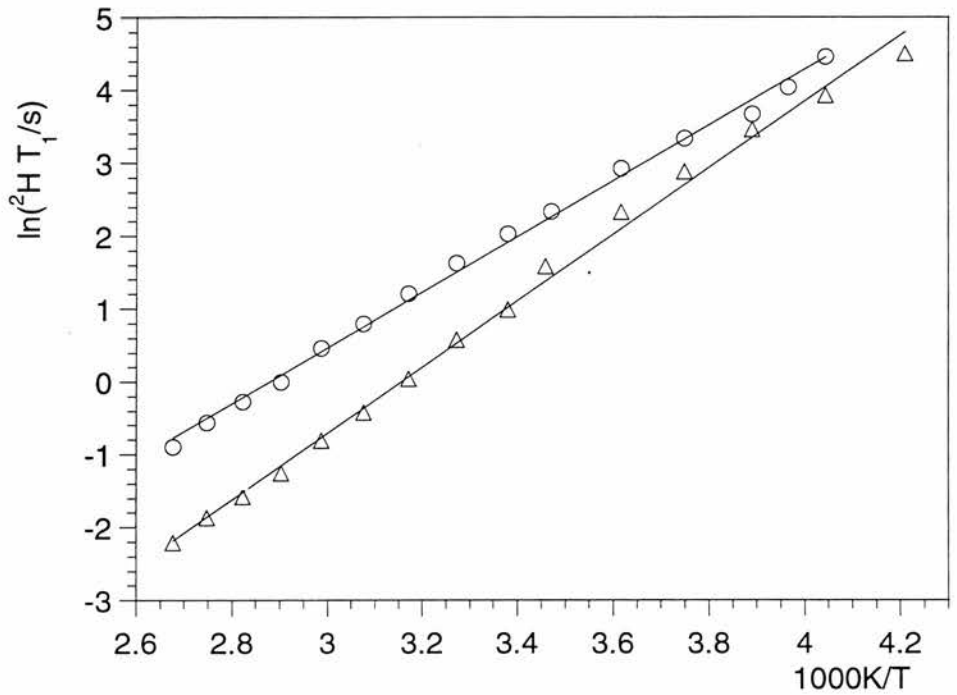

Figure 5.57. Plot of ln(^{2}H T_1) as a function of 1000K/T for 1,1,4,4-d_4- (o) and 2,2,3,3-d_4-butane-1,4-diyl bis(3,5-dimethoxybenzoate) (Δ). Apparent activation energy from the slope is 31.7 ± 1.0 and 37.9 ± 1.3 kJ mol^{-1}, respectively.

Figure 5.58 shows ^{2}H quadrupolar echo spectra for the 1,1,4,4-d_4-labelled derivative measured at different temperatures with 20 μs and 160 μs refocusing delays. A 117 kHz wide powder pattern is observed at 288 K. This spectrum is slightly narrowed down to 116 kHz at 325 K. A very small peak at zero frequency is visible in the spectrum measured with the 20 μs recycle delay. At 374 K, this central peak is considerably larger and the remaining powder pattern is narrowed down by a further kilohertz to 115 kHz. The spectrum is independent of the length of the refocusing delay indicating that the rate of the motion is in the fast motion limit.

The spectra were simulated using the conical libration model with a rate constant of 1×10^8 s^{-1}. The simulated spectra are shown in figure 5.59. The spectra at 288 and 325 K were produced with a distribution centred at 10° and having a standard deviation of 1°. At 374 K, a second distribution centred at 55° and having a standard deviation of 1° was added in 6:100 ratio (2^{nd}:1^{st}) to account for the peak in the centre.

Figure 5.60 shows the ^{2}H quadrupolar echo spectra for the 2,2,3,3-d_4-labelled derivative at different temperatures and for 20 and 160 μs refocusing delays. A 124 kHz wide powder pattern is observed at 276 K indicating very little molecular motion. The spectrum is narrowed down to 119 kHz at 364 K. This spectrum has also a small peak at the zero frequency. As for the 1,1,4,4-d_4-labelled derivative, the spectrum is independent of the length of the refocusing delay indicating that the rate of the motion is in the fast motion limit.

The spectra were simulated using the conical libration model with a rate constant of 1×10^8 s^{-1}. The simulated spectra are shown in figure 5.61. At 276 K, the distribution was centred at 0° with standard deviation of 1° while two different distributions were used at 364 K. The first distribution was centred at 5° and the second at 55° to account for the peak in the centre. The standard deviation was set to 1° at both temperatures. These two distributions were added in 100:1 (1^{st}:2^{nd}) ratio to produce the observed spectra.

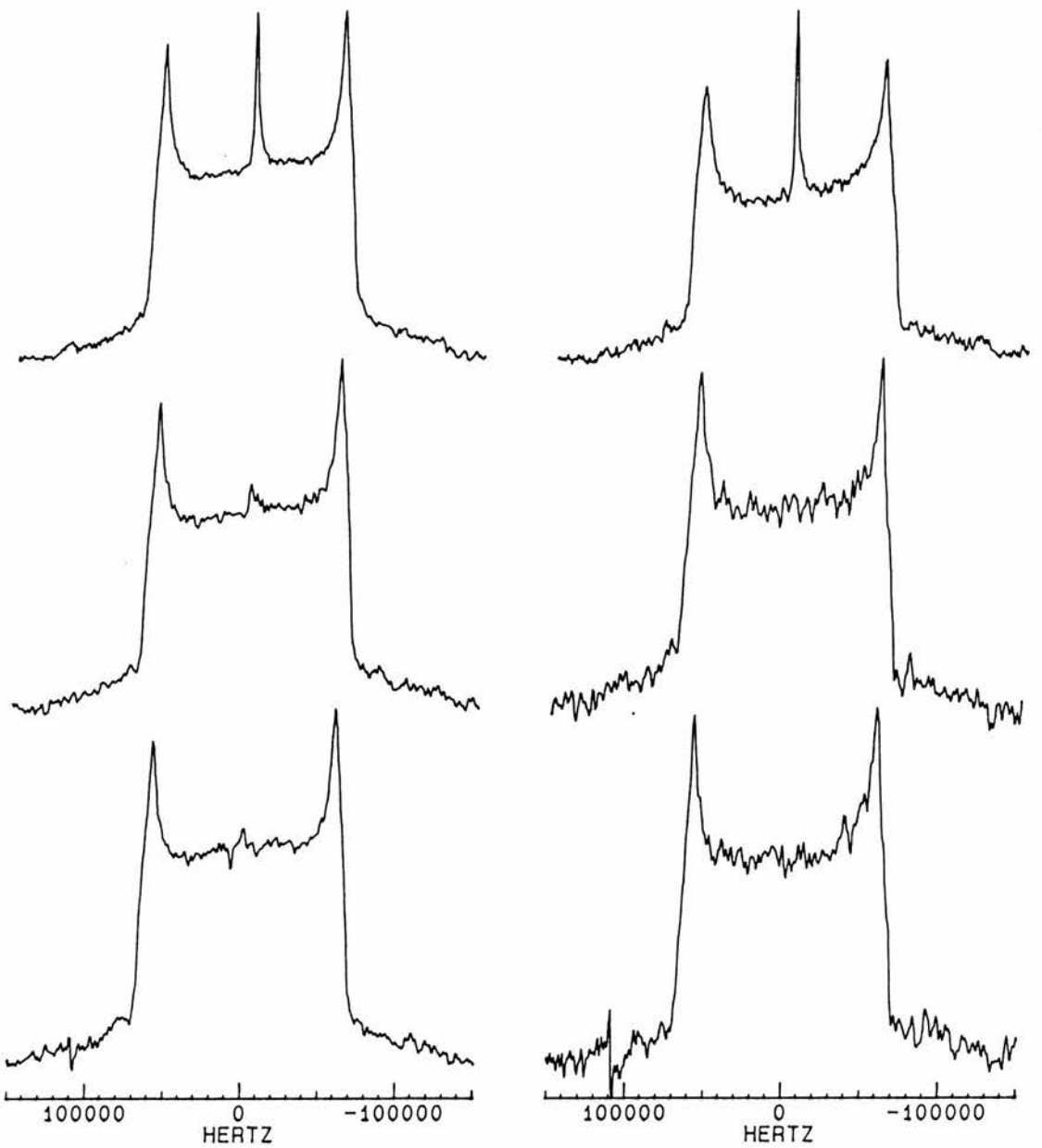

Figure 5.58. Measured ^2H quadrupolar echo spectra for 1,1,4,4-d_4-butane-1,4-diyl bis(3,5-dimethoxybenzoate) at different temperatures. Refocusing delay is 20 μs (left) and 160 μs (right). Temperatures are from top to bottom: 374, 325 and 288 K.

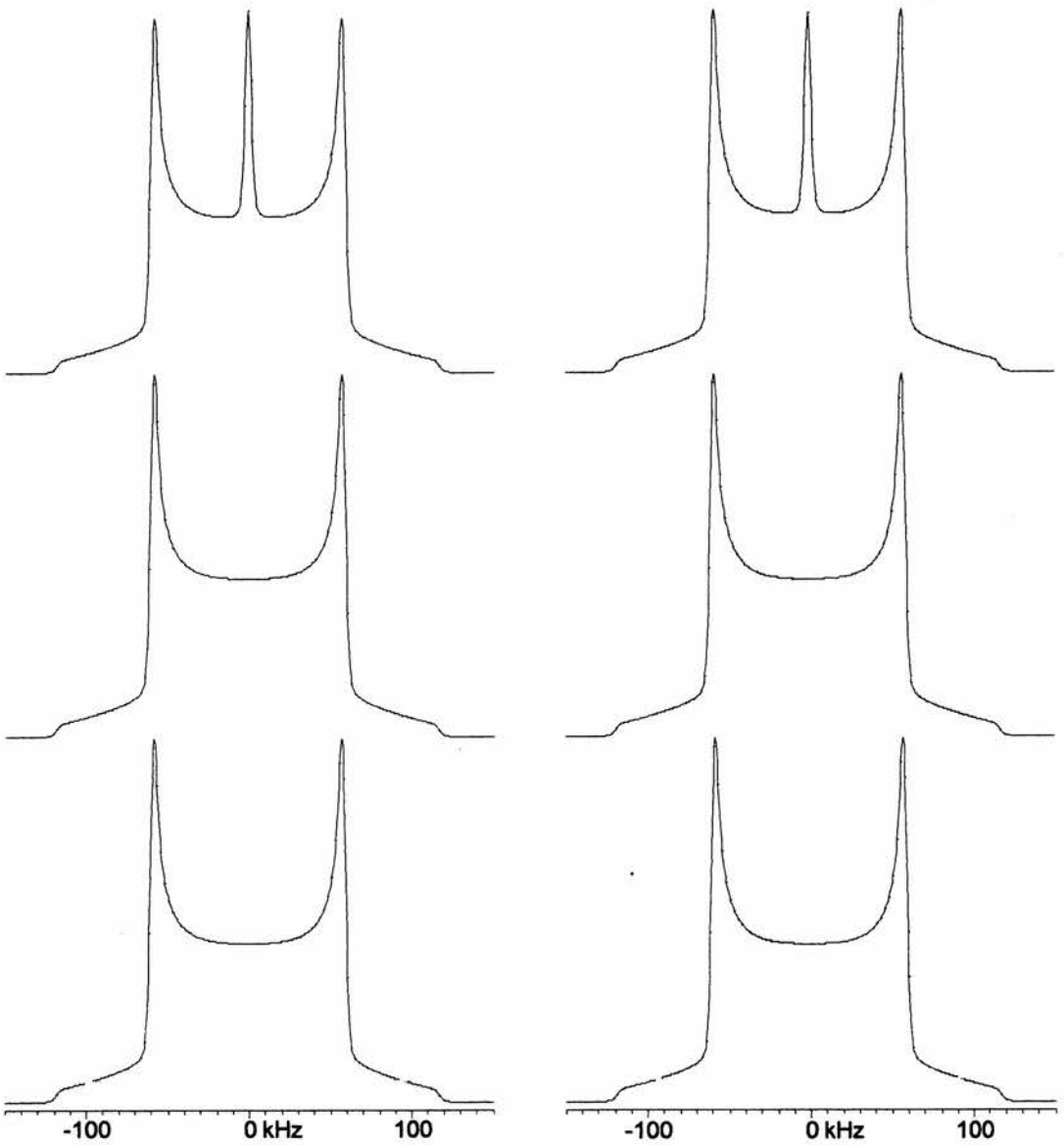

Figure 5.59. Simulated ^2H quadrupolar echo spectra for 1,1,4,4-d_4-butane-1,4-diyl bis(3,5-dimethoxybenzoate) corresponding to figure 5.58.

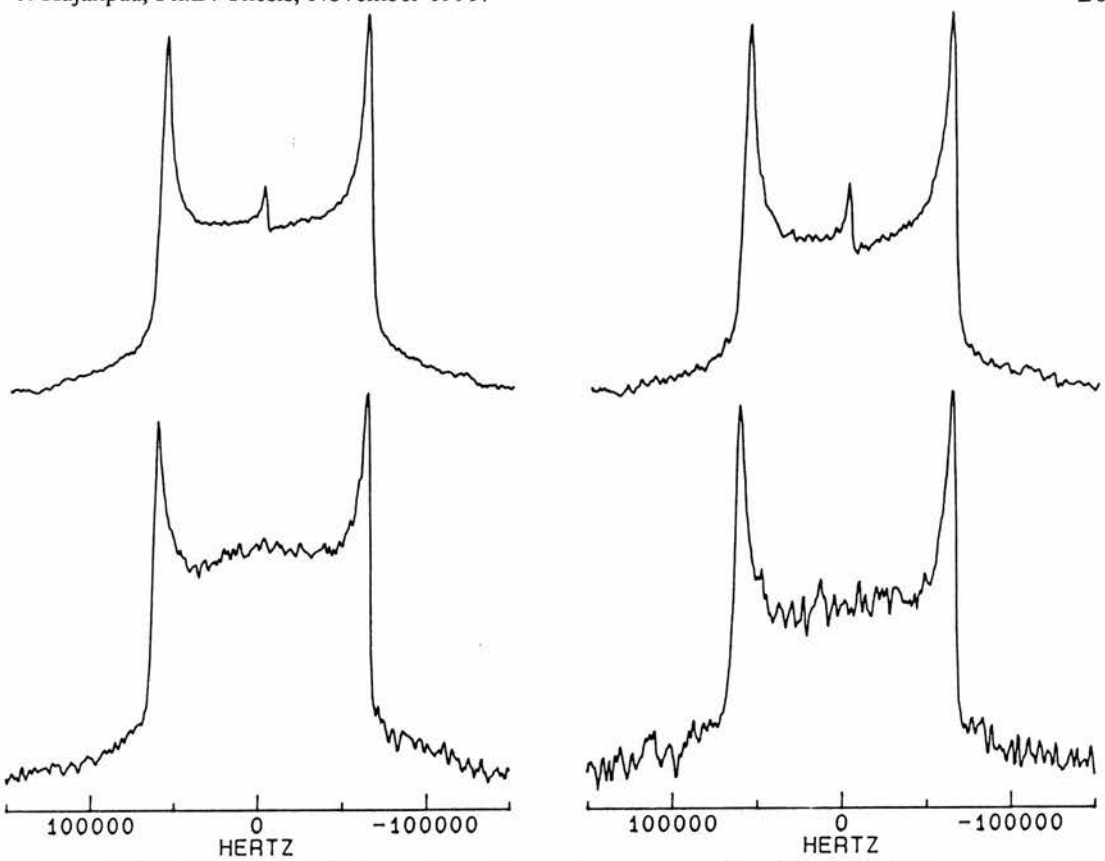

Figure 5.60. Measured ^{2}H quadrupolar echo spectra for 2,2,3,3-d_4-butane-1,4-diyl bis(3,5-dimethoxybenzoate) at 364 K (top) and 276 K (bottom).

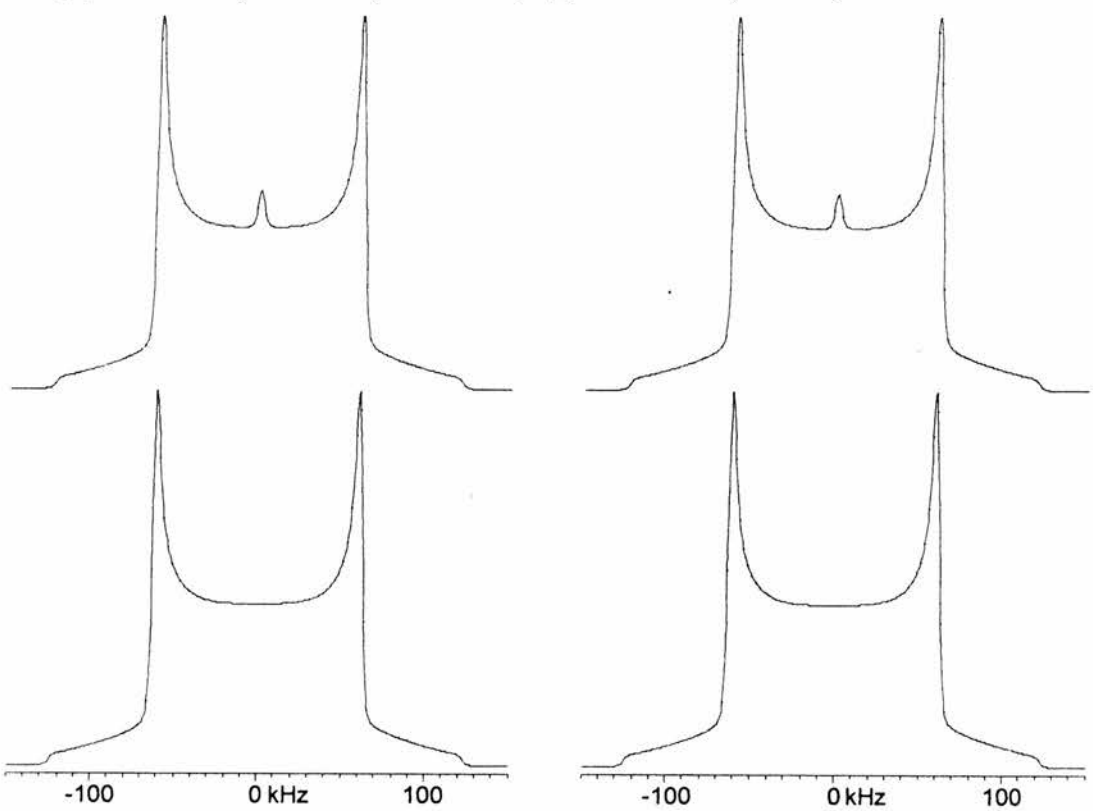

Figure 5.61. Simulated ^{2}H quadrupolar echo spectra for 2,2,3,3-d_4-butane-1,4-diyl bis(3,5-dimethoxybenzoate) corresponding to figure 5.60.

As for the hexyl series, compounds with *gauche* bonds in the alkyl chain were compared with compounds with an all-*trans* chain. According to Bocelli *et al.*[114] and Grenier-Loustalot *et al.*[115], the alkyl chain in butane-1,4-diyl bis(*m*-chlorobenzoate) is in all-*trans* conformation. Views of structure are given in the appendix (p. A-43).

Unfortunately, the measurement of ^{13}C CP/MAS spectra was difficult for this compound, and therefore, only one spectrum was measured at room temperature (fig. 5.62). Recycle delay of 60 s was needed to prevent saturation. Peaks are at 24.8 (-O-CH_2-$\underline{C}H_2$-), 65.9 (-O-$\underline{C}H_2$-CH_2-) 131.2 ($\underline{C}_{Ar}$) and 165.1 ppm (-$\underline{C}$=O). The peaks for the chain carbons show no evidence of dipolar broadening, and therefore, no attempt was made to measure ^{13}C $T_{1\rho}$ relaxation time. The single peak for the aryl carbons suggest a rapid rotation of the aryl group.

The central methylene groups of the alkyl chain were deuterated for deuteron NMR studies, and the ^2H spin-lattice relaxation time for this 2,2,3,3-d_4-butane-1,4-diyl bis(*m*-chlorobenzoate) was measured between 315 and 354 K. Below 315 K, the ^2H spin-lattice relaxation time was too long to be measured reliably. Measured ^2H spin-lattice relaxation times are listed in table 5.14 and shown as a function of temperature in figure 5.63. ^2H spin-lattice relaxation time decreases with temperature from 175 s at 315 K to *ca.* 80 s at 325 K. As expected for an all-*trans* chain, ^2H spin-lattice relaxation time is independent of temperature above 325 K.

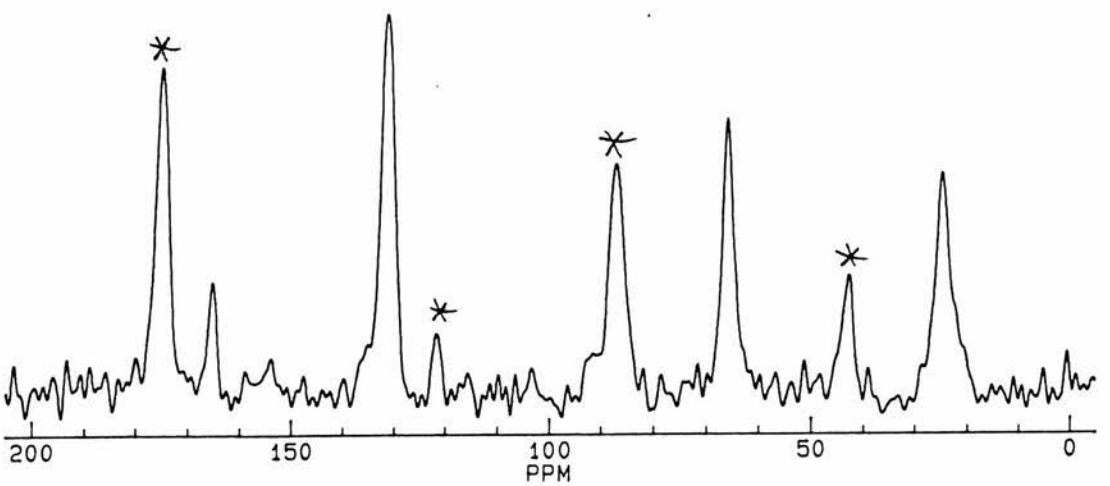

Figure 5.62. ^{13}C CP/MAS spectrum of butane-1,4-diyl bis(*m*-chlorobenzoate) at room temperature. Spinning sidebands are asterisked.

Table 5.14. Measured ^{2}H spin-lattice relaxation times for 2,2,3,3-d_4-butane-1,4-diyl bis(*m*-chlorobenzoate).

T(vtu)/K	T/K	^{2}H T_1/s
320	315	175
325	320	106
330	325	81
340	335	67
350	345	82
360	354	79

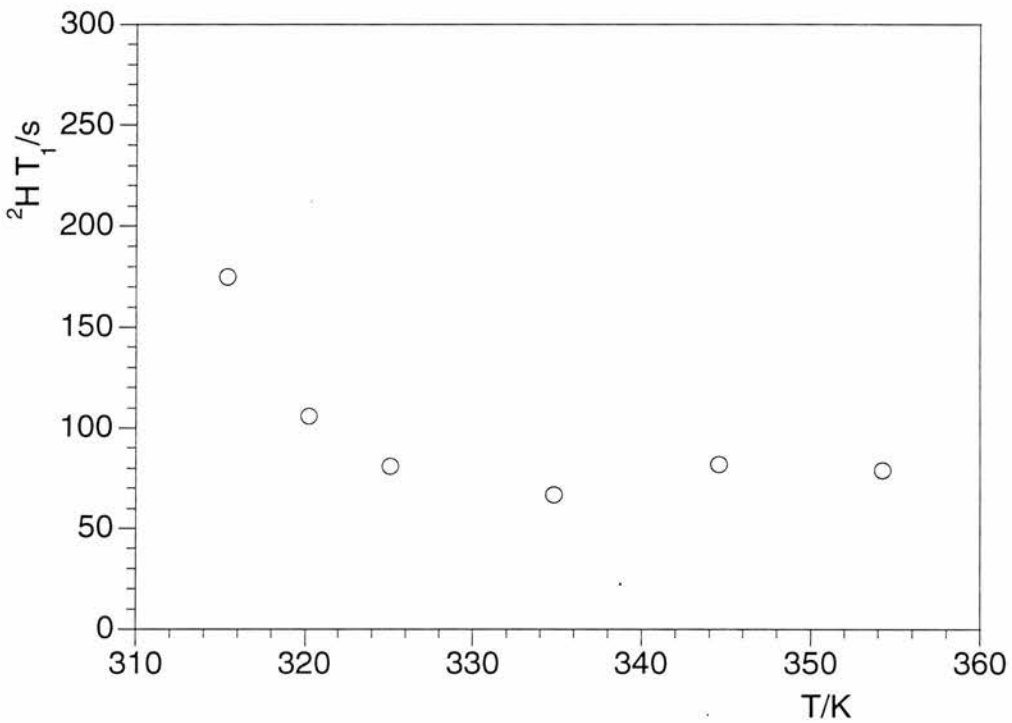

Figure 5.63. Measured ^{2}H spin-lattice relaxation time as a function of temperature for 2,2,3,3-d_4-butane-1,4-diyl bis(*m*-chlorobenzoate).

The long ^{2}H spin-lattice relaxation time for this compound made the measurement of ^{2}H quadrupolar echo spectra extremely time-consuming, and therefore, only one spectrum was measured at 325 K with a refocusing delay of 20 μs. This spectrum is shown in figure 5.64. A 118 kHz wide powder pattern was observed suggesting very little molecular motion. Almost any model would reproduce this spectrum but,

consistently with the other spectra in this thesis, the spectrum was simulated with the conical libration model (fig.5.64, right). The motion was assumed to be in the fast motion limit, and therefore, a rate constant of 1×10^8 s^{-1} was used. The distribution was centred at 5° and had a standard deviation of 1°.

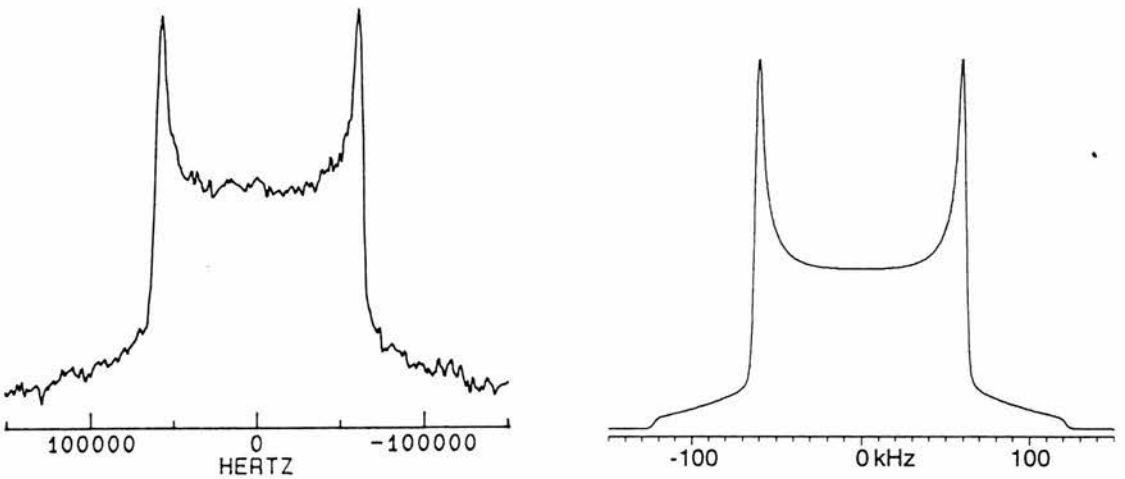

Figure 5.64. Measured ^2H quadrupolar echo spectrum for 2,2,3,3-d_4-butane-1,4-diyl bis(*m*-chlorobenzoate) (left) at 325 K together with a simulated spectrum (right).

5.11. Ethane-1,2-diyl bis(*p*-methylbenzoate)

As for the butyl series, two compounds with *gauche* bonds in the chain and one compound with all-*trans* chain were chosen to study in the ethyl series. The first compound in this ethyl series is ethane-1,2-diyl bis(*p*-methylbenzoate). Its structure has a been solved from single crystal x-ray data.[116] The structure (appendix, p. A-45) shows that the carbon-carbon bond in the chain is in the *gauche* conformation.

Because of the two fast rotating methyl groups, good quality ^{13}C CP/MAS spectra were obtained for this sample. Spectra measured at different temperatures are shown in figure 5.65. Peaks in the ^{13}C CP/MAS spectrum are at 21.8 ppm ($\underline{C}H_3$), 63.0 ppm ($\underline{C}H_2$), 127.3 ppm ($\underline{C}_{Ar}$-CH_3), 129.3 ppm ($\underline{C}_{Ar}$-H), 144.1 ($\underline{C}_{Ar}$-C=O) and 166.3 ppm ($\underline{C}$=O). Unfortunately, the spectrum fails to show any changes with temperature, and therefore, no attempt was made to measure ^{13}C $T_{1\rho}$ relaxation times at any temperature.

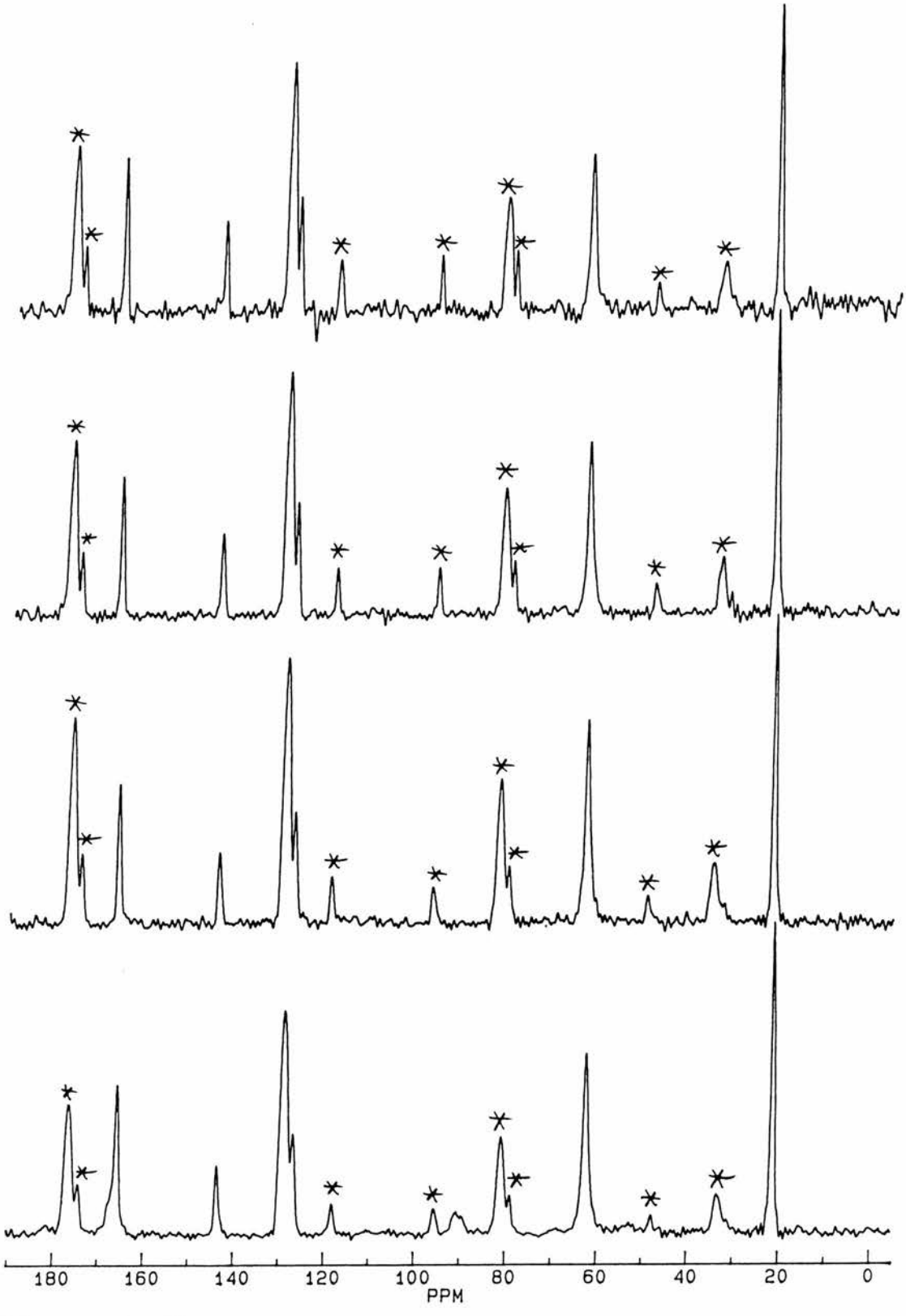

Figure 5.65. ^{13}C CP/MAS spectra for ethane-1,2-diyl bis(*p*-methylbenzoate) at different temperatures. Temperatures are from top to bottom: 374, 326, 270 and 198 K. Spinning sidebands (at 6 kHz) are asterisked.

The alkyl chain was deuterated and the ^{2}H spin-lattice relaxation time for this 1,1,2,2-d_4-ethane-1,2-diyl bis(*p*-methylbenzoate) was measured from 315 to 383 K. The measured ^{2}H spin-lattice relaxation times are listed in table 5.15 and shown as a function of temperature in figure 5.66. ^{2}H spin-lattice relaxation time decreases from 111 s at 315 K to *ca.* 7 s at 383 K. Figure 5.67. shows a plot of ln(^{2}H T_1) as a function of 1000K/T together with a best-fitting least-squares line. The slope of this line gives 45.6 ± 2.6 kJ mol^{-1} for the apparent activation energy.

Table 5.15. Measured ^{2}H spin-lattice relaxation time for 1,1,2,2-d_4-ethane-1,2-diyl bis(*p*-methylbenzoate)

T(vtu)/K	T/K	^{2}H T_1/s
320	315	111
330	325	97.0
340	335	56.0
355	349	30.6
365	359	20.0
370	364	18.0
375	369	12.5
380	374	9.90
385	379	7.90
390	383	7.10

The ^{2}H quadrupolar echo spectra were measured with 20 and 160 μs refocusing delays at 349 K and 379 K. The measured spectra are shown in figure 5.68. 114 kHz wide powder pattern was observed at both temperatures indicating little molecular motion in the chain. The spectrum is independent of the length of the refocusing delay indicating that the rate of the motion is in the fast motion limit. Almost any model would reproduce these spectra but, consistently with the other simulations in this thesis, the three conical libration model was used. The rate constant was set to 1×10^8 s^{-1} and the distribution was centred at 10° with a standard deviation of 1°.

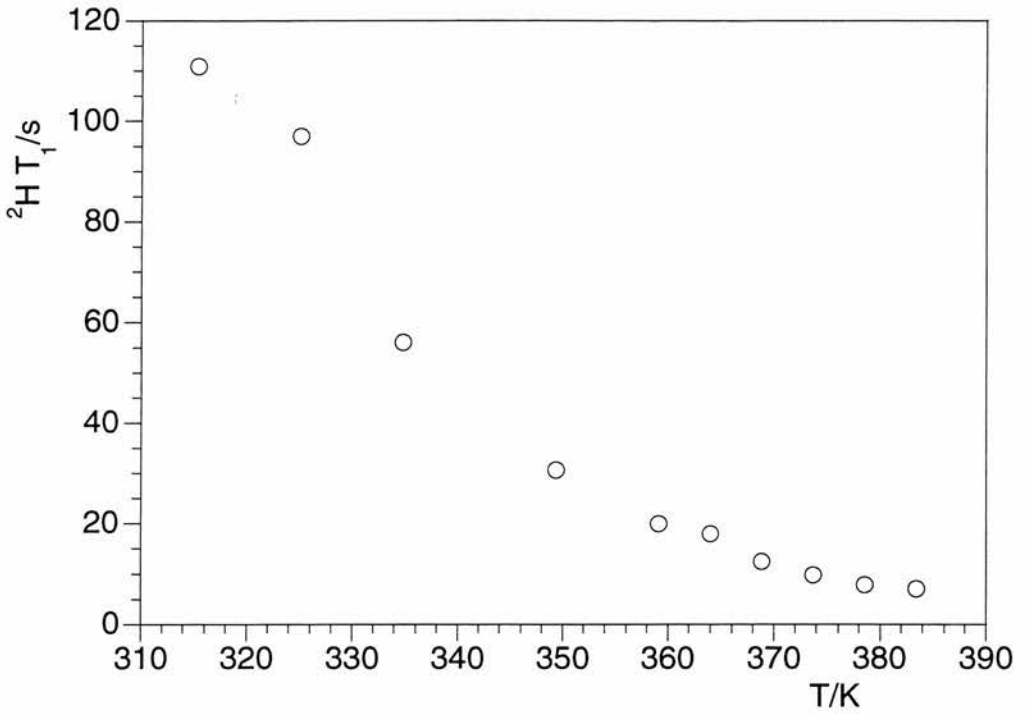

Figure 5.66. Measured ^{2}H relaxation time as a function of temperature for 1,1,2,2-d_4-ethyl 1,2-bis(*p*-methylbenzoate).

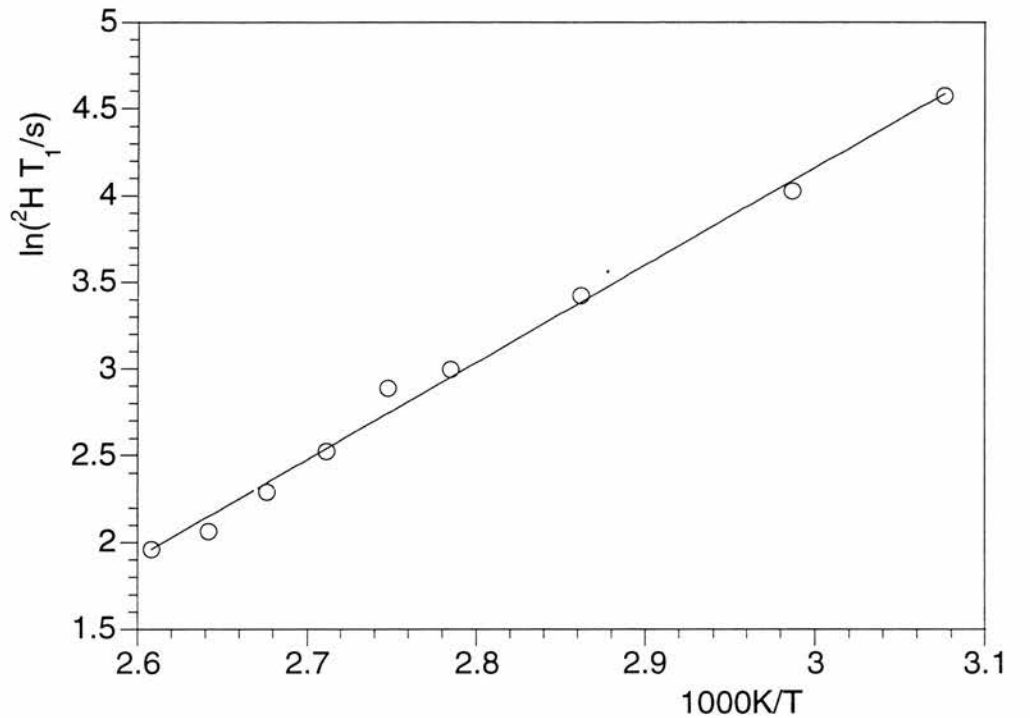

Figure 5.67. Plot of ln(^{2}H T_1) as a function of 1000/T for 1,1,2,2-d_4-ethyl 1,2-bis(*p*-methylbenzoate). Apparent activation energy from the slope is 45.6 ± 2.6 kJ mol^{-1}.

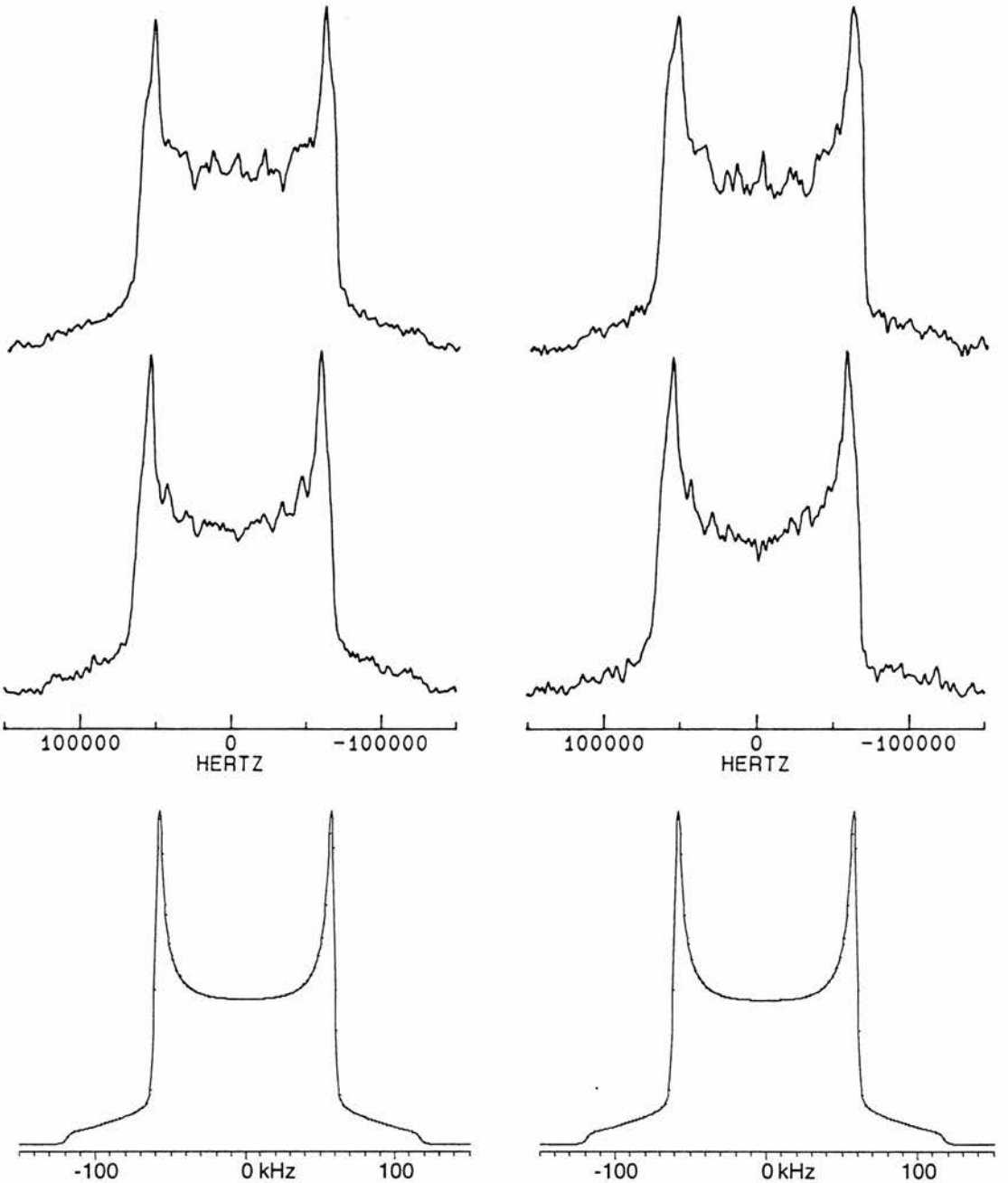

Figure 5.68. Measured ^2H quadrupolar echo spectra for 1,1,2,2-d_4-ethane-1,2-diyl bis(*p*-methylbenzoate) at 349 (middle) and 379 K (top) together with simulated spectra (bottom). Refocusing delay is 20 μs (left) and 160 μs (right).

5.12. Ethane-1,2-diyl bis(*p*-chlorobenzoate)

Another compound in this ethyl series is ethane-1,2-diyl bis(*p*-chlorobenzoate). Its crystal structure has been solved from single crystal x-ray diffraction data.[117] The

structure (appendix, p. A-46) indicates that the carbon-carbon bond in the chain is in *gauche* conformation, similarly to the alkyl chain in ethyl 1,2-bis(*p*-methyl-benzoate).

The measurement of ^{13}C CP/MAS spectra for this compound was difficult and a spectrum was only obtained at 374 K, which is the high temperature limit of the CP/MAS probe used. This spectrum is shown in figure 5.69. The signal to noise ratio is rather poor because a recycle delay of 90 s was needed to prevent saturation, and therefore, only 144 transients were collected. Peaks in the ^{13}C CP/MAS spectrum are at 64.9 ppm ($\underline{C}H_2$), 128.6 ppm ($\underline{C}_{Ar}$-H), 130.5 ppm ($\underline{C}_{Ar}$-H) 139.0 ($\underline{C}_{Ar}$-C=O), 142.2 ppm ($\underline{C}_{Ar}$-Cl) and 164.8 ppm ($\underline{C}$=O). The peak for the chain carbons shows no evidence of dynamic dipolar broadening, and therefore, no attempt was made to measure ^{13}C $T_{1\rho}$ relaxation time.

The alkyl chain was deuterated and the ^{2}H spin-lattice relaxation time for this 1,1,2,2-d_4-ethane-1,2-diyl bis(*p*-chlorobenzoate) was measured from 364 K to 403 K. The measured ^{2}H spin-lattice relaxation times are listed in table 5.16 and shown as a function of temperature in figure 5.70. The ^{2}H spin-lattice relaxation time decreases from *ca.* 100 s at 364 K to 9 s at 403 K. Figure 5.71 shows a plot of ln(^{2}H T_1) as a function of 1000K/T together with a least-squares line. The slope of this line gives 73.6 ± 9.8 kJ mol^{-1} for the apparent activation energy.

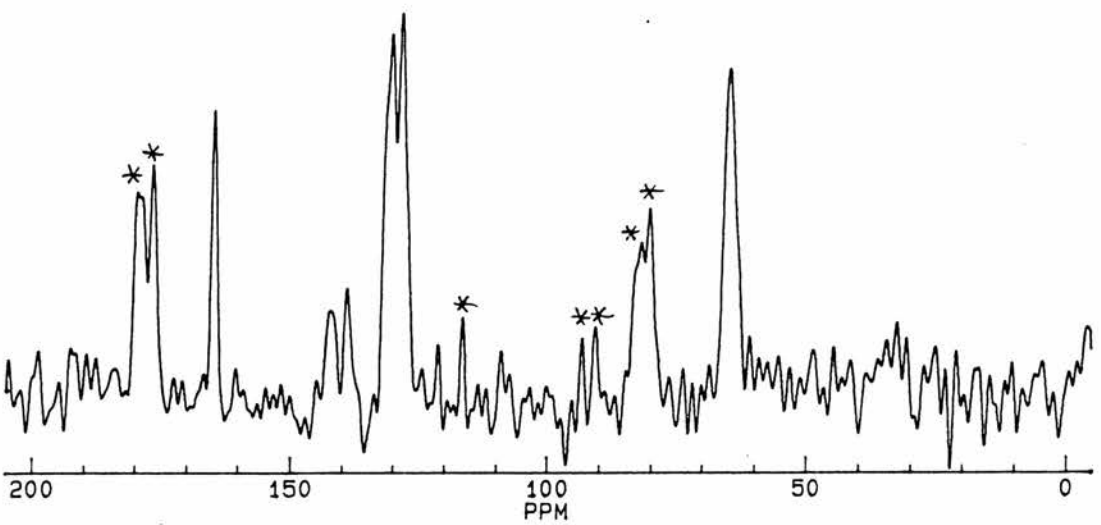

Figure 5.69. ^{13}C CP/MAS spectrum for ethane-1,2-diyl bis(*p*-chlorobenzoate) at 374 K. Spinning sidebands are asterisked.

Table 5.16. Measured ^{2}H spin-lattice relaxation time for 1,1,2,2-d_4-ethane-1,2-diyl bis(*p*-chlorobenzoate).

T(vtu)/K	T/K	^{2}H T_1/s
370	364	101
375	369	69.0
380	374	47.6
385	379	38.5
390	383	27.2
395	388	17.0
400	393	19.9
410	403	9.00

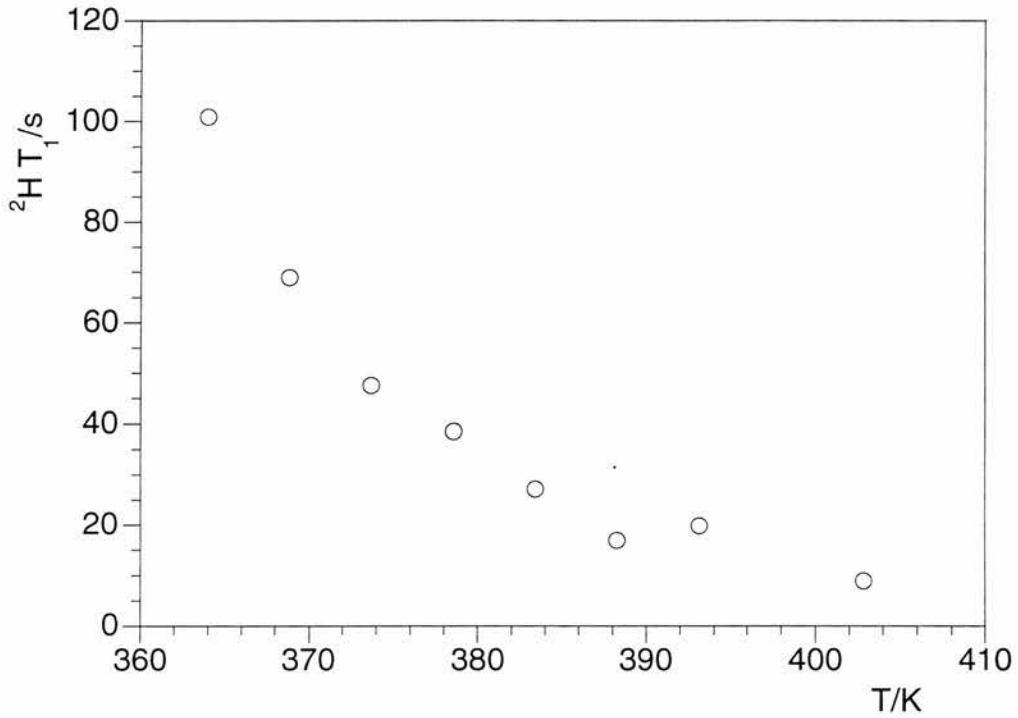

Figure 5.70. Measured ^{2}H spin-lattice relaxation time as a function of temperature for 1,1,2,2-d_4-ethane-1,2-diyl bis(*p*-chlorobenzoate).

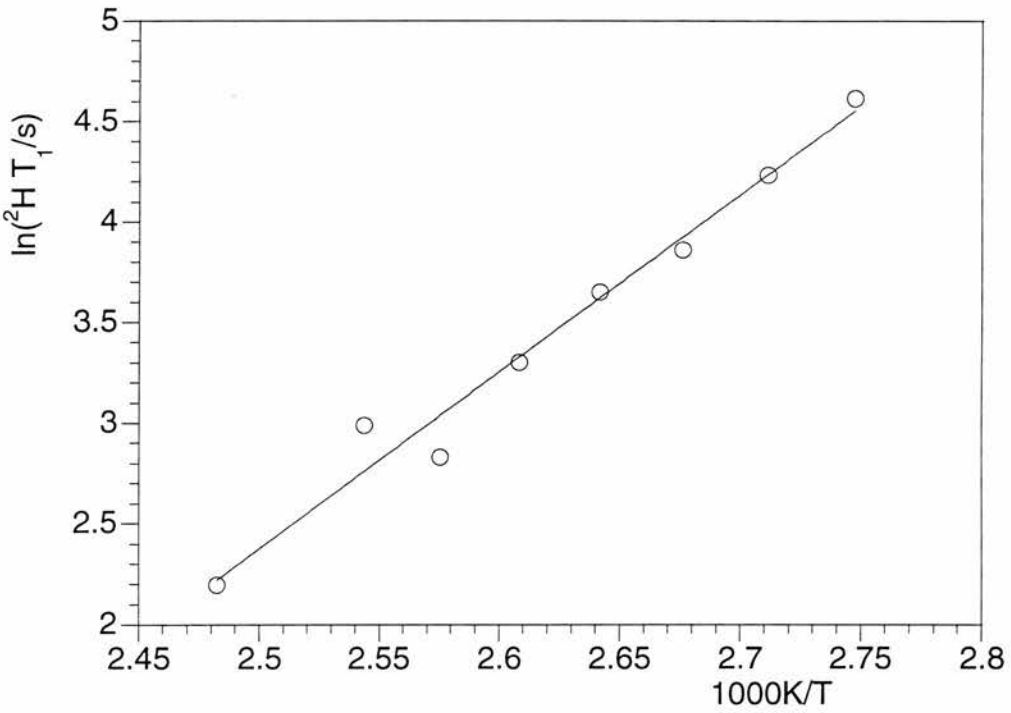

Figure 5.71. Plot of ln(^{2}H T_1) as a function of 1000/T for 1,1,2,2-d_4-ethane-1,2-diyl bis(*p*-chlorobenzoate) together with a least-squares line. Apparent activation energy from the slope is 73.6 ± 9.6 kJ mol^{-1}.

A ^{2}H quadrupolar echo spectrum was measured at 403 K with a 20 μs refocusing delay (fig. 5.72, left). No spectra were obtained with 30 μs or longer refocusing delays suggesting that the rate of the motion is in the intermediate rate regime where the echo intensity decreases strongly with the refocusing delay. In addition, the intensity in the central region of the spectrum is nearly zero. As was shown in chapter 3, this reduced intensity of the central region indicates that the rate of motion is in the intermediate regime. The width of the spectrum is 112 kHz indicating small amplitude motion.

The spectrum was simulated using the conical libration model. The rate constant was set to 1.0x10^5 s^{-1} and a distribution with a standard deviation of 1° and centred at 15° was used. The simulated spectrum (fig. 5.72, right) agrees well with the observed spectrum. Also, the measured ^{2}H spin-lattice relaxation time of 9 s is consistent with this model. The rate constant 1.0x10^5 s^{-1} corresponds to a correlation time of 1.7x10^{-6} s. Using a half-angle of 15° and a quadrupolar coupling constant of 165 kHz

equation 3.12. gives 13 s for the ^{2}H spin-lattice relaxation time, satisfyingly in agreement with the observed 9 s.

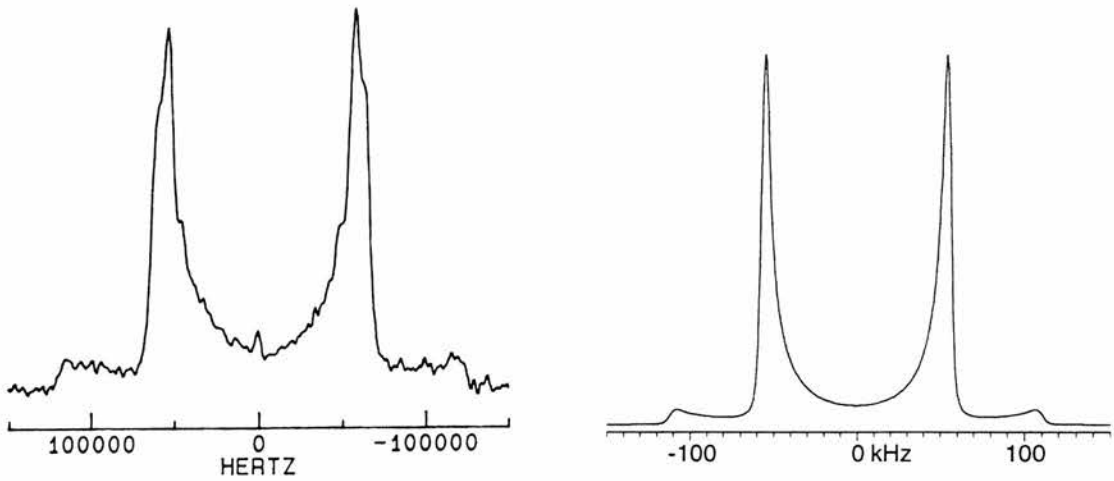

Figure 5.72. Measured ^{2}H quadrupolar echo spectrum for 1,1,2,2-d_4-ethane-1,2-diyl bis(*p*-chlorobenzoate) at 403 K (left) together with a simulated spectrum using the conical libration model with a rate constant is 1.0×10^5 s^{-1}.

5.13. Ethane-1,2-diyl bis(*m*-chlorobenzoate)

Again it is interesting to compare molecular dynamics in chains containing *gauche* bonds with chains in all-*trans* conformation. The all-*trans* compound chosen for the ethyl series is ethyl 1,2-bis(*m*-chlorobenzoate). Its crystal structure has been solved from single crystal x-ray data.[118] Views of the structure are given in the appendix (p. A-48).

Figure 5.73 shows ^{13}C CP/MAS spectra measured at different temperatures. Peaks in the ^{13}C CP/MAS spectrum are at 62.7 ppm (O$\underline{C}$H$_2$), 127.3 ppm ($\underline{C}_{Ar}$-H) 131.0 ppm ($\underline{C}_{Ar}$-H, 2 pos.), 133.9 ppm ($\underline{C}_{Ar}$-Cl) and 164.6 ppm ($\underline{C}$=O). Unfortunately, the spectra show no evidence of dipolar broadening, and therefore, no attempt was made to measure ^{13}C $T_{1\rho}$ relaxation time at any temperature.

The alkyl chain was deuterated and ^{2}H spin-lattice relaxation time was measured for this 1,1,2,2-d_4-ethane-1,2-diyl bis(*m*-chlorobenzoate) from 199 K to 359 K. The measured ^{2}H spin-lattice relaxation times are listed in table 5.17 and shown as a function of temperature in figure 5.74.

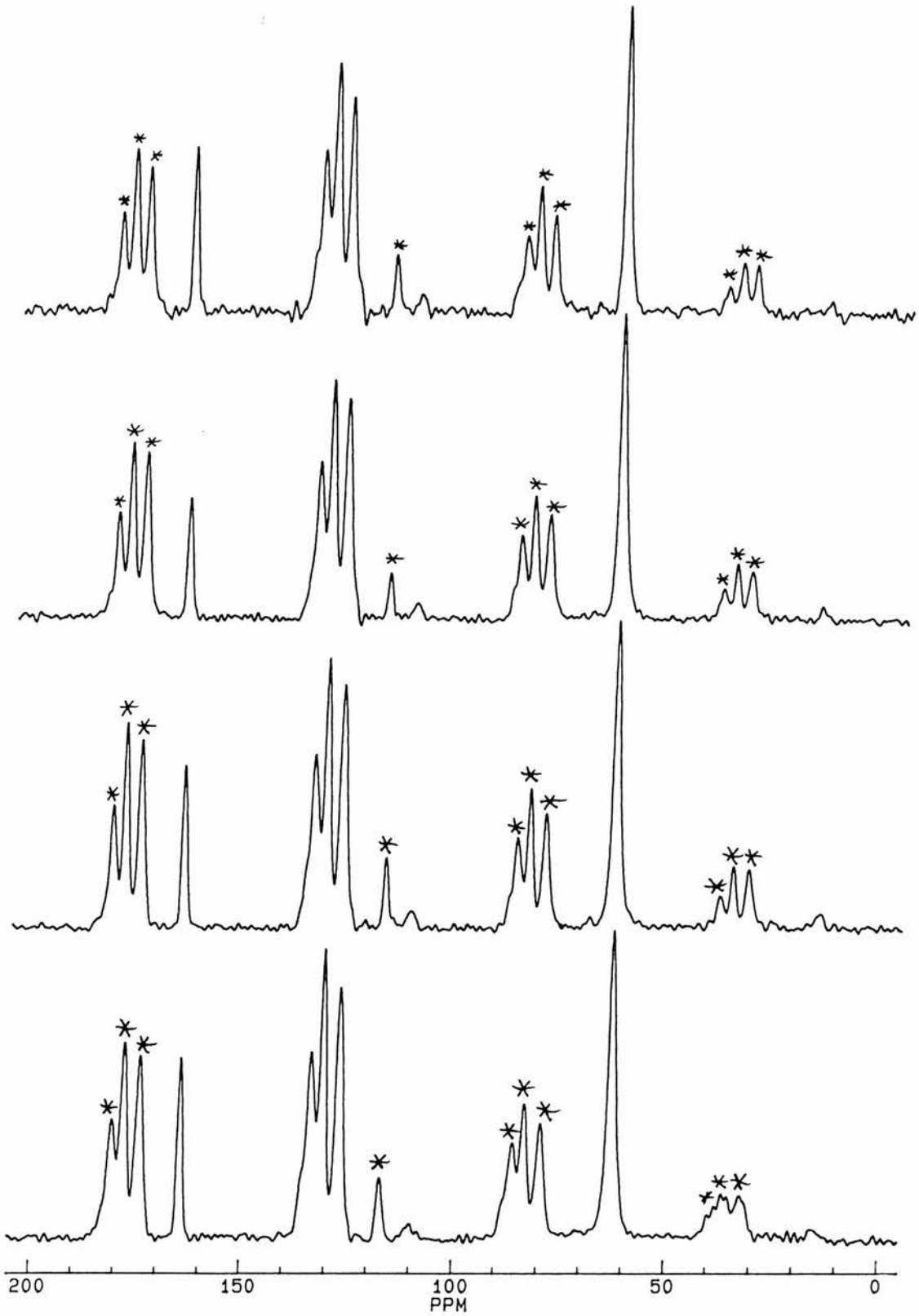

Figure 5.73. ^{13}C CP/MAS spectrum of ethane-1,2-diyl bis(*m*-chlorobenzoate) at different temperatures. Temperatures are from top to bottom: 350, 296, 246 and 198 K. Spinning sidebands (at 6 kHz) are asterisked.

Table 5.17. Measured ^{2}H spin-lattice relaxation time for 1,1,2,2-d_4-ethane-1,2-diyl bis(*m*-chlorobenzoate).

T(vtu)/K	T/K	^{2}H T_1/s
108	109	64.0
115	116	35.0
125	126	23.0
140	140	13.3
160	160	8.80
170	170	6.80
180	179	7.30
190	189	5.80
200	199	4.80
210	208	5.10
220	218	4.20
240	238	3.90
260	257	3.60
270	267	3.20
280	276	3.30
285	281	3.20
292	288	3.10
305	301	2.90
320	315	2.50
340	335	2.70
360	354	3.00
365	359	2.90

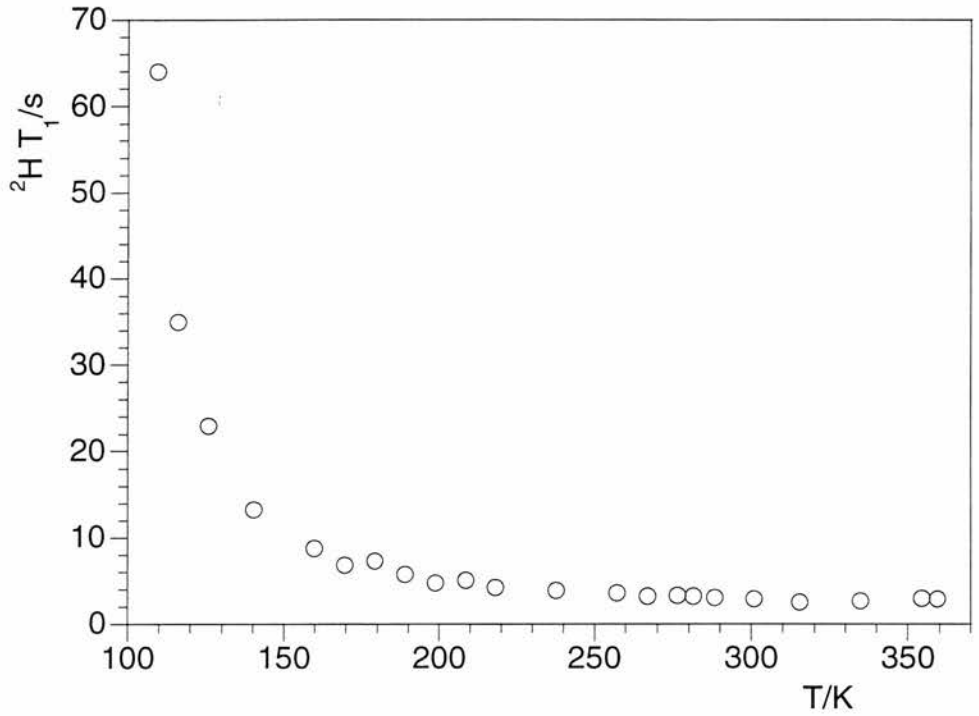

Figure 5.74. Measured ^{2}H spin-lattice relaxation time as a function of temperature for 1,1,2,2-d_4-ethane-1,2-diyl bis(*m*-chlorobenzoate).

As expected for an all-*trans* compound, ^{2}H spin-lattice relaxation time first decreases with temperature and then at higher temperatures is nearly independent of temperature. Similar temperature independent part has been observed for all the compounds with an all-*trans* chain but for none of the compounds containing *gauche* bonds, and therefore, could be a general property of short all-*trans* alkyl chains attached to rigid groups from both ends.

In the diacid series it was observed that the activation energy for the all-*trans* chain was *ca.* 5 kJ mol^{-1}. Therefore, it is interesting to estimate the activation energy for this two carbon all-*trans* chain in a diester. Figure 5.75 shows a plot of ln(^{2}H T_1/s) as a function of 1000K/T for the eight lowest temperature points of figure 5.74 together with a least-squares line. The slope of the least-squares line gives 4.9 kJ mol^{-1} for the apparent activation energy. This value agrees well with the values obtained for the diacids indicating that the motional behaviour of this all-*trans* chain is very similar to those in the diacids studied in chapter 4.

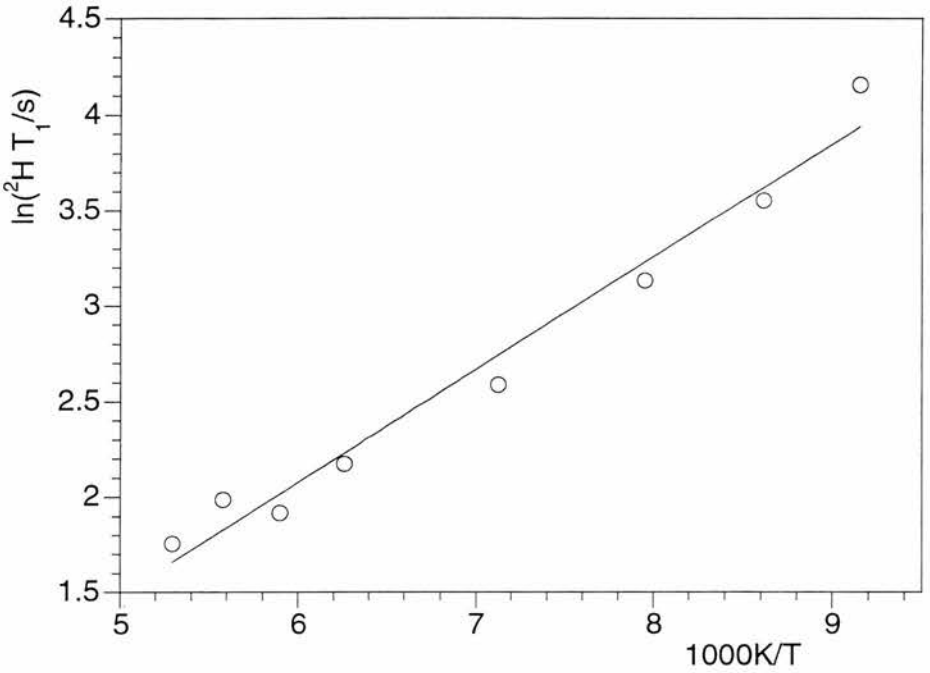

Figure 5.75. Plot of ln(^{2}H T_1) as a function of 1000K/T for 1,1,2,2-d_4-ethane-1,2-diyl bis(*m*-chlorobenzoate) in the low temperature region from 109 to 189 K.

^{2}H quadrupolar echo spectra were measured at four different temperatures from 199 to 359 K (fig. 5.76). A 115 kHz wide powder pattern was observed at 199 K. This spectrum narrows down to 100 kHz at 288 K, to 83 kHz at 335 K and to 74 kHz at 359 K. The spectra measured at the three highest temperatures are a superposition of two different spectra. The spectrum is independent of the length of the refocusing delay indicating that the rate of the motion is in the fast motion limit, and therefore, the spectra were simulated with the conical libration model using a rate constant of 1×10^8 s^{-1} (fig. 5.77). At 199 K, a distribution with a standard deviation of 1° and centred at 10° was used. Two distributions were needed at 288 K. A distribution with a standard deviation of 1° and centred at 15° was added to a distribution with a standard deviation of 1° and centred at 20° in a 100:80 ratio. Similarly at 335 K, a distribution with a standard deviation of 3° and centred at 15° was added to a distribution with a standard deviation of 3° and centred at 25° in a 100:80 ratio. Finally at 359 K, three distributions were used. The first and second had a standard deviation of 3° and were centred at 20° and 30°, respectively. These two distributions were added to a distribution with a standard deviation of 1° and centred at 55° in a 100:80:5 ratio to produce the measured spectra.

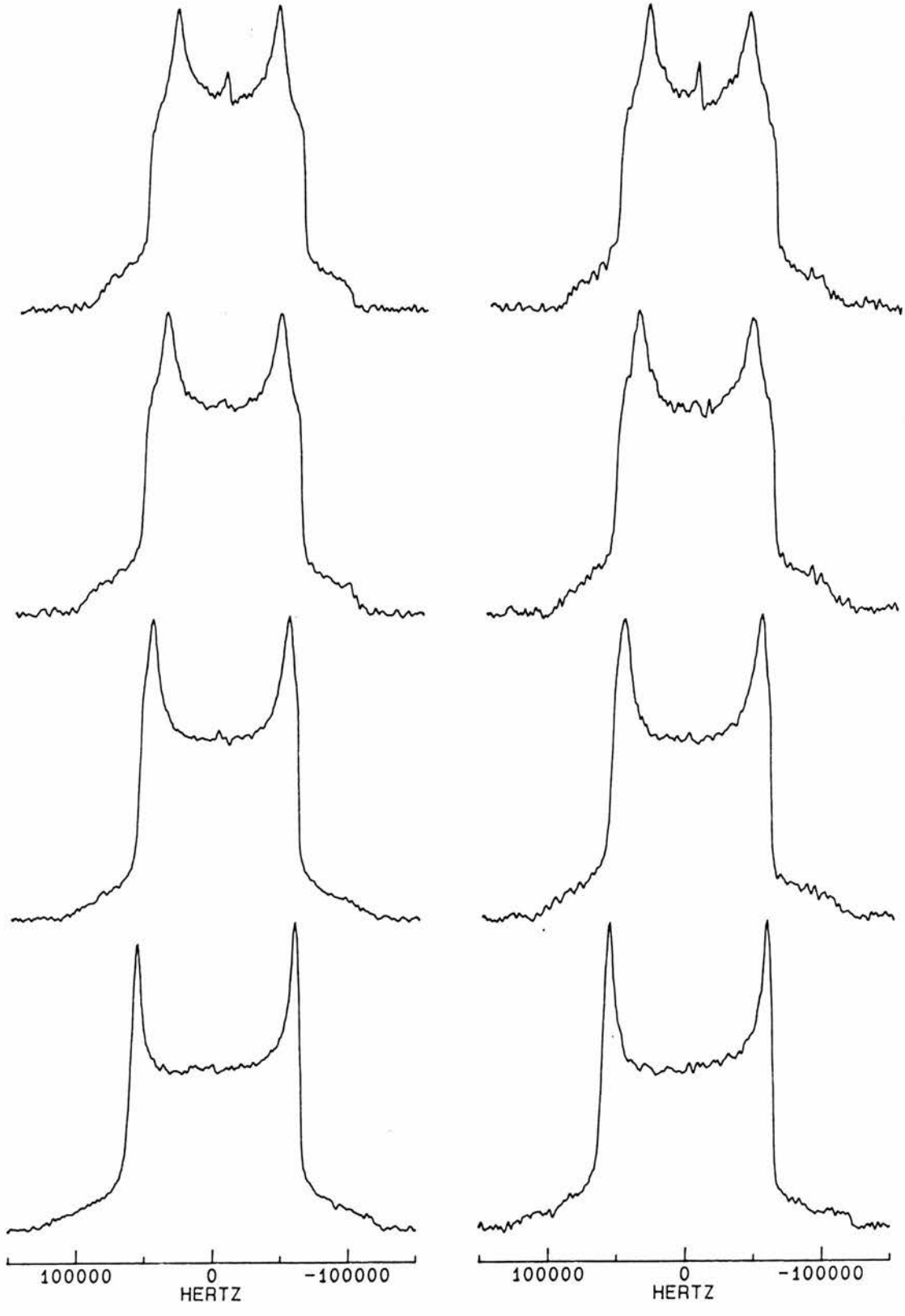

Figure 5.76. Measured ^{2}H quadrupolar echo spectra for 1,1,2,2-d_4-ethane-1,2-diyl bis(*m*-chlorobenzoate) at different temperatures. Temperatures are from top to bottom: 359, 335, 288 and 199 K.

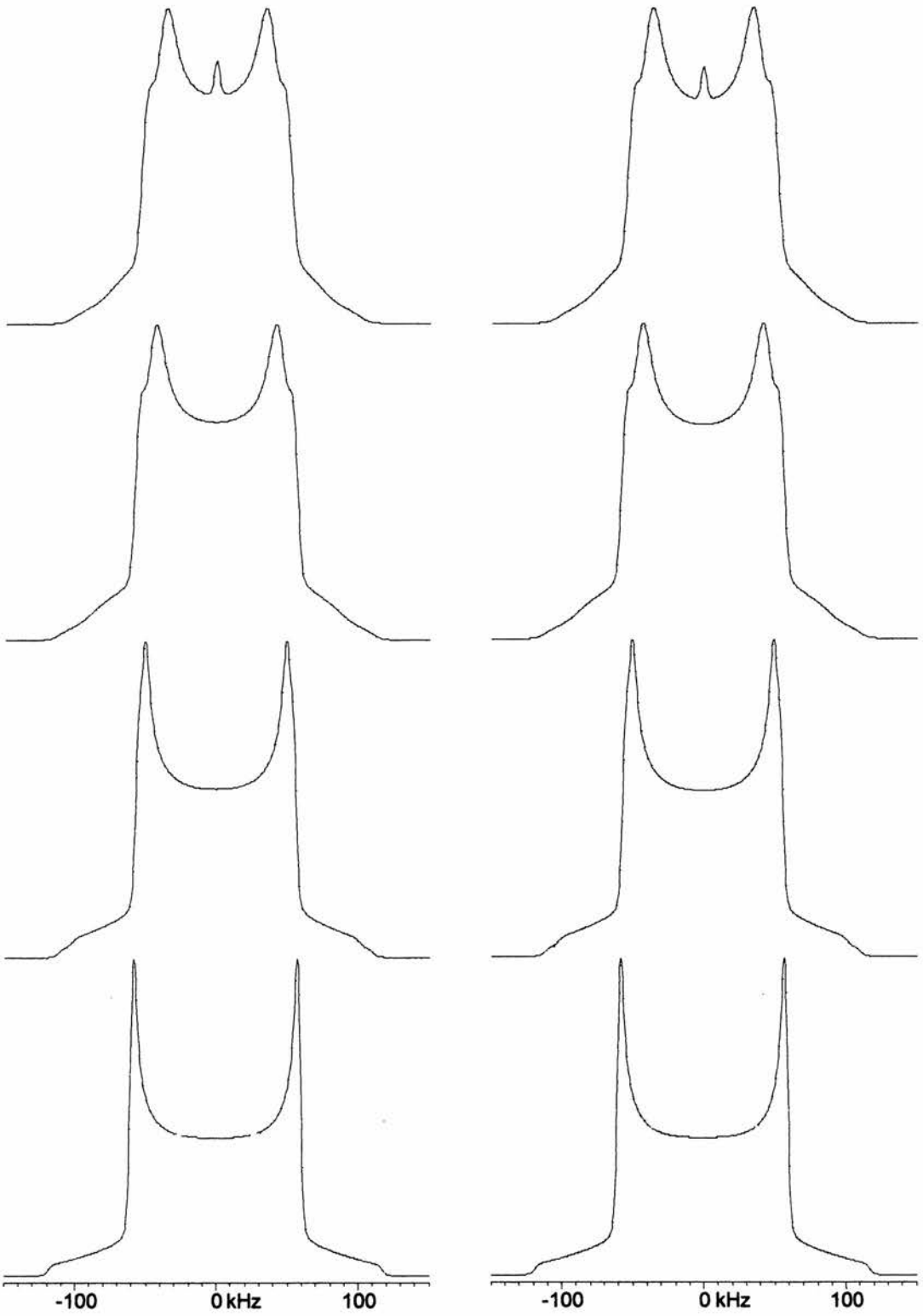

Figure 5.77. Simulated ^2H quadrupolar echo spectra for 1,1,2,2-d_4-ethane-1,2-diyl bis(*m*-chlorobenzoate) using the conical libration model.

5.14. Conclusions from the diester series

The dependence of ^{2}H spin-lattice relaxation time on temperature for all the all-*trans* diesters was similar to that observed for the diacids in chapter 4. As for the odd diacids, the spin-lattice relaxation time first decreases strongly with temperature and then is nearly independent of temperature at higher temperatures. This occurs because the angle of the librational motion increases with temperature, and therefore, compensates for the contribution of shortening correlation time in the fast motion limit.

Introducing a *gauche* bond to the chain allows for slower and larger angle librations to occur, possibly because *gauche* bonds tend to align carbon-carbon bonds in the chain, as opposed to the zig-zag shape of all-*trans* chains. Clear evidence for the slowing down of the librational motion was obtained from ^{13}C CP/MAS spectra, ^{2}H quadrupolar echo spectra and ^{2}H spin-lattice relaxation time for both hexane-1,6-diyl and butane-1,4-diyl bis(*p*-nitrobenzoates), and also from the ^{13}C $T_{1\rho}$ relaxation time and echo reduction factors for the hexanediyl derivative.

Similar motional behaviour was observed for hexane-1,6-diyl dibenzenesulfonate and ditosylate suggesting that the number of *gauche* bonds in the chain is insignificant. On the other hand, although the chain in hexane-1,6-diyl bis(3,5-dimethoxybenzoate) is similar to the chain in hexane-1,6-diyl bis(*p*-nitrobenzoate), they behaved differently in the NMR experiments suggesting that the chain dynamics are very sensitive to the molecular environment.

Apparent activation energies for the librational motion of the alkyl chains containing *gauche* bonds are listed in table 5.18. The apparent activation energy, including change both in the rate and in the angle of motion, is between 27 and 38 kJ mol^{-1} for the chains containing four and six carbons while it is larger than 45 kJ mol^{-1} for the chains containing only two carbons. This is an interesting result and indicates that the ethanediyl chain is much more rigid than the butanediyl and hexanediyl chains. As expected, the chains also become more rigid on cooling. This is evident from the apparent activation energy for the alkyl chain of butane-1,4-diyl bis(*p*-nitrobenzoate). The apparent activation energy is *ca.* 30 kJ mol^{-1} above 280 K

whereas it is *ca.* 50 kJ mol^{-1} below 280 K, indicating that at low temperatures the mobility of this butanediyl chain is comparable to the mobility of the ethanediyl chains.

Unfortunately, no crystal structures were obtained for diesters with odd number of carbons in the chain, and therefore, no NMR studies were carried out on these samples. As for the all-*trans* chains studied in the diacid series, it would be interesting to investigate whether an odd-even effect occurs also in chains containing *gauche* bonds.

Finally, all ^2H quadrupolar echo spectra in this chapter, and in the whole thesis, were satisfactorily simulated with the conical libration model indicating that the mode of the C-D bond motion is a complex but rather small angle librational motion arising from rotations of the carbon-carbon bonds in the chain. The NMR techniques used in this thesis did not indicate any *trans-gauche* isomerisation in the chain.

Table 5.18. Apparent activation energies E_a for the alkyl chains containing *gauche* bonds.

Compound	E_a(1 pos.) / kJ mol^{-1}	E_a(2 pos.) / kJ mol^{-1}
hexane-1,6-diyl		
bis(*p*-nitrobenzoate)	35	36
bis(3,5-dimethoxybenzoate)	27	-
dibenzenesulphonate	32.4	34.9
ditosylate	36.9	32.3
butane-1,4-diyl		
bis(*p*-nitrobenzoate) below 280 K	51.6	50.3
bis(*p*-nitrobenzoate) above 280 K	28.8	36.8
bis(3,5-dimethoxybenzoate)	31.7	37.9
ethane-1,2-diyl		
bis(*p*-methylbenzoate)	45.6	-
bis(*p*-chlorobenzoate)	73.6	-

6. EXPERIMENTAL

6.1. SYNTHESES

6.1.1. Diethyl adipate and diethyl glutarate

14.6 g (0.10 mol) of adipic acid, 36.0 ml of abs. ethanol (28.5 g = 0.62 mol), 18 ml of toluene and 0.2 ml of conc. sulphuric acid were measured into a 100 ml round-bottomed flask. A fractionating column filled with glass rods was attached to the flask and the equipment was set up for distillation. The mixture was heated in an oil bath until the azeotropic mixture of ethanol toluene and water had distilled off at 75 °C. The distillate was shaken with 15 g of anhydrous potassium carbonate. The mixture was filtered, and the filtrate was returned to the distillation flask. The azeotropic distillation was repeated. After the distillation, the solution in the distillation flask was transferred to a 100 ml Claisen flask. A vacuum distillation equipment was set up, and diethyl adipate was distilled at 138-140 °C. Yield 16.8 g (83 %).

Similarly was prepared diethyl glutarate from 13.2 g (0.10 mol) of glutaric acid. The product was collected at 134-136 °C. Yield 17.45 g (93 %).

6.1.2. 1,1,6,6-d_4-hexane-1,6-diol and 1,1,5,5-d_4-pentane-1,5-diol

10.0 ml (10 mmol) of 1.0 M $LiAlD_4$ was measured into a 100 ml three-necked flask. A reflux condenser and a dropping funnel, both provided with $CaCl_2$-tubes, were attached to the flask. 1.82 g (9.0 mmol) of diethyl adipate was dissolved in 10 ml of sodium dried ether, and the solution was transferred to the dropping funnel. The $LiAlD_4$ solution was stirred with a magnetic stirrer. Diethyl adipate was added so that the solution refluxed gently. The mixture became thick during the addition, and two times 10 ml of sodium dried ether was added to facilitate stirring. After addition, the mixture was stirred for additional 10 mins. Excess $LiAlD_4$ was destroyed by

adding 1 ml of ethyl acetate. The mixture was filtered with a sintered glass funnel. The filtrate was dried over anhydrous $MgSO_4$. The white powder that remained in the funnel was dissolved into ca. 20 ml of 20 % H_2SO_4. The solution was extracted six times with ether. The ethereal solution was dried with anhydrous $MgSO_4$ and combined with the previously dried filtrate. Ether was removed by rotary evaporator. A viscous liquid, that partly solidified in the freezer, was obtained. The liquid was heated in a Kügelrohr at 25 °C under vacuum (0.01 mbar) until 1,1,6,6-d_4-hexane-1,6-diol solidified. Yield 0.75 g (68 %).

Similarly was prepared 1,1,5,5-d_4-pentane-1,5-diol from 1.69 g of diethyl glutarate. The product was extracted from the aqueous solution with six times 30 ml of ethyl acetate. Yield 0.88 g (91 %).

6.1.3. 1,1,4,4-d_4-butane-1,4-diol and 2,2,3,3-d_4-butane-1,4-diol

1,1,4,4-d_4-butane-1,4-diol was prepared by Miss Jenny Anderson by adding 4.0 g of diethyl succinate in dry THF to 1.0 g of $LiAlD_4$ in dry THF. After refluxing for 30 mins, 50 % NaOH was added dropwise until a powdered granular solid formed. The THF layer was decanted and the solid layer washed with THF. Finally, THF was distilled off to give the product. The product was used without any purification.

2,2,3,3-d_4-butane-1,4-diol was purchased from Aldrich and was used without any further purification.

6.1.4. 1,1,2,2-d_4-ethylene glycol

1,1,2,2-d_4-ethylene glycol (97 D%) was purchased from Aldrich and was used without any further purification.

6.1.5. α,α,α′,α′-tetradeuteriodicarboxylic acids

All α,α,α′,α′-tetradeuteriodicarboxylic acids were prepared by the method of Atkinson *et al.*[119] The procedure was scaled down by a factor of 20 so that 25 mmol of the sodium salt was dissolved in 10 ml of D_2O containing 2.5 mmol of OD^-. This solution was heated at 150 °C in an autoclave for 24 hr. The procedure was repeated until the isotopic content was over 90 %.

2,2,7,7-d_4-suberic acid from 5.45 g (25 mmol) of disodium suberate; recrystallised twice from formic acid; yield 1.47 g (33 %), m.p. 142-4 °C (lit.[120] mp. for suberic acid 142-144°C). δ_H (200 MHz, DMSO-d_6) 1.25 (4H, m, -$CD_2CH_2C\underline{H}_2$), 1.46 (int. 28.5, 4H, t, -$CD_2C\underline{H}_2CH_2$), 2.17 (int. 0.6, t, -$C\underline{H}_2CH_2CH_2$ residue of 4H) and 11.99 (2H, s, COO$\underline{H}$). 98 atom % D from the integrals.

2,2,6,6-d_4-pimelic acid from 5.10 g (25 mmol) of disodium pimelate; recrystallised twice from formic acid; yield 1.52 g (37 %), m.p. 103-5 °C (lit.[120] mp. for pimelic acid 103-105°C). δ_H (200 MHz, DMSO-d_6) 1.28 (2H, m, -$CD_2CH_2C\underline{H}_2$), 1.47 (int. 29.3, 4H, t, -$CD_2C\underline{H}_2CH_2$), 2.17 (int. 1.6, t, -$C\underline{H}_2CH_2CH_2$ residue of 4H) and 12.00 (2H, s, COO$\underline{H}$). 95 atom % D from the integrals.

2,2,5,5-d_4-adipic acid from 4.75 g (25 mmol) of disodium adipate; recrystallised once from formic acid and once from water, yield 1.61 g (43 %), m.p. 151-154 °C (lit.[120] mp. for adipic acid 152-154°C). δ_H (200 MHz, DMSO-d_6) 1.48 (int. 78.0, 4H, s, -$CD_2C\underline{H}_2$), 2.19 (int. 2.6, t, -$C\underline{H}_2CH_2$ residue of 4H) and 12.04 (2H, s, COO$\underline{H}$). 97 atom % D from the integrals.

2,2,4,4-d_4-glutaric acid from 4.40 g (25 mmol) of disodium glutarate; recrystallised from toluene filtering NaCl off from the hot solution; yield 1.30 g (38 %), m.p. 96-98 °C (lit.[120] mp. for glutaric acid 95-98°C).. δ_H (200 MHz, DMSO-d_6) 1.67 (int. 129.3, 2H, s, $CD_2C\underline{H}_2CD_2$), 2.22 (int. 20.2, t, $C\underline{H}_2CH_2CD_2$ residue of 4H) and 12.09 (2H, s, COO$\underline{H}$). 92 atom % D from the integrals.

2,2,3,3-d_4-succinic acid from 4.05 g (25 mmol) of disodium succinate; recrystallised twice from acetone filtering NaCl off from the hot solution; yield 0.83 g (27 %), m.p. 188-191 °C (lit.[120] mp. for succinic acid 188-190°C). δ_H (200 MHz, DMSO-d_6) 2.39 (int. 8.5, s, C<u>H</u>$_2$ residue of 2H) and 12.18 (int. 75.1, 2H, s, COO<u>H</u>). 94 atom % D from the integrals.

6.1.6. 2,2,5,5-d_4-hexane-1,6-diol

5.00 g (33.3 mmol) of 2,2,5,5-d_4-adipic acid prepared as above was dissolved in 100 ml of methanol and the solution was cooled to 0 °C. 7.0 ml of thionyl chloride was added and the solution was refluxed for 5 hours. Methanol and excess of thionyl chloride were evaporated off in rotary evaporator. The remaining liquid was dissolved in 40 ml of sodium dried diethyl ether. 1.96 g (50.0 mmol) of $LiAlH_4$ was dissolved in 80 ml of sodium dried diethyl ether. The ester solution was added to the $LiAlH_4$ solution so that the mixture refluxed gently. After this addition, the mixture was refluxed on a steam bath for 10 minutes. The solid was collected by filtering the mixture using a sintered glass funnel. The ether phase was dried over $MgSO_4$. The solid was dissolved in 50 ml of 20 % H_2SO_4. The solution was extracted 8 times with 50 ml of diethyl ether. Ether phases were combined and dried over $MgSO_4$. After drying, ether was evaporated off in rotary evaporator. After removal of ether, a liquid remained. Ether was added to this liquid and the evaporation was repeated. A white solid remained. After drying in vacuum desiccator, this solid was used without any further purification. Yield 3.39 g (83 % from the acid).

6.1.7. Acid chlorides

p-Chlorobenzoyl chloride was obtained from a departmental store and was redistilled at 116-118 °C.

50 g (0.30 mol) of *p*-nitrobenzoic acid (BDH, 99 %) was mixed with 66 g (0.30 mol) of phosphorus pentachloride (Aldrich, 95 %) in a 250 ml round-bottomed flask. A

$CaCl_2$-tube was fitted to the flask, and the mixture was heated on a boiling water bath until the reaction took place. A pale yellow liquid formed. The mixture was heated for additional 30 mins. A Claisen distillation head was connected to the flask, and $POCl_3$ was distilled off at atmospheric pressure heating in an oil bath. After cooling, an air condenser was attached, and *p*-nitrobenzoyl chloride was distilled at 155 °C under water pump pressure. The liquid product was poured into a wide-mouthed bottle and allowed to solidify. Yield 48.9 g (88 %).

All other acid chlorides were prepared by refluxing the corresponding acid with an excess of thionyl chloride (ratio was 3.0 ml of thionyl chloride to 1.0 g of acid) until the evolution of hydrogen chloride was finished and then for an additional 10 minutes. The excess of thionyl chloride was removed by vacuum distillation, and acid chlorides were used without any further purification.

6.1.8. α,ω-Alkanediyl diesters

All diesters were prepared using a method similar to that of Heim and Poe[121] by adding two equivalents or a slight excess of liquid acid chloride or solid acid chloride dissolved 1,4-dioxane into a solution of one equivalent of diol and two equivalents of pyridine. During addition, heat was generated and pyridine hydrochloride precipitated. The mixture was stirred for an hour and then poured into distilled water with vigorous stirring. The white solid was collected by Buchner filtration. After drying, it was recrystallised from a suitable solvent.

Hexane-1,6-diyl bis(*p*-nitrobenzoate) from 0.60 g (5.0 mmol) of 1,6-hexanediol and 1.86 g (10 mmol) of *p*-nitrobenzoyl chloride: recrystallised twice from EtOAc-EtOH: yield 0.98 g (47 %), m.p. 121.5-122.5 °C (lit.[122] m.p. 120 °C). Found: C, 57.81; H, 4.67; N, 6.68. Calc. for $C_{20}H_{20}N_2O_8$: C, 57.69; H, 4.84%. δ_H (200 MHz; $CDCl_3$) 1.55 (4H, m, $OCH_2CH_2C\underline{H}_2$) 1.85 (4H, m, $OCH_2C\underline{H}_2CH_2$) 4.40 (4H, t, $OC\underline{H}_2CH_2CH_2$) and 8.25 (8H, m, aromatic). Crystals for single crystal x-ray diffraction were obtained by slow evaporation from CH_2Cl_2-acetone (1:1) solution. Structural parameters are listed in the appendix.

1,1,6,6-d_4-hexane-1,6-diyl bis(*p*-nitrobenzoate) from 0.75 g (6.1 mmol) of 1,1,6,6-d_4-hexane-1,6-diol and 2.78 g (15.0 mmol) of *p*-nitrobenzoyl chloride. The product was recrystallised twice from EtOAc-EtOH: yield 1.50 g (58 %), m.p. 121-122 °C; δ_H (200 MHz; $CDCl_3$) 1.55 (4H, m, $OCD_2CH_2C\underline{H}_2$) 1.84 (4H, t, $OCD_2C\underline{H}_2CH_2$) and 8.25 (8H, m, aromatic).

2,2,5,5-d_4-hexane-1,6-diyl bis(*p*-nitrobenzoate) from 0.45 g (3.7 mmol) of 2,2,5,5-d_4-hexane-1,6-diol and 1.37 g (7.4 mmol) of p-nitrobenzoyl chloride: recrystallised twice from EtOAc-EtOH; yield 1.10 g (71 %); m.p. 121-122 °C; δ_H (200 MHz; $CDCl_3$) 1.54 (4H, s, $OCH_2CD_2C\underline{H}_2$) 4.39 (4H, s, $OC\underline{H}_2CD_2CH_2$) and 8.25 (8H, m, aromatic).

Hexane-1,6-diyl bis(*p*-chlorobenzoate) from 0.44 g (99%, 3.7 mmol) of 1,6-hexanediol and 1.30 g (7.4 mmol) of *p*-chlorobenzoyl chloride: recrystallised from aq. MeOH. Yield 0.89 g (63 %), mp 78-80 °C, found: C, 60.51; H, 4.86. Calc. for $C_{20}H_{20}Cl_2O_4$: C, 60.77; H, 5.10%. δ_H (200 MHz; $CDCl_3$) 1.52 (4H, m, $OCH_2CH_2C\underline{H}_2$) 1.81 (4H, m, $OCH_2C\underline{H}_2CH_2$) 4.33 (4H, t, $OC\underline{H}_2CH_2CH_2$), 7.41 (4H, m, aromatic 3,5-pos.) and 7.96 (4H, m, aromatic 2,6-pos).

1,1,6,6-d_d-hexane-1,6-diyl bis(*p*-chlorobenzoate) from 0.45 g (3.7 mmol) of 1,1,6,6-d_4-hexane-1,6-diol and 1.30 g (7.4 mmol) of *p*-chlorobenzoyl chloride: recrystallised from aq. MeOH; yield 0.72 g (51 %); m.p. 78-80 °C. δ_H (200 MHz; $CDCl_3$) 1.51 (4H, m, $OCD_2CH_2C\underline{H}_2$) 1.79 (4H, t, $OCD_2C\underline{H}_2CH_2$), 7.40 (4H, m, aromatic 3,5-pos.) and 7.97 (4H, m, aromatic 2,6-pos).

2,2,5,5-d_4-hexane-1,6-diyl bis(*p*-chlorobenzoate) from 0.45 g (3.7 mmol) of 2,2,5,5-d_4-hexane-1,6-diol and 1.30 g (7.4 mmol) of *p*-chlorobenzoyl chloride: recrystallised from aq. MeOH; yield 0.87 g (61 %); m.p. 78-80 °C; δ_H (200 MHz; $CDCl_3$) 1.51 (4H, s, $OCH_2CD_2C\underline{H}_2$), 4.32 (4H, s, $OC\underline{H}_2CD_2CH_2$), 7.41 (4H, m, aromatic 3,5-pos.) and 7.96 (4H, m, aromatic 2,6-pos).

Hexane-1,6-diyl bis(*o*-chlorobenzoate) from 0.60 g (99 %, 5.0 mmol) of 1,6-hexanediol and 1.78 g (10 mmol) of *o*-chlorobenzoyl chloride: recrystallised from

aq. MeOH; yield 1.15 g (58 %); m.p. 50-52 °C, found: C, 60.75; H, 4.82. Calc. for $C_{20}H_{20}Cl_2O_4$: C, 60.77; H, 5.10%. δ_H (200 MHz; $CDCl_3$) 1.54 (4H, m, $OCH_2CH_2C\underline{H}_2$), 1.81 (4H, m, $OCH_2C\underline{H}_2CH_2$), 4.36 (4H, t, $OC\underline{H}_2CH_2CH_2$), 7.29-7.49 (6H, m, aromatic) and 7.79-7.84 (2H, m, aromatic).

1,1,6,6-d_4-hexane-1,6-diyl bis(*o*-chlorobenzoate) from 0.60 g (4.9 mmol) of 1,1,6,6-d_4-hexane-1,6-diol and 1.78 g (10 mmol) of *o*-chlorobenzoyl chloride: recrystallised from aq. MeOH; yield 0.53 g (27 %); m.p. 50-52 °C. δ_H (200 MHz; $CDCl_3$) 1.54 (4H, m, $OCD_2CH_2C\underline{H}_2$), 1.79 (4H, t, $OCD_2C\underline{H}_2CH_2$), 7.28-7.48 (6H, m, aromatic) and 7.79-7.83 (2H, m, aromatic 6-pos).

Hexane-1,6-diyl bis(3,5-dimethoxybenzoate) from 0.36 g of 1,6-hexanediol (99 %, 3.0 mmol) and 1.20 g (6.0 mmol) of 3,5-dimethoxybenzoyl chloride: recrystallised from aq. MeOH; yield 0.89 g (66 %); m.p. 108-110 °C; found: C, 64.44; H, 6.98. Calc. for $C_{24}H_{30}O_8$: C, 64.56; H, 6.77%. δ_H (200 MHz; $CDCl_3$) 1.52 (4H, m, $OCH_2CH_2C\underline{H}_2$), 1.80 (4H, m, $OCH_2C\underline{H}_2CH_2$), 3.83 (12H, s, $OC\underline{H}_3$), 4.32 (4H, t, $OC\underline{H}_2CH_2CH_2$), 6.64 (2H, t, aromatic 4-pos.) and 7.18 (4H, d, aromatic 2- and 6-pos.). Crystals for single crystal x-ray diffraction were obtained by slow evaporation from CH_2Cl_2-acetone (1:1) solution. Structural details are given in the appendix.

1,1,6,6-d_4-hexane-1,6-diyl bis(3,5-dimethoxybenzoate) from 0.55 g (4.5 mmol) of 1,1,6,6-d_4-hexane-1,6-diol and 1.80 g (9.0 mmol) of 3,5-dimethoxybenzoyl chloride; recrystallised from aq. MeOH; yield 0.71 g (35 %); m.p. 108-109 °C; δ_H (200 MHz; $CDCl_3$) 1.52 (4H, m, $OCD_2CH_2C\underline{H}_2$), 1.79 (4H, t, $OCD_2C\underline{H}_2CH_2$), 3.83 (12H, s, $OC\underline{H}_3$), 6.64 (2H, t, aromatic 4-pos.) and 7.19 (4H, d, aromatic 2- and 6-pos.).

Pentane-1,5-diyl bis(*p*-nitrobenzoate) from 0.88 g (8.1 mmol) of 1,5-pentanediol and 3.15 g (17 mmol) of *p*-nitrobenzoyl chloride; recrystallised from EtOH; Yield 2.42 g (74 %), m.p. 102-104 °C (lit. m.p.[123] 104 °C), found: C, 57.02; H, 4.51; N, 6.82. Calc. for $C_{19}H_{18}N_2O_8$: C, 56.72; H, 4.51; N, 6.96%. δ_H (200 MHz; $CDCl_3$) 1.66 (2H, m, $OCH_2CH_2C\underline{H}_2$), 1.91 (4H, m, $OCH_2C\underline{H}_2CH_2$), 4.42 (4H, t, $OC\underline{H}_2CH_2CH_2$) and 8.25 (8H, m, aromatic). Crystals for x-ray diffraction were obtained by slow

evaporation from CH_2Cl_2-acetone (3:1) solution. Crystals were left to Dr. Phil Lightfoot for x-ray structure determination but no structure was obtained.

1,1,5,5-d_4-pentane-1,5-diyl bis(*p*-nitrobenzoate) from 0.88 g (8.1 mmol) of 1,1,5,5-d_4-pentane-1,5-diol and 3.15 g (17 mmol) of *p*-nitrobenzoyl chloride: recrystallised twice from EtOH; yield 1.73 g (53 %); m.p. 102-104 °C. δ_H (200 MHz; $CDCl_3$) 1.63 (2H, m, $OCD_2CH_2C\underline{H}_2$), 1.90 (4H, t, $OCD_2C\underline{H}_2CH_2$) and 8.24 (8H, m, aromatic).

Butane-1,4-diyl bis(*p*-nitrobenzoate) from 0.45 g (5.0 mmol) of 1,4-butanediol and 1.86 g (10 mmol) of *p*-nitrobenzoyl chloride: recrystallised twice from glacial acetic acid and once from EtOAc; yield 0.53 g (27 %); m.p. 174-176 °C (lit.[123] m.p. 175 °C). δ_H (200 MHz; $CDCl_3$) 2.00 (4H, m, $OCH_2C\underline{H}_2$), 4.48 (4H, t, $OC\underline{H}_2CH_2$) and 8.26 (8H, m, aromatic).

1,1,4,4-d_4-butane-1,4-diyl bis(*p*-nitrobenzoate) from estimated 0.47 g (5.0 mmol) of 1,1,4,4-d_4-butane-1,4-diol and 1.86 g (10 mmol) of *p*-nitrobenzoyl chloride: recrystallised once from glacial acetic acid and once from EtOAc; yield 0.2 g (10 %); m.p. 174-175°C. δ_H (200 MHz; $CDCl_3$) 1.26 (4H, s, $OCD_2C\underline{H}_2$) and 8.26 (8H, m, aromatic)

2,2,3,3-d_4-butane-1,4-diyl bis(*p*-nitrobenzoate) from 0.33 g (3.5 mmol) of 2,2,3,3-d_4-butane-1,4-diol and 1.48 g (8.0 mmol) of *p*-nitrobenzoyl chloride; recrystallised twice from glacial acetic acid and once from EtOAc; yield 0.31 g (22 %); m.p. 174-176 °C. δ_H (200 MHz; $CDCl_3$) 4.47 (4H, s, $OC\underline{H}_2CD_2$) and 8.27 (8H, m, aromatic).

Butane-1,4-diyl bis(*m*-chlorobenzoate) from 0.45 g (5.0 mmol) of 1,4-butanediol and 1.93 g (11 mmol) of *m*-chlorobenzoyl chloride: recrystallised from acetone; yield 0.48 g (26 %); m.p. 93-95 °C; found: C, 59.06; H, 4.24. Calc. for $C_{18}H_{16}O_4Cl_2$: C, 58.87; H, 4.39%. δ_H (200 MHz; $CDCl_3$) 1.95 (4H, m, $OCH_2C\underline{H}_2$), 4.41 (4H, t, $OC\underline{H}_2CH_2$), 7.39 (2H, t, aromatic 5-pos.), 7.51-7.57 (2H, m, aromatic 4-pos), 7.91-7.95 (2H, m, aromatic 6-pos) and 8.01 (2H, t, aromatic 2-pos).

2,2,3,3-d_4-butane-1,4-diyl bis(*m*-chlorobenzoate) from 0.33 g (3.5 mmol) of 2,2,3,3-d_4-butane-1,4-diol and 1.40 g (8.0 mmol) of *m*-chlorobenzoyl chloride): recrystallised from acetone; yield 1.01 g (78 %); m.p. 93-95 °C; δ_H (200 MHz; $CDCl_3$) 4.40 (4H, s, $OC\underline{H}_2CD_2$), 7.38 (2H, t, aromatic 5-pos.), 7.51-7.56 (2H, m, aromatic 4-pos), 7.90-7.95 (2H, m, aromatic 6-pos) and 8.01 (2H, t, aromatic 2-pos).

Butane-1,4-diyl bis(3,5-dimethoxybenzoate) from 0.27 g (3.0 mmol) of 1,4-butanediol and 1.20 g (6.0 mmol) of 3,5-dimethoxybenzoyl chloride; recrystallised from aq. MeOH; yield 0.55 g (44 %); m.p. 117-118 °C; found: C, 63.42; H, 6.47. Calc. for $C_{22}H_{26}O_8$: C, 63.15; H, 6.26%. δ_H (200 MHz; $CDCl_3$) 1.94 (4H, m, $OCH_2C\underline{H}_2$), 3.83 (12H, s, $OC\underline{H}_3$), 4.39 (4H, t, $OC\underline{H}_2CH_2$), 6.65 (2H, t, aromatic 4-pos.) and 7.18 (4H, d, aromatic 2- and 6-pos.). Crystals for single crystal x-ray diffraction was obtained by slow evaporation from CH_2Cl_2-acetone (1:1) solution. Structural details are listed in the appendix.

1,1,4,4-d_4-butane-1,4-diyl bis(3,5-dimethoxybenzoate) from estimated 0.47 g (5.0 mmol) of 1,1,4,4-d_4-butane-1,4-diol and 2.61 g (13 mmol) of 3,5-dimethoxybenzoyl chloride: repeatedly recrystallised from aq. MeOH; yield 0.2 g (9.5 %); m.p. 116-117 °C. δ_H (200 MHz; $CDCl_3$) 1.92 (4H, s, $OCD_2C\underline{H}_2$), 3.83 (12H, s, $OC\underline{H}_3$), 6.65 (2H, t, aromatic 4-pos.) and 7.18 (4H, d, aromatic 2- and 6-pos.).

2,2,3,3-d_4-butane-1,4-diyl bis(3,5-dimethoxybenzoate) from 0.33 g (3.5 mmol) of 2,2,3,3-d_4-butane-1,4-diol and 1.60 g (8.0 mmol) of 3,5-dimethoxybenzoyl chloride; yield 0.81 g (55 %); m.p. 117-118 °C; δ_H (200 MHz; $CDCl_3$) 3.83 (12H, s, $OC\underline{H}_3$), 4.38 (4H, s, $OC\underline{H}_2CD_2$), 6.65 (2H, t, aromatic 4-pos.) and 7.18 (4H, d, aromatic 2- and 6-pos.).

Ethane-1,2-diyl bis(*p*-chlorobenzoate) from 0.33 g (5.3 mmol) of ethylene glycol and 1.93 g (11 mmol) of *p*-chlorobenzoate: recrystallised from a solution of petroleum ether (60:80) and EtOAc; yield 1.35 g (75 %); m.p. 143-145 °C (lit.[121] m.p. 140 °C). Found: C, 56.53, 3.42 %H. Calc. for $C_{16}H_{12}O_4Cl_2$: C, 56.66; H, 3.57%. δ_H (200 MHz; $CDCl_3$) 4.33 (4H, s, $OC\underline{H}_2$), 7.42 (4H, m, aromatic 3,5-pos.) and 7.98 (4H, m, aromatic 2,6-pos.).

1,1,2,2-d_4-ethane-1,2-diyl bis(*p*-chlorobenzoate) from 0.33 g (5.0 mmol) of 1,1,2,2-d_4-ethylene glycol and 1.93 g (11 mmol) of *p*-chlorobenzoyl chloride: yield 1.17 g (68 %); m.p. 143-145 °C; δ_H (200 MHz; $CDCl_3$) 7.42 (4H, m, aromatic 3,5-pos.) and 7.98 (4H, m, aromatic 2,6-pos).

Ethane-1,2-diyl bis(*p*-methylbenzoate) from 0.33 g (5.3 mmol) of ethylene glycol and 1.70 g (11 mmol) of *p*-methylbenzoyl chloride; recrystallised from petroleum ether (60:80), yield 1.18 g (75 %), m.p. 117-118 °C (lit.[116] m.p. 117 °C); found: C, 72.46; H, 5.84. Calc. for $C_{18}H_{18}O_4$: C, 72.47; H, 6.08%. δ_H (200 MHz; $CDCl_3$) 2.40 (6H, s, $C\underline{H}_3$), 4.64 (4H, s, $OC\underline{H}_2$), 7.24 (4H, d, aromatic 3,5-pos.) and 7.95 (4H, d, aromatic 2,6-pos.).

1,1,2,2-d_4-ethane-1,2-diyl bis(*p*-methylbenzoate) from 0.33 g (5.0 mmol) of 1,1,2,2-d_4-ethylene glycol and 1.70 g (11 mmol) of *p*-methylbenzoyl chloride: yield 1.22 g (81 %); m.p. 117-118 °C; δ_H (200 MHz; $CDCl_3$) 2.41 (6H, s, $C\underline{H}_3$), 7.24 (4H, d, aromatic 3,5-pos.) and 7.95 (4H, d, aromatic 2,6-pos.).

Ethane-1,2-diyl bis(*m*-chlorobenzoate) from 0.33 g (5.3 mmol) of ethylene glycol and 1.93 g (11 mmol) of *m*-chlorobenzoyl chloride; recrystallised from petroleum ether: yield 0.96 g (53 %); m.p. 98-100 °C (lit.[121] m.p. 91°C); found: C, 56.84; H, 3.28. Calc. for $C_{16}H_{12}O_4Cl_2$: C, 56.66; H, 3.57%. δ_H (200 MHz; $CDCl_3$) 4.67 (4H, s, $OC\underline{H}_2$), 7.39 (2H, t, aromatic 5-pos.), 7.52-7.58 (2H, m, aromatic 4-pos), 7.92-7.96 (2H, m, aromatic 6-pos) and 8.03 (2H, t, aromatic 2-pos).

1,1,2,2-d_4-ethane-1,2-diyl bis(*m*-chlorobenzoate) from 0.33 g (5.0 mmol) of 1,1,2,2-d_4-ethylene glycol and 1.93 g (11 mmol) of m-chlorobenzoyl chloride; yield 1.48 g (86 %) : m.p. 98-100 °C. δ_H (200 MHz; $CDCl_3$) 7.40 (2H, t, aromatic 5-pos.), 7.53-7.58 (2H, m, aromatic 4-pos), 7.92-7.97 (2H, m, aromatic 6-pos) and 8.03 (2H, t, aromatic 2-pos)

6.1.9. Dibenzenesulfonates and tosylates.

Dibenzenesulfonates and tosylates were prepared by adding a solution of benzenesulfonyl chloride or tosyl chloride in pyridine into a solution of a diol in pyridine at 0 °C. The solutions were stirred for 5 hours and then 2 M HCl was added. The solid that precipitated was collected by Buchner filtration. After drying, it was recrystallised from a suitable solvent.

Hexane-1,6-diyl dibenzenesulfonate from 0.60 g (99%, 5.0 mmol) of 1,6-hexanediol and 1.94 g (11 mmol) of benzenesulfonyl chloride; recrystallised from EtOH; yield 0.88 g (44 %); m.p. 59-61 °C. Found: C, 54.05, H, 5.40. Calc. for $C_{18}H_{22}S_2O_6$: C, 54.25; H, 5.56%. δ_H (200 MHz; $CDCl_3$) 1.27 (4H, m, $OCH_2CH_2C\underline{H}_2$) 1.60 (4H, m, $OCH_2C\underline{H}_2CH_2$) 4.01 (4H, t, $OC\underline{H}_2CH_2CH_2$), 7.52-7.71 (6H, m, aromatic 3,4,5-pos.) and 7.88-7.93 (4H, m, aromatic 2,6-pos.). Crystals for single crystal x-ray diffraction were obtained by slow evaporation from CH_2Cl_2 solution. Structural parameters are listed in the appendix.

1,1,6,6-d_4-hexane-1,6-diyl dibenzenesulfonate from 0.60 g (5.0 mmol) of 1,1,6,6-d_4-hexane-1,6-diol and 1.94 g (11 mmol) of benzenesulfonyl chloride; yield 1.34 g (67 %); m.p. 59-61 °C; δ_H (200 MHz; $CDCl_3$) 1.26 (4H, m, $OCD_2CH_2C\underline{H}_2$), 1.59 (4H, t, $OCD_2C\underline{H}_2CH_2$), 7.52-7.71 (6H, m, aromatic 3,4,5-pos.) and 7.88-7.93 (4H, m, aromatic 2,6-pos.)

2,2,5,5-d_4-hexane-1,6-diyl dibenzenesulfonate from 0.45 g (3.7 mmol) of 2,2,5,5-d_4-hexane-1,6-diol and 1.41 g (8.0 mmol) of benzenesulfonyl chloride; recrystallised from EtOH; yield 0.57 g (38 %); m.p. 59-61 °C; δ_H (200 MHz; $CDCl_3$) 1.25 (4H, s, $OCH_2CD_2C\underline{H}_2$), 4.00 (4H, s, $OC\underline{H}_2CD_2CH_2$), 7.52-7.71 (6H, m, aromatic 3,4,5-pos.) and 7.88-7.93 (4H, m, aromatic 2,6-pos.)

Hexane-1,6-diyl ditosylate from 0.60 g (99%, 5.0 mmol) of 1,6-hexanediol and 2.10 g (11 mmol) of tosyl chloride; recrystallised from EtOH; yield 1.37 g (64 %); m.p. 71.5-73.5 °C (lit.[124] m.p. 71-72 °C); found: C, 56.17; H, 6.22. Calc. for $C_{20}H_{26}S_2O_6$: C, 56.32; H, 6.14%. δ_H (200 MHz; $CDCl_3$) 1.26 (4H, m, $OCH_2CH_2C\underline{H}_2$), 1.59 (4H,

m, $OCH_2C\underline{H}_2CH_2$), 2.46 (6H, s, $\underline{C}H_3$), 3.98 (4H, t, $OC\underline{H}_2CH_2CH_2$), 7.35 (4H, d, aromatic 3,5-pos.) and 7.78 (4H, d, aromatic 2,6-pos.). Crystals for single crystal x-ray diffraction were obtained by slow evaporation from CH_2Cl_2 solution. Structural parameters are listed in the appendix.

1,1,6,6-d_4-hexane-1,6-diyl ditosylate from 0.60 g (4.9 mmol) of 1,1,6,6-d_4-hexane-1,6-diol and 2.10 g (11 mmol) of tosyl chloride; recrystallised from EtOH; yield 1.45 g (68 %); m.p. 71.5-73.5 °C. δ_H (200 MHz; $CDCl_3$) 1.26 (4H, m, $OCD_2CH_2C\underline{H}_2$), 1.58 (4H, t, $OCD_2C\underline{H}_2CH_2$), 2.45 (6H, s, $\underline{C}H_3$), 7.35 (4H, d, aromatic 3,5-pos.) and 7.78 (4H, d, aromatic 2,6-pos.).

2,2,5,5-d_4-hexane-1,6-diyl ditosylate from 0.45 g (3.7 mmol) of 2,2,5,5-d_4-hexane-1,6-diol and 1.52 g (8.0 mmol) of tosyl chloride; recrystallised from EtOH; yield 1.01 g (63 %); m.p. 71.5-73.5 °C; δ_H (200 MHz; $CDCl_3$) 1.25 (4H, s, $OCH_2CD_2C\underline{H}_2$), 2.46 (6H, s, $\underline{C}H_3$), 3.97 (4H, s, $OC\underline{H}_2CD_2CH_2$), 7.35 (4H, d, aromatic 3,5-pos.) and 7.78 (4H, d, aromatic 2,6-pos.).

6.2. INSTRUMENTATION

6.2.1. Melting point, ^{1}H NMR, elemental analysis and DSC.

All melting points were measured on an Electrothermal melting point apparatus and are uncorrected. All ^{1}H NMR solution spectra were obtained on a Varian Gemini 200 operating at 200.052 MHz. The spectra were referenced to TMS (0 ppm) as an internal standard. All elemental analyses were made by Mrs. S. Smith using a Carlo-Erba 1106 analyser. All differential scanning calorimetry measurements were made on a Perkin-Elmer DSC7 differential scanning calorimeter.

6.2.2. X-ray diffraction

All single crystal x-ray measurements and structure refinements were made by Dr. Phil Lightfoot. The data was collected on a Rigaku AFC7S diffractometer with graphite monochromated Mo-K_α radiation. The structures were solved by direct methods and expanded using Fourier techniques. The non-hydrogen atoms were refined anisotropically. Hydrogen atoms were included but not refined. All powder x-ray diffraction patterns were measured on a STOE powder diffraction system.

6.2.3. ^{13}C CP/MAS spectra

^{13}C CP/MAS spectra were obtained on a Brüker MSL500 spectrometer at 125.758 MHz using 4 mm o.d. zirconia rotors. Chemical shifts were referenced to the CH_2 resonance in an external adamantane sample at 38.56 ppm. ^{13}C $T_{1\rho}$ measurements were made using a standard CP sequence. The ^{13}C CP/MAS probe had been calibrated before using well-known phase changes.[49] Actual temperatures were calculated from the equation

$$T = 0.799 \cdot T(VTU) + 62.183 \qquad (6.1.)$$

^{13}C T_1 relaxation times were measured with a modified ^{13}C CP/MAS inversion-recovery sequence of Torchia.[43] The pulse sequence of Torchia involves continuous proton decoupling during the variable delay but the maximum time of decoupling with the power level needed for effective decoupling was estimated to be only *ca.* 0.5 s. Because this was not long enough for the ^{13}C T_1 measurements, a modification similar to that of Gabrys *et al.*[113] was used to replace the continuous decoupling with a train of saturating 90° pulses.

6.2.4. ^2H quadrupolar echo spectra

^2H quadrupolar echo spectra were measured using a MAS probe made by Doty Scientific Inc. Samples were packed into sapphire (Al_2O_3) rotors, and inserted into the stator block with a small pieces of paper to prevent sample spinning during variable temperature operation. Between room temperature and 330 K air was used as a heating gas whereas nitrogen gas was used above 330 K. Below room temperature, nitrogen gas was cooled with heat exchanger in a liquid nitrogen dewar. A flow of room temperature air was used to keep the electrical circuits at room temperature during the variable temperature operation. The 90° pulse length was determined with the multipulse tune-up sequences of Gernstein[125].

The spectra were measured with a standard quadrupolar echo sequence $90°_{\pm x}$-τ_1-$90°_{\pm y}$-τ_2-acq. Receiver phase followed the phase of the first 90° pulse and was adjusted so that the imaginary part of the signal was zero. Typical parameters used: 90° pulse length ca. 3.8-3.9 μs, τ_1 20 μs or 160 μs, τ_2 shorter than τ_1 so that the top of the echo was clearly visible, dwell time 0.2 μs (spectral width 2.5 MHz), filter width 5.0 MHz, 1024 - 3800 data points and recycle delay from 200 ms to 100 s with the standard quadrupolar echo pulse sequence and up to 1000 s with a modified pulse sequence. In the modified sequence, variable D0 for the recycling delay was replaced with a loop giving C1×D0 for the recycle delay. Before Fourier transformation, the fid was left-shifted to start at the top of the echo, the data were zero filled to 8192 data points and 1.0 kHz of Lorenzian line broadening was applied.

All ^{2}H quadrupolar echo spectra were measured on resonance. In separate experiments, the carrier frequency was set off-resonance to determine if the central peak was a phase glitch. In these experiments, the sharp peak remained in the centre of the powder pattern and did not follow the carrier frequency. This indicates that the sharp peak is an integral part of the powder pattern and not a phase glitch.

^{2}H spin-lattice relaxation times were measured using the saturation recovery method using quadrupolar echo detection similar to that of Hirschinger *et al.*[67] The pulse sequence was [90°-τ_0-]-90°-vd-90°-τ_1-90°-τ_2-acq. Where the delay τ_0 was 3 ms, variable delay vd was varied from 1 ms to 100 s, τ_1 was 20 μs and τ_2 shorter than t1 so that the top of echo was clearly visible. A short recycle delay of 200 ms was used to avoid any heating effects. ^{2}H spin-lattice relaxation times were calculated from the evolution of echo height as a function of the variable delay.

The probe was temperature calibrated by measuring the ^{27}Al spin-lattice relaxation time of an aluminum powder sample in the whole temperature range from 110 K to 400 K and then calculating the calibrated temperature T(cal) from

$$T(cal) = \frac{T_{1,293K} \cdot 293K}{T_1(meas.)} \qquad (6.2.)$$

Measured spin-lattice relaxation times are listed in table 6.1. together with calibrated temperatures. Figure 6.1. shows calibrated temperature as a function of the reading on the variable temperature unit together with the best least-squares line. The equation of the least-squares line is

$$T(cal) / K = 0.9711 \cdot T(vtu) + 4.283 \qquad (6.3.)$$

This equation was used to correct all temperatures when using the Doty probe.

Table 6.1. Measured ^{27}Al spin-lattice relaxation times.

T(vtu)/K	^{27}Al T_1/ms	T(cal)/K
108.8	17.452	102
122.0	15.570	114
130.0	14.095	126
140.0	13.036	137
150.0	12.288	145
160.0	11.106	160
170.0	10.561	169
180.0	9.6572	184
190.0	9.1483	195
200.0	8.6311	206
210.0	8.8378	201
220.0	8.1566	218
230.0	7.7489	230
240.0	7.3432	242
250.0	6.9940	254
260.0	6.7627	263
270.0	6.5907	270
280.0	6.2850	283
292.8	6.0789	293
300.0	5.8969	302
310.0	5.7366	310
320.0	5.5763	319
330.0	5.4849	325
340.0	5.3098	335
350.0	5.2127	341
360.0	5.0482	353
370.0	4.8821	365
380.0	4.7886	372
390.0	4.6882	380
400.0	4.6021	387
410.0	4.4859	397
420.0	4.3817	406

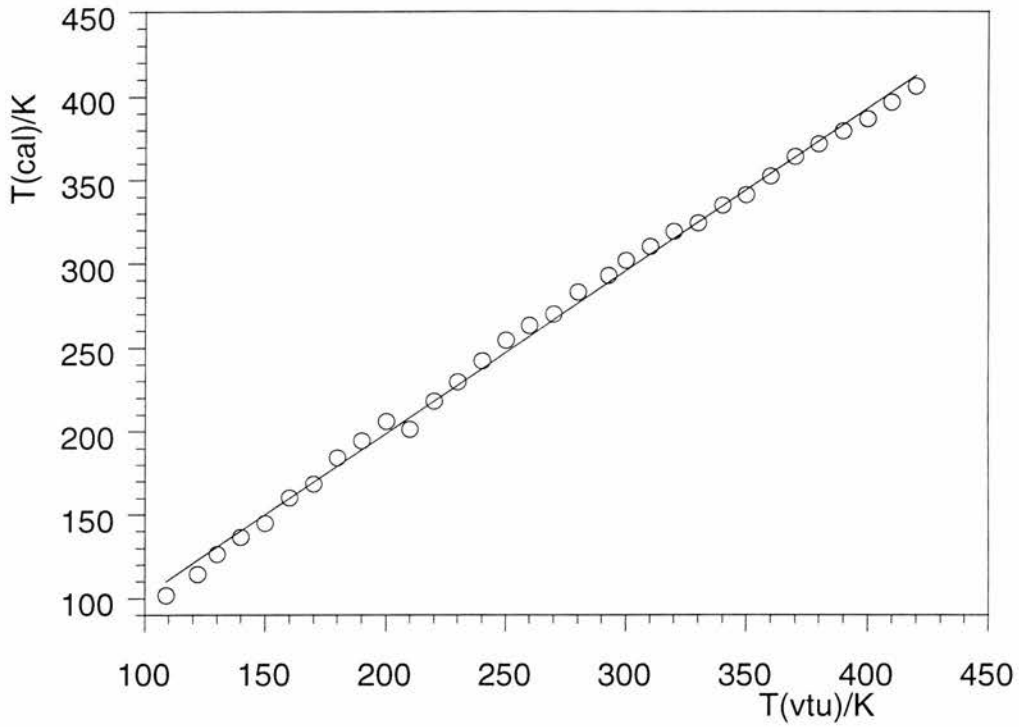

Figure 6.1. Calibrated temperature as a function of the reading on the variable temperature unit (vtu).

6.2.5. ^{2}H quadrupolar echo line shape simulations

The program MXET1 of Greenfield *et al.*[30] was compiled to a Sun Sparcstation 4 workstation. The parameter nbits in the main program was set to 52 which is the number of bits in the mantissa of the floating point representation excluding a sign bit. The parameter radix in the subprogram cbal was set to 2, the base number of the floating point representation. The program was compiled with f77 compiler. The compiler options -xtarget=ss5 and -O were used to optimise the code. The calculation time depended strongly on the number of exchange sites and powder orientations. Typically, a two-site exchange simulation took *ca.* 3 minutes for 400 powder orientations. For the conical libration model, the program was modified to write the Euler angle θ and the calculated (not normalised) fid into a file. A program was written to sum these raw files, calculated with different angles θ, according to eq. 3.14 and then write the resultant fid to an output file. This resultant fid was then apodised and Fourier transformed with routines extracted from the MXET1 program to obtain the spectrum.

REFERENCES

1. Harris K. D. M. and Aliev A. E., *Chem. Br.*, **1995**, 31, 132.
2. Perrin C. L. and Dwyer T. J., *Chem. Rev.*, **1990**, 90, 935.
3. Chmelka B. F. and Pines A., *Science*, **1989**, 246, 71.
4. Gray F. M., *Solid Polymer Electrolytes*, VCH Publishers, New York, 1991.
5. Blythe A. R., *Electrical Properties of Polymers*, Cambridge University Press, Cambridge, 1979.
6. Blümler P. and Blümich B., *Spectroscopy Europe*, **1995**, 7, 8.
7. Schaefer J., Stejskal E. O. and Buchdal R., *Macromolecules*, **1975**, 8, 291.
8. Fyfe C. A., *Solid State NMR for Chemists*, C. F. C. Press, Ontario, Canada, 1983.
9. Bovey F. A. and Jelinski L. W., *J. Phys. Chem.*, **1985**, 89, 571-583.
10. Vega A. J., 'Quadrupolar Nuclei in Solids' in *Encyclopedia of Nuclear Magnetic Resonance*, vol. 6, 3668, eds. Grant D. M. and Harris R. K., Wiley, Chichester, 1996.
11. Batchelder L. S., 'Deuterium NMR in Solids', in *Encyclopedia of Nuclear Magnetic Resonance*, vol. 3, 1574, eds. Grant D. M. and Harris R. K., Wiley, Chichester, 1996.
12. Bovey F. A., *Polym. Eng. Sci*, **1996**, 26, 1419-1428.
13. Henrichs P. M. and Hewitt J. M., 'Solid-State Nuclear Magnetic Resonance', in *Physical Methods of Chemistry*, vol. 5, 345, eds. Rossiter B. W. and Hamilton J. F., Wiley, New York, 1990.
14. Yannoni C. S., *Acc. Chem. Res.*, **1982**, 15, 201.
15. Schaefer J. and Stejskal E. O., 'High-Resolution ^{13}C NMR of Solid Polymers', in *Topics in Carbon-13 NMR Spectroscopy*, vol. 3, 283, ed. G. C. Levy, Wiley, New York, 1979.
16. Cheung T. T. P., 'Spin Diffusion in Solids', in *Encyclopedia of Nuclear Magnetic Resonance*, vol. 7, 4518, eds. Grant D. M. and Harris R. K., Wiley, Chichester, 1996.

17. Burum D. P., 'Cross Polarization in Solids', in *Encyclopedia of Nuclear Magnetic Resonance*, vol. 3, 1535, eds. Grant D. M. and Harris R. K., Wiley, Chichester, 1996.

18. Engelke F., 'Cross Polarization in Rotating Solids: Spin-1/2 Nuclei', in *Encyclopedia of Nuclear Magnetic Resonance*, vol. 3, 1529, eds. Grant D. M. and Harris R. K., Wiley, Chichester, 1996.

19. Pines A., Gibby M. G. and Waugh J. S., *J. Chem. Phys.*, **1973**, 53, 569.

20. Tegenfeldt J. and Haberlen U., *J. Magn. Reson.*, **1979**, 36, 453-457.

21. Sandström, J., *Dynamic NMR Spectroscopy*, Academic Press, London, 1982.

22. Rothwell W. P. and Waugh J. S., *J. Chem. Phys.*, **1981**, 74, 2721.

23. Everatt B., Harris R. K., Kenwright A. M., Packer K. J. and Stark B. P., *Magn. Reson. in Chem.*, **1987**, 25, 80.

24. Twyman J. M. and Dobson C. M., *J. Chem. Soc., Chem. Commun.*, **1988**, 786.

25. Long J. R., Sun B. Q., Bowen A. and Griffin R. G., *J. Am. Chem. Soc.*, **1994**, 116, 11950-11956.

26. Roy A. K. and Inglefield P. T., *Prog. Nucl. Mag. Res. Spectrosc.*, **1990**, 22, 569-603.

27. Müller K., Meier P. and Kothe G., *Prog. Nucl. Mag. Res. Spectrosc.*, **1985**, 17, 211-239.

28. Henrichs P. M., Hewitt J. M. and Linder M., *J. Magn. Reson.*, **1984**, 60, 280-298.

29. Ronemus A. D., Vold R. L. and Vold R. R., *J. Magn. Reson.*, **1986**, 70, 416-426.

30. Greenfield M. S., Ronemus A. D., Vold R. L., Vold R. R.,Ellis P. D. and Raidy T. E., *J. Magn. Reson.*, **1987**, 72, 89-107.

31. Schmidt C., Blümich B. and Spiess H. W., *J. Magn. Reson.*, **1988**, 79, 269.

32. Schmidt C., Wefing S., Blümich B. and Spiess H. W., *Chem. Phys. Lett.*, **1986**, 130, 84.

33. Schmidt C., Blümich B., Wefing S., Kaufmann S. and Spiess H. W., *Ber. Bunsenges. Phys. Chem.*, **1987**, 91, 1141-1145.

34. Spiess H. W., *Chem. Rev.*, **1991**, 91, 1321-1338.

35. Spiess H. W., 'Polymer Dynamics and Order from Multidimensional Solid State NMR', in *Encyclopedia of Nuclear Magnetic Resonance*, vol. 6, 3668, eds. Grant D. M. and Harris R. K., Wiley, Chichester, 1996.

36. Traficante D. D., 'Relaxation: An Introduction', in *Encyclopedia of Nuclear Magnetic Resonance*, vol. 6, 3988, eds. Grant D. M. and Harris R. K., Wiley, Chichester, 1996.

37. Günther H., *NMR Spectroscopy, Basic Principles, Concepts and Applications in Chemistry*, 2nd ed., Wiley, Chichester, 1996.

38. Marshall A. G. and Verdun F. R., *Fourier Transforms in NMR, Optical, and Mass Spectrometry, A User's Handbook*, Elsevier Science Publishers, Amsterdam, 1990.

39. Fukushima E. and Roeder S. B. W., *Experimental Pulse NMR, A Nuts and Bolts Approach*, Addison-Wesley, Reading, 1981.

40. Solomon I., *Phys. Rev.*, **1955**, 99, 559.

41. Menger E. M., Veeman W. S. and de Boer E., *Macromolecules*, 1982, **15**, 1406-1411.

42. Canet D., *Nuclear Magnetic Resonance, Concepts and Methods*, Wiley, Chichester, 1996.

43. Torchia D. A., *J. Magn. Reson.*, **1978**, 30, 613-616.

44. Torchia D. A. and Szabo A., *J. Magn. Reson.*, **1982**, 49, 107.

45. Gibby M. G., Pines A. and Waugh J. S., *Chem. Phys. Lett.*, **1972**, 16, 296-299.

46. Ailion D. C., 'Ultraslow Motions in Solids', in *Encyclopedia of Nuclear Magnetic Resonance*, vol. 8, 4874, eds. D. M. Grant and R. K. Harris, Wiley, Chichester, 1996.

47. McBrierty V. J., *Polymer*, **1974**, 15, 503 520.

48. Vega A. J., *J. Magn. Reson.*, **1985**, 65, 252-267.

49. Riddell F. G., Arumugan S., Harris K. D. M., Rogerson M. and Strange J. S., *J. Am. Chem. Soc.*, **1993**, 115, 1881.

50. VanderHart D. L. and Garroway A. N., *J. Chem. Phys.* , **1979**, 71, 2773.

51. Veeman W. S., Menger E. M., Ritchey W. and de Boer E., *Macromolecules*, **1979**, 12, 924-927.

52. Tekely P., Canet D., Delpuech J. -J. and Virlet J., *Magn. Reson. in Chem.*, **1990**, 28, S10-14.

53. Helfand E., *J. Chem. Phys.*, **1971**, 54, 4651-4661.

54. Huang T. H., Skarjune R. P., Wittebort R. J., Griffin R. G. and Oldfield E., *J. Am. Chem. Soc.*, **1980**, 102, 7379-7381.

55. Spiess H. W., *Colloid Polym. Sci.*, 1983, **261**, 193-209.

56. Hentschel D., Sillescu H. and Spiess H. W., *Makromol. Chem.*, **1979**, 180, 241-249.

57. Rosenke K., Sillescu H. and Spiess H. W., *Polymer*, **1980**, 21, 757-763.

58. Hentschel D., Sillescu H. and Spiess H. W., *Polymer*, **1984**, 25, 1078-1086.

59. Sefcik M. D., Schaefer J., Stejskal E. O. and McKay R. A., *Macromolecules*, **1980**, 13, 1132-1137.

60. Schaefer J., Stejskal E. O., Steger T. R., Sefic M. D. and McKay R. A., *Macromolecules*, **1980**, 13, 1121-1126.

61. Schaefer J., Stejskal E. O. and Buchdal R., *Macromolecules*, **1977**, 10, 384-405.

62. Jelinski L. W., Dumais J. J. and Engel A. K., *Macromolecules*, **1983**, 16, 492-496.

63. Jelinski L. W. and Dumais J. J., *Polym. Prepr., Am. Chem. Soc., Div. Polym. Chem.*, **1981**, 22, 273.

64. Jelinski L. W., Dumais J. J., Watnick P. I., Engel A. K. and Sefcik M. D., *Macromolecules*, **1983**, 16, 409.

65. Jelinski L. W., *Macromolecules*, **1981**, 14, 1341.

66. Kintanar A. and Jelinski L. W., *Macromolecules*, **1986**, 19, 1876, 1884.

67. Hirschinger J., Miura H., Gardner K. H. and English A. D., *Macromolecules*, **1990**, 23, 2153-2169.

68. Miura H., Hirschinger J. and English A. D., *Macromolecules*, **1990**, 23, 2169-2182.

69. Hatfield G. R. and Aharoni S. M., *Macromolecules*, **1989**, 22, 3807-3810.

70. Zemke K., Chmelka B. F., Schmidt-Rohr K. and Spiess H. W., *Macromolecules*, **1991**, 24, 6874-6876.

71. Hirschinger J., Schaefer D., Spiess H. W. and Lovinger A. J., *Macromolecules*, **1991**, 24, 2428-2433.

72. Schaefer D., Rietz R. R., Meyer W. H. and Spiess H. W., *Ber. Bunsenges. Phys. Chem.*, **1991**, 95, 1071-1076.

73. Rietz R. R., Schaefer D., Meyer W. H. and Spiess H. W., *Electrochimica Acta*, **1992**, 37, 1657-1661.

74. Abragam A., *The Principles of Nuclear Magnetism*, Oxford Univ. Press, Oxford, 1961.

75. Spiess H. W. and Sillescu H., *J. Magn. Reson.*, **1981**, 42, 381-389.

76. Schadt R. J., Cain E. J. and English A. D., *J. Phys. Chem.*, **1993**, 97, 8387-8392.

77. Lin T. -H and Vold R. R., *J. Magn. Reson., Ser. A*, **1995**, 113, 271-273.

78. Hirschinger J. and English A. D., *J. Magn. Reson.*, **1989**, 85, 542-553.

79. Rice D. M., Meinwald Y. C., Scheraga H. A. and Griffin R. G., *J. Am. Chem. Soc.*, **1987**, 109, 1636-1640.

80. Kennedy M. A., Vold R. R. and Vold R. L., *J. Magn. Reson.*, **1991**, 91, 301-315.

81. Ernst R. R., Bodenhausen G. and Wokaun A., *Principles of Nuclear Magnetic Resonance in One and Two Dimensions*, Oxford University Press, Oxford, 1994.

82. Sidhu P. S., Bell J., Penner G. H. and Jeffrey K. R., *Can. J. Chem.*, **1996**, 74, 1784-1794.

83. Heatley F., *Prog. Nucl. Magn. Res. Spectrosc.*, **1979**, 13, 47-85.

84. Wittebort R. J., Usha M. G., Ruben D. J., Wemmer D. E. and Pines A., *J. Am. Chem. Soc.*, **1988**, 110, 5668-5671.

85. Mack J. W. and Torchia D. A., *J. Phys. Chem.*, **1991**, 95, 4207-4213.

86. Ronemus A. D., Vold R. R. and Vold R. L., *J. Chem. Soc., Faraday Trans. 1*, **1988**, 84, 3761-3776.

87. Boas M. L., *Mathematical Methods in Physical Sciences*, 2nd ed., Wiley, 1983.

88. Atkins P. W., *Physical Chemistry*, 4th ed., Oxford Univ. Press, Oxford, 1992.

89. Rieck, *Rec. Trav. Chim. Pays-Bas*, **1944**, 63, 170.

90. Petropavlov N. N. and Yarantsev S. B., *Kristallografiya*, 1983, **28**, 1132.

91. Broadley J. S., Cruickshank D. W. J., Morrison J. D., Robertson J. M. and Shearer H. M. M., *Proc. R. Soc. London, Ser. A*, **1959**, 251, 441.

92. Leviel J. -L., Auvert G. and Savariault J. -M., *Acta Cryst., Sect. B.*, **1981**, 37, 2185.

93. Dunitz J. D., Maverick E. F. and Trueblood K. N., *Angew. Chem. Int. Ed. Engl.*, **1988**, 27, 880-895.

94. Schomaker V. and Trueblood K. N., *Acta Cryst.*, **1968**, B24, 63-76.

95. Davis J. H., 'Membranes: Deuterium NMR', in *Encyclopedia of Nuclear Magnetic Resonance*, vol. 3, 3008, eds. D. M. Grant and R. K. Harris, Wiley, Chichester, 1996.

96. Morrison J. D. and Robertson J. M., *J. Chem. Soc.*, **1949**, 1001.

97. Macgillavry C. H., *Rec. Trav. Chim. Pays-Bas*, **1941**, 60, 605.

98. Dupre la Tour, *C. R. Acad. Sci.*, **1932**, 194, 622.

99. a) Cingolani A. and Berchiesi G., *J. Therm. Anal.*, **1974**, 6, 87-90.
b) Petropavlov N. N., Tsygankova I. G. and Teslenko L. A., *Sov. Phys. Crystallogr.*, **1988**, 33, 853-855.

100. Morrison J. D. and Robertson J. M., *J. Chem. Soc.*, **1949**, 987.

101. Kirokawa S., *Bull. Chem. Soc. Jpn.*, **1950**, 23, 91.

102. Housty J. and Hospital M., *Acta Cryst.*, **1965**, 18, 693.

103. Macgillavry C. H., Hoogschagen G. and Sixma F. L. J., *Rec. Trav. Chim. Pays-Bas*, **1948**, 67, 869.

104. Kay M. I. and Katz L., *Acta Cryst.*, **1958**, 11, 289.

105. Housty J. and Hospital M., *Acta Cryst.*, **1966**, 21, 29.

106. Housty J. and Hospital M., *Acta Cryst.*, **1965**, 18, 753.

107. Gao Qi, Weber H. -P., Craven B. M. and McMullan R. K., *Acta Cryst., Sect. B*, **1994**, 50, 695.

108. He X. M. and Craven B. M., *Acta Cryst.*, **1993**, A49, 10-22.

109. Bocelli G. and Grenier-Loustalot M. F., *Acta Cryst., Sect. C*, **1984**, 40, 1391.

110. Bocelli G., Grenier-Loustalot M. F. and Marsh R. E., *Acta Cryst., Sect. C*, **1986**, 42, 127.

111. Palmer A. and Brisse F., *Acta Cryst., Sect. A.*, **1981**, 37, C243.

112. Palmer A., Poulin-Dandurand S. and Brisse F., *Can. J. Chem.*, **1985**, 63, 3079.

113. Gabrys B., Fumitaka H. and Kitamaru R., *Macromolecules*, **1987**, 20, 175-177.

114. Bocelli G. and Grenier-Loustalot M. F., *Acta Cryst., Sect. C*, **1984**, 40, 679.

115. Grenier-Loustalot M. -F. and Bocelli G., *Eur. Polym. J.*, **1984**, 20, 957-966.

116. Deguire S. and Brisse F., *Can. J. Chem.*, **1988**, 66, 2545.

117. Perez S. and Brisse F., *Can. J. Chem.*, **1975**, 53, 3551.

118. Bocelli G. and Grenier-Loustalot M. F., *Acta Cryst., Sect. C*, **1983**, 39, 1663.

119. Atkinson J. G., Csakvary J. J., Herbert G. T. and Stuart R. S., *J. Am. Chem. Soc.* **1968**, 90, 498-499.

120. *Aldrich Catalogue/Handbook of fine Chemicals*, U.K., 1996-1997.

121. Heim H. C. and Poe C. P., *J. Org. Chem.*, **1944**, 9, 299.

122. Heyns K. and Woyrsch O. F., *Chem. Abs.*, 48, 1262c.

123. Huntress E. H. and Mulliken S. P., *Identification of Pure Organic Compounds, Tables of Data on Selected Compounds of Order I*, Wiley, New York, 1946.

124. Drahowzal F. and Klamann D., *Chem. Abs.*, 46, 924d.

125. Gerstein B. C., Philos. Trans. R. Soc. London A, **1981**, 299, 521.

APPENDIX. CRYSTALLOGRAPHIC DATA

A.1. Data for hexane-1,6-diyl bis(*p*-nitrobenzoate)

Table A.1.1. Crystal data.

Empirical Formula	$C_{20}H_{20}N_2O_8$
Formula Weight	416.39
Crystal Colour, Habit	colourless, block
Crystal Dimensions	0.50 X 0.40 X 0.35 mm
Crystal System	monoclinic
Lattice Type	Primitive
No. of Reflections Used for Unit Cell Determination (2θ range)	25(23.5-24.9°)
Omega Scan Peak Width at Half-height	0.28°
Lattice Parameters:	a=8.982(3)Å b=12.471(3)Å c=9.086(3)Å β=92.91(3)° V=1016.4(5)Å^3
Space Group	$P2_1/n$ (#14)
Z value	2
D_{calc}	1.360 g/cm^3
$F_{(xx)}$	436.00
μ(MoKα)	1.06 cm^{-1}

Table A.1.2. Intensity measurements.

Diffractometer	RigakuAFC7S
Radiation	MoKα (λ = 0.71069Å) graphite monochromated
Attenuator	Zr foil (factor = 8.53)
Take-off Angle	6.0°
Detector Aperture	9.0 mm horizontal 13.0 mm vertical
Crystal to Detector Distance	235 mm
Temperature	20.0 °C
Scan Type	ω - 2θ
Scan Rate	16.0 °/min (in ω) (up to 4 scans)
Scan Width	(1.78 + 0.35 tanθ)°
$2\theta_{max}$	53.0°
No. of Reflections Measured	Total: 2360 Unique: 2219 (R_{int} = 0.028)
Corrections	Lorentz-polarization Secondary Extinction (coefficient: 3.28023e-06)

Table A.1.3. Structure solution and refinement.

Structure Solution	Direct Methods (SIR92)
Refinement	Full-matrix least-squares
Function Minimised	$\Sigma\omega(\|Fo\| - \|Fc\|)^2$
Least Squares Weights	$1/\sigma^2(Fo) = 4Fo^2/\sigma^2(Fo^2)$
p-factor	0.0030
Anomalous Dispersion	All non-hydrogen atoms
No. Observations($I > 3.00\sigma(I)$)	1209
No. Variables	137
Reflection/ParameterRatio	8.82
Residuals	R = 0.047, Rw = 0.037
Goodness of Fit Indicator	3.06
Max Shift/Error in Final Cycle	0.03
Maximum peak in Final Diff. Map	0.24 $e^-/Å^3$
Minimum peak in Final Diff. Map	-0.16 $e^-/Å^3$

Table A.1.4. Atomic co-ordinates and B_{iso}/B_{eq}.

atom	x	y	z	Beq
O(1)	-0.0180(3)	-0.2976(2)	0.2142(3)	8.94(8)
O(2)	-0.0932(2)	-0.1763(2)	0.0594(2)	7.94(7)
O(3)	0.3534(2)	0.0780(1)	0.6359(2)	5.28(5)
O(4)	0.2548(2)	0.2108(1)	0.5004(2)	7.33(6)
N(1)	-0.0257(3)	-0.2049(2)	0.1726(3)	6.05(8)
C(1)	0.0539(3)	-0.1226(2)	0.2640(3)	4.50(7)
C(2)	0.0343(3)	-0.0175(2)	0.2258(3)	5.26(8)
C(3)	0.1067(3)	0.0595(2)	0.3122(3)	5.02(7)
C(4)	0.1958(3)	0.0301(2)	0.4343(3)	3.90(6)
C(5)	0.2134(3)	-0.0770(2)	0.4691(3)	4.43(7)
C(6)	0.1423(3)	-0.1543(2)	0.3833(3)	4.79(7)
C(7)	0.2694(3)	0.1172(2)	0.5246(3)	4.64(7)
C(8)	0.4343(3)	0.1565(2)	0.7276(3)	5.65(8)
C(9)	0.5312(3)	0.0934(2)	0.8383(3)	6.02(9)
C(10)	0.4472(3)	0.0300(2)	0.9443(3)	5.52(8)
H(1)	-0.0273	0.0021	0.1422	6.3022
H(2)	0.0951	0.1332	0.2876	6.0265
H(3)	0.2749	-0.0974	0.5526	5.3087
H(4)	0.1543	-0.2282	0.4064	5.7470
H(5)	0.4945	0.2001	0.6689	6.7715
H(6)	0.3664	0.2005	0.7772	6.7715
H(7)	0.5911	0.0456	0.7855	7.2127
H(8)	0.5934	0.1425	0.8925	7.2127
H(9)	0.3913	0.0770	1.0024	6.6178
H(10)	0.3815	-0.0178	0.8919	6.6178

Table A.1.5. Anisotropic displacement parameters.

atom	U_{11}	U_{22}	U_{33}	U_{12}	U_{13}	U_{23}
O(1)	0.155(2)	0.087(2)	0.095(2)	-0.045(2)	-0.019(2)	-0.010(2)
O(2)	0.097(2)	0.116(2)	0.084(2)	0.015(1)	-0.036(1)	-0.032(1)
O(3)	0.084(1)	0.054(1)	0.059(1)	-0.014(1)	-0.017(1)	0.0019(10)
O(4)	0.109(2)	0.049(1)	0.117(2)	0.006(1)	-0.036(1)	0.003(1)
N(1)	0.076(2)	0.086(2)	0.068(2)	-0.006(2)	-0.001(1)	-0.021(2)
C(1)	0.055(2)	0.065(2)	0.051(2)	-0.002(1)	0.003(1)	-0.012(2)
C(2)	0.069(2)	0.077(2)	0.052(2)	0.013(2)	-0.012(1)	-0.004(2)
C(3)	0.073(2)	0.055(2)	0.061(2)	0.013(2)	-0.005(2)	0.005(1)
C(4)	0.050(2)	0.052(2)	0.046(1)	0.002(1)	0.003(1)	0.001(1)
C(5)	0.062(2)	0.055(2)	0.050(2)	-0.003(1)	-0.007(1)	0.006(1)
C(6)	0.071(2)	0.053(2)	0.058(2)	-0.004(1)	-0.003(1)	0.004(1)
C(7)	0.056(2)	0.059(2)	0.061(2)	0.000(2)	0.001(1)	0.003(2)
C(8)	0.082(2)	0.058(2)	0.073(2)	-0.021(2)	-0.010(2)	-0.005(2)
C(9)	0.074(2)	0.085(2)	0.068(2)	-0.024(2)	-0.008(2)	-0.009(2)
C(10)	0.071(2)	0.078(2)	0.059(2)	-0.005(2)	-0.008(1)	-0.012(2)

Table A.1.6. Bond lengths(Å).

atom	atom	distance	atom	atom	distance
O(1)	N(1)	1.217(3)	O(2)	N(1)	1.220(3)
O(3)	C(7)	1.324(3)	O(3)	C(8)	1.456(3)
O(4)	C(7)	1.193(3)	N(1)	C(1)	1.481(3)
C(1)	C(2)	1.364(3)	C(1)	C(6)	1.370(3)
C(2)	C(3)	1.382(3)	C(3)	C(4)	1.384(3)
C(4)	C(5)	1.380(3)	C(4)	C(7)	1.495(3)
C(5)	C(6)	1.377(3)	C(8)	C(9)	1.516(4)
C(9)	C(10)	1.482(4)	C(10)	C(10)	1.545(5)
C(2)	H(1)	0.95	C(3)	H(2)	0.95
C(5)	H(3)	0.95	C(6)	H(4)	0.95
C(8)	H(5)	0.95	C(8)	H(6)	0.95
C(9)	H(7)	0.95	C(9)	H(8)	0.95
C(10)	H(9)	0.95	C(10)	H(10)	0.95

Table A.1.7. Bond angles (°).

atom	atom	atom	angle	atom	atom	atom	angle
C(7)	O(3)	C(8)	115.9(2)	O(1)	N(1)	O(2)	123.9(3)
O(1)	N(1)	C(1)	117.8(3)	O(2)	N(1)	C(1)	118.4(3)
N(1)	C(1)	C(2)	118.1(3)	N(1)	C(1)	C(6)	119.2(3)
C(2)	C(1)	C(6)	122.7(3)	C(1)	C(2)	C(3)	118.2(2)
C(2)	C(3)	C(4)	120.5(3)	C(3)	C(4)	C(5)	119.7(2)
C(3)	C(4)	C(7)	118.0(2)	C(5)	C(4)	C(7)	122.3(2)
C(4)	C(5)	C(6)	120.2(2)	C(1)	C(6)	C(5)	118.7(2)
O(3)	C(7)	O(4)	123.7(3)	O(3)	C(7)	C(4)	111.7(2)
O(4)	C(7)	C(4)	124.6(3)	O(3)	C(8)	C(9)	106.5(2)
C(8)	C(9)	C(10)	114.5(2)	C(9)	C(10)	C(10)	111.6(3)
C(1)	C(2)	H(1)	120.9	C(3)	C(2)	H(1)	120.9
C(2)	C(3)	H(2)	119.8	C(4)	C(3)	H(2)	119.8
C(4)	C(5)	H(3)	119.9	C(6)	C(5)	H(3)	119.9
C(1)	C(6)	H(4)	120.7	C(5)	C(6)	H(4)	120.7
O(3)	C(8)	H(5)	110.2	O(3)	C(8)	H(6)	110.2
C(9)	C(8)	H(5)	110.2	C(9)	C(8)	H(6)	110.2
H(5)	C(8)	H(6)	109.5	C(8)	C(9)	H(7)	108.2
C(8)	C(9)	H(8)	108.2	C(10)	C(9)	H(7)	108.2
C(10)	C(9)	H(8)	108.2	H(7)	C(9)	H(8)	109.5
C(9)	C(10)	H(9)	109.5	C(9)	C(10)	H(10)	109.4
C(10)	C(10)	H(9)	105.0	C(10)	C(10)	H(10)	111.6
H(9)	C(10)	H(10)	109.5				

Table A.1.8. Torsion angles(°).

atom	atom	atom	atom	angle	atom	atom	atom	atom	angle
O(1)	N(1)	C(1)	C(2)	-173.9(3)	O(1)	N(1)	C(1)	C(6)	5.5(4)
O(2)	N(1)	C(1)	C(2)	7.1(4)	O(2)	N(1)	C(1)	C(6)	-173.5(3)
O(3)	C(7)	C(4)	C(3)	-178.8(2)	O(3)	C(7)	C(4)	C(5)	1.4(4)
O(3)	C(8)	C(9)	C(10)	-65.6(3)	O(4)	C(7)	O(3)	C(8)	-2.3(4)
O(4)	C(7)	C(4)	C(3)	1.5(4)	O(4)	C(7)	C(4)	C(5)	-178.3(3)
N(1)	C(1)	C(2)	C(3)	179.0(2)	N(1)	C(1)	C(6)	C(5)	-178.8(2)
C(1)	C(2)	C(3)	C(4)	-0.3(4)	C(1)	C(6)	C(5)	C(4)	-0.3(4)
C(2)	C(1)	C(6)	C(5)	0.6(4)	C(2)	C(3)	C(4)	C(5)	0.6(4)
C(2)	C(3)	C(4)	C(7)	-179.2(3)	C(3)	C(2)	C(1)	C(6)	-0.3(4)
C(3)	C(4)	C(5)	C(6)	-0.3(4)	C(4)	C(7)	O(3)	C(8)	177.9(2)
C(6)	C(5)	C(4)	C(7)	179.5(2)	C(7)	O(3)	C(8)	C(9)	-175.4(2)
C(8)	C(9)	C(10)	C(10)	-178.7(3)	C(9)	C(10)	C(10)	C(9)	180.0

Table A.1.9. Non-bonded contacts out to 3.30 Å.

atom	atom	distance	ADC	atom	atom	distance	ADC
O(1)	O(4)	3.142(4)	54502	O(4)	N(1)	3.144(3)	2

A.2. Data for hexane-1,6-diyl bis(3,5-dimethoxybenzoate)

Table A.2.1. Crystal data.

Empirical Formula	$C_{24}H_{30}O_8$
Formula Weight	446.50
Crystal Colour, Habit	colourless, plate
Crystal Dimensions	0.40 X 0.35 X 0.15 mm
Crystal System	monoclinic
Lattice Type	primitive
No. of Reflections Used for Unit Cell Determination (2θ range)	25(23.5-25.0°)
Omega Scan Peak Width at Half-height	0.28°
Lattice Parameters	a=4.846(5)Å b=15.805(4)Å c=15.121(3)Å β=92.11(4)° V=1157.2(9)Å^3
Space Group	$P2_1/c$ (#14)
Z value	2
D_{calc}	1.281 g/cm^3
F_{000}	476.00
μ(MoKα)	0.96 cm^{-1}

Table A.2.2. Intensity measurements.

Diffractometer	RigakuAFC7S
Radiation	MoKα (λ = 0.71069Å) graphite monochromated
Attenuator	Zr foil (factor = 8.53)
Take-off Angle	6.0°
Detector Aperture	9.0 mm horizontal, 13.0 mm vertical
Crystal to Detector Distance	235 mm
Temperature	20.0°C
Scan Type	ω-2θ
Scan Rate	16.0°/min (in ω) (up to 4 scans)
Scan Width	(1.15 + 0.35 tanθ)°
$2\theta_{max}$	50.0°
No. of Reflections Measured	Total: 2386, Unique: 2126 (R_{int} = 0.015)
Corrections	Lorentz-polarization Absorption (trans. factors: 0.8702 - 1.0000) Secondary Extinction (coefficient: 1.20398e-05)

Table A.2.3. Structure solution and refinement.

Structure Solution	Direct Methods (SIR92)
Refinement	Full-matrix least-squares
Function Minimised	$\Sigma\omega(\|Fo\| - \|Fc\|)^2$
Least Squares Weights	$1/\sigma^2(Fo) = 4Fo^2/\sigma^2(Fo^2)$
p-factor	0.0030
Anomalous Dispersion	All non-hydrogen atoms
No. Observations ($I > 3.00\sigma(I)$)	1401
No. Variables	146
Reflection/Parameter Ratio	9.60
Residuals	R = 0.085, Rw = 0.095
Goodness of Fit Indicator	6.87
Max Shift/Error in Final Cycle	0.01
Maximum peak in Final Diff. Map	0.32 $e^-/Å^3$
Minimum peak in Final Diff .Map	-0.35 $e^-/Å^3$

Table A.2.4. Atomic co-ordinates and B_{iso} /B_{eq}.

atom	x	y	z	B_{eq}
O(1)	0.619(1)	0.0473(3)	0.3227(3)	6.2(1)
O(2)	0.4620(9)	0.0601(3)	0.1826(3)	4.4(1)
O(3)	0.779(1)	0.3286(3)	0.0707(3)	6.3(1)
O(4)	1.3016(9)	0.2987(3)	0.3408(3)	5.1(1)
C(1)	0.611(1)	0.0850(4)	0.2532(4)	4.1(2)
C(2)	0.759(1)	0.1653(4)	0.2365(4)	3.6(1)
C(3)	0.705(1)	0.2121(4)	0.1609(4)	3.9(2)
C(4)	0.848(1)	0.2869(4)	0.1479(4)	4.3(2)
C(5)	1.051(1)	0.3131(4)	0.2077(4)	4.3(2)
C(6)	1.099(1)	0.2661(4)	0.2854(4)	3.9(2)
C(7)	0.957(1)	0.1924(4)	0.2999(4)	3.9(2)
C(8)	0.902(2)	0.4086(5)	0.0551(5)	7.0(2)
C(9)	1.353(2)	0.2550(4)	0.4227(5)	5.9(2)
C(10)	0.296(1)	-0.0171(4)	0.1925(4)	4.4(2)
C(11)	0.224(1)	-0.0456(4)	0.0973(4)	4.8(2)
C(12)	0.040(1)	0.0161(4)	0.0469(4)	4.5(2)
H(1)	0.5699	0.1937	0.1181	4.6848
H(2)	1.1570	0.3622	0.1966	5.0894
H(3)	0.9927	0.1606	0.3523	4.6639
H(4)	1.0968	0.4025	0.0546	8.2475
H(5)	0.8357	0.4301	-0.0005	8.2475
H(6)	0.8554	0.4469	0.1007	8.2475
H(7)	1.1906	0.2560	0.4562	6.9926
H(8)	1.4027	0.1981	0.4112	6.9926
H(9)	1.4990	0.2822	0.4552	6.9926
H(10)	0.4010	-0.0595	0.2232	5.3076
H(11)	0.1338	-0.0055	0.2233	5.3076
H(12)	0.3902	-0.0521	0.0667	5.7149
H(13)	0.1314	-0.0987	0.0995	5.7149
H(14)	0.1252	0.0703	0.0467	5.3810
H(15)	-0.1330	0.0201	0.0743	5.3810

Table A.2.5. Anisotropic displacement parameters.

atom	U_{11}	U_{22}	U_{33}	U_{12}	U_{13}	U_{23}
O(1)	0.112(4)	0.060(3)	0.061(3)	-0.029(3)	-0.027(3)	0.018(3)
O(2)	0.069(3)	0.040(3)	0.058(3)	-0.016(2)	-0.016(2)	0.004(2)
O(3)	0.131(5)	0.048(3)	0.059(3)	-0.030(3)	-0.036(3)	0.015(2)
O(4)	0.081(3)	0.047(3)	0.064(3)	-0.012(3)	-0.033(3)	0.002(2)
C(1)	0.060(4)	0.043(4)	0.051(4)	-0.002(3)	-0.011(3)	-0.001(3)
C(2)	0.051(4)	0.037(4)	0.050(4)	0.000(3)	-0.007(3)	-0.003(3)
C(3)	0.063(4)	0.042(4)	0.043(4)	-0.005(3)	-0.011(3)	-0.003(3)
C(4)	0.082(5)	0.038(4)	0.040(3)	-0.004(4)	-0.013(3)	0.000(3)
C(5)	0.074(5)	0.034(4)	0.052(4)	-0.009(3)	-0.011(3)	0.000(3)
C(6)	0.055(4)	0.041(4)	0.051(4)	0.003(3)	-0.013(3)	-0.006(3)
C(7)	0.059(4)	0.038(4)	0.050(4)	0.002(3)	-0.012(3)	0.002(3)
C(8)	0.144(8)	0.055(5)	0.064(5)	-0.024(5)	-0.013(5)	0.014(4)
C(9)	0.095(6)	0.059(5)	0.067(5)	-0.009(4)	-0.039(4)	-0.002(4)
C(10)	0.060(4)	0.047(4)	0.061(4)	-0.011(3)	-0.007(3)	0.009(3)
C(11)	0.080(5)	0.034(4)	0.067(4)	-0.013(4)	-0.018(4)	-0.004(3)
C(12)	0.064(4)	0.043(4)	0.062(4)	-0.006(3)	-0.015(3)	-0.008(3)

Table A.2.6. Bond lengths(Å).

atom	atom	distance	atom	atom	distance
O(1)	C(1)	1.208(7)	O(2)	C(1)	1.327(6)
O(2)	C(10)	1.471(7)	O(3)	C(4)	1.373(7)
O(3)	C(8)	1.422(8)	O(4)	C(6)	1.368(6)
O(4)	C(9)	1.432(7)	C(1)	C(2)	1.483(8)
C(2)	C(3)	1.378(8)	C(2)	C(7)	1.398(7)
C(3)	C(4)	1.389(8)	C(4)	C(5)	1.375(8)
C(5)	C(6)	1.402(8)	C(6)	C(7)	1.375(8)
C(10)	C(11)	1.537(8)	C(11)	C(12)	1.510(8)
C(12)	C(12)	1.54(1)			
C(3)	H(1)	0.95	C(5)	H(2)	0.95
C(7)	H(3)	0.95	C(8)	H(4)	0.95
C(8)	H(5)	0.95	C(8)	H(6)	0.95
C(9)	H(7)	0.95	C(9)	H(8)	0.95
C(9)	H(9)	0.95	C(10)	H(10)	0.95
C(10)	H(11)	0.95	C(11)	H(12)	0.95
C(11)	H(13)	0.95	C(12)	H(14)	0.95
C(12)	H(15)	0.95			

Table A.2.7. Bond angles(°).

atom	atom	atom	angle	atom	atom	atom	angle
C(1)	O(2)	C(10)	116.6(5)	C(4)	O(3)	C(8)	118.4(5)
C(6)	O(4)	C(9)	116.5(5)	O(1)	C(1)	O(2)	123.5(6)
O(1)	C(1)	C(2)	124.8(6)	O(2)	C(1)	C(2)	111.7(5)
C(1)	C(2)	C(3)	121.5(5)	C(1)	C(2)	C(7)	117.9(5)
C(3)	C(2)	C(7)	120.6(6)	C(2)	C(3)	C(4)	119.5(5)
O(3)	C(4)	C(3)	114.9(5)	O(3)	C(4)	C(5)	124.2(6)
C(3)	C(4)	C(5)	120.9(6)	C(4)	C(5)	C(6)	118.8(6)
O(4)	C(6)	C(5)	113.9(5)	O(4)	C(6)	C(7)	125.0(5)
C(5)	C(6)	C(7)	121.0(6)	C(2)	C(7)	C(6)	119.0(5)
O(2)	C(10)	C(11)	104.7(5)	C(10)	C(11)	C(12)	113.2(5)
C(11)	C(12)	C(12)	111.9(7)				
C(2)	C(3)	H(1)	120.4	C(4)	C(3)	H(1)	120.0
C(4)	C(5)	H(2)	120.6	C(6)	C(5)	H(2)	120.6
C(2)	C(7)	H(3)	120.7	C(6)	C(7)	H(3)	120.4
O(3)	C(8)	H(4)	109.6	O(3)	C(8)	H(5)	109.4
O(3)	C(8)	H(6)	109.5	H(4)	C(8)	H(5)	109.4
H(4)	C(8)	H(6)	109.5	H(5)	C(8)	H(6)	109.4
O(4)	C(9)	H(7)	109.4	O(4)	C(9)	H(8)	109.6
O(4)	C(9)	H(9)	109.3	H(7)	C(9)	H(8)	109.6
H(7)	C(9)	H(9)	109.5	H(8)	C(9)	H(9)	109.5
O(2)	C(10)	H(10)	110.6	O(2)	C(10)	H(11)	110.9
C(11)	C(10)	H(10)	110.5	C(11)	C(10)	H(11)	110.7
H(10)	C(10)	H(11)	109.5	C(10)	C(11)	H(12)	108.7
C(10)	C(11)	H(13)	108.4	C(12)	C(11)	H(12)	108.7
C(12)	C(11)	H(13)	108.4	H(12)	C(11)	H(13)	109.3
C(11)	C(12)	H(14)	109.4	C(11)	C(12)	H(15)	109.7
C(12)	C(12)	H(14)	112.9	C(12)	C(12)	H(15)	103.4
H(14)	C(12)	H(15)	109.4				

Table A.2.8. Torsion angles(°).

atom	atom	atom	atom	angle	atom	atom	atom	atom	angle
O(1)	C(1)	O(2)	C(10)	0.9(10)	O(1)	C(1)	C(2)	C(3)	-168.8(7)
O(1)	C(1)	C(2)	C(7)	11(1)	O(2)	C(1)	C(2)	C(3)	9.4(9)
O(2)	C(1)	C(2)	C(7)	-170.3(5)	O(2)	C(10)	C(11)	C(12)	-65.3(7)
O(3)	C(4)	C(3)	C(2)	-180.0(6)	O(3)	C(4)	C(5)	C(6)	178.6(6)
O(4)	C(6)	C(5)	C(4)	-178.8(6)	O(4)	C(6)	C(7)	C(2)	-178.5(6)
C(1)	O(2)	C(10)	C(11)	-162.7(5)	C(1)	C(2)	C(3)	C(4)	-179.8(6)
C(1)	C(2)	C(7)	C(6)	179.2(6)	C(2)	C(1)	O(2)	C(10)	-177.3(5)
C(2)	C(3)	C(4)	C(5)	2(1)	C(2)	C(7)	C(6)	C(5)	-1.3(10)
C(3)	C(2)	C(7)	C(6)	-0.5(9)	C(3)	C(4)	O(3)	C(8)	175.7(6)
C(3)	C(4)	C(5)	C(6)	-4(1)	C(4)	C(3)	C(2)	C(7)	-0.2(10)
C(4)	C(5)	C(6)	C(7)	3(1)	C(5)	C(4)	O(3)	C(8)	-6(1)
C(5)	C(6)	O(4)	C(9)	177.8(6)	C(7)	C(6)	O(4)	C(9)	-4.8(9)
C(10)	C(11)	C(12)	C(12)	-177.5(6)	C(11)	C(12)	C(12)	C(11)	180.0

Table A.2.9. Non-bonded contacts out to 3.30 Å.

atom	atom	distance	ADC	atom	atom	distance	ADC
O(3)	C(9)	3.266(8)	45404				

A.3. Data for hexane-1.6-diyl dibenzesulphonate

Table A.3.1. Crystal data.

Empirical Formula	$C_{18}H_{22}S_2O_6$
Formula Weight	398.49
Crystal Colour, Habit	colourless, block
Crystal Dimensions	0.50 X 0.45 X 0.40 mm
Crystal System	orthorhombic
Lattice Type	Primitive
No. of Reflections Used for Unit Cell Determination (2θ range)	25(22.8 - 24.8°)
Omega Scan Peak Width at Half-height	0.30°
Lattice Parameters	a = 16.707(8) Å b = 7.719(3) Å c=15.349(4)Å V=1979(1)Å^3
Space Group	Pbcn (#60)
Z value	4
D_{calc}	1.337 g/cm^3
F_{000}	840.00
μ(MoKα)	2.99 cm^{-1}

Table A.3.2. Intensity measurements.

Diffractometer	Rigaku AFC7S
Radiation	MoKα (λ = 0.71069 Å) graphite monochromated
Attenuator	Zr foil (factor = 8.53)
Take-off Angle	6.0°
Detector Aperture	9.0 mm horizontal 13.0 mm vertical
Crystal to Detector Distance	235 mm
Temperature	20.0°C
Scan Type	ω - 2θ
Scan Rate	16.0 °/min (in ω) (up to 4 scans)
Scan Width	(1.78 + 0.35tanθ)°
$2\theta_{max}$	50.0°
No. of Reflections Measured	Total: 2033
Corrections	Lorentz-polarization Absorption (trans. Factors: 0.8857 - 1.0000) Secondary Extinction (coefficient: 1.80828e-06)

Table A.3.3. Structure solution and refinement.

Structure Solution	Direct Methods (SIR92)
Refinement	Full-matrix least-squares
Function Minimised	$\Sigma\omega(\|Fo\| - \|Fc\|)^2$
Least Squares Weights	$1/\sigma^2(Fo) = 4Fo^2/\sigma^2(Fo^2)$
p-factor	0.0040
Anomalous Dispersion	All non-hydrogen atoms
No. Observations ($I > 3.00\sigma(I)$)	1219
No. Variables	119
Reflection/Parameter Ratio	10.24
Residuals	R = 0.098, Rw = 0.120
Goodness of Fit Indicator	9.75
Max Shift/Error in Final Cycle	0.06
Maximum peak in Final Diff. Map	0.75 $e^-/Å^3$
Minimum peak in Final Diff. Map	-0.57 $e^-/Å^3$

Table A.3.4. Atomic co-ordinates and B_{iso} /B_{eq}.

Atom	x	y	z	B_{eq}
S(1)	0.3554(2)	0.0828(4)	0.8029(2)	4.11(6)
O(1)	0.4180(4)	0.2223(9)	0.8301(4)	4.2(2)
O(2)	0.3977(5)	-0.0782(9)	0.8135(5)	6.0(2)
O(3)	0.2822(4)	0.112(1)	0.8488(4)	5.7(2)
C(1)	0.3942(7)	0.407(1)	0.8335(7)	5.0(3)
C(2)	0.4588(7)	0.499(1)	0.8809(7)	4.7(3)
C(3)	0.4656(6)	0.455(1)	0.9787(6)	4.2(3)
C(4)	0.3406(6)	0.118(1)	0.6896(6)	3.0(2)
C(5)	0.2706(6)	0.201(1)	0.6671(7)	4.3(3)
C(6)	0.2580(8)	0.232(1)	0.5758(8)	5.5(3)
C(7)	0.3135(9)	0.182(1)	0.5183(7)	5.3(3)
C(8)	0.3842(7)	0.101(2)	0.5426(8)	5.7(3)
C(9)	0.3938(6)	0.068(1)	0.6372(6)	4.0(2)
H(1)	0.3892	0.4516	0.7760	5.9042
H(2)	0.3448	0.4187	0.8632	5.9042
H(3)	0.5082	0.4716	0.8538	5.6052
H(4)	0.4489	0.6199	0.8758	5.6052
H(5)	0.4174	0.4851	1.0074	4.9496
H(6)	0.4755	0.3347	0.9853	4.9496
H(7)	0.2324	0.2353	0.7095	5.0666
H(8)	0.2105	0.2876	0.5570	6.4573
H(9)	0.3037	0.2039	0.4585	6.3674
H(10)	0.4239	0.0681	0.5016	6.7093
H(11)	0.4400	0.0087	0.6582	4.6920

Table A.3.5. Anisotropic displacement parameters.

Atom	U_{11}	U_{22}	U_{33}	U_{12}	U_{13}	U_{23}
S(1)	0.064(2)	0.054(2)	0.039(1)	-0.003(2)	-0.006(1)	-0.001(1)
O(1)	0.053(5)	0.055(5)	0.050(4)	0.007(4)	-0.015(4)	-0.016(4)
O(2)	0.109(7)	0.051(5)	0.067(5)	0.023(5)	-0.022(5)	0.000(5)
O(3)	0.074(5)	0.082(6)	0.062(5)	-0.003(5)	0.024(4)	-0.001(5)
C(1)	0.082(8)	0.046(7)	0.062(7)	0.010(6)	-0.021(6)	-0.009(6)
C(2)	0.070(8)	0.044(6)	0.065(7)	-0.004(6)	-0.012(7)	-0.006(6)
C(3)	0.067(7)	0.045(7)	0.047(6)	0.005(6)	-0.010(6)	-0.006(5)
C(4)	0.052(6)	0.029(5)	0.031(5)	-0.009(5)	-0.006(5)	-0.005(4)
C(5)	0.070(8)	0.038(6)	0.057(7)	0.007(6)	-0.009(6)	-0.015(6)
C(6)	0.081(9)	0.054(7)	0.075(8)	0.029(7)	-0.023(8)	-0.011(7)
C(7)	0.11(1)	0.044(7)	0.049(7)	-0.006(7)	-0.015(7)	0.006(6)
C(8)	0.075(9)	0.060(8)	0.080(9)	-0.034(7)	-0.010(7)	0.003(7)
C(9)	0.053(6)	0.058(7)	0.041(6)	-0.008(6)	-0.017(5)	-0.006(6)

Table A.3.6. Bond lengths(Å).

Atom	atom	distance	atom	atom	distance
S(1)	O(1)	1.557(7)	S(1)	O(2)	1.439(7)
S(1)	O(3)	1.429(7)	S(1)	C(4)	1.778(9)
O(1)	C(1)	1.48(1)	C(1)	C(2)	1.48(1)
C(2)	C(3)	1.54(1)	C(3)	C(3)	1.49(2)
C(4)	C(5)	1.37(1)	C(4)	C(9)	1.26(1)
C(5)	C(6)	1.44(1)	C(6)	C(7)	1.34(2)
C(7)	C(8)	1.39(1)	C(8)	C(9)	1.48(1)
C(1)	H(1)	0.95	C(1)	H(2)	0.95
C(2)	H(3)	0.95	C(2)	H(4)	0.95
C(3)	H(5)	0.95	C(3)	H(6)	0.95
C(5)	H(7)	0.95	C(6)	H(8)	0.95
C(7)	H(9)	0.95	C(8)	H(10)	0.95
C(9)	H(11)	0.95			

Table A.3.7. Bond angles(°).

atom	atom	atom	angle	atom	atom	atom	angle
O(1)	S(1)	O(2)	103.8(4)	O(1)	S(1)	O(3)	109.6(4)
O(1)	S(1)	C(4)	104.4(4)	O(2)	S(1)	O(3)	120.0(5)
O(2)	S(1)	C(4)	108.1(5)	O(3)	S(1)	C(4)	109.7(5)
S(1)	O(1)	C(1)	119.6(6)	O(1)	C(1)	C(2)	106.5(8)
C(1)	C(2)	C(3)	115.2(9)	C(2)	C(3)	C(3)	112(1)
S(1)	C(4)	C(5)	115.9(8)	S(1)	C(4)	C(9)	118.6(8)
C(5)	C(4)	C(9)	125.5(9)	C(4)	C(5)	C(6)	116.7(10)
C(5)	C(6)	C(7)	119(1)	C(6)	C(7)	C(8)	122(1)
C(7)	C(8)	C(9)	115(1)	C(4)	C(9)	C(8)	119(1)
O(1)	C(1)	H(1)	109.9	O(1)	C(1)	H(2)	110.1
C(2)	C(1)	H(1)	110.2	C(2)	C(1)	H(2)	110.5
H(1)	C(1)	H(2)	109.5	C(1)	C(2)	H(3)	108.1
C(1)	C(2)	H(4)	107.7	C(3)	C(2)	H(3)	108.3
C(3)	C(2)	H(4)	107.9	H(3)	C(2)	H(4)	109.6
C(2)	C(3)	H(5)	109.7	C(2)	C(3)	H(6)	109.4
C(3)	C(3)	H(5)	109.8	C(3)	C(3)	H(6)	105.9
H(5)	C(3)	H(6)	109.6	C(4)	C(5)	H(7)	121.9
C(6)	C(5)	H(7)	121.4	C(5)	C(6)	H(8)	119.8
C(7)	C(6)	H(8)	120.6	C(6)	C(7)	H(9)	118.0
C(8)	C(7)	H(9)	119.2	C(7)	C(8)	H(10)	122.4
C(9)	C(8)	H(10)	121.9	C(4)	C(9)	H(11)	120.2
C(8)	C(9)	H(11)	120.1				

Table A.3.8. Torsion angles(°).

atom	atom	atom	atom	angle	atom	atom	atom	atom	angle
S(1)	O(1)	C(1)	C(2)	166.6(7)	S(1)	C(4)	C(5)	C(6)	179.5(8)
S(1)	C(4)	C(9)	C(8)	-178.0(8)	O(1)	S(1)	C(4)	C(5)	-104.0(7)
O(1)	S(1)	C(4)	C(9)	75.9(9)	O(1)	C(1)	C(2)	C(3)	-68(1)
O(2)	S(1)	O(1)	C(1)	-175.8(7)	O(2)	S(1)	C(4)	C(5)	146.0(7)
O(2)	S(1)	C(4)	C(9)	-34.2(10)	O(3)	S(1)	O(1)	C(1)	-46.5(8)
O(3)	S(1)	C(4)	C(5)	13.4(9)	O(3)	S(1)	C(4)	C(9)	-166.7(8)
C(1)	O(1)	S(1)	C(4)	71.0(8)	C(1)	C(2)	C(3)	C(3)	176(1)
C(2)	C(3)	C(3)	C(2)	180.0	C(4)	C(5)	C(6)	C(7)	0(1)
C(4)	C(9)	C(8)	C(7)	-2(1)	C(5)	C(4)	C(9)	C(8)	1(1)
C(5)	C(6)	C(7)	C(8)	0(1)	C(6)	C(5)	C(4)	C(9)	0(1)
C(6)	C(7)	C(8)	C(9)	1(1)					

A.4. Data for hexane-1,6-diyl ditosylate

Table A.4.1. Crystal data.

Empirical Formula	$C_{20}H_{26}S_2O_6$
Formula Weight	426.54
Crystal Colour, Habit	colourless, block
Crystal Dimensions	0.50 X 0.40 X 0.35 mm
Crystal System	triclinic
Lattice Type	Primitive
No. of Reflections Used for Unit Cell Determination (2θ range)	16 (13.4 - 19.6°)
Omega Scan Peak Width at Half-height	0.33°
Lattice Parameters	a=8.111(2)Å b=9.167(2)Å c=7.365(2)Å α=90.25(2)° β=106.00(2)° γ=80.81(2)° V=519.2(2)Å^3
Space Group	P-1 (#2)
Z value	1
D_{calc}	1.364 g/cm^3
F_{000}	226.00
μ(MoKα)	2.77 cm^{-1}

Table A.4.2. Intensity measurements.

Diffractometer	Rigaku AFC7S
Radiation	MoKα (λ = 0.71069 Å) graphite monochromated
Attenuator	Zr foil (factor = 8.53)
Take-off Angle	6.0°
Detector Aperture	9.0 mm horizontal 13.0 mm vertical
Crystal to Detector Distance	235 mm
Temperature	20.0°C
Scan Type	ω - 2θ
Scan Rate	16.0 °/min (in ω) (up to 4 scans)
Scan Width	(1.73 + 0.35tanθ)°
$2\theta_{max}$	50.0°
No. of Reflections Measured	Total: 1972, Unique: 1832 (R_{int} = 0.012)
Corrections	Lorentz-polarization Secondary Extinction (coefficient: 5.56062e-06)

Table A.4.3. Structure solution and refinement.

Structure Solution	Direct Methods (SIR92)
Refinement	Full-matrix least-squares
Function Minimised	$\Sigma\omega(\|Fo\| - \|Fc\|)^2$
Least Squares Weights	$1/\sigma^2(Fo) = 4Fo^2/\sigma^2(Fo^2)$
p-factor	0.0030
Anomalous Dispersion	All non-hydrogen atoms
No. Observations ($I > 3.00\sigma(I)$)	1614
No. Variables	128
Reflection/Parameter Ratio	12.61
Residuals	R = 0.037, Rw = 0.037
Goodness of Fit Indicator	4.77
Max Shift/Error in Final Cycle	0.01
Maximum peak in Final Diff. Map	0.19 $e^-/Å^3$
Minimum peak in Final Diff. Map	-0.22 $e^-/Å^3$

Table A.4.4. Atomic co-ordinates and B_{iso} /B_{eq}.

atom	x	y	z	B_{eq}
S(1)	0.83692(7)	0.30075(7)	0.54106(9)	3.76(1)
O(1)	0.8058(2)	0.4447(2)	0.4130(2)	3.75(4)
O(2)	0.9930(2)	0.2086(2)	0.5326(2)	4.92(4)
O(3)	0.8203(2)	0.3547(2)	0.7178(2)	5.10(5)
C(1)	0.8382(3)	0.4301(3)	0.2266(3)	4.12(6)
C(2)	0.7295(3)	0.5592(3)	0.1020(3)	4.49(6)
C(3)	0.5329(3)	0.5637(3)	0.0573(3)	4.09(6)
C(4)	0.6580(3)	0.2141(2)	0.4311(3)	3.16(5)
C(5)	0.4944(3)	0.2807(2)	0.4351(3)	3.84(6)
C(6)	0.3523(3)	0.2181(3)	0.3429(3)	4.19(6)
C(7)	0.3712(3)	0.0901(3)	0.2466(3)	4.05(6)
C(8)	0.5362(3)	0.0233(3)	0.2490(3)	4.25(6)
C(9)	0.6816(3)	0.0844(2)	0.3409(3)	3.75(6)
C(10)	0.2123(3)	0.0259(3)	0.1403(4)	6.25(8)
H(1)	0.8068	0.3402	0.1739	4.7951
H(2)	0.9579	0.4301	0.2385	4.7951
H(3)	0.7592	0.5560	-0.0143	5.2768
H(4)	0.7564	0.6474	0.1628	5.2768
H(5)	0.4738	0.6485	-0.0214	4.7842
H(6)	0.4999	0.5677	0.1716	4.7842
H(7)	0.4796	0.3692	0.5014	4.5016
H(8)	0.2391	0.2642	0.3455	4.9086
H(9)	0.5513	-0.0670	0.1863	4.9795
H(10)	0.7952	0.0370	0.3412	4.3804
H(11)	0.1391	0.0961	0.0462	7.3802
H(12)	0.2480	-0.0616	0.0819	7.3802
H(13)	0.1508	0.0030	0.2260	7.3802

Table A.4.5. Anisotropic displacement parameters.

atom	U_{11}	U_{22}	U_{33}	U_{12}	U_{13}	U_{23}
S(1)	0.0356(3)	0.0507(4)	0.0525(4)	-0.0117(3)	0.0023(3)	-0.0014(3)
O(1)	0.0437(9)	0.0437(9)	0.054(1)	-0.0132(7)	0.0084(8)	-0.0032(7)
O(2)	0.0318(9)	0.061(1)	0.086(1)	-0.0012(8)	0.0050(9)	0.0057(9)
O(3)	0.070(1)	0.080(1)	0.046(1)	-0.0307(10)	0.0081(9)	-0.0133(9)
C(1)	0.035(1)	0.061(2)	0.061(2)	-0.013(1)	0.012(1)	-0.002(1)
C(2)	0.047(1)	0.062(2)	0.059(2)	-0.018(1)	0.005(1)	0.006(1)
C(3)	0.042(1)	0.055(2)	0.052(2)	-0.007(1)	0.003(1)	-0.003(1)
C(4)	0.033(1)	0.041(1)	0.044(1)	-0.0088(10)	0.0058(10)	0.000(1)
C(5)	0.042(1)	0.047(1)	0.058(2)	-0.008(1)	0.015(1)	-0.007(1)
C(6)	0.035(1)	0.062(2)	0.062(2)	-0.011(1)	0.012(1)	0.003(1)
C(7)	0.048(1)	0.061(2)	0.045(1)	-0.024(1)	0.004(1)	0.006(1)
C(8)	0.064(2)	0.047(1)	0.050(1)	-0.017(1)	0.009(1)	-0.009(1)
C(9)	0.042(1)	0.046(1)	0.052(1)	-0.003(1)	0.010(1)	-0.003(1)
C(10)	0.069(2)	0.102(2)	0.068(2)	-0.049(2)	0.000(2)	-0.001(2)

Table A.4.6. Bond lengths(Å).

atom	atom	distance	atom	atom	distance
S(1)	O(1)	1.571(2)	S(1)	O(2)	1.422(2)
S(1)	O(3)	1.424(2)	S(1)	C(4)	1.763(2)
O(1)	C(1)	1.469(3)	C(1)	C(2)	1.500(3)
C(2)	C(3)	1.530(3)	C(3)	C(3)	1.518(4)
C(4)	C(5)	1.378(3)	C(4)	C(9)	1.373(3)
C(5)	C(6)	1.377(3)	C(6)	C(7)	1.378(3)
C(7)	C(8)	1.375(3)	C(7)	C(10)	1.517(3)
C(8)	C(9)	1.389(3)			
C(1)	H(1)	0.95	C(1)	H(2)	0.95
C(2)	H(3)	0.95	C(2)	H(4)	0.95
C(3)	H(5)	0.95	C(3)	H(6)	0.95
C(5)	H(7)	0.95	C(6)	H(8)	0.95
C(8)	H(9)	0.95	C(9)	H(10)	0.95
C(10)	H(11)	0.95	C(10)	H(12)	0.95
C(10)	H(13)	0.95			

Table A.4.7. Bond angles(°).

atom	atom	atom	angle	atom	atom	atom	angle
O(1)	S(1)	O(2)	109.71(9)	O(1)	S(1)	O(3)	103.95(10)
O(1)	S(1)	C(4)	103.02(9)	O(2)	S(1)	O(3)	119.7(1)
O(2)	S(1)	C(4)	109.2(1)	O(3)	S(1)	C(4)	109.9(1)
S(1)	O(1)	C(1)	118.2(1)	O(1)	C(1)	C(2)	107.9(2)
C(1)	C(2)	C(3)	115.0(2)	C(2)	C(3)	C(3)	114.3(2)
S(1)	C(4)	C(5)	118.6(2)	S(1)	C(4)	C(9)	120.5(2)
C(5)	C(4)	C(9)	120.9(2)	C(4)	C(5)	C(6)	119.4(2)
C(5)	C(6)	C(7)	121.1(2)	C(6)	C(7)	C(8)	118.5(2)
C(6)	C(7)	C(10)	120.2(2)	C(8)	C(7)	C(10)	121.4(2)
C(7)	C(8)	C(9)	121.5(2)	C(4)	C(9)	C(8)	118.5(2)
O(1)	C(1)	H(1)	109.8	O(1)	C(1)	H(2)	109.9
C(2)	C(1)	H(1)	109.9	C(2)	C(1)	H(2)	109.9
H(1)	C(1)	H(2)	109.3	C(1)	C(2)	H(3)	108.2
C(1)	C(2)	H(4)	108.3	C(3)	C(2)	H(3)	108.0
C(3)	C(2)	H(4)	108.0	H(3)	C(2)	H(4)	109.4
C(2)	C(3)	H(5)	109.7	C(2)	C(3)	H(6)	109.5
C(3)	C(3)	H(5)	103.5	C(3)	C(3)	H(6)	110.2
H(5)	C(3)	H(6)	109.5	C(4)	C(5)	H(7)	120.3
C(6)	C(5)	H(7)	120.3	C(5)	C(6)	H(8)	119.4
C(7)	C(6)	H(8)	119.5	C(7)	C(8)	H(9)	119.3
C(9)	C(8)	H(9)	119.2	C(4)	C(9)	H(10)	120.8
C(8)	C(9)	H(10)	120.6	C(7)	C(10)	H(11)	109.4
C(7)	C(10)	H(12)	109.4	C(7)	C(10)	H(13)	109.5
H(11)	C(10)	H(12)	109.4	H(11)	C(10)	H(13)	109.6
H(12)	C(10)	H(13)	109.5				

Table A.4.8. Torsion angles(°).

atom	atom	atom	atom	angle	atom	atom	atom	atom	angle
S(1)	O(1)	C(1)	C(2)	155.0(1)	S(1)	C(4)	C(5)	C(6)	177.2(2)
S(1)	C(4)	C(9)	C(8)	-177.2(2)	O(1)	S(1)	C(4)	C(5)	-67.7(2)
O(1)	S(1)	C(4)	C(9)	111.2(2)	O(1)	C(1)	C(2)	C(3)	-65.4(2)
O(2)	S(1)	O(1)	C(1)	42.3(2)	O(2)	S(1)	C(4)	C(5)	175.7(2)
O(2)	S(1)	C(4)	C(9)	-5.4(2)	O(3)	S(1)	O(1)	C(1)	171.4(1)
O(3)	S(1)	C(4)	C(5)	42.5(2)	O(3)	S(1)	C(4)	C(9)	-138.5(2)
C(1)	O(1)	S(1)	C(4)	-73.9(2)	C(1)	C(2)	C(3)	C(3)	-64.6(3)
C(2)	C(3)	C(3)	C(2)	180.0	C(4)	C(5)	C(6)	C(7)	-0.1(4)
C(4)	C(9)	C(8)	C(7)	0.1(4)	C(5)	C(4)	C(9)	C(8)	1.7(3)
C(5)	C(6)	C(7)	C(8)	1.9(4)	C(5)	C(6)	C(7)	C(10)	-177.9(2)
C(6)	C(5)	C(4)	C(9)	-1.7(3)	C(6)	C(7)	C(8)	C(9)	-1.9(4)
C(9)	C(8)	C(7)	C(10)	177.9(2)					

A.5. Data for butane-1,4-diyl bis(3,5-dimethoxybenzoate)

Table A.5.1. Crystal data.

Empirical Formula	$C_{22}H_{26}O_8$
Formula Weight	418.44
Crystal Colour, Habit	colourless, needle
Crystal Dimensions	0.35 X 0.20 X 0.15 mm
Crystal System	monoclinic
Lattice Type	Primitive
No. of Reflections Used for Unit Cell Determination (2θ range)	20 (7.5 - 19.0°)
Omega Scan Peak Width at Half-height	0.28°
Lattice Parameters	a=14.353(6)Å b=17.013(6)Å c=4.291(8)Å β=98.1(1)° V=1037(1)Å^3
Space Group $P2_1/n$	(#14)
Z value	2
D_{calc}	1.340 g/cm^3
F_{000}	444.00
μ(MoKα)	1.02 cm^{-1}

Table A.5.2. Intensity measurements.

Diffractometer	RigakuAFC7S
Radiation	MoKα (λ=0.71069Å), graphite monochromated
Attenuator	Zr foil (factor = 8.53)
Take-off Angle	6.0°
Detector Aperture	9.0 mm horizontal, 13.0 mm vertical
Crystal to Detector Distance	235 mm
Temperature	20.0 °C
Scan Type	ω - 2θ
Scan Rate	16.0 °/min (in ω) (up to 4 scans)
Scan Width	(1.37 + 0.35 tanθ)°
$2\theta_{max}$	50.0°
No. of Reflections Measured	Total: 2884, Unique: 2441 (R_{int} = 0.029)
Corrections	Lorentz-polarization Secondary Extinction (coefficient: 1.16431e-06).

Table A.5.3. Structure solution and refinement.

Structure Solution	Direct Methods (SIR92)
Refinement	Full-matrix least-squares
Function Minimised	$\Sigma\omega(\|Fo\| - \|Fc\|)^2$
Least Squares Weights	$1/\sigma^2(Fo) = 4Fo^2/\sigma^2(Fo^2)$
p-factor	0.0160
Anomalous Dispersion	All non-hydrogen atoms
No. Observations ($I > 3.00\sigma(I)$)	1127
No. Variables	137
Reflection/Parameter Ratio	8.23
Residuals	R = 0.037,Rw = 0.039
Goodness of Fit Indicator	1.58
MaxShift/Error in Final Cycle	0.01
Maximum peak in Final Diff. Map	0.15 e-/Å^3
Minimum peak in Final Diff. Map	-0.14 e-/Å^3

Table A.5.4. Atomic co-ordinates and B_{iso} /B_{eq}.

atom	x	y	z	B_{eq}
O(1)	0.3353(1)	0.40232(9)	1.0483(4)	3.79(4)
O(2)	0.2769(1)	0.12659(9)	1.0610(4)	3.64(4)
O(3)	0.0206(1)	0.24510(10)	0.2331(4)	3.64(4)
O(4)	0.0489(1)	0.37435(9)	0.3013(4)	2.91(4)
C(1)	0.1517(2)	0.2870(1)	0.6027(5)	2.47(5)
C(2)	0.2062(2)	0.3497(1)	0.7227(5)	2.72(5)
C(3)	0.2849(2)	0.3363(1)	0.9472(5)	2.74(6)
C(4)	0.3072(2)	0.2611(1)	1.0547(6)	2.80(6)
C(5)	0.2501(2)	0.1989(1)	0.9336(6)	2.73(5)
C(6)	0.1737(2)	0.2106(1)	0.7057(6)	2.68(6)
C(7)	0.4203(2)	0.3914(2)	1.2606(7)	4.21(7)
C(8)	0.2148(2)	0.0626(2)	0.9751(8)	5.02(8)
C(9)	0.0673(2)	0.2980(1)	0.3609(5)	2.65(6)
C(10)	-0.0324(2)	0.3910(1)	0.0686(6)	2.92(6)
C(11)	-0.0425(2)	0.4791(1)	0.0487(6)	2.82(5)
H(1)	0.1903	0.4016	0.6529	3.2308
H(2)	0.3607	0.2520	1.2088	3.3184
H(3)	0.1364	0.1674	0.6201	3.1800
H(4)	0.4063	0.3666	1.4465	5.0269
H(5)	0.4622	0.3595	1.1636	5.0269
H(6)	0.4486	0.4411	1.3118	5.0269
H(7)	0.1556	0.0733	1.0405	5.9912
H(8)	0.2069	0.0560	0.7533	5.9912
H(9)	0.2406	0.0161	1.0745	5.9912
H(10)	-0.0232	0.3703	-0.1302	3.4750
H(11)	-0.0874	0.3683	0.1317	3.4750
H(12)	-0.0504	0.4995	0.2497	3.3341
H(13)	-0.0959	0.4923	-0.0992	3.3341

Table A.5.5. Anisotropic displacement parameters.

Atom	U_{11}	U_{22}	U_{33}	U_{12}	U_{13}	U_{23}
O(1)	0.047(1)	0.0304(10)	0.060(1)	0.0000(9)	-0.0159(9)	-0.0019(9)
O(2)	0.046(1)	0.0266(9)	0.062(1)	0.0039(8)	-0.0069(9)	0.0061(9)
O(3)	0.047(1)	0.035(1)	0.051(1)	-0.0063(9)	-0.0070(9)	-0.0028(9)
O(4)	0.0382(10)	0.0324(10)	0.0360(9)	0.0040(8)	-0.0084(7)	0.0011(8)
C(1)	0.031(1)	0.030(1)	0.033(1)	0.005(1)	0.005(1)	0.001(1)
C(2)	0.036(1)	0.027(1)	0.038(1)	0.005(1)	0.001(1)	0.002(1)
C(3)	0.036(1)	0.030(1)	0.038(1)	0.001(1)	0.002(1)	-0.004(1)
C(4)	0.033(1)	0.034(1)	0.037(1)	0.006(1)	0.000(1)	0.000(1)
C(5)	0.036(1)	0.027(1)	0.041(1)	0.007(1)	0.007(1)	0.004(1)
C(6)	0.034(1)	0.028(1)	0.039(1)	-0.001(1)	0.005(1)	-0.001(1)
C(7)	0.042(2)	0.045(2)	0.066(2)	0.000(1)	-0.015(1)	-0.009(1)
C(8)	0.068(2)	0.030(2)	0.087(2)	-0.003(2)	-0.012(2)	0.013(2)
C(9)	0.035(1)	0.031(1)	0.035(1)	0.002(1)	0.006(1)	0.001(1)
C(10)	0.032(1)	0.041(2)	0.035(1)	0.000(1)	-0.006(1)	0.001(1)
C(11)	0.031(1)	0.037(1)	0.035(1)	0.006(1)	-0.007(1)	0.003(1)

Table A.5.6. Bond lengths(Å).

Atom	atom	distance	atom	atom	distance
O(1)	C(3)	1.373(3)	O(1)	C(7)	1.427(3)
O(2)	C(5)	1.378(3)	O(2)	C(8)	1.422(3)
O(3)	C(9)	1.207(3)	O(4)	C(9)	1.342(3)
O(4)	C(10)	1.452(3)	C(1)	C(2)	1.378(3)
C(1)	C(6)	1.394(3)	C(1)	C(9)	1.491(3)
C(2)	C(3)	1.395(3)	C(3)	C(4)	1.383(3)
C(4)	C(5)	1.393(3)	C(5)	C(6)	1.377(3)
C(10)	C(11)	1.508(3)	C(11)	C(11)	1.521(5)
C(2)	H(1)	0.95	C(4)	H(2)	0.95
C(6)	H(3)	0.95	C(7)	H(4)	0.95
C(7)	H(5)	0.95	C(7)	H(6)	0.95
C(8)	H(7)	0.95	C(8)	H(8)	0.95
C(8)	H(9)	0.95	C(10)	H(10)	0.95
C(10)	H(11)	0.95	C(11)	H(12)	0.95
C(11)	H(13)	0.95			

Table A.5.7. Bond angles(°).

atom	atom	atom	angle	atom	atom	atom	angle
C(3)	O(1)	C(7)	117.4(2)	C(5)	O(2)	C(8)	116.8(2)
C(9)	O(4)	C(10)	115.9(2)	C(2)	C(1)	C(6)	120.8(2)
C(2)	C(1)	C(9)	121.6(2)	C(6)	C(1)	C(9)	117.6(2)
C(1)	C(2)	C(3)	119.5(2)	O(1)	C(3)	C(2)	115.1(2)
O(1)	C(3)	C(4)	124.4(2)	C(2)	C(3)	C(4)	120.5(2)
C(3)	C(4)	C(5)	118.8(2)	O(2)	C(5)	C(4)	114.5(2)
O(2)	C(5)	C(6)	124.1(2)	C(4)	C(5)	C(6)	121.5(2)
C(1)	C(6)	C(5)	118.8(2)	O(3)	C(9)	O(4)	123.6(2)
O(3)	C(9)	C(1)	124.5(2)	O(4)	C(9)	C(1)	111.9(2)
O(4)	C(10)	C(11)	107.1(2)	C(10)	C(11)	C(11)	113.9(3)
C(1)	C(2)	H(1)	120.2	C(3)	C(2)	H(1)	120.2
C(3)	C(4)	H(2)	120.6	C(5)	C(4)	H(2)	120.6
C(1)	C(6)	H(3)	120.5	C(5)	C(6)	H(3)	120.6
O(1)	C(7)	H(4)	109.4	O(1)	C(7)	H(5)	109.3
O(1)	C(7)	H(6)	109.3	H(4)	C(7)	H(5)	109.7
H(4)	C(7)	H(6)	109.6	H(5)	C(7)	H(6)	109.5
O(2)	C(8)	H(7)	109.3	O(2)	C(8)	H(8)	109.4
O(2)	C(8)	H(9)	109.4	H(7)	C(8)	H(8)	109.6
H(7)	C(8)	H(9)	109.6	H(8)	C(8)	H(9)	109.6
O(4)	C(10)	H(10)	110.1	O(4)	C(10)	H(11)	110.1
C(11)	C(10)	H(10)	110.0	C(11)	C(10)	H(11)	110.0
H(10)	C(10)	H(11)	109.5	C(10)	C(11)	H(12)	109.5
C(10)	C(11)	H(13)	109.5	C(11)	C(11)	H(12)	106.4
C(11)	C(11)	H(13)	108.0	H(12)	C(11)	H(13)	109.4

Table A.5.8. Torsion angles(°).

atom	atom	atom	atom	angle	atom	atom	atom	atom	angle
O(1)	C(3)	C(2)	C(1)	179.0(2)	O(1)	C(3)	C(4)	C(5)	179.9(2)
O(2)	C(5)	C(4)	C(3)	-178.5(2)	O(2)	C(5)	C(6)	C(1)	177.8(2)
O(3)	C(9)	O(4)	C(10)	0.0(3)	O(3)	C(9)	C(1)	C(2)	175.1(2)
O(3)	C(9)	C(1)	C(6)	-5.3(4)	O(4)	C(9)	C(1)	C(2)	-5.0(3)
O(4)	C(9)	C(1)	C(6)	174.6(2)	O(4)	C(10)	C(11)	C(11)	60.0(3)
C(1)	C(2)	C(3)	C(4)	-1.5(4)	C(1)	C(6)	C(5)	C(4)	-2.1(4)
C(1)	C(9)	O(4)	C(10)	-179.9(2)	C(2)	C(1)	C(6)	C(5)	0.9(4)
C(2)	C(3)	O(1)	C(7)	-175.6(2)	C(2)	C(3)	C(4)	C(5)	0.4(4)
C(3)	C(2)	C(1)	C(6)	0.8(4)	C(3)	C(2)	C(1)	C(9)	-179.6(2)
C(3)	C(4)	C(5)	C(6)	1.4(4)	C(4)	C(3)	O(1)	C(7)	4.9(4)
C(4)	C(5)	O(2)	C(8)	172.5(2)	C(5)	C(6)	C(1)	C(9)	-178.7(2)
C(6)	C(5)	O(2)	C(8)	-7.4(4)	C(9)	O(4)	C(10)	C(11)	177.6(2)
C(10)	C(11)	C(11)	C(10)	180.0					

Table A.5.9. Non-bonded contacts out to 3.30 Å

atom	atom	distance	ADC	atom	atom	distance	ADC
O(2)	C(10)	3.261(3)	55604	O(3)	C(7)	3.279(3)	45304

A.6. Plots of all crystal structures in the order of appearance in the text

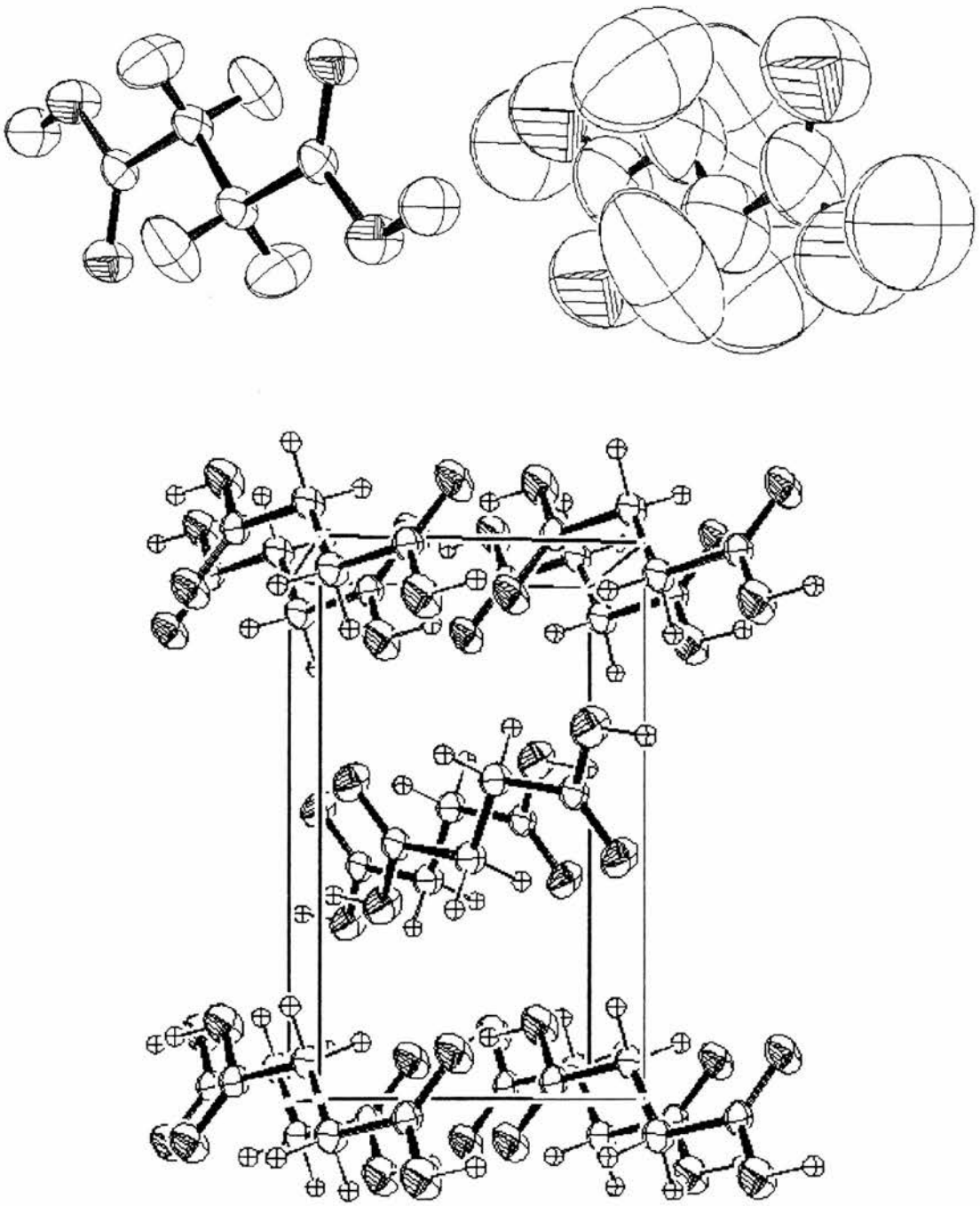

Figure A.1. A view of succinic acid at 300 K (top) together with a view of the unit cell (bottom).[92] The molecule is plotted with 50 % (top, left) and 99 % (top right) probability ellipsoids. The asymmetric unit is equal to half of the molecule. The unit cell is monoclinic with dimensions: a = 5.519, b = 8.862, c = 5.101 Å and β = 91.59°. The space group is $P2_1/c$.

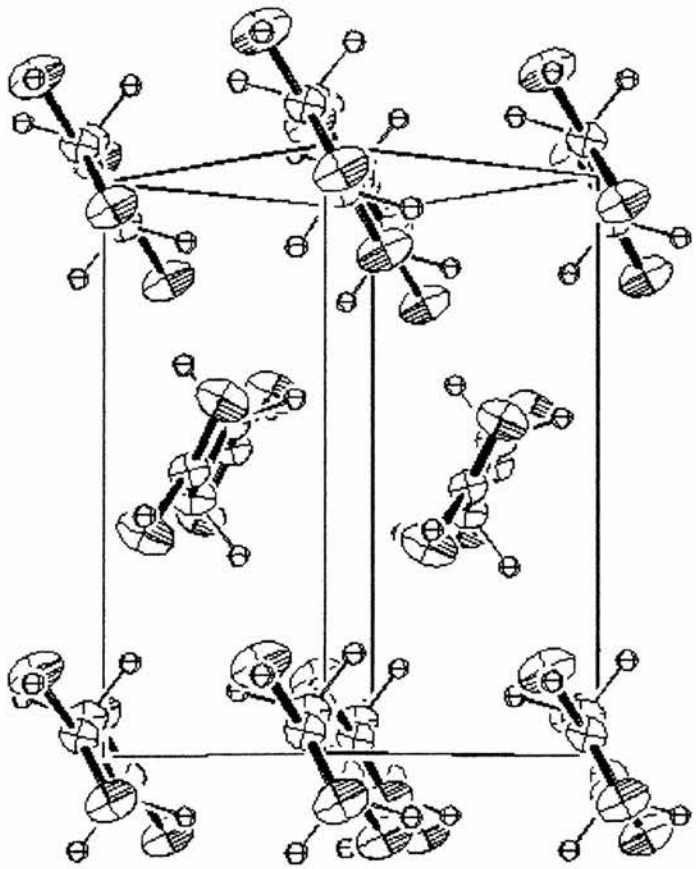

Figure A.1. (continued) The unit cell of succinic acid at 300 K viewed from a different angle.[92] The asymmetric unit is equal to half of the molecule. The unit cell is monoclinic with dimensions: a = 5.519, b = 8.862, c = 5.101 Å and β = 91.59°. The space group is $P2_1/c$.

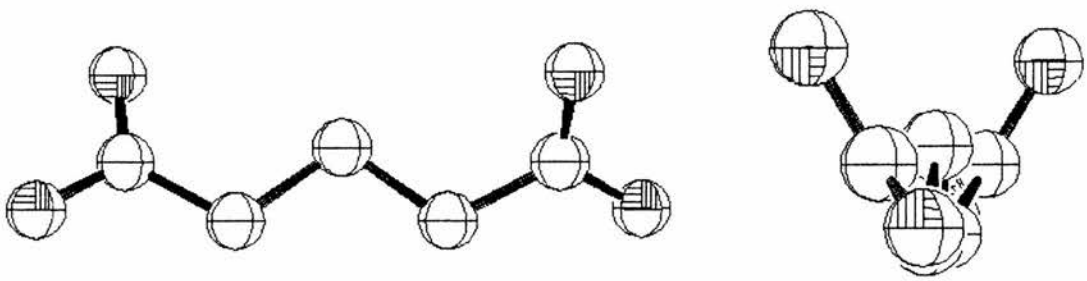

Figure A.2. Two different views of β-glutaric acid.[96]

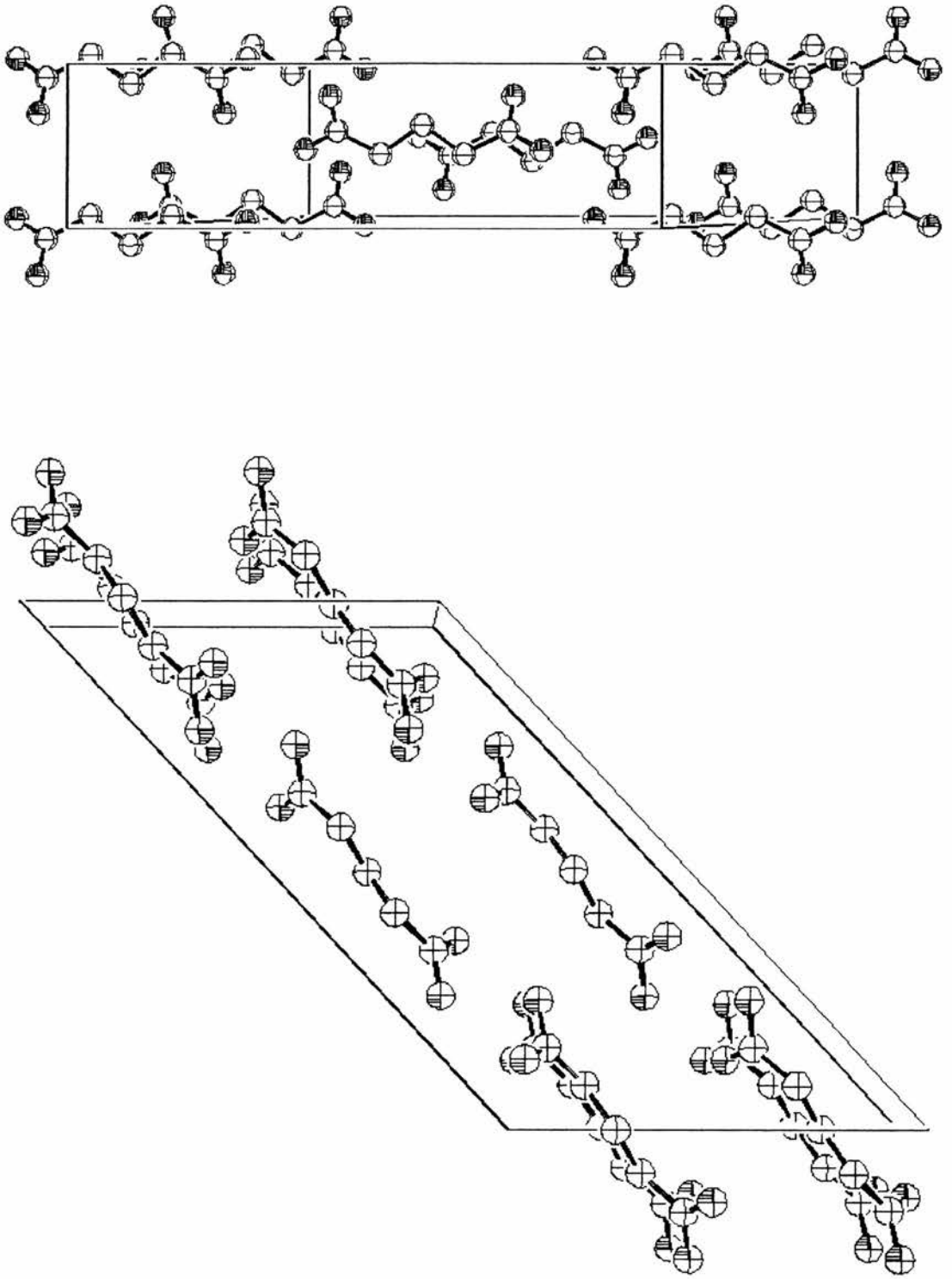

Figure A.2. (continued) The unit cell of β-glutaric acid plotted from two different angles.[96] The asymmetric unit is equal to half of the molecule. The unit cell is monoclinic with dimensions: a = 10.060, b = 4.870, c = 17.400 Å and β = 132.60°. The space group is $I2/a$.

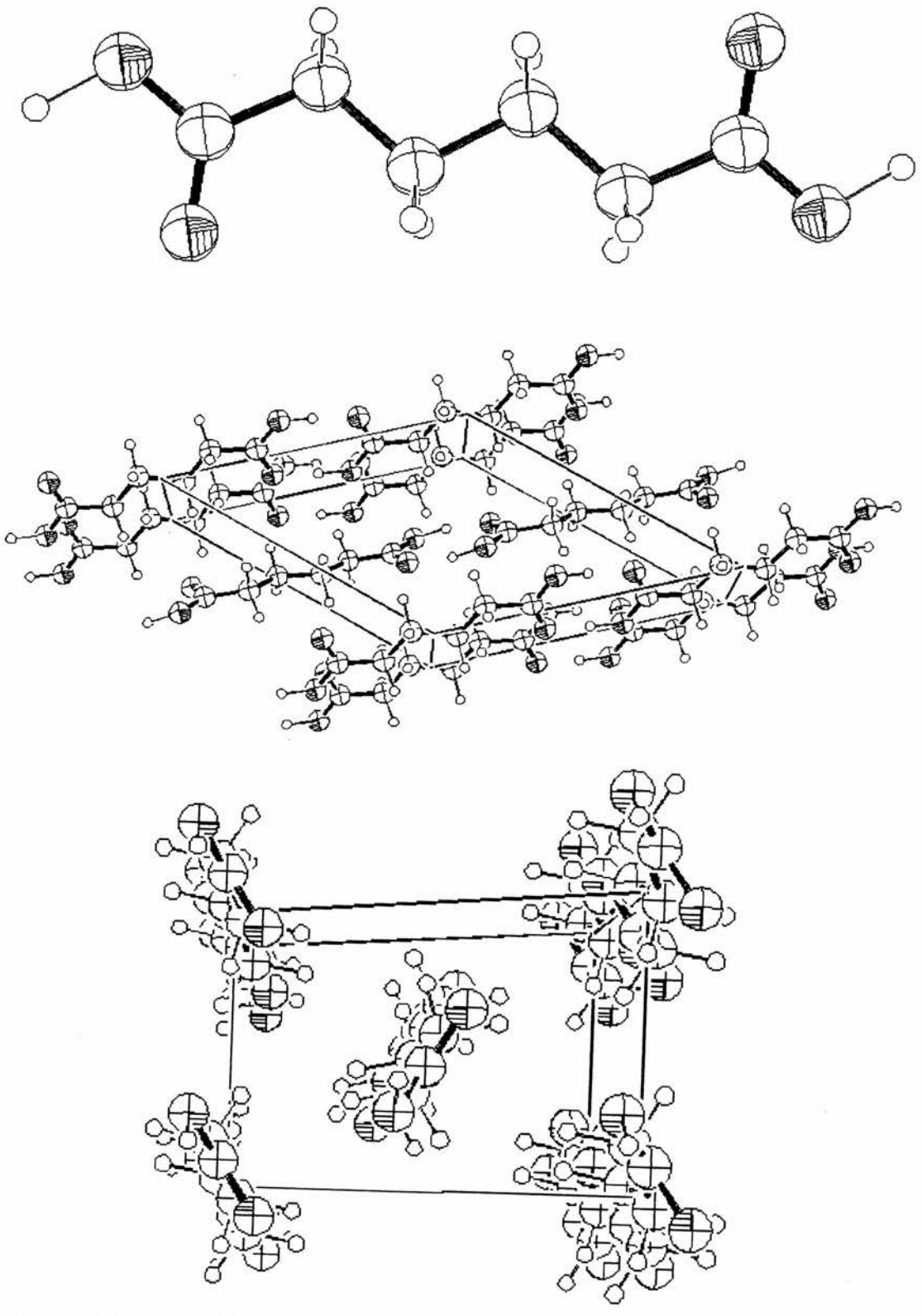

Figure A.3. A view of adipic acid (top) together with two different views of the unit cell (middle and bottom).[102] The asymmetric unit is equal to half of the molecule. The unit cell is monoclinic with dimensions: a = 10.010, b = 5.150, c = 10.060 Å and β = 136.75°. The space group is $P2_1/c$.

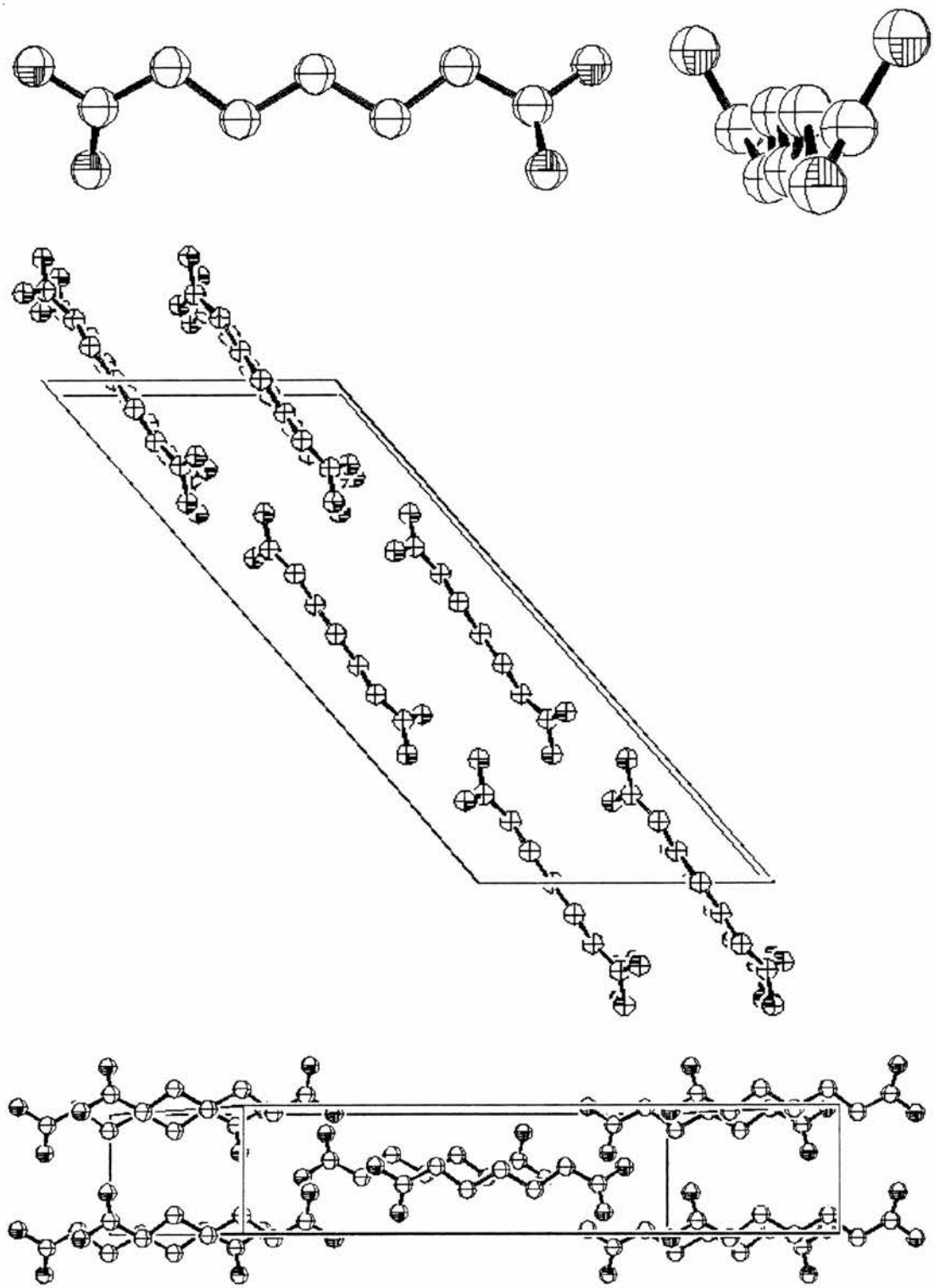

Figure A.4. Two different views of β-pimelic acid (top) together views of the unit cell (middle and bottom).[103] The asymmetric unit is equal to half of the molecule. The unit cell is monoclinic with dimensions: a = 9.840, b = 4.890, c = 22.430 Å and β = 130.67°. The space group is $I2/a$.

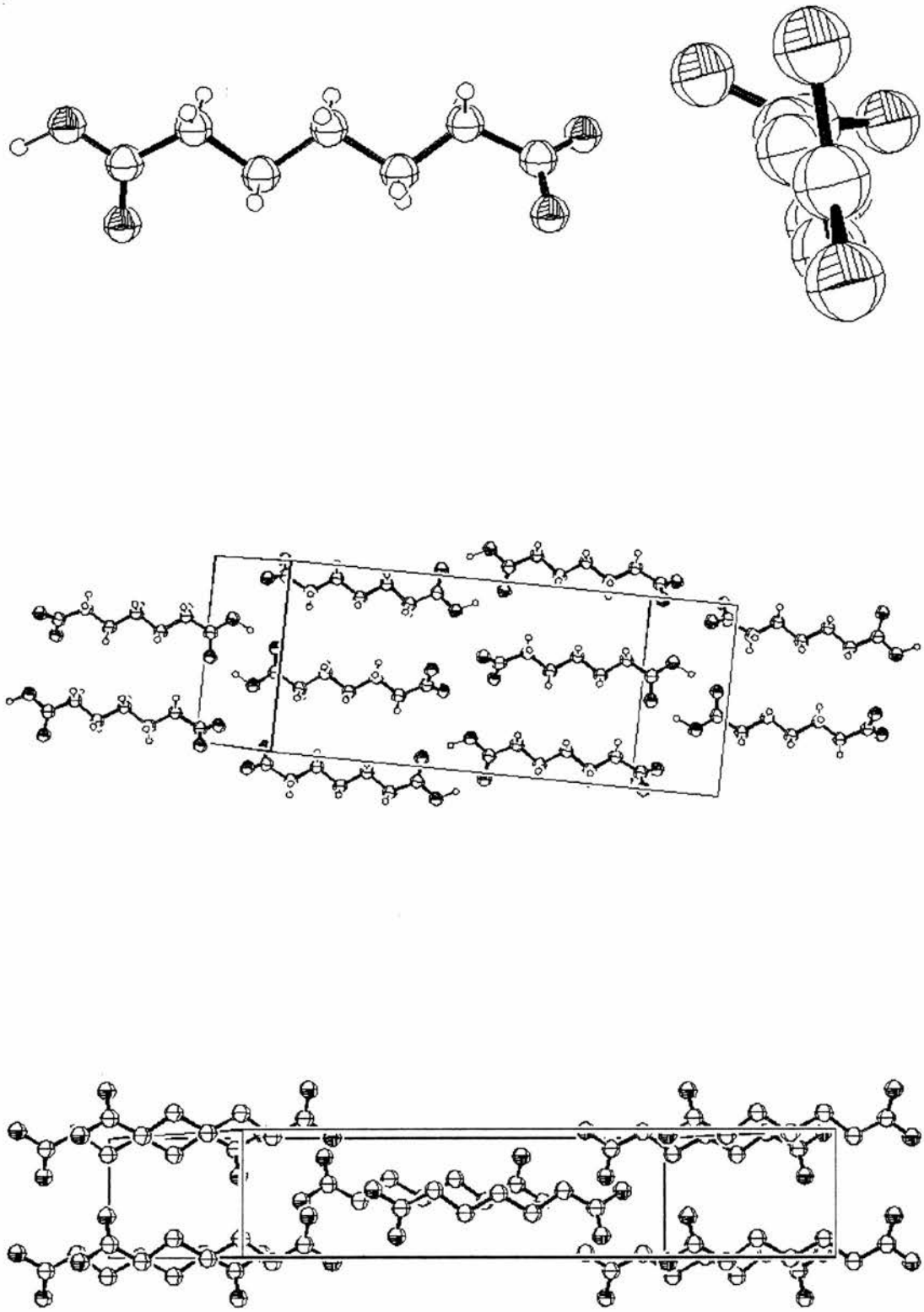

Figure A.5. Two different views of α-pimelic acid (top) together with views of the unit cell (middle and bottom).[105] The asymmetric unit is equal to the whole molecule. The unit cell is monoclinic with dimensions: a = 5.650, b = 9.680, c = 22.330 Å and β = 137.00°. The space group is $P2_1/c$.

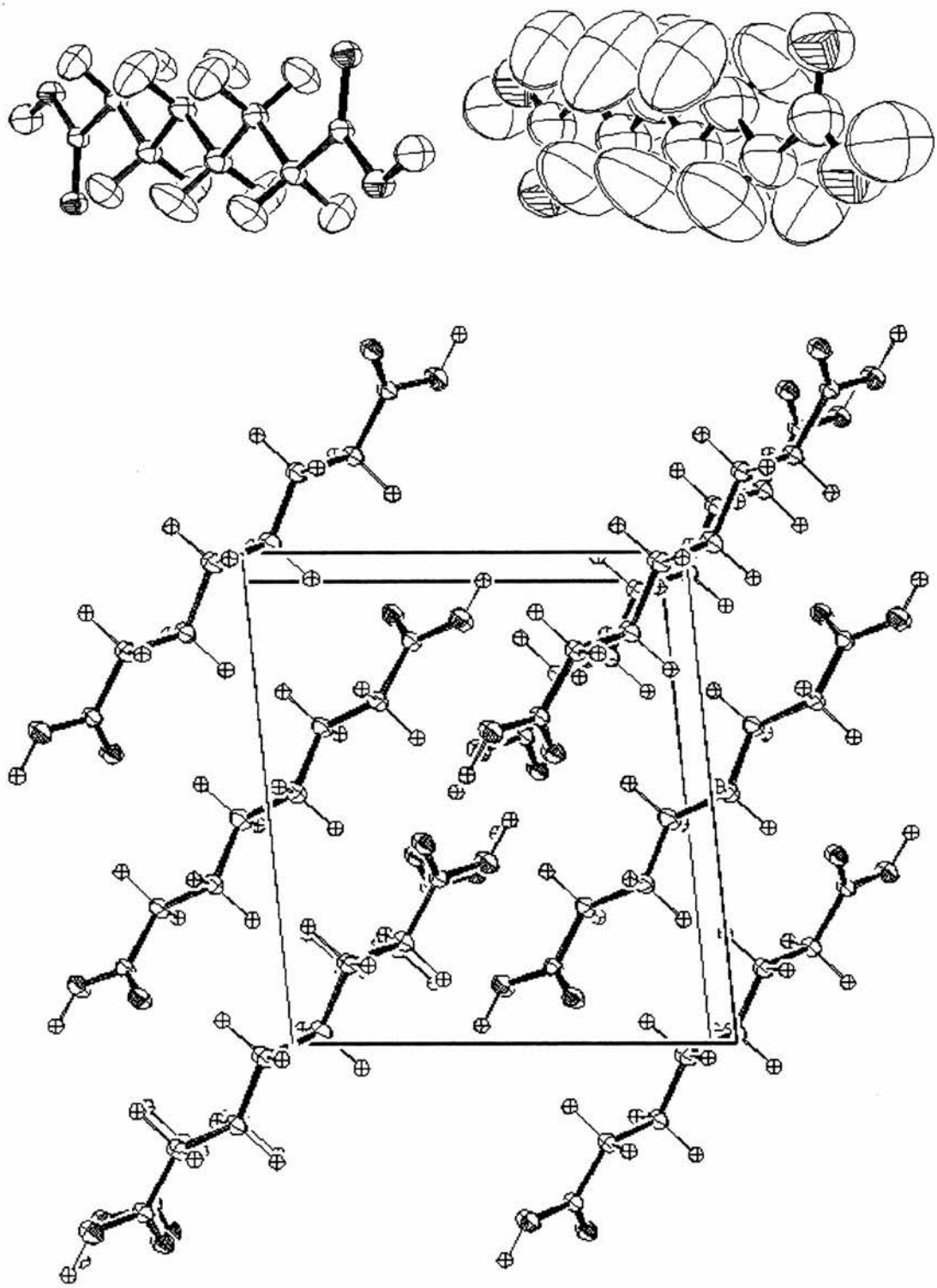

Figure A.6. Two different views of suberic acid (top) at 123 K together with a view of the unit cell (bottom).[107] The molecule is plotted with 50 % (top, left) and 99 % (top right) probability ellipsoids. The asymmetric unit is equal to half of the molecule. The unit cell is monoclinic with dimensions: a = 8.784, b = 5.072, c = 9.889 Å and β = 95.95°. The space group is $P2_1/c$.

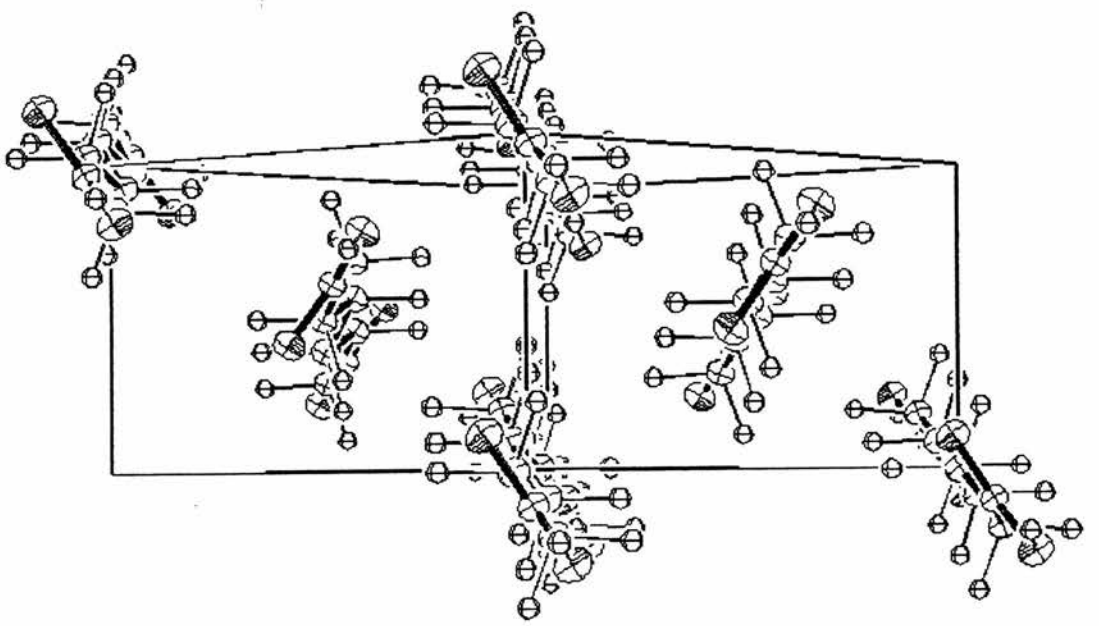

Figure A.6. (continued) The unit cell of suberic acid viewed from a different angle.[107] The asymmetric unit is equal to half of the molecule. The unit cell is monoclinic with dimensions: a = 8.784, b = 5.072, c = 9.889 Å and β = 95.95°. The space group is $P2_1/c$.

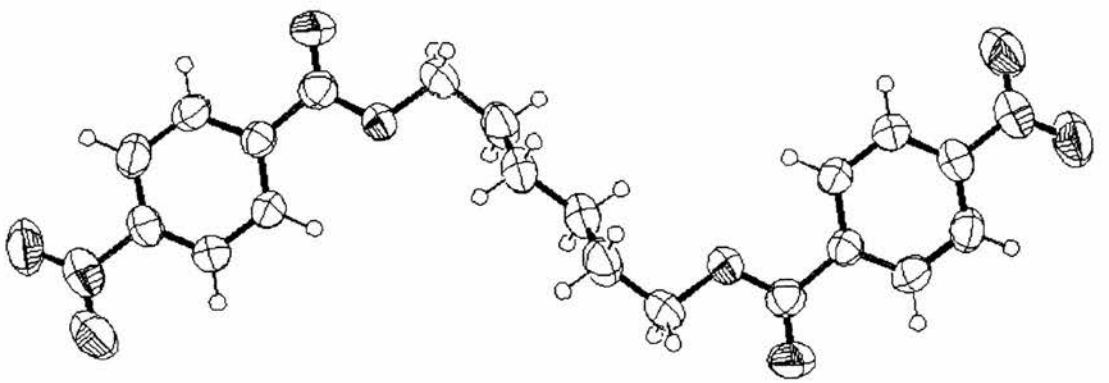

Figure A.7. A view of hexane-1,6-diyl bis(*p*-nitrobenzoate).

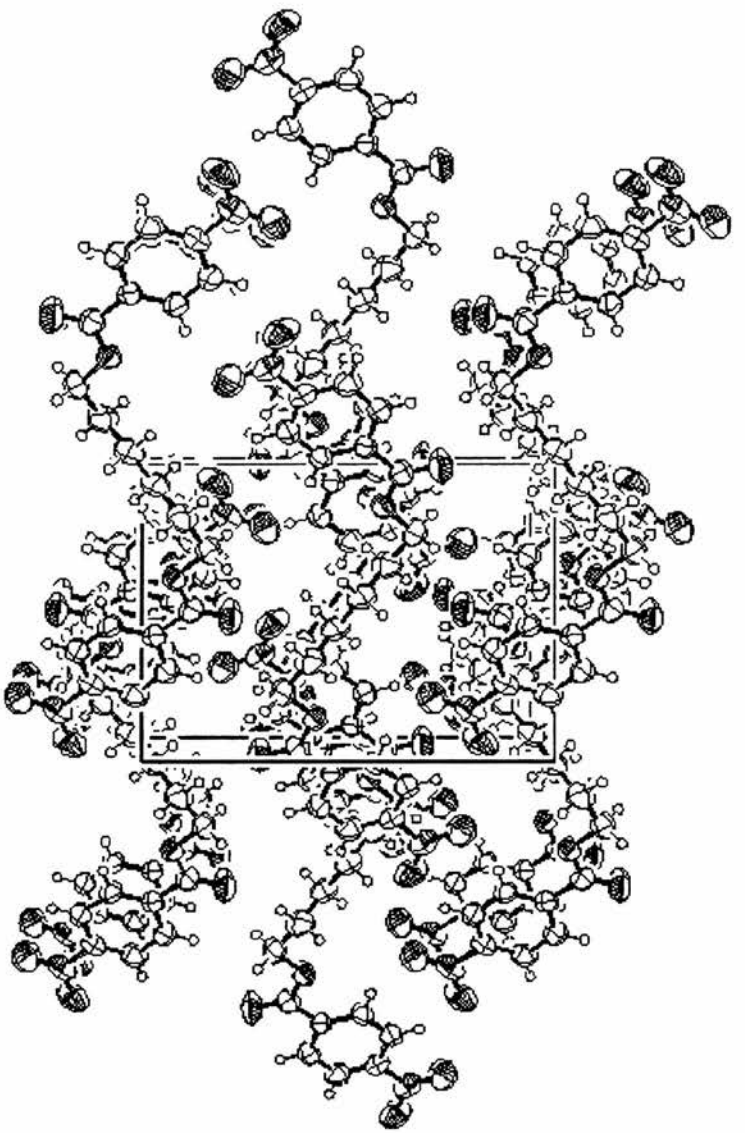

Figure A.7. (continued) The unit cell of hexane-1,6-diyl bis(*p*-nitrobenzoate). The asymmetric unit is equal to half of the molecule. The unit cell is monoclinic with dimensions: a = 8.982, b = 12.471, c = 9.086 Å and β = 92.91°. The space group is $P2_1/n$.

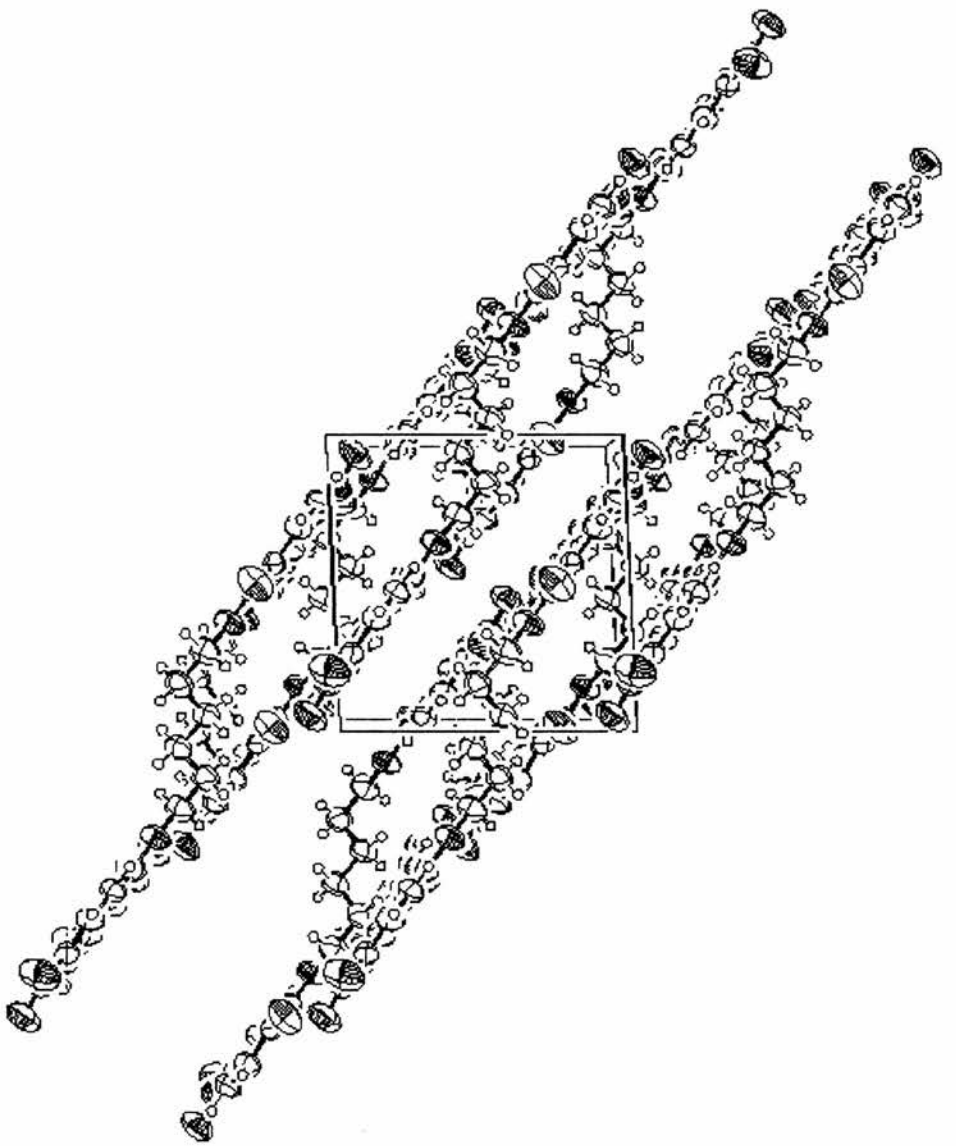

Figure A.7. (continued) The unit cell of hexane-1,6-diyl bis(*p*-nitrobenzoate) viewed from a different angle. The asymmetric unit is equal to half of the molecule. The unit cell is monoclinic with dimensions: a = 8.982, b = 12.471, c = 9.086 Å and β = 92.91°. The space group is $P2_1/n$.

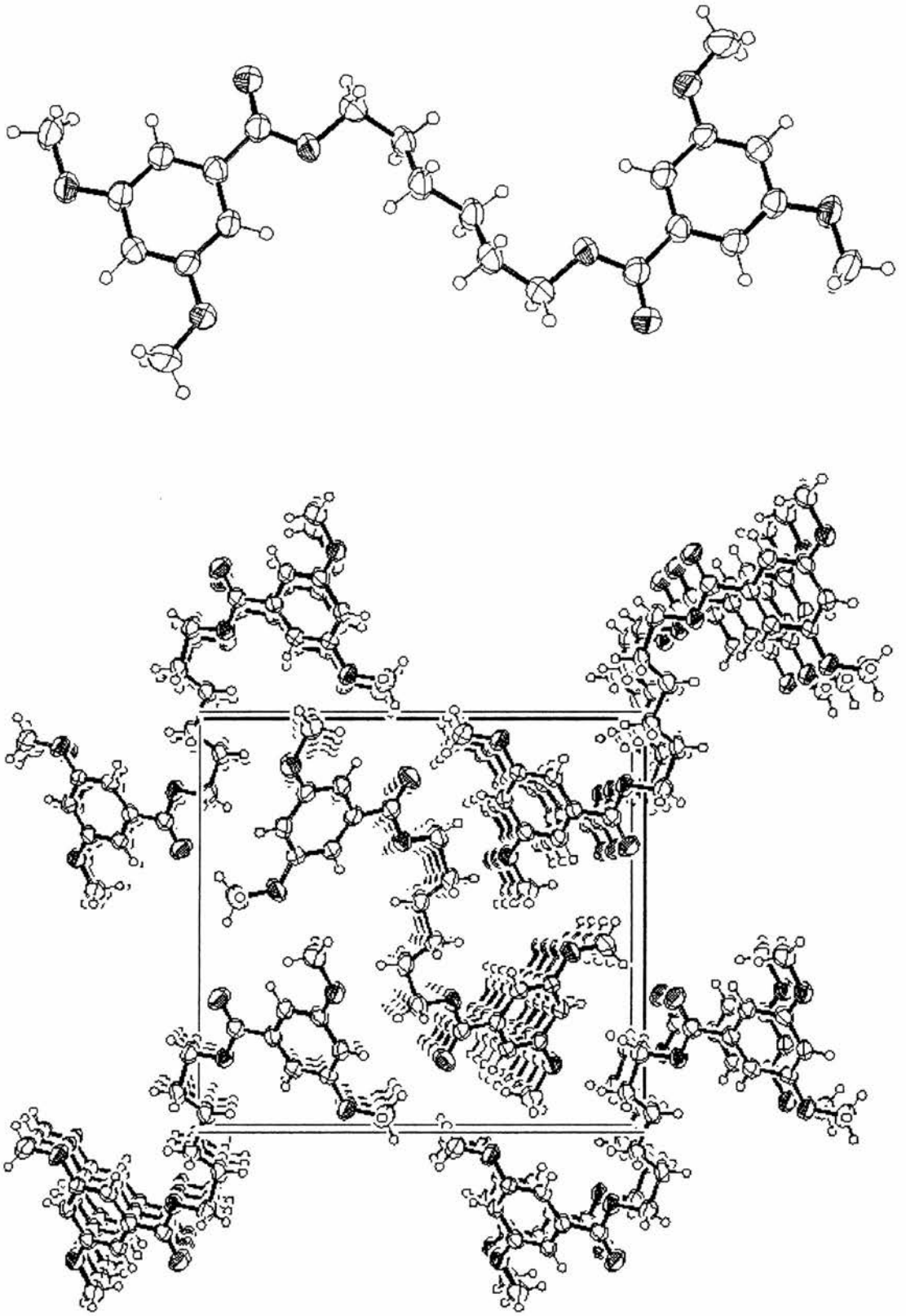

Figure A.8. A view of hexane-1,6-diyl bis(3,5-dimethoxybenzoate) (top) together with a view of the unit cell (bottom). The asymmetric unit is equal to half of the molecule. The unit cell is monoclinic with dimensions: a = 4.846, b = 15.805, c = 15.121 Å and β = 92.11°. The space group is $P2_1/c$.

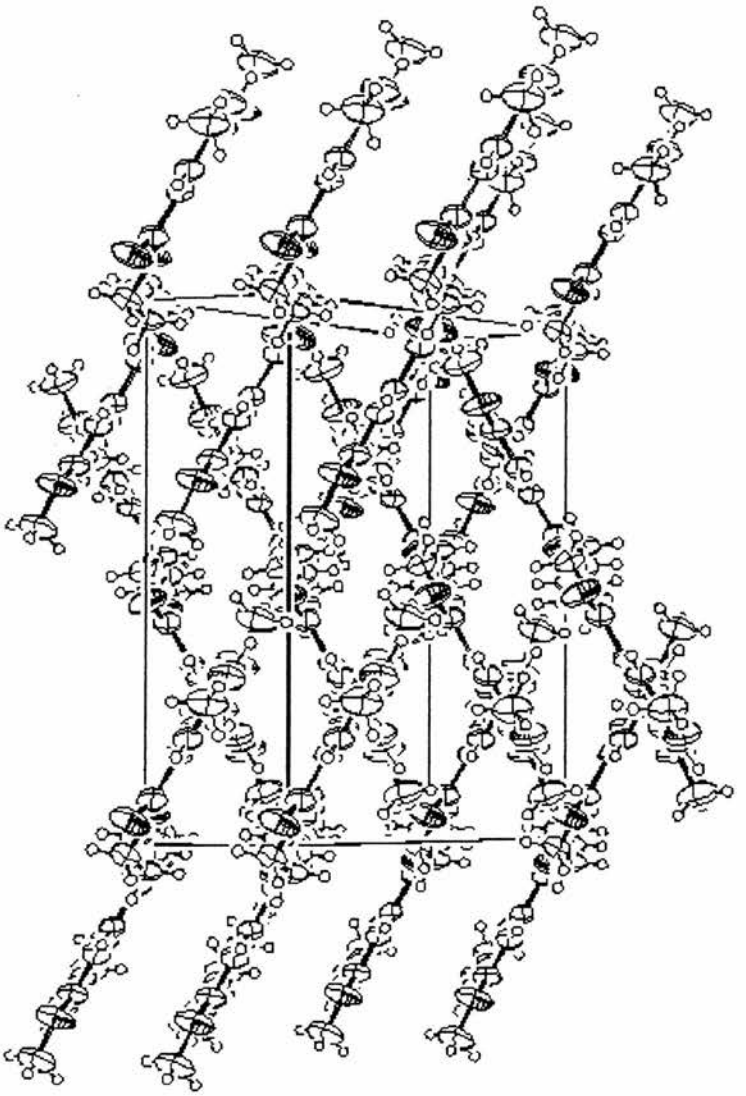

Figure A.8.(continued) The unit cell of hexane-1,6-diyl bis(3,5-dimethoxybenzoate) viewed from a different angle. The asymmetric unit is equal to half of the molecule. The unit cell is monoclinic with dimensions: a = 4.846, b = 15.805, c = 15.121 Å and β = 92.11°. The space group is $P2_1/c$.

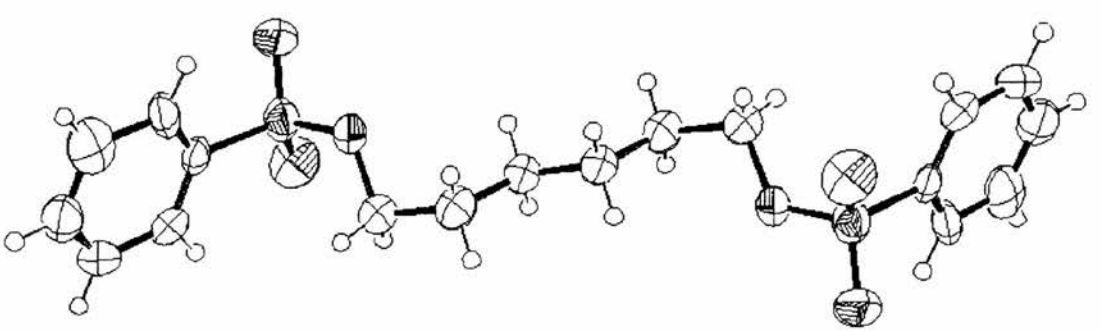

Figure A.9. A view of hexane-1,6-diyl dibenzenesulphonate.

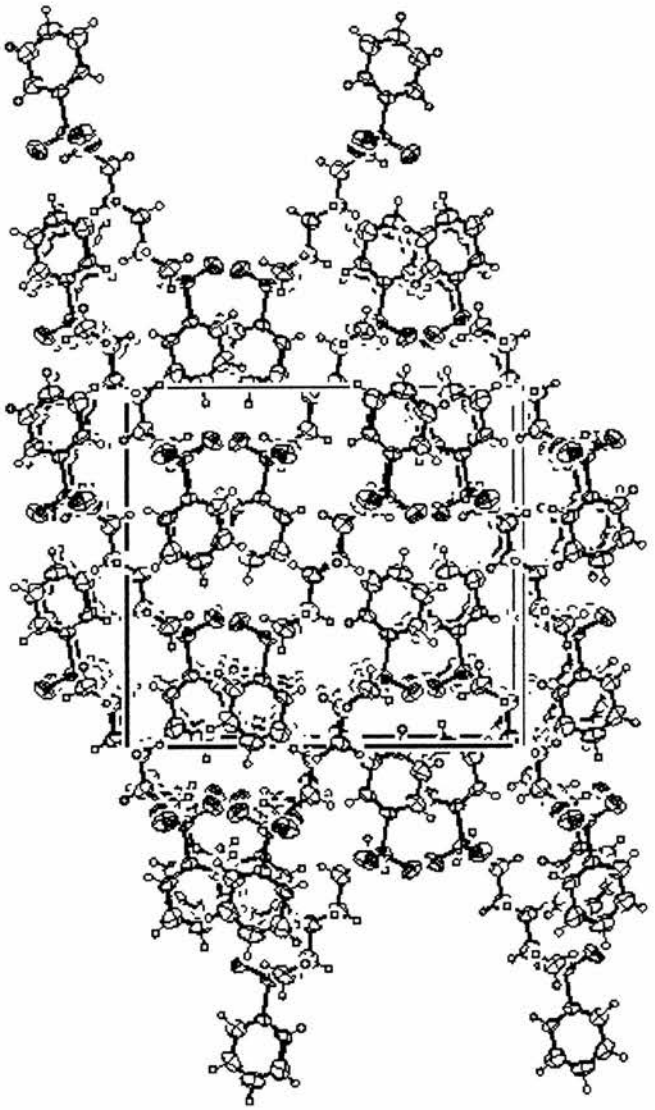

Figure A.9. (continued) The unit cell of hexane-1,6-diyl dibenzenesulphonate. The asymmetric unit is equal to half of the molecule. The unit cell is orthorhombic with dimensions: a = 16.707, b = 7.719 and c = 15.349 Å. The space group is *P*bcn.

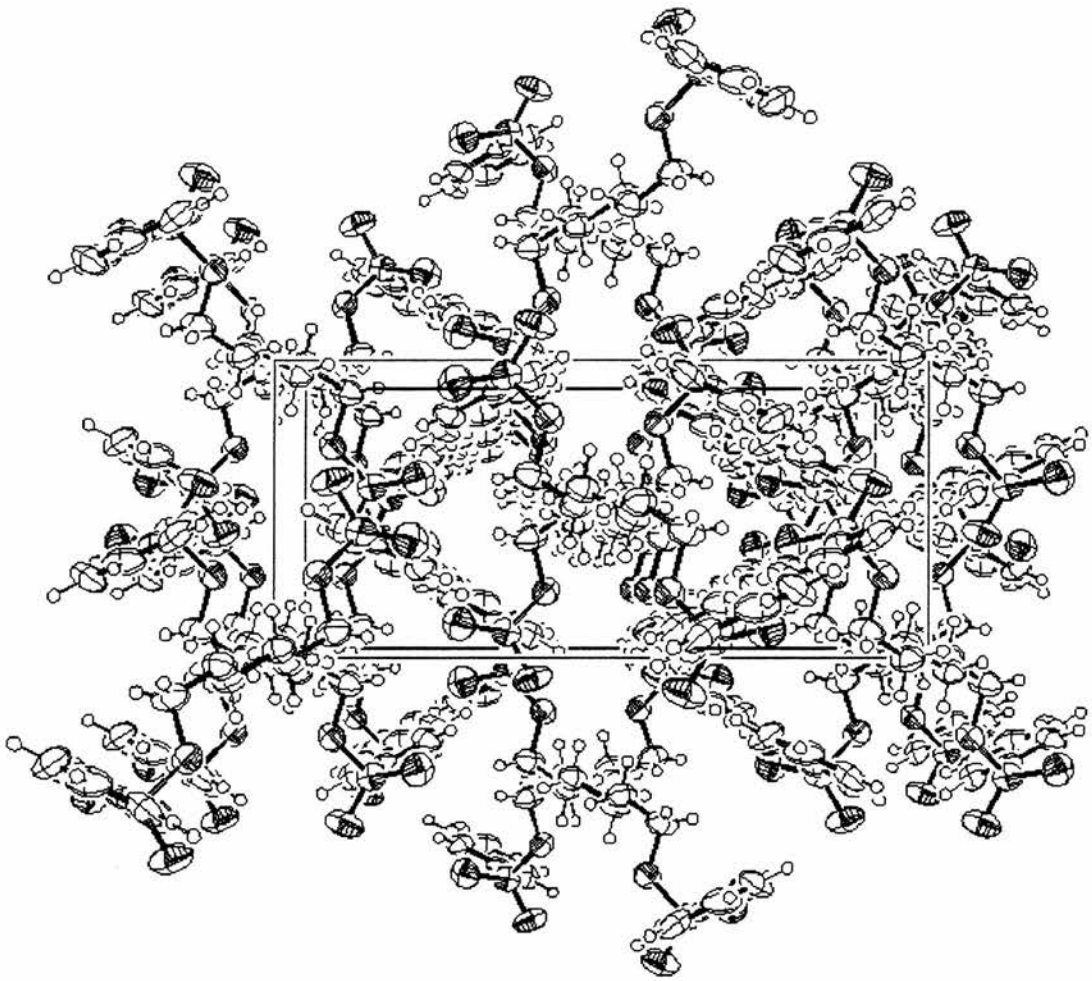

Figure A.9. (continued) The unit cell of hexane-1,6-diyl dibenzenesulphonate viewed from a different angle. The asymmetric unit is equal to half of the molecule. The unit cell is orthorhombic with dimensions: a = 16.707, b = 7.719 and c = 15.349 Å. The space group is *P*bcn.

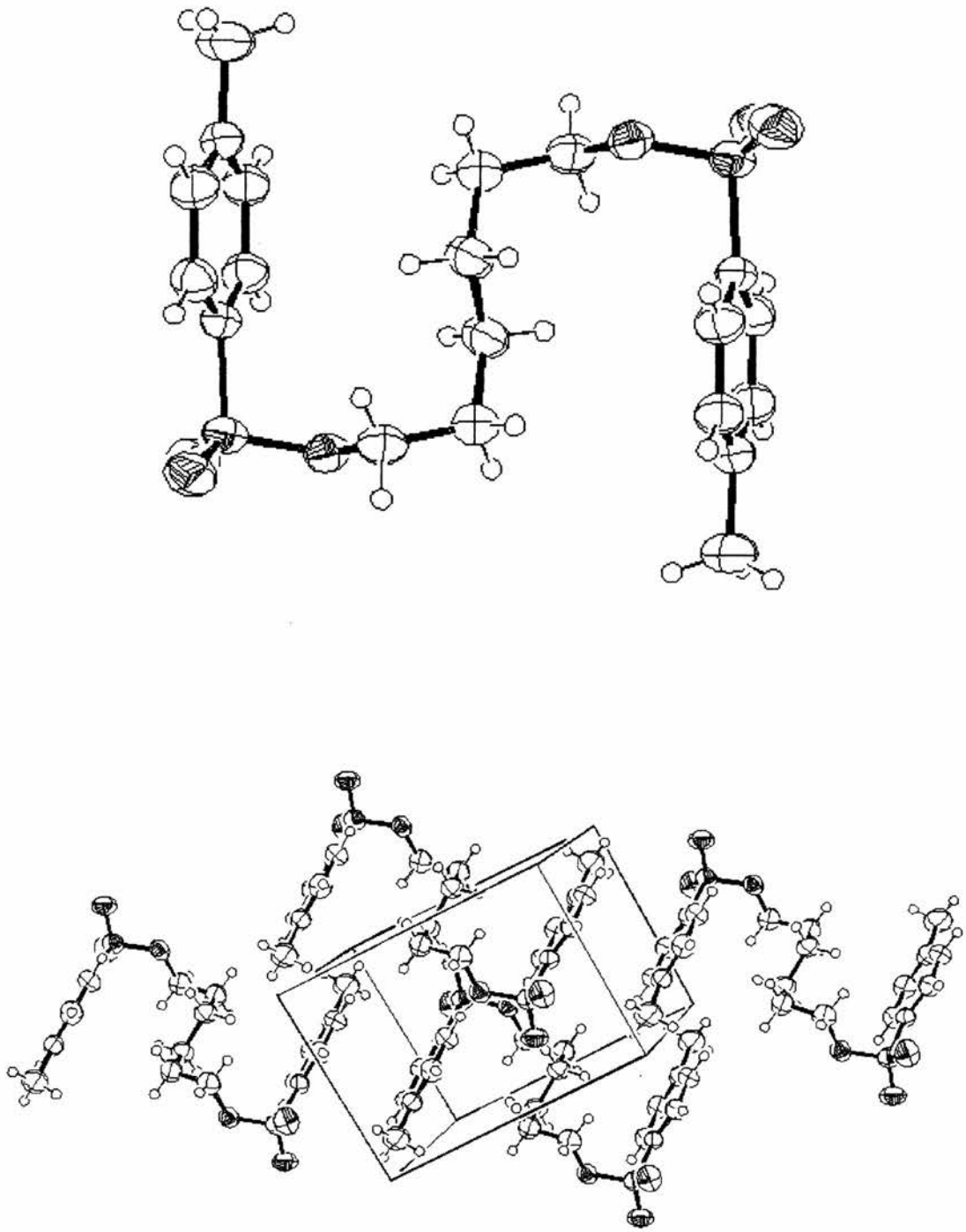

Figure A.10. A view of hexane-1,6-diyl ditosylate (top) together with a view of the unit cell (bottom). The asymmetric unit is equal to half of the molecule. The unit cell is triclinic with dimensions: a = 8.111, b =9.167, c = 7.365 Å, α = 90.25, β = 106.00 and γ = 80.81°. The space group is P-1.

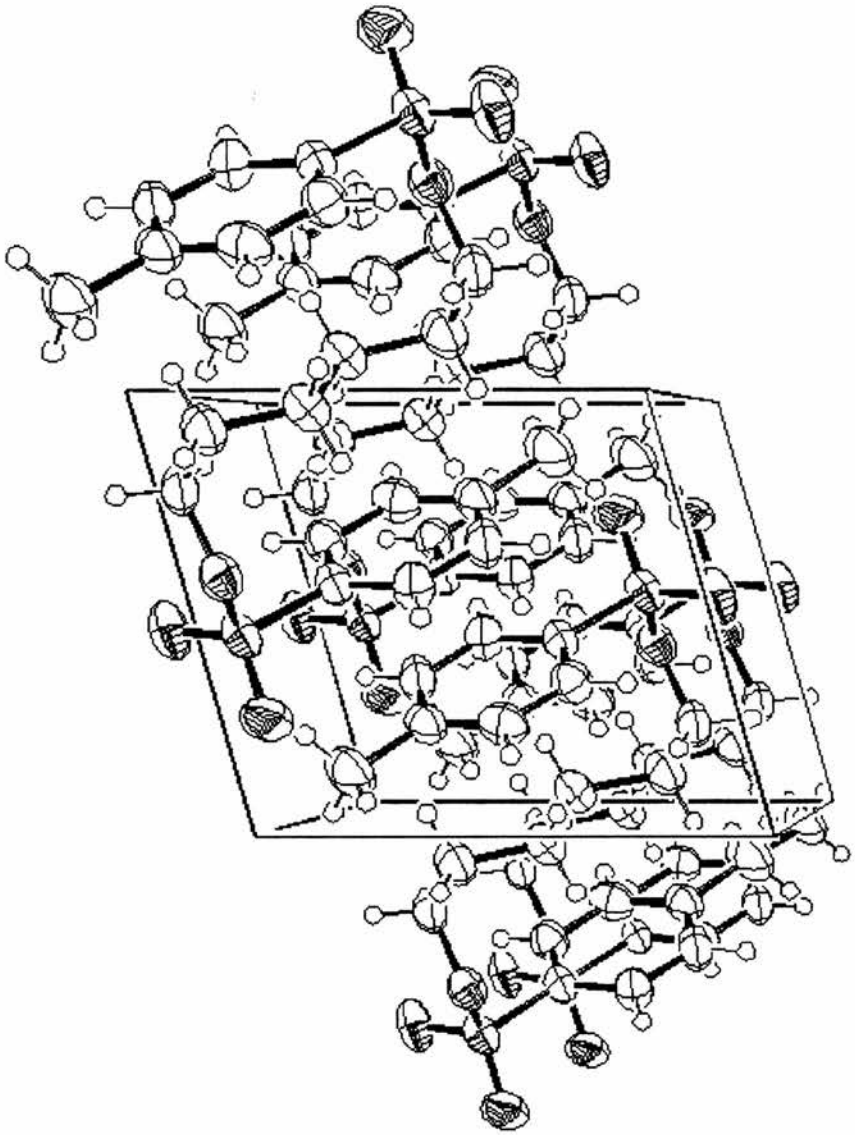

Figure A.10. (continued) The unit cell of hexane-1,6-diyl ditosylate viewed from a different angle. The asymmetric unit is equal to half of the molecule. The unit cell is triclinic with dimensions: a = 8.111, b =9.167, c = 7.365 Å, α = 90.25, β = 106.00 and γ = 80.81°. The space group is P-1.

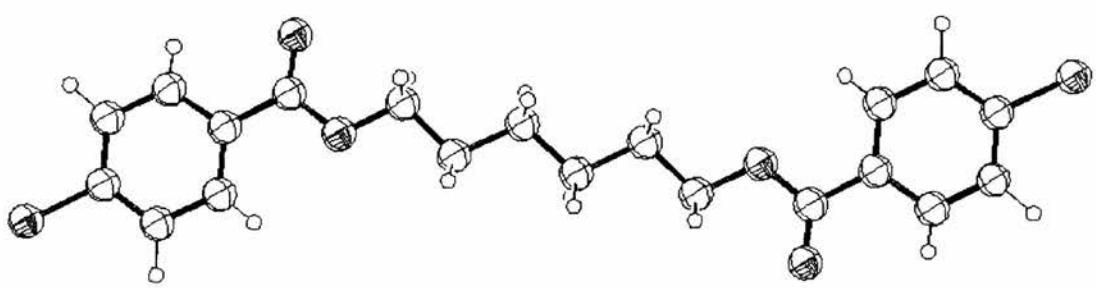

Figure A.11. A view of hexane-1,6-diyl bis(*p*-chlorobenzoate).[110]

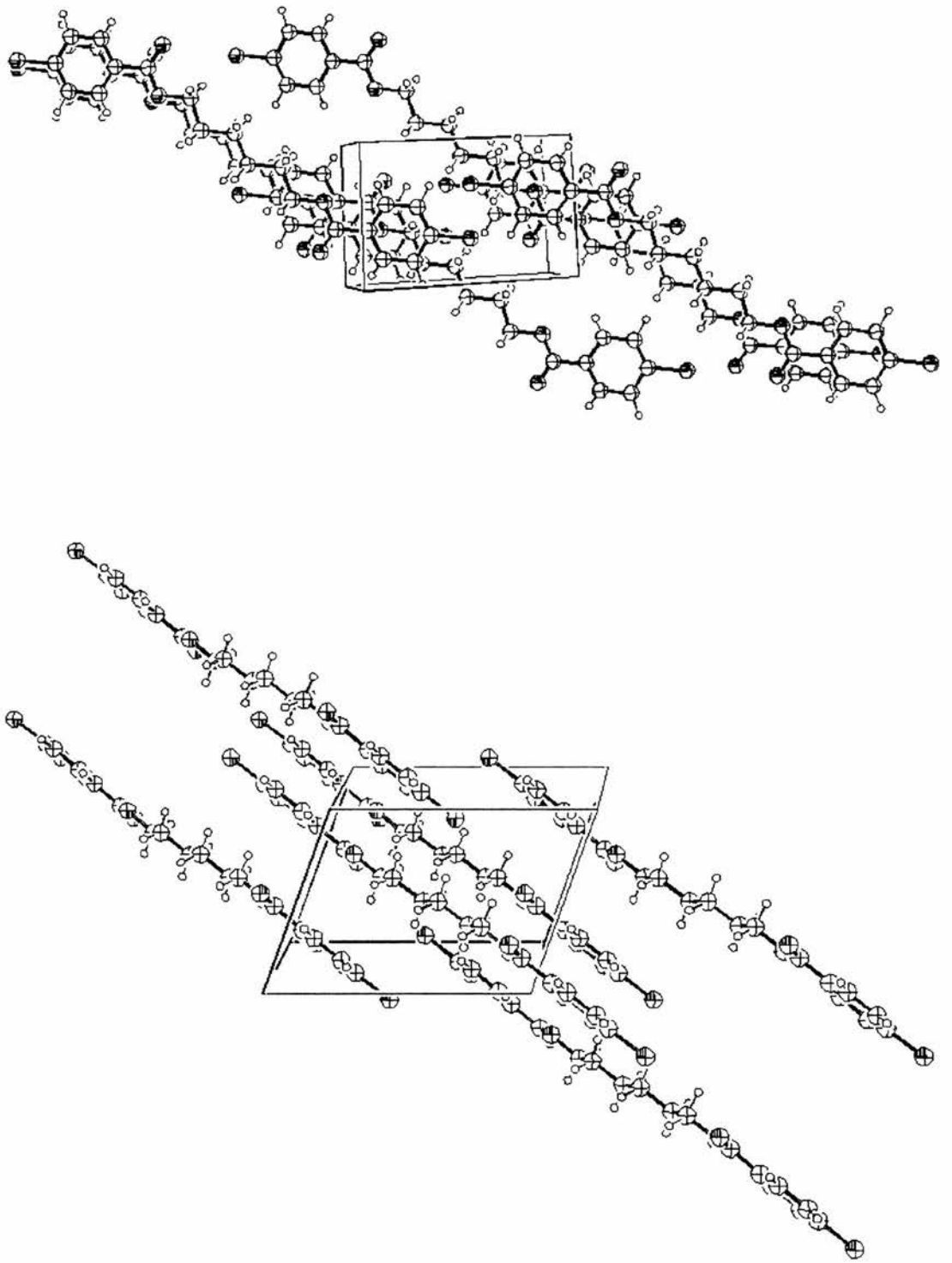

Figure A.11. (continued) The unit cell of hexane-1,6-diyl bis(*p*-chlorobenzoate) viewed from two different angles.[110] The asymmetric unit is equal to half of the molecule. The unit cell is triclinic with dimensions: a = 10.483, b = 7.760, c = 6.746 Å, α = 107.77, β = 98.32 and γ = 70.43°. The space group is P-1.

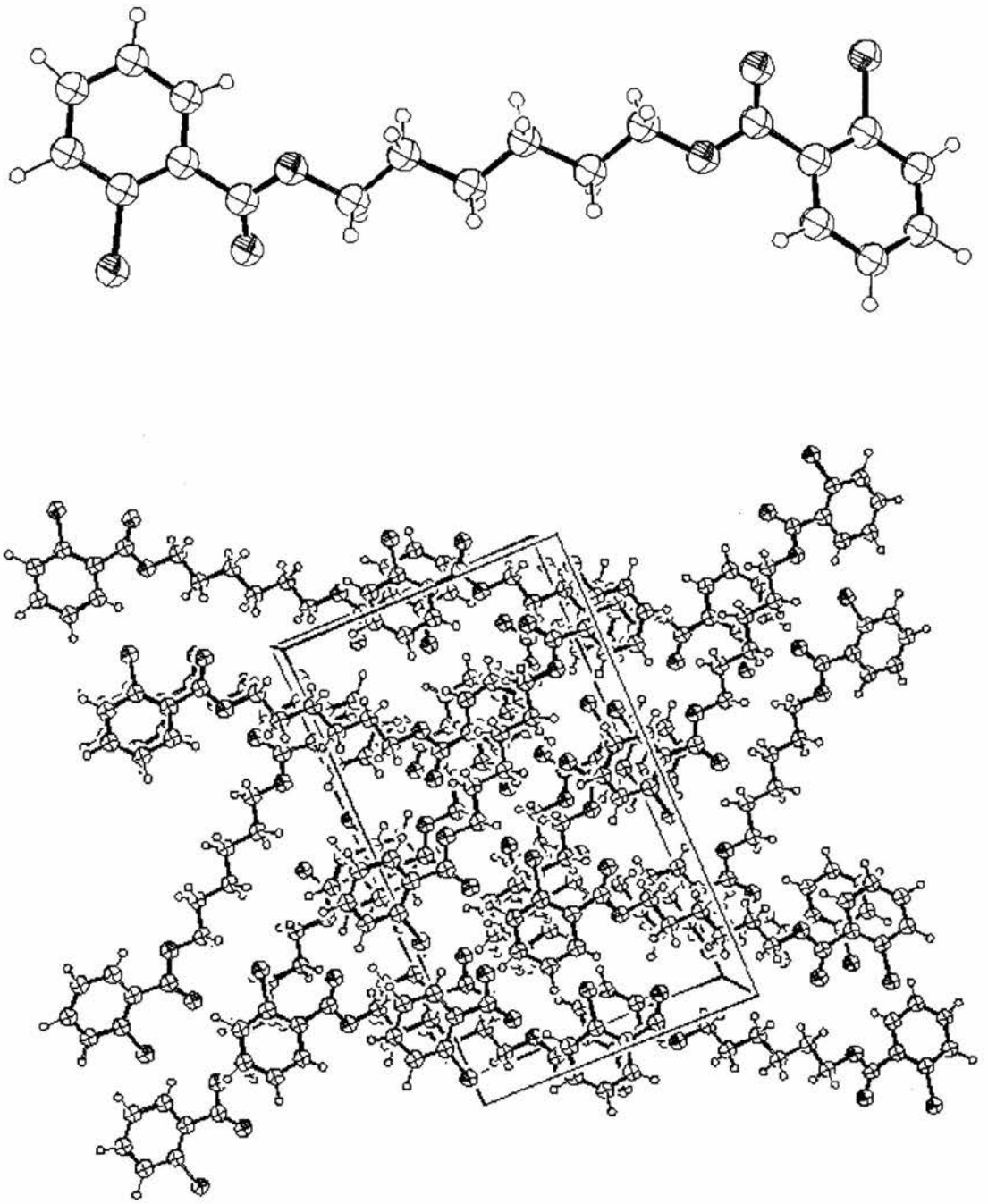

Figure A.12. A view of hexane-1,6-diyl bis(*o*-chlorobenzoate) (top) together with a plot of the unit cell (bottom).[109] The asymmetric unit is equal to the whole molecule. The unit cell is monoclinic with dimensions: a = 8.145, b = 20.359, c = 12.000 Å and β = 103.99°. The space group is $P21/c$.

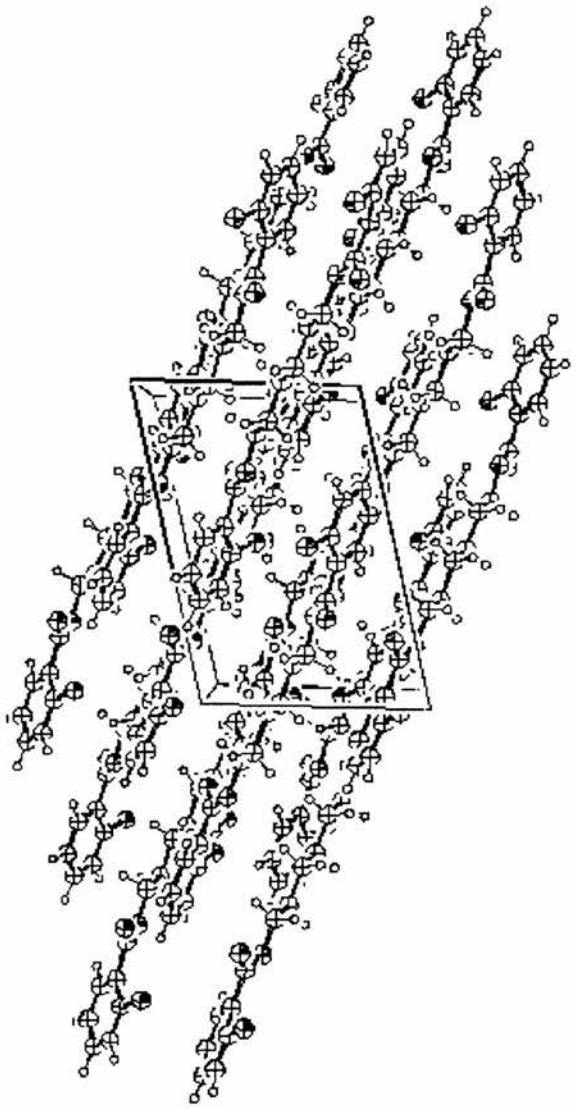

Figure A.12. (continued) The unit cell of hexane-1,6-diyl bis(*o*-chlorobenzoate) viewed from different angle.[109] The asymmetric unit is equal to the whole molecule. The unit cell is monoclinic with dimensions: a = 8.145, b = 20.359, c = 12.000 Å and β = 103.99°. The space group is $P21/c$.

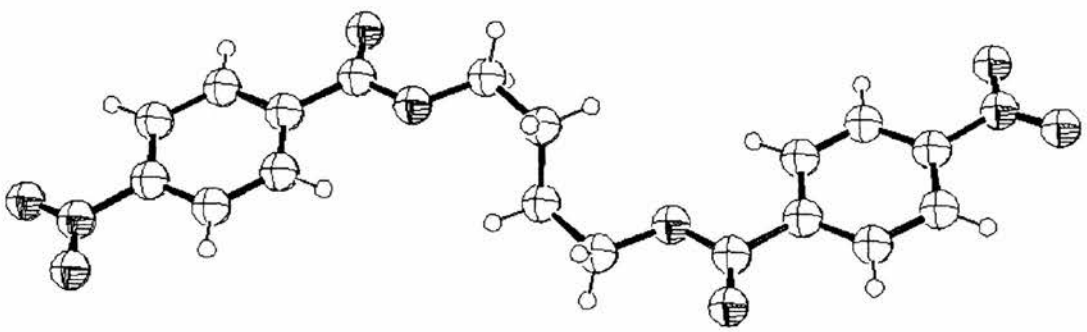

Figure A.13. A view of butane-1,4-diyl bis(*p*-nitrobenzoate).[112]

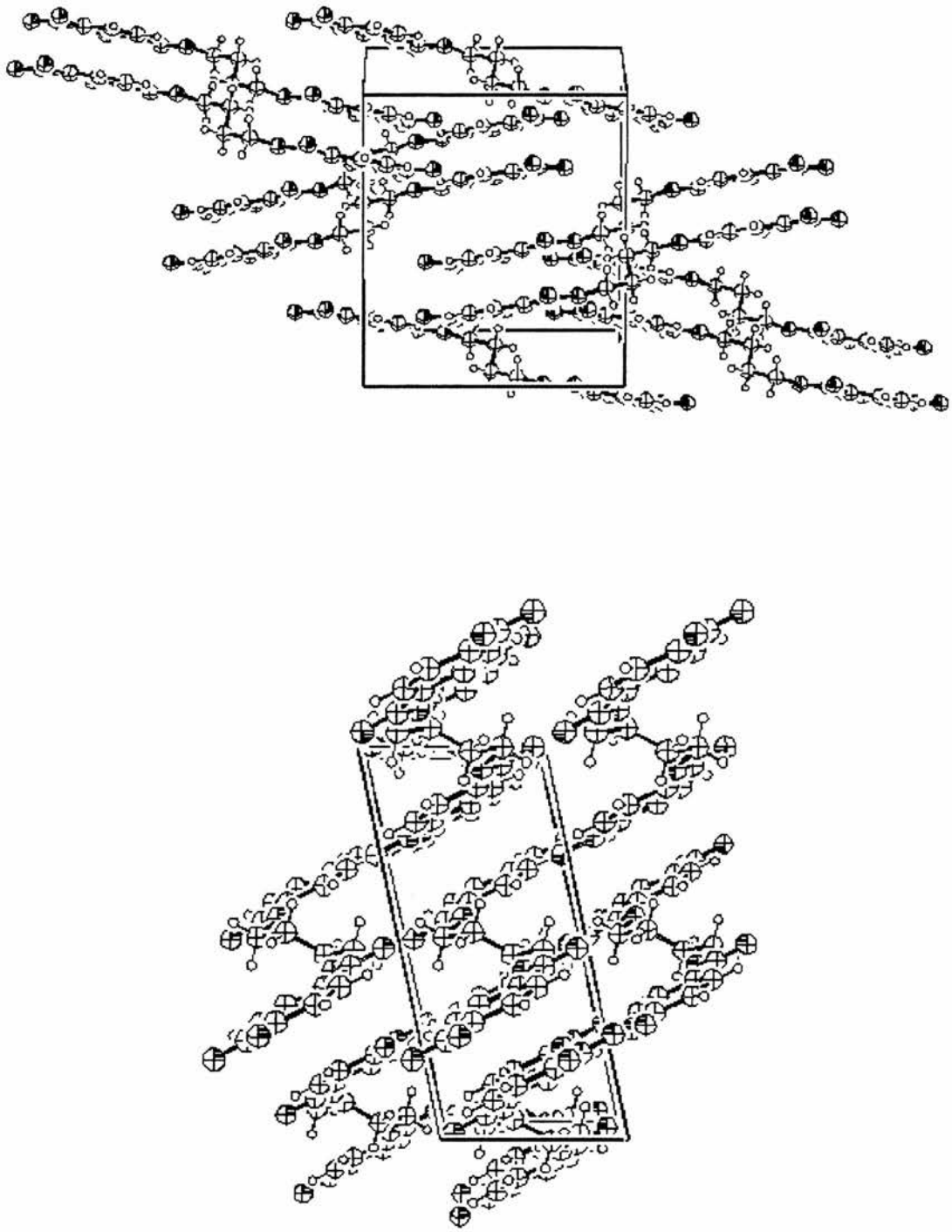

Figure A.13. (continued) The unit cell of butane-1,4-diyl bis(*p*-nitrobenzoate) viewed from two different angles.[112] The asymmetric unit is equal to half of the molecule. The unit cell is monoclinic with dimensions: a = 6.086, b = 11.475, c = 13.162 Å and β = 101.93°. The space group is $P2_1/c$.

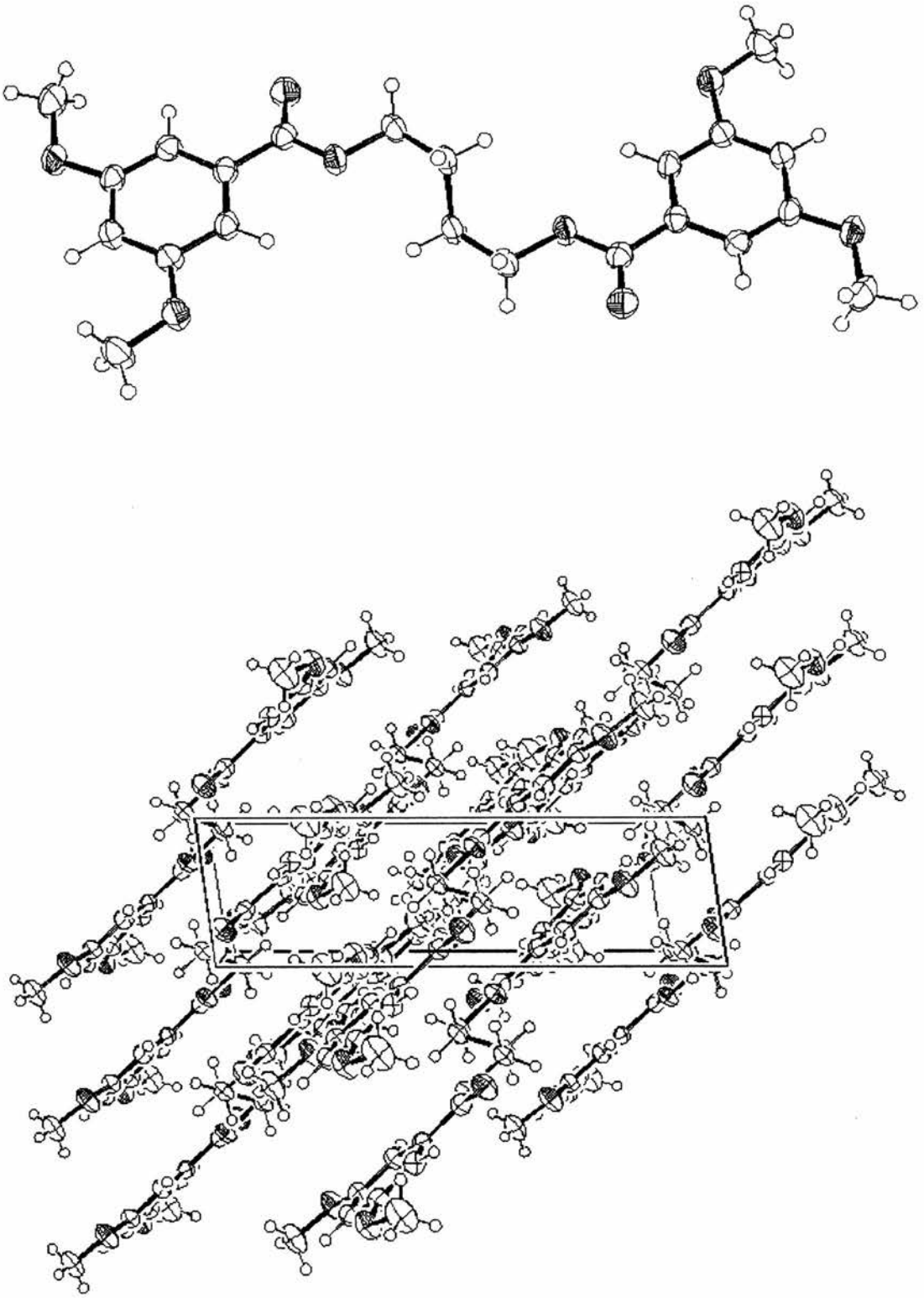

Figure A.14. A view of butane-1,4-diyl bis(3,5-dimethoxybenzoate) together with a view of the unit cell. The asymmetric unit is equal to half of the molecule. The unit cell is monoclinic with dimensions: a = 14.353, b = 17.013, c = 4.291 Å and β = 98.10°. The space group is $P2_1/n$.

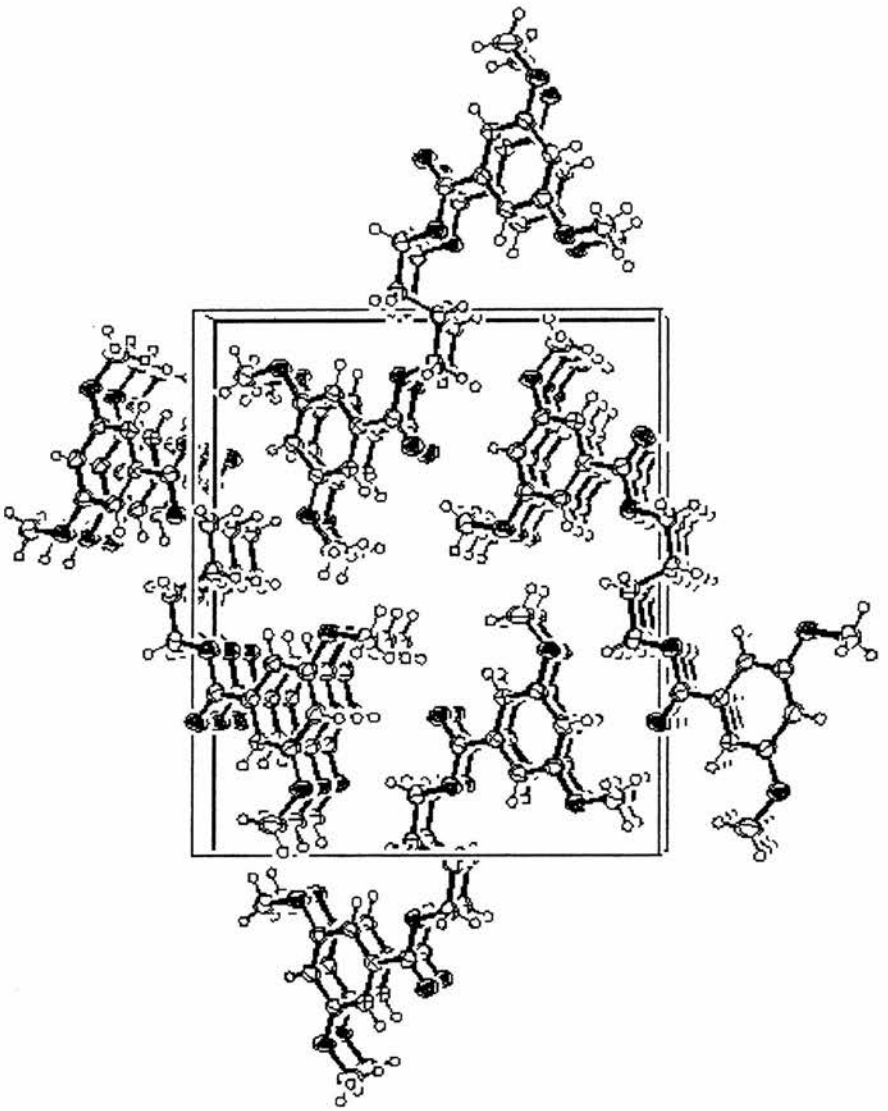

Figure A.14. (continued) The unit cell of butane-1,4-diyl bis(3,5-dimethoxy-benzoate) viewed from a different angle. The asymmetric unit is equal to half of the molecule. The unit cell is monoclinic with dimensions: a = 14.353, b = 17.013, c = 4.291 Å and β = 98.10°. The space group is $P2_1/n$.

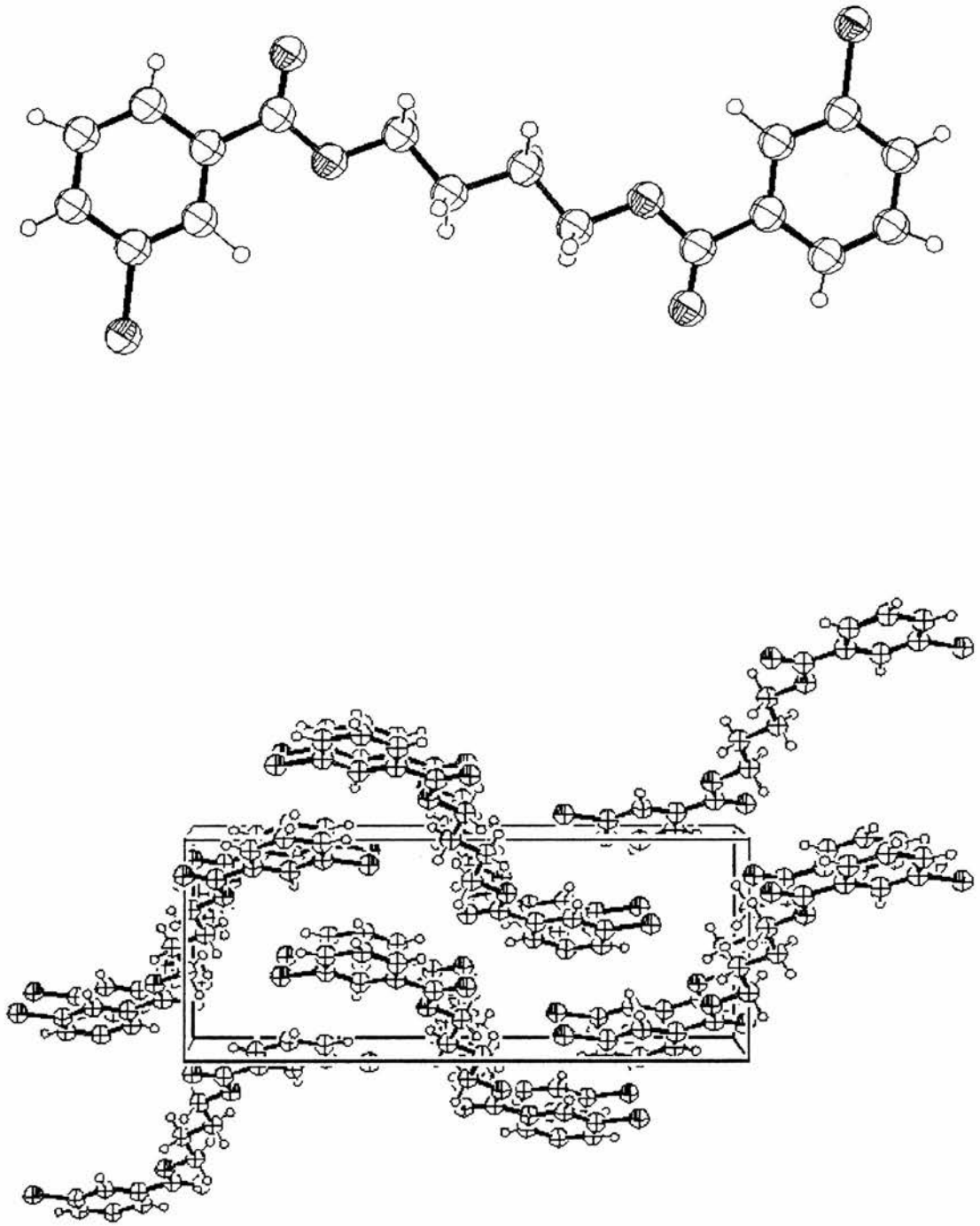

Figure A.15. A view of butane-1,4-diyl bis(*m*-chlorobenzoate) together with a view of the unit cell.[114] The asymmetric unit is equal to half of the molecule. The unit cell is monoclinic with dimensions: a = 5.870, b = 19.270, c = 7.651 Å and β = 97.29°. The space group is $P2_1/c$.

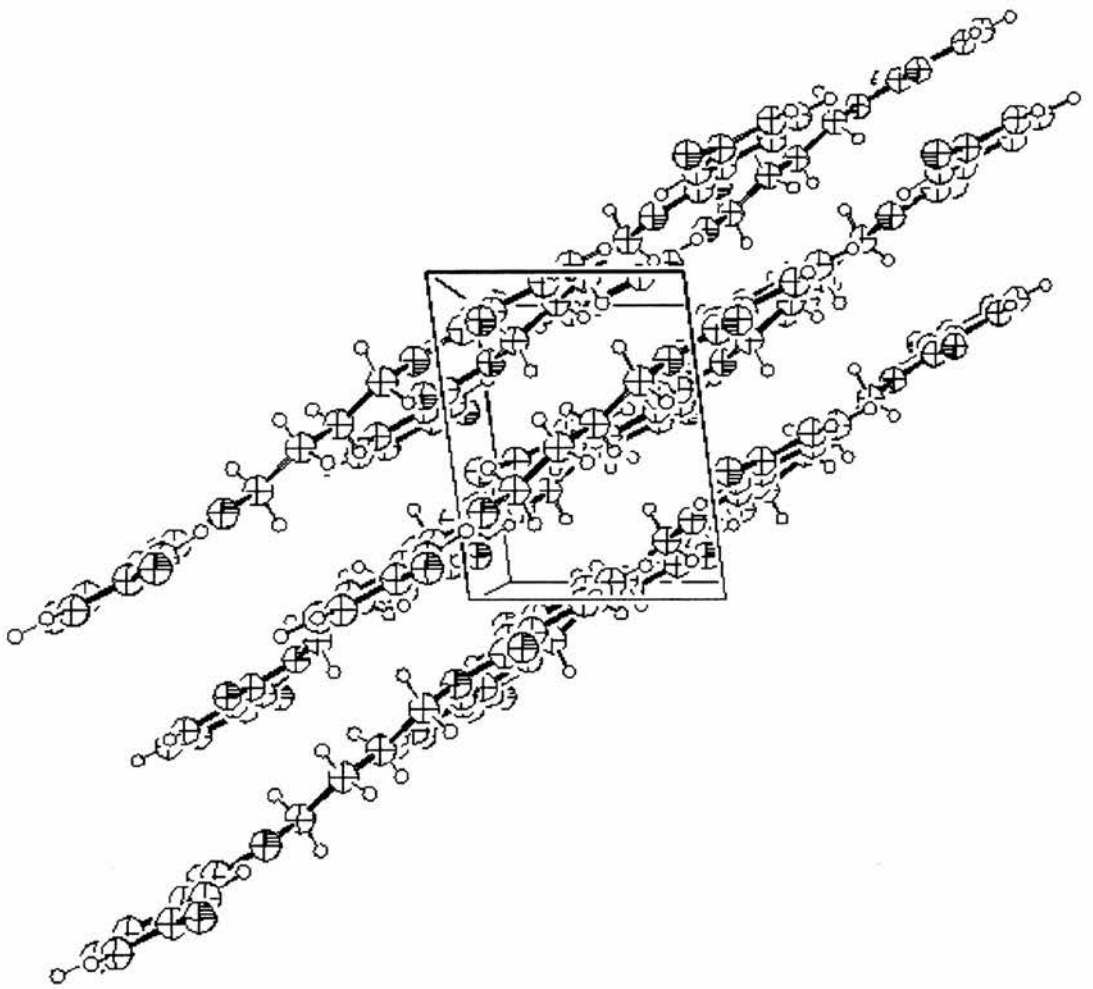

Figure A.15. (continued) The unit cell of butane-1,4-diyl bis(*m*-chlorobenzoate) viewed from a different angle.[114] The asymmetric unit is equal to half of the molecule. The unit cell is monoclinic with dimensions: a = 5.870, b = 19.270, c = 7.651 Å and β = 97.29°. The space group is $P2_1/c$.

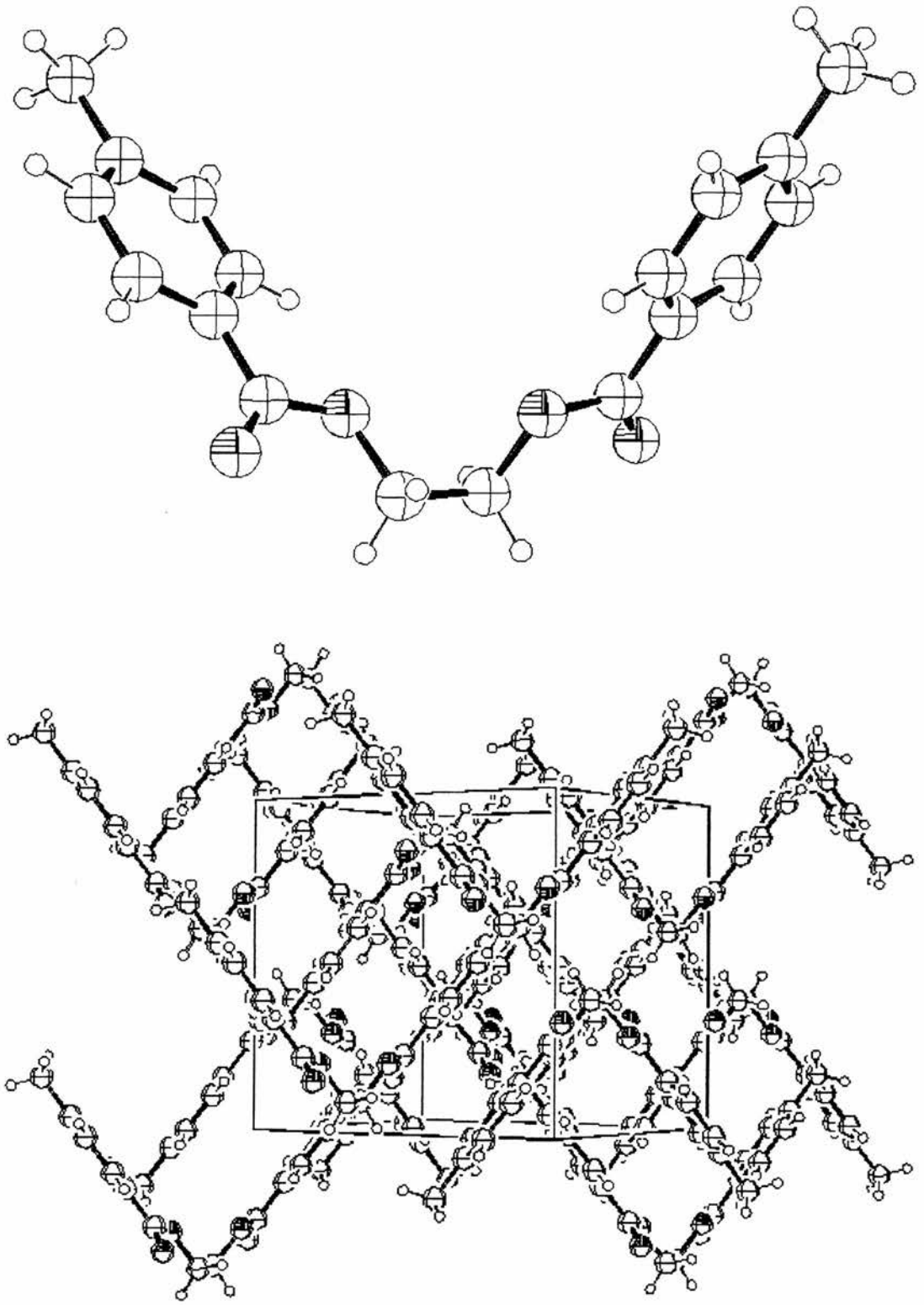

Figure A.16. A view of ethane-1,2-diyl bis(*p*-methylbenzoate) together with a view of the unit cell.[116] The asymmetric unit is equal to half of the molecule. The unit cell is monoclinic with dimensions: a = 12.203, b = 10.644, c = 12.288 Å and β = 75.80°. The space group is *C*2/*c*.

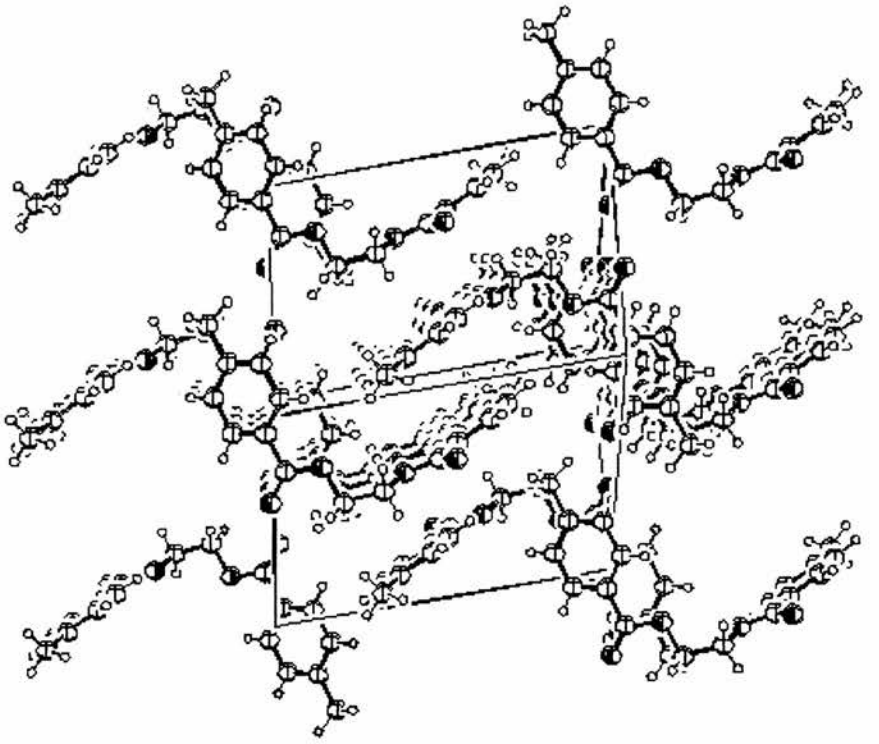

Figure A.16. (continued) The unit cell of ethane-1,2-diyl bis(*p*-methylbenzoate) viewed from a different angle.[116] The asymmetric unit is equal to half of the molecule. The unit cell is monoclinic with dimensions: a = 12.203, b = 10.644, c = 12.288 Å and β = 75.80°. The space group is *C*2/*c*.

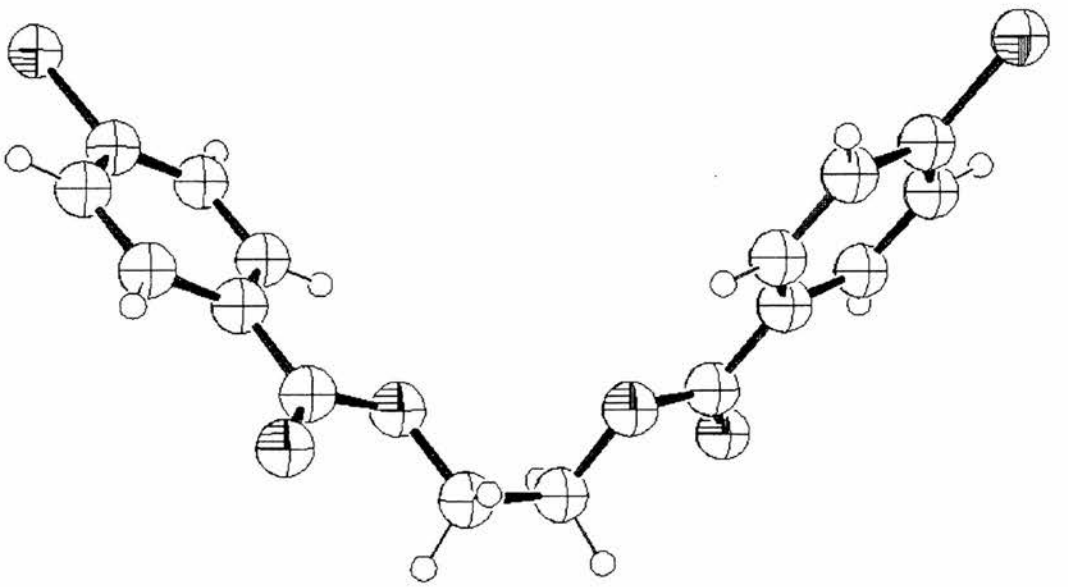

Figure A.17. A view of ethane-1,2-diyl bis(*p*-chlorobenzoate).[117]

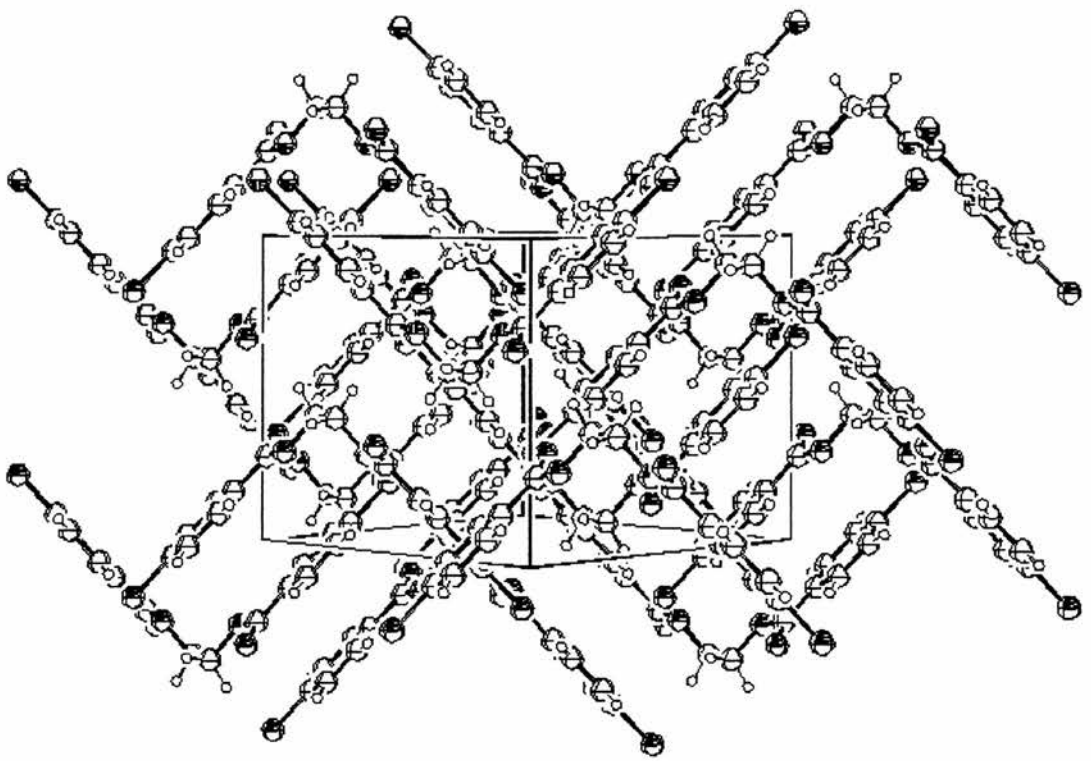

Figure A.17. (continued) The unit cell of ethane-1,2-diyl bis(*p*-chlorobenzoate).[117] The asymmetric unit is equal to half of the molecule. The unit cell is monoclinic with dimensions: a = 12.733, b = 9.522, c = 12.762 Å and β = 79.63°. The space group is *C*2/*c*.

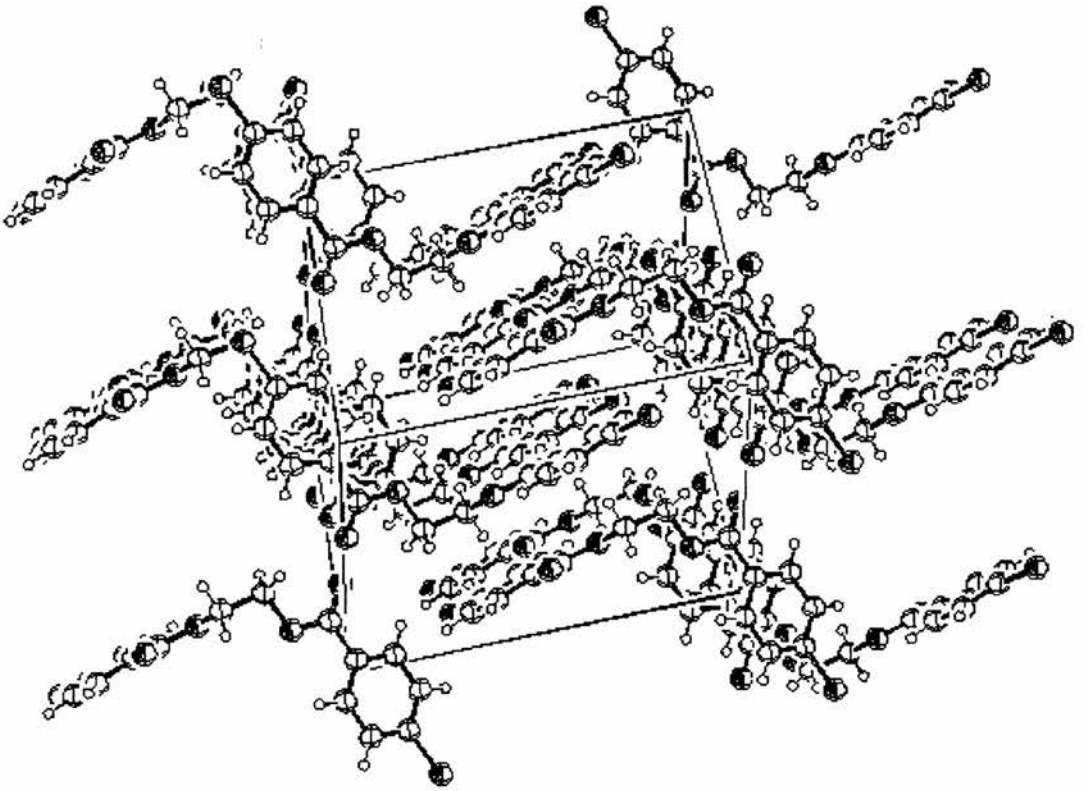

Figure A.17. (continued) The unit cell of ethane-1,2-diyl bis(*p*-chlorobenzoate) viewed from a different angle.[117] The asymmetric unit is equal to half of the molecule. The unit cell is monoclinic with dimensions: a = 12.733, b = 9.522, c = 12.762 Å and β = 79.63°. The space group is *C*2/*c*.

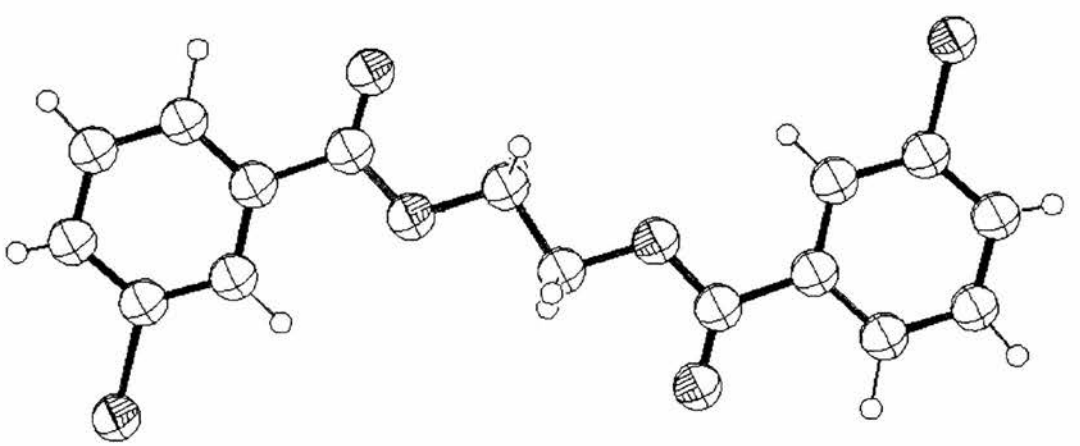

Figure A.18. A view of ethane-1,2-diyl bis(*m*-chlorobenzoate).[118]

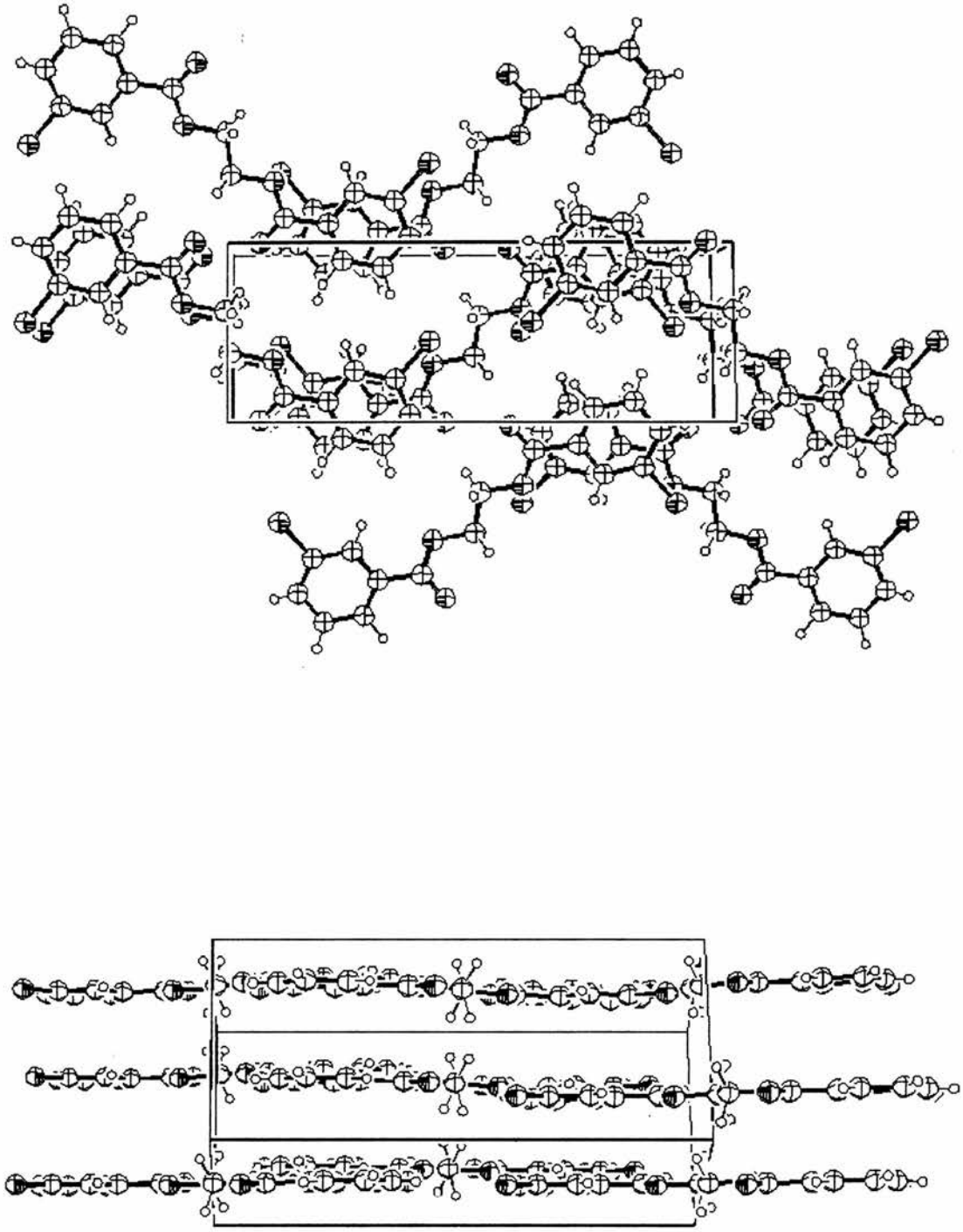

Figure A.18. (continued) The unit cell of ethane-1,2-diyl bis(*m*-chlorobenzoate) viewed from two different angles.[118] The asymmetric unit is equal to half of the molecule. The unit cell is monoclinic with dimensions: a = 6.136, b = 16.724, c = 7.351 Å and β = 81.40°. The space group is $P2_1/c$.